UNIVERSITY OF SUSSEX

Novel 3D printed biocompatible capsule with integrated macroscale triggerable anti-cancer drug delivery systems

by

Kejing Shi

Submitted for the degree of Doctor of Philosophy

University of Sussex

June 2021

I hereby declare that this thesis has not been and will not be, submitted in whole or in part to another University for the award of any other degree.

Kejing Shi

June 2021

Acknowledgements

I would like to thank my supervisor Professor Ali Nokhodchi for his supervision and guidance over the course of my PhD project. Without his guidance, this research would not have been possible, his theoretical and technical help was important for me. Dr Mohammed Maniruzzaman and Dr Taravat Ghafourian also provide many valuable suggestions for this project, and I would like to express my gratitude for their support and encouragement. I am grateful to the China Scholarship Council (CSC) / University of Sussex Joint Scholarships for funding this research project.

Special thanks my thesis committee members: Dr Qiao Chen and Dr Alfredo Vargas for their guidance and help. I would also like to thank Dr Lisa Woodbine, Dr Rodrigo Aviles-Espinosa, Dr Elizabeth Rendon-Morales and Dr Jonathan P. Salvage for their collaborative efforts.

Thanks are also given to members of Pharmaceutics Research Laboratory, it has been a pleasure working with you all.

Finally, I would like to give special thanks to my family, specifically my parents and grandparents who always give me their endless support. I am truly grateful for everything they did for me. I would especially like to thank my boyfriend Huai for his comprehension and patience getting me through this journey.

Abstract

In this project, the main objective is to develop a portable and integrated device that is suitable for the macro length scales relevant to human applications under externally applied magnetic fields. A novel release mechanism for the drug delivery system was investigated and optimized, which was aiming to realize remote and accurate control of the location, time, duration and amount of released drug. This study was separated into four tasks:

(1) Preparation and optimization of magnetic sponges:

Iron oxide nanoparticles, including magnetite (Fe_3O_4) and carbonyl iron, were embedded as magnetosensitive materials in polydimethylsiloxane (PDMS) resins for the fabrication of macroporous sponges via a sugar-template process. These magnetic sponges prepared with various sugar mold, magnetic particles content, weight ratios of PDMS prepolymer and curing agents display different porosity and magnetic field sensitivity.

(2) Development of anticancer drug solution:

A drop-on-powder 3D printer was applied to produce tablets with varying diameters. Pure 5-fluorouracil (FLU) solution of 2.5% (w/v) concentration and polymeric solutions containing either Soluplus alone or in combination with polyethylene glycol at drug: polymer(s) 1:1 (w/w) ratio was used to develop the coating solution on 3D printed tablets. According to the *in vitro* dissolution profiles, pure FLU solution was selected.

(3) Design and characterization of a novel 3D printed drug delivery system:

A novel magnetically triggerable drug delivery device composed of the optimized magnetic PDMS sponge cylinder and a 3D printed polylactic acid (PLA) reservoir was designed, fabricated and characterized. The switching “on” state of drug-releasing could be realized by the magnetic bar contacted with the side part of the device as the times needed to release 50%, 80% and 90% of 5-fluorouracil were observed to be 20, 55 and 140 min, respectively. In contrast, the switching “off” state of drug-releasing could be realized by the magnetic bar placed at the

bottom of the device where only 10% of 5-fluorouracil could be released within 12 h.

(4) Development of anti-inflammatory drug loaded filaments for fused deposition modelling (FDM) 3D printed reservoir:

Various release modifying excipients were used as a release modulating tool to control the drug release from 3D printed sustained release tablets. All ibuprofen (the model drug) loaded 3D printed tablets with ethyl cellulose (the polymeric matrix) matrix, especially with polyethylene glycol (PEG) as the release modifier, showed great potential in releasing ibuprofen in a zero-order reaction.

Abbreviations

3DP	three-dimensional printing
.stl	stereolithography
∇B	magnetic field gradient
β-CD	β-cyclodextrin
ε	relative permittivity or strain
θ	contact angle
γ	surface tension
γ-Fe_2O_3	maghemite
μ	magnetic permeability
ρ	density
σ	stress
σ_{UTS}	ultimate tensile strength
σ_y	yield strength
χ	magnetic susceptibility
A	absorbance
ABS	acrylonitrile butadiene styrene
AIC	Akaike Information Criteria
AMF	alternating current magnetic field
API	active pharmaceutical ingredient
B	magnetic field strength in Tesla
BCS	biopharmaceutics classification system
BFM	bright-field microscopy
C	capacitance or concentration
CAD	computer-assisted design
CI	carbonyl iron
CMC	critical micelle concentration
CNT	carbon nanotube
d	thickness

D	diameter
DBS	dibutyl sebacate
DDS	drug delivery system
DIP	N,N-diisopropyl tertiary amine group
DMEM	Dulbecco's modified Eagle's medium
DoP	drop-on-powder
DSC	differential scanning calorimetry
E	elasticity
EC	ethyl cellulose
EDS	energy-dispersive X-ray spectroscopy
EMA	European Medicines Agency
EPR	enhanced permeation and retention
E_r	radial expansion coefficient
EVA	ethylene vinyl acetate
f_2	similarity factor
Fc	ferrocene groups
FCS	foetal calf serum
FDA	the United States Food and Drug Administration
FDM	fused deposition modelling
Fe_3O_4	magnetite
FFF	fused filament fabrication
FLU	5-fluorouracil
F_{mag}	magnetic force
GC	glycol chitosan
GFP	green fluorescent protein
GI	gastrointestinal
h	height
H_c	coercivity or strain hardening capacity
HME	hot melt extrusion
HPC	hydroxypropyl cellulose

HPMC	hydroxypropyl methylcellulose
HPMCAS	hypromellose acetate succinate
IBP	ibuprofen
L	length
LCST	lower critical solution temperature
LD_{50}	median lethal dose
m	weight
MFH	magnetic fluid hyperthermia
MNP	magnetic nanoparticle
M_r	remnant magnetization
MRI	magnetic resonance imaging
M_{sat}	saturation magnetization
MSN	mesoporous silica nanoparticle
NSAID	non-steroidal anti-inflammatory drugs
N_w	water absorbency
ODT	orally disintegrating tablet
OHA	oxidized hyaluronate
PAAm	polyacrylamide
PB	powder-based
PBS	phosphate-buffered saline
PC	polycarbonate
PCL	polycaprolactone
PEG	polyethylene glycol
PEO	polyethylene oxide
PDMS	polydimethylsiloxane
PGA	poly(L-glutamic acid)
PLA	polylactic acid
PLLA	poly-L-lactic acid
PLGA	poly(lactic-co-glycolic acid)
P_m	particle size

PM	physical mixtures
PNIPAM	poly(N-isopropyl acrylamide)
pPTX	polymerized paclitaxel conjugate
PVA	poly(vinyl alcohol)
PVAc	polyvinyl acetate
PVC	polyvinyl caprolactam
PVP	polyvinyl pyrrolidone
r	radius
R^2_{adj}	adjusted coefficient of determination
RGD	arginine-glycine-aspartic acid
SEM	scanning electron microscopy
SLA	stereolithography
SLS	selective laser sintering
SOL	soluplus
SPION	superparamagnetic iron oxide nanoparticle
T_d	degradation temperature
TDDS	triggerable drug delivery system
TEC	triethyl citrate
T_g	glass transition temperature
TGA	thermogravimetric analysis
T_m	melting temperature
T_p	printing temperature
USP	United States Pharmacopeia
V	volume
VA	vinyl acetate
VDM	volume mean diameter
WCE	wireless capsule endoscope
XRD	X-ray diffraction

Index of Figures

Index of Tables

Table of Contents

(1) Shi, K.; Tan, D.; Nokhodchi, A.; Maniruzzaman, M. Drop-On-Powder 3D Printing of Tablets with an Anti-Cancer Drug, 5-Fluorouracil. *Pharmaceutics* **2019**, *11* (4), 150. https://doi.org/10.3390/pharmaceutics11040150.
(2) Shi, K.; Aviles-espinosa, R.; Rendon-morales, E.; Woodbine, L.; Maniruzzaman, M.; Nokhodchi, A. Novel 3D Printed Device with Integrated Macroscale Magnetic Field Triggerable Anti-Cancer Drug Delivery System. *Colloids Surfaces B Biointerfaces* **2020**, *192*, 111068. https://doi.org/10.1016/j.colsurfb.2020.111068.
(3) Shi, K.; Aviles-espinosa, R.; Rendon-morales, E.; Woodbine, L.; Salvage, J. P.; Maniruzzaman, M.; Nokhodchi, A. Magnetic Field Triggerable Macroporous PDMS Sponge Loaded with an Anticancer Drug , 5 - Fluorouracil. *ACS Biomater. Sci. Eng.* **2021**, *7*, 180–195. https://doi.org/10.1021/acsbiomaterials.0c01608.
(4) Shi, K.; Salvage, J. P.; Maniruzzaman, M.; Nokhodchi, A. Role of Release Modifiers to Modulate Drug Release from Fused Deposition Modelling (FDM) 3D Printed Tablets. Int. J. Pharm. 2021, 597, 120315. https://doi.org/10.1016/j.ijpharm.2021.120315.

1. Chapter 1: Introduction

1.1 An Overview of Remotely Triggerable Drug Delivery Systems

The major challenge of disease therapy is delivering therapeutic agents to the target location.[1] Traditional drug delivery approaches are limited by poor effectiveness, biodistribution and targeting ability.[1] With the development of drug discovery, much attention has been paid to the methods by which these active substances were administered.[2] Although conventional sustained release systems can improve patient compliance by reducing the frequency of drug administration, the maximum release duration is only 1 day and high fluctuation in drug concentration is inevitable from patient to patient.[3] Considering these limitations, drug delivery systems (DDSs) which can achieve repeatable, long-term, remote and precise drug release are of great importance in various medical applications for maintaining an ideal therapeutic plasma level between the minimum effective concentration and the maximum safe concentration (Figure 1.1).[4,5] Commercially available controlled release DDSs are superior to traditional drug dosage forms. For example, they can (1) provide more precise control over the location, timing and dosage of drug administration *in vivo* with fewer side effects, (2) maintain the drug concentration within the therapeutic window for a predetermined duration, (3) deliver drugs to a particular site, (4) minimize the frequency of administration, (5) protect medications from rapid clearance or degradation, (6) improve patient comfort and compliance.[3,6] However, the drug release rates in most controlled release DDSs have been predetermined by mechanisms such as degradation of polymers, diffusion, osmotic pressure, and microchannel design, so their release rates cannot be modified after administration of the devices.[5] Therefore, triggerable on-demand DDSs become necessary when the need and physiological circumstances of patients are variable, such as cancer chemotherapy, administration of insulin for diabetes patients, antiarrhythmics for heart rhythm disorders therapy and so on.[7]

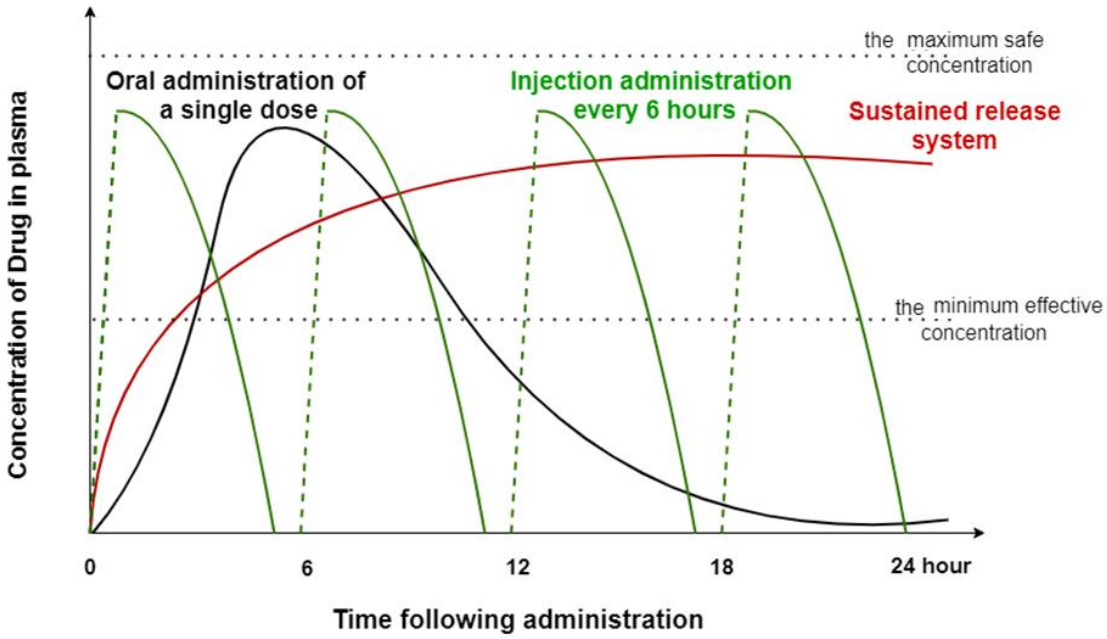

Figure 1.1. Blood plasma concentration-time curves following the oral administration of a single dose of a drug in a conventional tablet, the administration of a single dose of a sustained release system and the injection administration every 6 hours for 24 hours.

Triggerable DDSs can be classified as internally (self-regulated or closed-loop systems, which respond to a feedback mechanism happening inside the body: like pH, blood glucose level, and urea concentration) and externally (pulsed regulated or open-loop systems, which rely on externally applied stimuli, such as temperature, magnetic fields, ultrasound and light) controlled systems.[3,6] As a result, the development of externally applied stimuli triggerable drug delivery systems controlled either by an interaction between a sensor and environmental changes or by an operator (like using a remote device to control the implanted or injected drug delivery system) have attracted increasing interest, under the condition when the circadian dependence and patients' tolerance to the drug on a continuous level must be taken into consideration.[3] Patients, physicians or algorithms can decide to release the drug payload in response to the change of physiological factors and/or specific conditions or substances *in vivo*. Such drug delivery systems which contain a large enough amount of drug could be applied to determine the timing, duration, dosage, location and even achieve a remote,

noninvasive, repeatable and reliable switching of therapeutic compound flux.[7,8]

A typical triggerable DDS is mainly composed of a pump, a valve, a reservoir, and an actuation mechanism for adjusting the drug release rate.[5] The initial mode of the valve in triggerable DDSs (normally opened or normally closed) is vitally important for determining energy consumption.[5] Triggerable DDSs are required to show high drug loading capacity, the near-zero drug release volume in the switching off state, repeatable and switchable to the switch-on state, the adjustable dosage according to patients' conditions.[4] However, these DDSs exhibit many problems in translating from laboratory to clinic, such as low triggerability *in vivo*, low reproducibility after multiple cycles, weak sensitivity to stimuli and difficulties in modulating drug dosage for patients in real-time.[4,9] For fabricating external stimuli triggerable DDSs, the development of intelligent materials which are environmentally sensitive and capable of loading therapeutic agents, is of great importance.[10,11] These materials are required to exhibit a physical or chemical response to external stimuli, transform external signals into sensed information, and evaluate sensed information.[10] Polymeric assembly of intelligent materials shows advantages in drug loading and targeting drug delivery.[10] The fundamental principle of these external stimuli triggerable polymer-based DDSs is the fact that the stimulus can adjust structural composition or conformation for the DDSs.[12]

There is a wide range of sizes and shapes for DDSs. The nanoscale devices have advantages in systematic distribution (especially intravenous distribution) and enhanced permeation and retention (EPR), whereas macroscopic devices can load with a larger amount of drug and are easier to remain where they were placed. Consequently, repeatable triggering of macroscale DDSs can realize the delivery of multiple doses through a single administration or implantation.[7] Although the fundamental physics related to the devices of both microscale and macroscale are the same, the relative importance of physical effects is different.

Thus, researches should analyze and simulate every special device design rather than relying on their intuition from previous studies.[13] Brudno and Mooney pointed out that macroscale DDSs are commonly taking the form of a polymer or device implanted at a particular site.[14]

Similarly, triggerable DDSs can also be categorized by the frequency of the devices that can be triggered. The devices which are intended to be triggered only once are generally nanoparticulate. The nanocomposites can be injected at a particular location (like a depot system) or systematically (can be triggered at the desired locale to realize precise localization). Repeatable triggering devices tend to be larger in size and have more technical challenges. The major challenge is achieving highly reproducible drug dosing as the devices can be destroyed easily or deformed irreversibly by the triggering method. In addition, massive drug release may happen in larger devices because of the failure or breakage of devices. Meanwhile, a surgical procedure for implantation is inevitable for larger size devices and it may cause inflammation. In order to manage post-operative pain, non-steroidal anti-inflammatory drugs (NSAIDs) are commonly applied in implants.[15] Furthermore, it is vitally important to consider their biodegradability, biocompatibility, drug-related toxicity and whether they can be reloaded without reimplantation.[7]

Some physical stimuli can penetrate through human tissue, so these physical stimuli triggerable DDSs can release drugs even the devices are placed deeply within patients.[14] The specific design of these devices can be triggered by externally applied physical stimulations, such as magnetic fields, ultrasound, temperature, electricity and light. However, it is noteworthy that these stimulations show some limitations in their translation to the clinic, such as the relatively weak penetration ability of ultraviolet and infrared light in living tissues, and the infeasible application of electric fields in deep tissues of the body.[3]

1.2 Magnetic Field Triggerable Drug Delivery Systems

Although several external stimuli have been applied in triggerable DDSs, magnetic actuation is regarded as an attractive option, mainly because of the low toxicity of iron oxide particles, instantaneous and reversible response, remote actuation, strong penetration ability through human tissues, high controllability, the ability to produce significant force and displacements.[3,10] Therefore, magnetic actuation is especially attractive for biomedical applications where a noncontact feature is particularly necessary for *in vivo* environment with absolute safety.[16–18] The aims of magnetic field triggerable DDSs are the transportation of therapeutic agents with the blood flow and the release of the desired dosage within a targeted region under applied magnetic fields.[19,20] In the development of triggerable DDSs, magnetic actuation is unique because on-chip power sources are not required.[18] Additionally, many researches on magnetic devices in recent 50 years confirmed that this kind of DDSs could be remotely triggered deep inside biological tissues in various minimally invasive procedures, like tetherless robotic interventions and wireless capsule endoscopy.[21,22] For patients who require injection administered frequently, these magnetic field triggerable DDSs can provide a promising alternative to provide multiple cycles of small drug molecules and biomacromolecules in long term.[3] In recent years, magnetic fields are of great importance in optimizing the structure and improving the performance of materials.[23]

Fundamental researches on the design of magnetic DDSs, mechanism studies and preclinical research are key points to achieve wide clinical applications of magnetic DDSs.[24] Consequently, many factors should be considered when designing efficient magnetic DDSs, including safety, magnetic properties, magnetic particle size, magnetic field strength, drug loading capability, pharmacokinetic properties, the accessibility and depth of the target tissues and the blood flow rate.[1,25,26]

1.2.1 Magnet Systems

The design of the external magnets and the manipulation of magnetic nanoparticles (MNPs) are considered as the two major components in the development of magnetic field triggerable DDSs.[27] One of the main challenges for developing magnetic field triggerable DDSs is designing a suitable magnet system in order to generate a sufficient magnetic force for MNPs.[28] The simplest magnet for magnetic drug targeting is a single permanent magnet due to its ability to maintain a magnetic field without a power supply.[24,28] A large number of studies have focused on applying simple permanent magnets due to the advantages of inexpensiveness, versatility and do not require additional cooling or complex control algorithms.[18,25,29,30] Importantly, the single permanent magnet is required to be user friendly (small and light), to produce the desired magnetic field and the magnetic field gradient.[28] The main limitation of using external magnets is that the generated magnetic field strength and gradient usually drop exponentially with the distance from the skin surface.[31,32]

As external electromagnets and permanent magnets were commonly applied, the clinical studies of triggerable DDSs were limited to a poor penetration depth of 5 mm.[20,25] Nowadays, it has been demonstrated that the effective targeting depth can be improved significantly by using different magnet designs, for example, the pyramid magnet can be designed for producing a strong magnetically active space.[25] The design of a suitable magnet configuration can provide DDSs with sufficient magnet power and avoid the undesired accumulation of MNPs.[26] Recently, a two-magnet configuration has been proved to be able to enhance the accumulation and penetration of MNPs in a more advanced manner.[26] In addition, it has been demonstrated that the manipulation of oppositely polarized external magnets can realize the penetration and accumulation of magnetic nanocarriers into deeper tumors.[33] Various magnetic fields could be generated, like gradient magnetic field, uniform magnetic field and oscillation magnetic field.[34]

1.2.2 Magnetic Nanoparticles (MNPs)

Nanoparticles with three dimensions in the nanoscale (usually from 1 nm to 100 nm), show a similar size range with antibodies, receptors, proteins, nucleic acids and other biological molecules.[1,35] Nanoparticles are suitable for localized treatment, especially for transportation *in vivo* because these particles can pass through narrow blood vessels and penetrate through cell membranes without causing pain or emboli in surrounding tissues.[11,28,32,36,37] Nanoparticles showed a slower elimination rate from the bloodstream by the reticuloendothelial system when compared with larger micron-sized carriers.[25] Additionally, particles with smaller size possess passive targeting ability, longer plasma half-life and a higher tendency to accumulate in tumor tissues because of its enhanced vascularization.[30,38] Furthermore, nanoparticles could be conjugated with ligands to achieve active targeting.[30] Consequently, nanoparticles show great potential in targeting specific locations in the body, decreasing the dose of drugs for achieving effective concentration, minimizing side effects for nontarget locations.[37] These nanoparticles are required to possess suitable features such as nature, size, conjugation method for drugs, surface chemistry and functionalization, biodegradability, hydrophilic property and stimuli-responsive properties.[37]

Due to nanoparticle vectors show enhanced permeability and retention (EPR) effects and drug loading capacity for tumors, nanoparticle-based DDSs have been regarded as a promising candidate for overcoming the limitations of chemotherapeutic drugs in clinical cancer treatment.[39,40] However, the application of conventional nanoparticle-based DDSs is mainly limited by the passive release because of the difficulty in releasing a sufficient amount of drug in the target site.[39] Therefore, the next generation of nanoparticle-based DDSs are focusing on the development of stimuli-responsive properties, especially using magnetic actuation.[39] These smart controlled DDSs play an important role in cancer therapy.[41]

Magnetic nanoparticles (MNPs) have been widely applied in various fields (including bioseparation, cell labelling, hyperthermia, magnetic microdevices, magnetic resonance imaging (MRI) and drug delivery) because of their various physical and chemical properties, such as large surface area, chemical stability, low intraparticle diffusion rate and high loading capacity.[14,42,43] In recent years, MNPs have been applied as drug delivery carriers to facilitate several modes of targeted drug delivery technique (navigation through biological systems and efficient drug delivery) due to their magnetism, good compatibility, ease of fabrication and modification, potential to reduce the risk of systemic distribution of drugs for eliminating side effects (Figure 1.2A).[41,44–46] The response of MNPs could be achieved by the magnetic equilibrium between the magnetic force aligned along the magnetic field and the viscous force which is related to the fluid flow.[47,48] Similar to nanoparticles, smaller MNPs may result in enhanced penetration into tumors and a longer half-life, whereas the applied magnetic force may decrease accordingly.[25,26] As a result, it is necessary to find a balance between the magnetic force and the physiological stability in determining the suitable size of MNPs.[26] Additionally, the introduction of a magnet *in vivo*, can act as a guidance stimulus and a localizer for injected MNPs.[49] Furthermore, MNPs show great potential in the diagnosis and therapy of brain tumors.[45] The chemotherapy drug delivery efficiency of MNPs could be enhanced by direct binding with the agent or by functioning as nanocomposites.[20] For simulation experiments, sample containers and a permanent magnet could be used for evaluating DDSs (Figure 1.2B).[24]

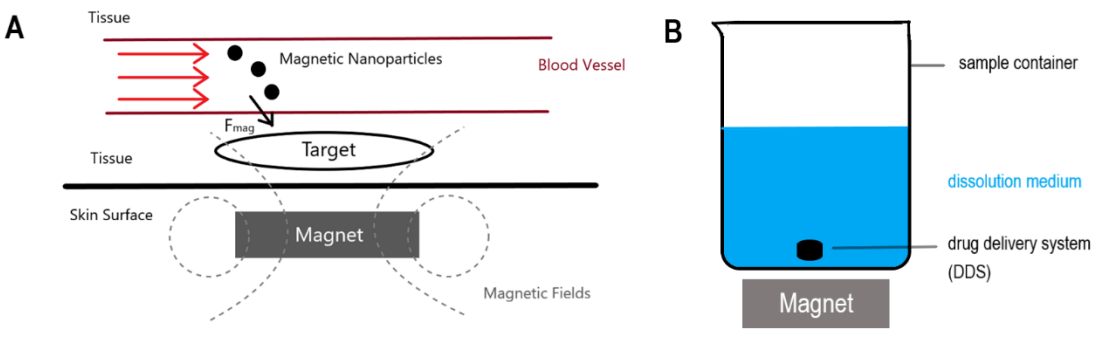

Figure 1.2. Schematic illustration of a magnetic targeting using a single permanent magnet. A. Attach the magnet to the skin near the target site, a magnetic nanoparticle-based drug delivery system can release drugs in response to magnetic fields. (F_{mag}: magnetic force vector). B. Place the magnet under the sample container, so the DDS can be attracted to the site close to the magnet.

The low colloidal stability of MNPs in biological fluids makes them tend to be cleared easily from the bloodstream.[50] Although MNPs showed many shortcomings in clinical applications, like the relatively short half-life, chemical instability, high tendency to agglomerate, low drug loading, and weak targeting specificity, many strategies could be used, including encapsulation, the introduction of navigation systems, surface modification with surfactants, polymeric materials, and thiol functional groups.[51,52] In order to improve the stability and biocompatibility, the addition of polymers as the stabilizer can achieve a highly stable dispersion of MNPs for biomedical applications.[37,50] The drug/MNP complex (MNPs attached to the drug molecules) could be injected intravenously or intraarterially to the target location. In physiological conditions, drugs will be released from the magnetic carriers.[44] Furthermore, their biocompatibility and long-term stability make this kind of material suitable for biomedical applications.[43] For example, PEGylation can protect MNPs from clearance from the circulation and facilitate their accumulation at the target site because of the stability, biocompatibility and hydrophilicity of poly-ethylene glycol (PEG).[53] To design an MNP-based targeting drug delivery system, more emphasis should be placed on physical parameters (including magnetic field strength, field geometry, magnetic properties, particle size of carriers and drug loading capacity) and physiological parameters (blood volume, blood flow rate, cardiac output, distance from the skin surface to the target and body weight).[37,44,54]

The drug/MNP complex can be attracted to an external magnetic field by a magnetic force (F_{mag}) because of the presence of a magnetic field gradient.[24,55]

According to the Eq. 1, the magnetic force was determined by the magnetic field strength in Tesla (B), the field gradient (∇B), the volume the MNPs (V), the magnetic permeability of free space (μ_0), the magnetic susceptibility of the magnetic particle (χ_2), and the magnetic susceptibility of the medium (χ_1).

$$F_{mag} = (\chi_2 - \chi_1)V\frac{1}{\mu_0}B(\nabla B) \quad \text{(Eq. 1)}$$

Obviously, only gradient magnetic fields can generate a magnetic force, whereas homogenous magnetic fields will exert no force on MNPs. Furthermore, MNPs with larger size and stronger magnetic properties, higher magnetic field strength and gradient will lead to a stronger F_{mag}.[55] Consequently, larger particles can move faster, and a higher concentration of particles also move faster due to the longer chains or needle-like aggregates formed.[27] As there are more significant physiological parameters in designing a practical DDS, such as many natural barriers (the blood-brain barrier and the blood-thymus barrier), a combination of forces (magnetic dipole interaction, buoyance, viscous resistance, and gravitational force), the complicated branching networks of blood vessels, and blood cells in the blood stream, further development of these theoretical models is vitally important for translating the magnetic targeting technique from the laboratory to the clinic.[24,28,55]

There are some basic classifications of magnetism for comparing magnetic behaviors: ferromagnetism, ferrimagnetism, antiferromagnetism and paramagnetism (Figure 1.3).[10] The ferric oxide nanoparticle form of magnetite (Fe_3O_4) and γ-Fe_2O_3 maghemite (γ-Fe_2O_3) have been used most widely because of their simple synthesis, stability in physiological conditions and flexibility in chemical modification (Table 1.1).[7,54] However, magnetite and maghemite will lose their permanent magnetization when the particle size is below 20 nm.[36] The bulk saturation magnetization of γ-Fe_2O_3 is significantly lower than that of Fe_3O_4.[56] Without being coated with biocompatible materials, these ferric oxide

nanoparticles could not be applied *in vivo*.[57] Various non-toxic, protective and non-permeable materials, including gold, polymers, silane and dendrimer could be used as the encapsulating shell in order to improve the biocompatibility and circulation time, diminish the toxicity and prevent oxidation of MNPs.[32,45,54,57] Additionally, different kinds of moieties could be used to decorate these MNPs with specific purposes (e.g. improved stability, prolonged retention time, etc.), so these functionalized MNPs could be applied clinically.[7] Therefore, MNPs are promising candidates for functional biomaterials because of their variety of practical properties. As MNPs can absorb biomolecules and form a bio-corona when exposed to *in vivo* conditions, coating of MNPs can affect the surface charge, corona formation and adhesion of particles to cells, resulting in differences in the ability to target and drug delivery.[20] It is noteworthy that the size, shape, composition, surface modification of these MNPs all have a critical effect on their toxicity.[7] As a result, the effects of these parameters of MNPs on their magnetic properties should be evaluated carefully for the fabrication process and biomedical applications.[45]

Table 1.1. Common iron oxides and their magnetism

MNPs	Formula	Magnetism
magnetite	Fe_3O_4	ferro(ferri)magnetism
maghemite	γ-Fe_2O_3	ferrimagnetism
hematite	α-Fe_2O_3	antiferromagnetism
carbonyl iron	$Fe(CO)_5$	ferromagnetism

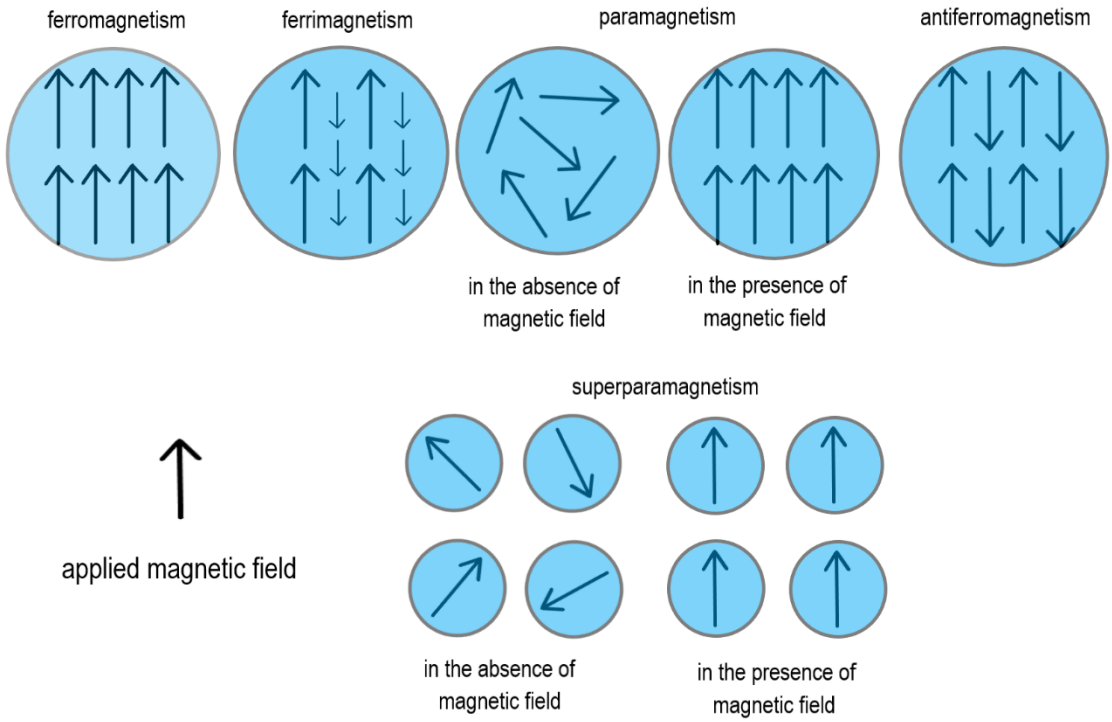

Figure 1.3. Basic classifications of magnetism showing orientations of magnetic moments.

Magnetic fluid hyperthermia (MFH) treatment is one of the important applications of MNPs and attracting more and more attention, but the higher temperature can lead to serious side effects, such as necrosis and coagulation.[11,36] Under exposure to an alternating current magnetic field (AMF), MNPs can generate heat because of the magnetic loss when the temperature is lower than their Curie temperature which is determined by the metal composition and size of the MNPs.[11,58] Direct injection of MNPs into targeted tissues or organs can be applied as a complementary cancer therapy strategy to heat the specific region because the temperatures of 42-45℃ can cause irreversible damage to cancerous cells and normal cells that are more tolerant to the heat.[36,38] The excellent targeting ability, produced high temperature and irreversible cell damage make magnetic-field-induced heating superior to other heating methods.[9] The concentration, distribution and size have a significant effect on the heating efficiency of MNPs.[36] To clarify, a higher concentration of MNPs can produce the desired treatment temperature with weaker magnetic field strength.[9] When the temperature is

higher than the Curie temperature, the heating process will be suspended because the value of saturation magnetization decline to zero.[11] The null overall magnetic moment is a result of the random fluctuation in the magnetization directions.[37]

Typically, MNPs can be classified into metals (including iron, manganese, rhenium, etc.), oxides (such as superparamagnetic oxides), alloys (such as FePt, PtCo and FeAu), ferrites (like $CoFe_2O_4$ and $CuFe_2O_4$) and multifunctional MNPs with different structures (like core/shell, hollow, dumbbell and hybrid).[32,35,59,60] Iron (Fe) is an essential element for the body, although an excess amount of Fe can cause toxicity *in vivo* (60 mg/kg).[57] Alloys exhibit higher saturation magnetization than pure metals.[61] The iron oxide nanoparticles are the only type of MNPs approved by the US Food and Drug Administration (FDA) for clinical applications.[1,62] They are the most used type for biomedicine because of the natural occurrence and the simple preparing process in nanometer ranges with a narrow distribution.[57]

The superior magnetic behavior, size- and material-dependent physicochemical properties and stability of superparamagnetic iron oxide nanoparticles (SPIONs) make this material widely applied as DDS derives.[10,36,63] The particle size of SPIONs is small enough (usually 10-20 nm) to exhibit a single large magnetic domain when the temperature is higher than the blocking temperature (Figure 1.3).[7,35,36] On the contrary, magnetic particles with a size larger than superparamagnetic radius normally exhibit a multidomain structure and these multidomain states were separated by domain walls because larger particles need less energy to form domain walls.[45,62] Once the particle size were below a critical size, these SPIONs possess the weaker magnetic moment, and show less reaction with magnetic fields.[54] With the particle size reduces, the coercivity (H_c) increases to the maximum and then drops to zero.[45] The magnetization curve of SPIONs exhibited an invertible S shape without hysteresis (Figure 1.4).[64] There

is no overall magnetic susceptibility because its fixed magnetic moment of individual particles is randomly oriented when there is no magnetic field.[7,45] High saturation magnetization (M_{sat}), no remnant magnetization (M_r) and zero H_c are key features of SPIONs in biomedical applications.[58,65] As a result, the prevention of particle agglomeration in the absence of magnetic fields can promote the injection of SPIONs dispersion into biological systems.[37,65] Furthermore, the effect of magnetic field strength on the magnetic force to SPIONs was reduced as a low magnetic field was required for SPIONs to reach M_{sat}.[26] Under the increase of static magnetic field strengths, magnetic moments will be aligned and the magnetic susceptibility will increase until a saturation point.[7] Once the magnetic field is removed, all magnetic moments will become direction randomization again (zero coercivity) due to the thermal fluctuation.[7] According to the FDA, magnetic fields up to 8 T are regarded as safe for adults.[35] When SPIONs were applied in combination with permanent neodymium-iron-boron (NdFeB) magnets, an effective magnetic field depth can reach 10-15 cm in the body.[37]

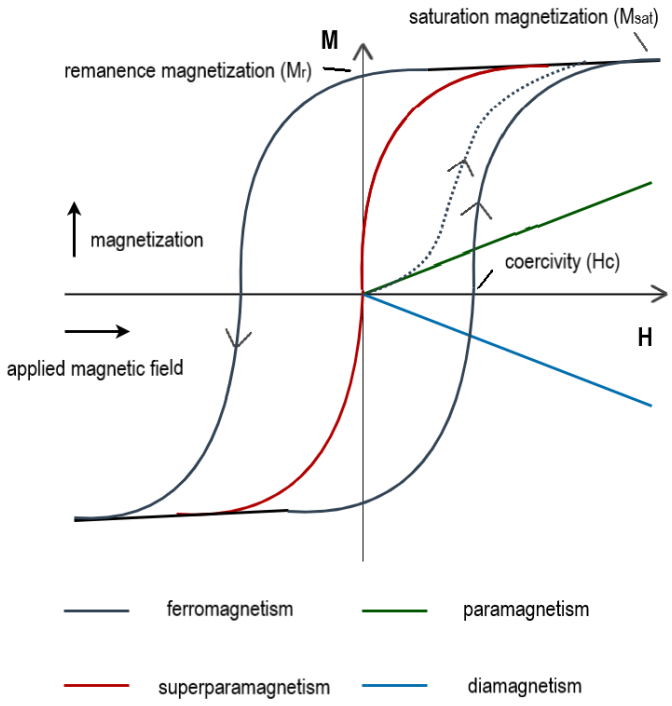

Figure 1.4. Schematic illustration of the magnetic hysteresis loop in the

magnetization *versus* field dependence.

There are many fabricating methods for SPIONs, including wet-chemical methods, co-precipitation methods, thermal decomposition methods and gas-phase methods.[32,36] Additionally, the surface polarities of SPIONs make them easier to be surface modified.[10] Furthermore, their promising biodegradability and the ability of binding to other substances broaden their application in biomedical areas.[10] Due to the high tendency for the particles to aggregate, the development of various nanostructures with the combination of SPIONs and polymers became a commonly used strategy.[63] It is vitally important to integrate SPIONs with polymers for creating novel structural characteristics and functions.[63] By coating SPIONs with polymers, the self-stability and anchoring capability could be enhanced without the addition of surfactants.[10]

However, the main concern of SPIONs for practical applications is the weak magnetization of individual nanoparticles, which is not efficient for target delivery in the body.[66] In order to increase the overall magnetic response in the physiological environment, many approaches have been proved to be feasible. Furthermore, as drug loading capability is the main limitation for translating MNPs from laboratory to clinical trial, developing a magnetic field triggerable DDSs with both high drug loading capability and good biocompatibility is of great importance.[35] The methods of drug loading and delivery are the main problem for MNP-based smart DDSs. Consequently, more attention should be focused on the drug loading method, surface chemistry, particle size, shape and material.

1.2.3 Magnetic Polymeric Nanocomposites

In recent years, nanoscale DDSs are critical strategies in chemotherapy as their physicochemical properties could be adjusted by controlling the shape, size and chemical composition.[61,67] Magnetically sensitive polymer-based nanocomposites show superior physicochemical and biological properties for the

development of biomedical devices.[68] Due to the larger surface areas and stronger reactivity of particles with a smaller size, the hydrodynamic diameter of particles in the range from 10 to 100 nm is regarded to show optimal pharmacokinetic properties.[1] There are many strategies for MNPs in the development of nanoscale DDSs: first, adjusting the size and shape of MNPs, as well as the type of matrix or medium; second, the encapsulation of MNPs with an external polymer coating; third, the porous nanocomposite mixture which is composed of MNPs and polymers; fourth, the grafting of drug molecules on the MNPs surface in the polymer matrix.[45] The approaches of conjugating therapeutic agents to the nanocarriers include absorption, covalent attachment, and encapsulation.[1] The targeting strategies are mainly divided into active (the application of specific ligands and physical stimuli) and passive (the result of EPR) mechanisms.[1]

1.2.3.1 Magnetic Micelles

A micelle, as one of the most important kinds of drug carriers for encapsulating hydrophobic drugs, is a supramolecular colloidal particle composed of a hydrophobic core (head) and a hydrophilic shell (tail).[69] The hydrophobic core is regarded as an optimum carrier compartment for hydrophobic drugs, and the hydrophilic shell can stabilize encapsulated particles in an aqueous solution.[70] It has been revealed that polymeric micelles showed great potential in increasing bioactivity, stability, tissue permeability, drug delivery efficiency and solubility of hydrophobic drugs.[71] Micelles are in dynamic equilibrium because they can form and stay constant when the concentration of surfactant or amphiphile solution is above the critical micelle concentration (CMC).[72] The CMC could be affected by the formation (hydrophobicity) and the molecular weight of the hydrophobic block.[73] These drug carriers have attracted much attention owing to multifunctional characteristics, such as storage and transportation of therapeutic substances and magnetic nanoparticles, cancer cells surface receptors targeting ability.[74] Various amphiphilic polymers which are responsive to external stimuli

(such as pH, temperature, magnetic field, etc.) could be fabricated with chemical modifications.[71] Therefore, these stimuli-responsive polymers could be used to prepare micelles for achieving controlled drug release.

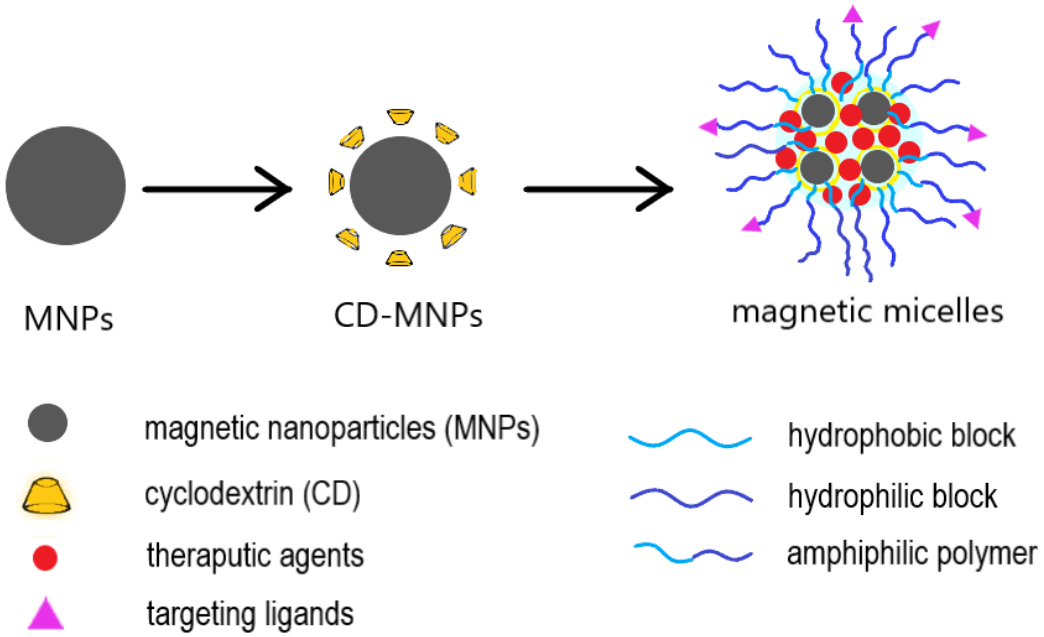

Figure 1.5. Schematic illustration of the preparing process of magnetic micelles composed of MNPs, therapeutic agents, amphiphilic polymer, cyclodextrin and targeting ligands.

For magnetic micelles, MNPs can be designed to located at the interface between the outer hydrophilic shell and the inner hydrophobic core (Figure 1.5). With the manipulation of magnetic fields, these magnetic micelles can maintain good chemical stability, biocompatibility, direct actuation, solubility and drug loading efficiency.[71] Zhang et al. applied guest molecules to graft on the surface of CD-MNPs (β-cyclodextrin capped onto the surface of Fe_3O_4 MNPs) via inclusion complexation between β-cyclodextrin (β-CD) and ferrocene groups (Fc).[75] Various polymers could be attached to MNPs as drug reservoirs for achieving multi-stimuli-responsive releasing carriers (Table 1.2), such as poly(N-isopropyl acrylamide) (PNIPAM), β-CD and glycerol monooleate.[41,75,76] Among them, β-CD molecules are the most common drug carriers and gatekeepers because of their

amphiphilic hollow structures and superior compatibility.[41,77] Furthermore, the specificity and efficacy of micelles could be improved because of the conjugation of targeting ligands, which can be connected to specific receptors on the surface of tumor cells and facilitate receptor-mediated endocytosis in cancer therapy.[73] The multivalent inclusion complexes between β-CD and the active pharmaceutical ingredients (API) can enhance stability, water-solubility, biological activity and prevent unwanted drug release.[51,78] As the size of SPIONs have a significant effect on the pharmacokinetics and tissue distribution *in vivo* and saturation magnetization, the tunable cluster size through changing the SPION/PEG ratio is of great importance.[51] Through the disassembly of micelles due to external stimuli, encapsulated drugs could be released. Many factors can influence the drug release from micelles, including micelle stability, the biodegradation rate of copolymers, drug diffusion rate, partition coefficient, drug concentration and localization in micelles.[73] In addition, the drug loading capacity could be adjusted through the hydrophobic block length and the volume of micelles.[74] Consequently, these nanocarriers showed great potential in both targeting cancer therapy and hyperthermia treatment.[11,76] Many hydrophobic anticancer drugs (Table 1.2) have been successfully loaded into the core of the micelles for increasing drug solubility and release rate.[70]

Table 1.2. Examples in the literature of magnetic micellar formulations

Stimulus	MNPs	Drug	Block copolymer	Targeting ligand	Ref.
magnetic field; tumor cells	SPIO	paclitaxel	PEG; β-CD	Arg–Gly–Asp (tumor targeting)	51
temperature, pH, H_2O_2, magnetic field	Fe_3O_4	doxorubicin	PEG/PNIPAM/CD-MNP PNIPAM (thermoresponsive) β-CD and Fc pair (redox responsive)	-	75

temperature, pH, magnetic field	Fe_3O_4	doxorubicin	PNIPAM@β-CD-BI-Fe_3O_4@mSiO_2 PNIPAM: thermoresponsive; β-CD: pH-responsive	-	76
magnetic field	Fe_3O_4	paclitaxel	pPTX/CD-SPION	-	78
magnetic field; acid; tumor cells	Fe_3O_4	doxorubicin	PEG-P(GA-DIP) poly(L- glutamic acid): acid-sensitive	folate (tumor targeting)	74
magnetic field; pH	Fe_3O_4	paclitaxel	amphipathic chitosan derivatives; (PEG)	-	71

However, this process is complicated, difficult to scale up, time-consuming and will lead to changes in the magnetic properties of MNPs.[32,51,71] Besides, it is difficult to control the size of magnetic micelles.[32] More attention should be paid to the drug loading capacity, drug release rate and saturation magnetization for these DDSs.[51,75]

1.2.3.2 Magnetoliposomes

Liposomes are composed of an aqueous lumen within a phospholipid bilayer, these vesicles have been applied as nanoscale DDSs.[36] The composition of the phospholipid bilayer has a critical effect on liposomes properties because the membrane structure should keep stable in blood flow and become permeable once reaching the target site.[79] Hence, membrane permeability, fusion and destabilization are all important tools for controlling drug release.[80] Their adjustable size, structure and chemical constituents all have critical effects on the membrane fluidity, charge density and permeability.[52] Additionally, the permeability and drug release rate of liposomes which depends on the lateral compressibility, could be adjusted by higher temperature (the melting temperature of lipid), pH, the conjunction with large headgroup amphiphiles,

defects or pores in the formulation.[81,82] The membrane is in the liquid phase (a thin and disordered membrane) when the temperature is higher than the lipid melting temperature (T_m), whereas the membrane will transfer to the gel phase (a thick and rigid membrane) below the T_m.[58,82] The gel to liquid phase transition of membranes with the rise of temperature will result in the increase in membrane permeability and the burst release of encapsulated drugs.[83] Liposomes show many advantages, like the modulated circulation of drugs *in vivo*, the protection and solubilization of drugs or nanoparticles against biomolecular adsorption by encapsulating them with various physicochemical properties.[54,82] In this kind of drug carriers, the drug released mainly through *trans*-membrane diffusion, but sustained the drug release for a long time is difficult to achieve.[81,83] Through intravenous injection, the drug delivery efficiency is restrained by the reticuloendothelial system and this limitation could be overcome by the functionalization of lipid headgroups with moieties, such as PEG.[54,84] The PEGylation of liposomes can prolong their storage and blood circulation time, decrease liver accumulation and uptake by macrophages because PEG can absorb plasma proteins, aggregate liposomes and protect the complex from the reticuloendothelial system.[45,82,85] Some bioactive molecules, such as enzymes and antibodies, can be used to conjugate on the phospholipid layer to endow them with more biological site-specific and selective properties due to the interaction between ligand and the receptors of specific cells.[52,85] Thus, the interaction between the targeting ligands of the carrier and the surface molecules of the targeted cells can ensure the targeting properties of liposomes.

Accordingly, magnetoliposomes have been developed to combine both the physical and magnetic properties of MNPs and liposomal drug nanocarriers for many purposes, including obtaining multivalent properties, preventing MNPs from aggregation and oxidation, increasing bioavailability, possessing specific target ability for biological applications.[36,52,54] There are three approaches to associate MNPs with liposomes: encapsulation of hydrophilic MNPs directly within the

liposome lumen (inner aqueous space), the embedding of hydrophobic MNPs between the lipid bilayer, and conjugation of MNPs to the bilayer outer surface (polymers, lipids and surfactants) (Figure 1.6).[36,54,85,86] The spatial location of the MNPs within the MNP-liposome hybrids is determined by the surface properties of MNPs.[36] Because MNPs can directly act on the capsule wall, the second approach is more preferable for DDSs.[54] The efficiency of encapsulation is determined by the size of MNPs.[54] However, the incorporation of MNPs in the bilayer lipid membrane will increase the rigidity of the membrane and thus decrease the drug diffusion.[85] The main limitations in the first approach are leakage caused by the reaction between the unstabilized MNPs and the membrane of liposomes, and the increase of temperature as a result of SPIONs heating.[54] The lipid composition can affect the efficiency of the incorporation of drugs into magnetoliposomes because the excess physical ligands may lead to the leakage of encapsulated drugs.[54,86] The third approach has not been widely accepted.[54] In addition, the saturation magnetization which is related to the amount of MNPs incorporated can be determined by the composition of magnetoliposomes bilayers.[86] Generally, fast and high drug release (permeability) from magnetoliposomes is related to the high drug loading capacity, high field frequency, the large size of MNPs, and long exposure time in a magnetic field.[81] Under the exposure of AMF, the magnetically induced heat and temperature increase of the magnetoliposomes will lead to the microstructure changes in the phospholipid bilayer from the gel to liquid phase, the enhanced membrane permeability and subsequent diffusion of encapsulated drugs.[58,83] Once the AMF was switched off, the temperature of membranes will cool down below T_m because of the superparamagnetic behavior. Herein, the membrane will revert to the gel phase and prohibit the drug release.[58]

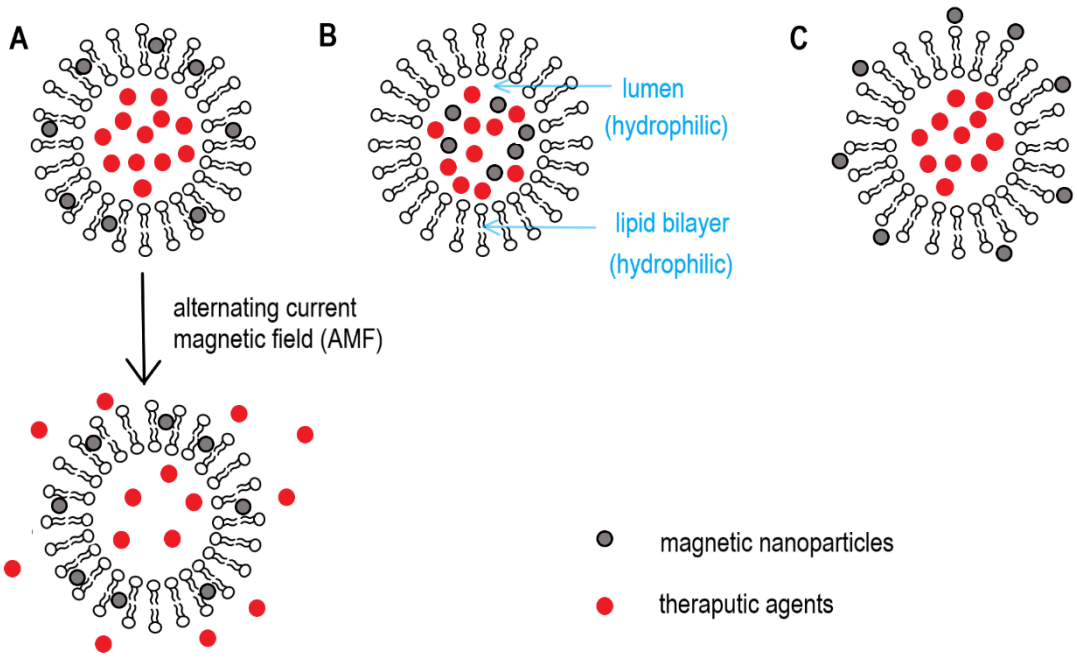

Figure 1.6. Schematic description of magnetoliposomes when MNPs were (A) located in the lipid bilayer, (B) the lumen (middle) or (C) attached on the surface of the liposome.

However, the investigation and fabrication of magnetoliposomes are limited by the inhibition of cell function, the clustering of MNPs, the formation of micelles, and increased passive drug release.[82,84] Therefore, it is necessary to find a balance between the concentration of encapsulated MNPs and cellular targeting.[84] It is noteworthy that the incorporation of larger MNPs (>5 nm) in the membrane may lead to the formation of magnetic micelles.[54] Besides, the density and stability of MNPs can affect the stability and membrane permeability of liposomes.[54] Moreover, the thermal-magnetic stimuli may cause damage and secondary effects to the neighboring tissues because of temperature increase and magnetically induced eddy currents, subsequently limit the clinical application of magnetoliposomes.[83] Also, the preparing method has a critical effect on the final shape, size distribution, surface chemistry and magnetic properties of magnetoliposomes.[54] During the process of developing magnetoliposomes, more attention needs to be paid to the selection of appropriate methods to synthesis and surface coating of MNPs, and appropriate

composition of the liposome bilayers.[36]

1.2.3.3 Ferrogels (Magnetic Hydrogels)

Gels can behave like solid-state under some deformation conditions.[19] Hydrogels possess 3D polymeric networks with high swellability in water because their hydrophilic chains cross-linked chemically or physically.[10,87,88] The crosslinking methods include covalent bonds, crystallization, hydrophobic interaction and so on.[23] Because of the dual nature (solid and liquid), high water content, softness, elasticity and diffusion ability of hydrogels, their structure show similarity and compatibility with living tissues.[9,19,23] According to the polymer category, hydrogels could be divided into synthetic and natural polymers.[9] In spite of the excellent processability and long service life of synthetic hydrogels, natural hydrogels are regarded to be more suitable for biocompatible applications because they are environmentally friendly and sustainable.[9] These synthetic hydrogels show many similarities with the biological objects in the structure and performance although common hydrogels show weak mechanical strength.[87,88]

As a common type of drug delivery carriers, hydrogels play an important role in sustained-release and controlled-release dosage forms because of their good biocompatibility, mechanical properties, high water content and flexible physicochemical structures.[10,89] However, the practical application of conventional hydrogels was limited by their unfavorable mechanical properties (e.g. stiffness and strength), insufficient functionality (e.g. conductivity, poor sensitivity and responsiveness), fatigue deterioration after multiple operation and difficulty in achieving accurate drug release (passive mechanisms is the main drug release pattern from hydrogels).[23,90]

Because the hydrogels show great potential for real-time alternation of swellablity, permeability and elasticity in response to environmental conditions, their applications as sensors draw much attention recently.[90] The drug release

behavior of traditional hydrogels were mainly dependent on the tunable pore size because channels and pores of hydrogels are reservoirs and diffusion pathways for drugs.[9] With the manipulation of physical and chemical stimuli (e.g. pH, temperature, magnetic field, electric field, change in solvent composition and pressure), various types of stimulus-sensitive hydrogels (smart hydrogels) exhibit an obvious and reversible change in volume and shape to achieve pulsatile release and position control.[19,87,89,91] Among these stimuli, pH and temperature stimulated hydrogels have been extensively studied for cancer therapy because of the relatively lower pH (around 5-6) and higher temperature (around 40-42℃) of cancerous cells.[92] For the application in DDSs, these stimuli sensitive hydrogels are required to be both biocompatible and biodegradable.[93]

Magnetic hydrogels (ferrogels), consisting of polymer hydrogels embedded with magnetic particles, have been intensively studied as smart materials for the development of DDSs because of their macroscopic changes in the shapes under magnetic fields.[56,90,94] Ferrogels mainly refer to magnetic gels prepared with MNPs rather than microparticles.[95] As the ferrogels show rapid response and remote control ability by controlling magnetic fields, the biological applications of ferrogels include controlled drug release and dialysis membranes.[9,68] As the critical step in ferrogels synthesis, MNPs were mainly integrated into hydrogels with three methods, including the blending, grafting and precipitation methods.[9,23] MNPs have many functions in preparing ferrogels, like crosslinking the hydrogels for absorbing or attaching to the polymeric chains, to be sensitive to external magnetic fields.[19] During exposure to magnetic fields, mechanical properties of the polymeric matrix could be improved and the deformation could be adjusted with the incorporation of MNPs.[95] Therefore, these materials with mechanical softness, viscoelastic nature and magneto sensitivity are commonly applied as carriers of drugs, proteins, cells and other small molecules.[10,19]

As shown in Table 1.3., MNPs and a polymeric matrix (usually using PVA, alginate,

NIPAM, polysaccharides and PDMS) are the main compositions of the ferrogels. The properties of ferrogels mainly depend on the size and distribution of MNPs, the type and concentration of gels and MNPs.[9] As ferrogels with a larger radius will lead to a stronger magnetic force and a faster movement, it will take less time for larger ferrogels to reach the target site.[48] Besides, ferrogels with a smaller size show a higher swelling rate due to the larger surface/volume ratio and more contact with the surrounding solvent.[48] Additionally, the type and concentration of base materials and MNPs can affect the swelling behavior of ferrogels significantly because the ratio of ironic and non-ionic functional groups in ferrogels can determine their swelling capacity.[19,96] The loose-structured ferrogels with high swellability and low cross-linking extent can retain more fluids for the development of DDSs.[19] Through coating MNPs with polymers, ferrogels can possess higher biocompatibility, pre-programming, self-regulation, precise actuation and lower risk for particles aggregation.[10,97] It has been proved that the extent of cross-linking, the intensity of the applied magnetic field and the concentration of MNPs all have a critical effect on the elastic modulus of fabricated ferrogels.[95] The high tendency of the MNPs to aggregate is one of the main challenges in coating MNPs with a polymer matrix, considering the result of surface roughness and stress concentration.[18] Hence, the main difficulty in achieving ferrogels with good mechanical properties and magnetic sensitivity is the compatibility of the polymer matrix with encapsulated MNPs.[95] Additionally, ferrogels show advantages in drug loading capacity, delivering drugs and phase transition for releasing drugs in a specific location because of time-dependent deformation and dynamic microstructural changes when external magnetic fields are exerted.[10,19,97] Diffusion is the main release mechanism of ferrogels.[10] With the manipulation of externally applied magnetic fields, the drug dosage and diffusion rate could be adjusted.[10] There are two main mechanisms for ferrogels drug release.

Table 1.3. Examples in the literature of ferrogels formulations

Stimulus	Base material	Crosslinker	Drug	MNPs	Ref.
magnetic field; pH	methacrylic acid or 2-aminoethyl methacrylate hydrochloride and N,N'-dimethylacrylamide	N,N'-methylene bisacrylamide	5-fluorouracil	Fe_3O_4	19
magnetic field	Acrylamide	PEG		$CoFe_2O_4$	98
magnetic field	PVA	polyethylenimine	-	Fe_3O_4	99
magnetic field; pH	PVA and *kappa*-Carrageenan	-	diclofenac sodium	Fe_3O_4	96
magnetic field	Alginate	calcium sulfate	doxorubicin	SPIONs	89
magnetic field; temperature	NIPAM	N,N'-methylene bisacrylamide	doxorubicin	$Mn_{0.6}Zn_{0.4}Fe_2O_4$ SPIONs	97
magnetic field	PAAm	N,N'-methylene bisacrylamide	-	γ-Fe_2O_3	87
magnetic field	glycol chitosan, oxidized hyaluronate	-	-	SPIONs	88
Magnetic field; temperature; pH	NIPAM	N,N'-methylene bisacrylamide	doxorubicin	Fe_3O_4	92
magnetic field	PVA	glutaraldehyde	theophylline	Fe_3O_4	93,100
	scleroglucan	-			

One mechanism is direct actuation through a physical deformation in ferrogels (Figure 1.7A). The accumulation of magnetic response of embedded MNPs could enable the ferrogels with magnetic macro-response and mechanical deformation properties because the magnetic moments of MNPs tend to align under the applied magnetic field.[7,23] As a result of fluid convection, adjustable drug release can be easily triggered from ferrogels.[56] Ferrogels will be stretched immediately according to the direction of magnetic fields, then return to the previous form after the magnetic field is disappeared.[14] Hence, the mechanical deformation property could be manipulated to control drug release from ferrogels through adjusting the amount of containing magnetic particles.[7] The drug release mechanism could be transferred from diffusion to magnetic field activation as the shrinkage of ferrogels will lead to a decrease in inner pore size and the release from the loaded drugs.[7] To achieve this aim, the size of MNPs ranging between 5 and 500 nm is regarded as the most appropriate size for ferrogels.[14] The particle size of magnetic particles has a significant effect on the deformation of ferrogels with a moderate magnetic field because larger particles show higher saturation magnetization values than smaller particles.[56] Ferrogels composed of MNPs with larger particle sizes showed better magnetic sensitivity due to their stronger saturation magnetization and weaker coercive force.[99] Importantly, the particle size of MNPs, the frequency of magnetic treatment and the switching duration time both have significant effects on the drug release behavior of ferrogels under the magnetic fields.[4,99] It has been proved that the concentration of MNPs also has a critical effect on the elastic properties of ferrogels because MNPs can improve the density of ferrogels matrix and inhibit the swelling process in some cases.[87] In addition, the roughness of ferrogel surface which is associated with the concentration of embedded MNPs, can influence the cell adhesive ability and proliferation.[87] Furthermore, ferrogels have the potential to be designed for multifunction through the conjunction with biological ligands or encapsulation with polymers for MNPs.[14] However, Zhao et al. pointed out that the deformation and volumetric change of typical nanoporous ferrogels applied in drug delivery are limited, and

the pore sizes are almost in the nanometer range.[94] Hence, the transport of large molecules and cells through gels will be limited (Figure 1.7A1). When the ferrogels are exposed to magnetic fields, the magnetic moments of MNPs can be aligned together and the aggregation of MNPs will lead to the "close" configuration of ferrogels.[96] The drug release kinetics will be decreased by the application of magnetic field because of the significant reduction in pore size and the increase in tortuosity (the ratio of the actual path length through the pores to the shortest linear distance) of diffusion channels of ferrogels.[93,100] When the size of the drug molecules is smaller than the pore size of ferrogels, the diffusion coefficients are inversely related to the tortuosity of the gels.[100] In contrast, the application of macroporous ferrogels with micrometer scale interconnected pores can overcome these problems because of simultaneous scaffold collapse and on-demand release of loaded drugs in response to magnetic fields (Figure 1.7A2).[14,94] Various ferrogel formulations have been used in clinical applications such as modulating drug delivery, MRI, cell tracking *in vivo* and hyperthermia treatment because of the promising combination of a safer stimulus with biocompatible magnetic particles, especially iron oxide nanoparticles. Also, it is noteworthy that the reduction in the size of ferrogels will lead to a decrease in ferrogels deformation as a result of less content of magnetic particles to be used to generate enough body force for smaller ferrogels.[56] For example, poly (vinyl alcohol) (PVA) can be cross-linked with MNPs because of its amphiphilicity for encapsulating drugs in either aqueous or organic solvent and dispersing MNPs uniformly.[99] The mixture of glycol chitosan (GC) and oxidized hyaluronate (OHA) solution (without additional chemical crosslinkers) could be used to fabricate ferrogels with the addition of SPIONs.[88] Polyacrylamide (PAAm) gels, which is regarded as the most common hydrogels, have been used to fabricate ferrogels networks with various cross-linking density because of low toxicity, cells compatibility and high elasticity.[87] However, the addition of cross-linking agent, initiator and catalyst are necessary for the synthesis of PAAm hydrogels.[87] As a physical cross-linking method, freezing-thawing could be applied in the

fabrication of PVA-based hydrogels due to its simple operation.[96] Similarly, other polymer systems also have been made with ferrogels, like gelatin-ferrite. In addition, injectable temperature-sensitive hydrogels have been connected with ferromagnetic particles.[7]

The other mechanism is drug release through de-gelling because of the conversion from high-frequency magnetic fields to heat (Figure 1.7B).[14,23] When the temperature is below the lower critical solution temperature (LCST), the polymer chains will absorb water and swell (decoil). Polar groups of hydrogels would result in water imbibition and volume increase.[10] Under an oscillating magnetic field, MNPs will heat inductively due to power absorption and the following magnetic relaxation of single-domain nanoparticles.[4,10] Generated heat can increase the degradation rate of these thermo-responsive ferrogels due to their reversible phase transition properties.[97] The polymer chains will de-swell and cluster to 'gel' phase because of the transformation from hydrophilicity to hydrophobicity when the temperature is higher than the LCST.[97] Porosity and diffusive pathways of ferrogels will be affected by the significant volume fluctuations in various temperatures.[10] Once the magnetic field was removed, the ferrogels will cool down and the phase transition will reverse.[4,91] PNIPAM is regarded as the most common polymers because its LCST is around 32°C.[11] Similarly, hydroxypropyl cellulose and poly(dimethyl aminoethyl methacrylate) also show thermosensitivity.[11] Therefore, a higher temperature can result in the hydrogel collapse and a burst release of encapsulated drug molecules (Figure 1.7B1).[3,14] This squeezing-controlled release is more desirable in a delayed triggering treatment because this mechanism can prevent the release of a large number of therapeutic agents before the trigger operation (heating process until reaching the Curie temperature).[11] However, the collapse of the hydrogel matrix was also observed to prevent the drug release because of the significant decrease in diffusive pathways (Figure 1.7B2).[7,14] This ability makes ferrogels suitable for implantable devices with tunable pharmacokinetics, noninvasivity and

precision.[14] The LCST of hydrogels could be altered by adjusting the hydrophilicity of polymers.[11] The LSCT could be enhanced when hydrophilic comonomers (like acrylic acid and acrylamide) were added to the hydrogels.[10,11] Consequently, the LSCT of thermo-responsive polymers could be tuned easily with the graft over MNPs.[10]

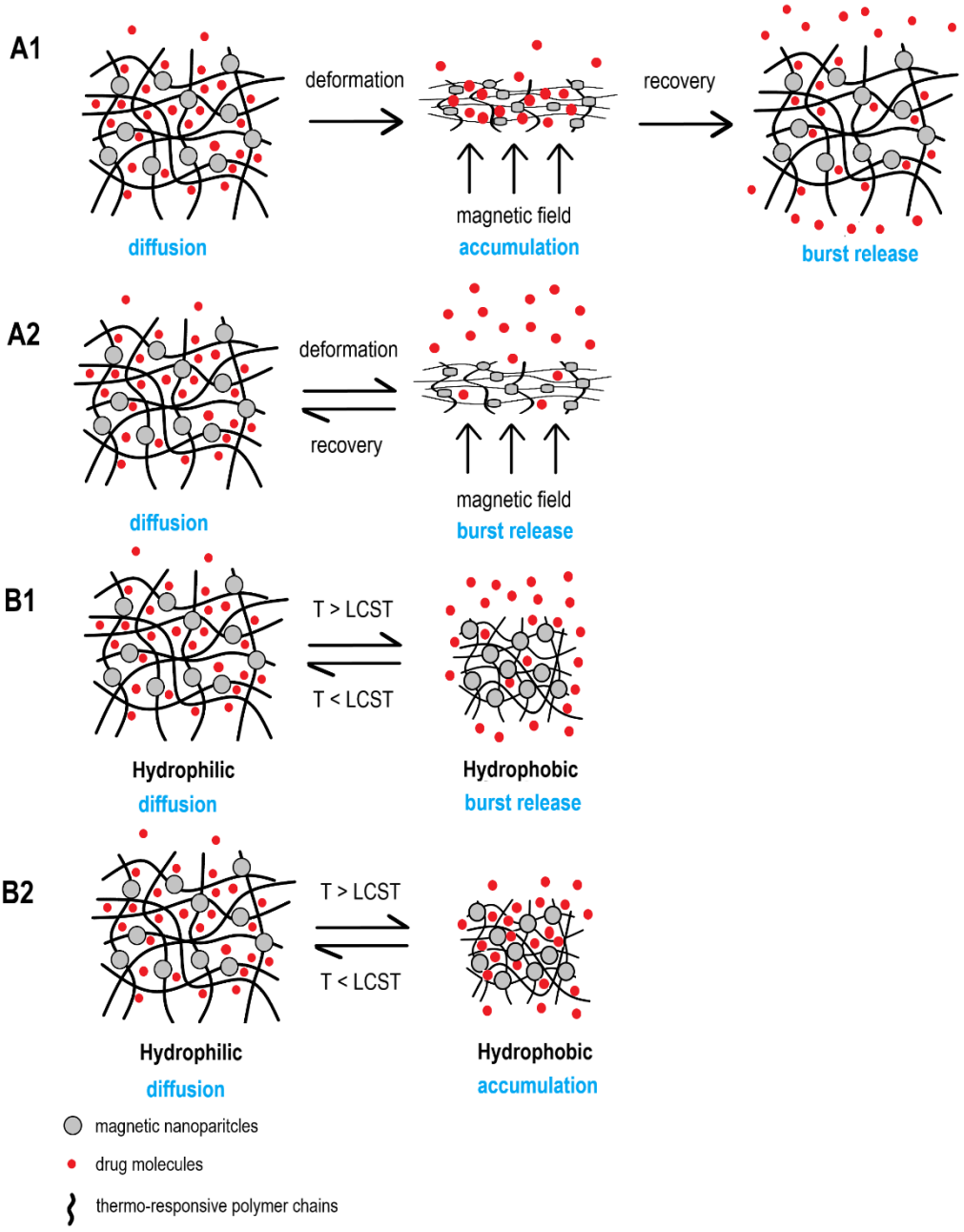

Figure 1.7. Schematic description of the drug release mechanisms of ferrogels: (A) matrix deformation induced by externally applied magnetic fields and (B) gelation induced by the association of polymeric chains beyond LCST.

The spatial distribution of MNPs in magnetic matrices shows parallel alignment to the direction of the magnetic field.[101] Accordingly, the spatial distribution of MNPs (including random distribution, parallel and perpendicular chain-like structure) fabricated under the exposure to magnetic fields can affect the mechanical properties (like elastic modulus shear modulus and Young's modulus) of composites significantly.[101,102] By modulating the nanochannels in ferrogels according to different directions of the externally applied magnetic field, the diffusion behavior of ferrogels could be adjusted.[68] As shown in Figure 1.8, MNPs were aligned in an end-to-end configuration under the exposure to magnetic fields (anisotropic ferrogels) whereas MNPs were distributed randomly in ferrogels without magnetic fields (isotropic ferrogels). As a result, the ferrogel nanochannels could be controlled according to the fabricated pearl-chain structure of ferrogels. In accordance with the drug diffusion direction and nanochannels which are decided by the direction of the magnetic field, the drug release rate of ferrogels is in the order of anisotropic perpendicular-aligned ferrogels < isotropic ferrogels < anisotropic parallel-aligned ferrogels. To conclude, the manipulation of magnetic field directions can realize the switch between "on" and "off" for the drug release from hydrogels.

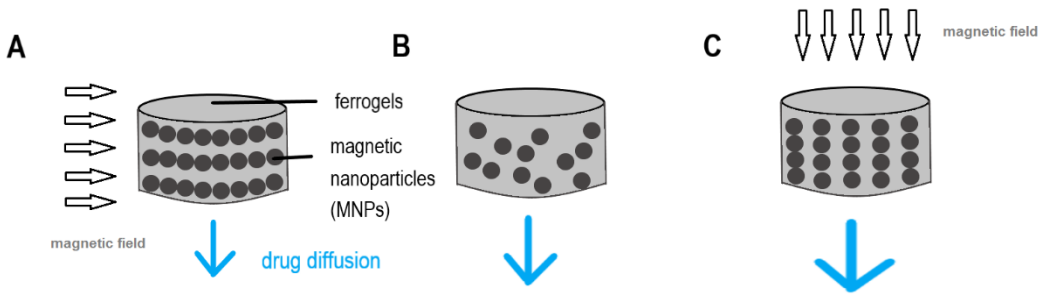

Figure 1.8. Schematic illustration of the effects of the direction of magnetic fields on the drug diffusion behavior of anisotropic and isotropic ferrogels: (A) the ferrogels were arranged by left-to-right magnetic fields (perpendicular to the drug diffusion direction), (B) isotropic ferrogels (randomly distributed MNPs), and (C) the ferrogels were arranged by top-to-down magnetic fields (parallel to the drug

diffusion direction).

The study of Zhao et al. suggested an active scaffold in the form of a macroporous ferrogel, which can achieve on-demand and reversible various biological agents delivery in response to external magnetic fields.[94] Alginates were used to fabricate the scaffolds, they were covalently coupled with peptides containing the arginine-glycine-aspartic acid (RGD) amino acid sequence. Pluronic-coated Fe_3O_4 nanoparticles were embedded in the RGD-modified alginate, and a superparamagnetic gel was formed. Under the externally applied magnetic field, the prompt deformation of the macroporous ferrogel can trigger the release of biological substances through the interconnected pores. To achieve suitable magnetic sensitivity, a high enough concentration of MNPs should be required in ferrogels formulations.[56]

However, the application of hydrogels is mainly limited by their poor drug loading capacity.[92] Moreover, swellable hydrogels may block blood vessels.[64] Although ferrogels have been widely studied for controlled drug delivery, it is difficult to achieve zero-order drug release before reaching the target sites as a result of the thermodynamic nature of diffusion.[103] Also, it is vitally important to entrap MNPs completely in the hydrogels to make sure the achievement of a uniform dispersion and optimized performance without the leakage of MNPs during the release of drugs.[11] Excess MNPs may create an extra burden to health, whereas insufficient MNPs cannot produce rapid responsibility to magnetic fields.[9] It is challenging to develop ferrogels with suitable physicochemical properties for the sophisticated *in vivo* environment.[23] Consequently, the development of ferrogels will be an inspiration to other magnetic elastomer materials with a more reasonable and safer design of structure and composition.

1.2.3.4 Magnetic Sponges (Ferrosponges)

Due to the interconnected nanopore structure, ferrosponges can accommodate

a large number of therapeutic agents.[90] Additionally, the ferrosponges with nanoporous networks possess strong magnetic sensitivity, high swellability, good elasticity and hydrophilicity.[90] Furthermore, the drug release from ferrosponges is dependent on the magnetism and the associated interactions between the MNPs and the polymer matrix during exposure to magnetic fields.[90] Although ferrosponges are similar to ferrogels, the porous structures endow them with better shape recovery ability, higher absorbency and stronger magnetic sensitivity because MNPs are distributed in a higher concentration within thinner polymeric walls.[90] Besides, the inclusion of MNPs in the polymeric walls can lead to lower wall permeability and drug release rate under magnetic fields (Figure 1.9).[90] It has been proved that the polymer matrix has a stronger influence than the amount of MNPs on the morphology and pore size of the fabricated ferrosponges.[90] Consequently, the ferrosponge formulation (including porosity, crosslinking degree, polymer type and concentration) can affect the release behaviors of loaded drugs significantly.[104]

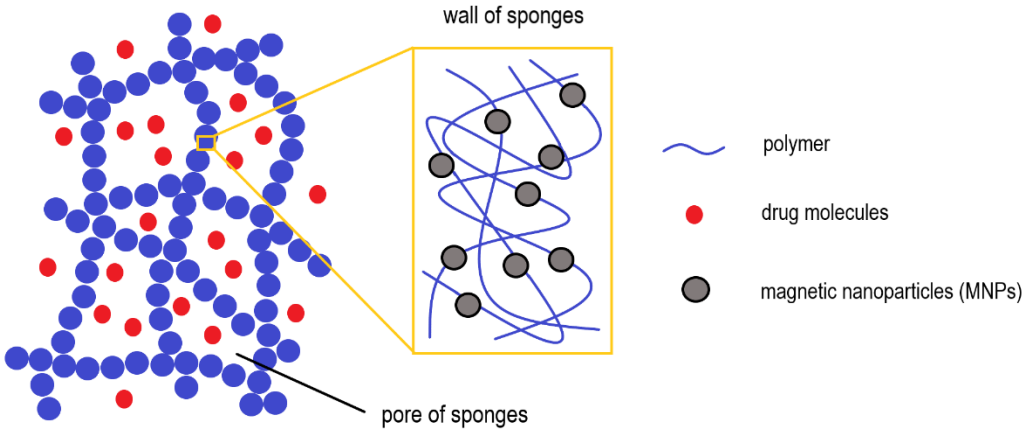

Figure 1.9. Schematic illustration of ferrosponges.

1.2.3.5 Magnetic Mesoporous Silica Nanoparticles

Mesoporous silica nanoparticles (MSNs) show great potential in biomedical applications because their structure makes them superior carriers for therapeutic

agents with various sizes, shapes and functionalities.[76] The most common MSNs present various pore sizes (between 2 and 10 nm) and structural characteristics (2D hexagonal and 3D cubic shape).[62] Therapeutic agents could be entrapped in the pores of the silica layer deposited over particle surfaces.[62]

Magnetic MSNs, core-shell structural mesoporous silica-coated MNPs, have been frequently studied because of their good biocompatibility, water dispersibility and wide biomedical applications.[76,105] The combination of MSNs with magnetic properties can be applied in magnetic targeting, MRI, and MFH.[62] Their appealing structural properties as DDSs including a large surface area, modifiable surface, a homogenous and large pore volume.[105] Additionally, their silica coating can prevent potential toxicity of MNPs due to the biochemical stability of silica shell and resistance to erosion.[105] Magnetic MSNs can be accumulated in the target site in response to externally applied magnetic fields.[76]

Similarly, the mesoporous structure on the surface of MNPs has a significant effect on improving drug loading capacity and increasing drug targeting efficiency.[106] Hollow mesoporous MNPs endowed with anticancer drugs could be prepared with a simple method and realize targeted drug delivery for cancer treatment.[106]

To promote the specific localization of therapeutic agent for MSNs, many efforts have been devoted, like the incorporation of hyaluronic acid in the mesoporous silica-coated Fe_3O_4 nanoparticles can target tumor cells selectively and release drug efficiently both *in vitro* and *in vivo*.[105]

1.2.3.6 Other Magnetic Nanocomposites

In addition, magnetic carbon nanotubes (CNTs), especially magnetic multiwalled CNTs, show several advantages as targeted DDSs, such as the simple synthesis and longer residence time for therapeutic agents through the application of

magnetic fields.[61,64,107]

Although various nanoscale magnetic DDSs have been developed for disease targeting, very few strategies have been translated into clinical applications and commercialization due to their main limitations, including poor controllability, hydrophilic drug loading capability, *in vivo* circulation instability and targeting efficiency.[67,108,109] Moreover, these strategies involve complicated chemical synthesis, inappropriate properties of MNPs, complex crosslinking agents and inadequate magnet system.[1,23,67] Consequently, the combination of microscale DDSs and nanocomposites are regarded as an emerging future strategy for the development of targeted drug delivery.[108]

1.2.4 Microscale Magnetic Drug Delivery Systems

Microscale magnetic DDSs are promising candidates in clinical therapy because of minimal invasiveness and wireless controllability.[108] The main problem that should be resolved is the controllability of microscale DDSs and the precision of drug release at the target site.[108]

1.2.4.1 Magnetic Microrobots

Microrobots are of great importance in biomedical applications because of their small size, minimal invasiveness, the ability to access most locations within the human body and targeted drug delivery.[47,110] The application of wirelessly controlled microrobots (such as tumor imaging and targeted drug delivery) can help increase drug retention, minimize patient trauma and side effects.[111] There are various kinds of magnetic robots, like capsule, earthworms, crawling and helical shape.[112] Nowadays, 3D printing technologies could be used to fabricate miniature components or complicated microrobot models designed with SolidWorks Software.[112–114] The developed device is required to be structurally compact and can be fit in the body.[112] Suitable and efficient actuation strategies

are the determining factor for minimizing microrobots, so the application of magnetic actuation can meet the demands without the requirement for on-board power or computation.[110,111] In order to maintain homeostasis, active and real-time control of the drug released amount from microrobots is required to be in response to the physiological changes and therapeutic needs.[110]

Wireless capsule endoscopes (WCEs), consisting of a miniature video camera, a battery and telemetry, have been developed to solve the problems in examining, diagnosing, and curing the inaccessible part of the gastrointestinal (GI) tract.[34,115] After oral administration, captured video can be sent to an external memory system through radiofrequency signals.[114] These systems can detect suspected disease in a comparatively safe, noninvasive and well-tolerated way. Although conventional WCEs show many advantages in good flexibility in swallowability, painlessness, the movement inside the body, drug delivery and surgery in the GI tract, they still have many technical problems in realizing active or real-time movement minimization without causing any damage *in vivo*.[34,114,116] Therefore, the actuating method of WCEs should be effective, accurate and versatile, as WCEs have low diagnostic accuracy and fewer abilities when compared with traditional endoscopes.[117] There are several approaches, such as magnetic actuation, battery-powered motor actuation and hybrid actuation.

Moreover, expensive energy supply is another challenge and it is difficult to realize multi-direction motion or achieve backward movement.[114,116] The application of magnetic torque is a hopeful approach to solve the problem of energy supply in the WCE movement. According to Munoz et al., an external magnetic system (outside the patients' body) and internal permanent magnets should interact with each other in magnetic devices of capsule endoscopes.[118] However, some commercial systems applied to actuate capsule endoscopes, such as electromagnets in MRI are too expensive for clinical applications. Therefore, applying external permanent magnets manipulated by robotic arms is

a feasible, easy and cheap way for remotely triggering magnetic modules, which are inserted in capsule endoscopes. The main challenge of triggering these magnetic devices with external PMs is the difficulties for real-time control strategies because of the complicated magnetic interaction between external and internal permanent magnetic systems.[119]

With the combination of a magnetic object and WCE, the device could be actively controlled in the GI tract in response to externally applied magnetic fields.[114] When equipped with a drug delivery module, the WCEs have been expected as a promising candidate in targeted drug delivery for non-invasive treatment due to less pain, tissue trauma and hospitalization time for patients.[34,114] In recent years, permanent magnets can be placed into the WCEs for achieving rotating and moving with the application of electromagnetic fields generated by the Helmholtz coils.[113] Several prototypes of drug delivery WCEs have been developed, although few of them can achieve complete control over drug release for clinical application.[114] The main problems are potential tissue damages and difficulties of both precise location control and real-time position control.[119]

Before the clinical trial and commercialization of magnetic microrobots, there are several obstacles to be overcome, such as developing multifunctional robots, tracking the device *in vivo*, and achieving real-time visualization.[112]

1.2.4.2 Magnetic Elastomers

Magnetic elastomers are composite materials composed of highly crosslinked polymeric matrices loaded with magnetic particles.[101,102] Due to the limitations of conventional magnetic elastomers, including low flexibility, deformation and sensitivity to externally applied magnetic fields, a new generation of magnetic elastomers was optimized with MNPs and highly elastic polymers for achieving obvious deformation, adjustable elastic modulus and high sensitivity to magnetic fields.[101] Although ferrogels and magnetic elastomers show some similarities, the

crosslinking degree of polymeric matrices in ferrogels is lower and MNPs in ferrogels show higher flexibility in diffusing through the network and form agglomerates.[102] According to the spatial distribution of MNPs (whether the composite was exposed to magnetic fields before the polymer crosslinking process), the magnetic elastomers can be classified into two types: isotropic (elastomer-ferromagnet composites) and anisotropic (magnetorheological elastomers).[102] Many studies illustrated that the elastic modulus and shear modulus of isotropic and anisotropic magnetic elastomers will both increase with the increase of applied magnetic fields.[102]

Apart from these DDSs, microbubbles incorporated with MNPs have been proven to be suitable drug delivery carriers for magnetic targeting.[22] Although much progress has been made to advance microscale magnetic field triggerable DDSs, challenges remain. Further study of the biocompatibility of polymer matrices with magnetic triggering is still necessary.[14] Besides, the systems should be designed not degrade obviously over various induction because the degradation may change the function of the device unpredictably.

1.2.5 Macroscale Magnetic Drug Delivery Systems

Owing to the limitation of low drug loading capacity, it is difficult for nanoscale and microscale DDSs to achieve extended drug release.[120] Moreover, their targeting ability could be affected by the complex biological environment *in vivo*. However, DDSs at the macroscale are receiving increasing attention because it is possible for these systems to spatiotemporally control drug availability at a target site.[120] According to the drug release mechanism, these macroscale DDSs can be roughly divided into two categories, polymer scaffolds (passive DDSs) and stimuli-triggered devices (active DDSs).[121]

1.2.5.1 Magnetic Macroporous Scaffolds

Porous scaffolds, which are made from natural or synthetic polymers, have been widely studied as drug carriers and scaffolds for tissue engineering because of the 3D environment.[94] Although porous scaffolds show excellent efficiency in preserving and delivering therapeutic agents and cells, it is difficult to achieve precise and on-demand drug delivery as the drug release is mainly governed by passive release mechanisms (e.g. molecular diffusion and scaffold degradation).[122] According to the pore size, the porous solid network structures were mainly categorized into two groups: macroporosity (between 100 and 200 nm) and mesoporosity (smaller than 100 nm).[90] Active porous scaffolds which can be responsive to external stimuli have been applied in controlled drug delivery.[94] As a result of their stimuli sensitivity, active drug release with high flexibility and reproducibility can be realized.

As an essential trace element in mammalian, silicon is widely distributed in human tissues.[29] Polydimethylsiloxane (PDMS) has been intensively studied as the matrix material for fabricating scaffolds with stochastic porous structures because of its special properties such as chemical inertness, elastomeric properties, biocompatibility, low toxicity, high flexibility, nonflammability, ease of fabrication, low manufacturing costs, optical transparency, and gas permeability.[123,124] In addition, it has been proved that PDMS sponge is a porous and hydrophobic polymer with attractive features like large absorption capacity, high porosity, lightweight, low density, low surface tension and energy, good elasticity (to be deformed into any shape), repeated compressibility (in either air or liquids without collapsing), and excellent recyclability.[123,125] Furthermore, only a few hours are enough for the preparing process of PDMS sponges and large-scale production can be easily realized for the benefits of the proposed sugar-templating process. Extrinsic magnetic stimulation and carbonyl iron (CI) microparticles which are incorporated into PDMS sponges (with 3D connected macropores) can provide a tunable force for triggering drug release from the

microspouter.[126]

Tolouei et al. designed and fabricated a two-compartment biomaterial system which is composed of a magnetically actuated biphasic ferrosponge nested within an outer macroporous gelatin hollow scaffold (Figure 1.10).[104] The outer scaffold is designed to provide infiltration and residence for cells due to its interconnected macroporous structure.[104] The inner compartment comprises a Fe_3O_4 loaded alginate sponge (top region) and a pure alginate sponge (bottom region). As a result, the biphasic ferrogels can exhibit obvious deformation under magnetic fields and release drug payloads from the bottom half, endowing the device with delayed and magnetic field triggerable drug delivery behaviors. [104]

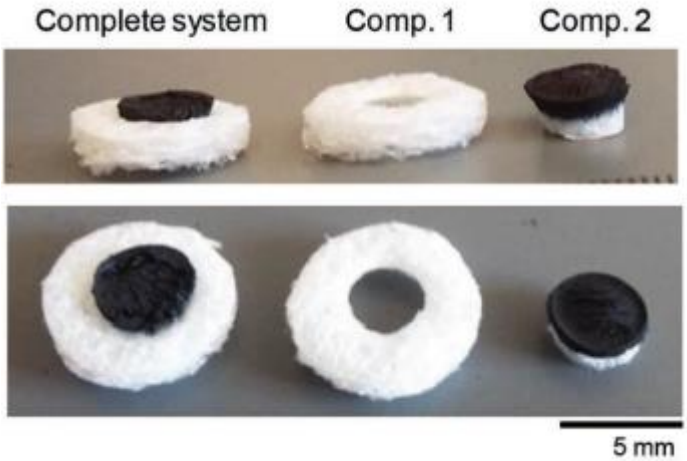

Figure 1.10. A two-compartment biomaterial system comprises an outer gelatin scaffold (Comp.1) and an inner biphasic ferrogel (Comp.2).[104]

1.2.5.2 Magnetically Triggerable Implants

In recent years, implantable DDSs have been extensively studied for achieving controlled drug release when oral drug administration is not the optimal choice.[121,127] In local disease treatment, these implants are superior to conventional injections because of their ability to go through physiological barriers without triggering pain for patients which are related to multiple invasive skin punctures.[127] Many studies have illustrated that implants can show great

efficiency in suppressing inflammation and angiogenesis.[128] Generally, an implantable DDS is composed of a reservoir, a micro-scaled chip and a pump.[127] The reservoir should be made up of biocompatible materials with strong mechanical properties. Most implantable DDSs in clinical applications were designed to be a cylinder without any sharp edge for easing the implantation and explantation.[127] The size should be customized according to the drug administration frequency and the drug release duration for the device.[127] Because active DDSs are more versatile than diffusion-based devices in achieving complex drug release kinetics, active drug release implants have been extensively studied for the treatment of cancer, diabetes and sclerosis.[127] There are some points to consider when developing these devices for actual clinical applications, for example, ideal implants should be small in size.[121] Notably, the retrieval of implants after use is also important as most commercially available implants are fabricated from non-biodegradable polymers.[110,129] Moreover, therapeutic agents loaded in the device should maintain stability until being released.[127] With the development of 3D printing technologies, the personalization of implantable DDSs could be realized.[129] In order to save space for the device, magnetic actuation shows great advantages over electric power supplies and electronic circuit components.[127]

Shademani et al. proposed a microspouter as a novel drug delivery device to provide an actively and precisely controllable approach for on-demand local drug delivery (Figure 1.11).[126] A 3D-printed positive mold was used to fabricate the PDMS reservoir. Then the magnetic sponge was installed in the demolded (peeled off from the mold) round shape reservoir (4 × 1.5 mm, diameter × depth) and the drug was loaded. In order to seal the microspouter, a thin PDMS membrane was firmly bonded to the top of the sponge and reservoir through plasma treatment. An aperture (90 × 90 μm^2) was made by laser ablation at the center of the PDMS membrane. Methylene blue (a good water-soluble model drug) and docetaxel (a hydrophobic drug with poor water solubility) were chosen

to investigate the drug release and functionalities for controlled drug release of the microspouter. The experiments demonstrated that the duration of release and dose can be simply and accurately controlled by this implantable device. Besides, the activity and effectiveness of docetaxel stored inside the device can be maintained even after over one month of encapsulation. Furthermore, a safe and long-term drug release would be possible to achieve because of a low background leakage and large drug loading ability.[126]

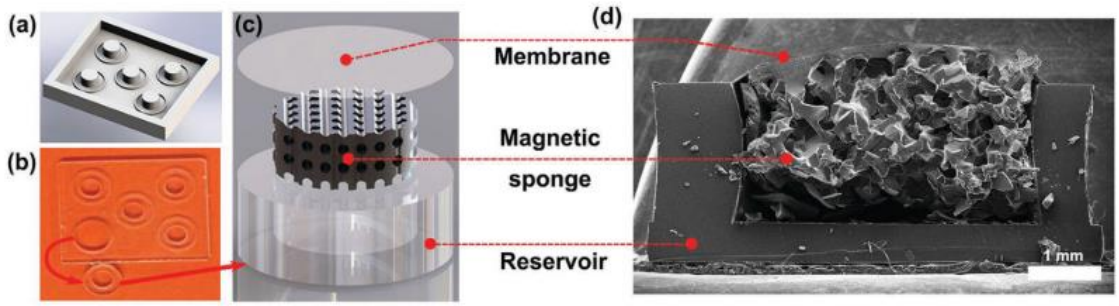

Figure 1.11. (a) 3D-printed mold for reservoir fabrication. (b) Image of demolded PDMS layer and one typical reservoir punched out. (c) Schematic-exploded diagram of the device components. (d) SEM image of the device from the cross-section view.[126]

Up till now, magnetic DDSs have not been successfully translated into clinical applications because of the relatively low efficacy and difficulties in controlling MNPs.[26] With the development of personalized medicine, more efforts should be devoted to developing novel magnetic field triggerable DDSs which can deliver and release drugs to individual patient safely and efficiently.[130]

1.3 Hot Melt Extrusion and Fused Deposition Modelling 3D Printing

Compression and injection molding are traditional approaches to fabricate medical implants which are loaded with API solutions or suspensions through the coating and spray-coating techniques for local drug delivery.[131] As a novel technology for rapid prototyping, 3D printing technology has been widely applied in many domains, such as fashion, architecture, defence, aerospace, automotive engineering and disease therapy in recent years.[129,132–134] With the development

of this promising technique, a more efficient and flexible tool was presented for obtaining digitally designed custom preparation of implantable dosage forms, medical devices, surgical instruments and tissue engineering scaffolds.[135,136] This instant desktop manufacturing is of great importance in emergency care and individualized therapy.[136] Additionally, pharmaceutical 3D printing plays an important role in precision medicine because of the ability to provide a more efficient method for targeted drug delivery.[137] In this way, APIs could be incorporated into scaffolds for sustained release instead of post-fabrication coating for burst release.[138] These properties are especially important for chemotherapeutic drugs with narrow therapeutic window and special patient groups, such as pediatric and geriatric patients.[137,139] Nowadays, 3D printing is regarded as a scalable manufacturing process and can be employed to prepare medical devices, implants, tissue regeneration, pharmaceutical dosage form, and personalized medicine.[131] Implants could be either directly manufactured using 3D printing technologies or prepared using a 3D printed mold with castables materials.[138]

3D printing technology which also known as additive manufacturing is a manufacturing process based on computer-assisted design (CAD) to describe the geometry and size of objects to be built.[138] The CAD model was then exported to rapid prototyping stereolithography (.stl) file format through creating sliced layers of the model.[139] Although the additive manufacturing process is relatively slow when compared with the traditional polymer manufacturing process (subtractive and formative manufacturing), it allows the CAD-guided manufacture of 3D structure with high shape complexity and multifunction.[136] The shape and geometry of the printed dosage forms can influence the drug release rate.[140] By modulating the dimensions and infill pattern/percentage, drug release dosage can be customized.[141] In practical applications, postprocessing is required for the 3D printing process to remove support structure or improve surface qualities because the fabricated layer thickness is normally between 15 and 500 μm

whereas naked eyes can recognize the layer thickness higher than 50 μm.[136]

The advantages of using 3D printing technologies in the development of DDSs are: (1) fabrication of complex shapes and geometrics with higher possible shape fidelity and accuracy, (2) on-demand production of various compositions for personalized dosage forms in an emergency, (3) reduce waste and solvent applications, (4) streamline the manufacturing process of pharmaceuticals, (5) precise control over the special distribution of APIs within the dosage form with a minimized medication error.[131,141–143] Last but not least, these 3D printed implants have been proved to be capable of eliminating burst release and achieving zero-order release due to the ability of this technique to modulate drug release kinetics through the control over geometry, surface/volume ratio and feed materials.[131]

Liquid-based, solid-based and powder-based are the three main categories of 3D printing technologies (Figure 1.12).[138] Among these 3D printing technologies, drop-on-powder and fused deposition modelling are the most common approaches to fabricate drug delivery implants.[131]

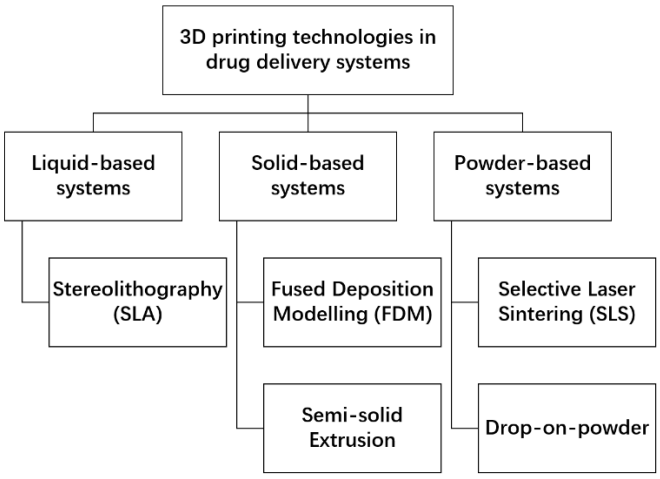

Figure 1.12. Schematic view of various 3D printing technologies that commonly used in fabricating drug delivery systems.

1.3.1 Powder-based 3D Printing

Drop-on-powder, also known as binder jetting, is a typical powder-based (PB) 3D printing technology. It was developed by the Massachusetts Institute of Technology (MIT) in the 1980s.[144] In 1994, this technology was licensed to Z-Corporation Inc. for commercialization.[138] It is regarded as the first technological adaption of 3D printing for pharmaceutical demands.[143] A wide variety of materials could be applied in the powder-based process, including metals, polymers, ceramics and metal-ceramic materials.[138] This process utilizes an ink-jet nozzle that can dispense the ink solution onto a flattened powder bed (Figure 1.13).[131] The ink solution are required not to dissolve or chemically react with powders.[145] The workflow can be divided into three steps: (1) the powder supply platform is lifted and the fabrication platform is lowered, (2) a new powder layer is spread onto the previous powder bed surface by using the roller horizontally across the fabrication platform, (3) particles of the powder carrier can be adhered together by organic or inorganic binders to form an agglomerated object in a layer-by-layer manner because of adhesive forces or a hydraulic cement setting reaction.[138,145] After completing these three steps, the unbound powder could be carefully removed from the remained parts through vacuuming or brushing because the de-powdering process is critical for printing porous objects especially when the pores and interconnections are small.[145] Postprocessing by resin infiltration or sintering is necessary to remove residual volatile solvents and improve the mechanical properties of final products.[136,139,145] In this event, the final 3D printed products with desired geometry can be created by stacking agglomerated layers in sequence. As a result, the PB 3D printed oral dosage forms, such as tablets, are similar to fast-disintegrating tablets because they are composed mainly of powders with loosely bound particles. Although there are many different 3D printing techniques suitable for pharmaceutical applications, the first Food and Drug Administration (FDA) approved 3D printed medicine (Spritam®) was developed through TheriForm® technology, which is originally

derived from a PB 3D printing technique.[137] Owing to the printing nature, formulations, and process optimization, the Spritam® (levetiracetam tablet) shows a highly porous internal environment and micron-scale pore size that can dramatically increase the surface area. The ultra-rapid drug dissolution and release after oral administration could be achieved.[146]

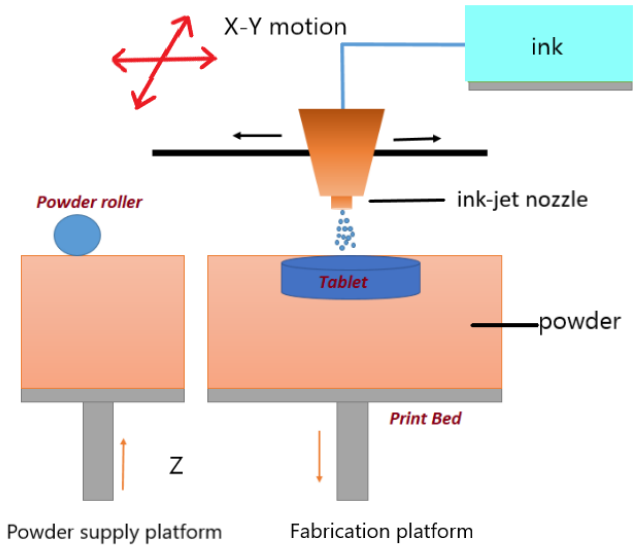

Figure 1.13. Schematic of the powder-based 3D printing process of a tablet.

1.3.1.1 Processing Parameters for Powder-based 3D Printing

The formulation development of PB 3D printing consists of two distinct formulation constituents, the ink and powder mixtures.[137] Hence, the powder topology and the reactivity between the powder and the ink are the two factors to influence this technology.[147] According to the location of the binder, PB 3D printing could be differentiated between the binder contained within the ink formulation and the binder distributed in the powder particles (Table 1.4).[136] In other words, there are three options for the ink composition: (1) API(s) and binder(s), (2) binder(s) and (3) solvent(s).[137] For the first option, applied APIs and binders are required to be dissolved or dispersed.[137] The binder which is composed of a solvent or solvent mixture will be responsible for particle fusion. Film-forming polymers and polymer dispersions are commonly used binders. The binder should be selected according to the powder type (Table 1.4), for example,

aqueous binders could be used for hydrophilic powders whereas organic solvents are suitable for hydrophobic polymer powders.[136] Additionally, the flowability and wettability of powders should be considered.[145] Physicochemical properties of the ink have a significant effect on the printability, so the surface tension and viscosity should be adjusted according to specific devices.[137] Jetting trials could be used to test the ink performance, then the particle size could be adjusted accordingly to ensure reliably jettable ink.[137] Therefore, the optimization for PB 3D printing is complex.[137]

Table 1.4. Classification of materials used in powder-based 3D printing.

PB 3D printing			
materials	binder component in the ink	binder component in the powder	
binder	inorganic (colloidal silica) organic (polymeric resin, polymeric emulsion)	organic solvents: e.g. chloroform	aqueous ink
powder	metal, ceramic	water-insoluble particles: PLA, PLGA, PCL	water-soluble particles: starch, plaster, cement

The typical mechanism of the PB 3D printing process can be described as three steps: (1) dissolution of binder in the printing liquid, (2) infiltration of binding liquid (ink) into the powder bed, and (3) solidification upon drying.[131] The concentration of binder is the determining factor for the mechanical strength of the final product as the increase of binder concentration can lead to lower porosity and enhanced strength.[131] As a result, the fluid properties of the ink should be evaluated. Besides, the particle size of the powder bed has a critical effect on the binder distribution, layer thickness and porosity of the final product.[145] However, the effect of particle size on the quality of the final structure is still contradictory. Some studies pointed out that fine powders (< 20 μm) can achieve higher strength, whereas others suggested that fine powders may cause bleaching issues during the printing process.[139] The ideal value of average particle size is between 50 and 150 μm.[131] Furthermore, other processing parameters worth consideration are

nozzle diameter, droplet distance, printing speed, droplet frequency and velocity.[131] As the typical layer thickness is around 100 μm, the resolution is a limiting factor for the geometry flexibility of the PB 3D printing process.[145] To ensure dimensional accuracy and repeatability of fabricated products, layer thickness, printing delay, build orientation, postprocessing methods, ink volume and geometric properties should also be considered.[145]

Therefore, the main challenges of the powder-based 3D printing technique are the limited selection of ink formulation and the adjustment of dose composition.[135] Despite the above-mentioned advantages, applications of this technology are limited by low resolution and large pore sizes of fabricated scaffolds.[145] Moreover, fabricated porous scaffolds usually possess low mechanical strength which is related to their pore volume and distribution.[145] As a result, common mechanical tests are not suitable for obtained products.[137] Furthermore, low fabrication speed and the reusability of materials should be further investigated.[137]

1.3.2 Fused Deposition Modelling 3D Printing

The fused deposition modelling (FDM), also known as fused filament fabrication (FFF), 3D printing technology was first patented by Stratasys Ltd. in 1989.[131] Commercially available filaments (with the diameter of 1.75 or 3.0 mm) from a spool are feed materials for the print head of FDM 3D printers (Figure 1.14).[136] The physical state of the feedstock changes from solid to semisolid or liquid during the heating process.[140] The operation principle of FDM 3D printers can be described by four modules: the feed zone, the hot zone, the deposition zone and the motion system (belt driven H-frame gantry).[148] The molten filament was extruded out from the printing nozzle and deposited onto the building platform in the x-y axis.[149] After the completion of one layer, the building platform moves down in the z-axis to allow the printing of the next layer on the previous one.[149] This process was repeated until the final layer was printed. In recent years, FDM

is the most widely studied 3D printing technology in fabricating DDSs because of its low cost, simple operation, high reproducibility and strong control over drug release kinetics.[135] The fabrication process can be simplified as follows: (1) extrusion of molten materials, (2) deposition of extrudates in a layer-by-layer manner for obtaining predetermined geometry, and (3) solidification upon cooling.[131] Postprocessing might be required for FDM 3D printed products due to their rough surface topography.[150] Although FDM can print objects without chemical modification, its limitation in biomedical applications should be considered, like high processing temperature, slow manufacturing speed, poor surface quality and low z-axis resolution.[138] Furthermore, FDM 3D printers equipped with multiple printheads can fabricate multiple-drug containing devices.[132]

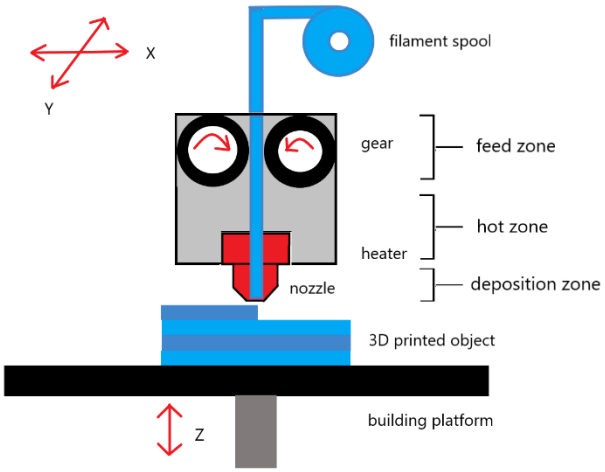

Figure 1.14. Schematic of a fused filament modelling (FDM) 3D printer.

As mentioned earlier, the printing materials of FDM are supplied in the form of filaments.[133] These materials are required to have high thermoplasticity whereas the majority of pharmaceutical grade polymers are not thermoplastic.[151] Therefore, acrylonitrile butadiene styrene (ABS) became the commercially available filament at the very beginning. Then other feedstock materials were applied, namely polycarbonate (PC), polyetherimide (PEI) resin,

polyphenylsulfone (PPSF), polyamides (Nylon), high-impact polystyrene (HIPS), high-density polyethylene (HDPE), polymethylmethacrylate (PMMA) and poly(ε-caprolactone) (PCL).[152] In the pharmaceutical field, plastics such as polylactic acid (PLA), ethylene vinyl acetate (EVA) and polyvinyl alcohol (PVA) in the form of filaments were also investigated for introducing APIs.[153] The 3D printed products of thermoplastics are light and some of them show excellent mechanical strength.[150] However, printable filaments with suitable physicochemical properties are required for the FDM printing process.[135] Until recently, the main challenges of FDM 3D printing are still related to the paucity of suitable filaments composed of pharmaceutical grade ingredients.[143,153–155]

As a common method for loading APIs in filaments, the impregnation method is always related to low drug loading capacity with a burst release.[135] As designing and developing new biomaterials that suit the current 3D printing instruments is one of the future trends in biomedical fields, hot melt extrusion (HME) was applied to fabricate filaments and achieve homogeneous molecular dispersion of APIs in the polymer matrix.[135,138]

1.3.2.1 Processing Parameters for Fused Deposition Modelling 3D Printing

Table 1.5. Common defects of FDM 3D printed products and possible reasons.

Defects	Reasons
banding (ripples on surface)	vibration in the building platform
leaning (off-axis products)	drift in the building platform
warping (product distortion)	thermal expansion/contraction
stringing (wisps of filament)	filament elongation during the off state of printing nozzles
collapse (loss of cavity)	sagging layers or excessive mass/energy input
imperfection (ununiform scaling)	poor and inconsistent flow of material
residuals (unbound parts)	incomplete printing

Several defects (Table 1.5) of FDM 3D printed products are related to the

equipment and processing parameters.[156] As a result, monitoring and controlling for these defects during the manufacturing and packaging process is vitally important to avoid affecting the appearance and properties of 3D printed products.[156]

Critical processing parameters of FDM can be categorized into machine-specific, operation-specific and material-specific parameters (Figure 1.15).[157] The main limitation of FDM 3D printing in pharmaceutical applications is the required high temperature for the softening of polymer filaments, which may cause the degradation of a large number of APIs and excipients.[143] As a result, consideration should be given to selecting suitable printing temperatures (T_p) for various polymers, otherwise, extrusion flow may not be adequate because of inappropriate melt viscosity.[158] Taking the higher T_p as an example, possible problems and reasons were listed in Table 1.6.[158]

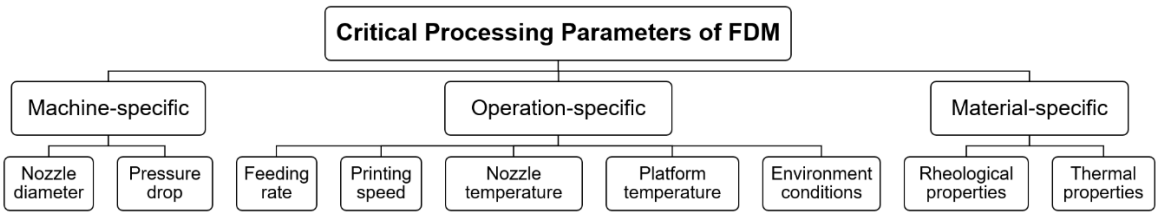

Figure 1.15. Critical processing parameters of FDM 3D printing.

Table 1.6. Possible problems and reasons in FDM 3D printing because of the higher printing temperature.

Problems	**Reasons**
long overall cycle time	longer cooling time
discoloration of extrusion	T_p>T_m of the drug
thermal instability	short residence time in the equipment
decomposition of drug	T_p>T_d of the drug
lower dissolution rate	more tortuous and less porous product smaller median pore radius increase of polymer-free volume less permeable matrix network inhibits drug diffusion better coalescence of molten polymer

Because feed materials are required to possess rheological properties in the FDM 3D printing process, more efforts should be made to the characterization of these parameters, including nozzle diameter, pressure drop, feeding rate, and thermal properties of feed materials.[131] Apart from these parameters, nozzle temperature, printing speed, platform temperature should be optimized according to the specific feed material.[131] The shape and geometry of the printed dosage forms also influence the drug release rate.[140] By modulating the dimensions and infill pattern/percentage, drug release dosage can be customized.[141] Furthermore, the surrounding environmental conditions (convection conditions and envelope temperature) can influence the cooling profile of the deposited products significantly and therefore determine the bond formation and strength of the fabricated structure.[131] Therefore, it is necessary to find a balance among all these parameters due to narrow processing windows for most FDM instruments.[136]

1.3.2.2 Hot Melt Extrusion

In pharmaceutical applications, extrusion is defined as a process for preparing solid dispersions or solutions of uniform shape and density through a die or an orifice under controlled conditions.[158,159] The main aim of this technology is to improve the bioavailability of poorly soluble drugs or to fabricate controlled release dosage forms because drug particles can be embedded in polymers homogeneously.[158] The screw extruders are the most commonly used category of extrusion equipment in the pharmaceutical industry.[159] Melt processing provides an approach to produce materials with high reproducibility and homogeneous distribution of drugs within the polymeric matrix because the polymer was melted instead of being solubilized in a solvent.[160]

Most available therapeutic agents are in a crystalline state, which is defined as a regularly sequenced lattice structure.[159] However, the application of crystalline

products is mainly limited by poor dissolution properties. The definition of solid dispersion is the API incorporated into an inert carrier being dispersed in the solid-state evenly.[161] Preparing amorphous solid dispersions from the crystalline state of the API has the potential to provide controlled, instant, delayed, sustained and targeted drug release with increased bioavailability.[142,148,162] HME was first used in the plastic and rubber industry in 1930, then has been promoted in pharmaceutical research since the 1970s as a preparation method for various dosage forms.[142,158,163] In recent years, it has been demonstrated that the HME process represents a feasible way to fabricate various acceptable DDSs, such as granules, pellets, implants, amorphous solid dispersion, transdermal patches and transmucosal films.[164–166] This technique can realize the combination of melting and mixing of materials through the rotation of screws in the heated barrel.[167] Since the development of pharmaceutical FDM 3D printing technique is mainly limited by available thermoplastics, thus impregnation and HME are regarded as the dominant methods to fabricate drug-loaded filaments.[136,140] However, the drug loading capacity of polymer filaments is low through the impregnation/incubation in organic solvents by passive diffusion (soaking).[168] Many problems are related to this method using organic solvents, including solvent emission, the residual solvent in final products, lower drug stability, long processing time and drying time.[166] Consequently, the combination of HME and FDM 3DP was developed to increase the range of materials that could be processable with FDM, this approach has the potential to produce more homogeneous filaments with higher drug loading capacity.[143,155] The rotation of screws inside the heated extruder can accelerate the spread and dispersion of APIs in the matrix.[169]

The possible mechanism of the filament fabrication using a typical twin-screw extruder was illustrated in Figure 1.16.[170] HME is a continuous and solvent-free process of forcing the raw materials to be blended in rotating screws at increased temperatures until being extruded through a die, resulting in a filament of uniform

characteristics.[132,171] At the end of the extruder, a rotating device coupled with a spool could be used to collect extruded filaments.[149] The rotating speed of the spool could be adjusted to obtain the desired diameter of filaments according to the stretching force if necessary.[149] The other aims of using HME is to increase the dissolution rate of insoluble drugs, generate a homogeneous blend, mask the bitter taste of the API and develop modified-release DDSs with delayed or sustained drug delivery profiles.[142,166] Also, the advantages of HME include simple operating process, ability to scale up, no need of solvents, low cost, environmentally friendly process and the potential of continuous processing.[166,172]

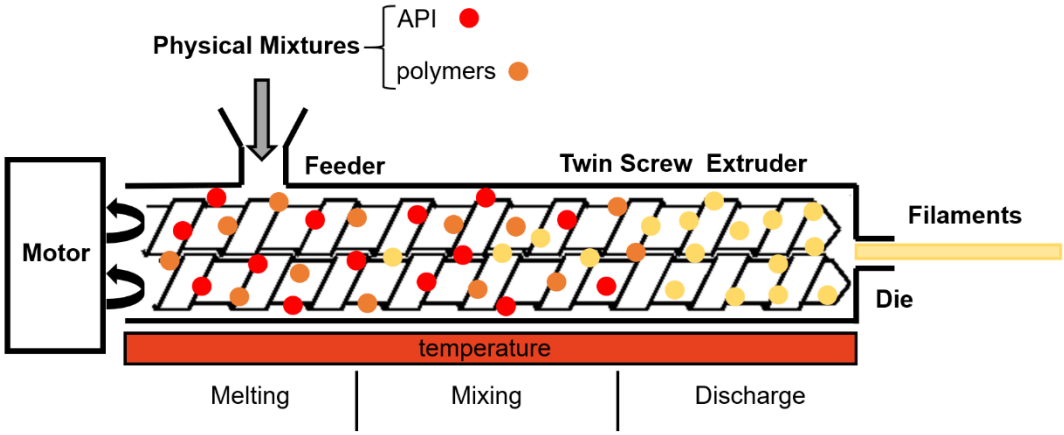

Figure 1.16. Schematic illustration of the filament fabrication using a twin-screw extruder.

Pharmaceutical polymers have been widely applied in HME formulations, such as synthetic cellulose derivatives, methacrylate polymers, polyvinyl pyrrolidone (PVP), polyethylene oxide (PEO) and pyrrolidone-co-vinyl acetate.[165] Because of the high processing temperature during the HME, the active molecules and additives may experience thermal degradation.[165] This leads to a limitation for using thermal sensitive drugs and excipients in the HME process.[165] Moreover, most hot melt extrudable pharmaceutical grade polymers are not suitable for FDM 3D printing in good quality because of deficient properties.[157] To clarify, more than 3000 materials are suitable for HME-based processes whereas only 30 materials

are available commercially for the FDM process.[173] Melt-blending can provide a cost-effective, convenient and mature solution by combining two or more different polymers with various properties into a single matrix material.[173] As a result, the final dosage form can be designed and fabricated with suitably flexible properties to overcome the material shortcomings of polymers for the following FDM process.

1.3.2.3 Processing Parameters for Hot Melt Extrusion

Various processing parameters have a great effect on the filament preparation of HME. These parameters can be classified as formulation-specific, equipment-specific, environment-specific and operation process-specific parameters (Figure 1.17).[163,170] These parameters should be optimized according to specific conditions, like the component weight fraction. For example, the higher content of the polymer matrix results in the induction of lower shear stress during the extrusion process and lower torque in the extruder.[170]

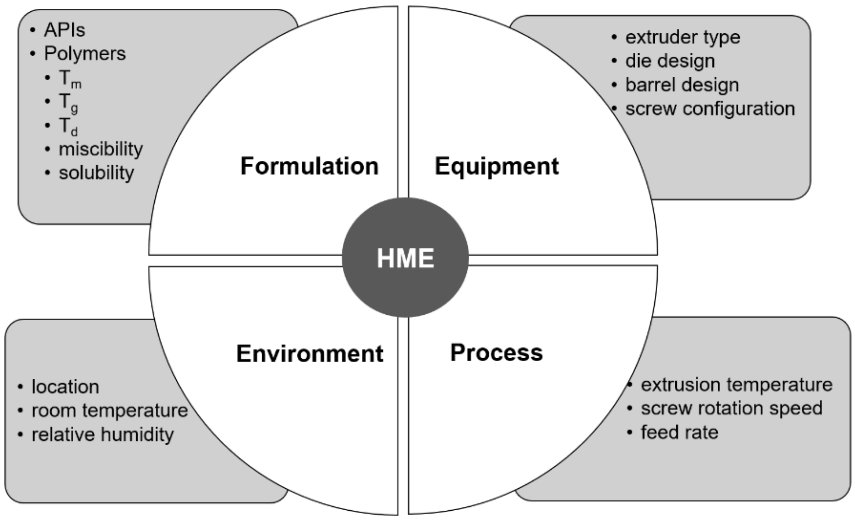

Figure 1.17. Matrix diagram of the critical processing parameters in hot melt extrusion.

It is believed that the selection of barrel temperature during the extrusion process has a critical effect on the viscosity of the molten mixture, the residence time in

the barrel and the physicochemical properties of the extrudates.[170] Therefore, the extrusion temperature should be set above the glass transition temperature (T_g) and the melting temperature (T_m), but below the degradation temperature (T_d) of raw materials at the same time.[170] If the extrusion temperature is too low, the viscosity of the melted materials is not low enough, the torque of the extruder will increase and the mixing ability will be weakened.[170] Therefore, the lower extrusion temperature may lead to the roughness imperfection on the surfaces of the filaments.[174] The selection of the suitable extruder type is important for increasing the efficiency of the process.[170] Most screws are made from surface-coated stainless steel for reducing friction and chemical reactions.[159] Twin-screw extruders present advantages over single-screw extruders for easier material feeding, high kneading and dispersing capability, shorter residence time, lower risk of overheating, better blending properties, higher flexibility and process productivity for pharmaceutical components.[150,159] A twin-screw extruder consists of two co-/counter rotating screws in a single barrel.[167] The fully-intermeshing twin-screw extruders are superior to non-intermeshing extruders as they can reduce the non-motion and prevent the localized overheating of materials.[159] Therefore, the fully-intermeshing co-rotating twin-screw extruders can provide an efficient approach to produce a homogeneous blend with finely distributed APIs.[159] To increase the mixing efficiency, an optimized screw configuration should be designed by using various screw elements, including conveying elements (Figure 1.18A), distributive mixing elements (Figure 1.18B), dispersive mixing elements (Figure 1.18C) and discharge elements (Figure 1.18D).[169,175] Distributive mixing includes melt division and recombination, whereas dispersive mixing includes shear and elongation mixing.[150] The screw design of the extruder could be described by two geometrical parameters, the diameter of the screw (D) and the ratio of the screw length to its diameter (L/D).[170] The decrease of the barrel filling volume and the increase of feeding rate or the screw rotation speed can both result in a decrease in the extrusion duration (residence time) of materials.[170] It is noteworthy that higher screw speed may lead to the degradation

or amorphization of the materials, whereas the lower screw speed is related to the formation of cocrystals.[170] Due to the increase of torque and pressure in the extruder die, the increase of feed rate may result in the blockage in the extruder and the failure of the extrusion process.[170] The increase of the screw diameter and barrel size can achieve continuous operation successfully.[163] Polymeric matrixes show a high tendency to absorb water according to the hygroscopic nature of the formulation.[148] The moisture absorption of filaments will lead to increased flexibility and subsequent squeezing problems by feed gears of FDM 3D printers.[176] Therefore, the products should be prepared and stored appropriately to prevent mass changes related to humidity and temperature.

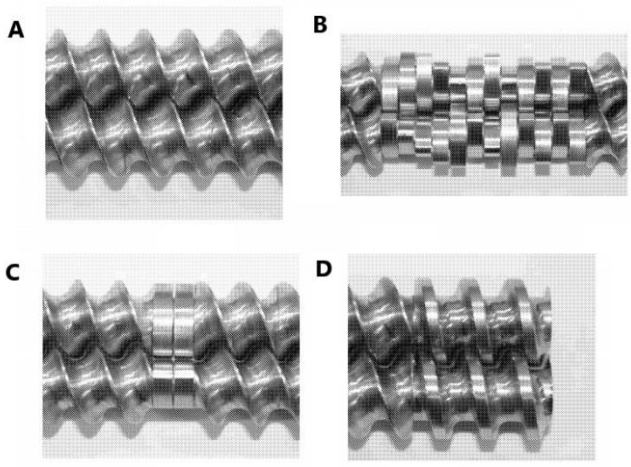

Figure 1.18. Photographs of four types of twin-screw elements: (A) conveying configuration, (B) distributive mixing configuration, (C) dispersive mixing configuration, and (D) discharge configuration.[175]

1.3.2.4 Suitable Polymeric Materials

Based on these premises, the fundamental steps of fabricating DDSs through continuous HME-FDM 3D printing are illustrated in (Figure 1.19).[142] As limited suitable feedstock materials are the main challenge for manufacturing controlled release dosage forms through FDM 3D printing, selecting suitable materials is an inevitable step for designing a pharmaceutical dosage form.[173,174] A pre-step (like milling or sieving) is necessary to ensure the form of polymers is compatible with

the API and to achieve homogeneous drug distribution in extruded filaments.[140] The functional excipients can be widely categorized into matrix carriers, release modifying agents, fillers, thermal lubricants, plasticizers, stabilizing agents and antioxidants.[159] The selection of appropriate excipients with specific properties in traditional dosage forms share similar results with hot melt extrudates and subsequently 3D printed products.[159] The matrix material plays important roles in storing loaded drugs before being released, determining the drug release rate of dosage forms, and providing adequate mechanical properties.[140] It is vitally important to carefully consider the suitable carrier for the HME-FDM process according to the drug-polymer miscibility, polymer solubility, and the desired function of the final dosage forms.[159] Hence, the physical properties and bulk properties of the material will influence the dissolution behavior and the processability respectively.[173] It is noteworthy that the selection of the suitable drug/polymer ratio is important because of the crystallinity of most API and the amorphous nature of polymers. Filaments loaded with a higher concentration of API can result in less risk of die swelling than pure polymeric filaments because the ordered crystal lattice occupies less molar volume than the randomly structured amorphous structure.[149]

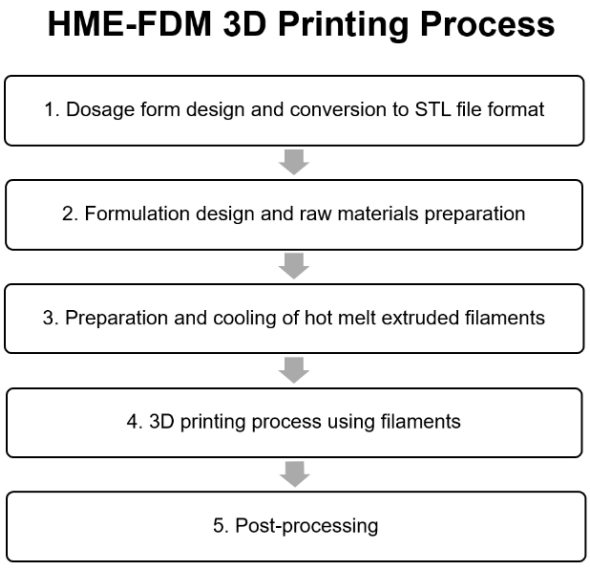

Figure 1.19. Process diagram of the HME-FDM 3D printing process.

Polymers are commonly used materials in API-matrix formulations for preparing high energy solid states, including amorphous solid dispersions.[170] Nowadays, polymers have been regarded as the most used materials for 3D printing technologies.[136] Although the pharmaceutical polymers suitable for HME are already limited, FDM is more strict in melt rheology and mechanical properties of materials than HME.[154] For example, these filaments will crumble once in contact with the feed gears.[148] Hot melt extruded filaments based on insoluble, soluble, enteric and swellable polymers have been successfully applied to fabricate DDSs through FDM (Figure 1.20).[153] Controlled drug release of 3D printed dosage forms can be achieved by adjusting the composition of the carrier polymers and combining these polymers of various categories.[140] An important challenge of FDM 3D printing is the incomplete drug release of 3D printed products due to the restricted drug diffusion rate from their compactness and high density.[174] Erosive or swellable polymers could be applied to increase the drug release rate through gradual disintegration.[174] Most thermoplastic polymers have been proved to be suitable for FDM because of their good thermal stability and melt viscosity at their specific printing temperature range.[141] The FDM processable polymeric substrates mainly include cellulosic, polymethacrylate, polyurethane, polyvinyl caprolactam derivates.[148] In some cases, plasticizers (low molecular weight compounds) are required for the HME process of most pharmaceutical polymers to increase their elasticity and flexibility because of their ability to reduce the interaction between molecules and increase molecular mobility.[148,172] In addition, plasticizers could be used to lower the processing temperature.[149] Consequently, plasticizers show great potential in lowing the risk for the degradation of thermolabile APIs.[159]

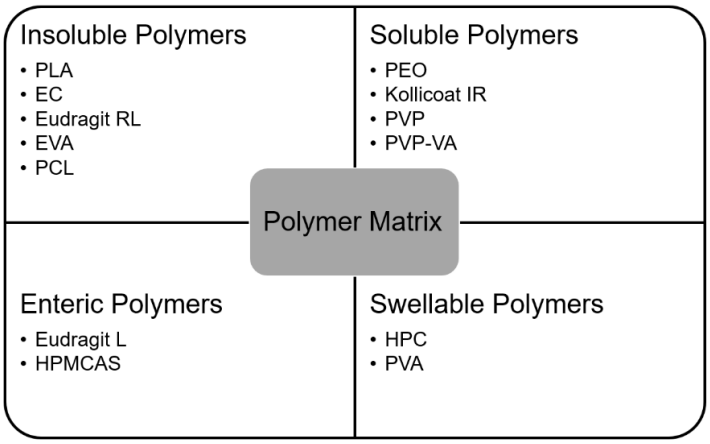

Figure 1.20. Commonly used polymeric carriers in the pharmaceutical HME-FDM process.

Many technological difficulties will appear during the development of new polymeric blends through FDM, so the structure and physical (thermal, mechanical and rheological) properties of these filaments should be carefully evaluated and optimized to ensure that the physicochemical integrity of the API was not affected during the HME-FDM process (Figure 1.21).[148]

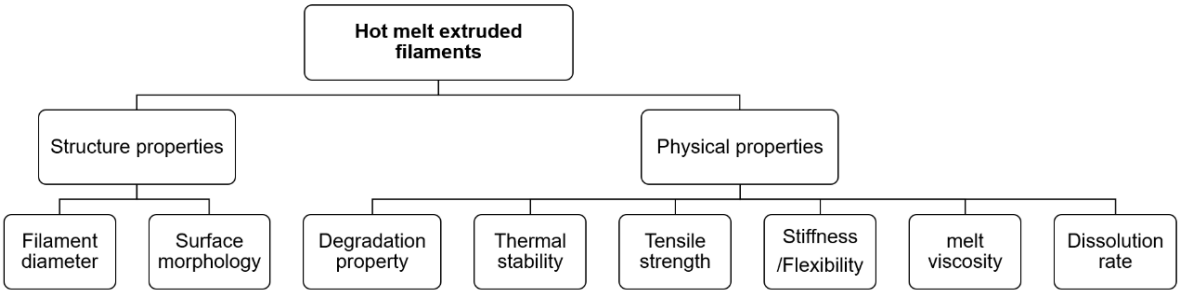

Figure 1.21. Significant properties of hot melt extruded filaments for the FDM 3D printing process.

The diameter of extruded filaments has a critical effect on their printability during the FDM printing process.[174] The die swelling (swelling of filaments once leaving the die) should be avoided to allow good feeding performance.[149] A smooth surface of filaments is necessary for adequate feeding in the FDM 3D printer, so the surface morphology should be evaluated.[149] In order to achieve a continuous

and high-quality FDM printing operation, the filaments are required to possess good mechanical properties to be feedable through the tensile and compressive force between feed gears of the printer and suitable melt flow properties to be printable in the heating zone of the printer nozzle.[157] Excellent thermal properties are required for the FDM 3D printing of drug-loaded filaments to achieve good printing quality because the filaments will withstand high temperature in the heater and nozzle.[150] Flexibility and elasticity are important parameters of the mechanical properties of filaments.[141] In other words, these two parameters can determine the FDM printability of extruded filaments. Stiff filaments can experience more force during feeding and less risk for bending or slipping.[148] Optimum flexibility means that filaments can deform but not break when an external force is applied.[141] Filaments with suitable elasticity can help to attain uniform printing with a lower risk of nozzle blockage and surface imperfections.[141] Suitable melt flow properties of filaments are required to form an adequate pressure drop for preventing clogging in the nozzle.[149] The viscosity and molecular weight of polymer both have a significant effect on the flow behavior of filaments.[149]

In conclusion, the development of suitable polymeric materials for fabricating implants through the HME-FDM process is complex. A comprehensive characterization should be carried out for hot melt extruded filaments and 3D printed dosage forms.

1.4 Aims and Objectives

In this project, the main aim is to develop a portable and integrated device that is suitable for the length scales relevant to human applications under externally applied magnetic fields. The novel hypothesis of the drug release mechanism from the DDS through the application of different magnetic fields and from different directions can be tested by *in vitro* dissolution studies. The composition

of the DDS, including anticancer drug solution, magnetic sponges and anti-inflammatory drug loaded capsule shell, can be fabricated, characterized and optimized.

Objective 1: investigate the development of magnetic field triggerable drug delivery systems and explore suitable pharmaceutical polymers to be used in fused deposition modelling three-dimensional (3D) printer in combination with the hot melt extrusion process.

Objective 2: design an implantable magnetic field triggerable drug delivery system which is simple, effective, feasible and reliable without the requirement of professional training for doctors.

Objective 3: fabricate, characterize and optimize magnetic PDMS sponges by adjusting the sugar mold, magnetic particles content, weight ratios of PDMS prepolymer and curing agents.

Objective 4: prepare and compare various 5-fluorouracil solutions through manually coating these drug solutions onto the surface of PB 3D printed tablets and analyzed the drug release properties.

Objective 5: develop ibuprofen loaded filaments using various release modifiers through HME and FDM 3D printing, then analyze their solid-states, mechanical properties, dissolution behaviors in order to achieve the zero-order drug release for the 3D printed reservoir.

2. Chapter 2: Materials and Methodologies

2.1 Introduction

In order to develop a novel magnetic field triggerable DDS for local cancer therapy, this project has mainly been divided into four parts. The first part is the preparation, characterization and optimization of magnetic-field-sensitive polydimethylsiloxane (PDMS) sponges for localized drug delivery. The second part is the preparation of suitable 5-fluorouracil (FLU) solutions to be loaded in the magnetic PDMS sponges. The third part is the investigation and optimization of the release mechanism for the DDS composed of a 3D printed reservoir and FLU solution loaded magnetic PDMS sponges. The fourth part is the fabrication and characterization of ibuprofen (IBP) loaded ethyl cellulose filaments and 3D printed tablets for developing suitable materials in the 3D printed reservoir. In this chapter, a comprehensive description of materials and methodologies was made based on the four parts described above.

2.2 Materials

The model drugs, 5-fluorouracil (FLU) with purity > 98% and ibuprofen (IBP), were purchased from Hangzhou Longshine Bio-tech Co., Ltd. (Hangzhou, China) and Spectrum Chemical Manufacturing Corp. (New Brunswick, NJ, USA) respectively. A SYLGARD® 184 silicone elastomer prepolymer (Sylgard 184A, Mw ≈ 22 000 $g \cdot mol^{-1}$) and the thermal curing agent (Sylgard 184B, Mw ≈ 15 000 $g \cdot mol^{-1}$) were purchased from Dow Corning Ltd. (Barry, UK). Carbonyl iron (CI) powder (purity ≥ 97%) and Fe_3O_4 powder (< 5 μm) with a purity of 95% were purchased from Sigma-Aldrich (Darmstadt, Germany). White granulated sugar and demerara sugar were purchased from Sainsbury's Supermarkets Ltd. (London, UK) and Co-operative Group Ltd. (Manchester, UK), respectively. The $CaSO_4$ powder of the PB 3D printer was obtained from EMCO Education Ltd. (Portsmouth, UK).

The PLA filament (FilaPrint® premium PLA, 1.75 mm) was purchased from 3D FilaPrint Ltd. (Essex, UK). Ethyl cellulose (EC, Ethocel® Standard 4/10/45 premium) and hydroxypropyl methylcellulose (HPMC) Methocel® K4M Premium CR were kindly donated by Colorcon Ltd. (Dartford, UK). HPMC Methocel® E10M Premium CR was obtained from Dow Chemical Company (Michigan, USA). HPMC Benecel™ K100M PHARM XR was donated by Ashland Industries Europe GmbH (Schaffhausen, Switzerland). Poly(vinyl alcohol) (PVA) with an average molecular weight of 22,000 was purchased from Acros Organics (Geel, Belgium). Soluplus® (SOL), Kollidon® 17 PF, 30 and vinyl acetate 64 (VA64) were obtained from BASF (Ludwigshafen, Germany). Polyethylene glycol (PEG) 6000 was procured from Alfa Aesar (Lancashire, UK). Eudragit® RL PO and RS PO powder were obtained from Evonik Industries AG (Darmstadt, Germany). Triethyl citrate (TEC) was purchased from Thermo Fisher Scientific Inc. (Geel, Belgium). Absolute ethanol (≥ 99.8%) was purchased from Sigma-Aldrich Co. Ltd. (Dorset, UK). Transcutol HP was kindly donated by Gattefosse SAS (Saint-Priest, France). All chemicals used were of analytical or food grade and used as received.

The chemical structure of raw materials is shown in Figure 2.1.

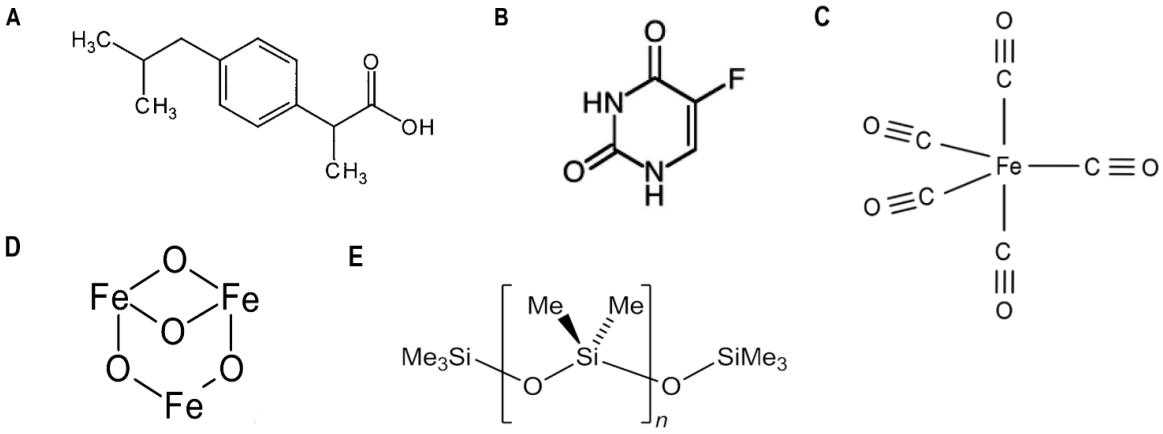

Figure 2.1. Chemical structure of (A) ibuprofen, (B) 5-fluorouracil, (C) carbonyl iron, (D) Fe_3O_4 and (E) PDMS.

2.3 Development of Magnetic Drug Delivery Systems

2.3.1 Preparation of Magnetic PDMS Sponges

About 15 g sugar was fully mixed with around 0.5 mL water with a spatula and then was pressed firmly in a Petri dish (diameter = 5 cm) to form a flat surface. To obtain a mold of connected sugar particles, the Petri dish with sugar was placed in a convection oven (Memmert, UF110, Schwabach, Germany) at 50°C for around 1 h to achieve fusion of sugar.[126,177]

SYLGARD®184 based PDMS sponges were prepared by polymerization of the blend of the prepolymer and the thermal curing agent (with the weight ratio of 10:1).[178] The ferromagnetic particles (CI and Fe_3O_4) were then loaded in the well-mixed PDMS at 0%, 30%, 50%, 100% and 150% (w/w) of the weight of the PDMS in the formulation (Table 2.1).

Table 2.1. Different kinds of PDMS sponge samples prepared with granulated sugar

Composition	Concentration of magnetic particles (%)
Pure PDMS sponge	0
CI/PDMS=30 wt% sponge	23.08
CI/PDMS=50 wt% sponge	33.33
CI/PDMS=100 wt% sponge	50.00
CI/PDMS=150 wt% sponge	60.00
Fe_3O_4/PDMS=30 wt% sponge	23.08
Fe_3O_4/PDMS=50 wt% sponge	33.33

The blend of PDMS (prepolymer and the curing agent) and magnetic microparticles were vortexed and sonicated for 10 min respectively to achieve homogeneous dispersion because the strong polarity and high density make these magnetic particles difficult to be well dispersed in common solvents.[179] After that, the well-mixed blend was poured onto the dried sugar mold and then

infiltrated into the sugar template because of capillary force.[123,180] The Petri dish was placed in the oven again at 70°C for 3 h for the curing process. Finally, the cured blend was immersed in water to dissolve the sugar completely with an ultrasonic cleaning bath (Fisherbrand FB15050, Leicestershire, UK) at 50°C. The obtained sponges containing magnetic particles were removed from the ultrasonic bath and dried in the oven at 60°C for 1 h. After the complete removal of sugar templates, 3D interconnected macroporous PDMS sponges were formed.

2.3.2 Characterization of Magnetic PDMS Sponges

2.3.2.1 Physical Appearance

A Celestron 44347 TetraView LCD digital microscope (Celestron LLC, Torrance, CA, USA) was used to check the uniformity of sugar particles for sponge molds. The formed sponges were physically evaluated concerning color, transparency, brittleness, and integrity. A ROTEK digital microscope (Shenzhen, China) was employed to obtain the surface image of the fabricated sponges.

2.3.2.2 Porosity (Absorbency) Measurement

During the leaching process, the porous structure is generated by dissolving sugar in the sponge, which makes the drug delivery system more porous. Hence, the total pore volume of sponges could be used for the mathematical calculation of the porosity value.[181] Dried sponge cubes (1×1×0.5 cm, length × width × height) were weighed (m_s) and placed in distilled water at room temperature. Then the sponge cubes were compressed gently to let air bubbles come out, so the sponges were filled with water after the removal of the force from the sponge. Finally, the sponges were taken out of the water after water absorption equilibrium and were weighed again (m) to calculate the volume of absorbed water in the sponge cubes (V_w). The water absorbency (N_w) of the sample was calculated by Eq. 2.[125] The porosity of the sponge was eventually determined by both the

volume of the sponge cube (V_s) and the volume of absorbed water as $V_w/V_s \times 100\%$ in Eq. 3. The bulk density (ρ) of the sponge was calculated with Eq. 4. Because the structure of the sugar template has a significant effect on the porosity of the PDMS sponge, three separate samples (different fabricated molds) were used to attain the average value of each kind of sponge.[182] All experiments were conducted at room temperature.

$$N_w = \frac{m-m_s}{m_s} \times 100\% \quad \text{Eq. 2}$$

$$\text{porosity}(\%) = \frac{V_w}{V_s} \times 100\% = \frac{m_w}{\rho_w \times V_s} \times 100\% = \frac{m-m_s}{1\ g/cm^3 \times V_s} \times 100\% \quad \text{Eq. 3}$$

$$\rho = \frac{m_s}{V} = \frac{m_s}{0.5cm^3} \quad \text{Eq. 4}$$

2.3.2.3 Measurement of Sponge Deformation under A Magnetic Field

Magnetic PDMS sponge cylinders (diameter × thickness = 12 mm × 7 mm) with various contents of magnetic particles were placed on a microscope glass slide (thickness = 1 mm). Magnet D (Table 2.2) was placed underneath the sponge cylinder (attached to a glass slide) to provide a magnetic field strength (magnetic flux density) of 355 mT for compressing these sponge cylinders. Then the displacement of the front surface of each sponge cylinder in three different locations under different magnetic flux densities and the average deformation were recorded. Three separate sponge samples from independently fabricated sugar molds were applied for the deformation measurements (n = 3).

Table 2.2. Dimensions of neodymium grade N42 magnets used in the current studies to provide different magnetic flux densities with a distance of 5 mm

Magnets	A	B	C	D
diameter (mm)	19.5	19.5	21.5	19.5
thickness (mm)	2.5	4.5	5.5	9.5
magnetic field (mT)	110	150	204	355

A noncontact rig for characterizing the compression of magnetic sponges was designed. This method is based on a bright-field microscopy (BFM) metrology

system (Figure 2.2) consisting of an Olympus PLN4X (working distance of 18.5 mm, a numerical aperture of 0.1, Olympus Corporation, Tokyo, Japan), a tube lens with a focal length of 180 mm, and an Imaging Source DMK31BF03 CCD camera (The Imaging Source Europe GmbH, Bremen, Germany) mounted on top of a custom-made linear stage having a coarse resolution of around 3.3 µm.

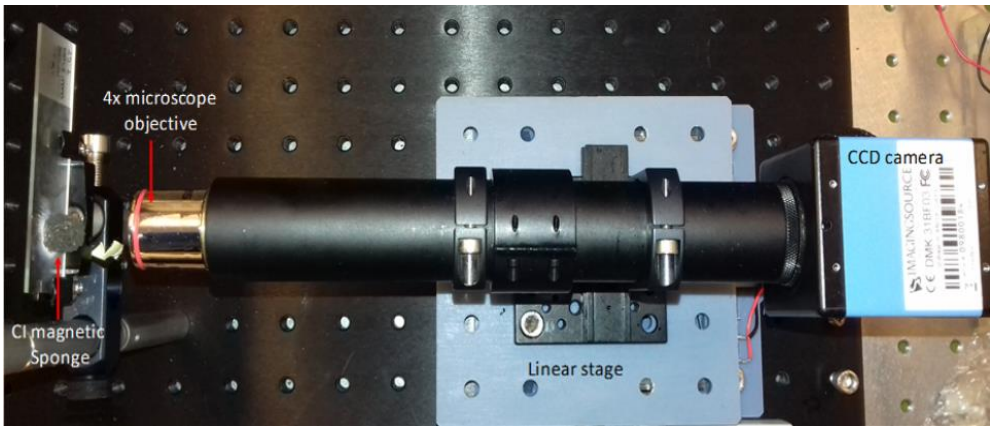

Figure 2.2. Bright-field microscopy metrology system.

As the sponges are made of PDMS and ferromagnetic particles, the illumination source was placed parallel to the measurement device, i.e., facing toward the surface of the sample. The sponges under test were fixed on microscope slides and positioned at the focal point of the metrology system. The measurements were performed by applying different magnetic field strengths using custom-designed neodymium grade N42 magnets (Table 2.2).

By placing the magnets in contact with the back of the microscope slide, visible deformation was observed. This was measured by employing the bright-field measurement device without making contact with the actual sponge (i.e., opposed to contacting methods based on the use of a calliper) to determine the average deformation of the sponge at different magnetic field strengths.

By focusing the microscope on the magnetic sponge surface, the reference position was recorded. Then, placing the magnet near the magnetic sponge, a

deformation was produced, taking the sample out of the focal plane. By refocusing the measuring device and recording the linear stage digital readout, the deformation was accurately measured.

2.3.2.4 Dielectric Constant (Relative Permittivity) Measurement

The dielectric constant (relative permittivity) is measured with an LCR meter (4274A multifrequency LCR meter 100 Hz to 100 kHz, HP/Agilent, Japan) and a parallel plate capacitor (dielectric loss test Jig TJ155B/1, Marconi Instruments Ltd., UK) with two disks (25.4 mm in diameter). The sponge sample was sandwiched between the two plates, so the capacitance (C) was measured out on the screen. As the area of parallel plates (A) is 5.07×10^{-4} m^2, the separation (d) is the thickness of the sponge sample, the permittivity of space (ε_0) is 8.854×10^{-12} F/m, the relative permittivity of the dielectric material between the plates (k or ε_r) could be calculated with Eq. 5.

$$k = \frac{\varepsilon}{\varepsilon_0} = \frac{\mathrm{Cd}}{\varepsilon_0 \mathrm{A}} \qquad \text{Eq. 5}$$

2.3.3 Optimization of Magnetic PDMS Sponges

According to Choi *et al.*, the less uniform the sugar particles are, the higher the porosity of the PDMS sponge can be achieved.[123] PDMS sponges replicated with different sugar templates were fabricated and characterized for comparison. Besides, sponges prepared with different weight ratios of the prepolymer and the curing agent of PDMS were prepared and analyzed.

2.3.3.1 Particle Size Analysis

Data were collected over selected Scanning Electron Microscopy (SEM) images of sugar samples in Section 2.5.4. The average particle size of each kind of sugar magnetic particles and were calculated from 100 random individual measurements through ImageJ software (National Institutes of Health, USA) respectively. Particle size distribution graphs were plotted and analyzed using

OriginPro 8.5.

2.3.3.2 PDMS Sponges Prepared with Different Sugar Molds

The demerara sugar and the mixture of granulated and demerara sugar (in a weight ratio of 1:1) were employed as templates for the preparation of PDMS sponges. All other conditions of the fabrication process were the same as in Section 2.3.1.

2.3.3.3 PDMS Sponge Formulation Optimization

To explore the differences among sponges prepared with different prepolymer/curing agent weight ratios, PDMS prepolymer and curing agents were blended by weight ratios of 15:1, 20:1, 25:1 and 30:1, and followed by the same process of CI particles addition.

2.3.3.4 Recyclability

The measurement of repeated absorption and desorption on water absorbency of sponges is applied for the evaluation of their reusability. To achieve absorption equilibrium, the sponge cylinder samples (diameter × thickness = 12 mm × 7 mm) was immersed in water at room temperature and was compressed gently until no air bubbles came out. Then the absorbency value was calculated by weighing the sponge samples with absorbed water. The samples were squeezed and dried in an oven at 60 °C until the weight was stable. The absorption−desorption procedure was repeated 10 times to check if the absorbency property of the sponge remained intact.

2.3.4 Assemble and Drug Loading of the Device

2.3.4.1 Preparation of Drug Solution

The model drug in this study, 5-fluorouracil (FLU), is sparingly soluble in water and slightly soluble in ethanol, so it is necessary to design how to increase the

dose of FLU loaded into the device.[183] However, the solubility of 5-fluorouracil can be affected significantly by temperature as it can increase more than 12-fold by enhancing the temperature between 25 and 200°C under the constant pressure of 5.1 MPa.[184] Additionally, Singh et al. point out that 5-fluorouracil has good thermal stability when the temperature is less than 278°C.[185] Therefore, the temperature of the solution was increased in the preparing process. 250 mg FLU was precisely weighed and dissolved in a 10 mL volumetric flask with deionized water under magnetic stirring at 70°C until complete dissolution.

2.3.4.2 Device Integration and Assembly

The sponge cylinders which can fit the shape of the hollow space of the reservoir bottom were cut and then immersed into the drug solution. After the sponge cylinder absorbed enough drug solution, it was taken out and placed into the bottom hollow. Then the two parts of the reservoir were closed tightly.

2.3.4.3 Drug Loading of the Device

By comparing the weight change of the device before and after the drug loading process, the amount of drug loaded into the device could be calculated every time afterwards because the weight ratio of the drug to the solution was constant.

2.4 3D Printing Process

2.4.1 PB 3D Printing of Tablets and Anti-cancer Drug Coating

2.4.1.1 Powder-based 3D Printing of Tablets

The tablets with diameters of 10 mm and 13 mm were printed using a ZCorp printer (Z-Corporation, Rock Hill, SC, USA) with a print layer thickness of ~100 µm. The tablet matrix was composed of a $CaSO_4$ based powder, which was a mixture of $CaSO_4$ (< 90%) and vinyl polymer (< 20%) with carbohydrate (< 10%), whereas the liquid binding solution was an aqueous solution containing 2-pyrrolidinone, whose viscosity is similar to water. The printing process only took

< 5 min for one tablet. The printing parameters such as binder volume, jet-dispensing speed, and drops fired were optimized and recorded throughout the printing process. The print head operated at a maximum temperature of 50 °C with a maximum current of 1.7 A and a firing voltage of 0.5 V, which was found to be optimal for the successful and smooth printing of the tablets. An AutoCAD design of the tablets was made using Solidworks (2017 SP5, Waltham, MA, USA) and transferred to the computer connected with the printer in stereolithography (.stl) file format prior to the actual printing process. After the printing process was finished, all tablets were subject to quick drying in the build box before being removed from the powder bed. This drying process was conducted to ensure that the printed tablets were robust enough to withstand the handling process and that any redundant powders were removed easily after the cycle. Since this study aimed to prove the concept of PB 3D printing for the fabrication of anti-cancer drug loaded tablets, only the powder suitable for printing with Z-Corp was used herein. This also eliminated any possibility for the intrusion of the performance and/or safety of the printer. Therefore, the incorporation of the drug in the tablet matrix was not performed at this stage.

2.4.1.2 Coating Process

As mentioned in Section 2.3.3.1, the solubility of FLU in water is very low and could be increased significantly at higher temperatures, therefore, the temperature was increased to 70°C to load more drug in a limited volume of water during the FLU solution preparation.[183] The coating aqueous solutions containing the drug FLU was prepared at the concentration of 2.5% (w/v). Either SOL alone or in combination with PEG was used to develop the coating solution. The composition of the polymeric solutions was adjusted at a drug: polymer(s) 1:1 (w/w) ratio. Various compositions were prepared as depicted in Table 2.3. The coating of the 3D printed tablets was performed using the drop-on-demand technique via utilizing a micro-pipette and depositing the solution onto the surface of the tablet until a homogenous coating was achieved. As mentioned earlier, for

the purpose of this proof of concept study, no additional materials except suitable carrier powders were used in the printer. For this reason, the drug was added to the printed tablets by the coating method. Briefly, around 0.1 and 0.2 mL of the drug solution were dropped manually onto the surface of tablets (diameters of 10 mm and 13 mm) separately by using a 20–200 µL Research® plus pipette (Eppendorf Ltd, Stevenage, UK). After that, the tablet samples were put into the oven at 50 °C for 1 h. The drying process was finished until the weight of tablets would not decrease.

Table 2.3. Drug coating solution 2.5% (w/v) compositions (weight ratio)

Excipients	Solution A	Solution B	Solution C
5-fluorouracil	1	1	1
Soluplus	1	0.5	0
PEG	0	0.5	0

2.4.1.3 Particle Size Distribution Analysis of Printing Powder

The geometric primary particle size distribution of the printing powder was measured with a laser light diffraction analyzer (Helos/Rodos, Sympatec GmbH, Clausthal-Zellerfeld, Germany) equipped with the HELOS sensor and Windox software (version 5, Sympatec, Clausthal-Zellerfeld, Germany). Detection of the particles was carried out using the R3 and R5 lenses with the detection range of 0.5–175 µm and 0.5–875 µm, respectively.

2.4.2 FDM 3D Printing of PLA Reservoirs

The model reservoir was designed using Solidworks (2017 SP5, Waltham, MA, USA) and converted to a stereolithography (.stl) file. For the ease of printing operation, the geometry of the 3D printed reservoirs was selected as cylinder shape because of the large surface area in contact with the building plate.[186] In addition, the cylinder shape without sharp edges has been widely applied in implantable DDSs in clinical uses owing to less invasive implantation and explantation.[127] The currently optimized design was flat cylindrical with a

smoothed edge and consisting of two parts: top and bottom (Figure 2.3A and B). The diameter and height of the reservoir are 19mm and 7mm, respectively. Considering the diameter of the human small intestine is smaller than around 25 mm, the diameter and height of the hollow space for sponges are 12.5 mm and 5mm, respectively.[115] In addition, there is a small aperture (diameter = 1.5 mm) at the center of the top part surface.

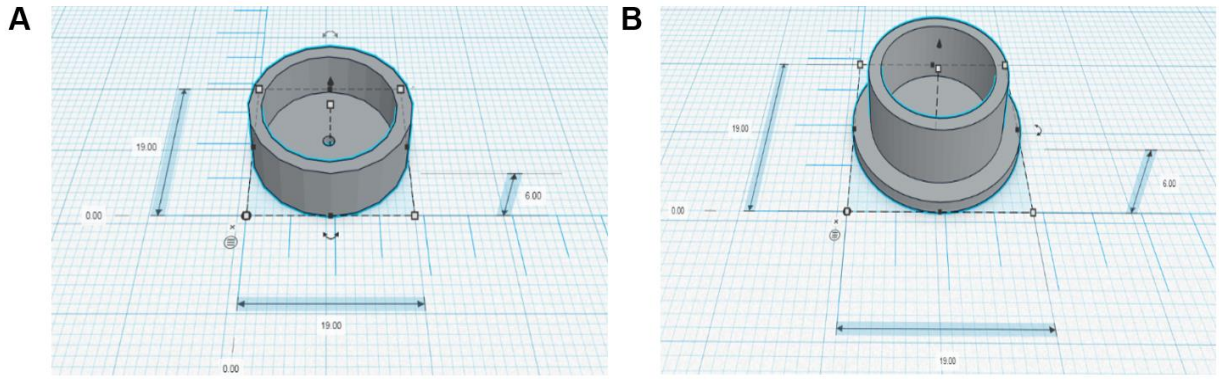

Figure 2.3. CAD images of (A) the bottom part and (B) the top part of the reservoir.

Printing was performed in a Robo R2 (San Diego, CA, USA) using a nozzle with a diameter of 0.4mm for printing PLA 1.75mm 3D printer filaments. The following settings were employed: the printing temperature (T_p) was set at 195 °C, $T_{platform}$ = 60 °C, infill pattern = light, layer height = 0.1 mm.

Samples prepared by FDM were photographed and were visually investigated. The diameter and height of the 3D printed reservoirs were measured with a vernier calliper. The radial expansion coefficient (E_r) of filaments was calculated according to Eq. 6, where D_f and D_0 represent the diameters of filament and die of the printer, respectively.[154]

$$E_r(\%) = \frac{D_f}{D_0} \times 100\% \qquad \text{Eq. 6}$$

2.4.3 Preparation of Physical Mixtures and Directly Compressed Tablet

2.4.3.1 Preparation of Physical Mixtures

All materials (except PEG 6000 and TEC) were placed in a convection oven (Memmert, UF110, Schwabach, Germany) at 50 °C for approximately 2 h before use because the removal of residual moisture can help prevent these powders from aggregating and sticking to the feeder surface of the hot melt extruder at high processing temperature. Physical mixtures were prepared by dry mixing of the composition as outlined in Table 2.4 using a mortar and pestle for 5 min. Then, powder mixtures were further mixed with a Turbula blender (T2F, Willy A. Bachofen AG, Muttenz, Switzerland) for 10 min. Before the extrusion process, the blend was left overnight for better migration of the plasticizer TEC (liquid form) into the polymer.[158]

Table 2.4. Composition of the filament formulations for HME

Group number	Ibuprofen, (% w/w)	EC (% w/w)	Release modifier (w/w)
G1	20	80	-
G2	20	60	20% PVA
G3	20	60	20% Soluplus
G4	20	60	20% PEG 6000
G5	20	60	20% Eudragit RSPO
G6	20	60	20% Eudragit RLPO
G7	20	60	20% HPMC K4M
G8	20	60	20% HPMC E10M
G9	20	60	20% HPMC K100M
G10	20	60	20% Kollidon VA 64
G11	20	60	20% Kollidon 17 PF
G12	20	60	20% Kollidon 30
G13	20	60	15% Kollidon VA 64, 5% TEC
G14	20	60	10% Kollidon VA 64, 10% Eudragit RSPO

2.4.3.2 Tablets Prepared by Direct Compression

A manual tablet compression machine (Model MTCM-I, Globe Pharma, USA) equipped with 10 mm diameter flat-faced punches was used to prepare tablet compacts of physical mixtures. All punches and dies were carefully cleaned

before the compression process. For a better comparison between 3D printed tablets and tablets prepared via direct compression, based on the weights of prepared 3D printed tablets (Table 2.4), physical mixtures of the same weight in each group were accurately weighed and filled into the die manually (Figure 2.4). Tablets were compressed at 30 MPa for 3 s dwell time.

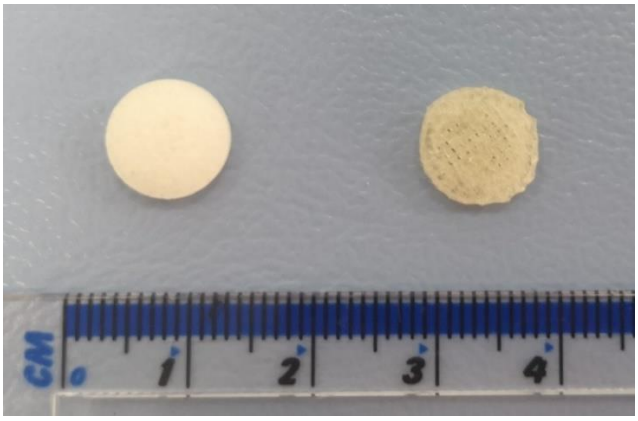

Figure 2.4. Images of the directly compressed physical mixtures tablet (left) and the 3D printed tablet (right).

2.4.4 Hot Melt Extrusion of Ibuprofen-loaded Filaments

The powder mixtures were fed into a 10 mm twin-screw extruder L/D 20 (assembled by Point 1 Control System Ltd., Stoke-on-Trent, UK) at a screw speed of 60 rpm. As IBP has a plasticizing effect, the glass transition temperature (T_g) of EC and the processing temperature during HME should decrease.[187] Hence, the extrusion temperatures of four heating zones and the die along the extrusion barrel were set at 80, 100, 100, 100 and 100 °C respectively. The extruded filaments were collected with a filament winder (FilaFab™, D3D Innovations Limited, Bristol, UK).

2.4.5 FDM 3D Printing of Tablets Using Ibuprofen-loaded Filaments

The model tablet (diameter × height = 10 × 2 mm) was designed online on TinkerCAD (https://www.tinkercad.com/) and then downloaded as a stereolithographic (.stl) file format (Figure 2.5). The .stl file was then imported into

a MakerBot Replicator 2X 3D Printer (MakerBot Inc., Brooklyn, NY, USA), which was equipped with two MK8 dual-head extruders (diameter = 0.4 mm). Model tablets were printed with 100% infill density. The layer height was set at 0.2 mm. The printing was performed at 178 °C whereas the build plate was set to 65 °C.

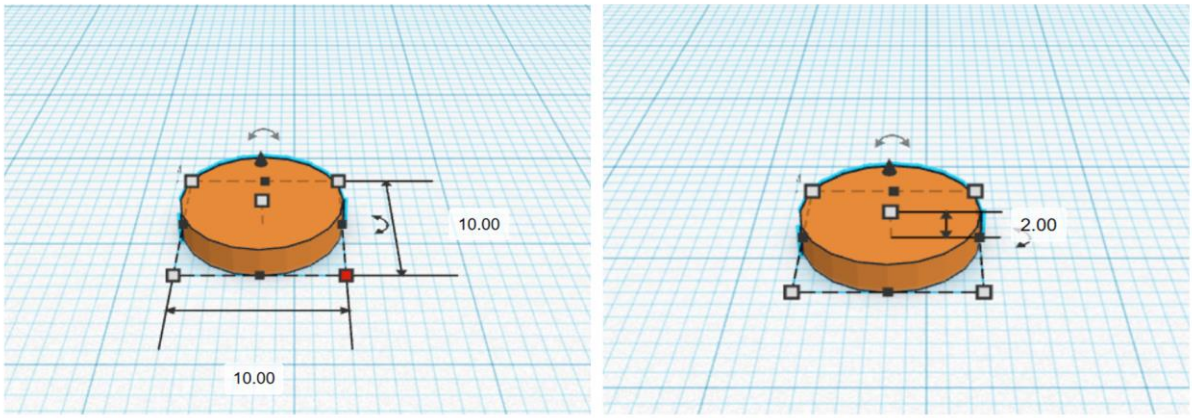

Figure 2.5. Designed CAD model of the tablet (diameter × height = 10 × 2 mm) for FDM 3D Printing.

2.5 Microscopic Analysis

2.5.1 SEM Analysis of PB 3D Printed Tablets, PLA Filaments and FDM 3D Printed PLA Reservoirs

The surface morphology was examined by Jeol JMS 820 (Freising, Munich, Germany) at the accelerating voltage of 3 kV. The samples were mounted on an aluminum stub using adhesive carbon tape and were sputter-coated with gold under vacuum (Edwards S-150 sputter coater, Edwards High Vacuum Co. International, Albany, NY, USA).

2.5.2 Confocal Microscopic Analysis of Drug-coated PB 3D Printed Tablets

As fluorescence and UV-Vis irradiation are important photophysical properties of FLU, the homogeneity of FLU on the surface of 3D-printed tablets was checked with an SP8 confocal microscope (Leica, Microsystems Ltd., Milton Keynes, UK).

Also, the 3D-printed tablet without the drug solution was analyzed for negative control.

2.5.3 SEM and Energy-Dispersive X-ray Spectroscopy (EDS) Analysis of PDMS Sponges

The PDMS sponge samples were mounted on 12.5 mm diameter aluminum pin stubs (Agar Scientific, UK) using Leit-C conductive carbon cement (Agar Scientific, UK) and sputter-coated with 4 nm of platinum using a Q150T-ES sputter coater (Quorum Technologies, UK) to improve sample conductivity.

SEM imaging and EDS analysis were performed under high vacuum using a Zeiss Sigma FEG-SEM (Carl Zeiss, UK) and AZtec EDS system (Oxford Instruments, UK). The SEM working condition parameters were 20 kV accelerating voltage, 60 µm column aperture, and 8.5 mm working distance, using an Everhart−Thornley secondary electron detector (Carl Zeiss, UK) for imaging. The EDS analysis used a 10-frame acquisition per map, 20 µs pixel dwell time, AZtec software signal processer time setting 5, and an X-Max 80 mm^2 silicon drift detector (SDD) (Oxford Instruments, UK) for X-ray signal detection.

2.5.4 SEM Analysis of Magnetic Particles, Sugar, Filaments and FDM 3D Printed Tablets

The SEM analysis of magnetic particles, sugar, hot melt extruded filaments and FDM 3D printed tablets was conducted the same way as in Section 2.5.3, but SEM working condition parameters were set to 5 kV accelerating voltage with a 30 µm column aperture.

2.6 X-ray Diffraction (XRD)

XRD measurements were performed using a Siemens D500 X-ray Diffractometer (Munich, Germany). The samples were scanned between 2 Theta (θ) from 5° to

50° at a step width of 0.01° and 1 s time count. The divergence slit was 1 mm and the scatter slit was 0.6 mm. The X-ray wavelength was 0.154 nm in Cu source and at a voltage of 40 kV.

2.7 Thermal Analysis

2.7.1 Thermogravimetric Analysis (TGA)

TGA was performed with a TGA Q50 (TA Instruments, Leatherhead, UK) to measure the water content and the degradation temperature of samples. Data were recorded and analyzed with the TA Universal Analysis software (TA Instruments-Waters LLC, New Castle, DE, USA).

2.7.1.1 TGA Analysis of PDMS Sponges

Around 5 mg of each sample was placed in an open aluminum pan and then heated from 20 °C at a heating rate of 10 °C/min up to 500 °C with 25 mL/ min purified nitrogen purging.

2.7.1.2 TGA analysis of Extruded Filaments and FDM 3D Printed Tablets

Around 5 mg of each sample was placed in an open aluminum pan and then heated from 25 °C to 500 °C at a heating rate of 20 °C/min under 20 mL/min purified nitrogen gas for purging.

2.7.2 Differential scanning calorimetry (DSC)

A differential scanning calorimeter 4000 system (Perkin Elmer, Waltham, MA, USA) was utilized to conduct a thermal analysis of all raw materials, physical mixtures, extruded filaments, and 3D printed tablets. Samples (approximately 5 mg) were accurately weighed and placed in a 40 µL aluminum pan (Mettler Toledo GmbH, Greifensee, Switzerland). All experiments were conducted under a nitrogen environment (flow rate = 20 mL/min). All samples were heated from 25 °C to 200 °C at 20 °C /min. The data were collected using Pyris software

version 5.0 (Perkin Elmer, Waltham, MA, USA).

2.8 Mechanical Characterization

2.8.1 Compression Test of Sponges

To do the compression test, all the fabricated PDMS sponges were cut into cylinders (with 12 mm in diameter and 7 mm in height). A texture analyzer (TA.XT Plus, Texture Technologies, Scarsdale, NY, USA) and a radiused cylinder probe (P/0.5R) were used for measuring the elasticity modulus of all PDMS sponge samples. The modulus of elasticity (E) of the sample was calculated with Eq. 7, and it could be represented as the slope of the stress-strain curve in the elastic region. The stress (σ) is the pressing force that brings the deformation to the object. The strain (ε) is defined as the ratio of the height change of the object due to the deformation to its original height.[188] These PDMS samples were compressed with a trigger force of 0.005 kg at the test speed of 2.00 mm/sec. All samples were run in triplicate (n = 3).

$$E = \frac{\sigma}{\varepsilon} \qquad \text{Eq. 7}$$

2.8.2 Mechanical Characterization of Filaments

A TA.XT plusC Texture Analyser (Stable Micro Systems Ltd., Godalming, UK) equipped with a 50 kg load cell and tensile grips (A/TG) probe was used to measure the tensile strength of extruded filaments which were accurately cut into 10 cm segments (diameter × length = 1.75 mm × 10 cm). The filament pieces were fixed vertically between two screw-down grips. The original distance between the two grips was set to 8 cm and then stretched gradually at an elongation speed of 1 mm/s until the filament was broken (Figure 2.6). The stress and strain values were collected through the Exponent Software version 7.0.3.0 (Stable Micro Systems Ltd., Godalming, UK). Then the elastic modulus could be calculated according to the elastic region (linear region) in the stress-strain curve. At least three replicates were conducted for each batch of extruded filaments.

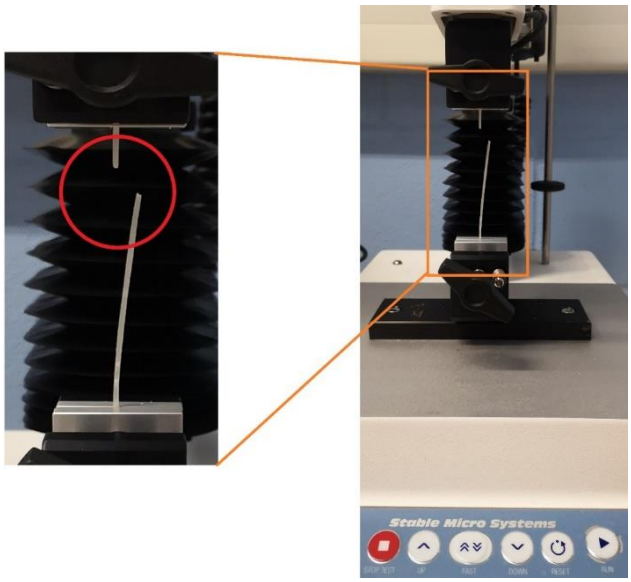

Figure 2.6. The rig of filaments texture analysis.

2.9 *In Vitro* Drug Release Studies

2.9.1 Dissolution Test of PB 3D Printed Tablets Coated with FLU

In vitro dissolution tests under sink conditions were performed with a US Pharmacopeia (USP) type II paddle apparatus (708-DS Dissolution Apparatus, Agilent Technologies, Santa Clara, CA, USA) in 900 mL of phosphate-buffered saline (PBS) (pH 6.8) at 37 ± 0.3 °C with a paddle speed of 100 rpm. All samples were run in triplicate (*n* = 3). The drug concentration of the dissolution medium was measured automatically by using Cary 60 UV-Vis (Agilent Technologies) at a wavelength of 265 nm in a 1 cm cell versus a blank solution consisting of a phosphate buffer (pH 6.8). Then, the release profiles were plotted as a percentage of cumulative drug release versus time. Additionally, there was no interference from Soluplus® or PEG 6000 on drug assay observed at the detection wavelength. The standard curve was prepared in the concentration of 0.625-20 μg/mL ($A = 0.0514C + 0.002$, $R^2 = 0.9995$) where A is the absorbance and C is the concentration (μg/ml) (Figure 2.7).

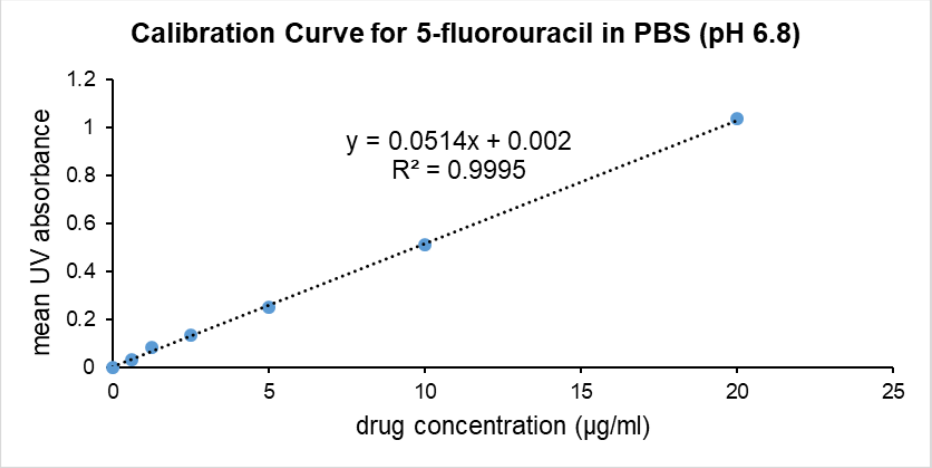

Figure 2.7. Calibration curve for 5-fluorouracil in PBS (pH 6.8).

The similarity factor (f_2) in Eq. 8 was developed by Moore and Flanner as a model-independent mathematical method to analyze the closeness between two dissolution profiles.[189] where n is the number of dissolution time points, R_t and T_t are the dissolution value of the reference and test sample at the time t, respectively.

$$f_2 = 50 \times \log\{[1 + \frac{1}{n}\sum_{t=1}^{n}(R_t - T_t)^2]^{-0.5} \times 100\} \quad \text{Eq. 8}$$

The mathematical method of f_2 has been adopted by many guidance, like Food and Drug Administration (FDA) and European Medicines Agency (EMA), as a criterion for measurement of the similarity between *in vitro* dissolution profiles.[190] As the value of f_2 equals to 100 when the two profiles are identical and the value is 50 when an average variation of 10% at all determined time points, a public standard for f_2 value between 50 and 100 can indicate the two dissolution profiles are similar, whereas the value of less than 50 can show the two profiles are different.

2.9.2 Dissolution Test of Magnetic Field Triggerable Device

Similar to Section 2.9.1, *in vitro* dissolution tests of the FLU loaded magnetic field triggerable device under sink conditions were performed with a US

Pharmacopeia (USP) type Ⅰ basket or type Ⅱ paddle apparatus according to different designed modes (Figure 2.8). The preliminary results showed that the materials used in 3D printing such as PLA do not interfere with drug detection and UV absorbance.

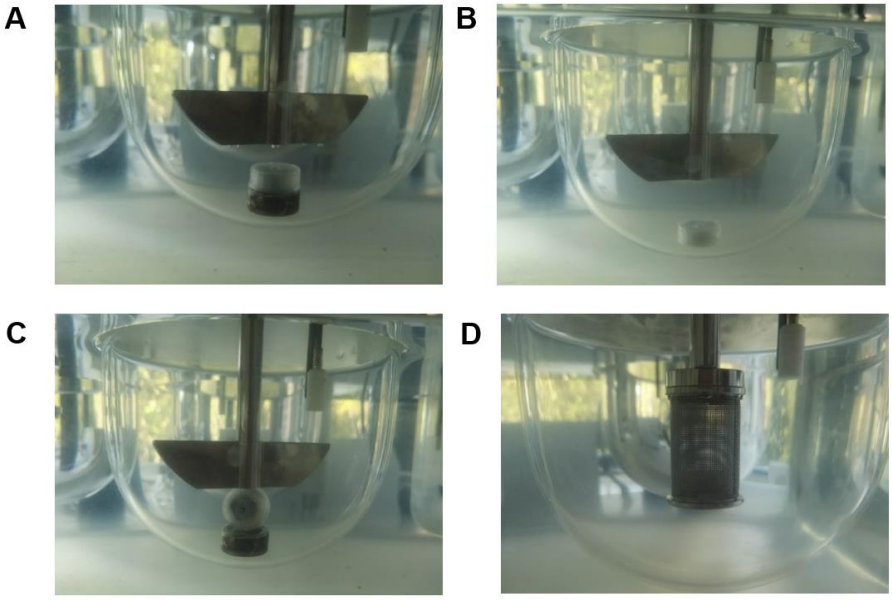

Figure 2.8. Various modes for comparing the drug release from the device. (A) Mode 1: the device was laid flat on the magnet; (B) Mode 2: the device with no magnets; (C) Mode 3: the device was placed vertically on the magnet; (D) Mode 4: the device was placed in the basket without a magnet.

To study the effect of the position of magnet versus device containing the sponge, various modes were employed. In Mode 1 (Figure 2.8A), the device was lying on the magnet. In Mode 2 (Figure 2.8B), there is no magnet. In Mode 3 (Figure 2.8C), the device was standing on the magnet. In Mode 4 (Figure 2.8D), the device was placed in the basket without a magnet.

2.9.3 Determination of Drug Content

Around 30 mg segments of hot melt extruded filaments or 3D printed tablets were placed into a volumetric flask with 25 mL ethanol under magnetic stirring until the segments were completely dissolved. Then the homogenous solution was filtered through a 10 mL SOL-M^{TM} syringe (SOL-MILLENNIUM Medical Group, Aichwald,

Germany) and a 0.45 μm Fisherbrand™ syringe filter (Fisher Scientific International, Inc., Guangzhou, China). The amount of IBP was determined with a Biochrom WPA Biowave II+ UV/Visible Spectrophotometer (Biochrom Ltd., Cambourne, UK) at an absorption wavelength of 264 nm. To calculate the concentration of IBP in ethanol, the calibration curve (Figure 2.9) was prepared in the range of 3.125-100 μg/mL ($A = 0.0014C + 0.0046, R^2 = 0.9956$) where A represents the absorbance and the C represents the concentration (μg/mL). There was no interference between IBP and the other materials at the wavelength. The drug loading and dose accuracy were calculated according to Eq. 9 and Eq. 10. All measurements were conducted in triplicate (n = 3).

$$Drug\ Loading = \frac{Amount\ of\ drug}{Amount\ of\ drug+polymers} \times 100\% \quad \text{Eq. 9}$$

$$Dose\ Accuracy = \frac{Calculated\ drug\ loading}{Theoretical\ drug\ loading} \times 100\% \quad \text{Eq. 10}$$

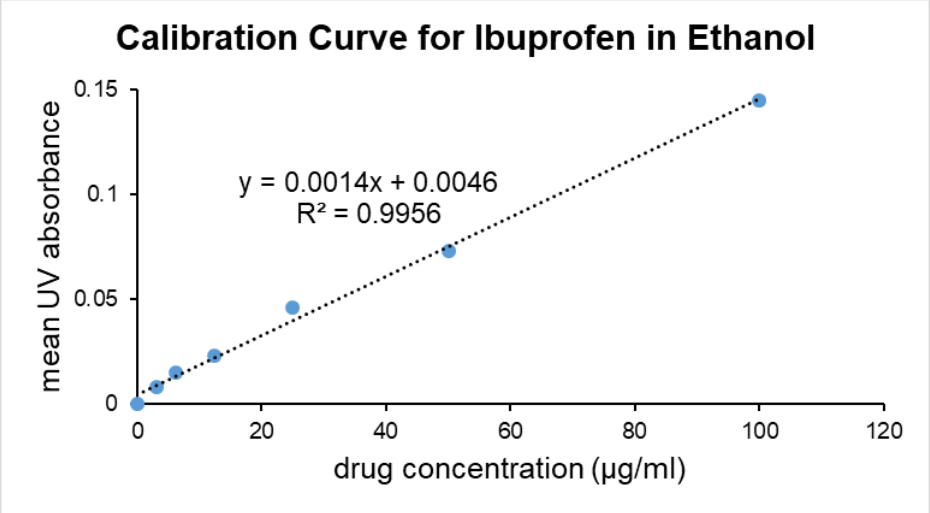

Figure 2.9. Calibration curve for ibuprofen in ethanol.

2.9.4 Dissolution Test of Extruded Filaments and 3D Printed Tablets

In vitro dissolution tests of hot melt extruded filaments and 3D printed tablets under sink conditions were performed in 900 mL of phosphate-buffered saline (PBS) solution (pH = 7.2) at 37 ± 0.3 °C with a paddle speed of 100 rpm. All samples were run in triplicate (n = 3). At different time intervals (0, 20, 40, 60,

then every 60 min up to 24 h) the dissolution medium was automatically pumped into a UV spectrophotometer. The drug concentration of the dissolution medium was measured at a wavelength of 221 nm in a 1 cm cell versus a blank solution consisting of PBS solution (pH = 7.2). The solubility of IBP in this medium is 4.48 ± 0.08 mg/mL at 37 °C.[191] The calibration curve (Figure 2.10) from 0.78125 to 25 µg/mL was prepared ($A = 0.0424C + 0.0024, R^2 = 0.9997$) to calculate the concentration of IBP. Then, the release profiles were plotted as a percentage of cumulative drug release versus time. Additionally, there is no interference from other raw materials on the drug assay observed at the detection wavelength.

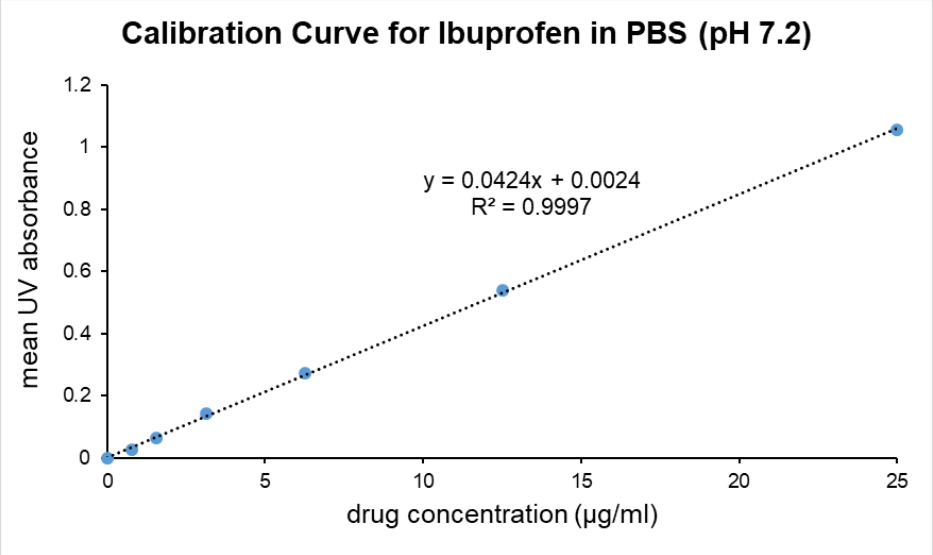

Figure 2.10. Calibration curve for ibuprofen in PBS (pH 7.2).

An add-in program (DDSolver) in Microsoft Excel was used to evaluate the drug release kinetics of the acquired dissolution curves by fitting the data to various equations listed in Table 2.5.[192] The zero-order drug release model where the dissolution rate is constant is regarded as the ideal model for release data as this type of drug release pattern can maintain the drug concentration in blood plasma at a constant level for prolonged periods.[193,194] The first-order model (the dissolution rate is exponential) has been used to describe drug absorption, elimination and decomposition.[193,194] The Higuchi model (square root time-

dependent) mainly describes drug release as a diffusion process according to Fick's law.[194,195] The Korsmeyer-Peppas model (relating exponentially the drug release to the elapsed time) could be used to analyze the drug release mechanism.[158,174] In the case of cylindrical tablets, the value of n could be used as an approximation to describe the mechanism of drug release. The $n < 0.45$ (Fickian diffusion), $0.45 < n < 0.89$ (anomalous transport) and $n > 0.89$ (case-II transport).[196] It is noteworthy that only the portion of the dissolution curve where $F < 60\%$ should be used to calculate the exponent n.[196] If the n value of 0.45 or 0.89 is an indication of diffusion or erosion mechanism, respectively.

Two statistical criteria, the adjusted coefficient of determination (R^2_{adj}) and the Akaike Information Criteria (AIC) were applied to determine the most suitable model for fitting dissolution data.[148,158] When comparing different models for a given dissolution profile, the model with the highest value of R^2_{adj} and the lowest value of AIC could be regarded as the best fit among all models.[192,194]

Table 2.5. Kinetic release model equations in this study

Model	Equation	Parameters
Zero-order	$F = k_0 \cdot t$	k_0 -- zero-order release constant
First-order	$F = 100 \cdot (1 - e^{-k_1 \cdot t})$	k_1 -- first-order release constant
Higuchi	$F = k_H \cdot t^{0.5}$	k_H -- Higuchi release constant
Korsmeyer-Peppas	$F = k_{KP} \cdot t^n$	k_{KP} -- release constant with structural & geometric information n -- diffusional exponent indicating release mechanism

(F is the fraction or percentage of drug released in time t)

2.10 Cell Culture Studies

As the sponge samples are very porous, it is easy for them to absorb the drug solution (Table 2.3) inside. Three samples of each kind of sponges (diameter × thickness = 5 mm × 2 mm) were immersed in the FLU solution with a concentration of 25 mg/mL or 12.5 mg/mL. After the complete absorption of the

drug solution, the sponge samples were taken out and left at room temperature for 3 days before sterilization.

HeLa and Trex cells both stably express green fluorescent protein (GFP) constructs. Cell lines were maintained in Dulbecco's modified Eagle's medium (DMEM) supplemented with 10% fetal calf serum (FCS), penicillin/streptomycin, and L-glutamine at 37 °C and 5% CO_2.

Substrates were sterilized and transferred to 12-well plates. Cells were plated at a density of 0.4×10^5 on day 0. On day 1, the media in wells were changed. On day 1 or 2, substrates were transferred to new wells and the remaining cells were trypsinized using trypsin EDTA and counted using a hemocytometer. Cells were replated onto the substrates in fresh media. On day 4, substrates were washed three times with PBS and transferred to new wells and fresh media. The remaining cells were trypsinized, counted, and discarded.

3. Chapter 3: Preparation and Characterization of Magnetic PDMS Sponge

3.1 Introduction

There are many approaches to fabricate porous PDMS structures, like templating with self-assembled colloidal microspheres, emulsion polymerization, surface treatment using a CO_2-pulsed laser, phase separation, one-pot method with the reaction of $NaHCO_3$ and HCl, NaCl microparticles templating with dimethicone, and suspension polymerization with gelation as the surfactant.[180,197,198] However, these methods are expensive, time-consuming and difficult to manipulate the shape and size of porous structures because of sophisticated fabrication procedures.[180,197] Zhao *et al.* pointed out that PDMS sponges must be washed repeatedly with ethanol and dichloromethane for removing the NaCl microparticles completely which is not the case when sugar was used.[199] Furthermore, the porosity of sponges made from salt molds is lower because the wall thickness of the pores increased significantly, and the compressive modulus is higher. Additionally, it has been proved that the sponge pores of sugar molds are more amorphous because of higher connectivity.[120] In this study, a simple, cheap and eco-friendly sugar templating method was applied to fabricate porous PDMS sponges using commercial household sugar.

Carbonyl iron (CI) is a unique form of elemental iron with a small particle size and very low toxicity (LD_{50}: 50 g/kg).[200] As a novel food additive or iron supplementation, CI has therapeutic potential for iron deficiency anaemia because of its safety and potent bioavailability.[201] In addition, the relatively high permeability and high saturation magnetization at the microwave frequency band make CI have the potential to be used as an electromagnetic wave absorbing material.[179,202] It has been proved that black iron oxide Fe_3O_4 (magnetite) particles are biocompatible, can respond quickly to an extrinsic magnetic field

and display fast reverse behaviour once removing the magnetic field.[42,203,204] Therefore, these two kinds of magnetic particles are promising candidates in fields of biomaterials, implant technology and biosensors for biomedical applications.

This chapter described the preparation and characterization of magnetic field sensitive sugar-templated PDMS sponges. Different concentrations of carbonyl iron (CI) and magnetite Fe_3O_4 nanopowders were embedded as magnetosensitive materials in PDMS resins for the fabrication of macroporous sponges via a sugar template process. The process is environmentally friendly and simple. The prepared magnetic PDMS sponges were evaluated for their morphology, the particle size of magnetic particles, solid-state, porosity (absorbency), elastic modulus, deformation under a magnetic field and dielectric constant. All physicochemical and magneto-mechanical analysis confirmed that the magnetic field sensitive PDMS sponges are promising candidates as active porous scaffolds for delivering drugs. Furthermore, the magnetic field sensitivity of the fabricated PDMS sponges under magnetic fields can be controlled by adjusting the concentration and the type of magnetic particles.

3.2 Methods

3.2.1 Preparation of Macroporous PDMS Sponges

Refer to Section 2.3.1.

3.2.2 Characterization of PDMS Sponge Properties

3.2.2.1 Physical Appearance

Refer to Section 2.3.2.1.

3.2.2.2 SEM and Particle Size Analysis of Magnetic Particles

Refer to Section 2.3.3.1.

3.2.2.3 XRD

Refer to Section 2.6.

3.2.2.4 Porosity

Refer to Section 2.3.2.2.

3.2.2.5 Compression Test

Refer to Section 2.8.1.

3.2.2.6 Sponge Deformation under Magnetic Fields

Refer to Section 2.3.2.3.

3.2.2.7 Dielectric Constant (Relative Permittivity)

Refer to Section 2.3.2.4.

3.3 Results and Discussion

3.3.1 Preparation of Magnetic PDMS Sponges

Pure PDMS sponges and magnetic PDMS sponges with different concentrations of magnetic microparticles were fabricated and sectioned into different thicknesses by using the water-soluble sugar template. The macroporous sponges with interconnected pores, larger pore sizes, a higher concentration of magnetic particles and lower compressive modulus were selected as the main scaffold in this study. The main reasons behind the selection of sponges were that sponges with large pore sizes and high connectivity can preserve and transport drug more efficiently, and a higher magnetic particle density can produce a higher body force under the same magnetic field, and sponges with lower compressive moduli have the potential to show larger deformation (leads to a more obvious effect on the drug release) when subject to the same body force.[94]

Highly monodisperse Fe_3O_4 microparticles were embedded in sponges at predetermined concentrations (30, 50, and 100 w/w% of the PDMS). Unlike Fe_3O_4, CI microparticles can be used to prepare 30, 50, 100 and 150 (w/w % of the weight of PDMS) CI-loaded PDMS sponges which could be due to the lower density of CI (1.45 g/cm^3) when compared with Fe_3O_4 (5.2 g/cm^3).[204–206]

3.3.2 Characterization of Magnetic PDMS Sponges

3.3.2.1 Physical Appearance of Sponges

The optical microscope image of granulated sugar particles (Figure 3.1A) reveals that the size of granulated sugar particles used in this experiment is not so uniform. This will help to increase the porosity of PDMS sponges because the less uniform the sugar particles are, the higher the porosity of the sponges is.[182]

Macroporous sponges of various shapes and dimensions (Figure 3.1B) can readily be fabricated and cut to accommodate specific requirements. Additionally, large-scale production of PDMS sponges can be accessible through the proposed sugar-templating process as the total processing time only lasts for a few hours.[182]

The Fe_3O_4 loaded PDMS sponges were black and porous. The sponges become stiffer when the concentration of Fe_3O_4 microparticles increases due to the stiffness of the magnetic microparticles. The CI loaded PDMS sponges are dark grey and porous (Figure 3.1C). The sponges also become stiffer when the concentration of CI microparticles increases.

As shown in Figure 3.1D, the fabricated magnetic PDMS sponges display a rarely observed structural flexibility in porous materials.[123] These sponges show significant compliance and springiness for a remarkable volume reduction of

more than 50% in manual compression. Additionally, these sponges can be bent to a large extent without breaking apart and they are reversible to their original shape. It is inferred that these sponges are suitable for recycling. Furthermore, the absorbed solution in PDMS sponges can be removed and reutilized through slightly squeezing sponges manually because of the springy nature of these PDMS sponges.

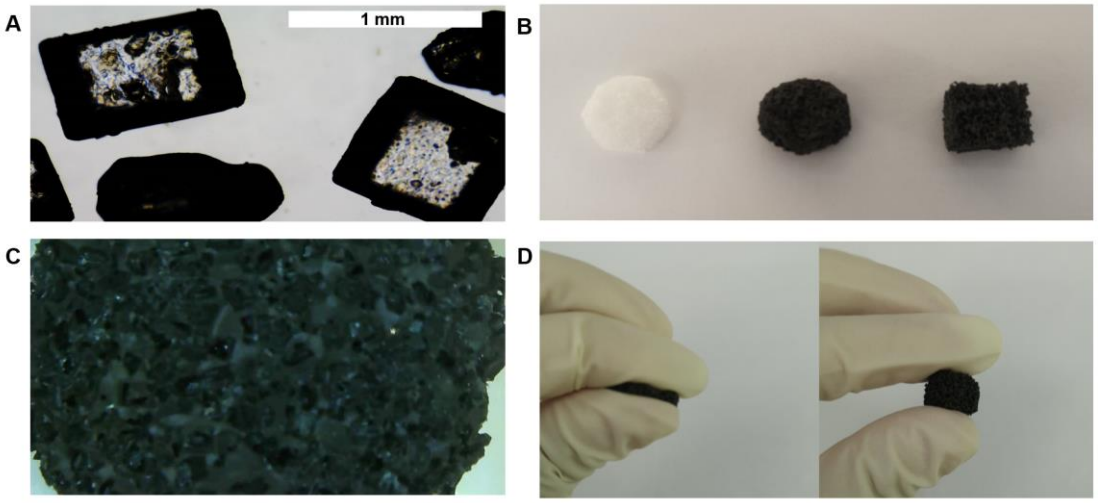

Figure 3.1. (A) Optical microscope image of granulated sugar particles, (B) Photograph of the pure PDMS sponge cylinder, CI loaded PDMS sponge cylinder and Fe_3O_4 loaded PDMS sponge cube fabricated with granulated sugar template, (C) Macroscopic appearance of 100 w/w% CI/PDMS sponge cylinder surface, (D) Manual compression and recovery of 100 w/w% CI/PDMS sponge cylinder.

3.3.2.2 SEM and Particle Size Analysis of Magnetic Particles

The SEM images of Fe_3O_4 and CI particles were shown in Figure 3.2. The CI particles showed a spherical shape, whereas cubic Fe_3O_4 particles have a smaller particle size. As shown in the particle size frequency diagrams, the calculated average particle sizes (P_m) of Fe_3O_4 and CI particles are 177 and 1354 nm respectively. According to Eq. 1, the larger volume of CI particles can lead to a stronger magnetic force under the same magnetic field.

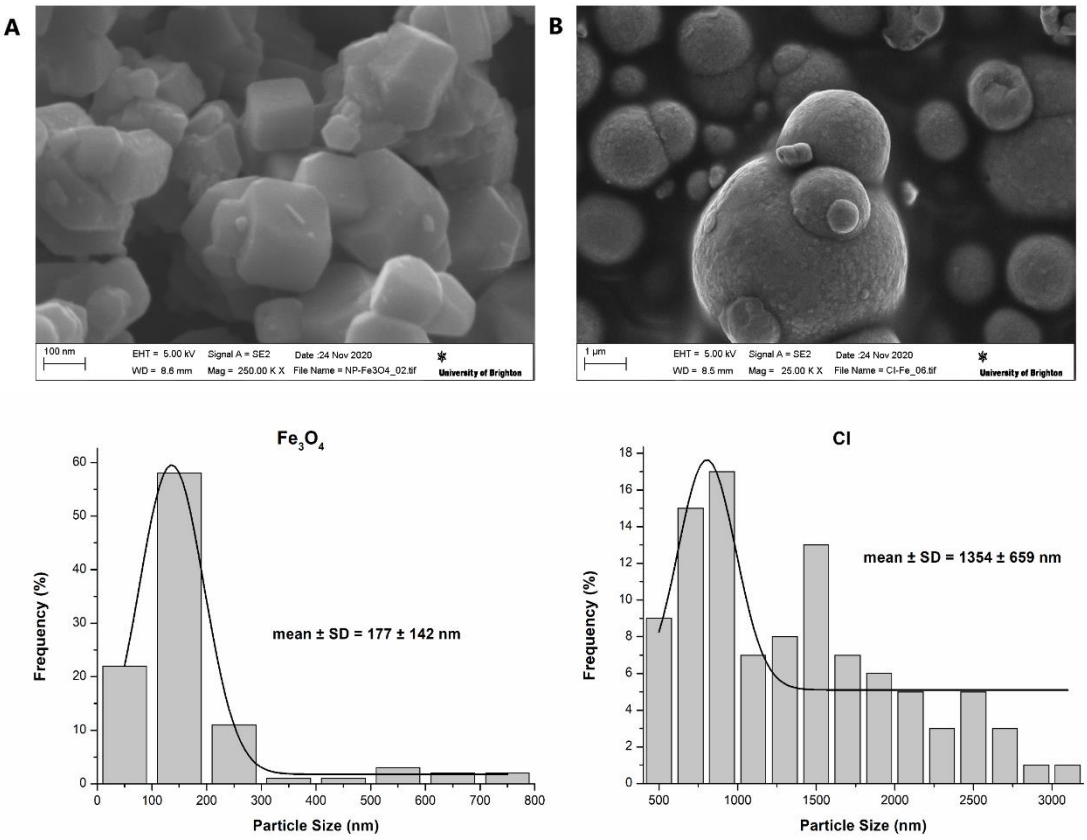

Figure 3.2. SEM images and particle size frequency diagrams of (A) Fe_3O_4 and (B) CI particles.

3.3.2.3 XRD Analysis

XRD measurements are important to analyze the dispersion of magnetic particles in these fabricated magnetic PDMS sponges. The XRD diffractograms (Figure 3.3) of raw materials and pure PDMS sponges showed that white granulated sugar, Fe_3O_4 and CI particles all have a crystalline nature because of the sharp intense peaks throughout their diffraction patterns, whereas the XRD pattern of pure PDMS sponges is mostly in the amorphous state as it shows a halo pattern. The XRD patterns of Fe_3O_4 particles exhibit five peaks at 2 thetas of 29.4°, 34.9°, 42.6°, 56.5° and 62.1°, whereas CI particles show two peaks at 2 thetas of 44.2° and 64.9°which are the main peaks for these two chemicals.[207–209] Two broad and low-intensity peaks at around 12° and 23° from the pattern of pure PDMS sponges confirm their amorphous nature because it has been revealed that the XRD diffraction peak at around 24° is one of the evidence for the existence of large

quantities of amorphous materials.[207,208]

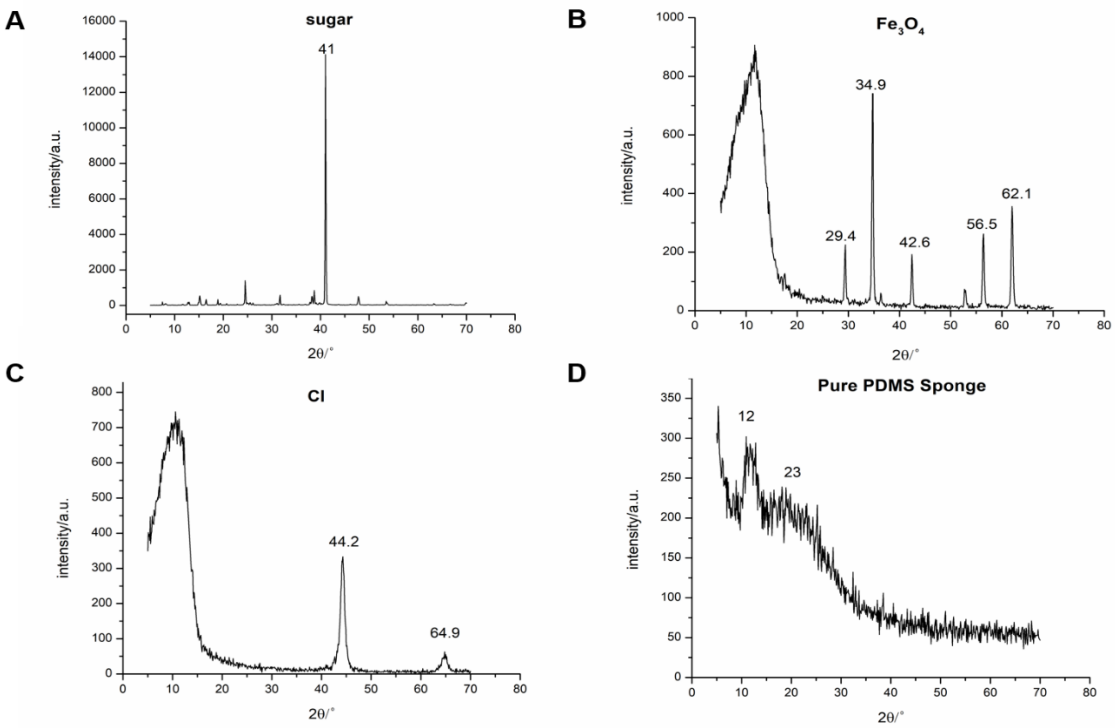

Figure 3.3. XRD patterns of raw materials (sugar, Fe_3O_4 and CI) and PDMS sponges.

There are obvious sharp intense peaks in all diffraction patterns of Fe_3O_4/PDMS sponges and CI/PDMS sponges so they all have a crystalline nature. The comparisons of XRD traces (Figure 3.4) of different Fe_3O_4-loaded PDMS sponges / CI-loaded PDMS sponges and Fe_3O_4 / CI were made to find out the relationship between the peaks of Fe_3O_4-loaded / CI-loaded PDMS sponges with raw materials. Most peaks in Fe_3O_4-loaded / CI-loaded PDMS sponges are inconsistent with peaks of Fe_3O_4 / CI. Consequently, a certain amount of crystalline Fe_3O_4 / CI can be confirmed in these Fe_3O_4-loaded / CI-loaded PDMS sponges through these graphs. Furthermore, there is also no trace of sugars in the formulation, which means all sugars have been washed away during the leaching process. However, 100% Fe_3O_4 / PDMS sponges seemed to have reduced the crystallinity because the mixture of Fe_3O_4 and PDMS solution was so sticky that Fe_3O_4 cannot penetrate through the sugar mold to form the sponge.

As a result, most of Fe_3O_4 particles were agglomerated at the top surface of the sugar mold in the fabricating process of 100 w/w % Fe_3O_4 / PDMS sponges.

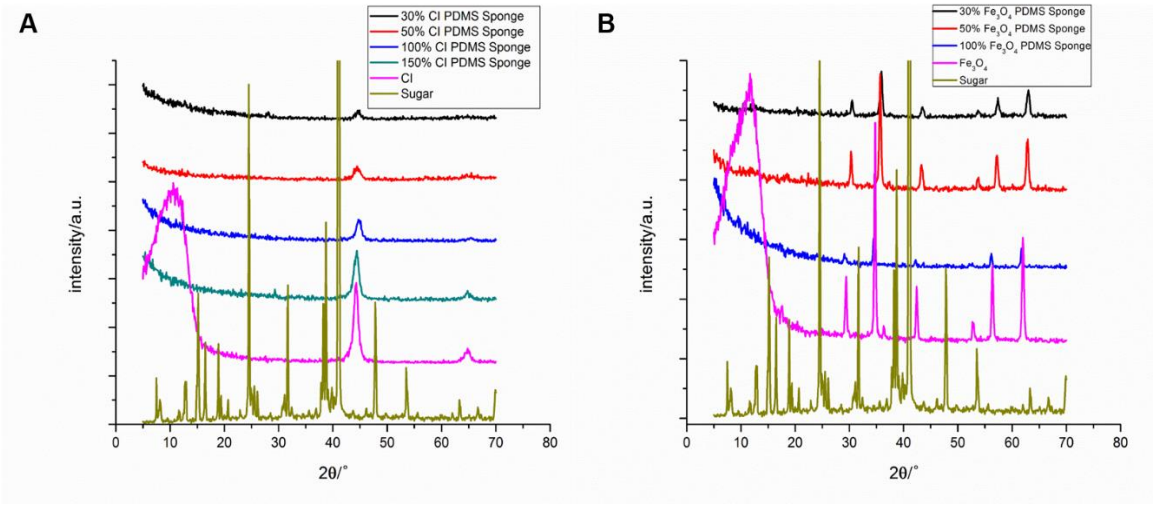

Figure 3.4. Comparison of XRD patterns of raw materials (sugar and Fe_3O_4 / CI) with corresponding (A) Fe_3O_4-loaded / (B) CI-loaded PDMS sponges.

Since the specimens for XRD studies were selected from the midsection of the mold for all formulations, this proves less penetration of Fe_3O_4 in the sponges due to the unsatisfactory penetration of 100 w/w % Fe_3O_4 / PDMS through the sugar mold. Because it has been proved that the non-uniform distribution of magnetic particles could lead to poor magnetic and mechanical properties, this sponge was not used in the following experiments.[210,211]

3.3.2.4 Porosity of Sponges

As can be seen from Table 3.1, pure PDMS sponges exhibited the highest porosity and water absorption. However, the differences among the porosity values of CI/PDMS sponge samples with the weight ratios of 30, 50, and 100 w/w% of PDMS are not very remarkable ($P > 0.05$). The porosity of 150 w/w% CI/PDMS sponges is the lowest. Also, the porosity values of 30 w/w% and 50 w/w% Fe_3O_4/PDMS sponges are much lower than the same ratio of CI/PDMS sponges respectively. The possible reason is the higher density of Fe_3O_4 when compared with CI. By immersing these sponges fabricated from the granulated sugar mold

directly into water, up to 146 wt% of the original weight could be absorbed. These PDMS sponges were immediately wetted in water, although higher absorption was expected to achieve in long immersion time. This time-independent absorbing property also illustrates the strong water absorption of these sponges. Furthermore, the standard deviations of the water absorption of Fe_3O_4 loaded PDMS sponges are higher than CI loaded PDMS sponges.

Table 3.1. Calculated mean ± standard deviation values of bulk density, porosity and water absorption of different kinds of PDMS sponge samples prepared with granulated sugar (n = 3)

Composition	Bulk density (g/cm^3)	Porosity (%)	Water absorption (%)
Pure PDMS sponge	0.31±0.02	64.97±5.50	145.51±6.15
CI/PDMS=30 wt%	0.35±0.01	63.57±2.44	128.33±10.10
CI/PDMS=50 wt%	0.43±0.06	61.90±4.37	119.01±12.56
CI/PDMS=100 wt%	0.49±0.06	59.04±2.93	102.87±5.48
CI/PDMS=150 wt%	0.56±0.02	41.01±2.16	63.10±10.30
Fe_3O_4/PDMS=30 wt%	0.46±0.12	53.96±3.36	117.18±11.85
Fe_3O_4/PDMS=50 wt%	0.49±0.20	49.71±1.42	83.08±14.58

According to Jurin's Law (Eq. 11), the height of liquid (h) in a capillary tube is associated with the surface tension (γ) of the liquid, the contact angle (θ) of the liquid, the mass density (ρ) and the tube radius (r).[212] Although these sponges were all prepared with granulated sugar mold, the depth of liquid columns of the PDMS and magnetic particles blend penetrated in sugar mold is lower because of the higher density of the magnetic PDMS blend. The slow penetration of the solution can completely remove the air between sugar crystals from the sugar template compared to the fast penetration of pure PDMS. As a result, the sponges prepared with magnetic PDMS blends show thicker walls inside the sponge. After the leaching process, magnetic PDMS sponge can show lower porosity as the

density of PDMS blends increases. When the concentration of magnetic particles increases in the PDMS solution (which the density of the solution will increase accordingly) the porosity of the sponges decreases as a result of the high density of the solution (Table 3.1).

$$h = \frac{2\gamma \cos \theta}{\rho g r} \quad \text{Eq. 11}$$

Additionally, the absorption capacity of these PDMS sponges after multiple cycles was normalized by the initial weight gain. Complete removal of the remaining water from PDMS sponges in an oven can ensure the PDMS sponges could be recycled.[125]

3.3.2.5 Mechanical Testing

The inclusion of heterogeneous materials can affect the mechanical properties of PDMS sponges, so compressive stress-strain curves were used to analyze their moduli.[213] Figure 3.5A exhibits the measured stress-strain data of various prepared PDMS sponge cylinders fabricated with the granulated sugar mold, which proves that these porous materials possess a three-phase behaviour (Figure 3.5B).[214] At the beginning of curves, the intact sponges deform linearly with respect to the stress. Region Ⅰ was depicted as the elastic region. This region is followed by a relative plateau (Region Ⅱ), in which the curves demonstrate that these scaffolds are buckled and collapsed. With the increase of stress (Region Ⅲ), the PDMS sponges are crushed together and exhibit great mechanical performances. During the releasing process, these curves can return to the origin without plastic deformation. The cycled compression-relaxation test of these sponges illustrated their excellent reversible deformation ability.[120] Obvious hysteresis loops could be found in all stress-strain curves. The area inside the loop represents the energy lost during the pressing-releasing cycle. This is mainly contributed to the viscoelastic characteristics of these PDMS sponges. It indicates that strong mechanical forces could be applied to these

prepared PDMS sponges as they possess high deformability. As expected, pure PDMS sponges showed the maximum strain at about 90%, which started decreasing with the increase in the content of magnetic iron particles. This is because of the stiffness of the crystalline particles. However, the presence of iron particles contributed to the enhanced stress values of the sponges, where the maximum stress of about 540 kPa was observed for CI-loaded PDMS sponges compared to about 460 kPa for pure PDMS sponges. Nonetheless, all developed sponges exhibited 70% more strain values with the capacity of full deformation.

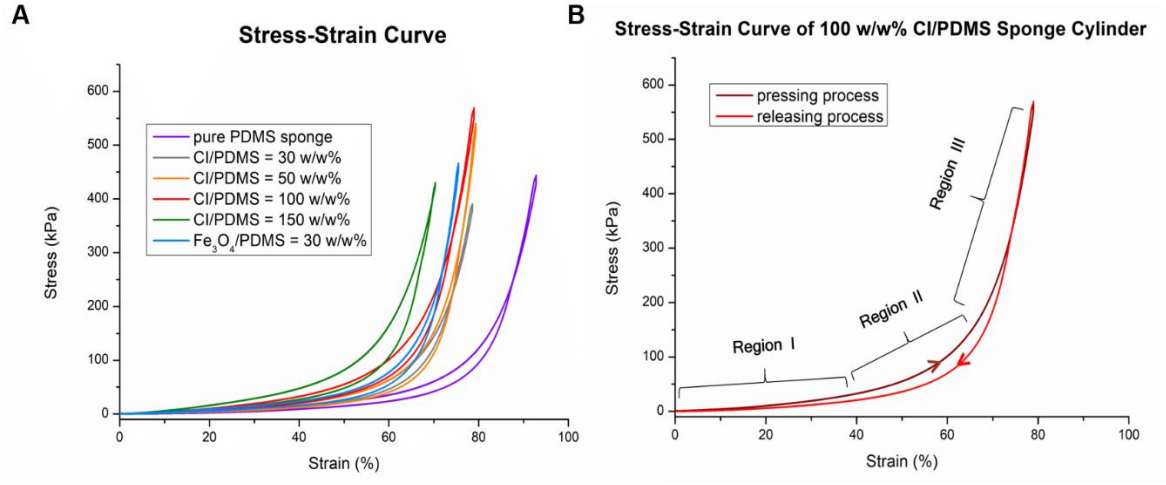

Figure 3.5. (A) The compressive stress-strain curves of various PDMS sponge cylinders prepared with granulated sugar molds. (B) Illustration of different phases (the brown curve represents the pressing process with three regions and the red curve represents the releasing process) in the stress-strain curve of 100 w/w% CI/PDMS sponge cylinders.

The measured data within the elastic region (Region Ⅰ) are shown in the stress-strain curves (Figure 3.6A). Based on the slope of strain versus stress (Eq. 7), the elastic modulus of these sponge samples can be calculated. The measured elastic modulus of prepared PDMS sponges is between 20 and 90 kPa (Figure 3.6B), which is significantly lower than that of rubber (10485.76~104857.6 kPa) and bulk PDMS materials (786.432 kPa).[123]

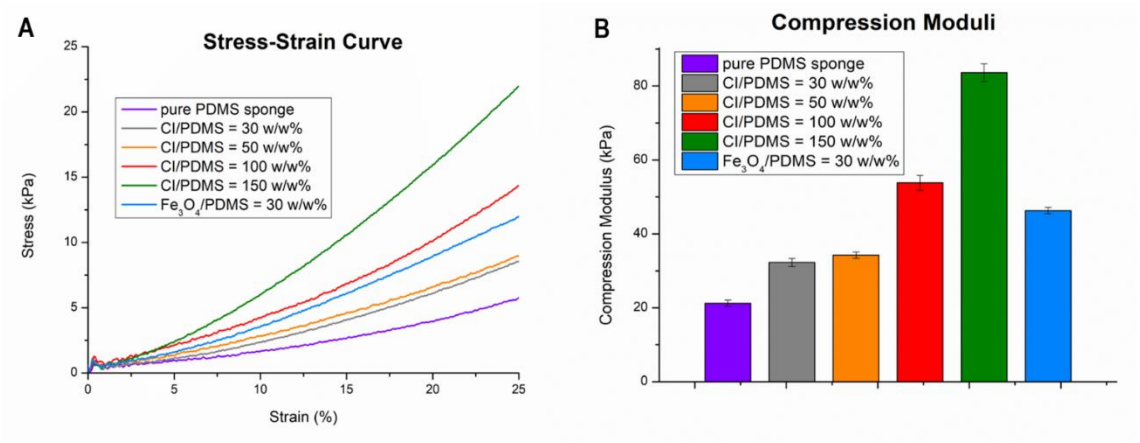

Figure 3.6. (A) The compressive stress-strain curves with a maximum strain of 25% for various magnetic particles loaded PDMS sponges prepared with granulated sugar molds, (B) Calculated compression moduli of sponges with different concentrations of magnetic particles. The average ± standard deviation was represented by the error bars (*n* = 3).

As shown in Figure 3.6B, the compression modulus will increase when the CI/PDMS w/w% ratio is increased because the interaction between the CI particles and the polymer scaffold was strengthened.[202] The possible reason for these enhanced moduli is the increased rigidity of the sponge samples because of the participation of magnetic microparticles. However, the sponge samples with lower compression modulus are more desirable because they can deflect more under the same external magnetic field. The surface properties of embedded particles have a crucial effect on the physicochemical interaction between the filler materials and the polymer scaffold network, then can further influence the mechanical properties of the composites.[202] Therefore, these PDMS sponges with excellent mechanical properties and resilience from large deformation could be potentially applied in drug-releasing devices and implantable biomedical devices.

3.3.2.6 Sponge Deformation under Magnetic Field

The height of prepared sponge cylinders can decrease obviously under the magnetic field provided by Magnet D (Table 2.2). At the same time, the volume of the interconnected pores of sponges will be minimized. Like manual compression

(Figure 3.1D), all deformations due to the magnetic force would be reversible. The deformation of these magnetic sponge samples increases linearly as a function of magnetic field strength. Under Magnet D, the height changes of various sponge samples were compared in Figure 3.7. When the CI concentration in PDMS sponges was increased, a stronger magnetic force can be applied to the magnetic PDMS sponge in a specific magnetic field and the volume variations subsequently would increase. It is clear from the figure that the sponge with the lowest CI concentration (CI/PDMS=30 w/w%) presents the least compression. The sponge with the CI/PDMS weight ratio of 150 w/w% shows less deformation, similarly to the 50 w/w% CI/PDMS sponge and 30 w/w% Fe_3O_4/PDMS sponge.

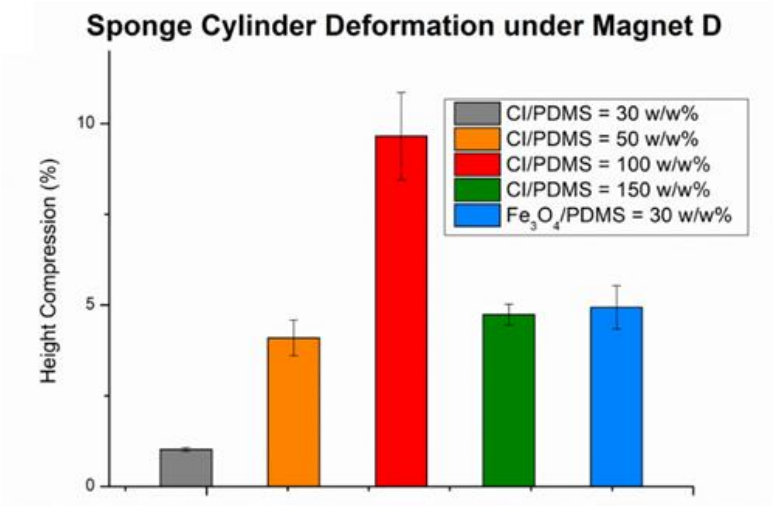

Figure 3.7. Average configuration changes of sponges prepared with granulated sugar molds under Magnet D, the average ± standard error was represented by the error bars (*n* = 3).

Given its deformation of 10%, the sponge prepared with the most magnetic field sensitive weight ratio of CI and PDMS (100 w/w%) in the experiment was selected for further sponge optimization study.

3.3.2.7 Dielectric Constant (Relative Permittivity) Measurement

In this study, embedded magnetic particles in polymer scaffolds can also be regarded as conductive fillers for improving the conductivity of this material.[215]

The dielectric constant of a material is its absolute permittivity represented as a ratio relative to the permittivity of vacuum or free space. The value could show how easily this material can become polarized by the imposition of an electric field on an insulator. From Figure 3.8, it is obvious that the relative permittivity value of pure PDMS sponge is the lowest. When the concentration of magnetic powders increases, the relative permittivity value also increases. When compared with the relative permittivity value of water ($\varepsilon_r(H_2O)$= 78) at room temperature, the relative permittivity for these sponge samples is very low.[216]

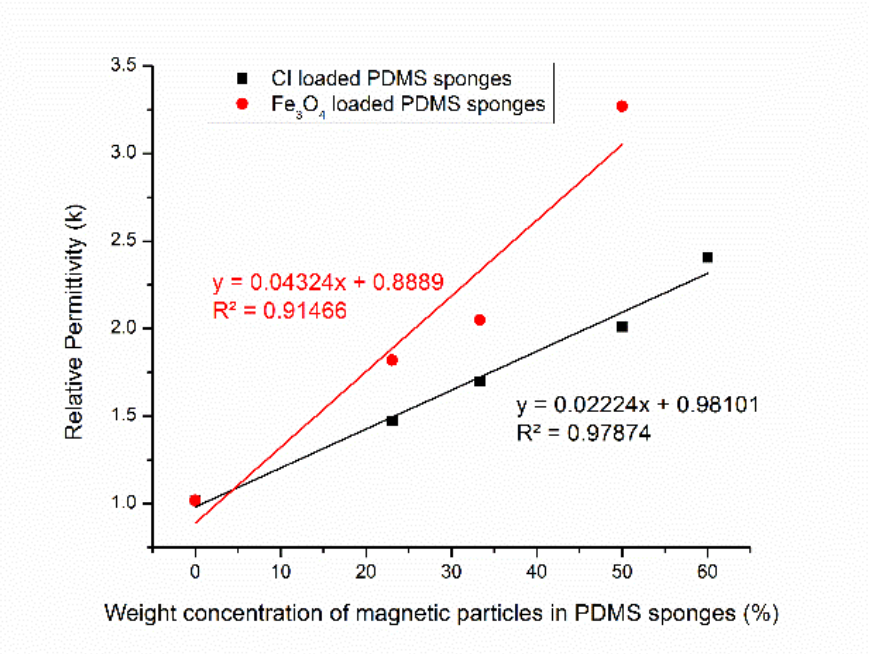

Figure 3.8. The comparison of the relative permittivity of Fe_3O_4 loaded PDMS sponges and CI loaded PDMS sponges.

Through the comparison of relative permittivity values of Fe_3O_4 loaded and CI loaded PDMS sponges (Figure 3.8), the PDMS sponges loaded with Fe_3O_4 show higher relative permittivity when the concentrations of magnetic powders are the same. The correlation coefficient (R^2) values of the trendlines are 0.979 and 0.915, respectively (very close to 1), so the data fit the lines well. As a result, the relative permittivity of PDMS sponge samples loaded with different concentrations of magnetic powders could be predictable with these equations included in Figure

3.8. As the magnetic particles were uniformly embedded on the PDMS scaffold, the holistic impedance matching was enhanced.[179]

When external pressure is applied, the sponge is compressed and the air holes shrink.[217] According to Eq. 5, the capacitance (C) of the PDMS sponge will increase primarily due to the reduction in the thickness of sponge samples (d). Capacitance has been used as one of conversion mechanisms for transforming external pressure signals (including stretch and compression) into electrical signals in the applications of implantable flexible pressure sensors, such as wearable devices, intelligent robots and electronic skin.[214,215] In recent years, various PDMS-based porous conductive sponges were developed and these sponges were considered as ideal scaffolds for stretchable flexible sensors and piezoresistive sensors because of their exceptional deformability, failure strain, synchronous reflection to stimulations, and magnetic-mechanic-electric coupling property.[215,218] Consequently, the prepared PDMS sponges have the potential to be applied in wireless flexible pressure sensors as a dielectric layer to overcome the disadvantages of most flexible sensors, like weak stretchability, low gauge factor and long hysteresis.[217]

3.4 Conclusion

Different concentrations of CI and Fe_3O_4 particles were embedded as magneto-sensitive materials in PDMS resins for the fabrication of macroporous sponges via a sugar-templated process. Various PDMS sponges were successfully fabricated with different magnetic particles and concentrations. The sugar templating method for fabricating porous scaffolds has the advantages of low cost, flexible formulation design, simple process, and no other materials required. The prepared magnetic PDMS sponges were evaluated for their morphology, the particle size of magnetic particles, solid-state, porosity (absorbency), elastic modulus, deformation under a magnetic field and dielectric constant. The 100

w/w% CI/PDMS sponge has been proved to be a promising candidate as scaffolds for delivering drug solutions in the local treatment of diseases and further applications on innovative medical devices. However, the deformation of these sponge cylinders under the magnetic field of 355 mT is not higher than 10%. As a result, it is necessary to optimize these magnetic PDMS sponges for achieving higher magnetic field sensitivity and an accurate drug release rate in DDSs. According to the preparation process of PDMS sponges, the effects of various sugar molds and weight ratios between the prepolymer and the curing agent of PDMS will be analyzed in the following chapter.

4. Chapter 4: Optimization of Magnetic PDMS Sponges

4.1 Introduction

To investigate the influence of the fabrication process on the deformation of these PDMS sponges under varying magnetic fields, 100 w/w% CI/PDMS sponges prepared in the same way just except different sugar moulds and/or different weight ratios between the PDMS prepolymer and curing agents were characterized for comparison in this chapter.

Although the PDMS prepolymer and curing agent should be blended at the weight ratio of 10:1 according to the instruction manual provided by the manufacturer, the PDMS substrate prepared with the weight ratio of 30:1 showed significantly higher stretchability and lower elastic modulus.[219] Additionally, the porous PDMS scaffold prepared with the weight ratio of 30:1 has been studied as magnetically controllable and flexible sensors due to its excellent deformability, strain-dependent electrical properties and magnetic controllability.[218]

Choi *et al.* proved that the optimization of the sugar template employed in the formation of the PDMS sponges can increase the absorption capacity of these sponges significantly by combining various sugar particles (i.e., granulated, sanding, and black sugar particles) in the template.[182] The PDMS sponges prepared with the sugar template consisted of heterogeneously mixed sugar particles of different sizes exhibited higher absorption capacity and enhanced porosity.[182] This inspired me to focus on the selection of sugar mold for the magnetic PDMS sponge fabrication.

In this chapter, a novel method of measuring the deformation of prepared magnetic PDMS sponge cylinders was developed with the manipulation of a

bright-field microscopy metrology system. The optimized sponges were characterized for their elastic modulus, recyclability and thermostability. Furthermore, *in vitro* cell studies were conducted to illustrate the inhibition behaviour of drug-loaded sponges on the growth of cancerous cells. The mechanical property and magnetic field sensitivity of PDMS sponge cylinders could be modulated by controlling the sugar mold and the weight ratio of the PDMS prepolymer and curing agent. These results confirmed that these magnetic PDMS sponges fabricated with a simple, economical and effective approach can be applied as a component of smart stimuli-responsive drug delivery systems for the localized on-demand delivery of chemotherapeutic drugs.

4.2 Methods

4.2.1 Optimization of the Sponges

Refer to Section 2.3.3.

4.2.2 SEM and EDS

Refer to Section 2.5.3.

4.2.3 Recyclability

Refer to Section 2.3.2.5.

4.2.4 TGA

Refer to Section 2.7.1.1.

4.2.5 Cell Culture Studies

Refer to Section 2.10.

4.3 Results and Discussion

4.3.1 Particle Size Analysis of Sugar

The calculated average particle sizes (P_m) of granulated sugar and demerara sugar (Figure 4.1A-B) are 0.68 and 1.60 mm respectively. The particle size

frequency diagrams are shown in Figure 4.1C. As a result, PDMS sponges prepared with the demerara sugar mold may show weaker stiffness because the interconnected pore size is much bigger when compared with sponges prepared with granulated sugar. For increasing the porosity of sponges, the mixture of granulated and demerara sugar could be employed as the sugar mould for fabrication as well.

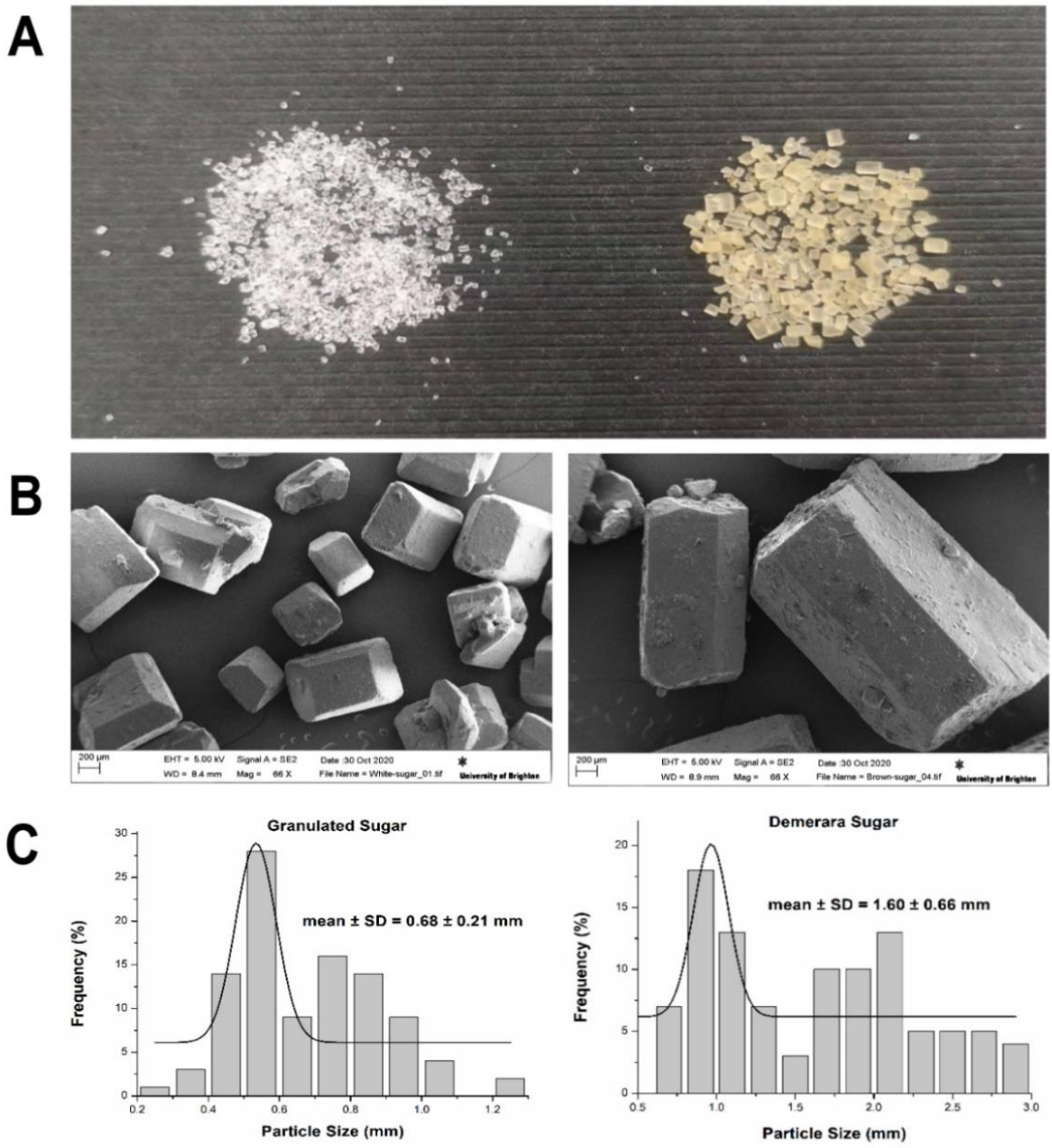

Figure 4.1. (A) Photographs, (B) SEM images and (C) particle size frequency diagrams of granulated sugar and demerara sugar.

The 100 w/w% CI/PDMS sponge prepared with three different sugar templates will be characterized for comparison.

4.3.2 Sponges Prepared with Different Sugar Molds

The stress-strain curves with a maximum strain of 25% for 100 w/w% CI/PDMS sponge cylinders (diameter × thickness = 12 mm × 7 mm) fabricated with different sugar moulds are shown in Figure 4.2A. The sponge cylinder fabricated with the granulated sugar mould is more rigid and resistant to compression than the demerara sugar mould and the mixed sugar mould, which could be explained by the smaller interconnected pore size. Consequently, PDMS sponge cylinders prepared with demerara sugar or mixed sugar particles will possess a looser structure, higher porosity, less rigidity and may show more deformation under the same magnetic field because of the less uniform sugar particle size.[120]

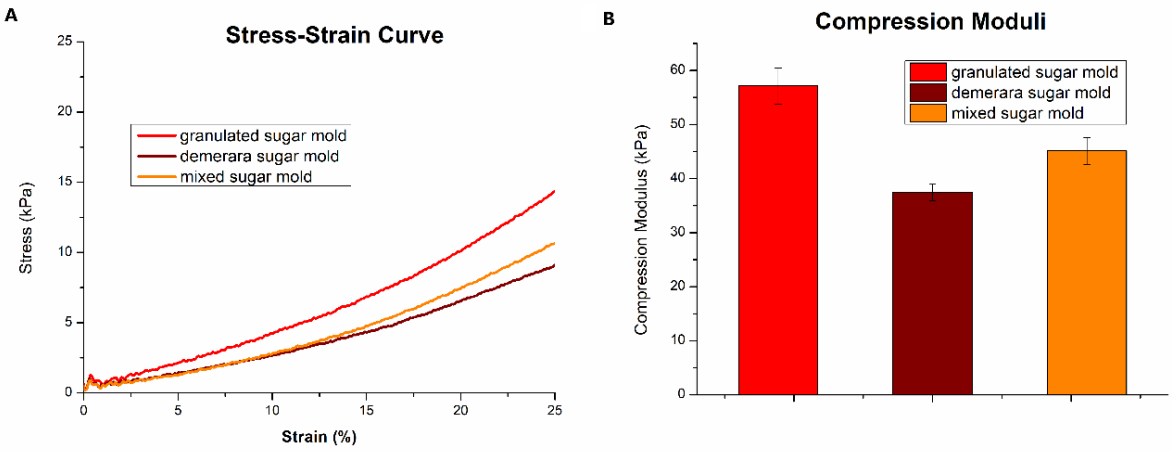

Figure 4.2. (A) The compressive stress-strain curves with a maximum strain of 25% for 100 w/w% CI/PDMS sponges prepared with different sugar molds. (B) Calculated compression moduli of sponges prepared with different sugar molds. The average ± standard deviation was represented by the error bars (n = 3).

As the 100 w/w% CI/PDMS sponge prepared with the demerara sugar mould showed the lowest elastic modulus (38 kPa) in Figure 4.2B, it will be further investigated in the following section.

4.3.3 PDMS Sponge Formulation Optimization

According to Li *et al.*, the PDMS prepared with different prepolymer and curing agent weight ratios showed different compression modulus values.[202] 100 w/w% CI/PDMS sponges prepared with the PDMS prepolymer and curing agents weight ratios of 15:1, 20:1, 25:1 and 30:1 were fabricated with the demerara sugar mold aiming to overcome the problems encountered when using the previous prepolymer/curing agent ratio (10:1). The sponge sample prepared with the weight ratio of 30:1 had an increased viscosity and therefore it was difficult to be fully cured. According to Figure 4.3, the rigidity of the sponge decreases when the prepolymer and curing agents weight ratio increases. The elastic modulus of the 100 w/w% CI/PDMS sponges prepared with the demerara sugar mold decreased significantly when the curing agent content decreased. The possible reason is the low cross-linking density of the sponge with the lower ratio of curing agents.[120] However, inadequate cross-linking may cause unwanted stickiness and relative low recoverability. Hence, the less amount of curing agents is added into the PDMS prepolymer in the preparation process, the PDMS sponges will show more deformation under magnetic fields.

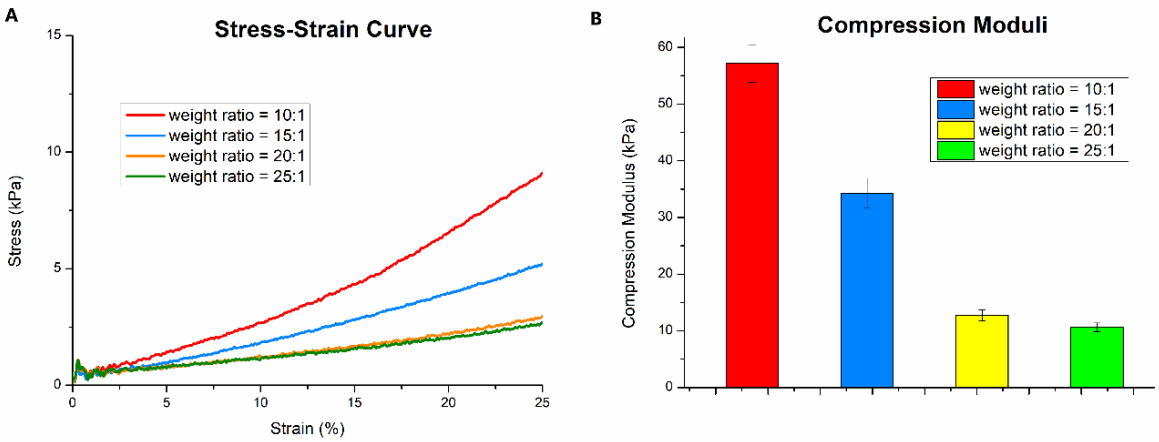

Figure 4.3. (A) The compressive stress-strain curves with a maximum strain of 25% for 100 w/w% CI/PDMS sponge cylinder prepared with the demerara sugar mold and various weight ratios of PDMS prepolymer and curing agents. (B) Calculated compression moduli of these sponges. The average ± standard deviation was represented by the error bars (n = 3).

As can be observed from Figure 4.4, the 100 w/w% CI/PDMS sponge cylinder prepared with demerara sugar and PDMS prepolymer/curing agents = 25:1 w/w showed the maximum compression as a function of the applied magnetic field provided by four different magnets (Magnet A, B, C and D) in Table 2.2. Generally, decreasing the curing agent's concentration can lead to softer PDMS sponges and consequently increases the volume change under a specific magnetic field. The R^2 values of all trendlines are close to 1, so the data fit these lines well. Based on the equation mentioned in Figure 4.4, the deformation of each kind of sponge cylinder (diameter × thickness = 12 mm × 7 mm) in a given magnetic field could be easily predicted.

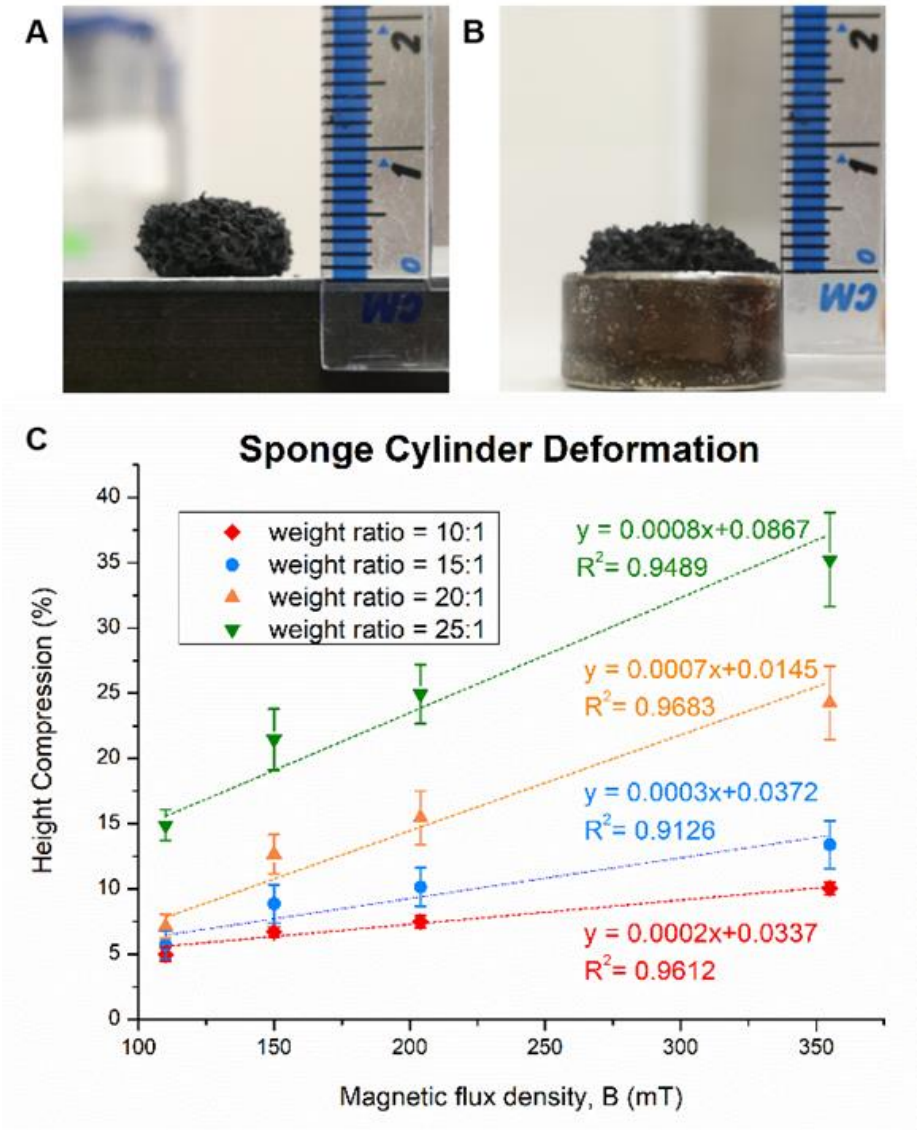

Figure 4.4. (A) Image of the original shape of the 100 w/w% CI/PDMS sponge cylinder prepared with demerara sugar and PDMS prepolymer/curing agents = 25:1 w/w, (B) the deformed shape of sponge cylinder under Magnet D. (C) Height compression of sponge cylinders versus different magnetic fields, the average ± standard error was represented by the error bars (*n* = 3).

4.3.4 SEM and EDS Analysis

From these SEM images of thin sponge slices (Figure 4.5), no obvious difference in the morphology or distribution of magnetic particles was discovered among all these PDMS sponges. All sponge samples possess a similar open network of pores with a large surface area and a perfect porous structure. It indicates that the mixture of magnetic particles and PDMS (prepolymer and curing agents) filled the sugar mold completely and is capable of forming porous scaffolds.[214] Interconnected pores of these sponge samples were spread evenly across the PDMS and their pore size is around 200-500 μm mainly because the same sugar template was used. With the addition of magnetic particles, the surface of the sponge becomes rugged. As magnetic particles were wrapped completely, the risk of oxidation will be minimized, the stability will be enhanced and the surface roughness will be increased.[179,202,218] However, the rough surface and the 3D interconnected pores of magnetic powder loaded PDMS sponges could enhance the hydrophobic property of the sponges.[198]

In conjunction with advanced SEM, EDS has been widely applied as a chemical microanalysis technology because of many advantages, such as high-resolution imaging, semi-quantitative elemental analysis and qualitative X-ray elemental maps.[220] It is difficult to fabricate sponges with both high contents of magnetic particles and superior distribution of magnetic particles at the same time due to the tendency for these Fe_3O_4 and CI particles with large surface areas and high free energy to cluster and precipitate.[210] To investigate the chemical composition and spatial distribution of magnetic particles in sponges, EDS was also used in this study.

The EDS analysis of the cross-section area in these sponges showed various distributions of elements (Figure 4.5). The pure PDMS sponges only exhibited a large number of signals of C, O and Si as well as trace amounts of Pt because of the sputter coating process. With the addition of CI particles in the PDMS sponges, the signals of Fe increased, whereas the signals of Si decreased gradually.

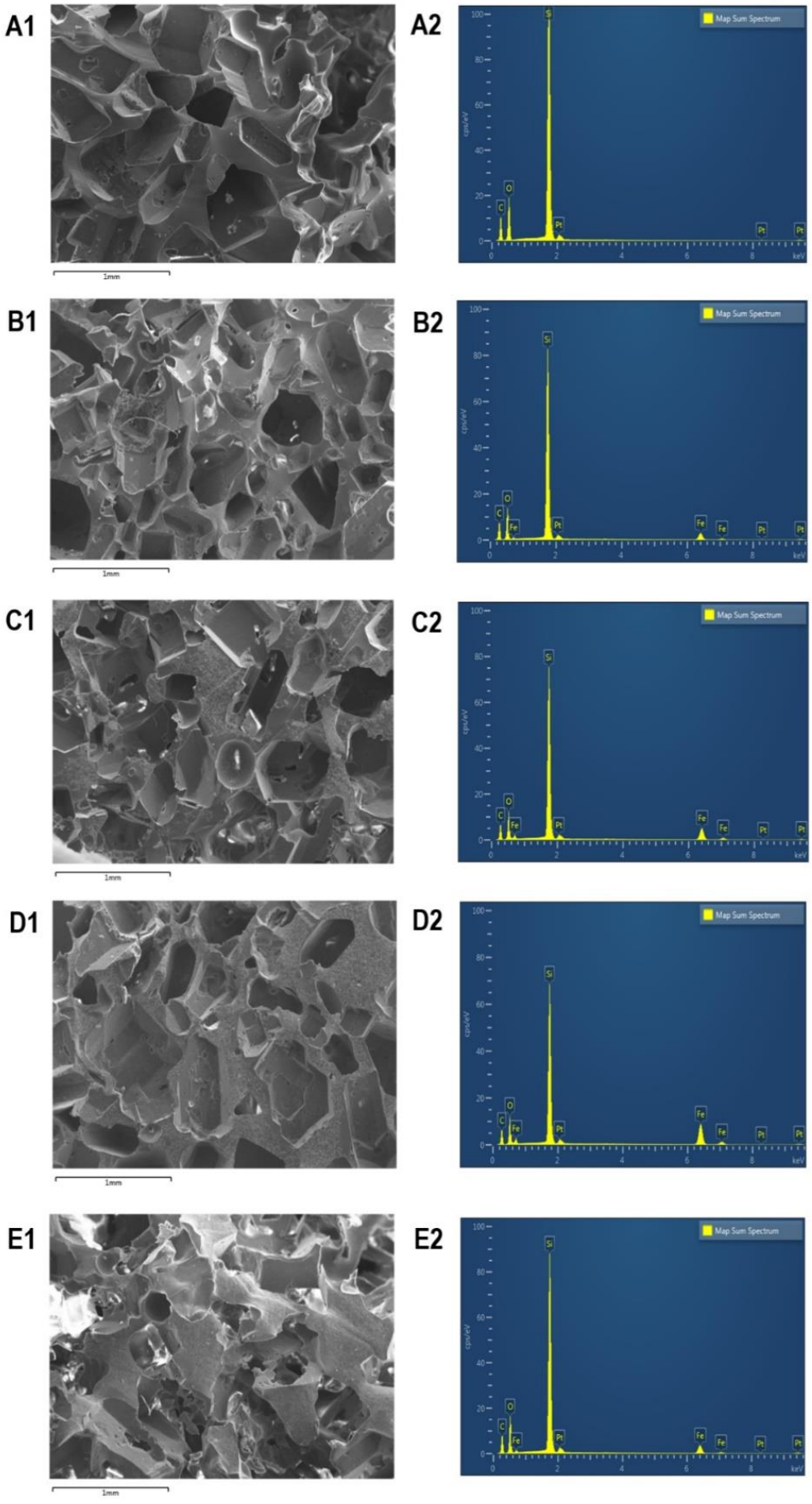
A1
A2
B1
B2
C1
C2
D1
D2
E1
E2
1mm
Map Sum Spectrum
cps/eV
keV
O
C
Fe
Pt
Si

Figure 4.5. SEM images of the morphology and EDS spectra in the cross-section of (A) pure PDMS sponges, (B) 30 w/w% CI/PDMS sponges, (C) 100 w/w% CI/PDMS sponges (D) 150 w/w% CI/PDMS sponges and (E) 30 w/w% Fe_3O_4/PDMS sponges.

Multi-elemental EDS mapping images of C, Fe, O and Si are shown in Figure 4.6. The bright spots of these elements in corresponding maps indicate a homogeneous distribution of these elements in the field of view of the partial cross-section. Furthermore, the magnetic particles showed no agglomeration and were distributed in PDMS uniformly.

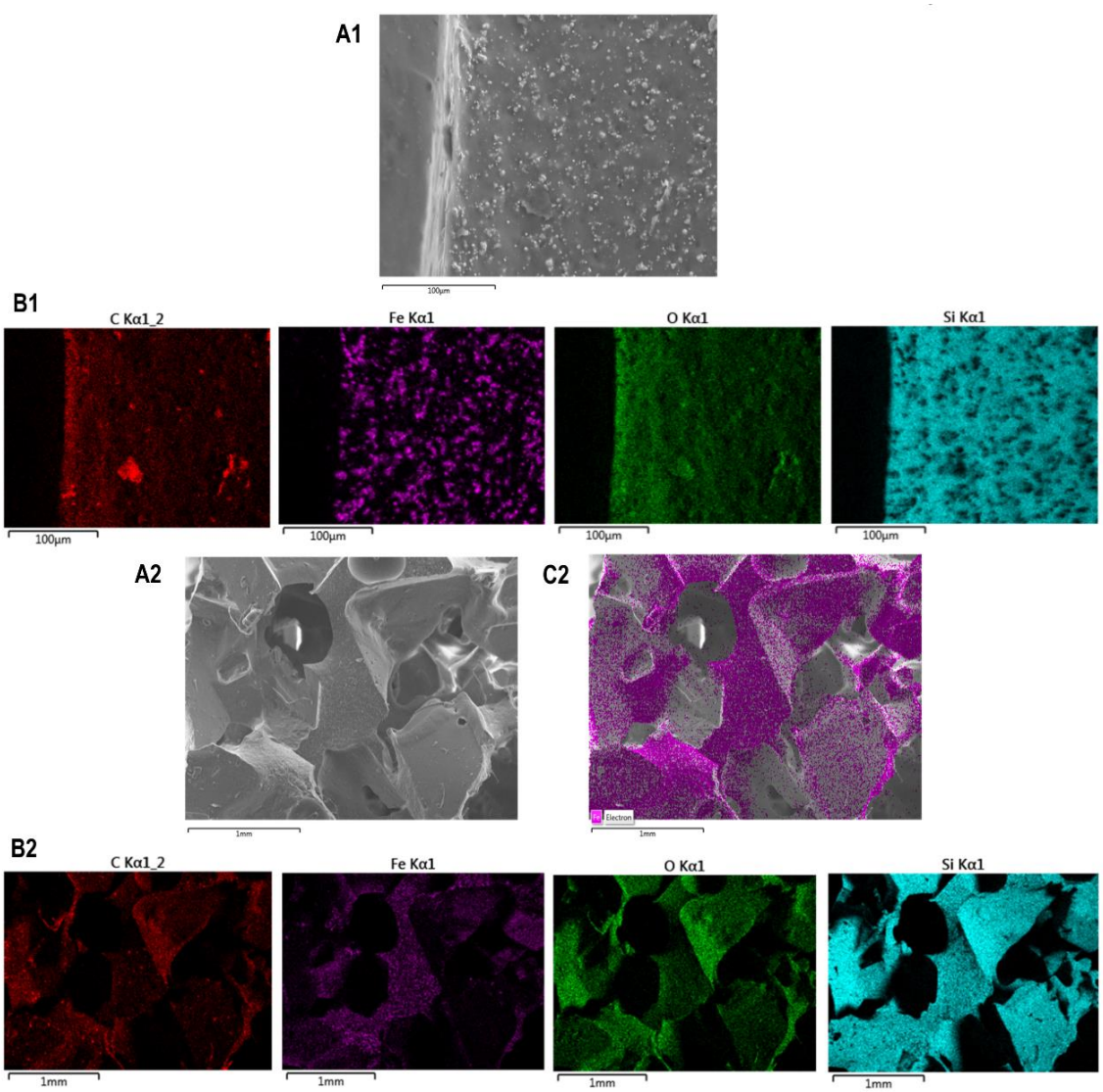

Figure 4.6. The cross-sectional (A) SEM image, (B) multi-element EDS mapping of C, Fe, O and Si, and (C) SEM-EDS digital image of elements Fe in 100 w/w% CI/PDMS sponges.

4.3.5 Recyclability

After finishing all tests on the sponges, an attempt was made to test their recyclability, which is a crucial property in actual applications.[221] The most fragile 100 w/w% CI/PDMS sponge prepared with demerara sugar (PDMS prepolymer/curing agents = 25:1 w/w) was selected as the model for the recyclability test. The results showed that the sponge cylinder weight was constant before absorption and after desorption of water. The sponge samples exhibited almost no change in their absorption capacities and their weights after 10 absorbing/desorbing cycles shown in Figure 4.7.

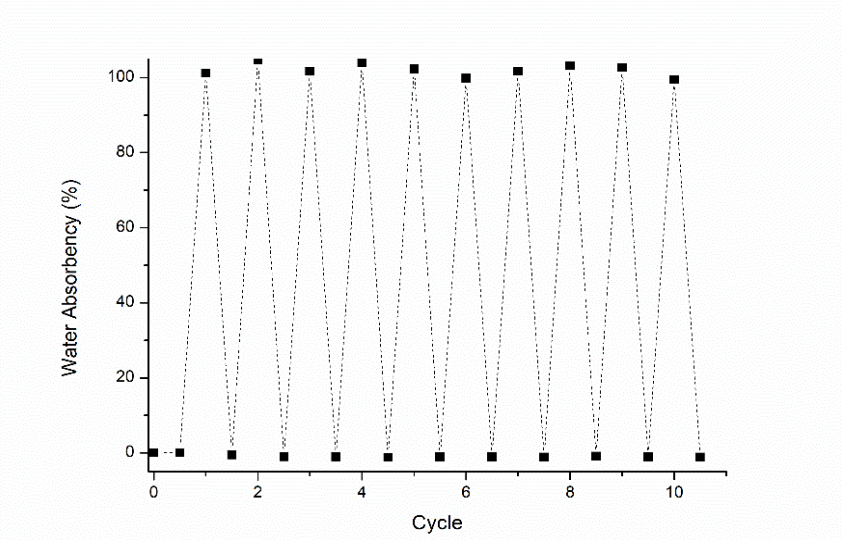

Figure 4.7. Demonstration of recyclability of 100 w/w% CI/PDMS sponge cylinders (prepared with demerara sugar and PDMS prepolymer/curing agents = 25:1 w/w).

4.3.6 Thermal Characterization

The TGA analysis (Figure 4.8) of CI particles exhibits a slight ring trend, possibly due to oxidation of the particles caused by the impurity of the nitrogen gas.[207] The fabricated PDMS sponges showed almost no weight loss below 100°C, which is related to the relatively low weight ratio of absorbed moisture.[209] Their weight loss begins from 200°C, mainly due to the onset of thermal degradation. With the temperature increasing to 400°C, significant weight loss for these sponge

samples (especially the pure PDMS sponge) occurred as a result of the decomposition of methyl groups.[198,221] Also, it was observed that the pure PDMS sponge sample shows the highest weight loss, indicating the most obvious chemical degradation. When the ferromagnetic particles (Fe_3O_4 or CI) concentration of the PDMS sponge is the same, the weight loss of PDMS sponges keeps constant. With the increase of ferromagnetic particles in the PDMS sponge, the total weight loss will decrease. It indicates that the introduction of magnetic particles can improve the thermostability of the PDMS matrix.[207] Furthermore, the degradation at a processing temperature will be decreased and the degradation rate will be slowed down owing to the interactions between the PDMS matrix and embedded magnetic particles.[207] Karimzadeh *et al.* proved that the TGA curve of bare Fe_3O_4 nanoparticles shows only 1.6% weight loss between 25°C and 200°C and no obvious weight loss from 200°C to 600°C.[222] This result is in consistence with our hypothesis that the degradation is mainly due to PDMS whereas bare ferromagnetic particles are thermally stable even at elevated temperatures. Consequently, these fabricated magnetic PDMS sponges can keep the drug thermally stable during the preparing process and under real operating conditions.

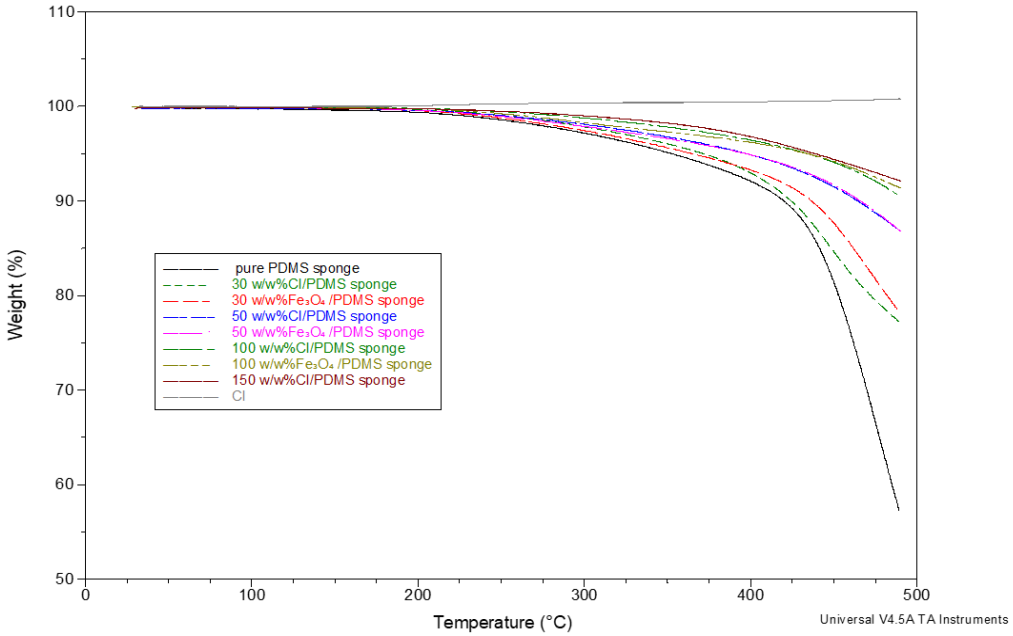

Figure 4.8. TGA thermal traces of CI particles, pure fabricated PDMS sponge and various magnetic PDMS sponge samples. (The initial weight shows 100%).

4.3.7 Cell Studies *in Vitro*

To explore the inhibition behaviours of different sponges, different magnetic fields and different concentrations of FLU solution on the growth of cancerous cells, various groups of assessments were designed (Table 4.1). By comparing the numbers of HeLa cells in four days, the differences in the inhibition of HeLa cells among these groups could be observed.

Table 4.1. Sponge samples loaded with different solutions and under different magnetic fields

Group	Magnet	Sponge	FLU Solution
A1	B	×	×
A2	C	×	×
A3	×	pure PDMS	×
A4	×	pure PDMS	25 mg/mL
A5	B	pure PDMS	×
A6	B	pure PDMS	25 mg/mL
A7	C	pure PDMS	25 mg/mL
A8	×	CI/PDMS=100 wt%	×
A9	×	CI/PDMS=100 wt%	25 mg/mL
A10	B	CI/PDMS=100 wt%	×
A11	C	CI/PDMS=100 wt%	×
A12	B	CI/PDMS=100 wt%	25 mg/mL
A13	C	CI/PDMS=100 wt%	25 mg/mL
A14	B	CI/PDMS=100 wt%	12.5 mg/mL
A15	C	CI/PDMS=100 wt%	12.5 mg/mL

Comparing Group A3 with A5, Group A1 with A2, Groups A8, A10 with A11 in terms of the number of cells (Figure 4.9), it is obvious that a stronger magnetic field can exhibit stronger inhibition effects on the growth of HeLa cells. Similarly, the increase of HeLa cell numbers in groups with these PDMS sponges (especially CI loaded PDMS sponges) is not as obvious as the increase in groups without sponge samples as reflected by the data of Groups A1, A5 with A10 and Group A2 with A11. The possible reason is the volume of PDMS sponge samples

in the well plates affect the growth of HeLa cells because the number of cells in all these groups still showed an increasing trend. Additionally, sponge samples loaded with FLU solution (both 12.5 and 25 mg/mL) can kill almost all HeLa cells within 4 days (Groups A4, A6, A7, A9 and A12-15). The differences between pure PDMS sponges (Groups A4, A6 and A7) and CI loaded PDMS sponges (Groups A9, A12 and A13) under various magnetic fields illustrate that the main reason for the decrease in cell numbers in Group A13 is the addition of a magnetic field which can trigger the release of FLU solution from magnetic sponges. Also, there is no significant difference in cell numbers between Groups A12 and A14, Groups A13 and A15. The possible reason may be that both concentrations of FLU solutions are high enough to inhibit the growth of the HeLa cells. Lower concentrations will be applied in the future to test the effect of various FLU concentrations loaded into the sponges on the growth of cancerous cells. Additionally, drug release dynamics based on magnetic PDMS sponge types and external magnetic fields will be further explored.

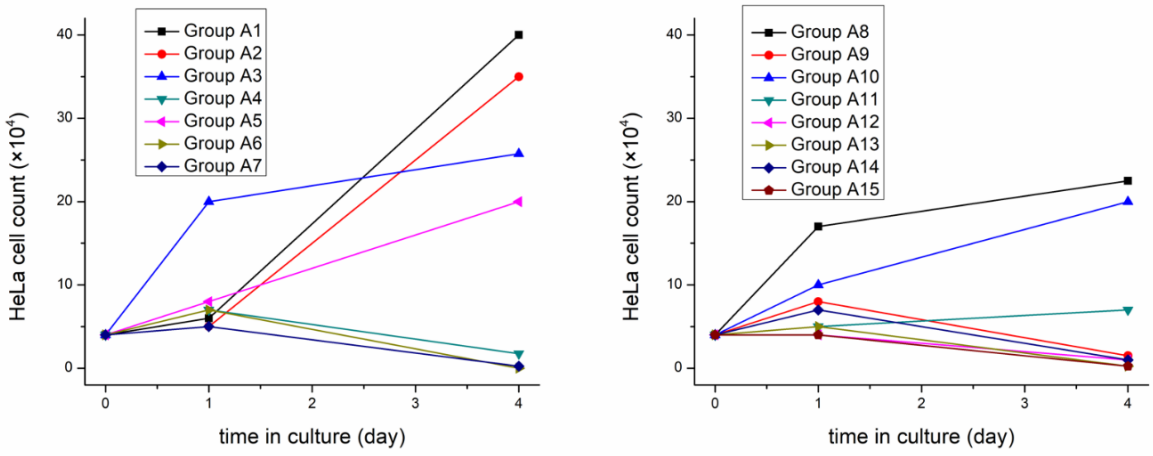

Figure 4.9. Numbers of HeLa cells under different conditions.

4.4 Conclusion

In this chapter, the required porous scaffolds for DDSs with suitable porosity and magnetic field sensitivity could be prepared by controlling the fabrication process.

Besides, the study showed that these magnetic sponges can be reused as the water absorption capacity of the prepared CI-loaded PDMS sponge did not change after 10 absorbing/desorbing cycles. The fabricated interconnected microporous magnetic particles loaded PDMS sponges possess flexible skeletons and good recyclability because of their recoverability after compression (deformation) without any breakdown. All these promising features and simple fabrication make the CI-loaded PDMS sponge a superior scaffold for delivering drug solutions in the local treatment of diseases and further applications in innovative medical devices. All physicochemical and magneto-mechanical analysis confirmed that the optimized magnetic field sensitive PDMS sponge can provide an efficient method for delivering an on-demand dose of anti-cancer drug solutions at a specific location and timing with the aid of controlled magnetic fields.

5. Chapter 5: Comparison of 5-fluorouracil Solutions Using Drug-coated Powder-based 3D Printed Tablets

5.1 Introduction

In this chapter, three different 5-fluorouracil (FLU) solutions were designed and evaluated for further drug loading process of the fabricated PDMS sponges. The powder-based (PB) three-dimensional (3D) printing technology was applied to produce tablets (diameters of 10 mm and 13 mm), then coated with the anticancer model drug (FLU). For this study, a composition of the powder carrier containing $CaSO_4$ hydrates, vinyl polymer, and carbohydrate was used as the matrix former, whereas 2-pyrrolidone with a viscosity like water was used as a binding liquid or inkjet ink. All tablets were printed using a commercial ZCorp 3D printer with modifications. The resultant tablets were subject to coating with various drug solutions, including 5-fluorouracil solution and polymeric solutions containing 5-fluorouracil. The composition of the polymeric solutions was adjusted at a drug: polymer(s) 1:1 (w/w) ratio. Either Soluplus® (SOL) alone or in combination with polyethylene glycol (PEG) was used to develop the FLU coating solution of 2.5% (w/v) concentration.

5-fluorouracil has been widely applied as a first-line chemotherapeutic agent in various cancer therapies, such as colon cancer, rectal cancer, gastric cancer, breast cancer, bladder cancer, liver cancer, etc.[184] FLU, a BCS class Ⅲ drug, is a pyrimidine-analogue drug which can inhibit the biosynthesis of deoxyribonucleotides for DNA replication.[223,224] FLU can result in apoptosis of cancer cells because of its broad spectrum of activity against cancer.[225] The main challenges to applying FLU are the short half-life, non-selective distribution, non-uniform oral bioavailability and toxicity.[225] As a result, many side effects are commonly observed during its clinical applications, such as mucositis, dermatitis,

diarrhoea, gastric disturbance and myelosuppression.[226] High and frequent dose administration is a common method to achieve an effective blood drug concentration, but side effects of FLU become severe at the same time.[223,227] Nowadays, topical and injectable formulations of FLU are commercially available, whereas oral formulations are not available because of serious side effects and low bioavailability.[228] Localization of FLU in the targeted tissues can reduce its toxicity and improve its pharmacokinetic profile.[229]

Therefore, FLU was selected as the model drug to prove the concept of our printing process. This model drug is highly potent and available in low dosage. Though FLU is fairly heat stable, the successful optimization and subsequent development of its tablets using PB heat-less 3D printing will provide an ideal platform to process and evaluate many other model drugs that are highly thermo-sensitive, such as biologics or macromolecules. Optimized powder carrier containing $CaSO_4$ hydrates were used as powder bed materials. The drug solution compositions were optimized using hydrophilic polymer combinations. This study proves that an optimized powder-based 3D printing approach can also be used to develop pharmaceutical products using pharmaceutical grade excipients by eliminating the need for thermal processing. In addition, PB 3D printing is much easier and less time consuming than making filaments to fabricate tablets through the FDM 3D printing technology.

5.2 Methods

5.2.1 PB 3D Printing and Characterization of Tablets

Refer to the Section 2.4.1.1.

5.2.2 Coating Process

Refer to the Section 2.4.1.2.

5.2.3 Particle Size Distribution of Printing Powder

Refer to the Section 2.4.1.3.

5.2.4 SEM of PB 3D Printed Tablets

Refer to the Section 2.5.1.

5.2.5 Confocal Microscopic Analysis of Drug-coated PB 3D Printed Tablets

Refer to the Section 2.5.2.

5.2.6 Dissolution Studies

Refer to the Section 2.9.1.

5.3 Results and Discussion

5.3.1 PB 3D Printed Tablets

The powder-based 3D printing platform used the maximum layer resolution in accordance with the slicing fragments counted, which resulted in the estimated time for the printing of the single tablet at about 5 min. This can be fairly scaled up for pilot scale manufacturing and a commercially viable process. The jet-dispensing rate plays a pivotal role in the texture and binding properties of the particles with the printed 3D objects (Figure 5.1). The printing process was optimized so that all printed tablets were almost instantly ready for further evaluation, although an optional drying step can be introduced to produce tablets as robust as possible to withstand the handling process. This eliminates the wait time for the eradication of the residual solvent. The printing process utilized an aqueous solution of 2-pyrrolidone, which is largely available in various pharmaceutical formulations.[230] The use of this binding liquid assisted in a smooth and faster printing process without any further post-processing steps. It has been reported that 2-pyrrolidone is an acceptable solvent to be used in DDSs

for humans. It is also widely present in foodstuffs and food additives.[230]

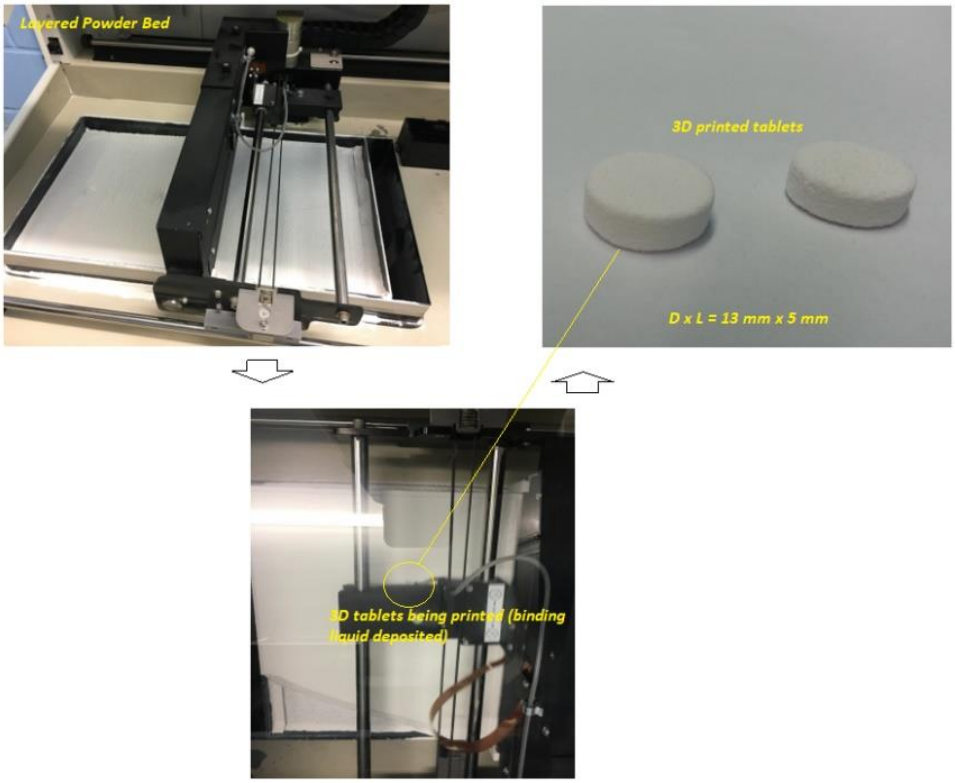

Figure 5.1. Schematic diagram of the printing process of PB 3D printing process utilized in this study.

5.3.2 Particle Size Distribution Analysis

The carrier powder was composed of pharmaceutical grade $CaSO_4$ granules, vinyl polymer, and carbohydrate with narrow particle size distribution. The particle size and shape of active and non-active pharmaceutical ingredients in most pharmaceutical products can affect various significant physical properties and quality attributes, such as physicochemical stability and dissolution rate.[231] In Figure 5.2B, as the mode average diameter according to the peak is around 50 µm, the flowability of these particles may just be at the threshold of good flow. This can sometimes result in the appearance of incomplete layers during the printing process.[137] However, the optimization of processing conditions, various tablets with high accuracy and shape fidelity (Figure 5.2A) were still printed successfully despite the moderate to poor flowability of the printing powder

carriers.

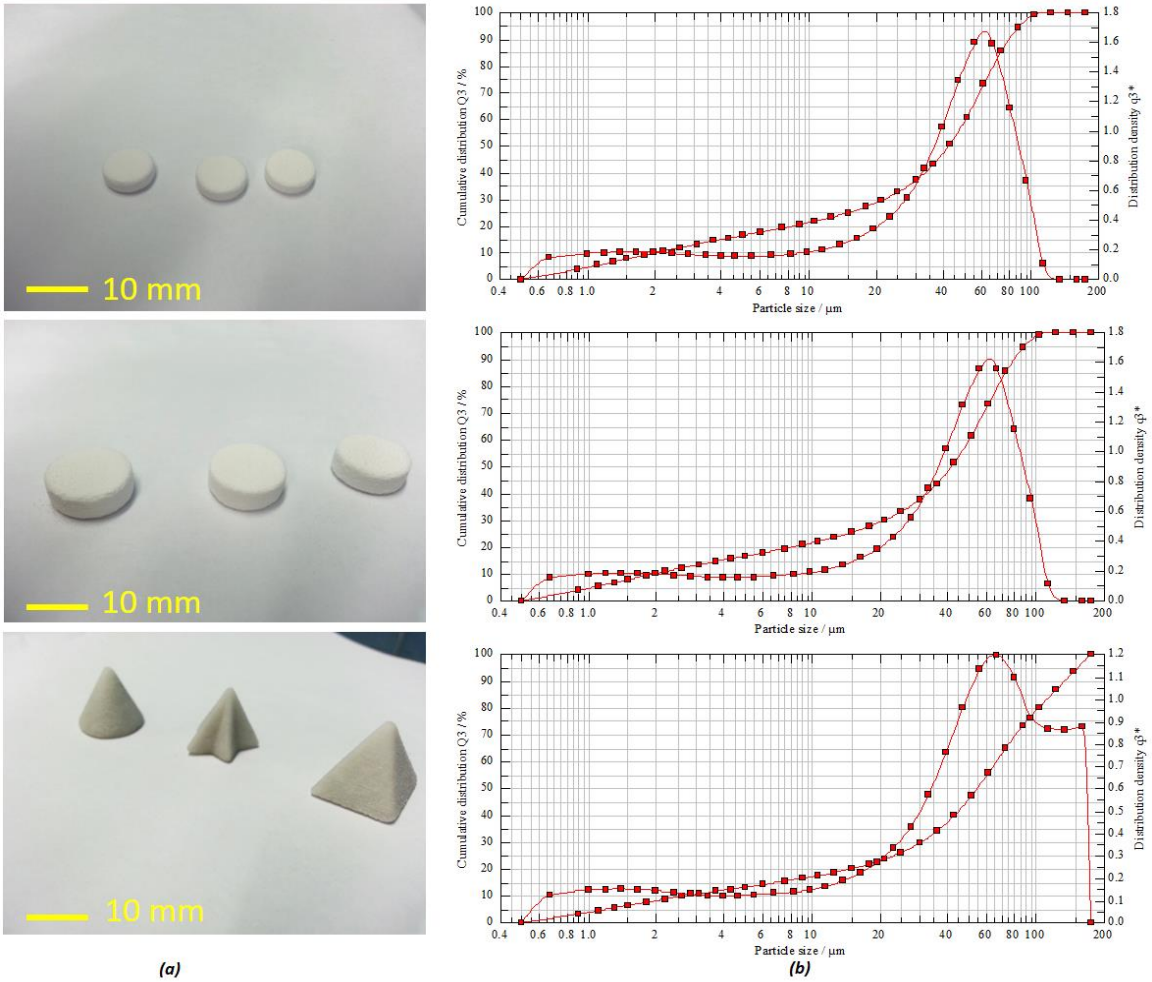

Figure 5.2. (A) 3D printed tablets with different shape and dimensions, (B) volume-weighted particle size distribution of the printing powder carriers.

The mean particle size distribution was found to be in the range of about 41.65–54.44 µm ($D_{50\%}$) with a volume mean diameter (VMD) of 41.46 µm (Figure 5.2B). The powder flowability test via both Carr's index and angle of repose estimation for formulation powders exhibited good flow properties. This is reflected in the calculated values of Carr's index and angle of repose as 25 and 22.05 degrees, respectively. Moreover, the calculated bulk density value of the powder indicates that it rendered good compatibility as well (Table 5.1). It has been reported that the particle morphology of $CaSO_4$ hydrates based powder with high performance can assist in the preparation of strong, accurate, and high-definition models. In

an optimized process, by simply spraying the suitable binding solution, this calcium sulfate hemihydrate ($CaSO_4$ + nH2O) powder undergoes a self-hydration process, resulting in a semi-solid calcium plaster-like paste ($CaSO_4 \cdot \frac{1}{2}H_2O + 1\frac{1}{2}H_2O = CaSO_4 \cdot 2H_2O$).[145,232] This process was adopted and repeated for each depositing layers in sequence until the 3D object was printed herein. As shown in Figure 5.2A, the tablets with various shape fidelity and dimensions were printed with high accuracy, uniformity, and reproducibility.

Table 5.1. Properties of the powders used for printing matrices

Printing Powder Carrier Properties				
Viscosity(cP_0)	**Flowability**		**Bulk Density (g/cm^3)**	**$D_{50\%}$, $D_{90\%}$ (μm)**
	Carr's Index	**Angle of Repose**		
220.8 (Torque: 18.4% Speed: 5.00 rpm)	25	22.05°	1.172	42.32, 80.12

5.3.3 SEM of PB 3D Printed Tablets

The surface morphology of the printed tablets examined via SEM is depicted in Figure 5.3. It is obvious from the SEM images that all printed tablets had a highly porous surface with matrix-forming particles loosely bound with the binding liquid. This can be ideal for the formulation of fast disintegrating dosage forms, such as orally disintegrating tablets (ODTs). All tablet formulations exhibited micron-scale interconnected pore size. A high-resolution SEM image revealed the pore diameter in the region of about ~90 μm (Figure 5.3F). As a result, upon contact with an aqueous medium such as a dissolution solution, the surface area could be increased significantly, resulting in the faster dissolution of the drug from the tablets.

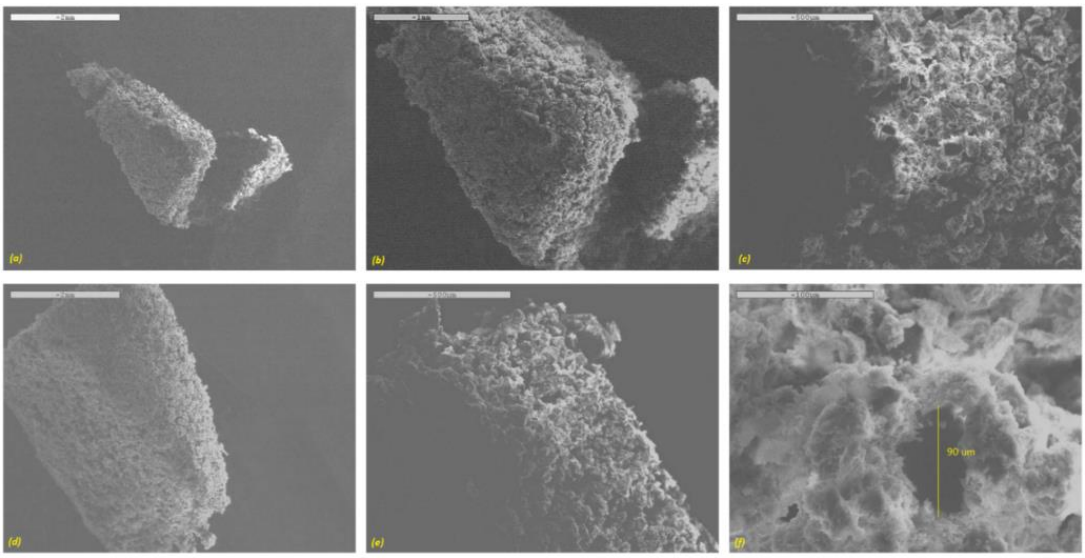

Figure 5.3. SEM images of the surface of PB 3D-printed tablets.

5.3.4 Preparation of Coating Solution

The model anti-cancer drug, FLU, is sparingly soluble in water and slightly soluble in ethanol.[233] However, the solubility of FLU can be affected significantly by temperature, and it can be increased more than 12-fold by enhancing the temperature between 25 and 200 °C under a constant pressure of 5.1 MPa.[184] Additionally, Singh *et al.* pointed out that FLU has high thermal stability when the temperature is less than 278 °C.[185] Having considered this property, during the preparation of the drug-loaded coating solution, the temperature was increased to around 70 °C in order to increase the concentration of the drug in the solution. As a result, the maximum concentration of the solution was optimized at 25 mg/mL. According to the concentration of prepared solutions and the weight changes of tablets before and after the coating process, compositions of drug solution coated on different tablets could be calculated (Table 5.2).

Table 5.2. Compositions of drug solution coated on different tablets

Tablets	Components	Solution A	Solution B	Solution C
Tablet (batch 1) (Diameter = 10 mm)	5-fluorouracil (mg)	2.5	2.5	2.5
	Soluplus (mg)	2.5	1.25	0
	PEG (mg)	0	1.25	0
Tablet (Batch 2) (Diameter = 13mm)	5-fluorouracil (mg)	5	5	5
	Soluplus (mg)	5	2.5	0
	PEG (mg)	0	2.5	0

Soluplus® (SOL) is a graft co-polymer of polyvinyl caprolactam (PVC)-polyvinyl acetate (PVAc)-polyethylene glycol (PEG) that can help drug dispersed molecularly in its matrix in the preparation of solid dispersion. As a result, Thakral *et al.* proved Soluplus® can increase the water solubility of an anti-cancer drug with poor aqueous solubility (camptothecin) in a colon-targeted delivery system.[234] Their solid dispersion formulation of camptothecin in Soluplus® with citric acid had great potential for colorectal cancer therapy. Uddin *et al.* studied Soluplus® as a drug carrier and the coating formulations (consisting of drug-polymer solutions at various ratios).[235] They found that Soluplus® helped the drug release for various anti-cancer substances (5-fluorouracil, curcumin, and cisplatin), especially for the water-insoluble drugs (curcumin and cisplatin) because of their solubilizing enhancement capacity. In addition, Homayouni *et al.* pointed out that this polymer can perform as a stabilizer and a solubilizing agent in poorly water-soluble drug formulation.[236] Because Soluplus® contains a polyethylene glycol backbone as the hydrophilic portion and vinyl caprolactam/vinyl acetate side chain as the lipophilic part, the significant amphipathic property gives it good surface activity, wettability, ability to enhance the aqueous solubility, and oral bioavailability.[237,238] As a result, all developed polymeric solutions (SOL alone or in combination with PEG) contained FLU dispersed homogeneously within the matrices.

5.3.5 Confocal Microscopic Analysis of Drug-coated PB 3D Printed Tablets

In order to evaluate the homogeneity of the drug distribution upon depositing onto the formulated tablets, an optical microscopic analysis was conducted. As can be seen in Figure 5.4, an uncoated tablet without the drug solution exhibited no fluorescence traces in the mapping image (Figure 5.4A). There were some bright green dots that may be attributed to some degree of contamination during the

sample preparation or handling process. These green dots were also present in the FLU loaded tablets, indicating that these are not relevant to the presence of the drug. It could also have been due to the presence of dust on the surface of the tablet. However, the images of tablets coated with drug solution showed significant differences compared to the tablet without drug solution. In contrast, the FLU loaded tablet surface showed a homogenous distribution of the drug throughout the surface of the tablets, represented by the dark green pattern. From these images, the edge of the tablet can be figured out easily. It can be concluded that the drug was coated homogeneously on the surface of these 3D printed tablets.

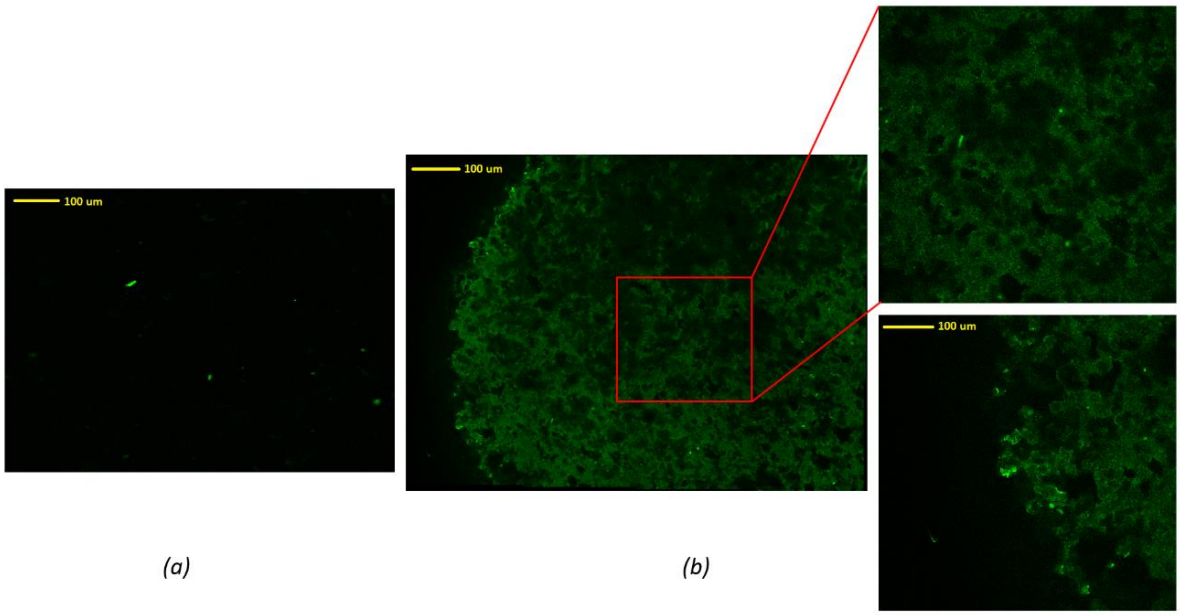

Figure 5.4. Confocal microscopic images of (A) tablets without drug solution, (B) tablets with drug solution C.

5.3.6 Dissolution Studies

In vitro drug release profiles from both 10 mm and 13 mm tablets coated with FLU solution A, B, and C for 2 h are depicted in Figure 5.5. Tablets with a bigger diameter (13 mm) showed a faster dissolution rate when compared with small tablets. The probable reason is the larger volume of 3D printed tablets for absorbing the drug solution and the larger surface area for partial hydration

reaction in the dissolution media. The dissolution test was carried out for 6 h; as over 80% of the drug was released within the first 120 min, only data up to 120 min were picked up for further evaluations. The aim of the current research was not to show sustained release behavior of printed tablets. Rather, it was to show that the drug release from printed tablets can be modified to reach the dissolution profile needed. Asadi-Eydivand *et al.* pointed out that calcium sulphate hydrated powder could absorb moisture from the environment.[232] The comparison graphs of solutions A, B, and C clearly illustrate that all these drug solution coated tablets showed a sustained release over 2 h. Tablets coated with solutions A and B showed slightly slower release compared to that of solution C, which contained only FLU. About 90% of the drug had been released from polymeric solutions, whereas the bulk FLU solution showed about 100% release in 2 h. The slight delay in the release of the drug from the polymeric solution could be attributed to the chemistry of the amphiphilic polymer, Soluplus®. It has been reported that Soluplus® tends to retard the release of the sparingly water-soluble drug upon swelling in the dissolution media.[171] Comparing the dissolution profiles of the 13 mm and the 10 mm tablets coated by solution C showed that these dissolution profiles were different (f_2 value of 43) because similarity factor (f_2) less than 50 indicates that they are different. This indicates that the size of printed tablets has a significant effect on the dissolution profiles of FLU. Comparing the effect of the coating solution showed that the type of solution cannot make a big difference (the similarity factor f_2 value was higher than 50). Nonetheless, our developed formulation compositions (solutions A and B) could be ideal for prolonging the release of the drug for a longer time or sustained release drug delivery, as may be required for chemotherapeutic DDSs.

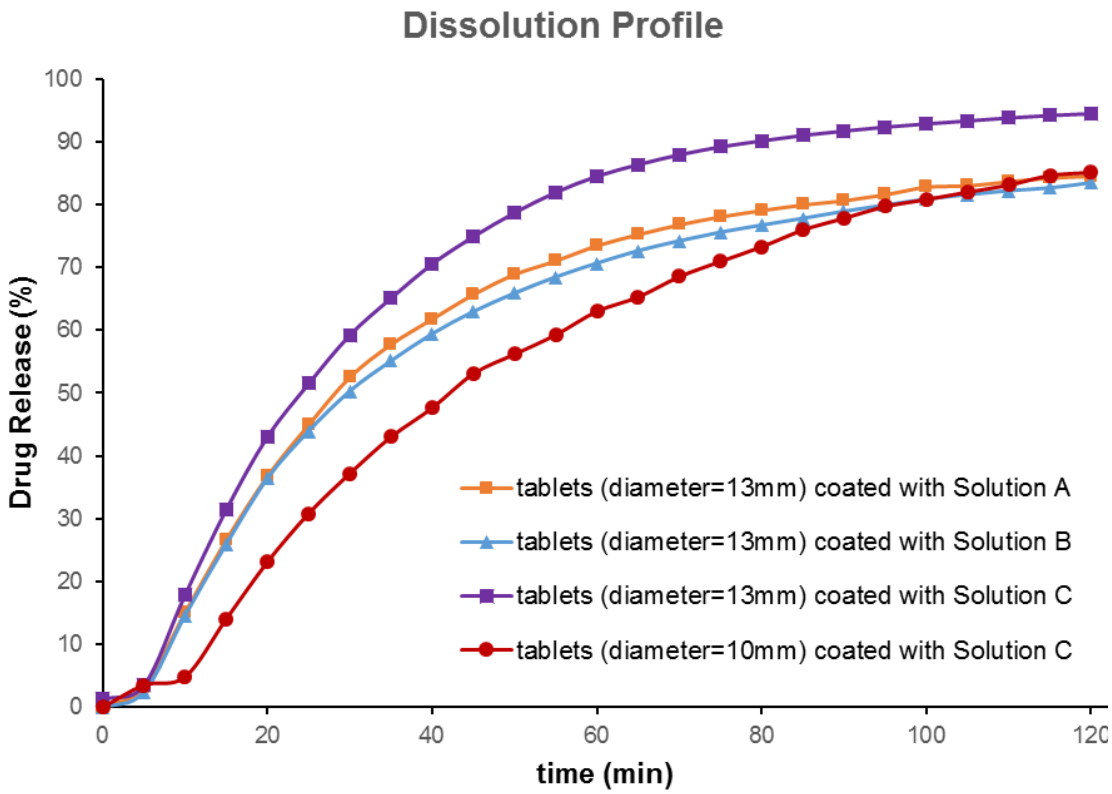

Figure 5.5. *In vitro* drug release profiles (under sink condition) of various printed tablets coated with solutions A, B, and C containing 5-fluorouracil (FLU) at pH 6.8 (n = 3).

5.4 Conclusion

This chapter demonstrated an optimized PB 3D printing process that can be applied for the fabrication of oral dosage forms, such as tablets with varying shapes and morphology. A detailed investigation of the powder compositions revealed that particle size, flow, and morphology play pivotal roles in the printing process. The produced tablets were also coated with various anticancer drug solutions, where drug particles were observed homogenously dispersed throughout the surface of the printed tablets. Furthermore, it could be claimed that the PB 3D printing process demonstrated here was able to adjust the dose, release rate, and loading amount of the drug substances by changing the formulation composition and the processing parameters. This method can be further scaled up for pilot scale manufacturing in personalized medicine. In conclusion, it can be claimed that the PB 3D printing process reported herein can be exploited for a number of drugs, including thermolabile drugs, by optimizing

the powder bed composition using pharmaceutical grade excipients such as polymers. This presents an emerging technique at the forefront of the additive manufacturing process which enables the immediate release of drug for personalized medicine.

According to the drug dissolution test, the 5-fluorouracil solution of 2.5% (w/v) concentration (Solution C) will be further applied in the development of the novel magnetic field triggerable DDS.

6. Chapter 6: Assembly and Characterization of Magnetic Field Triggerable Drug Delivery System

6.1 Introduction

Triggerable drug delivery systems (TDDSs), capable of releasing drug through applying external physical signals (such as magnetic field, ultrasound, pH, enzymes, temperature, electric, light, and near-infrared radiation) are gaining more and more attention in pharmaceutical sciences.[94,126,239] Such systems containing a large amount of drug can present remote, noninvasive, tunable, and reliable switching of therapeutic compound flux.[7] Hence, spatio-temporal management of drug availability could be realized through these triggerable drug delivery systems by the physicians or patients with the utilization of either the interaction between a 'responsive' material and the surrounding environment or a remotely controllable activation device.[126,240,241] Also, these systems loaded with a large amount of drug can achieve multiple dosing after a single administration through repeatable triggering.[126] However, there are still some limitations, like low controllability because of an initial burst release or a drug leakage via diffusion, difficulty in disposing of the systems after therapy, and increasing toxicity-associated risks due to the possible degradation of the matrix and the reduction of stability and reliability of the systems.[126,240]

Implantable reservoir-based devices have been designed to overcome these limitations efficiently.[121] Targeted therapy could be achieved through these devices at different length scales with high anatomical variability.[168] The performing procedure and working environment will affect the features, sizes, and operation mechanisms significantly.[240] Herein, it is highly desirable to fabricate untethered macroscale triggerable DDSs with low cost, simple preparation, facile operation, simplified structural morphology, and the ability to move through body

channels and perform on-demand drug administration.[129,240]

Although several external stimuli have been studied in TDDSs, controlled drug targeting through magnetic actuation is still one of the principal approaches because of many advantages, such as instantaneous and reversible response, remote actuation, nondestructive and high controllability, which are especially attractive for biomedical fabrication where the noncontact feature is particularly necessary *in vivo* environment with absolute safety.[16,17,200] Those magnetic systems also play an important role in cancer research due to the superior ability in chemotherapy by realizing: (1) selective delivery of the maximum fraction of anticancer molecules to the desired site without any increase in side effects to normal cells; (2) prior distribution of anticancer drugs to targeted cells; (3) stable systemic drug concentration and (4) elimination of normal tissue clearance with the application of external magnetic fields.[200] Various types of magnetic particles have been widely applied in these systems as switching carriers, including Fe_3O_4 particles, NdFeB powders and carbonyl iron (CI) powders.[16,17,94,203,240] With the addition of magnetic enclosures, these magnetically responsive systems can move and deform due to applied magnetic fields.[210] Furthermore, with the manipulation of external permanent magnets, magnetically triggered drug delivery systems have the ability to remote locomotion through biological tissues in real-time because magnetic fields can transmit high force or torques wirelessly with multiple degrees of freedom to medical robots.[21,240]

Polylactic acid (PLA) is the most common material used for FDM because it is a non-toxic, renewable, thermoplastic, biodegradable and biocompatible polymer.[242,243] Additionally, its suitable properties like high mechanical strength, low coefficient of thermal expansion and processability for extrusion applications make this material ideal for pharmaceutical and biomedical applications.[243] Furthermore, various polymers, such as Pluronic, poly(vinyl alcohol) and polycaprolactone, could be blended with PLA to provide extra features with the

addition of APIs to the final composite material in healthcare applications.[166,242–244] Although the hydrolysis rate of PLA is low, it has been widely studied as a base polymer in recent years because of its biodegradability and biocompatibility.[166] PLA have other advantages for the FDM printing, such as easy availability and a melting range from 180 to 220°C.[245] Additionally, the degradation products from PLA are non-toxic and can be excreted from kidneys, so PLA has been applied in tissue engineering, sutures and prostheses.[245] According to FDA, PLA is regarded as a safe material.

An appropriate 5-fluorouracil (FLU) DDS should meet the following requirements: (1) physical stability; (2) small size for uniform perfusion; (3) enough drug loading capacity; (4) prevention of degradation; (5) minimized drug leakage; (6) controllable drug release rate from the carrier at the desired target site; (7) surface properties allowing maximum biocompatibility and minimum antigenicity; and (8) degradation products with minimized toxicity.[229]

In this chapter, a novel magnetically triggerable DDS composed of a magnetic polydimethylsiloxane (PDMS) sponge cylinder and a 3D printed PLA reservoir was designed, fabricated and characterized. This system can realize a switch between the “on” and “off” state easily through the application of different magnetic fields and from different directions. Active and repeatable control of the localized drug release could be achieved by the utilization of magnetic fields to this device due to the shrinking extent of the macro-porous magnetic sponge inside. An anticancer substance, FLU, was used as the model drug to illustrate the drug release behaviour of the device under different strengths of magnetic fields applied. *In vitro* cell culture studies also demonstrated that the stronger the magnetic field applied, the higher the drug release from the deformed PDMS sponge cylinder and thus the more obvious inhibition effects on Trex cell growth. All results confirmed that the device can provide a safe, long-term, triggerable and reutilizable way for localized disease treatment such as cancer.

6.2 Methods

6.2.1 Preparation of PDMS Sponges

Refer to the Section 2.3.1.

6.2.2 Preparation and Characterization of the Reservoir

Refer to the Section 2.4.2.

6.2.3 SEM Analysis of FDM 3D Printed PLA Reservoirs

Refer to the Section 2.5.1.

6.2.4 Assemble and Drug Loading of the Device

Refer to the Section 2.3.4.

6.2.5 Dissolution Test under Sink Conditions

Refer to the Section 2.9.2.

6.3.6 Cell Studies of the Devices *in Vitro* with FLU Solution

Refer to the Section 2.10.

6.3 Results and Discussion

6.3.1 Fabrication and Characterization of Magnetic PDMS Sponges

Among all prepared magnetic PDMS sponges (Figure 6.1), 100 w/w% CI/PDMS sponge was selected for the scaffold in this experiment as it exhibited the most deformation tendency at the given reflux under the given magnetic field. The underlying reason is that the ferromagnetic particles were homogeneously distributed throughout the PDMS sponges as such it was enough to deform the sponges to a suitable extent to trigger drug release from the system. The lower

or higher amount of CI particles in the formulation exhibited insufficient magnetic field sensitivity in the experimental set-up, respectively. Based on the preliminary results, 100% w/w CI/PDMS formulation was selected for the additional studies.

Figure 6.1. Photograph of the pure PDMS sponge cylinder, CI loaded PDMS cylinder and cube.

6.3.2 Fabrication and Characterization of the Reservoir

6.3.2.1 Printing the Device

The PLA filaments were transformed into reservoirs via a Robo R2 FDM 3D printer (Figure 6.2A). The suitable size of the sponge cylinder was cut and subsequently installed into the PLA reservoir bottom before the top part assembling and drug loading. The reservoir could be opened later, meanwhile, both the reservoir and PDMS sponge cylinders could be washed completely and reutilized (Figure 6.2B). These printed reservoirs showed satisfactory mechanical properties. These two parts of the reservoir are white, non-friable, plastic-like and can be closed tightly. The printed reservoirs show low variability in both size and weight (Figure 6.2) because the relative standard deviation values of the diameter, height and weight are 0.052, 0.087 and 0.066 respectively (n = 3).

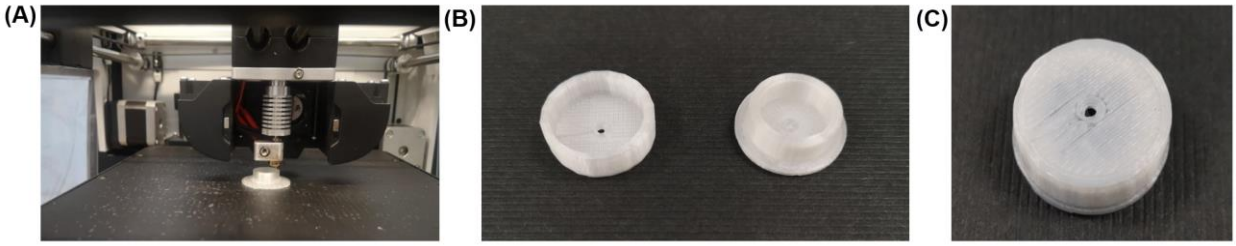

Figure 6.2. (A) The printing process of the PLA reservoir with Robo R2. (B) Macroscopic appearance of 3D-printed PLA reservoir (left: top, right: bottom). (C) Macroscopic appearance of the assembled 3D-printed PLA reservoir loaded with 100% CI/PDMS sponge and drug solution.

6.3.2.2 Characterization of 3D Printed Reservoirs

The extruded PLA filament was smooth and uniform with a diameter of 0.403 ± 0.001 mm. The value of E_r (100.75 %) reduced the possibility of die swelling, which may cause uneven filament blocking the feed nozzle (ø = 0.4 mm) of the 3D printer. SEM analysis (Figure 6.3) confirmed that the printed reservoir has a layered structure as the printing process was conducted in a layer-by-layer manner.

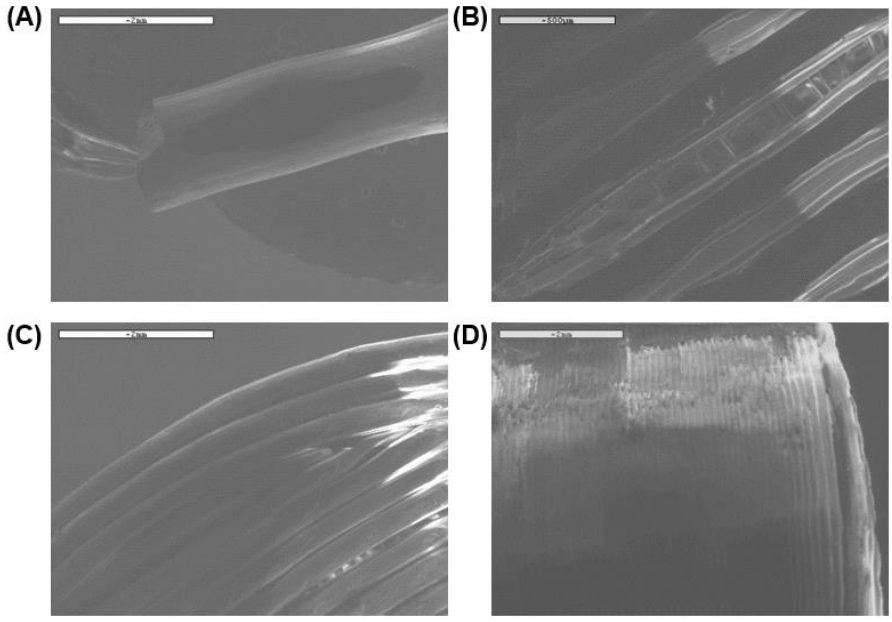

Figure 6.3. SEM images of (A) PLA filaments, (B) the bottom surface of the reservoir, (C) the top surface of the reservoir, (D) the side surface of the reservoir.

6.3.3 Assemble and Drug Loading of the TDDS

The sponge cylinders with the diameter and height of 12.5 mm and 5 mm respectively were cut carefully and then placed into the hollow space of the reservoir bottom. Then the two parts of the reservoir were closed tightly (Figure 6.2C).

After the pure PDMS sponge or the CI-loaded PDMS sponge was assembled into the reservoir, around 0.3 mL solution could be loaded into the device because of the strong water absorption property of the sponge samples. The dose of FLU loaded into the device could be calculated by analyzing the weight change (weight of solution) of the device before and after the drug loading process. The maximum concentration of the FLU solution was optimized at 25 mg/mL. As a result, the device containing around 7~8 mg FLU was assembled successfully.

6.3.4 Dissolution Test under Sink Conditions

It is assumed that the location of the magnetic bar with respect to the location of the reservoir containing a sponge cylinder can deform the sponge cylinder differently and this, in turn, releases the drug with different patterns when compared to the release behavior of the device without magnets (Figure 6.4). Some drug solutions can release from the small aperture gradually without magnets (Mode 2). When the magnet bar is contacted with the side part of the device, the magnetic sponge loaded with the drug solution can move close to the magnetic bar because of the magnetic field and the drug solution is squeezed out through the small aperture (Mode 3). In contrast, the magnetic sponge and drug solution move away from the aperture when the magnetic bar is at the bottom of the device, so only a little amount of drug solution will be released (Mode 1). To prove this hypothesis, dissolution tests under sink conditions were carried out (Figure 2.6).

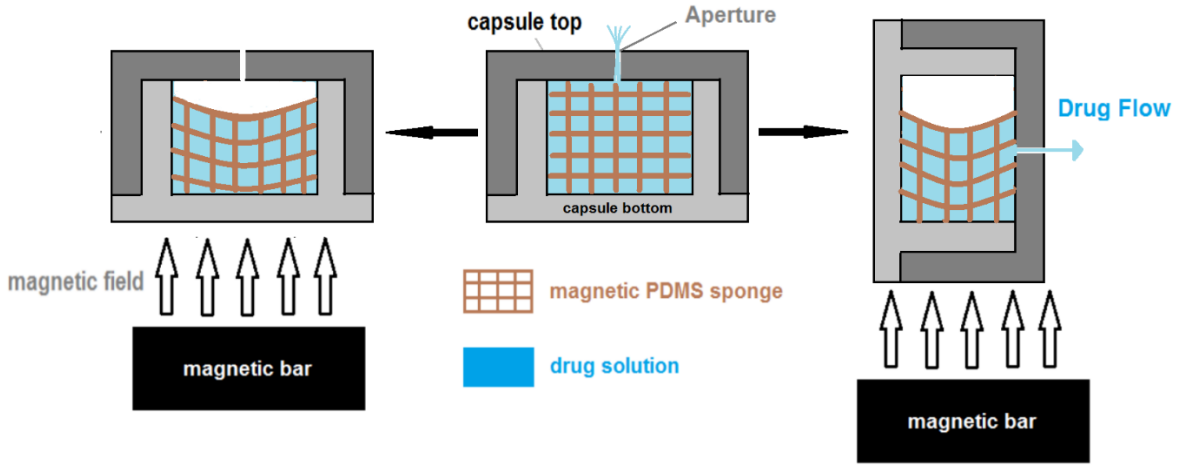

Figure 6.4. A schematic cross-section view diagram showing the release mechanism of the device with the utilization of the magnetic field from different directions (left: Mode 1, middle: Mode 2, right: Mode 3).

In vitro drug release profiles from the same drug-loaded device but with different utilizations of magnets are depicted in Figure 6.5. The dissolution test was carried out for 12 h, and the results showed that over 80% of the drug was released in Model 3 within the first 720 min.

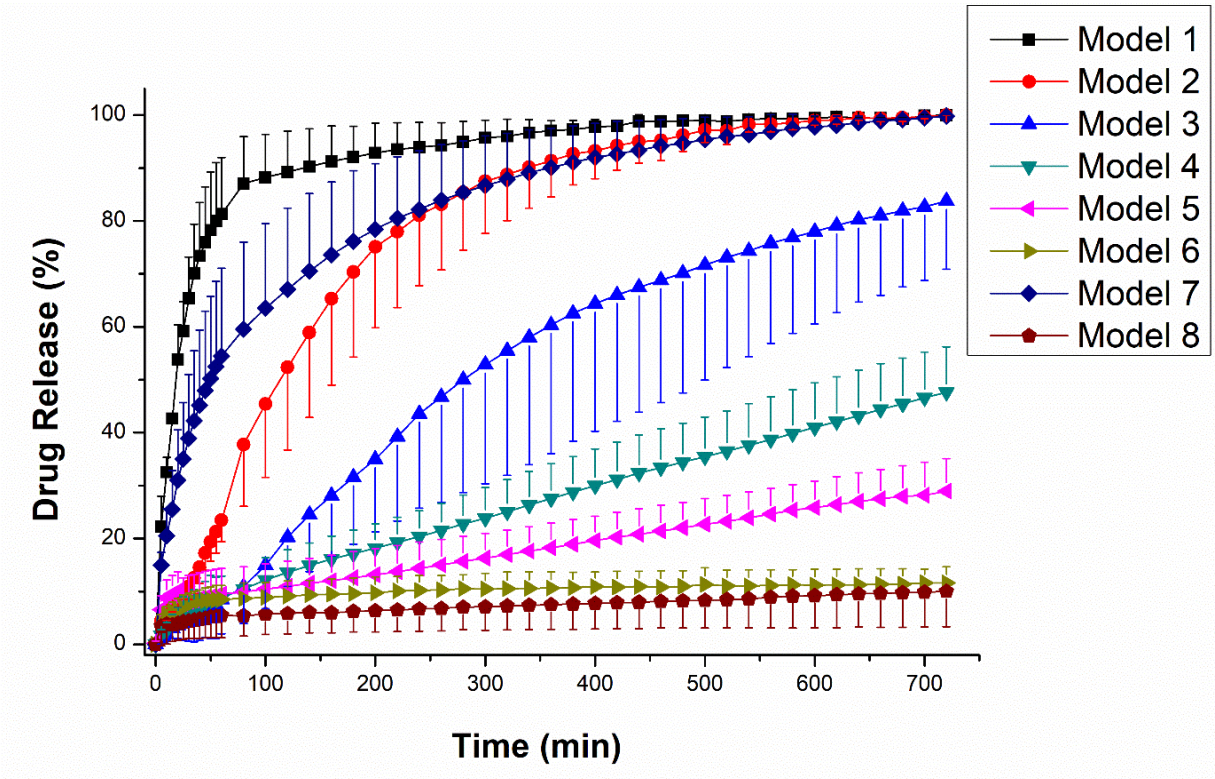

Figure 6.5. *In vitro* mean drug release profiles (±SD) (under sink condition) in PBS (pH 6.8) of the device loaded with 25 mg/mL FLU solution (*n* =3).

When the device was standing on Magnet D (Model 1), the dissolution rate was faster than other models. The probable reasons may have been the drug solution could release from the small aperture because of the deformation caused by the magnetic field. In particular, the times at which 50%, 80% and 90% of the drug were dissolved ($T_{50\%}$, $T_{80\%}$ and $T_{90\%}$ respectively) are observed at 20, 55 and 140 min (Table 6.1). When Model 7 which the device was standing on Magnet B (the smaller magnetic field) and compared with Model 1 (the stronger magnetic field), the drug release of Model 1 is much faster (f_2 =40.58). This confirmed that the quicker drug release is mainly due to the more obvious deformation caused by a stronger magnetic field.

Table 6.1. Different models and the time at which 10%, 50%, 80% and 90% of the drug were dissolved are clarified underneath the dissolution profiles for the comparison of drug release behaviors of the device.

Model	Apparatus	Magnet	Mode	Aperture	$T_{10\%}$	$T_{50\%}$	$T_{80\%}$	$T_{90\%}$
1	Paddle	D	3	√	<5 min	20 min	55 min	140 min
2	Paddle	×	2	√	25 min	120 min	240 min	340 min
3	Basket	×	4	√	80 min	280 min	640 min	-
4	Basket	D	1	√	80 min	-	-	-
5	Paddle	D	1	√	80 min	-	-	-
6	Paddle	×	2	×	220 min	-	-	-
7	Paddle	B	3	√	<5 min	50 min	220 min	360 min
8	Paddle	B	1	√	720 min	-	-	-

However, the drug release from the device which was lying on the magnet (Model 5) is dramatically slow. The comparison of dissolution profiles of Model 1 with model 5 demonstrated that the deformation of the magnetic sponge in Model 1 is more efficient than Model 5 because of the position of the small aperture and the size differences between the diameter and height of the sponge samples assembled in the reservoir (f_2 =9.71).

Besides, there are also significant differences between Models 1 and 2 ($f_2 = 30.03$), Models 2 and 5 ($f_2 = 15.66$). This indicates that the different utilizations of the external magnetic field have crucial influences on the dissolution behaviour of drug release from the device. The dissolution behaviours of the drug-loaded device are different in basket and paddle methods because of the obvious difference between Model 2 and 3 ($f_2 = 30.03$), Model 4 and 5 ($f_2 = 50.56$).

To prove the small aperture on the top of the reservoir is the main pathway for drug-releasing, the device without any aperture was designed, fabricated and analyzed (Model 6) in the same way as Model 2. During the 12 h, only 16% of drug loading was released from the device and the amount is much lower than that of Model 2. This indicates that the drug solution is mainly released from the small aperture. However, the slower drug release in Model 8 when compared with Model 5 indicates that the weaker magnetic field can release less drug in Mode 1.

It can be concluded that the switching “on” state in the release pattern from the device can be triggered when the magnet is employed like Model 1, and the switching “off” drug-releasing of the device can also be realized when we change the position of the magnets like Model 8. Consequently, the release of drugs from this device can be controlled repeatedly and quickly. All these features make this novel implantable drug delivery device a promising candidate for on-demand and control the release of therapeutic substances in local disease therapy. The device could be navigated to the target site *in vivo* wirelessly with the application of magnetic fields. With the development of this TDDS, the anticancer agent (FLU) could be navigated to the target site and released at an adjustable rate in accordance with patients’ specific conditions for minimizing adverse effects during cancer treatment. Herein, the bioavailability of FLU could be enhanced significantly. Furthermore, this device shows superior potential in hormone

deficiencies and chronic pain treatments. Desirable doses of these drugs, like hormones and painkillers, can be released by loading these drug solutions of various concentrations into the DDS.

6.3.5 Cell Studies *In Vitro*

It was necessary to analyze the cell inhibition behavior of FLU loaded 3D printed reservoir and sponge samples. The assessment of cell numbers of Trex cells was designed (Table 6.2). The cell numbers in Figure 6.6 (Group B1, B9 with B11, Group B2 with B10) display that these PDMS sponges, especially CI loaded PDMS sponge without the drug can inhibit the growth of Trex cells to some extent, but the number of Trex cells still increased within 4 days because there is no FLU solution. Through comparing the data of groups under the same conditions just except for applying magnetic fields (Group B9 with B10, Group B1 with B2, and Group B3 with B4), it can be concluded that the stronger magnet will lead to more drugs being released from the deformation of magnetic sponges and more obvious inhibition effects on Trex cell growth. Importantly, sponge samples loaded with a higher concentration of FLU solution (Group B3 with B5, Group B4 with B6) presented a stronger inhibition effect on Trex cells. The results showed that there is no difference between Group 7 and 8 and this is not surprising because the magnet would not trigger the release of the drug solution loaded in the device when the magnets were placed at the bottom of the whole device as reflected by the results highlighted in the dissolution section.

In summary, stronger magnetic fields can lead to larger deformations of CI-loaded PDMS sponge cylinders and a higher volume of drug solution will be released from the drug-loaded magnetic PDMS sponges. By adjusting the concentration of the drug solution, the dose of the drug could be changed. Because the prepared magnetic sponge sample can release a specific volume of drug solution under the same magnetic field, the lower loaded solution concentration can lead

to the lower loaded dose of the drug. With the assembly of a 3D printed PLA reservoir, there will be no obvious difference in the released dose of drug from the whole device between the device having magnets placed underneath and the device alone without magnets.

Table 6.2. 3D printed PLA reservoir and sponge samples loaded with different solutions under different magnetic fields

Group	Magnet	Sponge	FLU Solution	PLA Reservoir
B1	B	CI/PDMS=100 wt%	×	×
B2	C	CI/PDMS=100 wt%	×	×
B3	B	CI/PDMS=100 wt%	12.5 mg/mL	×
B4	C	CI/PDMS=100 wt%	12.5 mg/mL	×
B5	B	CI/PDMS=100 wt%	25 mg/mL	×
B6	C	CI/PDMS=100 wt%	25 mg/mL	×
B7	×	CI/PDMS=100 wt%	12.5 mg/mL	√
B8	B	CI/PDMS=100 wt%	12.5 mg/mL	√
B9	B	×	×	×
B10	C	×	×	×
B11	B	pure PDMS	×	×

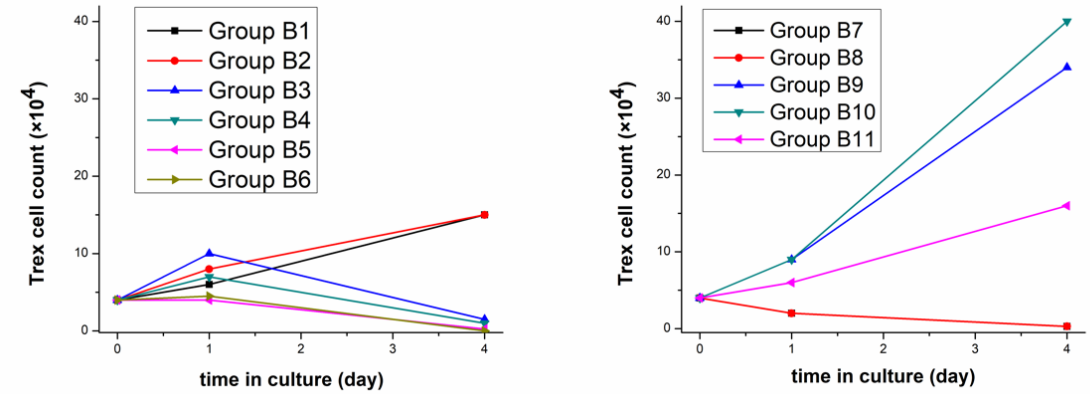

Figure 6.6. Numbers of Trex cells under different conditions.

6.3.6 Optimization of 5-fluorouracil Solution

Although the FLU solution of 2.5% (w/v) concentration loaded into the device showed great performance in cell studies and *in vitro* dissolution tests, the FLU solution could be further optimized with other solvents for long term implantation. Highly purified diethylene glycol monoethyl ether, which commercially known as

Transcutol®, has been widely used as a solvent in many medicines for solubility improvement.[246] Transcutol is a transparent liquid with low viscosity and pleasant odor, and its physicochemical properties are comparable to protic solvents (e.g. ethanol and water).[246] A significant application of this solvent is to dissolve a wide range of hydrophilic and lipophilic substances. Transcutol HP (mass fraction purity > 99.90%) was selected as a solvent in this study because of its nontoxicity, biocompatibility and strong solubilization effect.[247,248] According to Siddalingam and Chidambaram, Transcutol HP showed the highest solubility of FLU (94.62 mg/mL) and good solubility was also observed in Capyrol PGMC (78.94 mg/mL) and PEG 400 (93.12 mg/mL).[248] Therefore, Transcutol HP could be applied to prepare FLU solution with a concentration of 25 mg/mL with no need to increase the temperature.

6.4 Conclusion

This chapter illustrates the design and development of a novel implantable drug delivery device assembled from a magnetic PDMS sponge cylinder and a 3D-printed PLA reservoir to provide a triggerable and remotely controllable system for on-demand drug delivery in localized disease treatment. This device utilized different extrinsic magnetic fields for offering a tunable force to trigger drug release through reversible magnetic sponge deformations. The geometric shape and dimensions of the reservoir could be adjusted easily through FDM 3D printing technology according to the requirement of patients. In addition, the drug-releasing dose and timing can be reliably and flexibly controlled by different applications of the magnetic field to fit the prescribed needs. Furthermore, this device has the potential to be optimized as a safe and long-term implant because of its large drug loading ability. It can be the key component of a multi-functional, implantable and smart drug delivery system for the controlled release of therapeutic substances to avoid frequent injections or various sophisticated dosing regimens. In the future, combining the device with a sensing system can

also offer protection for biosensors because biofouling and exposure to the body may lead to the failure of biosensors *in vivo*.

7. Chapter 7: Development of Hot Melt Extruded Filaments for Fused Deposition Modelling 3D Printing

7.1 Introduction

Hot melt extrusion (HME) was first used in the plastic and rubber industry, since the 1970s, it has been promoted in pharmaceutical research as a method of preparing solid dispersions through distributing poorly soluble drugs into a polymeric matrix for manufacturing various dosage forms (e.g. implants, granules, pellets, films).[142,158,174] An early investigation revealed that the percentage of drug loading into the polymers would be low when drugs were loaded through impregnation/incubation in organic solvents as a function of passive diffusion (soaking).[157,168] In recent years, HME has been used in combination with fused deposition modelling (FDM) 3DP, which is one of the most promising 3DP technologies in pharmaceutical applications to date.[143,155,249,250] Consequently, HME is of great importance in providing an increasing number of materials processable by FDM, increasing the drug loading capacity of filaments, and achieving on-demand fabrication of a unit dose for patients.

Ibuprofen (IBP) is one of the most commonly used non-steroidal anti-inflammatory drugs (NSAIDs).[251] Its short biological half-life (2 h) makes this drug suitable for sustained DDSs development.[191] Solid dispersions of IBP with various carriers have been investigated in recent years for improving the solubility and dissolution properties of IBP, even though IBP shows poor pharmaceutical behaviors and flow properties.[161,194] Moreover, IBP has a high tendency to adhere to punches during direct compression.[251] IBP was selected as the model drug in this study mainly due to its plasticizing effect on ethyl cellulose (EC).[154,187]

Plasticizers always play an essential role in HME with those pharmaceutical

polymers for enhancing the workability, melt flow property and flexibility (strain bearing ability) of filaments because of their ability to decrease the interaction between the polymer chains and soften the polymer matrix.[250,252] Also, they can help to decrease the elastic modulus, tensile strength, polymer melt viscosity, glass transition temperature (T_g) and increase shear resistance.[157,165,187] Additionally, the risk of thermal decomposition of the drug molecular will decrease because a lower processing temperature can be applied during the extrusion process.[158] However, the addition of plasticizers may affect gastric and intestinal transit times, then have an impact on drug absorption especially in hydrophilic matrices and chronic disease treatment.[250] Traditional plasticizers (often with low molecular weight) include triethyl citrate (TEC), propylene glycol, triacetin, polyethylene glycols (PEG), dibutyl sebacate (DBS), Tween® 80 and diethyl phthalate.[157,158,165] Some drugs (e.g. IBP) were also found to possess the plasticizing effect which will bring some technological advantages during the HME process, such as lower the extrusion temperature.[187] It is noteworthy that the plasticizer content has a significant influence on the processability of HME filaments during the FDM 3D printing process (Table 7.1) because sufficient plasticizer can promote the appearance and minimize the variations in the weight of printed objects.[154] Hence, it is important to figure out the best polymer-plasticizer ratio for each drug load.[253]

Table 7.1. The comparison of unsuitable content of plasticizer during FDM

	Insufficient plasticizer	Redundant plasticizer
Problems	• cavities • aggregation formulation	• a great decrease in the average weight of FDM printed objects • low rigidity • bend and deformation in heater
Reasons	• low flowability • high viscosity of melts	• more adhesive melts on FDM nozzle due to low viscosity • interfere with the instant solidification of extruded layers
Solutions	• improve FDM printing temperature • addition of thermoplastic materials	• decrease FDM printing temperature

EC is a well-known polymer to be used in the manufacture of tablets by direct compression for achieving sustained release profiles.[191] EC with various molecular weights is suitable for HME because of its excellent thermo-plasticity when the temperature is higher than its T_g (129-133°C).[158,165] As a result, EC formulations without plasticizers could only be extruded at temperatures above 133°C and the extrudates will be too brittle to be further printed through FDM.[158] With the addition of traditional plasticizers (e.g. dibutyl sebacate), the extrusion process will become easier by decreasing the T_g and melt viscosity of EC, then the risk of thermal decomposition of the API will be minimized because of the lower processing temperature.[158] Many studies have illustrated that the addition of IBP to the HME formulations can lower the extrusion temperature significantly and increase the stability due to the plasticizing effect of IBP.[154,187,191] However, the drug release rate from the IBP and EC hot melt extrudates is very slow due to the water insolubility and inertia of EC.[158,191,254] Consequently, other polymers were also introduced to modify the drug release behavior of FDM 3D printed tablets fabricated from hot melt extruded filaments of IBP and EC matrix. In this way, HME can provide an effective combining method for melt-blending different polymers into one homogenous final dosage form.[173] Because the printability of filaments will be affected significantly by the physicochemical properties of the starting materials, the hot melt extruded filaments were characterized comprehensively.[255]

In the current research, release modifiers with different viscosity grades were added to IBP-EC hot melt extruded matrix separately to modulate the drug release. Although FDM 3DP is a promising method for preparing controlled release dosage forms, the high compactness and high density of FDM 3D printed objects place a significant restriction on the drug release through diffusion.[154,174] In this situation, the introduction of erosive polymers (e.g. PVA, Soluplus, HPMC) into the 3D printed matrix is an efficient method for improving the drug release

through surface erosion of the intact matrix in the dissolution media.[132,174] Yang *et al.* have used PVA and HPMC K100LV as release modifiers in combination with IBP and EC because HPMC can increase the drug release through water uptake, swelling and erosion.[154] PVA possesses great thermo-plasticity and mechanical properties, so PVA filaments are one of the commercially available filaments for FDM 3DP.[141,242,256] Similarly, Soluplus is another swellable polymer for HME in pharmaceutical applications due to its outstanding thermal stability and extrudability, although pure Soluplus filaments are too brittle for FDM 3D printers.[151] Traditional plasticizers, such as TEC and various grades of PEG, show a facilitating effect on FDM 3DP for increasing the melt flow properties of thermoplastic polymers and decreasing the T_g.[157] The pH-independent swelling behavior and low permeability make Eudragit RL and RS promising release modifiers for release retardation because the drug release from these two water-insoluble polymers is mainly governed by the diffusion mechanism in many studies of 3DP.[155,168,257] Various grades of HPMC are processable in HME without the addition of plasticizers and they are the most widely used polymers in drug-loaded filament development for sustained drug release 3D printed tablets.[250,258] Kollidon® VA64 (a copolymer of polyvinylpyrrolidone and vinyl acetate) has been used as a water-soluble polymer matrix material in the HME process, but the pure Kollidon® VA64 filaments are so brittle that would collapse in the 3D printer.[173,252] To the best of our knowledge, Kollidon® 17 PF and 30 have not been employed in the FDM 3DP technology, but Kollamaram *et al.* proved that Kollidon® 12PF is a suitable excipient for FDM 3DP.[259] Kollidon® 12PF and 17PF are soluble low molecular polyvinylpyrrolidone which is used as common solubilizing agents and crystallization inhibitors.[259] Similarly, Kollidon® 30 (medium-molecular polyvinylpyrrolidone) could also be applied as a solubilizing agent and a crystallization inhibitor.

In the development of sustained DDSs, high drug loading should be considered due to the requirement for high amounts of drug and low volume of drug

systems.[191] As IBP shows a plasticizing effect on EC and has a significant effect on improving the thermo-plasticity of EC during the HME process, therefore, sufficient IBP was necessary to ensure the processability of hot melt extruded filaments in the following FDM printing process.[154,191] According to Yang et al., FDM 3D printed tablets with 20% ibuprofen perform better than tablets prepared with other drug contents from 16% to 24% in printing quality.[154]

7.2 Methods

7.2.1 Preparation of Physical Mixtures

Refer to the Section 2.4.3.1.

7.2.2 Tablets Prepared by Direct Compression

Refer to the Section 2.4.3.2.

7.2.3 TGA

Refer to the Section 2.7.1.2.

7.2.4 Preparation of Polymeric Filaments

Refer to the Section 2.4.4.

7.2.5 SEM

Refer to the Section 2.5.4.

7.2.6 DSC Analysis

Refer to the Section 2.7.2.

7.2.7 XRD

Refer to the Section 2.6.

7.2.8 Mechanical characterization

Refer to the Section 2.8.2.

7.2.9 Determination of Drug Content

Refer to the Section 2.9.3.

7.2.10 *In Vitro* Drug Release Studies

Refer to the Section 2.9.4.

7.3 Results and Discussion

7.3.1 Characterization of Raw Materials

7.3.1.1 Matrix Selection

As mentioned above, EC is available in various molecular weights. Lower molecular weight grades are related to solutions of lower viscosity. According to the manufacture's report, Ethocel™ (premium ethyl cellulose polymers) with an ethoxyl content of 48.0-49.5% and various viscosity grades are common polymers in pharmaceutical applications. To study the effect of the viscosity of EC in the HME-FDM process, different viscosity grades of EC were used: Ethocel™ standard 4 (EC 4), Ethocel™ standard 10 (EC 10) and Ethocel™ standard 45 (EC 45) with respective viscosities of 5.3, 10.3 and 43.5 mPa.s (cP).[158] Therefore, three different filaments composed of IBP (20 w/w%) and EC (80 w/w%) were fabricated according to Group 1 in Table 2.4. The morphology of these filaments was shown in Figure 7.1. These three filaments with a diameter of 1.75 mm showed similar morphology.

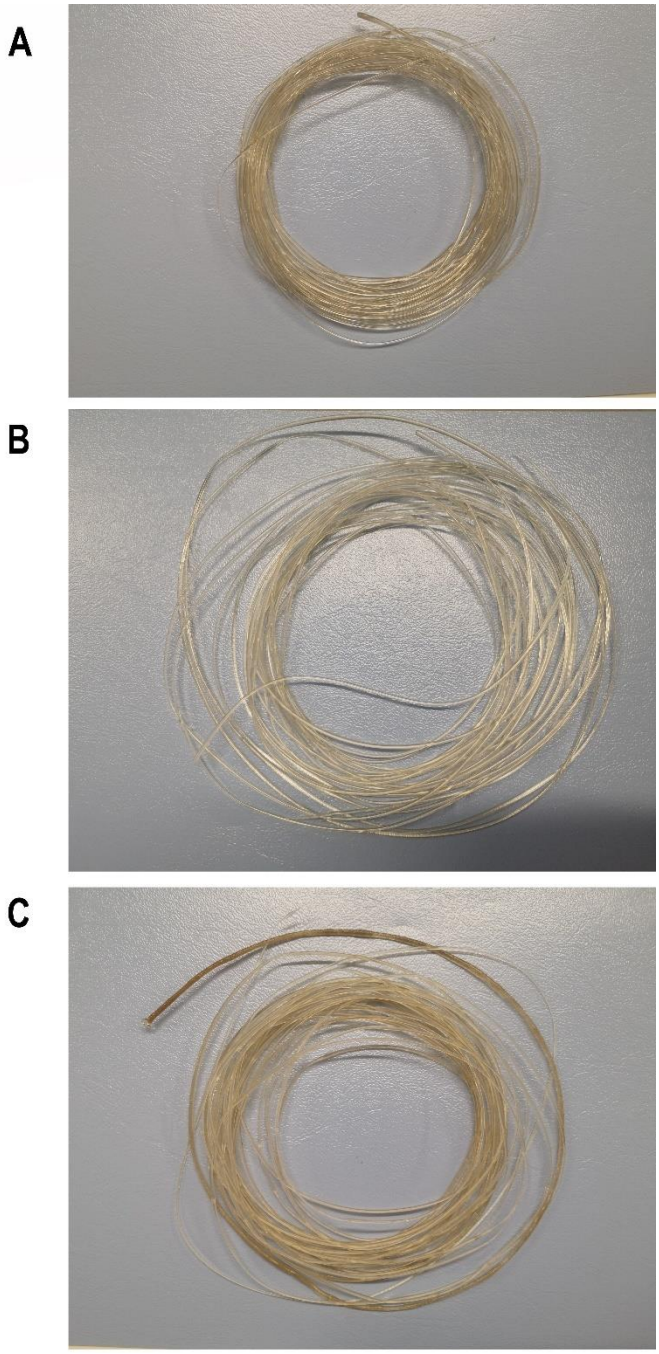

Figure 7.1. Photograph of hot melt extruded filaments prepared with 20 w/w% IBP and 80 w/w% (A) EC 4, (B) EC 10 and (C) EC 45.

Mechanical properties of hot melt extruded filaments were evaluated using a texture analyzer to predict the printability of these filaments during the FDM 3DP process.[242] Commercial polylactic acid (PLA) filaments (FilaPrint® premium PLA, 1.75 mm, 3D FilaPrint Ltd., Essex, UK) without drug deposition were used as the reference standard (Figure 7.2). The yield strength (elastic limit) represents the

maximum stress that the filament could tolerate before permanent deformation happens. The ultimate tensile strength is represented by the highest point in the stress-strain curve because it is the minimum stress (ratio of applied force to the cross-sectional area filaments) that the material will break during the stretching process. The elastic modulus (Young's modulus) could be represented by the slope of the elastic region (linear part) in the stress-strain curve.[174] The elastic modulus was calculated to evaluate the stiffness of filaments. To guarantee the filaments could tolerate the operation in the drive gears of the 3D printer, the elongation at break (the ratio of increase in length to original length) is needed to be higher.[148,174] Furthermore, stiffer filaments show higher Young's modulus and less brittle filaments show higher elongation at break.[142]

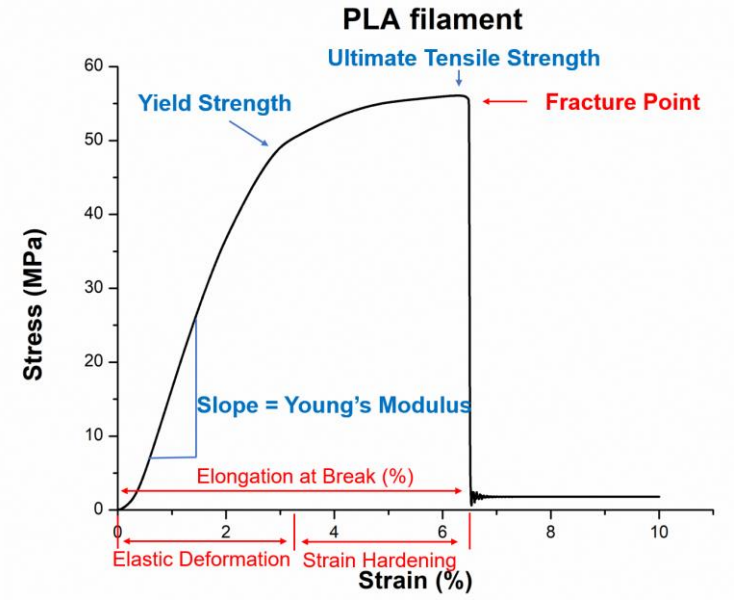

Figure 7.2. Illustration of the stress-strain curve of commercial PLA filaments.

The stress-strain curves of these three filaments were shown in Figure 7.3. As demonstrated in Table 7.2, the filaments prepared with Ethocel™ standard 10 showed the highest elastic modulus (~1100 MPa), whereas the elastic modulus of filaments prepared with Ethocel™ standard 4 and 45 are around 95 and 182 MPa respectively. Therefore, the stiffness of the other two filaments is much lower than the IBP-EC 10 filaments. It is also noteworthy that the IBP-EC 4 and 45

filaments both illustrated elongation at break of 24% and 30%, which are more than three times that of IBP-EC 10 filaments (8%). The much lower value of elongation at break for IBP-EC 10 filaments indicates the higher brittleness of the filaments. Ductile filaments showed a high tendency to deform when being passed forward in the feed zone and then block the printing head, although brittle filaments which cannot bear the mechanical strain generated from the compression and pushing of gears in the feed zone are likely to fracture and cause a blockage as well.[157] Additionally, the molecular weight of EC has a critical effect on the tensile strength of filaments. The highest value (34.47 MPa) was observed for formulations consisting of EC 45. This result is in good agreement with the previous literature report.[158]

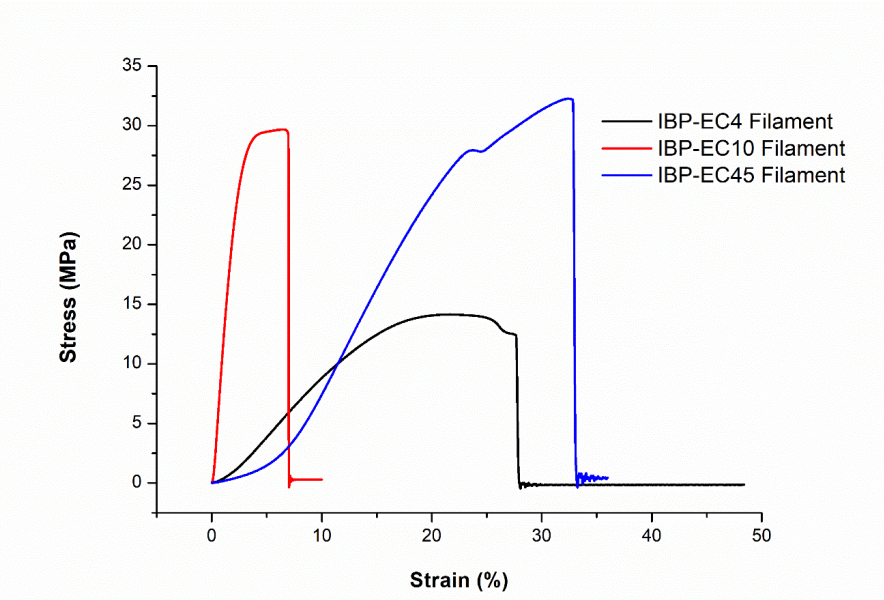

Figure 7.3. Stress-Strain curves of various IBP-loaded EC filaments using Ethocel™ standard 4, 10 and 45 respectively.

Table 7.2. Mechanical properties of hot melt extruded IBP-loaded EC filaments (n = 3, mean ± SD)

Filament	Yield strength (MPa)	Tensile strength (MPa)	Elastic modulus (MPa)	Elongation at break (%)	Strain hardening capacity
IBP-EC 4	11.64 ± 2.23	13.62 ± 3.21	95.10 ± 3.90	23.73 ± 6.38	0.17 ± 0.08
IBP-EC 10	26.59 ± 3.30	32.71 ± 4.29	1099.37 ± 0.06	7.88 ± 1.29	0.23 ± 0.01
IBP-EC 45	23.65 ± 4.75	34.47 ± 1.93	181.59 ± 23.19	30.29 ± 4.46	0.51 ± 0.37

The dissolution profiles of filaments containing IBP and different EC viscosity grades are given in Figure 7.4. It can be observed that filaments prepared from low molecular weight EC polymers had faster release rates. The possible reason is that low molecular weight polymers are related to short chains and weaker mechanical properties.[260] Additionally, there is no obvious difference among these filaments as the f_2 value between IBP-EC 4 and 45 is 96.74.

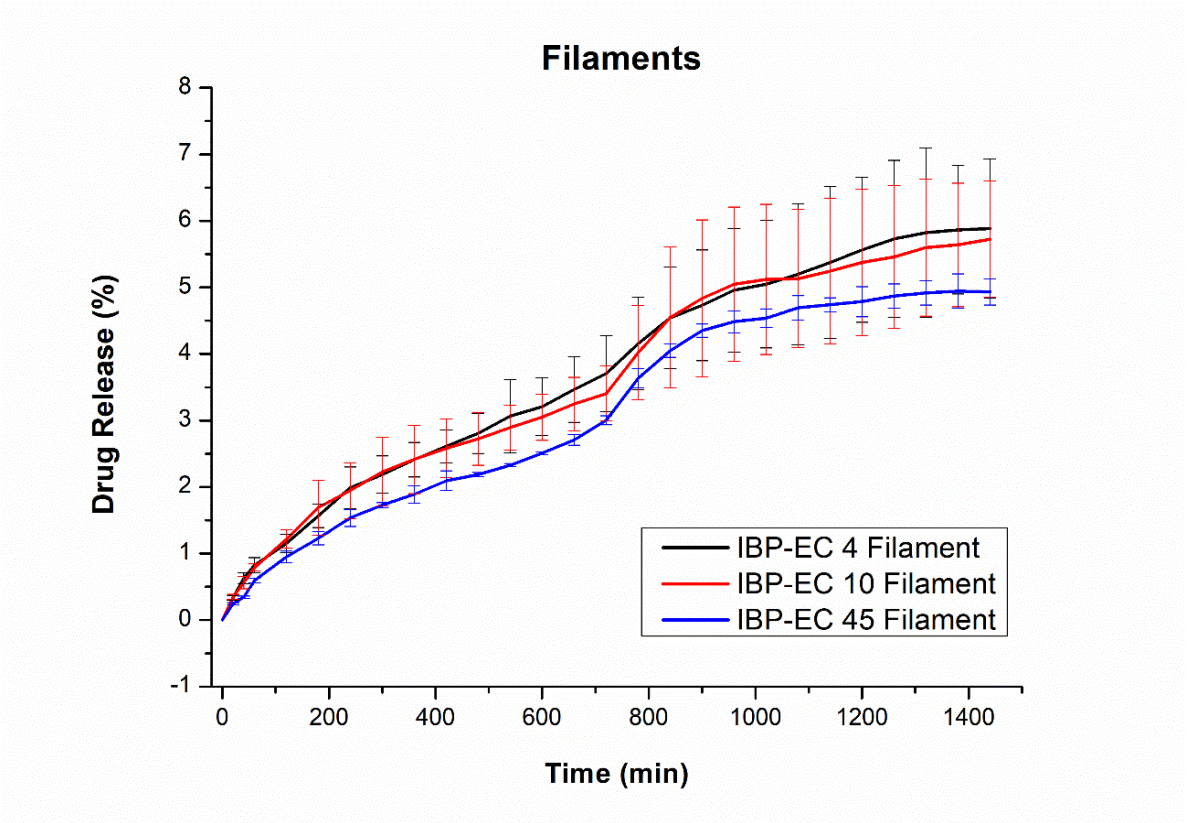

Figure 7.4. *In vitro* drug release study of various IBP-EC filament pieces fabricated with EC 4, 10 and 45 (n = 3).

These filaments were then evaluated for their printability using an FDM 3D printer. However, the tablets (Figure 7.5) showed significantly different appearance due to the mechanical properties of filaments and the performance during in printing process. Only the IBP-EC 10 filaments can complete the whole printing process to obtain tablets with uniform morphology.

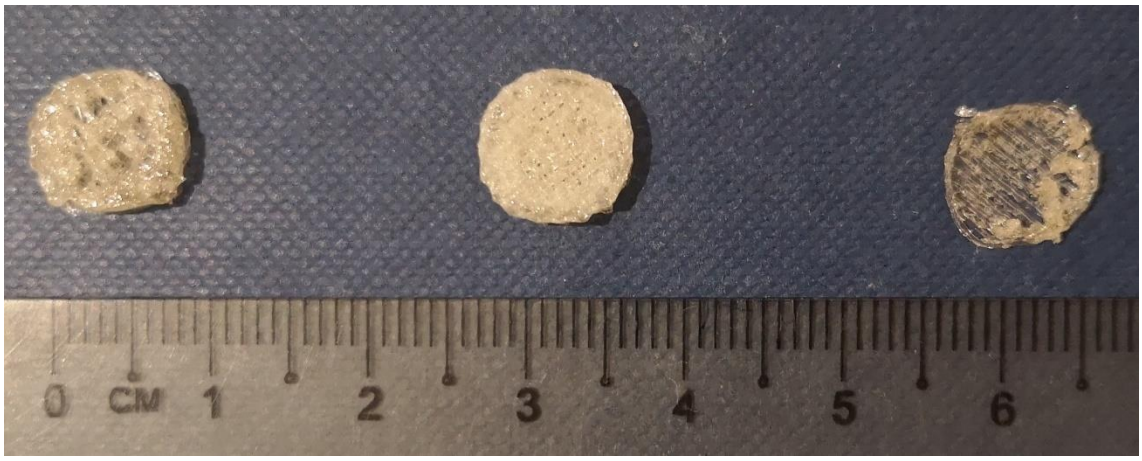

Figure 7.5. Photograph of the FDM 3D printed tablets using filaments prepared with (left) IBP-EC 4, (middle) IBP-EC 10 and (right) IBP-EC 45 under the same settings.

Because of the printability of IBP-EC filaments using Ethocel™ standard 4/10/45 and no obvious difference in the dissolution rate of these filaments, only Ethocel™ 10 (EC 10) was selected for the following study to analyze the effect of various polymers on the printability and dissolution behavior of extruded filaments and printed tablets.

7.3.1.2 TGA of Raw Materials

The processing temperature plays an important role in this study because a higher processing temperature will lead to a higher risk of thermal API decomposition.[158] It has also been shown that printing quality could be affected significantly by printing temperatures.[154] Objects printed through lower temperatures tend to be more viscous in the heater and show weaker bond strength between layers, which then lead to nozzle blockage and the disintegration of final products.[154] However, if the printing temperature is too high, thermolabile drugs and polymers will degrade.[155] Hence, the TGA was conducted to compare the thermal decomposition pattern of all raw materials.

As shown in Figure 7.6A, the TGA diagram of pure ibuprofen showed a small decrease below 100°C, indicating the loss of moisture in the IBP particles.[261] The

start point of IBP thermal degradation is around 151°C, and 201°C is regarded as the degradation acceleration peak. All other raw materials (Figure 7.6B) exhibited no obvious weight loss up to 220°C, where the thermal degradation begins to occur for HPMC K4M. Among these materials, Kollidon 30 and HPMC K100M both demonstrated an obvious weight loss below 100 °C, which is related to the relatively higher weight ratio of absorbed moisture. Therefore, all other polymers applied in this study are thermally stable up to around 300 °C. In addition, Pietrzak *et al.* pointed out that FDM 3DP temperature is required to be at least 40-50 °C higher than the ideal HME processing temperature.[155] The possible reason is the difference between the heating duration of HME (longer than 5 min under shear mixing of powder mixtures) and 3DP (normal extrusion rate of extruded filaments at 3 mm^3/s through the heated nozzle).[155] To minimize the decomposition of the API during extrusion and printing processes, printing temperatures were tested from 150°C to determine the lowest processable printing temperature. Based on the results, all fabricated filaments could only be printed until 178°C.

Hence, 178°C was selected as the optimum printing temperature without compromising the quality of the print as well as the products. Apart from IBP, no significant weight loss of other excipients could be observed in the HME zone (80-100 °C) nor the FDM printing zone (178 °C). Therefore, the drug content test was necessary to evaluate the amount of IBP loaded in the filaments and printed tablets after repetitive exposure to high temperature.

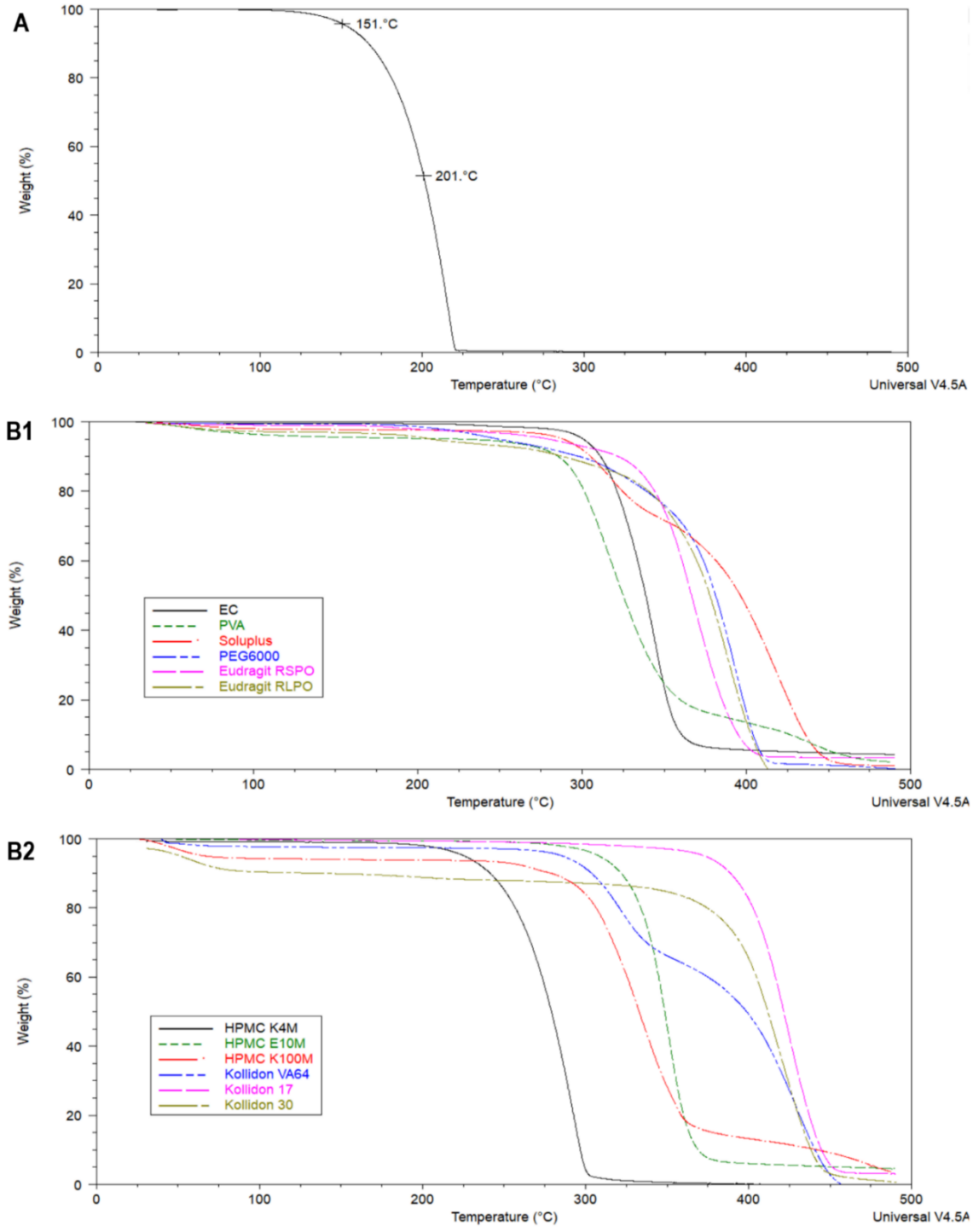

Figure 7.6. Thermal degradation profiles of (A) IBP and (B) other raw materials.

In addition, physical mixtures (PM) of all groups (Figure 7.7) exhibited no obvious weight loss during the extrusion zone (80-100°C) as most of these curves started to degrade from 200°C. All these TGA curves showed relatively lower weight ratios of absorbed moisture (< 5%) below 100°C.

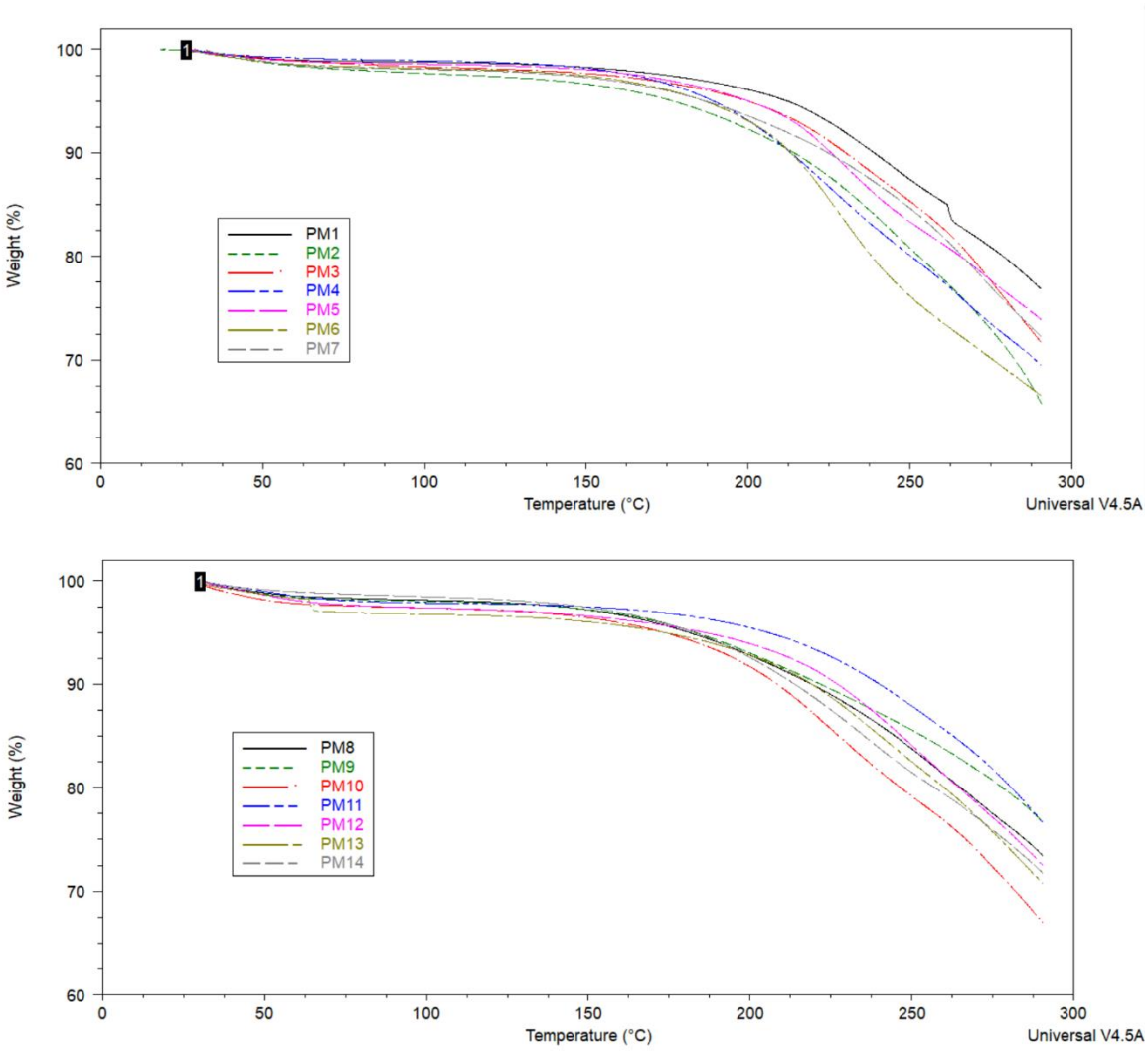

Figure 7.7. Thermal degradation profiles of physical mixtures in all groups.

7.3.1.3 DSC Analysis of Raw Materials and Physical Mixtures

The optimal processing temperatures during extrusion and printing processes should be determined by both the melting and degradation temperature values of IBP and other raw materials to minimize degradation and incomplete incorporation of the model drug in the carrier. For evaluating the solid-state of the drug in the extruded filaments and 3D printed tablets, DSC and XRD analyses were applied. As shown in Figure 7.8A, the DSC profile of IBP showed a sharp endothermic peak with an onset temperature of about 78.9 °C. The melting point of IBP also confirmed its crystalline state. EC and other excipients (except for PEG 6000 which is a semi-crystalline substance) showed no endothermic peaks, indicating that they are in an amorphous state. The DSC thermograms of physical

mixtures of all formulations exhibited an IBP endothermic peak but with smaller intensity due to the low amount of IBP (20 w/w%) compared to DSC traces of pure IBP. Additionally, it could be due to partial drug-polymer miscibility and interaction.[262] The presence of the characteristic endothermic peak of IBP in all physical mixtures indicates that the mixing process cannot change the solid states of the API and excipients (Figure 7.8B).

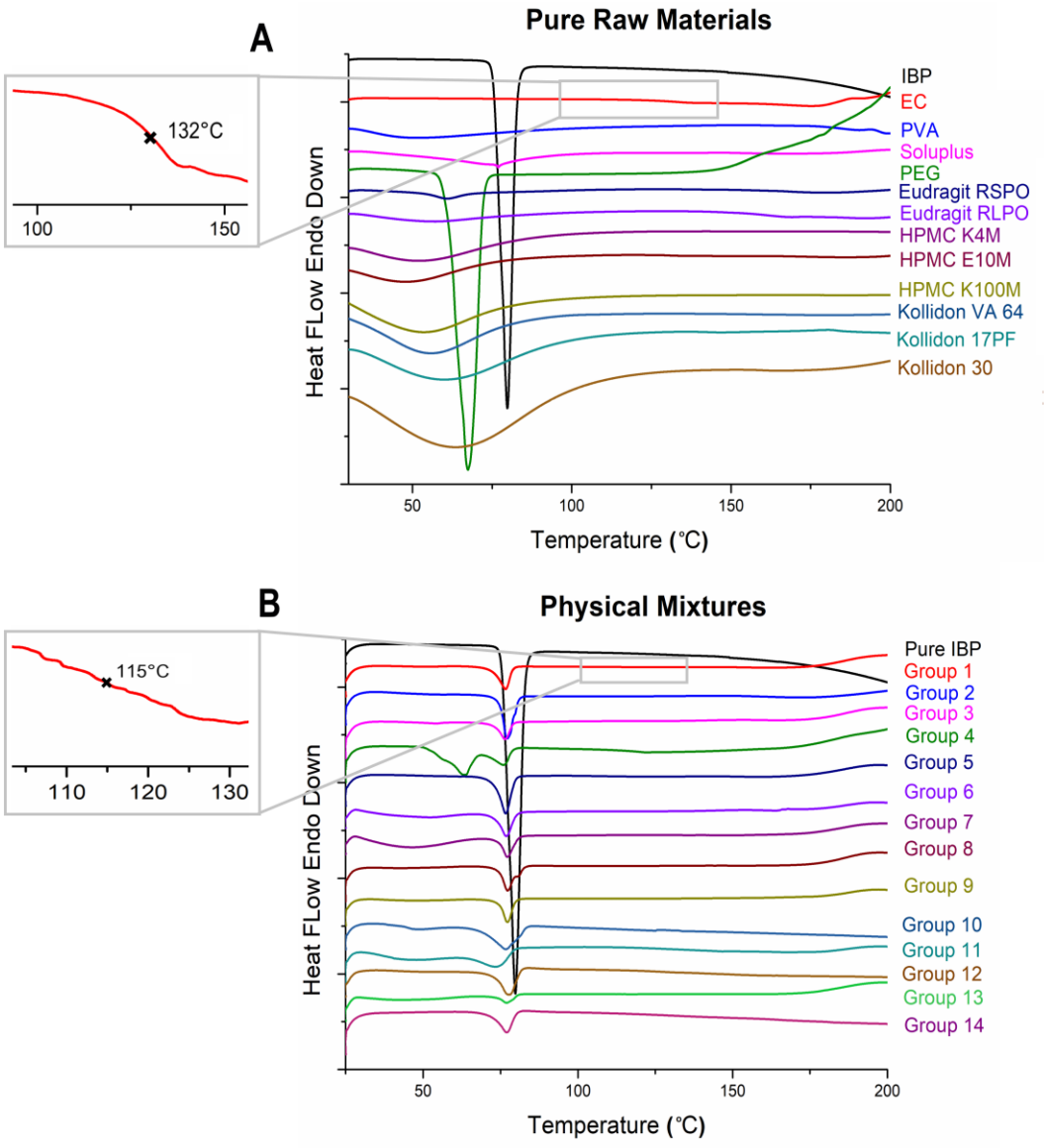

Figure 7.8. DSC thermograms of (A) pure raw materials and (B) physical mixtures.

The single shift in the baseline of unprocessed EC powder was observed at around 132 °C, which could be attributed to its T_g.[187] Additionally, De Brabander

et al. pointed out that the T_g of amorphous IBP was determined at -43.6°C.[187] According to the Gordon-Taylor equation, the significant decrease in the T_g of EC from 132°C to 115°C reflects the miscibility between IBP and EC in the physical mixtures of Group 1 (IBP and EC without release modifiers) because the T_g of physical mixtures lies between the T_g of two individual components.[162] This decreasing effect of IBP on the T_g of EC can also confirm that IBP showed the plasticizing effect and mobility enhancing effect on EC chains.[174]

7.3.1.4 XRD Analysis

XRD studies were conducted to analyze the physicochemical properties of raw materials and the crystalline-amorphous transformation of the API through the preparing process. XRD diffractograms of raw materials (Figure 7.9) were illustrated to identify the original solid-state of IBP, polymer and various release modifiers. Diffraction patterns of IBP showed an obvious crystalline nature due to multiple sharp intense peaks at around 6.2°, 12.3°, 16.7°, 19.1°, 20.2° and 22.4° (2-theta position), whereas other raw materials showed the halo structure which is an indication of amorphous nature of these materials with an exception of PEG.[263] The diffraction pattern of PVA and PEG 6000 revealed a complete agreement of their semi-crystalline nature.[141,151,253]

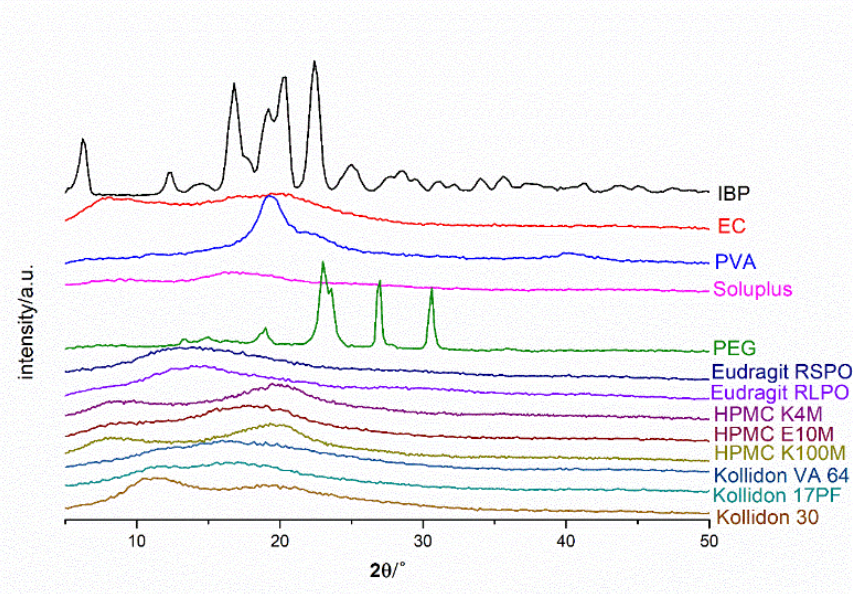

Figure 7.9. XRD diffractograms of raw materials.

7.3.2 Characterization of Filaments

7.3.2.1 Surface Morphology

The filaments of F1, F5 and F6 were translucent and others had a slightly white opaque appearance (Figure 7.10). This indicates that most release modifiers of each group still existed in the form of particles after the HME process to some extent except F5 and F6.[264]

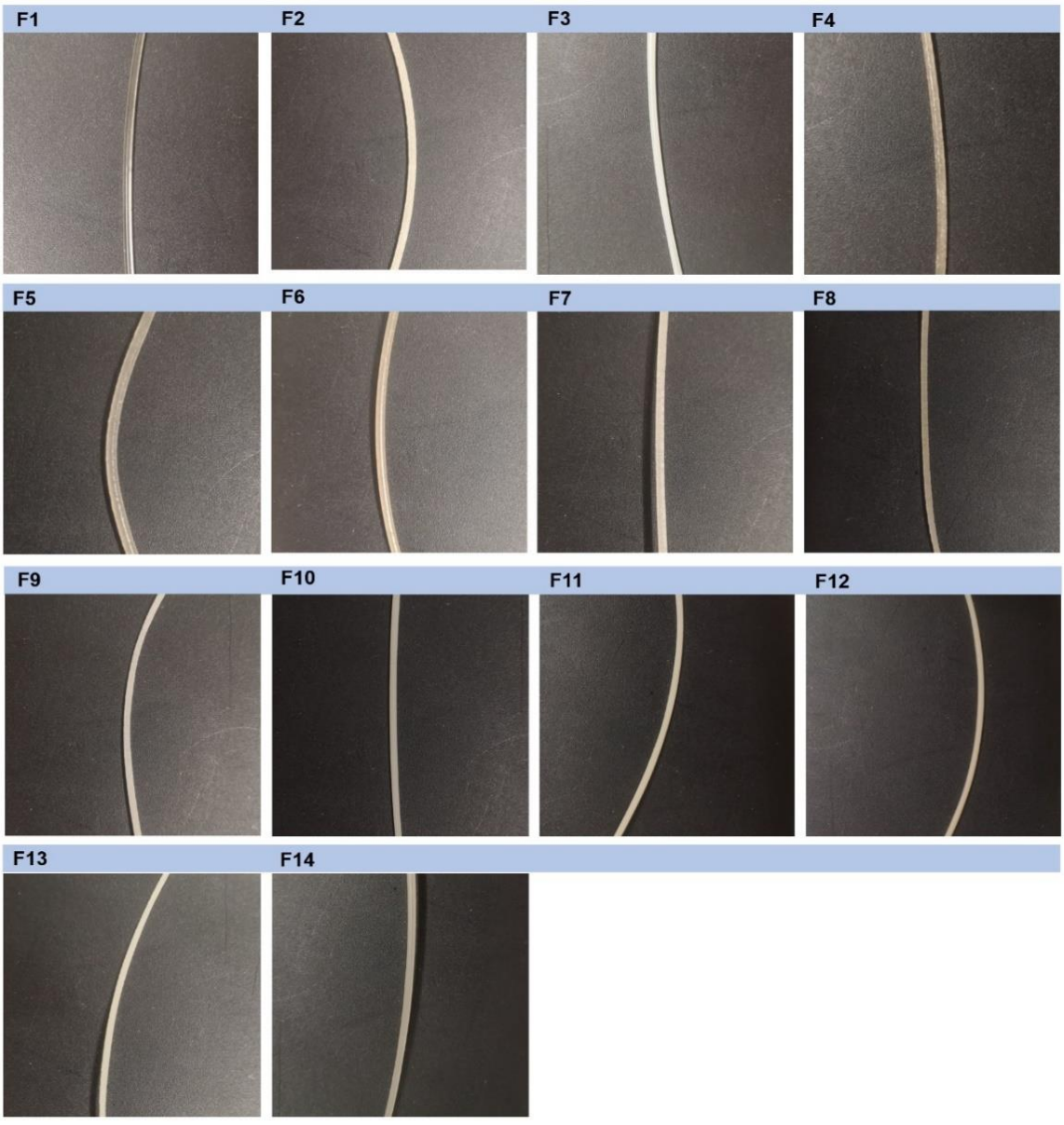

Figure 7.10. Images of hot melt extruded filaments containing IBP.

As shown in Figure 7.11, no defects, bubbles or holes were observed on the cross-section or surface of all drug-loaded filaments. Homogeneous morphology and the absence of drug crystals in SEM images of Group 1 (Figure 7.11A1 and B1) illustrated that IBP was distributed evenly in the EC matrix of IBP containing filaments.[174] However, a small number of IBP crystals could be seen in the filaments of Groups 2 and 9 at high magnification when compared with other groups. The external surface of hot melt extruded filaments in Groups 1, 3, 4, 5 and 6 was smoother, possibly due to the better coalescence of the API and polymers during processing.[158] On the contrary, the roughness imperfections on the surface of filaments in Group 2, and Group 7 to Group 14 might be contributed to the low processing temperature during HME (80-100 °C) which is not high enough for melt flowing and mixing of EC and release modifiers.[174] According to Crowley *et al.*, the processing temperature has a significant effect on the surface morphology of extrudates because lower processing temperature is related to visible crystalline API particles and higher processing temperature can lead to striated appearance.[265]

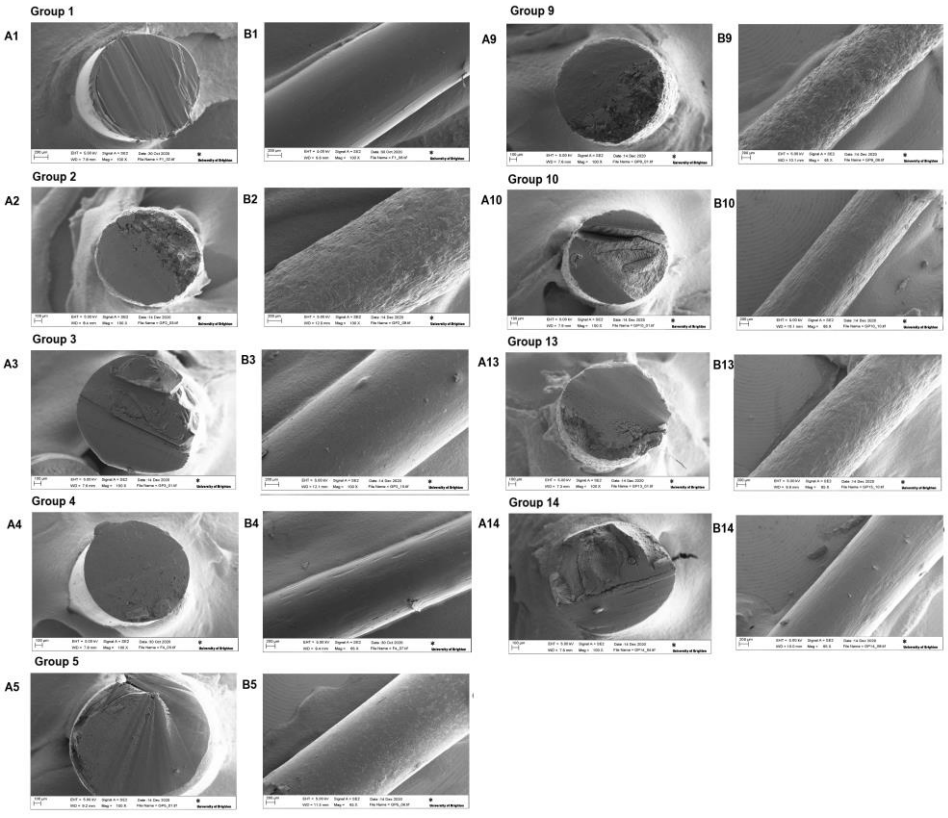

Figure 7.11. SEM images of (A) cross-section and (B) surface of filaments.

7.3.2.2 Mechanical Properties

Elasticity, stiffness, homogenous dimension and drug distribution are key factors for filaments to be printed into high-quality dosage forms with FDM technology.[255] Most pharmaceutical polymers possess high viscosity and poor melt flow properties, which are undesirable factors for FDM.[157] The filaments are required to possess both suitable stiffness and elasticity.[176] Otherwise, those filaments could not be printed successfully due to several states, such as fragmentation (related to high brittleness), shear/erosion (related to lower resistance to traction), buckle (high viscosity and /or low column strength) and so forth.[148,255]

The commercial PLA filaments (Figure 7.2) showed higher yield strength, Young's modulus and tensile strength when compared with hot melt extruded IBP loaded EC filaments (Figure 7.12) due to higher stiffness. Filaments prepared without release modifiers (F1) were used to ascertain the original printing properties of IBP and EC. It is noteworthy that filaments prepared without release modifiers (F1) exhibited slightly higher elongation at break than PLA filaments because of lower brittleness. Filaments extruded with only IBP and EC (F1) displayed a significantly higher tensile strength of 30 MPa than all other fabricated filaments with the addition of various release modifiers (F2-14). Additionally, the elongation at break of F1 (7.88%) was also the highest. Nasereddin *et al.* have pointed out that pure Soluplus filaments showed almost no strain bearing capacity, which is in agreement with the low elongation at break of F3 filaments.[157] The IBP-EC filaments with the addition of Kollidon VA 64 (F10) and Kollidon 30 (F12) showed similar mechanical properties. The addition of TEC in F13 can lower the brittleness and stiffness of filaments in F10, whereas the addition of Eudragit RSPO in F14 can increase the stiffness and brittleness slightly.

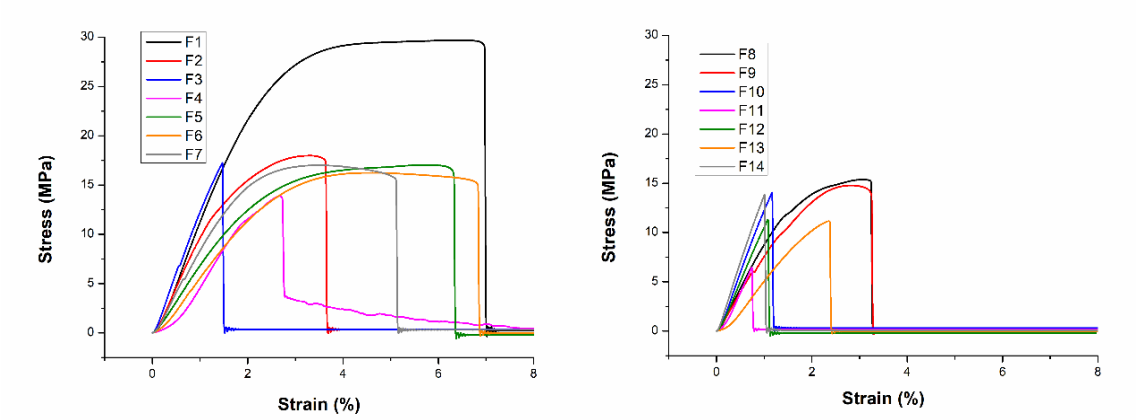

Figure 7.12. Stress-Strain curves of various IBP-loaded EC filaments.

As shown in Table 7.3, the addition of these release modifiers decreased the stiffness and increased the brittleness because of the significant decrease in both tensile strengths and elongations at the break. No obvious difference could be observed among F7, F8 and F9, indicating that the mechanical properties of filaments prepared with the addition of HPMC K4M, E10M and K100M are similar. Similar trends could be found in F5 (Eudragit RSPO) and F6 (Eudragit RLPO) even though F5 showed the second-highest elongation at break (6.90%) among all these 14 batches. The addition of plasticizer (TEC) can increase the strain bearing ability and decrease the elastic modulus of F13 compared to F10 filaments.[157,174,176]

The strain hardening behavior could be applied as a parameter to evaluate the conditions for material processing as it has a significant influence on strength and ductility.[266] As shown in Eq. 12, the strain hardening capacity (H_c) was defined as a ratio of the ultimate tensile strength (σ_{UTS}) to the yield strength (σ_y). According to Hall-Petch relationship, materials with the higher H_c value are considered as ideal because they reflect homogeneous yielding and the increase in formability and grain size.[267,268] Strain hardening capacity is related to the material condition as higher hardening capacity will lead to higher ductility.[269] As shown in Table 7.3, the values of H_c in F1 and F4 to F9 are all obviously higher than that of commercial PLA filaments. Among them, the addition of HPMC E10M (F8), K4M

(F7) and PEG 6000 (F4) can increase the value of H_c in IBP-EC filaments (F1). However, the hardening capacity values of filaments in F3, F10, F11, F12 and F14 are 0. In this case, these extruded filaments experienced a sudden fracture during the tensile test without the strain hardening process.

$$H_c = \frac{\sigma_{UTS}}{\sigma_y} - 1 \qquad \text{Eq. 12}$$

Table 7.3. Mechanical properties of hot melt extruded IBP-loaded EC filaments (n = 3, mean ± SD)

Filament	Yield strength (MPa)	Tensile strength (MPa)	Elastic modulus (MPa)	Elongation at break (%)	Strain hardening capacity
PLA	50.43 ± 0.97	54.64 ± 2.02	2171.62 ± 62.13	6.38 ± 0.17	0.08 ± 0.06
F1	26.59 ± 3.30	32.71 ± 4.29	1099.37 ± 0.06	7.88 ± 1.29	0.23 ± 0.01
F2	16.84 ± 0.28	17.59 ± 0.54	1015.58 ± 116.19	2.96 ± 0.97	0.04 ± 0.01
F3	15.48 ± 2.40	15.48 ± 2.40	1272.24 ± 96.03	1.28 ± 0.30	0±0
F4	13.05 ± 2.09	15.15 ± 0.40	697.12 ± 140.55	2.81 ± 0.06	0.26 ± 0.01
F5	15.50 ± 0.86	17.99 ± 1.39	701.82 ± 32.67	6.90 ± 0.79	0.16 ± 0.03
F6	14.18 ± 0.42	15.52 ± 1.01	932.81 ± 47.35	4.53 ± 3.27	0.09 ± 0.04
F7	12.66 ± 0.35	17.46 ± 0.66	916.60 ± 114.56	4.31 ± 1.15	0.38 ± 0.09
F8	11.43 ± 0.02	17.02 ± 2.35	961.00 ± 159.81	2.99 ± 0.37	0.54 ± 0.13
F9	13.09 ± 0.26	14.84 ± 0.08	707.00 ± 129.50	2.96 ± 0.42	0.13 ± 0.02
F10	11.67 ± 2.98	11.67 ± 2.98	1068.67 ± 227.76	1.13 ± 0.07	0±0
F11	5.23 ± 1.63	5.23 ± 1.63	825.05 ± 60.01	0.65 ± 0.16	0±0
F12	12.19 ± 1.41	12.19 ± 1.41	966.50 ± 120.75	1.48 ± 0.54	0±0
F13	8.89 ± 2.02	9.51 ± 2.49	457.27 ± 79.36	2.79 ± 0.90	0.06 ± 0.04
F14	9.66 ± 3.51	9.66 ± 3.51	1183.67 ± 202.46	0.80 ± 0.20	0±0

All these prepared filaments showed no breaking or squeezing problems during the 3DP process, indicating suitable mechanical properties of these filaments for FDM 3DP and the fabrication of high-quality 3D printed tablets.

7.3.2.3 XRD Analysis of Filaments

The peaks of XRD traces of physical mixtures (Figure 7.13A) are in good consistent with the peaks of IBP in each batch because EC and most of the release modifiers (Soluplus, Eudragit RL PO/RS PO, HPMC K4M/E10M/ K100M, Kollidon VA 64/17PF/30) exist in the amorphous state. No characteristic peaks

for IBP were detected in the diffractograms for the extruded filaments (Figure 7.13B), confirming the absence of crystalline IBP in the extruded filaments with the 20 w/w% drug load. It suggests that HME processes had a significant effect on the crystallinity of the API. The XRD diffractograms of drug-loaded hot melt extruded filaments from all groups only reflect the EC characteristic peaks. Multiple high-intensity peaks of IBP were not seen in the XRD patterns of filaments, mainly because of the formation of the IBP solid dispersion in the filaments which overshadowed its crystalline nature.[249]

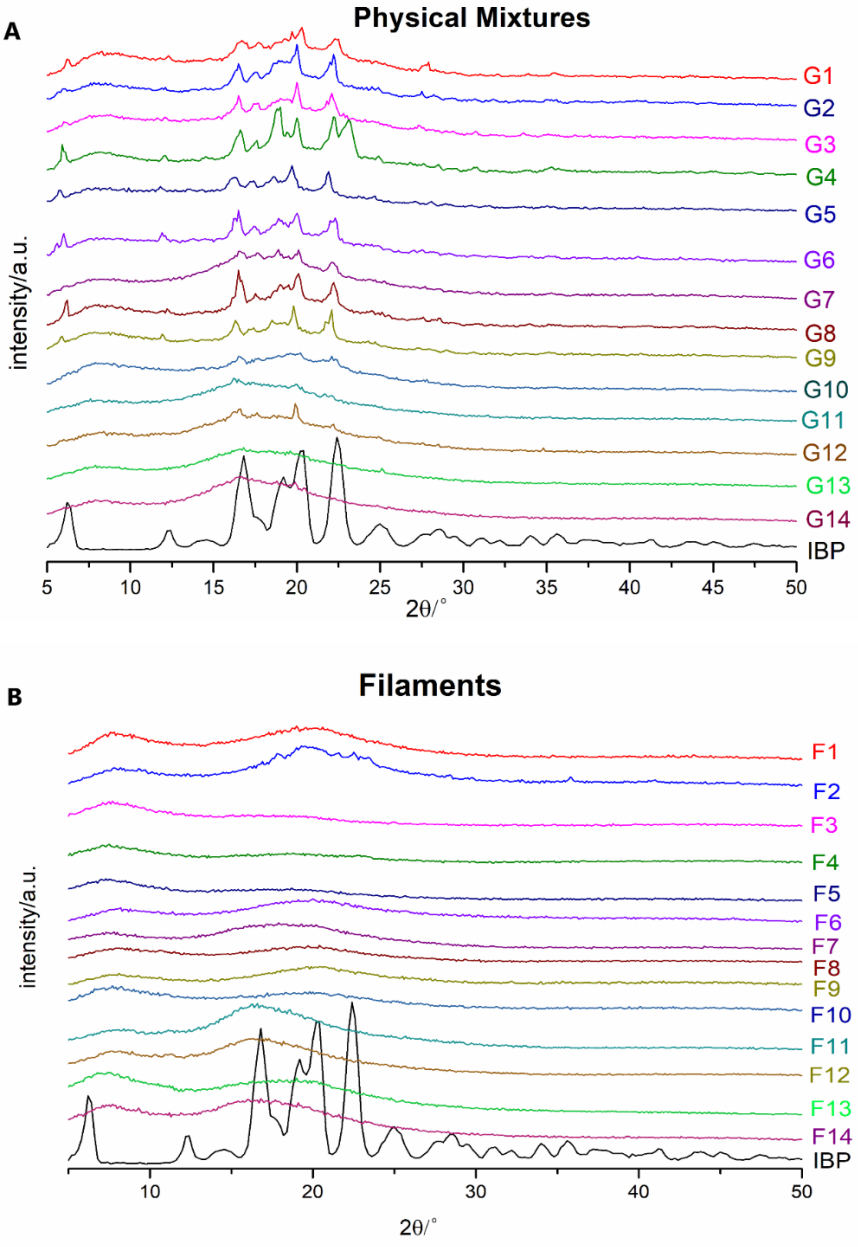

Figure 7.13. XRD diffractograms of (A) physical mixtures and (B) hot melt extruded filaments of all groups when compared with pure ibuprofen.

7.3.2.4 TGA of Filaments

The thermal stability of these hot melt extruded filaments was evaluated by TGA to understand how each filament performs during the FDM 3D printing process.[270] As shown in Figure 7.14, these extruded filaments showed no higher than 5% weight loss up to 200°C, where thermal degradation begins to occur. Based on this result, all filaments are predicted to remain thermally stable throughout the FDM 3D printing process at 178°C.

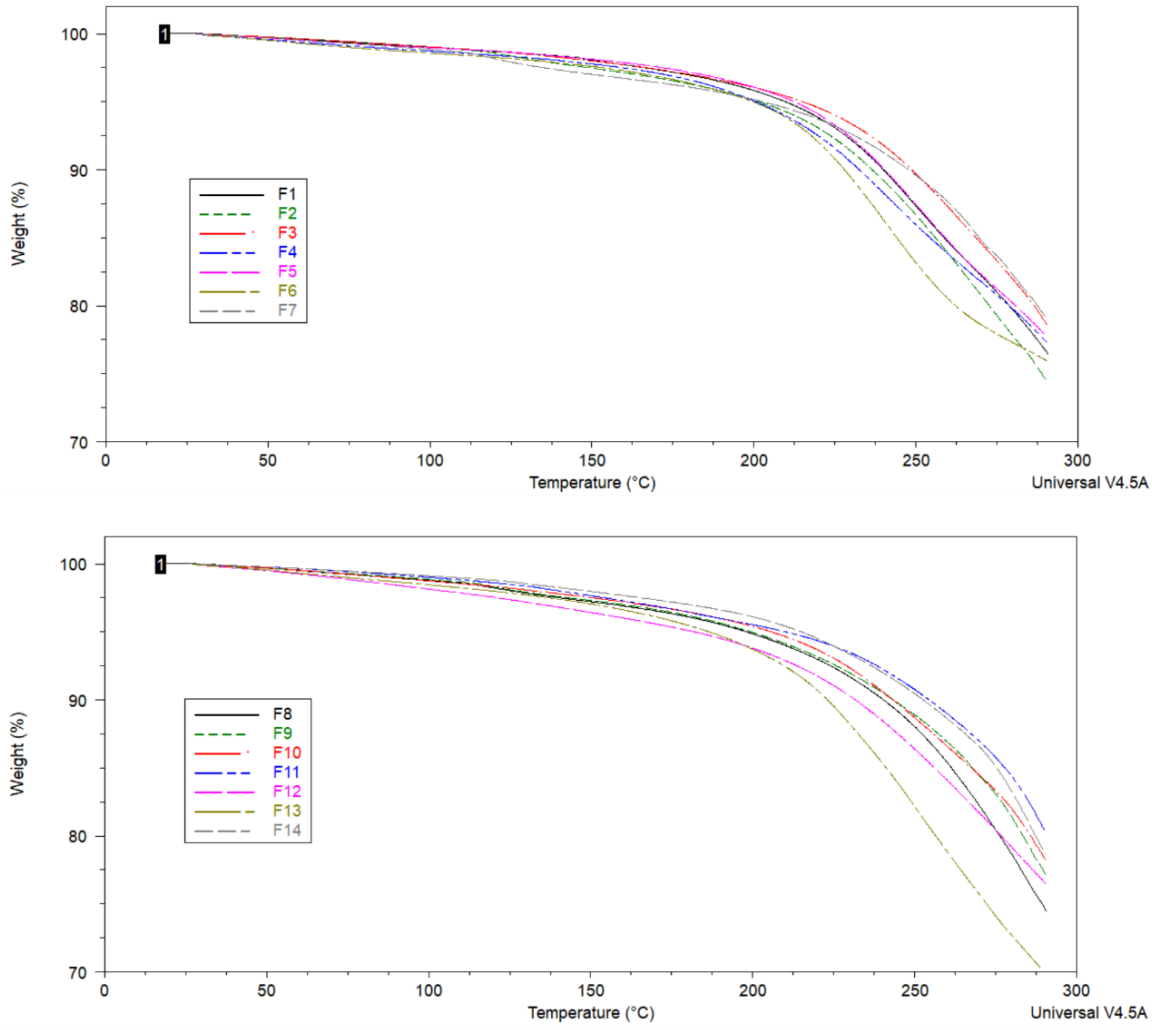

Figure 7.14. Thermal degradation profiles of hot melt extruded filaments in all groups.

7.3.2.5 Drug Content Determination

During the HME and FDM processes for developing amorphous dispersions, identifying drug loading is vitally important for checking the chemical and physical stability of the final formulation.[258] Ethanol was used to completely dissolve EC based filaments and 3D printed tablets.[158] The percentage of IBP in the filaments was shown in Table 7.4. Reasonable under-content or overage is common and acceptable in pharmaceutical products across regulatory agencies.[249] This indicates that there is no major loss or degradation of IBP during the extrusion processes.

Table 7.4. Drug loading and dose accuracy (mean ± standard deviation) of filaments in each group

Group	Theoretical drug loading (%)	Filaments	
		Drug Loading (%)	Dose Accuracy (%)
G1	20	20.09 ± 0.10	100.47 ± 0.52
G2	20	20.72 ± 0.13	103.62 ± 0.64
G3	20	20.14 ± 0.20	100.72 ± 1.01
G4	20	19.98 ± 0.06	99.92 ± 0.30
G5	20	19.99 ± 0.18	99.94 ± 0.89
G6	20	19.98 ± 0.04	99.92 ± 0.20
G7	20	20.03 ± 0.26	100.16 ± 1.29
G8	20	19.97 ± 0.29	99.86 ± 1.45
G9	20	19.97 ± 0.28	99.83 ± 1.40
G10	20	20.42 ± 0.42	102.12 ± 2.11
G11	20	20.38 ± 0.07	101.92 ± 0.37
G12	20	20.08 ± 0.11	100.42 ± 0.57
G13	20	20.75 ± 0.17	103.75 ± 0.83
G14	20	19.92 ± 0.44	99.62 ± 2.19

7.3.2.6 *In Vitro* Dissolution Studies

The drug dissolution behaviors from hot melt extruded filament segments and directly compressed physical mixture tablets were evaluated. The main polymer in this study was EC, which is barely soluble in water and has been applied in producing sustained-release tablets by direct compression.[142,191] As expected, the directly compressed physical mixture tablets (in Group 1) released only 37%

of IBP within 24 h (Figure 7.15A). However, tablets from other groups exhibited different dissolution behaviors. Typically, the dissolution rate of tablets from Groups 7, 8 and 9 (physical mixtures of IBP, EC and HPMC) showed the fastest among all fourteen formulations studied, although the addition of PVA, Soluplus, PEG and Kollidon can also enhance drug release to some extent in Groups 2, 3, 4 and 10-12. On the contrary, the incorporation of Eudragit RSPO (Group 5) or RLPO (Group 6) showed a reduction in drug release.

Generally, the drug release rate from filament segments (Figure 7.15B) is much lower than directly compressed physical mixture tablets due to the compacted nature of the molten polymers. It is clear from the results, the addition of Soluplus in F3 has an increasing effect on the dissolution rate of the IBP and EC matrix when compared with other filaments. Many researchers proved that Soluplus, a water-soluble polymer, could be used to increase the dissolution of poorly soluble drugs during the preparation of hot melt extruded solid dispersions.[151] Although Soluplus has promising thermostability and extrudability in pharmaceutical HME, pure hot melt extruded Soluplus filaments are not FDM printable.[151] The excellent thermoplastic and FDM printability of PVA make it a benchmark release modifier in this study.[151] Similarly, PEG was also applied to improve the FDM printability of the blends and have a plasticizing effect on poorly water-soluble drugs.[151] Many studies pointed out that diffusion is the main mechanism for the API to be released from the insoluble macromolecular matrix of Eudragit.[155] Eudragit® RLPO and RSPO are both copolymers of acrylic and methacrylic acid esters.[271] Eudragit® RLPO exhibits more permeable to aqueous media than Eudragit® RSPO because of the higher molar ratio of ionizable groups.[271] As a result, the drug release rates of extruded filaments and physical mixture tablets in Group 6 are both slightly higher than those in Group 5. Commonly, sustained-release compacts prepared with higher viscosity grades of HPMC result in a decrease in the drug release rate because of stronger polymer entanglement and slower polymer erosion.[191] However, it has been proved that hot melt extrudates

prepared with IBP, EC and higher viscosity grades of HPMC will show a faster drug release rate and higher initial burst drug release when compared with similar extrudates containing lower viscosity grades of HPMC.[158,191] The possible reasons are: (1) the high drug load and the presence of EC can weaken the HPMC chains entangled within the matrix; (2) the higher water uptake and swelling capability of higher viscosity HMPC grades can make the matrix more accessible to the dissolution medium.[158,191] The viscosity of HPMC used in this study was in the order of K4M < E10M < K100M.[272] This is in good agreement with the order of drug release rates for their filaments (Figure 7.15B). It can be observed that the Kollidon® VA64, 17PF and 30 showed similar increasing effects on the dissolution rate of hot melt extruded filaments of the IBP-EC matrix. It is noteworthy that the dissolution rate of F14 decreased significantly with the addition of Eudragit® RSPO when compared with F10 as it can be seen that F5 showed the lowest dissolution rate among all groups. All these data indicate that the behaviors of polymers in their physical mixtures and in the filament are entirely different and the drug release from filaments cannot be predicted based on the dissolution data of physical mixtures of IBP and polymers.

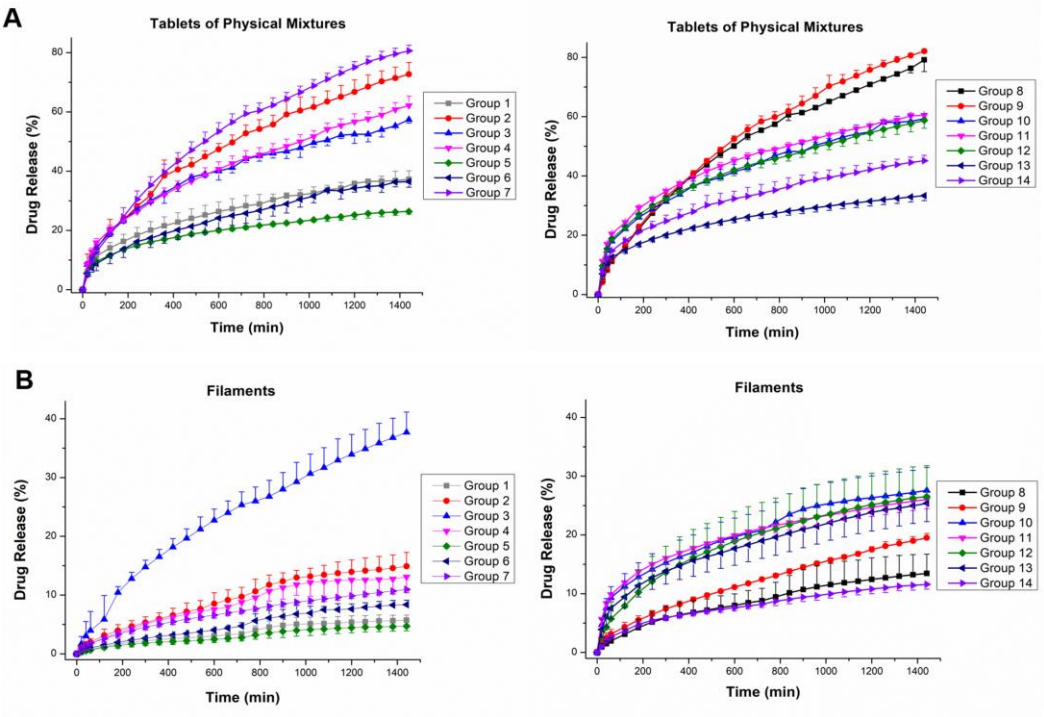

Figure 7.15. *In vitro* drug release study of (A) physical mixture tablets and (B) filament pieces (*n* = 3).

7.3.2.7 Determination of Drug Release Kinetics

The dissolution data of tablets prepared by direct compression and filaments were plotted based on the zero-order, first-order, Higuchi and Korsmeyer-Peppas equations and calculated kinetic parameters with fitting results are summarized in Table 7.5. The best fit for the kinetics of almost all tablets and filaments was obtained with the Korsmeyer-Peppas model (Figure 7.16). The n values of physical mixture tablets are much lower and in some groups (Groups 1, 3, 5, 10-14) are less than 0.45 (indicating Fickian diffusion).[174]

Table 7.5. Drug release kinetics parameters of physical mixture tablets and filaments for various drug release models

Group	Parameter	Tablets of Physical Mixtures				Filaments			
		Zero-order	First-order	Higuchi	Korsmeyer-Peppas	Zero-order	First-order	Higuchi	Korsmeyer-Peppas
1	R^2_{adj}	0.691	0.792	0.983	0.999	0.928	0.934	0.977	0.998
	AIC	183	172	105	35	49	47	11	-34
	n	----	----	----	0.408	----	----	----	0.658
2	R^2_{adj}	0.780	0.964	0.997	0.999	0.923	0.989	0.982	0.997
	AIC	502	401	245	150	98	93	72	23
	n	----	----	----	0.542	----	----	----	0.665
3	R^2_{adj}	0.514	0.795	0.971	0.986	0.914	0.954	0.989	0.999
	AIC	515	470	352	302	157	140	97	27
	n	----	----	----	0.424	----	----	----	0.626
4	R^2_{adj}	0.629	0.833	0.996	0.998	0.912	0.928	0.976	0.989
	AIC	496	450	238	188	102	96	58	43
	n	----	----	----	0.453				0.640
5	R^2_{adj}	0.178	0.357	0.922	0.997	0.941	0.945	0.961	0.993
	AIC	452	439	318	166	27	26	20	-25
	n	----	----	----	0.344	----	----	----	0.669
6	R^2_{adj}	0.798	0.868	0.987	0.997	0.964	0.968	0.938	0.983
	AIC	401	377	251	174	51	48	66	27
	n	----	----	----	0.478	----	----	----	0.771
7	R^2_{adj}	0.843	0.991	0.993	0.999	0.886	0.903	0.998	1.000
	AIC	499	335	322	136	95	91	-15	-77
	n	----	----	----	0.647	----	----	----	0.572

	R^2_{adj}	0.872	0.989	0.989	1.000	0.891	0.905	0.998	1.000
8	AIC	208	141	138	28	89	85	3	-61
	n	----	----	----	0.651	----	----	----	0.581
	R^2_{adj}	0.879	0.997	0.987	0.999	0.934	0.954	0.995	1.000
9	AIC	208	110	149	20	115	105	38	-16
	n	----	----	----	0.684	----	----	----	0.619
	R^2_{adj}	0.572	0.788	0.976	0.999	0.530	0.624	0.974	0.996
10	AIC	216	197	138	65	171	165	93	48
	n	----	----	----	0.404	----	----	----	0.384
	R^2_{adj}	0.392	0.704	0.951	0.999	0.246	0.386	0.917	0.999
11	AIC	227	207	159	51	184	179	125	20
	n	----	----	----	0.358	----	----	----	0.318
	R^2_{adj}	0.470	0.740	0.964	0.998	0.800	0.852	0.995	0.996
12	AIC	221	204	151	64	151	143	55	50
	n	----	----	----	0.377	----	----	----	0.475
	R^2_{adj}	0.286	0.479	0.927	0.999	0.588	0.675	0.985	0.999
13	AIC	198	190	139	31	165	160	77	16
	n	----	----	----	0.326	----	----	----	0.402
	R^2_{adj}	0.492	0.672	0.965	0.997	0.709	0.743	0.995	0.997
14	AIC	204	192	132	65	119	116	6	-9
	n	----	----	----	0.376	----	----	----	0.461

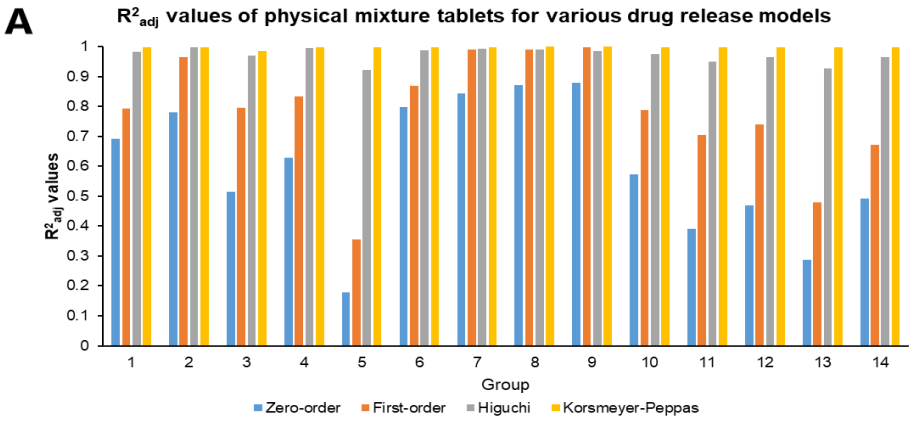

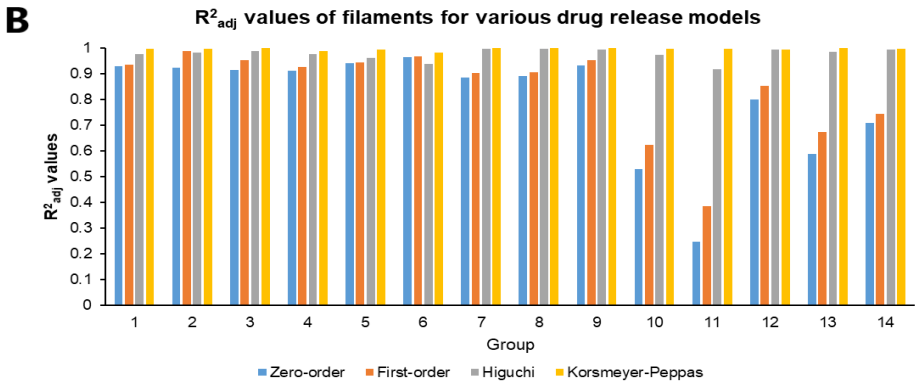

Figure 7.16. The adjusted coefficient of determination (R^2_{adj}) values of (A) physical mixture tablets and (B) filaments for various drug release models.

7.4 Conclusion

In this chapter, IBP (as the model drug) and EC (as the polymeric matrix), along with various release modifiers, were blended and extruded into filaments through a twin-screw extruder. EC polymers with various molecular weights (viscosity grades) were applied to fabricate IBP loaded filaments. A comprehensive characterization was made to select the most suitable filament formulation for the following FDM 3D printing process. Due to the excellent performance of the IBP-EC 10 filament, the Ethocel™ Standard 10 Premium was selected as the main polymer matrix. To modulate the FDM printability and release behavior of the IBP loaded filaments, various release modifying materials, namely, PVA, Soluplus, PEG 6000, Eudragit® RL PO/RS PO, HPMC K4M/E10M/K100M, Kollidon® vinyl acetate 64 (VA 64)/17PF/30 were added into the formulation. We successfully fabricated various solid dispersion filaments with IBP in an EC and release modifiers matrix through the HME process, which all showed good mechanical properties. The mechanical characterization showed that the filament stiffness and brittleness could be adjusted significantly by changing the type of release modifiers. Furthermore, *in vitro* drug release studies revealed that these release modifying materials can adjust the drug release rate significantly. In comparison with directly compressed physical mixture tablets, slower drug release can be obtained from these hot melt extruded filaments.

8. Chapter 8: Fused Deposition Modelling 3D Printed Devices Prepared Using Filaments

8.1 Introduction

Pharmaceutical polymers have been widely applied in HME formulations, such as synthetic cellulose derivatives, methacrylate polymers, polyvinyl pyrrolidone (PVP), polyethylene oxide (PEO) and pyrrolidone-co-vinyl acetate.[165] However, only 30 materials are available commercially for the FDM process, whereas there are more than 3000 materials that are suitable for other HME-based processes.[173] It is difficult to fabricate suitable hot melt extruded filaments for the following 3D printing process due to the importance of filament mechanical characteristics.[273] Melt-blending can provide a cost-effective, convenient and mature solution by combining two or more different polymers with various properties into a single matrix material.[173,249] As a result, the final dosage form can be designed and fabricated with suitably flexible properties to overcome the material shortcomings of polymers for the FDM process.

Conventional manufacture of zero-order release dosage forms is complicated, time-consuming, difficult and low in flexibility.[274] In recent years, additive manufacturing technology has been developed into a promising platform to fabricate sustained-release tablets or implants with many advantages, such as the ability to prepare objects in almost any shape to meet the growing need for personalized medicine.[168,255] It has been proved that 3DP can be of great importance in many practical medical applications which are required to meet a wide range of anatomical and pathological requirements, like vaginal rings and localized cancer treatment.[129,168] In addition, although the HME can be used to improve the solubility and bioavailability of poorly soluble drugs, the combination of HME and FDM 3DP into a continuous process can become a promising strategy for the preparation of patient-centred and abuse-deterrent dosage forms

of opioids,[275] offer a cost-effective and convenient manufacturing platform for sustained release DDSs,[276] fabricate zero-order release dosage forms consisting of an insoluble shell and a controlled release core,[274] create osmotically controlled dosage forms with a core-shell structure for achieving sustained and/or delayed-release,[277] develop floating zero-order release dosage forms with complex hollow structure,[278] provide an alternative to the development of multilayer polypills with optimized release profiles for individualized therapy,[279] and prolong the drug release from dosage forms in a continuous and controlled manner simultaneously.[174]

Although HME has been used in combination with FDM 3DP, suitable feedstock materials such as polymeric filaments with optimum properties are still limited. In this chapter, various release modifying excipients, namely, poly(vinyl alcohol) (PVA), Soluplus®, PEG 6000, Eudragit® RL PO/RS PO, hydroxypropyl methylcellulose (HPMC) K4M/E10M/K100M, Kollidon® vinyl acetate 64 (VA 64)/17PF/30, were used as a release modulating tool to control the drug release from 3D printed sustained-release tablets. Hot melt extruded filaments were printed into cylindrical tablets through the FDM 3DP technique and their surface morphology, thermal stability, solid-state, mechanical properties, dose accuracy and drug release behaviors were investigated. In the current research, tablets were also prepared using a manual tablet compression machine by mixing all raw materials prior to direct compression and compared with 3D printed tablets.

The purposes of this research were (1) to develop suitable materials for preparing HME filaments and FDM 3DP of sustained-release tablets, (2) to compare the impact of different release modifiers on the mechanical properties and drug dissolution behaviors of filaments and FDM 3D printed tablets, and (3) to test the applicability of these processes in the preparation of 3D printed objects for achieving adjustable drug release profiles. For these purposes, a comprehensive evaluation of the suitability of a series of EC formulations containing both IBP and

a range of release modifiers for HME and FDM 3DP processes was conducted.

8.2 Methods

8.2.1 3D Printing of Tablets

Refer to the Section 2.4.5.

8.2.2 Characterization of Tablets

The weight, diameter and thickness of tablets from each batch were assessed for uniformity (n = 3). The diameter and thickness of 3D printed tablets were measured using a digital micrometer (Series 293 MDC-MX Lite, Mitutoyo Ltd., Hampshire, UK). Then the weight of tablets was measured accurately using a digital analytical balance (Sartorius, 0.1 mg).

8.2.3 SEM of Tablets

Refer to the Section 2.5.4.

8.2.4 DSC Analysis

Refer to the Section 2.7.2.

8.2.5 XRD

Refer to the Section 2.6.

8.2.6 TGA

Refer to the Section 2.7.1.2.

8.2.7 Determination of Drug Content

Refer to the Section 2.9.3.

8.2.8 *In Vitro* Drug Dissolution Studies

Refer to the Section 2.9.4.

8.3 Results and Discussion

8.3.1 Surface Morphology

The physical characteristics of tablets printed with filaments were evaluated. As shown in Table 8.1, the ability of fabricated filaments to reproduce the predesigned 3D structure was high. The tablets in each group were found to have uniform weights, diameters and heights with acceptable variation (Table 2.4 and Figure 8.1). The weight variations seen for these batches could be attributed to the differences among the fluidity potentials of these release modifiers.[148] Raw materials with enhanced mechanical and rheological properties can lead to a higher extrusion rate, then bigger and heavier final tablets could be produced. The geometry of these tablets is relatively constant with similar surface area/volume ratios from 1.32 to 1.40. Because the mechanical strength of these tablets was high, the friability values were zero and conventional hardness test methods are not feasible for FDM 3D printed formulations.[174,280]

Table 8.1. Physical parameters for 3D printed tablets (n = 3, mean ± SD).

3DP Tablets	Weight (mg)	Diameter (mm)	Height (mm)	Volume (mm^3)	Density (mg/mm^3)	Surface area (mm^2)	Surface area/volume
Group 1	116.00 ± 5.02	9.67 ± 0.12	2.21 ± 0.09	162.43 ± 3.18	0.71 ± 0.04	214.07 ± 1.87	1.32 ± 0.03
Group 2	119.73 ± 5.65	9.74 ± 0.15	2.14 ± 0.13	159.20 ± 12.35	0.75 ± 0.03	214.41 ± 7.92	1.35 ± 0.06
Group 3	144.97 ± 1.12	9.84 ± 0.19	2.13 ± 0.09	162.09 ± 11.35	0.90 ± 0.06	217.99 ± 8.84	1.35 ± 0.05
Group 4	137.17 ± 1.00	9.71 ± 0.24	2.12 ± 0.11	156.57 ± 9.71	0.88 ± 0.05	212.53 ± 8.60	1.36 ± 0.05
Group 5	116.17 ± 4.10	9.82 ± 0.10	2.10 ± 0.04	158.59 ± 5.67	0.73 ± 0.03	216.00 ± 4.58	1.36 ± 0.02
Group 6	118.73 ± 4.36	9.78 ± 0.15	2.09 ± 0.05	156.90 ± 6.84	0.76 ± 0.05	214.30 ± 6.22	1.37 ± 0.03
Group 7	126.13 ± 4.55	9.58 ± 0.01	2.14 ± 0.05	154.62 ± 3.37	0.82 ± 0.05	208.77 ± 1.45	1.35 ± 0.02
Group 8	130.53 ± 0.78	9.80 ± 0.12	2.02 ± 0.05	152.25 ± 6.48	0.86 ± 0.03	212.97 ± 5.39	1.40 ± 0.03
Group 9	135.47 ± 5.06	9.85 ± 0.12	2.07 ± 0.01	157.62 ± 3.59	0.86 ± 0.05	216.36 ± 4.26	1.37 ± 0.01
Group 10	116.43 ± 3.32	9.64 ± 0.09	2.03 ± 0.05	148.24 ± 5.80	0.79 ± 0.05	207.43 ± 4.45	1.40 ± 0.03
Group 11	113.20 ± 1.40	9.76 ± 0.23	2.01 ± 0.02	150.68 ± 7.36	0.75 ± 0.04	211.41 ± 8.69	1.40 ± 0.01
Group 12	102.37 ± 3.40	9.61 ± 0.21	2.15 ± 0.04	155.90 ± 10.07	0.66 ± 0.04	210.06 ± 9.16	1.35 ± 0.03
Group 13	103.30 ± 1.30	9.51 ± 0.11	2.12 ± 0.08	150.53 ± 8.97	0.69 ± 0.03	205.34 ± 6.16	1.37 ± 0.04
Group 14	118.10 ± 1.61	9.70 ± 0.05	2.11 ± 0.04	156.00 ± 4.21	0.76 ± 0.02	212.09 ± 2.90	1.36 ± 0.02

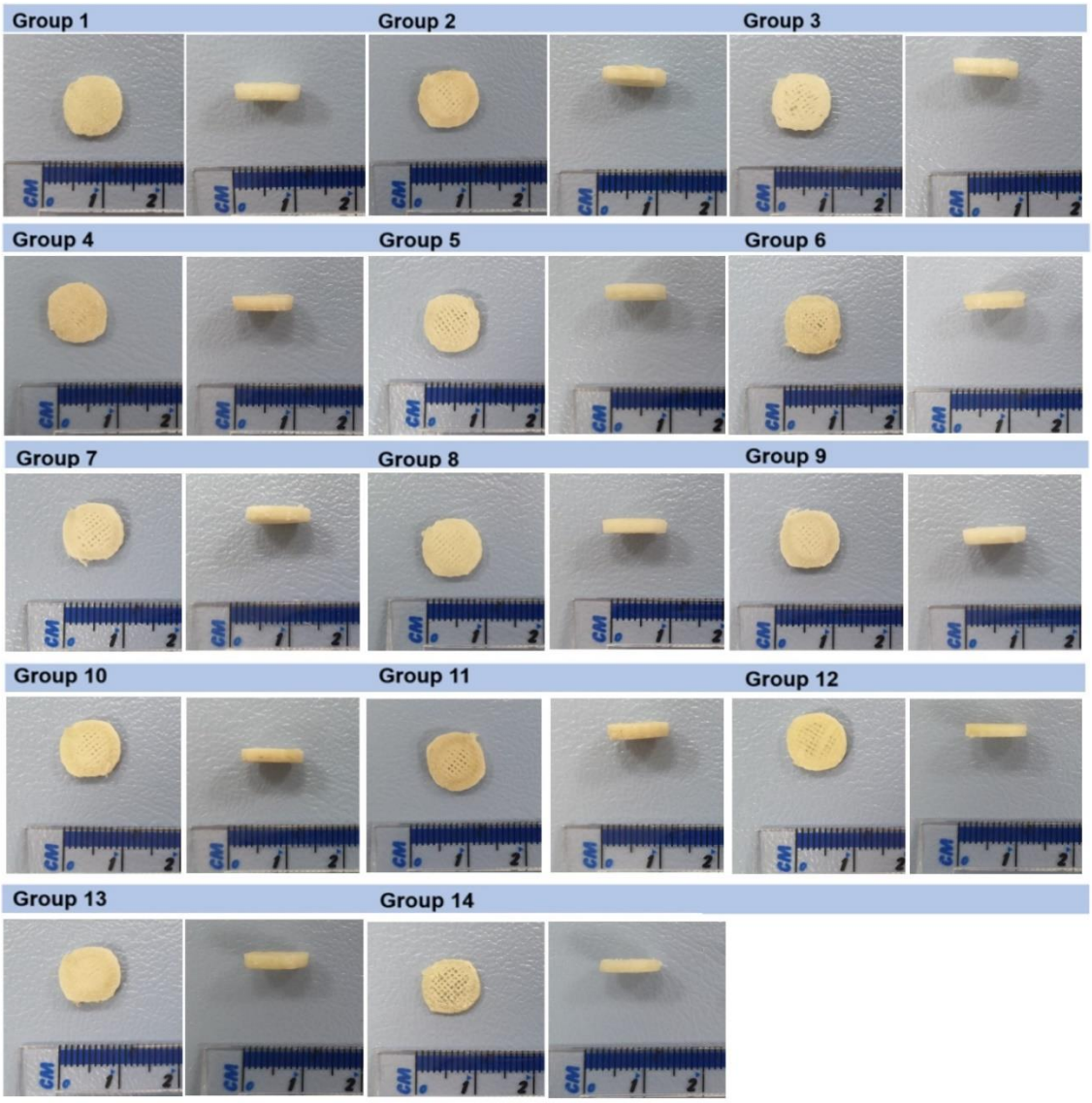

Figure 8.1. Images of 3D printed tablets prepared with hot melt extruded filaments.

The SEM images of 3D printed tablets (Figure 8.2A and B) illustrated that IBP was distributed in the tablets homogenously after further exposure to heat. The excellent surface morphology of all these 3D printed tablets confirmed that the formulation composition of 14 groups is suitable for HME and FDM 3DP processes.

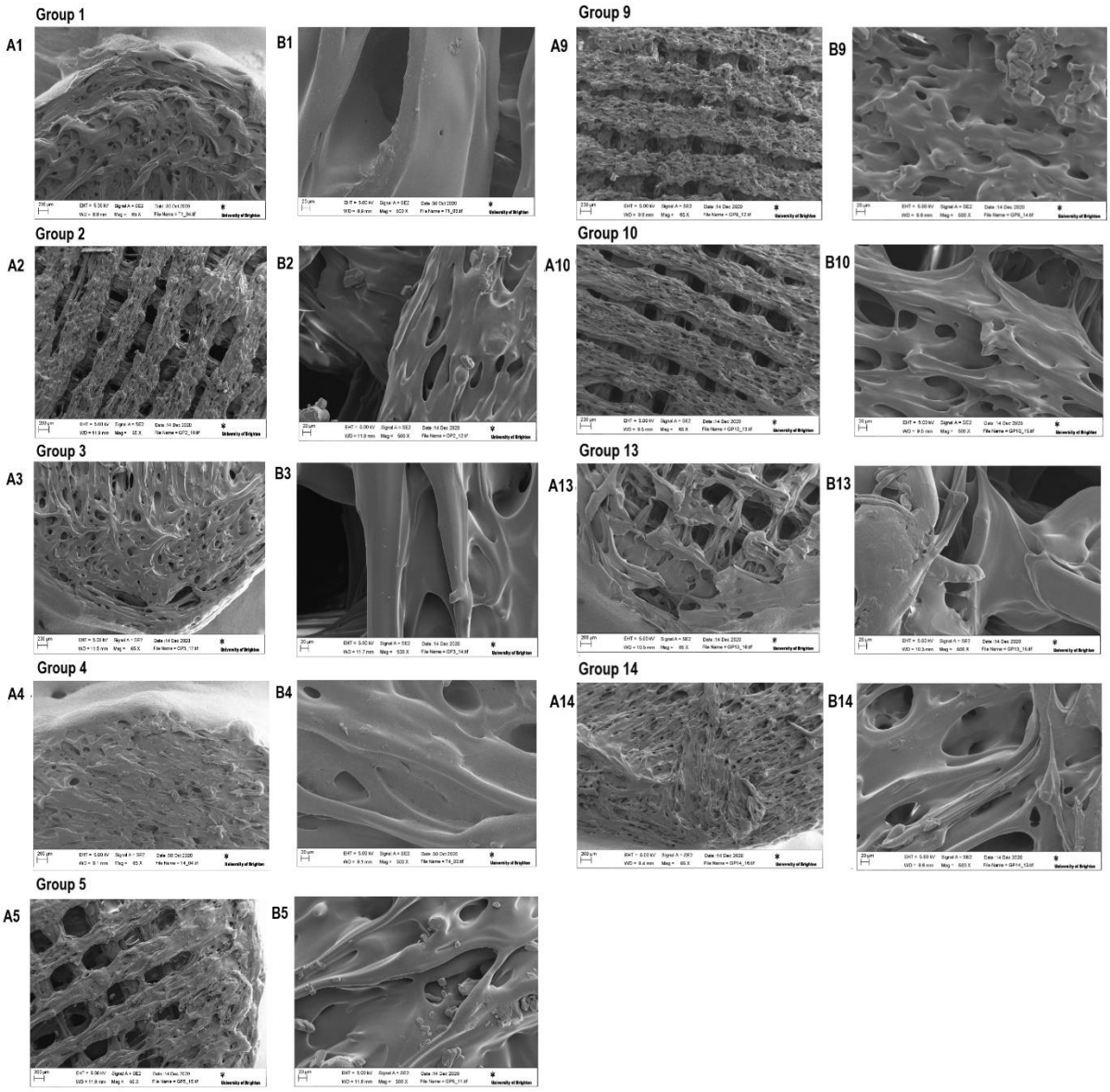

Figure 8.2. SEM images of top surface of 3D printed tablets loaded with IBP in Group 1, 2, 3, 4, 5, 9, 10, 13 and 14.

8.3.2 DSC Analysis

A complete absence of the IBP endothermic peak in the IBP loaded extruded filaments (Figure 8.3A) and 3D printed tablets (Figure 8.3B) from all groups was attributed to the conversion of IBP from the crystalline state to the amorphous state during the HME process.[154] It is noteworthy that the endothermic peak of PEG could be observed in F4 filaments instead of 3D printed tablets because semi-crystalline PEG was transformed into the amorphous state mainly during the printing process.

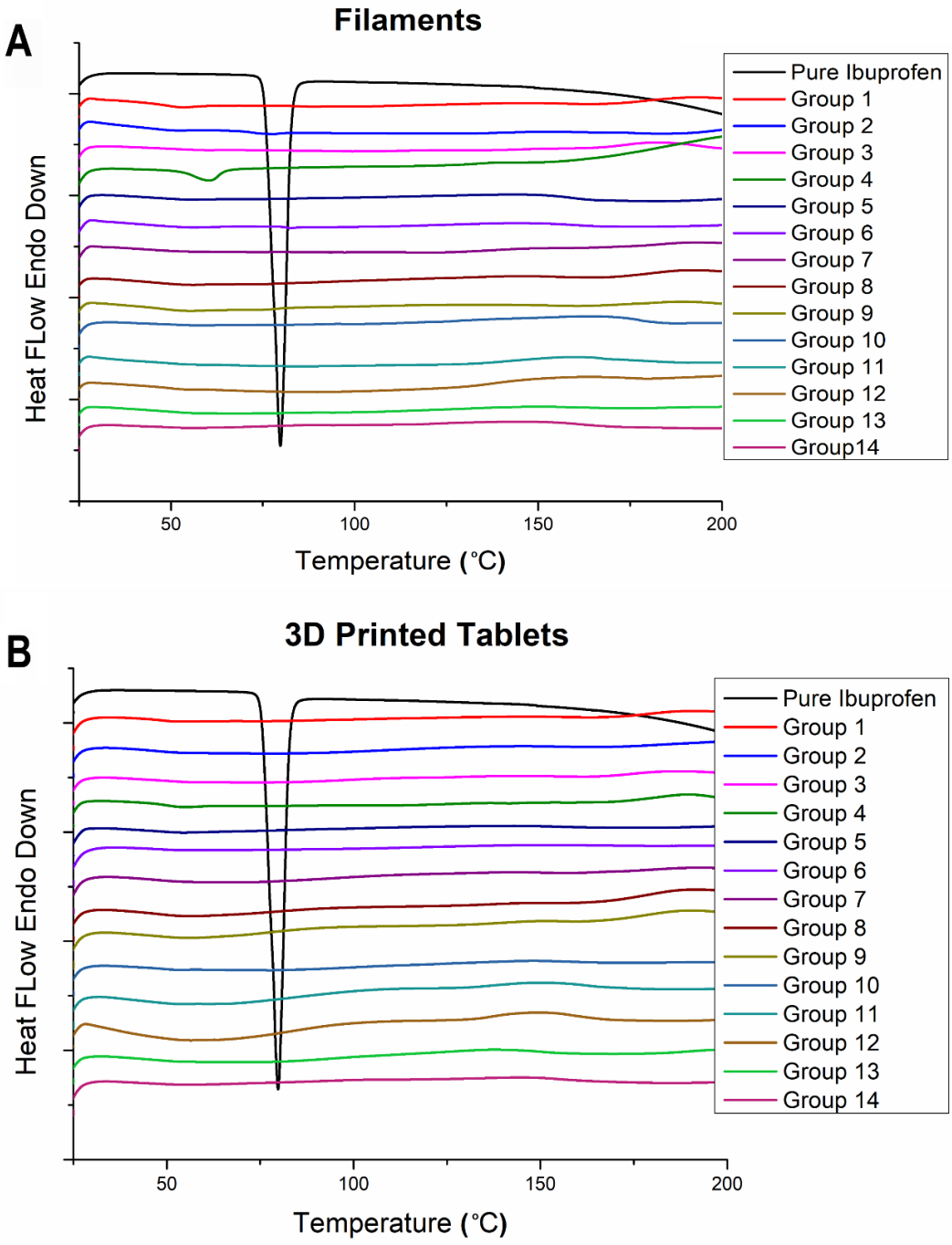

Figure 8.3. DSC thermograms of (A) hot melt extruded filaments and (B) 3D printed tablets of each group.

8.3.3 XRD Analysis

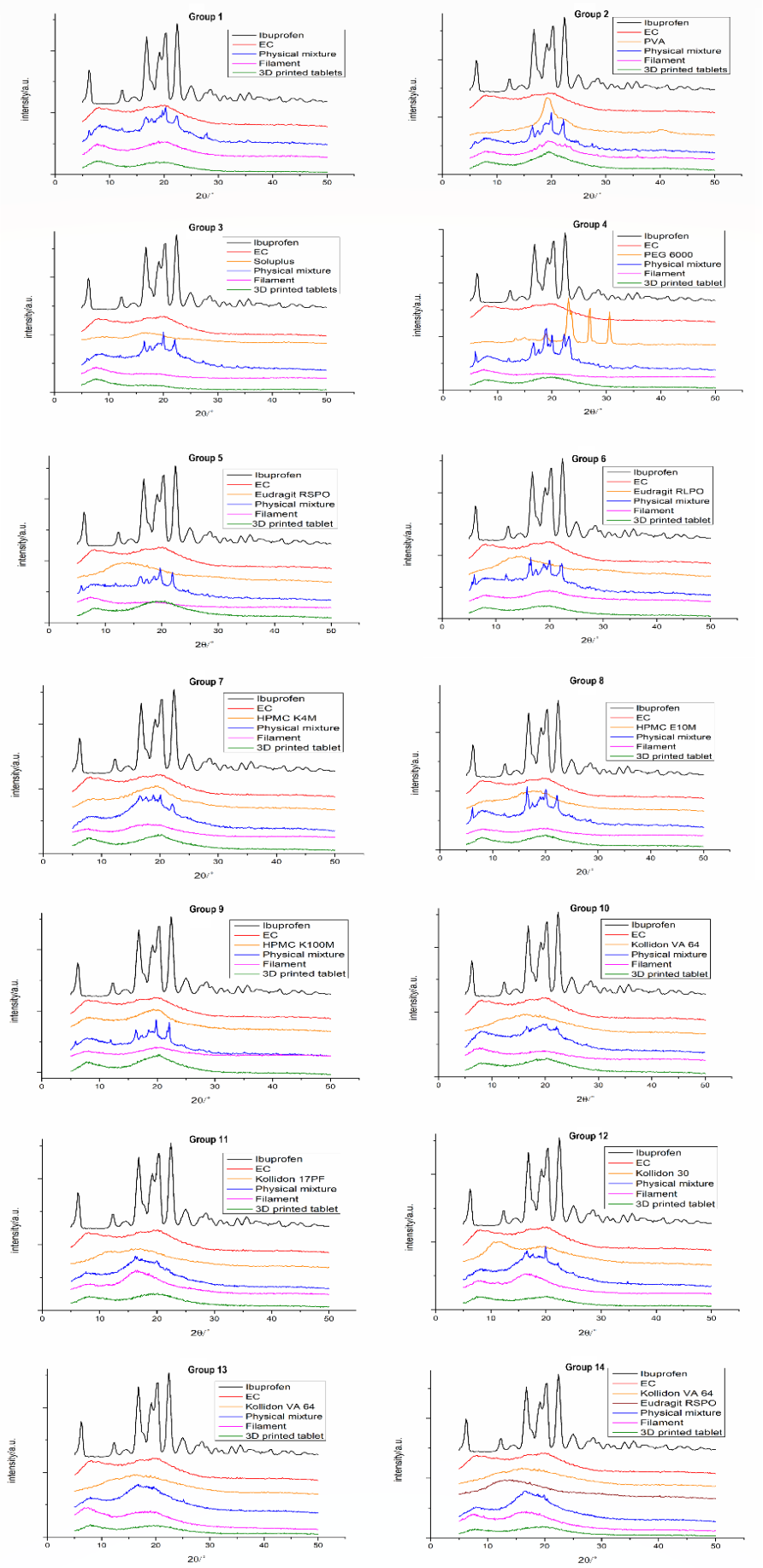
Group 1
Ibuprofen
EC
Physical mixture
Filament
3D printed tablets
Group 2
Ibuprofen
EC
PVA
Physical mixture
Filament
3D printed tablets
Group 3
Ibuprofen
EC
Soluplus
Physical mixture
Filament
3D printed tablets
Group 4
Ibuprofen
EC
PEG 6000
Physical mixture
Filament
3D printed tablet
Group 5
Ibuprofen
EC
Eudragit RSPO
Physical mixture
Filament
3D printed tablet
Group 6
Ibuprofen
EC
Eudragit RLPO
Physical mixture
Filament
3D printed tablet
Group 7
Ibuprofen
EC
HPMC K4M
Physical mixture
Filament
3D printed tablet
Group 8
Ibuprofen
EC
HPMC E10M
Physical mixture
Filament
3D printed tablet
Group 9
Ibuprofen
EC
HPMC K100M
Physical mixture
Filament
3D printed tablet
Group 10
Ibuprofen
EC
Kollidon VA 64
Physical mixture
Filament
3D printed tablet
Group 11
Ibuprofen
EC
Kollidon 17PF
Physical mixture
Filament
3D printed tablet
Group 12
Ibuprofen
EC
Kollidon 30
Physical mixture
Filament
3D printed tablet
Group 13
Ibuprofen
EC
Kollidon VA 64
Physical mixture
Filament
3D printed tablet
Group 14
Ibuprofen
EC
Kollidon VA 64
Eudragit RSPO
Physical mixture
Filament
3D printed tablet
intensity/a.u.
2θ/°

Figure 8.4. Comparison of XRD diffractograms of each group.

No characteristic peaks for IBP were detected in the diffractograms for the extruded filaments and 3D printed tablets (Figure 8.4), confirming the absence of crystalline IBP in the extruded filaments and 3D printed tablets with the 20 w/w% drug load. It suggests that HME and 3DP processes had a significant effect on the crystallinity of the API. The XRD diffractograms of drug-loaded hot melt extruded filaments and 3D printed tablets from all groups only reflect the EC characteristic peaks. Multiple high-intensity peaks of IBP were not seen in the XRD patterns of filaments or 3D printed tablets, mainly because of the formation of the IBP solid dispersion in the filaments or 3D printed tables which overshadowed its crystalline nature.[249]

8.3.4 TGA

The TGA results of 3D printed tablets in all groups are shown in Figure 8.5. The initial weight loss below 100°C was attributed to the evaporation of absorbed moisture.[281] Most of these tablets exhibited rapid weight loss above 200°C due to the chemical degradation that produced volatiles. The obvious weight loss from 200°C is probably due to the onset of thermal degradation for all these tablets.

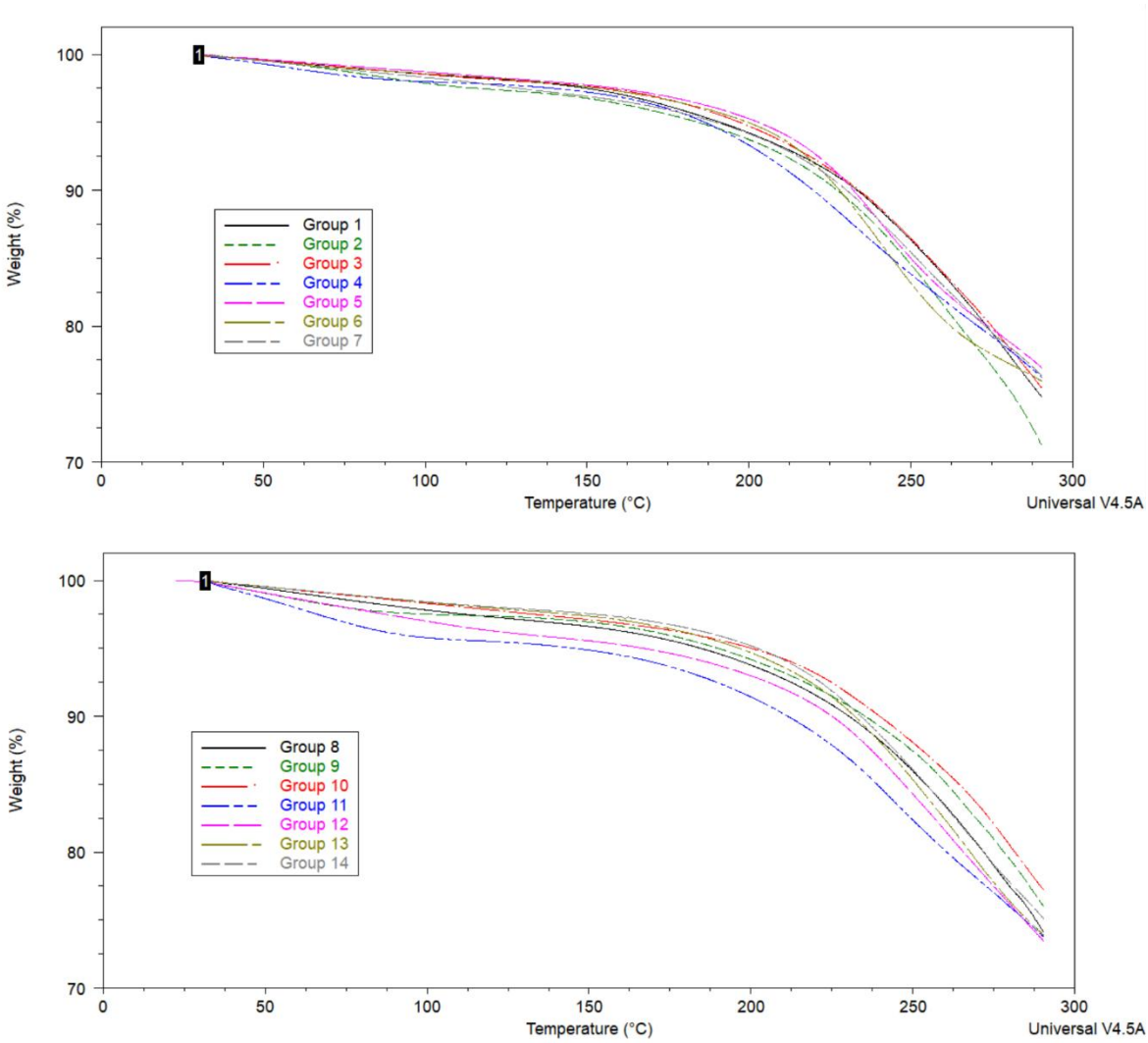

Figure 8.5. Thermal degradation profiles of 3D printed tablets in all groups.

8.3.5 Drug Content Determination

The percentage of IBP in 3D printed tablets was shown in Table 8.2. This indicates that there is no major loss or degradation of IBP during the printing processes. When the printing temperature is set below the degradation temperature of filaments according to the TGA results, degradation of ibuprofen is presumed to be negligible due to the limited retention time of filaments within the heated nozzle of the printer with a high printing speed.[148] The good drug content uniformity in IBP containing filaments (Table 7.4) and 3D printed tablets illustrated that the HME process can provide an effective method for loading IBP into EC polymer matrix homogeneously and minimizing the drug content

differences among the 3D printed tablets.[174] Consequently, the drug loading in the filaments or 3D printed tablets was 20 w/w%, which allowed for adjusting the amount of IBP by controlling the total weight of the final products.

Table 8.2. Drug loading and dose accuracy (mean ± standard deviation) of 3D printed tablets in each group

Group	Theoretical drug loading (%)	3D Printed Tablets	
		Drug Loading (%)	Dose Accuracy (%)
G1	20	19.94±0.05	99.70±0.24
G2	20	19.98±0.20	99.88±1.00
G3	20	20.06±0.14	100.32±0.71
G4	20	20.07±0.06	100.37±0.29
G5	20	20.28±0.10	101.39±0.50
G6	20	20.03±0.99	100.14±4.94
G7	20	20.00±0.40	99.98±1.99
G8	20	19.96±0.17	99.79±0.87
G9	20	20.05±0.11	100.25±0.57
G10	20	19.96±0.27	99.78±1.35
G11	20	19.93±0.61	99.67±3.07
G12	20	19.97±0.42	99.86±2.12
G13	20	20.01±0.61	100.05±3.06
G14	20	20.16±0.19	100.82±0.94

8.3.6 *In Vitro* Dissolution Studies

The dissolution efficiency, the area under the dissolution curve, was calculated to analyze whether the behavior of the release modifier added to the formulation is the same trend when it is subjected to HME or 3DP process.[282] The results were shown in Figure 8.6. The figure showed that the data were scattered everywhere, and no pattern and correlation can be deduced from the figures. This indicates that the behavior of polymers (release modifiers) can be changed via the HME or FDM 3DP process.

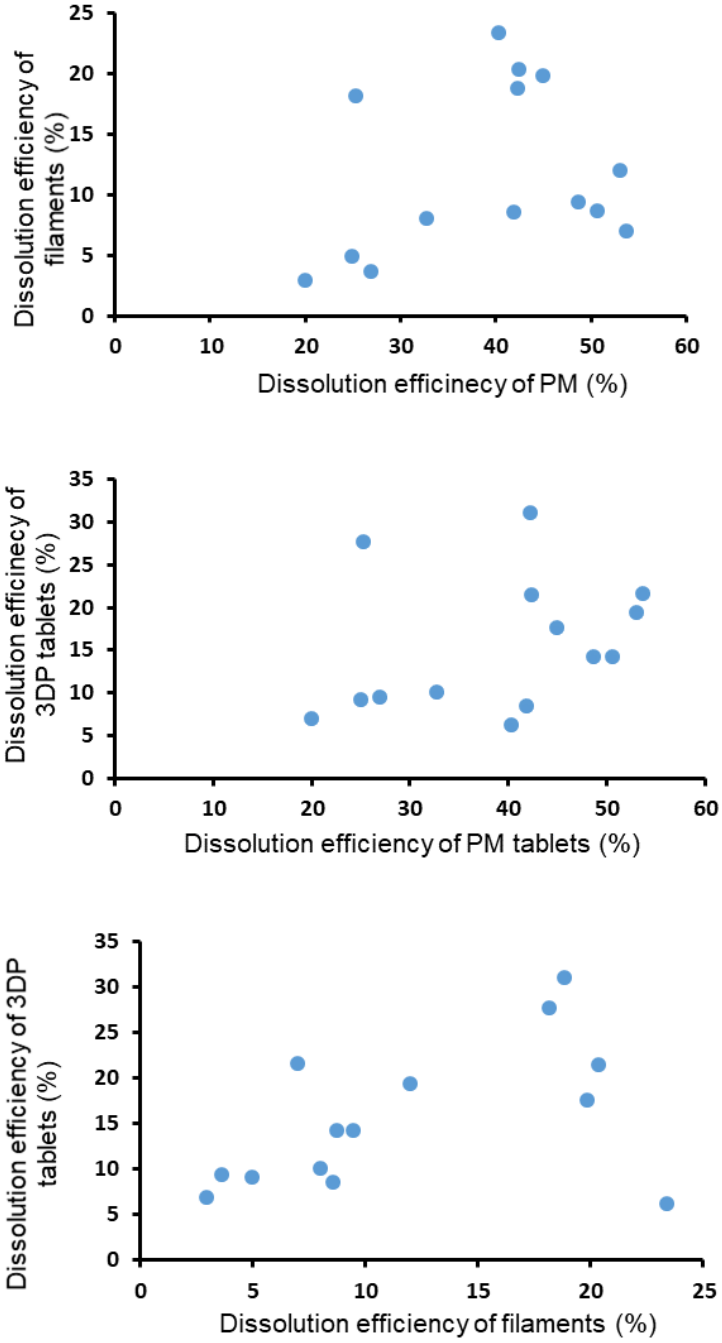

Figure 8.6. Correlating dissolution efficiency of physical mixture tablets, filaments and 3DP tablets.

Generally, the dissolution profiles of 3D printed tablets (Figure 8.7) showed a slightly faster release than filaments (Figure 7.15B) because of the denser structure of filaments generated via thermal treatment during the HME process.[154] 3D printed tablets of Group 1 released only 16% of IBP within 24 h.

The incorporation of Soluplus (Group 3), PEG (Group 4) and Eudragit (Groups 5 & 6) decreased the drug release rate. However, other release modifiers can enhance the drug release rate. When Kollidon 30 was applied as the release modifier (Group 12), 3D printed tablets had the highest release rate with more than 47% drug content released after 24 h, which is two times higher than in Group 1.

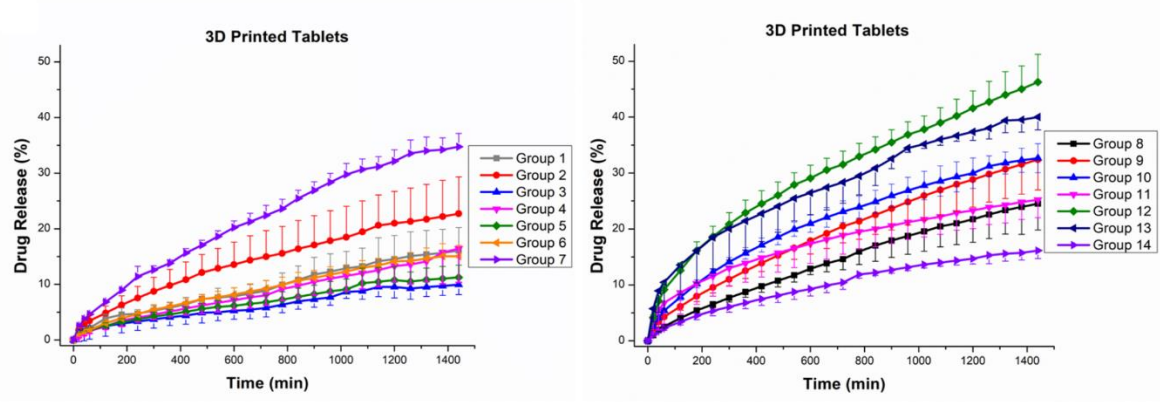

Figure 8.7. *In vitro* drug release study of 3D printed tablets (n = 3).

Consequently, these fabricated IBP-EC 3D printed tablets showed various dissolution profiles with the polymer blending method. By changing the type and concentration of release modifiers, the drug release rate from 3D printed tablets could be modulated. If the drug release rate from these 3D printed tablets is required to be further enhanced, lower fill density could be applied because an increase in the surface area/mass ratio of tablets can lead to the improvement in water permeation and drug diffusion.[154]

8.3.7 Determination of Drug Release Kinetics

The dissolution data of 3D printed tablets were plotted based on the zero-order, first-order, Higuchi and Korsmeyer-Peppas equations and calculated kinetic parameters with fitting results are summarized in Table 8.3. The best fit for the kinetics of almost all tablets was obtained with the Korsmeyer-Peppas model. In each group, 3D printed tablets showed significantly higher n values than

physical mixture tablets (Table 7.5) except Groups 7-9 (with the addition of HPMC). The possible reason is the high swelling capacity of HPMC makes HPMC swell and form a viscous layer, the diffusion and swelling rates are comparable in physical mixture tablets.[158] Hence, the release of IBP from IBP loaded 3D printed tablets of all groups could occur by diffusion of water through EC and release modifiers matrix and swelling/relaxation of chains between EC and release modifiers.[174] Among them, the 3D printed tablets from Group 4 showed the highest n value (0.817) indicates that the IBP release of these tablets almost followed zero-order kinetics, and this is consistent with the parameters in the zero-order model because of its highest R^2_{adj} (0.9876) and lowest AIC (53.15) values. It is necessary to mention that 3D printed tablets from all groups (except Group 10-13) presented a near-zero-order release with $R^2_{adj} > 0.9$.

Table 8.3. Drug release kinetics parameters of 3D printed tablets for various drug release models

Group	Parameter	3D printed tablets			
		Zero-order	First-order	Higuchi	Korsmeyer-Peppas
1	R^2_{adj}	0.961	0.970	0.973	0.992
	AIC	101	93	57	48
	n	----	----	----	0.696
2	R^2_{adj}	0.921	0.944	0.995	0.999
	AIC	122	113	36	-13
	n	----	----	----	0.610
3	R^2_{adj}	0.966	0.971	0.914	0.983
	AIC	51	47	99	33
	n	----	----	----	0.672
4	R^2_{adj}	0.988	0.991	0.967	0.9974
	AIC	53	45	67	-1
	n	----	----	----	0.817
5	R^2_{adj}	0.916	0.930	0.973	0.996
	AIC	79	76	45	6
	n	----	----	----	0.648
6	R^2_{adj}	0.942	0.958	0.966	0.999
	AIC	97	92	82	15
	n	----	----	----	0.685

7	R^2_{adj}	0.937	0.973	0.985	0.999
	AIC	147	125	102	47
	n	----	----	----	0.660
8	R^2_{adj}	0.984	0.994	0.973	0.999
	AIC	99	74	91	1
	n	----	----	----	0.737
9	R^2_{adj}	0.953	0.984	0.979	1.000
	AIC	138	113	102	1
	n	----	----	----	0.674
10	R^2_{adj}	0.834	0.929	0.998	0.998
	AIC	161	148	51	46
	n	----	----	----	0.553
11	R^2_{adj}	0.782	0.842	0.999	0.999
	AIC	152	145	15	4
	n	----	----	----	0.445
12	R^2_{adj}	0.894	0.953	0.999	0.999
	AIC	172	150	47	49
	n	----	----	----	0.518
13	R^2_{adj}	0.871	0.931	0.996	0.998
	AIC	168	151	77	58
	n	----	----	----	0.474
14	R^2_{adj}	0.914	0.932	0.987	0.999
	AIC	110	104	61	-23
	n	----	----	----	0.631

IBP loaded 3D printed tablets showed a significantly lower release rate of IBP compared to directly compressed physical mixture tablets (Figure 8.8). Therefore, the HME and FDM printing processes not only decreased the IBP release rate from 3D printed tablets but also changed the drug release mechanism from the diffusion of directly compressed tablets to the diffusion and erosion of 3D printed tablets. Furthermore, these IBP loaded 3D printed tablets show great potential in releasing IBP in a zero-order reaction.

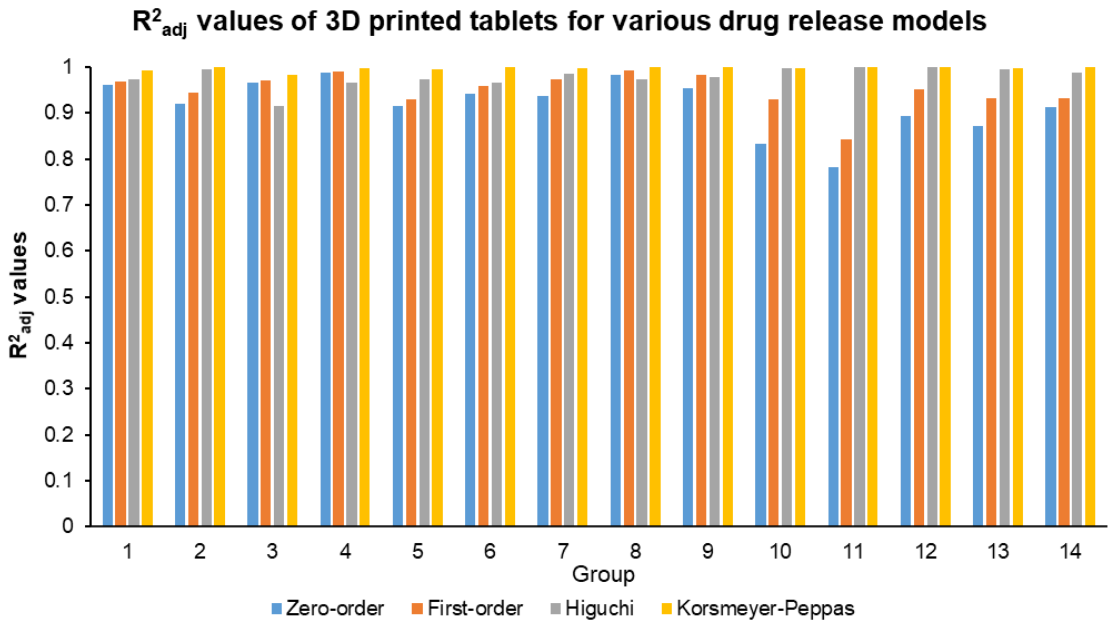

Figure 8.8. The adjusted coefficient of determination (R^2_{adj}) values of 3D printed tablets for various drug release models

The drug release mechanism was further verified by SEM. The cross-sections of 3D printed tablets in Group 9 before and after dissolution are shown in Figure 8.9. A large number of pores and cracks could be observed in Figure 8.9B. This indicates that ibuprofen gradually released and the EC-release modifier matrix slowly eroded during the 24 hours.[154] The observation was consistent with the drug release mechanism of diffusion and erosion.

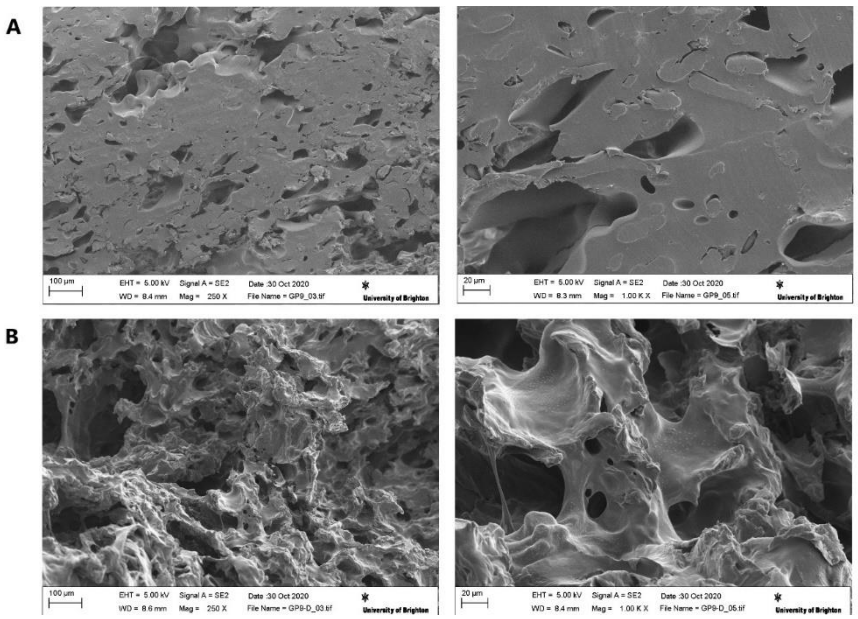

Figure 8.9. Cross-section of 3D printed tablets in Group 9 at (A) 0 h and (B) 24 h during dissolution, observed by SEM.

8.3.8 3D Printed Reservoirs Using Various Filaments

According to the drug release kinetics parameters of all 3D printed tablets, filaments from Group 4 of 20% IBP, 60% EC and 20% PEG 6000 (w/w) were selected to fabricate the reservoir due to its potential to release IBP in the zero-order model. The photograph of the reservoir printed using a MakerBot Replicator 2X 3D Printer according to the CAD model (Figure 2.2) is shown in Figure 8.10. The morphology and mechanical properties of the reservoir printed using F4 are similar to the PLA reservoir printed using a Robo R2 3D printer. Furthermore, different reservoirs could be printed using filaments from other groups for achieving slower or higher drug release requirements.

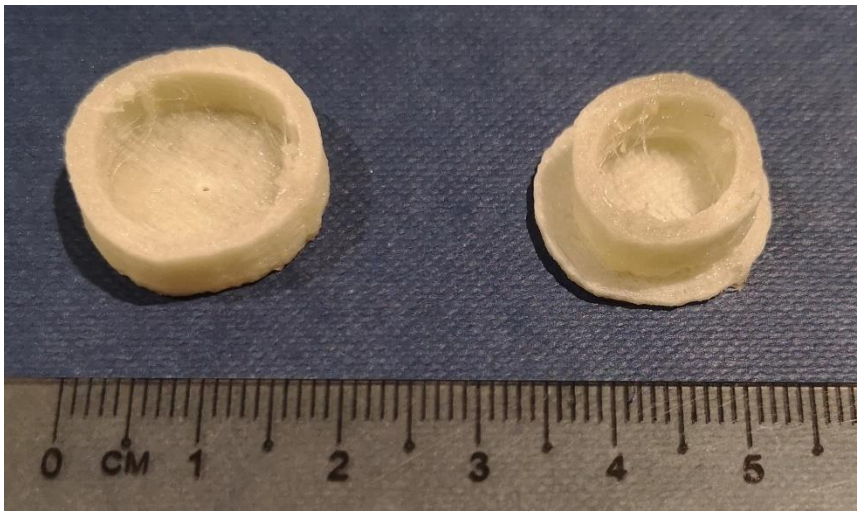

Figure 8.10. Images of FDM 3D printed reservoir using hot melt extruded filaments from Group 4

8.4 Conclusion

All these 3D printed tablets possess elegant appearance, suitable mechanical properties, and good constancy in both physical parameters and drug content. It has been proved that by only changing the release-modifying agents, a tunable release profile of the model drug from various 3D printed tablets can be achieved.

Hot melt extruded filaments prepared with a proportion of 20% IBP, 60% EC and 20% release modifiers (w/w) exhibited high processability for the preparation of tablets using FDM 3DP technique. The solid-state analysis of 3D printed tablets exhibited the amorphous nature of the drug dispersed in the polymer matrices. Moreover, *in vitro* drug release studies revealed that the drug release could simply be controlled over 24 h by only changing the type of release modifiers. All IBP loaded 3D printed tablets with EC matrix, especially with PEG as the release modifier, showed great potential in releasing IBP in a zero-order reaction. In conclusion, all results illustrated that the HME-FDM approach and optimized formulation compositions can be an attractive option for the development of pharmaceutical tablets and implants where adjustable drug release patterns are necessary.

In order to inhibit the inflammatory response caused by the DDS, ibuprofen was utilized in fabricating the reservoir with site-specific and controlled release. This chapter proved the suitability of preparing several modified dosage forms of IBP and EC using FDM 3DP technology with various pharmaceutical-grade polymers. All these results illustrated that these dosage forms developed in this study are promising candidates for sustained release devices and implants development.

9. Chapter 9: General Discussions and Future Work

9.1 General Discussions

Various medical treatments of gastrointestinal diseases have been studied, including oral drug delivery, microrobots, traditional endoscopes and capsule endoscopes.[115] As a major health burden worldwide, cancer is a sophisticated and multifactorial disease which has been well known for high mortality and recurrence rates.[105,135,283] There are various therapeutic approaches for the treatment of different kinds of cancers, including chemotherapy, targeted therapy, surgical resections, and radiation.[283] Among them, chemotherapy is the most common therapy method.[283] Due to the low therapeutic efficacy of chemotherapy and poor targeting ability of chemotherapeutic drugs, serious side effects on healthy rapid proliferating cells have caught much attention.[40] A high dose of chemotherapeutic drugs was required due to the low therapeutic indices, this will lead to multi-drug resistant cancers.[135] Therefore, it is a biologically demanding and technically challenging task to improve the efficacy of chemotherapeutic drugs in cancer.[26] The development of DDSs is an efficient method for enhancing the efficiency and safety of chemotherapeutic agents.

This project provides some insights for the future development of magnetic field triggerable DDSs using 3D printing technologies. From the DDS which composed of an anticancer drug, 5-fluorouracil (FLU) solution loaded magnetic PDMS sponge cylinder and a 3D printed NSAID (IBP) loaded reservoir, the FLU release can realize a switch between the “on” and “off” state easily through the application of different magnetic fields and from different directions. Owing to the satisfactory results of *in vitro* dissolution test, filaments composed of 20% IBP, 60% EC and 20% PEG 6000 (w/w) were applied to print the reservoir for achieving the release of IBP in a zero-order reaction. Consequently, the 3D printed reservoir has great

potential in delivering anti-inflammatory drugs to the implant site.

In Chapter 3, different concentrations of CI and Fe_3O_4 particles were embedded as magneto-sensitive materials in PDMS resins for the fabrication of macroporous sponges via a sugar-templated process. According to the evaluation for their morphology, the particle size of magnetic particles, solid-state, porosity, elastic modulus, deformation under a magnetic field and dielectric constant, the 100 w/w% CI/PDMS sponge has been proved to be a promising candidate as scaffolds for delivering drug solutions in the local treatment of diseases and further applications in innovative medical devices. However, the deformation of these sponge cylinders under the magnetic field of 355 mT is not higher than 10%.

In Chapter 4, the macroporous PDMS sponges were optimized by controlling the fabrication process for increasing the porosity and magnetic field sensitivity. The 100 w/w% CI/PDMS sponge cylinder prepared with demerara sugar and PDMS prepolymer/curing agents = 25:1 w/w showed the maximum compression (35%) under the magnetic field of 355 mT. Besides, the study showed that these magnetic sponges can be reused as the water absorption capacity of the prepared CI-loaded PDMS sponge did not change after 10 absorbing/desorbing cycles. All these promising features and simple fabrication make the CI-loaded PDMS sponge a superior scaffold for delivering drug solutions in the local treatment of diseases and further applications in innovative medical devices.

In Chapter 5, an optimized PB 3D printing process is applied for the fabrication of oral dosage forms, such as tablets with varying shapes and morphologies. A detailed investigation of the powder compositions revealed that particle size, flow, and morphology play pivotal roles in the printing process. The produced tablets were then coated with various anticancer drug solutions, where drug particles were observed homogenously dispersed throughout the surface of the printed

tablets. Furthermore, the PB 3D printing process demonstrated in this research was able to adjust the dose, release rate, and drug loading by changing the formulation composition and the processing parameters. According to the *in vitro* dissolution test, the 5-fluorouracil solution of 2.5% (w/v) concentration will be further applied in the development of the novel magnetic field triggerable DDS.

Chapter 6 illustrated the design and development of a novel implantable drug delivery device assembled from a magnetic PDMS sponge cylinder and a 3D printed PLA reservoir to provide a triggerable and remotely controllable system for on-demand drug delivery in localized disease treatment. In addition, the drug-releasing dose and timing can be reliably and flexibly controlled by different applications of the magnetic field to fit the prescribed needs. The switching “on” state of drug-releasing could be realized by the magnetic bar contacted with the side part of the device because the times at which 50%, 80% and 90% (w/w) of the drug were dissolved are observed to be 20, 55 and 140 min, respectively. In contrast, the switching “off” state of drug-releasing could be realized by the magnetic bar placed at the bottom of the device as only 10% (w/w) of the drug could be released within 12 h. Furthermore, this device has the potential to be optimized as a safe and long-term implant because of its large drug loading ability. It can be the key component of a multi-functional, implantable and smart drug delivery system for the controlled release of therapeutic substances to avoid frequent injections or various sophisticated dosing regimens.

In Chapter 7, EC polymers with various molecular weights (viscosity grades) were applied to fabricate IBP loaded filaments through HME. The obtained filaments were subjected to a comprehensive characterization and analysis in order to select the most suitable filament formulation for the FDM 3D printing process. Due to the excellent performance of the IBP-EC 10 filament, the Ethocel™ Standard 10 Premium was selected as the main polymer matrix. To modulate the FDM printability and release behavior of the IBP loaded filaments, various release

modifying materials, namely, PVA, Soluplus, PEG 6000, Eudragit® RL PO/RS PO, HPMC K4M/E10M/K100M, Kollidon® vinyl acetate 64 (VA 64)/17PF/30 were added into the formulation. Various solid dispersion filaments with ibuprofen in an EC and release modifier matrix were successfully fabricated through the HME process, which all showed good mechanical properties. Furthermore, *in vitro* drug release studies revealed that these release modifying materials can adjust the drug release rate from these filaments significantly. In comparison with directly compressed physical mixture tablets, slower drug release can be obtained from these hot melt extruded filaments.

In Chapter 8, all these prepared filaments could be successfully printed without failing during the FDM 3DP process. These 3D printed tablets possess an elegant appearance with suitable mechanical properties and good reliability in both physical parameters and drug content. It has been proved that by only changing the release-modifying agents, a tunable release profile of the model drug from various 3D printed tablets can be achieved. To our knowledge, this is the first research for adjusting the drug release behavior of IBP by adding various release modifiers to the EC matrix. Hot melt extruded filaments prepared with a proportion of 20% IBP, 60% EC and 20% release modifiers (w/w) exhibited high processability for the preparation of tablets using the FDM 3DP technique. Sustained-release tablets with different dissolution behaviors were fabricated by coupling HME and FDM 3DP processes. Consequently, the sustained release of IBP from these dosage forms showed significant potential in minimizing its plasma fluctuations and side effects, as well as enhancing its patient compliance. This study proved the suitability of preparing several modified dosage forms of IBP and EC using FDM technology with various pharmaceutical-grade polymers. All these results illustrated that these dosage forms developed in this study are promising candidates for sustained release devices (tablets) development.

9.2 Future Work

In this project, a novel magnetic field triggerable drug delivery system was designed, fabricated and characterized. This device can provide a simple method for localized gastrointestinal cancer therapy to minimize the side effects of chemotherapeutic drugs and improve patient compliance. Nevertheless, there is still room for improvement since clinical situations should be taken into account. With the development of personalized medicine and 3D printing technology, this novel drug delivery system could be optimized to achieve more precise results.

Firstly, efforts should be made to minimize the size of the device. In clinical practice, targeted therapy is required at various length scales to be used in different body regions, so implantable devices are expected to transport through small-diameter canals and endoluminal access points. Therefore, FDM 3D printing technology may be not competent to obtain microscale and high-resolution devices. In this case, stereolithography (SLA) 3D printing technology is superior to others due to its high accuracy and ability to achieve z-resolution (layer thickness) of < 10 μm when compared with 100 μm. An object could be produced by the consequent deposition of thin layers of a liquid resin when exposed to a scanning laser beam in accordance with a CAD file. With the development of microstereolithography which can achieve the resolution of 1 μm, the fabrication of devices with more precise and complex geometries becomes possible. Additionally, SLA showed advantages in spatial control and flexibility because of improved surface smoothness of printed objects, printing efficiency and bonding between layers.

Secondly, biodegradable materials should be explored for fabricating this device. Because most available implants are required to be removed from the body after the therapy has been performed, this operation is always related to toxicity-associated risks. Despite the numerous advantages of PDMS sponges, they also

have limitations in that silicon substrate is not biodegradable. Consequently, biodegradable materials could be analyzed to fabricate magnetic field sensitive sponges. For example, keratin structural protein which is a kind of biodegradable peptide-based biomaterials can be used to prepare macroporous sponges with various porosities using freeze-drying technology. Alginate, a naturally occurring polysaccharide, is another promising candidate in fabricating porous scaffolds because of its good biocompatibility and biodegradability. Additionally, other biodegradable polymers including poly-L-lactic acid (PLLA), PLGA and chitosan could be used to fabricate porous scaffolds through freeze-extraction and freeze-gelation methods.

Thirdly, further study should focus on improving the tumor-targeting efficiency through developing a DDS exhibiting a multi-targeting mechanism. As magnetic PDMS sponges have been proved to be conductive in this project, this device showed great potential to be developed into wireless flexible pressure sensors. Multi-stimuli-responsive releasing carriers could be prepared with various polymers, such as PNIPAM, β-CD and glycerol monooleate. With the manipulation of physical and chemical stimuli (e.g. pH, temperature, magnetic field, electric field, change in solvent composition and pressure), various types of stimulus-sensitive sponges could be fabricated to exhibit an obvious and reversible change in volume and shape for achieving pulsatile release and position control. Among these stimulus-sensitive sponges, pH and temperature stimulated hydrogels have been extensively studied for cancer therapy because of the relatively lower pH (around 5-6) and higher temperature (around 40-42℃) of cancerous cells. In the future, combining the device with a sensing system can also offer protection for biosensors because biofouling and exposure to the body may lead to the failure of biosensors *in vivo*.

Fourthly, *in vivo* animal studies should be carried out following animal welfare guidelines and approved by the local animal ethics committee. Despite *in vitro*

techniques for the early stage of drug assessment have made significant progress in recent years, they cannot replace *in vivo* evaluations due to the large blind areas in animal physiology. Prior to human tests in a clinical setting, animals studies play an important role in safety evaluation and minimizing toxicity of novel drug compounds, optimized formulation and specific targeting. Although cell studies and *in vitro* dissolution tests were conducted in this project, *in vivo* (drug absorption) performance needs to be further explored in the future. Moreover, many physiological parameters should be considered in the extrapolation from animal models to humans due to the differences in weight, blood volume, cardiac output, circulation time and tumor volume/location/blood flow. Additionally, the tumor and tissue receptors in animals and humans have a significant difference. Therefore, the analysis of hematocompatibility, biodegradation, immunogenicity, pharmacokinetics, toxicity in cellular and animal models should be performed before the clinical testing. Multiple animals instead of a single animal species in drug delivery modelling may be required to simulating various parameters accurately. The spatial geometry to which magnetic field generation systems may function with respect to the target location is the main difficulty in scaling up this technique from small animals (e.g. rabbits and rats) with near skin surface targets to large animals (e.g. pigs, monkeys) and humans. There have been some successful examples of magnetic targeting systems in larger animals and early clinical human trials, further work on solving this problem is continuing.

References

(1) Wilczewska, A. Z.; Niemirowicz, K.; Markiewicz, K. H.; Car, H. Nanoparticles as Drug Delivery Systems. *Pharmacol. reports* **2012**, *64*, 1020–1037.

(2) Kost, J.; Langer, R. Responsive Polymeric Delivery Systems. *Adv. Drug Deliv. Rev.* **2001**, *46*, 125–148. https://doi.org/10.1016/j.addr.2012.09.014.

(3) Lanier, O. L.; Monsalve, A. G.; Mcfetridge, P. S.; Dobson, J. Magnetically Triggered Release of Biologics. *Int. Mater. Rev.* **2019**, *64* (2), 63–90. https://doi.org/10.1080/09506608.2018.1446280.

(4) Hoare, T.; Santamaria, J.; Goya, G. F.; Irusta, S.; Lin, D.; Lau, S.; Padera, R.; Langer, R.; Kohane, D. S. A Magnetically Triggered Composite Membrane for On-Demand Drug Delivery. *Nano Lett.* **2009**, *9* (10), 3641–3657. https://doi.org/10.1021/nl9018935.

(5) Kim, H.; Seo, J. Fabrication of Magnetically Actuated Fluidic Drug Delivery Device Using Polyvinyl Chloride Adhesive Stencils. *micromachines* **2018**, *9*, 358. https://doi.org/10.3390/mi9070358.

(6) Sonawane, S. J.; Kalhapure, R. S.; Govender, T. Hydrazone Linkages in PH Responsive Drug Delivery Systems. *Eur. J. Pharm. Sci.* **2017**, *99*, 45–65. https://doi.org/10.1016/j.ejps.2016.12.011.

(7) Timko, B. P.; Dvir, T.; Kohane, D. S. Remotely Triggerable Drug Delivery Systems. *Adv. Mater.* **2010**, *22*, 4925–4943. https://doi.org/10.1002/adma.201002072.

(8) Wang, Y.; Li, B.; Zhang, L.; Song, H.; Zhang, L. Targeted Delivery System Based on Magnetic Mesoporous Silica Nanocomposites with Light-Controlled Release Character. *ACS Appl. Mater. Interfaces* **2013**, *5*, 11–15.

(9) Liao, J.; Huang, H. Review on Magnetic Natural Polymer Constructed Hydrogels as Vehicles for Drug Delivery. *Biomacromolecules* **2020**, *21*, 2574–2594. https://doi.org/10.1021/acs.biomac.0c00566.

(10) Ganguly, S.; Margel, S. Review : Remotely Controlled Magneto-Regulation

of Therapeutics from Magnetoelastic Gel Matrices. *Biotechnol. Adv.* **2020**, *44*, 107611. https://doi.org/10.1016/j.biotechadv.2020.107611.

(11) Brazel, C. S. Expert Review Magnetothermally-Responsive Nanomaterials : Combining Magnetic Nanostructures and Thermally-Sensitive Polymers for Triggered Drug Release. *Pharm. Res.* **2009**, *26* (3), 644–656. https://doi.org/10.1007/s11095-008-9773-2.

(12) Marín, T.; Montoya, P.; Arnache, O.; Pinal, R.; Calderón, J. Bioactive Films of Zein / Magnetite Magnetically Stimuli-Responsive for Controlled Drug Release. *J. Magn. Magn. Mater.* **2018**, *458*, 355–364. https://doi.org/10.1016/j.jmmm.2018.03.046.

(13) Nelson, B. J.; Kaliakatsos, I. K.; Abbott, J. J. Microrobots for Minimally Invasive Medicine. *Annu. Rev. Biomed. Eng.* **2010**, *12*, 55–85. https://doi.org/10.1146/annurev-bioeng-010510-103409.

(14) Brudno, Y.; Mooney, D. J. On-Demand Drug Delivery from Local Depots. *J. Control. Release* **2015**, *219*, 8–17. https://doi.org/10.1016/j.jconrel.2015.09.011.

(15) Luo, J. D.; Miller, C.; Jirjis, T.; Nasir, M.; Sharma, D. The Effect of Non-Steroidal Anti- Inflammatory Drugs on the Osteogenic Activity in Osseointegration : A Systematic Review. *Int. J. Implant Dent.* **2018**, *4*, 30.

(16) Jiang, S.; Hu, Y.; Wu, H.; Zhang, Y.; Zhang, Y.; Wang, Y.; Zhang, Y.; Zhu, W.; Li, J.; Wu, D.; et al. Multifunctional Janus Microplates Arrays Actuated by Magnetic Fields for Water/Light Switches and Bio-Inspired Assimilatory Coloration. *Adv. Mater.* **2019**, *31*, 1807507(1-8). https://doi.org/10.1002/adma.201807507.

(17) Kim, J. H.; Kang, S. M.; Lee, B. J.; Ko, H.; Bae, W. G.; Suh, K. Y.; Kwak, M. K.; Jeong, H. E. Remote Manipulation of Droplets on a Flexible Magnetically Responsive Film. *Sci. Rep.* **2015**, *5* (1), p.17843. https://doi.org/10.1038/srep17843.

(18) Pirmoradi, F. N.; Cheng, L.; Chiao, M. A Magnetic Poly (Dimethylesiloxane) Composite Membrane Incorporated with Uniformly Dispersed , Coated Iron

Oxide Nanoparticles. *J. Micromechanics Microengineering* **2010**, *20*, 015032. https://doi.org/10.1088/0960-1317/20/1/015032.

(19) Muzzalupo, R.; Tavano, L.; Rossi, C. O.; Picci, N.; Ranieri, G. A. Novel PH Sensitive Ferrogels as New Approach in Cancer Treatment : Effect of the Magnetic Field on Swelling and Drug Delivery. *Colloids Surfaces B Biointerfaces* **2015**, *134*, 273–278. https://doi.org/10.1016/j.colsurfb.2015.06.065.

(20) Willis, A. J.; Pernal, S. P.; Gaertner, Z. A.; Lakka, S. S.; Sabo, M. E.; Creighton, F. M.; Engelhard, H. H. Rotating Magnetic Nanoparticle Clusters as Microdevices for Drug Delivery. *Int. J. Nanomedicine* **2020**, *15*, 4105–4123.

(21) Munoz, F.; Alici, G.; Zhou, H.; Li, W.; Sitti, M. Analysis of Magnetic Interaction in Remotely Controlled Magnetic Devices and Its Application to a Capsule Robot for Drug Delivery. *IEEE/ASME Trans. Mechatronics* **2018**, *23* (1), 298–310. https://doi.org/10.1109/TMECH.2017.2764902.

(22) Barnsley, L. C.; Gray, M. D.; Beguin, E.; Carugo, D.; Stride, E. A Combined Magnetic-Acoustic Device for Simultaneous , Coaligned Application of Magnetic and Ultrasonic Fields. *Adv. Mater. Technol.* **2018**, *3* (7), 1800081. https://doi.org/10.1002/admt.201800081.

(23) Shi, W.; Huang, J.; Fang, R.; Liu, M. Imparting Functionality to the Hydrogel by Magnetic-Field-Induced Nano-Assembly and Macro-Response. *ACS Appl. Mater. Interfaces* **2020**, *12*, 5177–5194. https://doi.org/10.1021/acsami.9b16770.

(24) Liu, Y.; Chen, D.; Shang, P.; Yin, D.-C. A Review of Magnet Systems for Targeted Drug Delivery. *J. Control. Release* **2019**, *302*, 90–104. https://doi.org/10.1016/j.jconrel.2019.03.031.

(25) Mohseni, M.; Connell, J. J.; Payne, C.; Patrick, P. S.; Baker, R.; Yu, Y.; Siow, B.; Zaw-thin, M.; Kalber, T. L.; Pankhurst, Q. A.; et al. Scalable Magnet Geometries Enhance Tumour Targeting of Magnetic Nano-Carriers. *Mater. Des.* **2020**, *191*, 108610. https://doi.org/10.1016/j.matdes.2020.108610.

(26) Zhou, Z.; Shen, Z.; Chen, X. Tale of Two Magnets : An Advanced Magnetic Targeting System. *ACS Nano* **2020**, *14*, 7–11. https://doi.org/10.1021/acsnano.9b06842.

(27) Benhal, P.; Broda, A.; Najafali, D.; Malik, P.; Mohammed, A.; Ramaswamy, B.; Depireux, D. A.; Shimoji, M.; Shukoor, M.; Shapiro, B. On-Chip Testing of the Speed of Magnetic Nano- and Micro-Particles under a Calibrated Magnetic Gradient. *J. Magn. Magn. Mater.* **2019**, *474*, 187–198. https://doi.org/10.1016/j.jmmm.2018.10.148.

(28) Li, D.; Ren, Y. High-Gradient Magnetic Field for Magnetic Nanoparticles Drug Delivery System. *IEEE Trans. Appl. Supercond.* **2018**, *28* (6), 4402107.

(29) Gu, L.; Park, J.; Duong, K. H.; Ruoslahti, E.; Sailor, M. J. Magnetic Luminescent Porous Silicon Microparticles for Localized Delivery of Molecular Drug Payloads. *Small* **2010**, *6* (22), 2546–2552. https://doi.org/10.1002/smll.201000841.

(30) Zahn, D.; Klein, K.; Radon, P.; Berkov, D.; Erokhin, S.; Nagel, E.; Eichhorn, M.; Wiekhorst, F.; Dutz, S. Investigation of Magnetically Driven Passage of Magnetic Nanoparticles through Eye Tissues for Magnetic Drug Targeting. *Nanotechnology* **2020**, *31*, 495101.

(31) Marcus, M.; Smith, A.; Maswadeh, A.; Shemesh, Z.; Zak, I.; Motiei, M.; Schori, H.; Margel, S.; Sharoni, A.; Shefi, O. Magnetic Targeting of Growth Factors Using Iron Oxide Nanoparticles. *Nanomaterials* **2018**, *8*, 707. https://doi.org/10.3390/nano8090707.

(32) Mcbain, S. C.; Yiu, H. H.; Dobson, J. Magnetic Nanoparticles for Gene and Drug Delivery. *Int. J. Nanomedicine* **2008**, *3* (2), 169–180.

(33) Liu, J. F.; Lan, Z.; Ferrari, C.; Stein, J. M.; Higbee-dempsey, E.; Yan, L.; Amirshaghaghi, A.; Cheng, Z.; Issadore, D.; Tsourkas, A. Use of Oppositely Polarized External Magnets To Improve the Accumulation and Penetration of Magnetic Nanocarriers into Solid Tumors. *ACS Nano* **2020**, *14*, 142–152. https://doi.org/10.1021/acsnano.9b05660.

(34) Fu, Q.; Zhang, S.; Guo, S.; Guo, J. Performance Evaluation of Amagnetically Actuated Capsulemicrorobotic System Formedical Applications. *Micromachines* **2018**, *9*, 641. https://doi.org/10.3390/mi9120641.

(35) Xiong, F.; Huang, S.; Gu, N. Magnetic Nanoparticles : Recent Developments in Drug Delivery System. *Drug Dev. Ind. Pharm.* **2018**, *44* (5), 697–706. https://doi.org/10.1080/03639045.2017.1421961.

(36) Monnier, C. A.; Burnand, D.; Rothen-rutishauser, B.; Lattuada, M.; Petri-Fink, A. Magnetoliposomes : Opportunities and Challenges. *Eur. J. nanomedicine* **2014**, *6* (4), 201–215. https://doi.org/10.1515/ejnm-2014-0042.

(37) Arruebo, M.; Fernández-pacheco, R.; Ibarra, M. R.; Santamaría, J. Magnetic Nanoparticles for Drug Delivery. *nanotoday* **2007**, *2* (3), 22–32. https://doi.org/10.1016/S1748-0132(07)70084-1.

(38) Clares, B.; Biedma-ortiz, R. A.; Sáez-fernández, E.; Prados, J. C.; Melguizo, C.; Cabeza, L.; Ortiz, R.; Arias, J. L. Nano-Engineering of 5-Fluorouracil-Loaded Magnetoliposomes for Combined Hyperthermia and Chemotherapy against Colon Cancer. *Eur. J. Pharm. Biopharm.* **2013**, *85*, 329–338. https://doi.org/10.1016/j.ejpb.2013.01.028.

(39) Lee, J.; Chen, K.; Noh, S.; Garcia, M. A.; Wang, H.; Lin, W.; Jeong, H.; Kong, B. J.; Stout, D. B.; Cheon, J.; et al. On-Demand Drug Release System for In Vivo Cancer Treatment through Self-Assembled Magnetic Nanoparticles. *Angew. Chemie* **2013**, *52* (16), 4384–4388. https://doi.org/10.1002/anie.201207721.

(40) Zhao, C.; Feng, H.; Zhang, L.; Li, Z.; Zou, Y.; Tan, P.; Ouyang, H.; Jiang, D.; Yu, M.; Wang, C.; et al. Highly Efficient In Vivo Cancer Therapy by an Implantable Magnet Triboelectric Nanogenerator. *Adv. Funct. Mater.* **2019**, *29*, 1808640. https://doi.org/10.1002/adfm.201808640.

(41) Luo, Z.; Cai, K.; Hu, Y.; Li, J.; Ding, X.; Zhang, B.; Xu, D.; Yang, W.; Liu, P. Redox-Responsive Molecular Nanoreservoirs for Controlled Intracellular

Anticancer Drug Delivery Based on Magnetic Nanoparticles. *Adv. Mater.* **2012**, *24*, 431–435. https://doi.org/10.1002/adma.201103458.

(42) Ali, A.; Zafar, H.; Zia, M.; Ul Haq, I.; Phull, A. R.; Ali, J. S.; Hussain, A. Synthesis, Characterization, Applications, and Challenges of Iron Oxide Nanoparticles. *Nanotechnol. Sci. Appl.* **2016**, *9*, 49–67. https://doi.org/10.2147/NSA.S99986.

(43) Municoy, S.; Á, I.; Antezana, P. E.; Galdop, J. M.; Olivetti, C.; Mebert, A. M.; Foglia, L.; Tuttolomondo, V.; Alvarez, G. S.; Hardy, J. G.; et al. Stimuli-Responsive Materials for Tissue Engineering and Drug Delivery. *Int. J. Mol. Sci.* **2020**, *21* (13), 4724.

(44) Dobson, J. Magnetic Nanoparticles for Drug Delivery. *DRUG Dev. Res.* **2006**, *67*, 55–60. https://doi.org/10.1002/ddr.20067.

(45) Mody, V. V; Cox, A.; Shah, S.; Singh, A.; Bevins, W.; Parihar, H. Magnetic Nanoparticle Drug Delivery Systems for Targeting Tumor. *Appl. Nanosci.* **2014**, *4*, 385–392. https://doi.org/10.1007/s13204-013-0216-y.

(46) Jafari, S.; Soleimani, M.; Salehi, R. Nanotechnology-Based Combinational Drug Delivery Systems for Breast Cancer Treatment. *Int. J. Polym. Mater. Polym. Biomater.* **2019**, *68* (14), 859–869. https://doi.org/10.1080/00914037.2018.1517348.

(47) Jeong, J.; Jang, D.; Kim, D.; Lee, D.; Chung, S. K. Acoustic Bubble-Based Drug Manipulation : Carrying , Releasing and Penetrating for Targeted Drug Delivery Using an Electromagnetically Actuated Microrobot. *Sensors Actuators A Phys.* **2020**, *306*, 111973. https://doi.org/10.1016/j.sna.2020.111973.

(48) Liu, Q.; Li, H.; Lam, K. Y. Optimization of Deformable Magnetic-Sensitive Hydrogel-Based Targeting System in Suspension Fluid for Site-Specific Drug Delivery. *Mol. Pharm.* **2018**, *15*, 4632–4642. https://doi.org/10.1021/acs.molpharmaceut.8b00626.

(49) Denyer, S.; Bhimani, A. D.; Papastefan, S.; Kheirkhah, P.; Aguilar, T.; Zakrzewski, J.; Rosinski, C. L.; Patel, A. S.; Patel, S.; Zakrzewski, V.; et al.

Magnetic Kyphoplasty : A Novel Drug Delivery System for the Spinal Column. *PLoS One* **2018**, *13* (7), e0201402.

(50) Amini-fazl, M. S.; Mohammadi, R.; Kheiri, K. 5 - Fluorouracil Loaded Chitosan / Polyacrylic Acid / Fe 3 O 4 Magnetic Nanocomposite Hydrogel as a Potential Anticancer Drug Delivery System. *Int. J. Biol. Macromol.* **2019**, *132*, 506–513. https://doi.org/10.1016/j.ijbiomac.2019.04.005.

(51) Nguyen, D. H.; Lee, J. S.; Choi, J. H.; Park, K. M.; Lee, Y.; Park, K. D. Hierarchical Self-Assembly of Magnetic Nanoclusters for Theranostics: Tunable Size, Enhanced Magnetic Resonance Imagability, and Controlled and Targeted Drug Delivery. *Acta Biomater.* **2016**, *35*, 109–117. https://doi.org/10.1016/j.actbio.2016.02.020.

(52) Sangregorio, C.; Wiemann, J. K.; Connor, C. J. O.; Rosenzweig, Z. A New Method for the Synthesis of Magnetoliposomes. *J. Appl. Phys.* **1999**, *85* (8), 5699.

(53) Chiu, C.; Chung, T.; Chen, S.; Ma, Y. Effects of PEGylation on Capture of Dextran-Coated Magnetic Nanoparticles in Microcirculation. *Int. J. Nanomedicine* **2019**, *14*, 4767–4780.

(54) Namdari, M.; Cheraghi, M.; Negahdari, B.; Eatemadi, A.; Daraee, H. Recent Advances in Magnetoliposome for Heart Drug Delivery. *Artif. Cells, Nanomedicine, Biotechnol.* **2017**, *45* (6), 1051–1057. https://doi.org/10.1080/21691401.2017.1299159.

(55) Dobson, J. Magnetic Micro- and Nano-Particle-Based Targeting for Drug and Gene Delivery. *Nanomedicine* **2006**, *1* (1), 31–37. https://doi.org/10.2217/17435889.1.1.31.

(56) Cezar, C. A.; Kennedy, S. M.; Therapies, R.; Weaver, J. C.; Mooney, D. J. Biphasic Ferrogels for Triggered Drug and Cell Delivery. *Adv. Healthc. Mater.* **2014**, *3* (11), 1869–1876. https://doi.org/10.1002/adhm.201400095.Biphasic.

(57) Kiaie, N.; Emami, S. H.; Rabbani, S.; Aghdam, R. M.; Tafti, H. A. Targeted and Controlled Drug Delivery to a Rat Model of Heart Failure Through a

Magnetic Nanocomposite. *Ann. Biomed. Eng.* **2020**, *48* (2), 709–721. https://doi.org/10.1007/s10439-019-02394-y.

(58) Qiu, D.; An, X. Controllable Release from Magnetoliposomes by Magnetic Stimulation and Thermal Stimulation. *Colloids Surfaces B Biointerfaces* **2013**, *104*, 326–329. https://doi.org/10.1016/j.colsurfb.2012.11.033.

(59) Tian, B.; Liu, Y.; Liu, J. Smart Stimuli-Responsive Drug Delivery Systems Based on Cyclodextrin : A Review. *Carbohydr. Polym.* **2021**, *251*, 116871. https://doi.org/10.1016/j.carbpol.2020.116871.

(60) Ziarani, G. M.; Malmir, M.; Lashgari, N.; Badiei, A. The Role of Hollow Magnetic Nanoparticles in Drug Delivery. *RSC Adv.* **2019**, *9*, 25094–25106. https://doi.org/10.1039/c9ra01589b.

(61) Kaniukov, E.; Shumskaya, A.; Yakimchuk, D.; Kozlovskiy, A.; Korolkov, I.; Ibragimova, M.; Zdorovets, M.; Kadyrzhanov, K.; Rusakov, V.; Fadeev, M.; et al. FeNi Nanotubes : Perspective Tool for Targeted Delivery. *Appl. Nanosci.* **2019**, *9*, 835–844. https://doi.org/10.1007/s13204-018-0762-4.

(62) Ansari, L.; Jaafari, M. R.; Bastami, T. R.; Malaekeh-Nikouei, B. Improved Anticancer Efficacy of Epirubicin by Magnetic Mesoporous Silica Nanoparticles : In Vitro and in Vivo Studies. *Artif. Cells, Nanomedicine, Biotechnol.* **2018**, *46* (S2), S594–S606. https://doi.org/10.1080/21691401.2018.1464461.

(63) Ulbrich, K.; Holá, K.; Šubr, V.; Bakandritsos, A.; Tuček, J.; Zbořil, R. Targeted Drug Delivery with Polymers and Magnetic Nanoparticles : Covalent and Noncovalent Approaches , Release Control , and Clinical Studies. *Chem. Rev.* **2016**, *116* (9), p.5338-5431. https://doi.org/10.1021/acs.chemrev.5b00589.

(64) Suo, N.; Wang, M.; Jin, Y.; Ding, J.; Gao, X.; Sun, X.; Zhang, H.; Cui, M.; Zheng, J.; Li, N.; et al. Magnetic Multiwalled Carbon Nanotubes with Controlled Release of Epirubicin : An Intravesical Instillation System for Bladder Cancer. *Int. J. Nanomedicine* **2019**, *14*, 1241–1254.

(65) Frey, N. A.; Peng, S.; Cheng, K.; Sun, S. Magnetic Nanoparticles :

Synthesis , Functionalization , and Applications in Bioimaging and Magnetic Energy Storage. *Chem. Soc. Rev.* **2009**, *38*, 2532–2542. https://doi.org/10.1039/b815548h.

(66) Price, P. M.; Mahmoud, W. E.; Al-ghamdi, A. A.; Bronstein, L. M. Magnetic Drug Delivery : Where the Field Is Going. *Front. Chem.* **2018**, *6*, 619. https://doi.org/10.3389/fchem.2018.00619.

(67) Sun, Z.; Yi, Z.; Zhang, H.; Ma, X.; Su, W.; Sun, X.; Li, X. Bio-Responsive Alginate-Keratin Composite Nanogels with Enhanced Drug Loading Efficiency for Cancer Therapy. *Carbohydr. Polym.* **2017**, *175*, 159–169. https://doi.org/10.1016/j.carbpol.2017.07.078.

(68) Liu, T.; Chan, T.; Wang, K.; Tsou, H. RSC Advances In Fl Uence of Magnetic Nanoparticle Arrangement in Ferrogels for Tunable Biomolecule Di Ff Usion. *RSC Adv.* **2015**, *5*, 90098–90102. https://doi.org/10.1039/c5ra17306j.

(69) Biswas, S.; Vaze, O. S.; Movassaghian, S.; Torchilin, V. P. Polymeric Micelles for the Delivery of Poorly Soluble Drugs. In *Drug Delivery Strategies for Poorly Water-Soluble Drugs*; Douroumis, D., Fahr, A., Eds.; John Wiley & Sons, Ltd., 2013; pp 411–476. https://doi.org/https://doi.org/10.1002/9781118444726.ch14.

(70) Ai, B. H.; Flask, C.; Weinberg, B.; Shuai, X.; Pagel, M. D.; Farrell, D.; Duerk, J.; Gao, J. Magnetite-Loaded Polymeric Micelles as Ultrasensitive Magnetic-Resonance Probes **. *Adv. Mater.* **2005**, *17*, 1949–1952. https://doi.org/10.1002/adma.200401904.

(71) Chu, L.; Zhang, Y.; Feng, Z.; Yang, J.; Tian, Q.; Yao, X.; Zhao, X.; Tan, H.; Chen, Y. Synthesis and Application of a Series of Amphipathic Chitosan Derivatives and the Corresponding Magnetic Nanoparticle-Embedded Polymeric Micelles. *Carbohydr. Polym.* **2019**, *223*, 114966. https://doi.org/10.1016/j.carbpol.2019.06.005.

(72) Attwood, D. Disperse Systems. In *Aulton's pharmaceutics: the design and manufacture of medicines*; Aulton, M. E., Taylor, K. M. ., Eds.; Churchill

Livingstone, 2018; pp 60–92.

(73) Oerlemans, C.; Bult, W.; Bos, M.; Storm, G.; Nijsen, J. F. W.; Hennink, W. E. Polymeric Micelles in Anticancer Therapy: Targeting , Imaging and Triggered Release. *Pharm. Res.* **2010**, *27*, 2569–2589. https://doi.org/10.1007/s11095-010-0233-4.

(74) Li, X.; Li, H.; Yi, W.; Chen, J.; Liang, B. Acid-Triggered Core Cross-Linked Nanomicelles for Targeted Drug Delivery and Magnetic Resonance Imaging in Liver Cancer Cells. *Int. J. Nanomedicine* **2013**, *8*, 3019–3031.

(75) Zhang, X.; Guo, K.; Li, L.; Zhang, S.; Li, B. Multi-Stimuli-Responsive Magnetic Assemblies Astunable Releasing Carriers. *J. Mater. Chem. B* **2015**, *3*, 6026–6031. https://doi.org/10.1039/c5tb00845j.

(76) Pourjavadi, A.; Tehrani, Z. M. Poly (N-Isopropylacrylamide)-Coated β-Cyclodextrin-Capped Magnetic Mesoporous Silica Nanoparticles Exhibiting Thermal and PH Dual Response for Triggered Anticancer Drug Delivery. *Int. J. Polym. Mater. Polym. Biomater.* **2017**, *66* (7), 336–348. https://doi.org/10.1080/00914037.2016.1217531.

(77) Hegazy, M.; Zhou, P.; Rahoui, N.; Wu, G.; Taloub, N. A Facile Design of Smart Silica Nanocarriers via Surface-Initiated RAFT Polymerization as a Dual-Stimuli Drug Release Platform. *Colloids Surfaces A* **2019**, *581*, 123797. https://doi.org/10.1016/j.colsurfa.2019.123797.

(78) Jeon, H.; Kim, J.; Mi, Y.; Kim, J.; Woo, H.; Lee, J.; Park, H.; Kang, Y.; Kim, I.; Lee, B.; et al. Poly-Paclitaxel / Cyclodextrin-SPION Nano-Assembly for Magnetically Guided Drug Delivery System. *J. Control. Release* **2016**, *231*, 68–76. https://doi.org/10.1016/j.jconrel.2016.01.006.

(79) Nakagawa, H.; Ohuchi, M.; Tadokoro, T. Application of Spin-Correlated Radical Pair System to Liposomal Drug-Delivery System under Exposure to Magnetic Fields. *J. Magn. Magn. Mater.* **2019**, *479*, 161–165. https://doi.org/10.1016/j.jmmm.2019.01.099.

(80) Nakagawa, H.; Ohuchi, M. Photomagnetic Control of Nanoparticles With Radical Pair System : A Promising New Area of Liposomal Drug-Delivery

System. *IEEE Trans. Magn.* **2019**, *55* (2), 5000104.

(81) Nappini, S.; Bombelli, F. B.; Bonini, M.; Nord, B.; Baglioni, P. Magnetoliposomes for Controlled Drug Release in the Presence of Low-Frequency Magnetic Field. *Soft Matter* **2010**, *6* (1), 154–162. https://doi.org/10.1039/b915651h.

(82) Shaghasemi, B. S.; Virk, M. M.; Reimhult, E. Optimization of Magneto-Thermally Controlled Release Kinetics by Tuning of Magnetoliposome Composition and Structure. *Sci. Rep.* **2017**, *7*, 7474. https://doi.org/10.1038/s41598-017-06980-9.

(83) Spera, R.; Apollonio, F.; Liberti, M.; Paffi, A.; Merla, C.; Pinto, R.; Petralito, S. Controllable Release from High-Transition Temperature Magnetoliposomes by Low-Level Magnetic Stimulation. *Colloids Surfaces B Biointerfaces* **2015**, *131*, 136–140. https://doi.org/10.1016/j.colsurfb.2015.04.030.

(84) Bothun, G. D.; Lelis, A.; Chen, Y.; Scully, K.; Anderson, L. E.; Stoner, M. A. Multicomponent Folate-Targeted Magnetoliposomes : Design , Characterization , and Cellular Uptake. *Nanomedicine Nanotechnology, Biol. Med.* **2011**, *7*, 797–805. https://doi.org/10.1016/j.nano.2011.02.007.

(85) Szuplewska, A.; Aleksandra, R. Magnetic Field-Assisted Selective Delivery of Doxorubicin to Cancer Cells Using Magnetoliposomes as Drug Nanocarriers. *Nanotechnology* **2019**, *30*, 315101.

(86) Faria, M. R.; Cruz, M. M.; Gonc, M. C.; Carvalho, A.; Feio, G.; Martins, M. B. F. Synthesis and Characterization of Magnetoliposomes for MRI Contrast Enhancement. *Int. J. Pharm.* **2013**, *446*, 183–190. https://doi.org/10.1016/j.ijpharm.2013.02.025.

(87) Blyakhman, F. A.; Makarova, E. B.; Fadeyev, F. A.; Lugovets, D. V; Safronov, A. P.; Shabadrov, P. A.; Shklyar, T. F.; Melnikov, G. Y.; Orue, I.; Kurlyandskaya, G. V. The Contribution of Magnetic Nanoparticles to Ferrogel Biophysical Properties. *Nanomaterials* **2019**, *9*, 232. https://doi.org/10.3390/nano9020232.

(88) Ko, E. S.; Kim, C.; Choi, Y.; Lee, K. Y. 3D Printing of Self-Healing Ferrogel Prepared from Glycol Chitosan , Oxidized Hyaluronate , and Iron Oxide Nanoparticles. *Carbohydr. Polym.* **2020**, *245*, 116496. https://doi.org/10.1016/j.carbpol.2020.116496.

(89) Kim, C.; Kim, H.; Park, H.; Yong, K. Controlling the Porous Structure of Alginate Ferrogel for Anticancer Drug Delivery under Magnetic Stimulation. *Carbohydr. Polym.* **2019**, *223*, 115045. https://doi.org/10.1016/j.carbpol.2019.115045.

(90) Hu, S.; Liu, T.; Liu, D.; Chen, S. Nano-Ferrosponges for Controlled Drug Release. *J. ofControlled Release* **2007**, *121*, 181–189. https://doi.org/10.1016/j.jconrel.2007.06.002.

(91) Jackson, D. K.; Leeb, S. B.; Mitwalli, A. H.; Narvaez, P.; Fusco, D.; Lupton, E. C. Power Electronic Drives for Magnetically Triggered Gels. *IEEE Trans. Ind. Electron.* **1997**, *44* (2), 217–225.

(92) Bardajee, G. R.; Hooshyar, Z. Thermo/PH/Magnetic-Triple Sensitive Poly(N-Isopropylacrylamide-Co-2-Dimethylaminoethyl) Methacrylate)/Sodium Alginate Modified Magnetic Graphene Oxide Nanogel for Anticancer Drug Delivery. *Polym. Bull.* **2018**, *75*, 5403–5419. https://doi.org/10.1007/s00289-018-2329-7.

(93) François, N. J.; Allo, S.; Jacobo, S. E.; Daraio, M. E. Composites of Polymeric Gels and Magnetic Nanoparticles : Preparation and Drug Release Behavior. *J. Appl. Polym. Sci.* **2007**, *105* (2), 647–655. https://doi.org/10.1002/app.26321.

(94) Zhao, X.; Kim, J.; Cezar, C. A.; Huebsch, N.; Lee, K.; Bouhadir, K.; Mooney, D. J. Active Scaffolds for On-Demand Drug and Cell Delivery. *Proc. Natl. Acad. Sci.* **2011**, *108* (1), 67–72. https://doi.org/10.1073/pnas.1007862108.

(95) Furlan, M.; Lattuada, M. Use of Magnetic Nanoparticles for the Preparation of Micro- and Nanostructured Materials. In *Advanced Hierarchical Nanostructured Materials*; Zhang, Q., Wei, W., Eds.; Wiley-VCH: Weinheim, 2014; pp 71–108.

(96) Mahdavinia, G. R.; Etemadi, H. In Situ Synthesis of Magnetic CaraPVA IPN Nanocomposite Hydrogels and Controlled Drug Release. *Mater. Sci. Eng. C* **2014**, *45*, 250–260. https://doi.org/10.1016/j.msec.2014.09.023.

(97) Monfared, A. H.; Zamanian, A.; Sharifi, I.; Mozafari, M. Reversible Multistimuli-Responsive Manganese–Zinc Ferrite/P(NIPAAM-AAc-AAm) Core-Shell Nanoparticles: A Programmed Ferrogel System. *Mater. Chem. Phys.* **2019**, *226*, 44–50. https://doi.org/10.1016/j.matchemphys.2019.01.016.

(98) Bonini, M.; Lenz, S.; Falletta, E.; Ridi, F.; Carretti, E.; Fratini, E.; Wiedenmann, A.; Baglioni, P. Acrylamide-Based Magnetic Nanosponges : A New Smart Nanocomposite Material. *Langmuir* **2008**, *24* (21), 12644–12650. https://doi.org/10.1021/la802425k.

(99) Liu, T.; Hu, S.; Liu, T.; Liu, D.; Chen, S. Magnetic-Sensitive Behavior of Intelligent Ferrogels for Controlled Release of Drug. *Langmuir* **2006**, *22* (14), 5974–5978. https://doi.org/10.1021/la060371e.

(100) Bertoglio, P.; Jacobo, S. E.; Daraio, M. E. Preparation and Characterization of PVA Films with Magnetic Nanoparticles : The Effect of Particle Loading on Drug Release Behavior. *J. Appl. Polym. Sci.* **2010**, *115* (3), 1859–1865. https://doi.org/10.1002/app.

(101) Varga, Z.; Filipcsei, G.; Zrínyi, M. Magnetic Field Sensitive Functional Elastomers with Tuneable Elastic Modulus. *Polymer (Guildf).* **2006**, *47* (1), 227–233. https://doi.org/10.1016/j.polymer.2005.10.139.

(102) Ivaneyko, D.; Toshchevikov, V.; Saphiannikova, M.; Heinrich, G. Magneto-Sensitive Elastomers in a Homogeneous Magnetic Field : A Regular Rectangular Lattice Model. *Macromol. theory simulations* **2011**, *20* (6), 411–424.

(103) Hu, S.; Chen, S.; Liu, D.; Hsiao, C. Core / Single-Crystal-Shell Nanospheres for Controlled Drug Release via a Magnetically Triggered Rupturing Mechanism. *Adv. Mater.* **2008**, *20*, 2690–2695. https://doi.org/10.1002/adma.200800193.

(104) Tolouei, A. E.; Dülger, N.; Ghatee, R.; Kennedy, S. A Magnetically Responsive Biomaterial System for Flexibly Regulating the Duration between Pro- and Anti-Inflammatory Cytokine Deliveries. *Adv. Healthc. Mater.* **2018**, *7*, 1800227. https://doi.org/10.1002/adhm.201800227.

(105) Fang, Z.; Li, X.; Xu, Z.; Du, F.; Wang, W.; Shi, R.; Gao, D. Hyaluronic Acid-Modified Mesoporous Silica-Coated Superparamagnetic Fe3O4 Nanoparticles for Targeted Drug Delivery. *Int. J. Nanomedicine* **2019**, *14*, 5785–5797.

(106) Zhang, Z.; Zhuang, L.; Lin, Y.; Yan, M.; Lv, J.; Li, X.; Lin, H.; Zhu, P.; Lin, Q.; Xu, Y. Novel Drug Delivery System Based on Hollow Mesoporous Magnetic Nanoparticles for Head and Neck Cancers--Targeted Therapy in Vitro and in Vivo. *Am. J. Cancer Res.* **2020**, *10* (1), 350–364.

(107) Ghoderao, P.; Sahare, S.; Alegaonkar, P.; Kulkarni, A. A.; Bhave, T. Multiwalled Carbon Nanotubes Decorated with Fe 3 O 4 Nanoparticles for E Ffi Cacious Doxycycline Delivery. *ACS Appllied Nano Mater.* **2019**, *2*, 607–616. https://doi.org/10.1021/acsanm.8b02268.

(108) Park, J.; Kim, J.; Pané, S.; Nelson, B. J.; Choi, H. Acoustically Mediated Controlled Drug Release and Targeted Therapy with Degradable 3D Porous Magnetic Microrobots. *Adv. Healthc. Mater.* **2021**, *10*, 2001096. https://doi.org/10.1002/adhm.202001096.

(109) Grifantini, R.; Taranta, M.; Gherardini, L.; Naldi, I.; Parri, M.; Grandi, A.; Giannetti, A.; Tombelli, S.; Lucarini, G.; Ricotti, L.; et al. Magnetically Driven Drug Delivery Systems Improving Targeted Immunotherapy for Colon-Rectal Cancer. *J. Control. Release* **2018**, *280*, 76–86. https://doi.org/10.1016/j.jconrel.2018.04.052.

(110) Park, J.; Jin, C.; Lee, S.; Kim, J.; Choi, H. Magnetically Actuated Degradable Microrobots for Actively Controlled Drug Release and Hyperthermia Therapy. *Adv. Healthc. Mater.* **2019**, *8*, 1900213. https://doi.org/10.1002/adhm.201900213.

(111) Niedert, E. E.; Bi, C.; Adam, G.; Lambert, E.; Solorio, L.; Goergen, C. J.;

Cappelleri, D. J. A Tumbling Magnetic Microrobot System for Biomedical Applications. *micromachines* **2020**, *11*, 861.

(112) Nam, J.; Lee, W.; Kim, J.; Jang, G. Magnetic Helical Robot for Targeted Drug-Delivery in Tubular Environments. *IEEE/ASME Trans. mechatronics* **2017**, *22* (6), 2461–2468.

(113) Guo, S.; Zhang, L.; Yang, Q. The Structural Design of a Magnetic Driven Wireless Capsule Robot for Drug Delivery. In *IEEE International Conference on Mechatronics and Automation (ICMA)*; IEEE: Tianjin, China, 2019; pp 844–849. https://doi.org/10.1109/ICMA.2019.8816504.

(114) Nguyen, K. T.; Hoang, M. C.; Choi, E.; Kang, B.; Park, J.; Kim, C.-S. Medical Microrobot - A Drug Delivery Capsule Endoscope with Active Locomotion and Drug Release Mechanism : Proof of Concept. *Int. J. Control. Autom. Syst.* **2020**, *18* (1), 65–75.

(115) Lee, J.; Lee, H.; Kwon, S.; Park, S. Active Delivery of Multi-Layer Drug-Loaded Microneedle Patches Using Magnetically Driven Capsule. *Med. Eng. Phys.* **2020**, *85*, 87–96. https://doi.org/10.1016/j.medengphy.2020.09.012.

(116) Wang, Z.; Guo, S.; Fu, Q.; Guo, J. Characteristic Evaluation of a Magnetic-Actuated Microrobot in Pipe with Screw Jet Motion. *Microsyst. Technol.* **2019**, *25*, 719–727. https://doi.org/10.1007/s00542-018-4000-5.

(117) Sun, Z.-J.; Cheng, X.-G.; Cao, S.; Ye, B.; Zhang, H.-H.; Liu, S. Multi-Applications of a Magnet Configuration in Actuating Capsule Endoscope. In *2014 IEEE/ASME International Conference on Advanced Intelligent Mechatronics*; IEEE, 2014; pp 106–111. https://doi.org/10.1109/AIM.2014.6878063.

(118) Munoz, F.; Alici, G.; Zhou, H.; Li, W.; Sitti, M. Analysis of Magnetic Interaction in Remotely Controlled Magnetic Devices and Its Application to a Capsule Robot for Drug Delivery. *IEEE/ASME Trans. mechatronics* **2018**, *23* (1), 298–310.

(119) Yim, S.; Sitti, M. Design and Rolling Locomotion of a Magnetically

Actuated Soft Capsule Endoscope. *IEEE Trans. Robot.* **2012**, *28* (1), 183–194. https://doi.org/10.1109/TRO.2011.2163861.

(120) Shi, J.; Zhang, H.; Jackson, J.; Shademani, A.; Chiao, M. A Robust and Refillable Magnetic Sponge Capsule for Remotely Triggered Drug Release. *J. Mater. Chem. B* **2016**, *4* (46), 7415–7422. https://doi.org/10.1039/c6tb02762h.

(121) Maloney, J. M.; Uhland, S. A.; Polito, B. F.; Sheppard, N. F.; Pelta, C. M.; Santini, J. T. Electrothermally Activated Microchips for Implantable Drug Delivery and Biosensing. *J. Control. Release* **2005**, *109* (1–3), 244–255. https://doi.org/10.1016/j.jconrel.2005.09.035.

(122) Xu, C.; Wei, Z.; Gao, H.; Bai, Y.; Liu, H.; Yang, H.; Lai, Y.; Yang, L. Bioinspired Mechano-Sensitive Macroporous Ceramic Sponge for Logical Drug and Cell Delivery. *Adv. Sci.* **2017**, *4* (6). https://doi.org/10.1002/advs.201600410.

(123) Choi, S. J.; Kwon, T. H.; Im, H.; Moon, D. Il; Baek, D. J.; Seol, M. L.; Duarte, J. P.; Choi, Y. K. A Polydimethylsiloxane (PDMS) Sponge for the Selective Absorption of Oil from Water. *ACS Appl. Mater. Interfaces* **2011**, *3* (12), 4552–4556. https://doi.org/10.1021/am201352w.

(124) Zhang, H.; Chiao, M. Anti-Fouling Coatings of Poly(Dimethylsiloxane) Devices for Biological and Biomedical Applications. *J. Med. Biol. Eng.* **2015**, *35* (2), 143–155. https://doi.org/10.1007/s40846-015-0029-4.

(125) Si, P.; Wang, J.; Guo, J.; Li, S.; Cai, W.; Xu, H. Mussel-Inspired One-Step Modification of a Porous Structured Surface with Self-Cleaning Properties for Oil Sorption. *New J. Chem.* **2015**, *39* (9), 6823–6829. https://doi.org/10.1039/c5nj00971e.

(126) Shademani, A.; Zhang, H.; Jackson, J. K.; Chiao, M. Active Regulation of On-Demand Drug Delivery by Magnetically Triggerable Microspouters. *Adv. Funct. Mater.* **2017**, *27* (6). https://doi.org/10.1002/adfm.201604558.

(127) Lee, S. H.; Kim, B. H.; Park, C. G.; Lee, C.; Lim, B. Y.; Choy, Y. Bin. Implantable Small Device Enabled with Magnetic Actuation for On-Demand

and Pulsatile Drug Delivery. *J. Control. Release* **2018**, *286*, 224–230. https://doi.org/10.1016/j.jconrel.2018.07.037.

(128) Moura, S. A. L.; Lima, L. D. C.; Andrade, S. P.; Da Silva-Cunha, A.; Órefice, R. L.; Ayres, E.; Da Silva, G. R. Local Drug Delivery System: Inhibition of Inflammatory Angiogenesis in a Murine Sponge Model by Dexamethasone-Loaded Polyurethane Implants. *J. Pharm. Sci.* **2011**, *100* (7), 2886–2895. https://doi.org/10.1002/jps.

(129) Stewart, S. A.; Domínguez-Robles, J.; McIlorum, V. J.; Mancuso, E.; Lamprou, D. A.; Donnelly, R. F.; Larrañeta, E. Development of a Biodegradable Subcutaneous Implant for Prolonged Drug Delivery Using 3D Printing. *Pharmaceutics* **2020**, *12* (2). https://doi.org/10.3390/pharmaceutics12020105.

(130) Alomari, M.; Mohamed, F. H.; Basit, A. W.; Gaisford, S. Personalised Dosing: Printing a Dose of One's Own Medicine. *Int. J. Pharm.* **2015**, *494* (2), 568–577. https://doi.org/10.1016/j.ijpharm.2014.12.006.

(131) Prasad, L. K.; Smyth, H. 3D Printing Technologies for Drug Delivery : A Review. *Drug Dev. Ind. Pharm.* **2016**, *42* (7), 1019–1031.

(132) Goyanes, A.; Wang, J.; Buanz, A.; Martínez-Pacheco, R.; Telford, R.; Gaisford, S.; Basit, A. W. 3D Printing of Medicines: Engineering Novel Oral Devices with Unique Design and Drug Release Characteristics. *Mol. Pharm.* **2015**, *12* (11), 4077–4084. https://doi.org/10.1021/acs.molpharmaceut.5b00510.

(133) Melocchi, A.; Parietti, F.; Maroni, A.; Foppoli, A.; Gazzaniga, A.; Zema, L. Hot-Melt Extruded Filaments Based on Pharmaceutical Grade Polymers for 3D Printing by Fused Deposition Modeling. *Int. J. Pharm.* **2016**, *509* (1–2), 255–263. https://doi.org/10.1016/j.ijpharm.2016.05.036.

(134) Moulton, S. E.; Wallace, G. G. 3-Dimensional (3D) Fabricated Polymer Based Drug Delivery Systems. *J. Control. Release* **2014**, *193*, 27–34. https://doi.org/10.1016/j.jconrel.2014.07.005.

(135) Shafiee, A. Design and Fabrication of Three-Dimensional Printed

Scaffolds for Cancer Precision Medicine. *Tissue Eng. Part A* **2020**, *26* (5–6), 305–317. https://doi.org/10.1089/ten.tea.2019.0278.

(136) Ligon, S. C.; Liska, R.; Gurr, M.; Mu, R.; Gmbh, H. B. F. D.; Bleiche, A. D. R.; D-, L. Polymers for 3D Printing and Customized Additive Manufacturing. *Chem. Rev.* **2017**, *117*, 10212−10290. https://doi.org/10.1021/acs.chemrev.7b00074.

(137) Infanger, S.; Haemmerli, A.; Iliev, S.; Baier, A.; Stoyanov, E.; Quodbach, J. Powder Bed 3D-Printing of Highly Loaded Drug Delivery Devices with Hydroxypropyl Cellulose as Solid Binder. *Int. J. Pharm.* **2019**, *555*, 198–206. https://doi.org/10.1016/j.ijpharm.2018.11.048.

(138) Touri, M.; Kabirian, F.; Saadati, M.; Ramakrishna, S.; Mozafari, M. Additive Manufacturing of Biomaterials À The Evolution of Rapid Prototyping. *Adv. Eng. Mater.* **2019**, *21*, 1800511. https://doi.org/10.1002/adem.201800511.

(139) Goole, J.; Amighi, K. 3D Printing in Pharmaceutics : A New Tool for Designing Customized Drug Delivery Systems. *Int. J. Pharm.* **2016**, *499*, 376–394. https://doi.org/10.1016/j.ijpharm.2015.12.071.

(140) Shaqour, B.; Samaro, A.; Verleije, B.; Beyers, K.; Vervaet, C.; Cos, P. Production of Drug Delivery Systems Using Fused Filament Fabrication : A Systematic Review. *Pharmaceutics* **2020**, *12*, 517.

(141) Palekar, S.; Nukala, P. K.; Mishra, S. M.; Kipping, T.; Patel, K. Application of 3D Printing Technology and Quality by Design Approach for Development of Age-Appropriate Pediatric Formulation of Baclofen. *Int. J. Pharm.* **2019**, *556*, 106–116. https://doi.org/10.1016/j.ijpharm.2018.11.062.

(142) Zhang, J.; Feng, X.; Patil, H.; Tiwari, R. V.; Repka, M. A. Coupling 3D Printing with Hot-Melt Extrusion to Produce Controlled-Release Tablets. *Int. J. Pharm.* **2017**, *519* (1–2), 186–197. https://doi.org/10.1016/j.ijpharm.2016.12.049.

(143) Alhnan, M. A.; Okwuosa, T. C.; Sadia, M.; Wan, K. W.; Ahmed, W.; Arafat, B. Emergence of 3D Printed Dosage Forms: Opportunities and Challenges.

Pharm. Res. **2016**, *33* (8), 1817–1832. https://doi.org/10.1007/s11095-016-1933-1.

(144) Gharaie, S. H.; Morsi, Y.; Masood, S. H. Tensile Properties of Processed 3D Printer ZP150 Powder Material. *Adv. Mater. Res.* **2013**, *699*, 813–816. https://doi.org/10.4028/www.scientific.net/AMR.699.813.

(145) Farzadi, A.; Solati-hashjin, M.; Asadi-eydivand, M.; Osman, N. A. A. Effect of Layer Thickness and Printing Orientation on Mechanical Properties and Dimensional Accuracy of 3D Printed Porous Samples for Bone Tissue Engineering. *PLoS One* **2014**, *9* (9), e108252. https://doi.org/10.1371/journal.pone.0108252.

(146) Qi, S.; Craig, D. Recent Developments in Micro- and Nanofabrication Techniques for the Preparation of Amorphous Pharmaceutical Dosage Forms ☆. *Adv. Drug Deliv. Rev.* **2016**, *100*, 67–84. https://doi.org/10.1016/j.addr.2016.01.003.

(147) Zhou, Z.; Buchanan, F.; Mitchell, C.; Dunne, N. Printability of Calcium Phosphate : Calcium Sulfate Powders for the Application of Tissue Engineered Bone Scaffolds Using the 3D Printing Technique. *Mater. Sci. Eng. C* **2014**, *38*, 1–10. https://doi.org/10.1016/j.msec.2014.01.027.

(148) Ilyés, K.; Kovács, N. K.; Balogh, A.; Borbás, E.; Farkas, B.; Casian, T.; Marosi, G.; Tomuță, I.; Nagy, Z. K. The Applicability of Pharmaceutical Polymeric Blends for the Fused Deposition Modelling (FDM) 3D Technique: Material Considerations–Printability–Process Modulation, with Consecutive Effects on in Vitro Release, Stability and Degradation. *Eur. J. Pharm. Sci.* **2019**, *129*, 110–123. https://doi.org/10.1016/j.ejps.2018.12.019.

(149) Samaro, A.; Janssens, P.; Vanhoorne, V.; Renterghem, J. Van; Eeckhout, M.; Cardon, L.; De Beer, T.; Vervaet, C. Screening of Pharmaceutical Polymers for Extrusion-Based Additive Manufacturing of Patient-Tailored Tablets. *Int. J. Pharm.* **2020**, *586*, 119591.

https://doi.org/10.1016/j.ijpharm.2020.119591.

(150) Tan, D. K.; Maniruzzaman, M.; Nokhodchi, A. Advanced Pharmaceutical Applications of Hot-Melt Extrusion Coupled with Fused Deposition Modelling (FDM) 3D Printing for Personalised Drug Delivery. *Pharmaceutics* **2018**, *10* (4). https://doi.org/10.3390/pharmaceutics10040203.

(151) Alhijjaj, M.; Belton, P.; Qi, S. An Investigation into the Use of Polymer Blends to Improve the Printability of and Regulate Drug Release from Pharmaceutical Solid Dispersions Prepared via Fused Deposition Modeling (FDM) 3D Printing. *Eur. J. Pharm. Biopharm.* **2016**, *108*, 111–125. https://doi.org/10.1016/j.ejpb.2016.08.016.

(152) Genina, N.; Holländer, J.; Jukarainen, H.; Mäkilä, E.; Salonen, J.; Sandler, N. Ethylene Vinyl Acetate (EVA) as a New Drug Carrier for 3D Printed Medical Drug Delivery Devices. *Eur. J. Pharm. Sci.* **2016**, *90*, 53–63. https://doi.org/10.1016/j.ejps.2015.11.005.

(153) Melocchi, A.; Parietti, F.; Maroni, A.; Foppoli, A.; Gazzaniga, A.; Zema, L. Hot-Melt Extruded Filaments Based on Pharmaceutical Grade Polymers for 3D Printing by Fused Deposition Modeling. *Int. J. Pharm.* **2016**, *509* (1–2), 255–263. https://doi.org/10.1016/j.ijpharm.2016.05.036.

(154) Yang, Y.; Wang, H.; Li, H.; Ou, Z.; Yang, G. 3D Printed Tablets with Internal Scaffold Structure Using Ethyl Cellulose to Achieve Sustained Ibuprofen Release. *Eur. J. Pharm. Sci.* **2018**, *115* (December 2017), 11–18. https://doi.org/10.1016/j.ejps.2018.01.005.

(155) Pietrzak, K.; Isreb, A.; Alhnan, M. A. A Flexible-Dose Dispenser for Immediate and Extended Release 3D Printed Tablets. *Eur. J. Pharm. Biopharm.* **2015**, *96*, 380–387. https://doi.org/10.1016/j.ejpb.2015.07.027.

(156) Norman, J.; Madurawe, R. D.; Moore, C. M. V; Khan, M. A.; Khairuzzaman, A. A New Chapter in Pharmaceutical Manufacturing : 3D-Printed Drug Products. *Adv. Drug Deliv. Rev.* **2017**, *108*, 39–50. https://doi.org/10.1016/j.addr.2016.03.001.

(157) Nasereddin, J. M.; Wellner, N.; Alhijjaj, M.; Belton, P.; Qi, S. Development of a Simple Mechanical Screening Method for Predicting the Feedability of a Pharmaceutical FDM 3D Printing Filament. *Pharm. Res.* **2018**, *35* (8). https://doi.org/10.1007/s11095-018-2432-3.

(158) Quinten, T.; Beer, T. De; Vervaet, C.; Remon, J. P. Evaluation of Injection Moulding as a Pharmaceutical Technology to Produce Matrix Tablets. *Eur. J. Pharm. Biopharm.* **2009**, *71* (1), 145–154. https://doi.org/10.1016/j.ejpb.2008.02.025.

(159) Patil, H.; Tiwari, R. V; Repka, M. A. Hot-Melt Extrusion : From Theory to Application in Pharmaceutical Formulation. *AAPS PharmSciTech* **2016**, *17* (1), 20–42. https://doi.org/10.1208/s12249-015-0360-7.

(160) Arora, A.; Aggarwal, G.; Chander, J.; Maman, P.; Nagpal, M. Drug Eluting Sutures : A Recent Update. *J. Appl. Pharm. Sci.* **2019**, *9* (07), 111–123. https://doi.org/10.7324/JAPS.2019.90716.

(161) Al-hamidi, H.; Edwards, A. A.; Mohammad, M. A.; Nokhodchi, A. To Enhance Dissolution Rate of Poorly Water-Soluble Drugs: Glucosamine Hydrochloride as a Potential Carrier in Solid Dispersion Formulations. *Colloids Surfaces B Biointerfaces* **2010**, *76*, 170–178. https://doi.org/10.1016/j.colsurfb.2009.10.030.

(162) Maniruzzaman, M.; Morgan, D. J.; Mendham, A. P.; Pang, J.; Snowden, M. J.; Douroumis, D. Drug-Polymer Intermolecular Interactions in Hot-Melt Extruded Solid Dispersions. *Int. J. Pharm.* **2013**, *443* (1–2), 199–208. https://doi.org/10.1016/j.ijpharm.2012.11.048.

(163) Chavan, R. B.; Thipparaboina, R.; Yadav, B.; Shastri, N. R. Continuous Manufacturing of Co-Crystals : Challenges and Prospects. *Drug Deliv. Transl. Res.* **2018**, *8*, 1726–1739.

(164) Goyanes, A.; Robles Martinez, P.; Buanz, A.; Basit, A. W.; Gaisford, S. Effect of Geometry on Drug Release from 3D Printed Tablets. *Int. J. Pharm.* **2015**, *494* (2), 657–663. https://doi.org/10.1016/j.ijpharm.2015.04.069.

(165) Maru, S. M.; De Matas, M.; Kelly, A.; Paradkar, A. Characterization of

Thermal and Rheological Properties of Zidovidine, Lamivudine and Plasticizer Blends with Ethyl Cellulose to Assess Their Suitability for Hot Melt Extrusion. *Eur. J. Pharm. Sci.* **2011**, *44* (4), 471–478. https://doi.org/10.1016/j.ejps.2011.09.003.

(166) Li, D.; Guo, G.; Fan, R.; Liang, J.; Deng, X.; Luo, F.; Qian, Z. PLA/F68/Dexamethasone Implants Prepared by Hot-Melt Extrusion for Controlled Release of Anti-Inflammatory Drug to Implantable Medical Devices: I. Preparation, Characterization and Hydrolytic Degradation Study. *Int. J. Pharm.* **2013**, *441* (1–2), 365–372. https://doi.org/10.1016/j.ijpharm.2012.11.019.

(167) Karimi-jafari, M.; Padrela, L.; Walker, G. M.; Croker, D. M. Creating Cocrystals : A Review of Pharmaceutical Cocrystal Preparation Routes and Applications. *Cryst. Growth Des.* **2018**, *18*, 6370–6387. https://doi.org/10.1021/acs.cgd.8b00933.

(168) Kempin, W.; Franz, C.; Koster, L. C.; Schneider, F.; Bogdahn, M.; Weitschies, W.; Seidlitz, A. Assessment of Different Polymers and Drug Loads for Fused Deposition Modeling of Drug Loaded Implants. *Eur. J. Pharm. Biopharm.* **2017**, *115*, 84–93. https://doi.org/10.1016/j.ejpb.2017.02.014.

(169) Li, S.; Yu, T.; Tian, Y.; Lagan, C.; Jones, D. S.; Andrews, G. P. Mechanochemical Synthesis of Pharmaceutical Cocrystal Suspensions via Hot Melt Extrusion: Enhancing Cocrystal Yield. *Mol. Pharm.* **2018**, *15*, 3741–3754. https://doi.org/10.1021/acs.molpharmaceut.7b00979.

(170) Gajda, M.; Nartowski, K. P.; Pluta, J.; Karolewicz, B. Continuous , One-Step Synthesis of Pharmaceutical Cocrystals via Hot Melt Extrusion from Neat to Matrix-Assisted Processing – State of the Art. *Int. J. Pharm.* **2019**, *558*, 426–440. https://doi.org/10.1016/j.ijpharm.2019.01.016.

(171) K, T. A.; Moravkar, K.; Maniruzzaman, M.; Amin, P. Effect of Melt Extrudability and Melt Binding Efficiency of Polyvinyl Caprolactam Polyvinyl Acetate Polyethylene Glycol Graft Copolymer (Soluplus®) on Release

Pattern of Hydrophilic and High Dose Drugs. *Mater. Sci. Eng. C* **2019**, *99*, 563–574. https://doi.org/10.1016/j.msec.2019.01.126.

(172) Almeida, A.; Possemiers, S.; Boone, M. N.; De Beer, T.; Quinten, T.; Van Hoorebeke, L.; Remon, J. P.; Vervaet, C. Ethylene Vinyl Acetate as Matrix for Oral Sustained Release Dosage Forms Produced via Hot-Melt Extrusion. *Eur. J. Pharm. Biopharm.* **2011**, *77* (2), 297–305. https://doi.org/10.1016/j.ejpb.2010.12.004.

(173) Fuenmayor, E.; Forde, M.; Healy, A. V.; Devine, D. M.; Lyons, J. G.; McConville, C.; Major, I. Material Considerations for Fused-Filament Fabrication of Solid Dosage Forms. *Pharmaceutics* **2018**, *10* (2), 1–27. https://doi.org/10.3390/pharmaceutics10020044.

(174) Homaee Borujeni, S.; Mirdamadian, S. Z.; Varshosaz, J.; Taheri, A. Three-Dimensional (3D) Printed Tablets Using Ethyl Cellulose and Hydroxypropyl Cellulose to Achieve Zero Order Sustained Release Profile. *Cellulose* **2020**, *27* (3), 1573–1589. https://doi.org/10.1007/s10570-019-02881-4.

(175) PARADKAR, A.; KELLY, A.; COATES, P.; YORK, P. Method and Product. WO 2010/013035 Al, 2010.

(176) Dumpa, N. R.; Bandari, S.; Repka, M. A. Novel Gastroretentive Floating Pulsatile Drug Delivery System Produced via Hot-Melt Extrusion and Fused Deposition Modeling 3D Printing. *Pharmaceutics* **2020**, *12*, 52. https://doi.org/10.3390/pharmaceutics12010052.

(177) Wang, J.; Guo, J.; Si, P.; Cai, W.; Wang, Y.; Wu, G. Polydopamine-Based Synthesis of an In(OH) 3 -PDMS Sponge for Ammonia Detection by Switching Surface Wettability. *RSC Adv.* **2016**, *6* (6), 4329–4334. https://doi.org/10.1039/c5ra23484k.

(178) Chemical., T. D. C. SYLGARD ™ 184 Silicone Elastomer APPLICATIONS. *Silicone Elastomer Tech. Data Sheet* **2017**, No. 11, 4. https://doi.org/Form No. 11-3184-01 C.

(179) Quan, B.; Gu, W.; Chen, J.; Xu, G.; Ji, G. Integrating Carbonyl Iron with

Sponge to Enable Lightweight and Dual-Frequency Absorption. *Nanotechnology* **2019**, *30* (19), p.195703 (10pp).

(180) Li, J.; Zhang, Y. Porous Polymer Films with Size-Tunable Surface Pores. *Chem. Mater.* **2007**, *19* (10), 2581–2584. https://doi.org/10.1021/cm070197v.

(181) Hazzah, H. A.; Farid, R. M.; Nasra, M. M. A.; El-Massik, M. A.; Abdallah, O. Y. Lyophilized Sponges Loaded with Curcumin Solid Lipid Nanoparticles for Buccal Delivery: Development and Characterization. *Int. J. Pharm.* **2015**, *492* (1–2), 248–257. https://doi.org/10.1016/j.ijpharm.2015.06.022.

(182) Choi, S. J.; Kwon, T. H.; Im, H.; Moon, D. Il; Baek, D. J.; Seol, M. L.; Duarte, J. P.; Choi, Y. K. A Polydimethylsiloxane (PDMS) Sponge for the Selective Absorption of Oil from Water. *ACS Appl. Mater. Interfaces* **2011**, *3* (12), 4552–4556. https://doi.org/10.1021/am201352w.

(183) Shi, K.; Tan, D.; Nokhodchi, A.; Maniruzzaman, M. Drop-On-Powder 3D Printing of Tablets with an Anti-Cancer Drug, 5-Fluorouracil. *Pharmaceutics* **2019**, *11* (4), 150. https://doi.org/10.3390/pharmaceutics11040150.

(184) Akay, S.; Kayan, B.; Yang, Y. Solubility and Chromatographic Separation of 5-Fluorouracil under Subcritical Water Conditions. *J. Chem. Eng. Data* **2017**, *62* (4), 1538–1543. https://doi.org/10.1021/acs.jced.7b00015.

(185) Singh, P.; Tyagi, G.; Mehrotra, R.; Bakhshi., A. K. Thermal Stability Studies of 5‐fluorouracil Using Diffuse Reflectance Infrared Spectroscopy. *Drug Test. Anal.* **2009**, *1*, 240–244. https://doi.org/10.1002/dta.41.

(186) Li, Q.; Wen, H.; Jia, D.; Guan, X.; Pan, H.; Yang, Y.; Yu, S.; Zhu, Z.; Xiang, R.; Pan, W. Preparation and Investigation of Controlled-Release Glipizide Novel Oral Device with Three-Dimensional Printing. *Int. J. Pharm.* **2017**, *525* (1), 5–11. https://doi.org/10.1016/j.ijpharm.2017.03.066.

(187) De Brabander, C.; Van Den Mooter, G.; Vervaet, C.; Remon, J. P. Characterization of Ibuprofen as a Nontraditional Plasticizer of Ethyl Cellulose. *J. Pharm. Sci.* **2002**, *91* (7), 1678–1685. https://doi.org/10.1002/jps.10159.

(188) Beer, F. P.; Johnston, E. R.; DeWolf, J. T.; Mazurek, D. F. *Mechanics of Materials*, Seventh Ed.; New York, 2015. https://doi.org/10.4135/9781452276076.n265.

(189) Moore, J. W.; Flanner, H. H. Mathematical Comparison of Dissolution Profiles. *Pharm. Technol.* **1996**, *20*, 64–74.

(190) Xie, F.; Ji, S.; Cheng, Z. In Vitro Dissolution Similarity Factor (F2) and in Vivo Bioequivalence Criteria, How and When Do They Match? Using a BCS Class II Drug as a Simulation Example. *Eur. J. Pharm. Sci.* **2015**, *66*, 163–172. https://doi.org/10.1016/j.ejps.2014.10.002.

(191) De Brabander, C.; Vervaet, C.; Remon, J. P. Development and Evaluation of Sustained Release Mini-Matrices Prepared via Hot Melt Extrusion. *J. Control. Release* **2003**, *89* (2), 235–247. https://doi.org/10.1016/S0168-3659(03)00075-0.

(192) Zhang, Y.; Huo, M.; Zhou, J.; Zou, A.; Li, W.; Yao, C.; Xie, S. DDSolver: An Add-in Program for Modeling and Comparison of Drug Dissolution Profiles. *AAPS J.* **2010**, *12* (3), 263–271. https://doi.org/10.1208/s12248-010-9185-1.

(193) Williams, G. R. Kinetics. In *Aulton's pharmaceutics: the design and manufacture of medicines*; Aulton, M. E., Taylor, K. M. ., Eds.; Churchill Livingstone, 2018; pp 114–127.

(194) Samaha, D.; Shehayeb, R.; Kyriacos, S. Modeling and Comparison of Dissolution Profiles of Diltiazem Modified-Release Formulations. *Dissolution Technol.* **2009**, *16* (2), 41–46. https://doi.org/10.14227/DT160209P41.

(195) Higuchi, T. Mechanism of Sustained-action Medication. Theoretical Analysis of Rate of Release of Solid Drugs Dispersed in Solid Matrices. *J. Pharmaceirtical Sci.* **1963**, *52* (12), 1145–1149. https://doi.org/10.1002/jps.2600521210.

(196) Peppas, N. A.; Sahlin, J. J. A Simple Equation for the Description of Solute Release. III. Coupling of Diffusion and Relaxation. *Int. J. Pharm.*

1989, *57*, 169–172. https://doi.org/10.1016/0378-5173(89)90306-2.

(197) Cha, K. J.; Kim, D. S. A Portable Pressure Pump for Microfluidic Lab-on-a-Chip Systems Using a Porous Polydimethylsiloxane (PDMS) Sponge. *Biomed. Microdevices* **2011**, *13* (5), 877–883. https://doi.org/10.1007/s10544-011-9557-z.

(198) Guo, J.; Wang, J.; Wang, W.; Bai, Z.; Zhang, Z.; Zhang, Y.; Zhang, S. The Fabrication of 3D Porous PDMS Sponge for Oil and Organic Solvent Absorption. *Environ. Prog. Sustain. Energy* **2019**, *38* (s1), S86–S92. https://doi.org/10.1002/ep.12924.

(199) Zhao, X.; Li, L.; Li, B.; Zhang, J.; Wang, A. Durable Superhydrophobic/Superoleophilic PDMS Sponges and Their Applications in Selective Oil Absorption and in Plugging Oil Leakages. *J. Mater. Chem. A* **2014**, *2* (43), 18281–18287. https://doi.org/10.1039/c4ta04406a.

(200) Arias, J. L.; Gallardo, V.; Linares-Molinero, F.; Delgado, A. V. Preparation and Characterization of Carbonyl Iron/Poly(Butylcyanoacrylate) Core/Shell Nanoparticles. *J. Colloid Interface Sci.* **2006**, *299* (2), 599–607. https://doi.org/10.1016/j.jcis.2006.03.005.

(201) Zhu, Q.; Qian, Y.; Yang, Y.; Wu, W.; Xie, J.; Wei, D. Effects of Carbonyl Iron Powder on Iron Deficiency Anemia and Its Subchronic Toxicity. *J. Food Drug Anal.* **2016**, *24* (4), 746–753. https://doi.org/10.1016/j.jfda.2016.04.003.

(202) Li, J.; Zhang, M.; Wang, L. Design and Fabrication of Microfluidic Mixer from Carbonyl Iron – PDMS Composite Membrane. *Microfluid Nanofluid* **2011**, *10*, 919–925. https://doi.org/10.1007/s10404-010-0712-2.

(203) Cai, K.; Luo, Z.; Hu, Y.; Chen, X.; Liao, Y.; Yang, L.; Deng, L. Magnetically Triggered Reversible Controlled Drug Delivery from Microfabricated Polymeric Multireservoir Devices. *Adv. Mater.* **2009**, *21*, 4045–4049. https://doi.org/10.1002/adma.200900593.

(204) Ghazanfari, M. R.; Kashefi, M.; Shams, S. F.; Jaafari, M. R. Perspective of Fe3O4 Nanoparticles Role in Biomedical Applications. *Biochem. Res. Int.*

2016, *2016*. https://doi.org/10.1155/2016/7840161.

(205) Bernardes, C. E. S.; Canongia Lopes, J. N.; Da Piedade, M. E. M. All-Atom Force Field for Molecular Dynamics Simulations on Organotransition Metal Solids and Liquids. Application to M(CO) n (M = Cr, Fe, Ni, Mo, Ru, or W) Compounds. *J. Phys. Chem. A* **2013**, *117* (43), 11107–11113. https://doi.org/10.1021/jp407739h.

(206) Blaney, L. Magnetite (Fe3O4): Properties, Synthesis, and Applications. *Lehigh Rev.* **2007**, *15–2007*, Paper 5. https://doi.org/10.1016/j.jallcom.2010.10.211.

(207) Perales-Martínez, I. A.; Palacios-Pineda, L. M.; Lozano-Sánchez, L. M.; Martínez-Romero, O.; Puente-Cordova, J. G.; Elías-Zúñiga, A. Enhancement of a Magnetorheological PDMS Elastomer with Carbonyl Iron Particles. *Polym. Test.* **2017**, *57*, 78–86. https://doi.org/10.1016/j.polymertesting.2016.10.029.

(208) Beshkar, F.; Khojasteh, H.; Salavati-niasari, M. Recyclable Magnetic Superhydrophobic Straw Soot Sponge for Highly Efficient Oil / Water Separation. *J. Colloid Interface Sci.* **2017**, *497*, 57–65. https://doi.org/10.1016/j.jcis.2017.02.016.

(209) Liu, Y.; Wang, X.; Feng, S. Nonflammable and Magnetic Sponge Decorated with Polydimethylsiloxane Brush for Multitasking and Highly Efficient Oil – Water Separation. *Adv. Funct. Mater.* **2019**, *29* (29), 1902488. https://doi.org/10.1002/adfm.201902488.

(210) Hu, X.; Nian, G.; Liang, X.; Wu, L.; Yin, T.; Lu, H.; Qu, S.; Yang, W. Adhesive Tough Magnetic Hydrogels with High Fe 3 O 4 Content. *ACS Appl. Mater. Interfaces* **2019**, *11* (10), 10292–10300. https://doi.org/10.1021/acsami.8b20937.

(211) Tang, J.; Tong, Z.; Xia, Y.; Liu, M.; Lv, Z.; Gao, Y.; Lu, T.; Xie, S.; Pei, Y.; Fang, D.; et al. Super Tough Magnetic Hydrogels for Remotely Triggered Shape Morphing. *J. Mater. Chem. B* **2018**, *6* (18), 2713–2722. https://doi.org/10.1039/c8tb00568k.

(212) Liu, S.; Li, S.; Liu, J. Jurin ' s Law Revisited : Exact Meniscus Shape and Column Height. *Eur. Phys. J. E* **2018**, *41* (3), 46. https://doi.org/10.1140/epje/i2018-11648-1.

(213) Yin, T.; Wu, L.; Wu, T.; Mao, G.; Nian, G.; Chen, Z.; Hu, X.; Wang, P.; Xiang, Y.; Yu, H.; et al. Ultrastretchable and Conductive Core / Sheath Hydrogel Fibers with Multifunctionality. *ournal Polym. Sci. Part B Polym. Phys.* **2019**, *57*, 272–280. https://doi.org/10.1002/polb.24781.

(214) Song, Y.; Chen, H.; Su, Z.; Chen, X.; Miao, L.; Zhang, J.; Cheng, X.; Zhang, H. Highly Compressible Integrated Supercapacitor–Piezoresistance-Sensor System with CNT–PDMS Sponge for Health Monitoring. *Small* **2017**, *13* (39), 201702091.

(215) Hu, T.; Xuan, S.; Ding, L.; Gong, X. Stretchable and Magneto-Sensitive Strain Sensor Based on Silver Nanowire-Polyurethane Sponge Enhanced Magnetorheological Elastomer. *Mater. Des.* **2018**, *156*, 528–537. https://doi.org/10.1016/j.matdes.2018.07.024.

(216) Pawliszyn, J. *Theory of Solid-Phase Microextraction*; Elsevier Inc., 2012. https://doi.org/10.1016/B978-0-12-416017-0.00002-4.

(217) Kou, H.; Zhang, L.; Tan, Q.; Liu, G.; Dong, H.; Zhang, W.; Xiong, J. Wireless Wide-Range Pressure Sensor Based on Graphene/PDMS Sponge for Tactile Monitoring. *Sci. Rep.* **2019**, *9* (1), 1–7. https://doi.org/10.1038/s41598-019-40828-8.

(218) Ding, L.; Xuan, S.; Pei, L.; Wang, S.; Hu, T.; Zhang, S.; Gong, X. Stress and Magnetic Field Bimode Detection Sensors Based on Flexible CI/CNTs − PDMS Sponges. *ACS Appl. Mater. Interfaces* **2018**, *10*, 30774–39784. https://doi.org/10.1021/acsami.8b11333.

(219) Liu, J.; Yang, S.; Liu, Z.; Guo, H.; Liu, Z.; Xu, Z.; Liu, C.; Wang, L. Patterning Sub-30 μ m Liquid Metal Wires on PDMS Substrates via Stencil Lithography and Pre-Stretching. *J. Micromechanics Microengineering* **2019**, *29* (9), 095001. https://doi.org/10.1088/1361-6439/ab2839.

(220) Chang, H.-H.; Cheng, C.-L.; Huang, P.-J.; Lin, S.-Y. Application of

Scanning Electron Microscopy and X-Ray Microanalysis : FE-SEM , ESEM-EDS , and EDS Mapping for Studying the Characteristics of Topographical Microstructure and Elemental Mapping of Human Cardiac Calcified Deposition. *Anal. Bioanal. Chem.* **2014**, *406* (1), 359–366. https://doi.org/10.1007/s00216-013-7414-z.

(221) Guo, J.; Wang, J.; Zhang, S.; Ma, X.; Qiu, Z.; Peng, X.; Ying, J.; Wang, Y.; Wu, G. One-Step Modification of PU Sponges for Selective Absorption of Oil-Water Mixtures. *New J. Chem.* **2016**, *41* (1), 90–96. https://doi.org/10.1039/c6nj03239g.

(222) Karimzadeh, I.; Aghazadeh, M.; Doroudi, T.; Ganjali, M. R.; Kolivand, P. H. Superparamagnetic Iron Oxide (Fe3O4) Nanoparticles Coated with PEG/PEI for Biomedical Applications: A Facile and Scalable Preparation Route Based on the Cathodic Electrochemical Deposition Method. *Adv. Phys. Chem.* **2017**, *2017*. https://doi.org/10.1155/2017/9437487.

(223) Azhar, F. F.; Olad, A. A Study on Sustained Release Formulations for Oral Delivery of 5-Fluorouracil Based on Alginate-Chitosan/Montmorillonite Nanocomposite Systems. *Appl. Clay Sci.* **2014**, *101*, 288–296. https://doi.org/10.1016/j.clay.2014.09.004.

(224) Goindi, S.; Arora, P.; Kumar, N.; Puri, A. Development of Novel Ionic Liquid-Based Microemulsion Formulation for Dermal Delivery of 5-Fluorouracil. *AAPS PharmSciTech* **2014**, *15* (4), 810–821. https://doi.org/10.1208/s12249-014-0103-1.

(225) Haggag, Y. A.; Osman, M. A.; El-Gizawy, S. A.; Goda, A. E.; Shamloula, M. M.; Faheem, A. M.; McCarron, P. A. Polymeric Nano-Encapsulation of 5-Fluorouracil Enhances Anti-Cancer Activity and Ameliorates Side Effects in Solid Ehrlich Carcinoma-Bearing Mice. *Biomed. Pharmacother.* **2018**, *105* (May), 215–224. https://doi.org/10.1016/j.biopha.2018.05.124.

(226) Man, L.; Zhen, L.; Xun, S.; Tao, G.; Zhirong, Z. A Polymeric Prodrug of 5-Fluorouracil-1-Acetic Acid Using a Multi-Hydroxyl Polyethylene Glycol Derivative as the Drug Carrier. *PLoS One* **2014**, *9* (11).

https://doi.org/10.1371/journal.pone.0112888.

(227) Hussain, A.; Haque, M. W.; Singh, S. K.; Ahmed, F. J. Optimized Permeation Enhancer for Topical Delivery of 5-Fluorouracil-Loaded Elastic Liposome Using Design Expert: Part II. *Drug Deliv.* **2016**, *23* (4), 1242–1253. https://doi.org/10.3109/10717544.2015.1124473.

(228) Shakeel, F.; Haq, N.; Al-Dhfyan, A.; Alanazi, F. K.; Alsarra, I. A. Chemoprevention of Skin Cancer Using Low HLB Surfactant Nanoemulsion of 5-Fluorouracil: A Preliminary Study. *Drug Deliv.* **2015**, *22* (4), 573–580. https://doi.org/10.3109/10717544.2013.868557.

(229) Arias, J. L. Novel Strategies to Improve the Anticancer Action of 5-Fluorouracil by Using Drug Delivery Systems. *Molecules* **2008**, *13* (10), 2340–2369. https://doi.org/10.3390/molecules13102340.

(230) *Committee for Veterinary Medicinal Products 2-PYRROLIDONE*; 1998.

(231) Shekunov, B. Y.; Chattopadhyay, P.; Tong, H. H. Y.; Chow, A. H. L. Particle Size Analysis in Pharmaceutics : Principles , Methods and Applications. *Pharm. Res.* **2007**, *24* (2), 203–227. https://doi.org/10.1007/s11095-006-9146-7.

(232) Asadi-eydivand, M.; Solati-hashjin, M.; Shafiei, S. S. Structure , Properties , and In Vitro Behavior of Heat-Treated Calcium Sulfate Scaffolds Fabricated by 3D Printing. *PLoS One* **2016**, 1–29. https://doi.org/10.1371/journal.pone.0151216.

(233) Jeddipelly, S. R. FORMULATION AND INVITRO EVALUATION OF 5-FLUOROURACIL MICROCAPSULES BY USING DIFFERENT METHODS OF MICROENCAPSULATION | PharmaTutor, The Tamil Nadu Dr. M.G.R. Medical University, 2013.

(234) Thakral, N. K.; Ray, A. R.; Bar-Shalom, D.; Eriksson, A. H.; Majumdar, D. K. Soluplus-Solubilized Citrated Camptothecin—A Potential Drug Delivery Strategy in Colon Cancer. *AAPS PharmSciTech* **2012**, *13* (1), 59–66. https://doi.org/10.1208/s12249-011-9720-0.

(235) Uddin, J.; Scoutaris, N.; Klepetsanis, P.; Chowdhry, B.; Prausnitz, M. R.;

Douroumis, D. Inkjet Printing of Transdermal Microneedles for the Delivery of Anticancer Agents. *Int. J. Pharm.* **2015**, *494*, 593–602. https://doi.org/10.1016/j.ijpharm.2015.01.038.

(236) Homayouni, A.; Sadeghi, F.; Varshosaz, J.; Garekani, H. A.; Nokhodchi, A. Promising Dissolution Enhancement Effect of Soluplus on Crystallized Celecoxib Obtained through Antisolvent Precipitation and High Pressure Homogenization Techniques. *Colloids Surfaces B Biointerfaces* **2014**, *122*, 591–600. https://doi.org/10.1016/j.colsurfb.2014.07.037.

(237) Yang, H.; Teng, F.; Wang, P.; Tian, B.; Lin, X.; Hu, X.; Zhang, L.; Zhang, K.; Zhang, Y.; Tang, X. Investigation of a Nanosuspension Stabilized by Soluplus® to Improve Bioavailability. *Int. J. Pharm.* **2014**, *477* (1–2), 88–95. https://doi.org/10.1016/j.ijpharm.2014.10.025.

(238) Zeng, Y.; Li, S.; Liu, C.; Gong, T.; Sun, X.; Fu, Y.; Zhang, Z. Soluplus Micelles for Improving the Oral Bioavailability of Scopoletin and Their Hypouricemic Effect in Vivo. *Acta Pharmacol. Sin.* **2017**, *38*, 424–433. https://doi.org/10.1038/aps.2016.126.

(239) Sitti, M.; Ceylan, H.; Hu, W.; Giltinan, J.; Turan, M.; Yim, S.; Diller, E. Biomedical Applications of Untethered Mobile Milli/Microrobots. *Proc. IEEE* **2015**, *103* (2), 205–224. https://doi.org/10.1109/JPROC.2014.2385105.

(240) Iacovacci, V.; Lucarini, G.; Ricotti, L.; Dario, P.; Dupont, P. E.; Menciassi, A. Untethered Magnetic Millirobot for Targeted Drug Delivery. *Biomed. Microdevices* **2015**, *17* (3). https://doi.org/10.1007/s10544-015-9962-9.

(241) Rwei, A. Y.; Paris, J. L.; Wang, B.; Wang, W.; Axon, C. D.; Vallet-Regí, M.; Langer, R.; Kohane, D. S. Ultrasound-Triggered Local Anaesthesia. *Nat. Biomed. Eng.* **2017**, *1* (8), 644–653. https://doi.org/10.1038/s41551-017-0117-6.

(242) Liang, K.; Carmone, S.; Brambilla, D.; Leroux, J.-C. 3D Printing of a Wearable Personalized Oral Delivery Device: A First-in-Human Study. *Sci. Adv.* **2018**, *4* (5), eaat2544.

(243) Domínguez-Robles, J.; Martin, N.; Fong, M.; Stewart, S.; Irwin, N.; Rial-

Hermida, M.; Donnelly, R.; Larrañeta, E. Antioxidant PLA Composites Containing Lignin for 3D Printing Applications: A Potential Material for Healthcare Applications. *Pharmaceutics* **2019**, *11* (4), 165. https://doi.org/10.3390/pharmaceutics11040165.

(244) Fu, J.; Yu, X.; Jin, Y. 3D Printing of Vaginal Rings with Personalized Shapes for Controlled Release of Progesterone. *Int. J. Pharm.* **2018**, *539* (1–2), 75–82. https://doi.org/10.1016/j.ijpharm.2018.01.036.

(245) Mathew, E.; Dom, J.; Larrañeta, E.; Lamprou, D. A. Fused Deposition Modelling as a Potential Tool for Antimicrobial Dialysis Catheters Manufacturing: New Trends vs. Conventional Approaches. *coatings* **2019**, *9*, 515.

(246) Osborne, D. W.; Musakhanian, J. Skin Penetration and Permeation Properties of Transcutol®—Neat or Diluted Mixtures. *AAPS PharmSciTech* **2018**, *19* (8), 3512–3533. https://doi.org/10.1208/s12249-018-1196-8.

(247) Ha, E. S.; Kuk, D. H.; Kim, J. S.; Kim, M. S. Solubility of Trans-Resveratrol in Transcutol HP + Water Mixtures at Different Temperatures and Its Application to Fabrication of Nanosuspensions. *J. Mol. Liq.* **2019**, *281*, 344–351. https://doi.org/10.1016/j.molliq.2019.02.104.

(248) Siddalingam, R.; Chidambaram, K. Topical Nano-Delivery of 5-Fluorouracil : Preparation and Characterization of Water-in-Oil Nanoemulsion. *Trop. J. Pharm. Res.* **2016**, *15* (November), 2311–2319.

(249) Kadry, H.; Al-Hilal, T. A.; Keshavarz, A.; Alam, F.; Xu, C.; Joy, A.; Ahsan, F. Multi-Purposable Filaments of HPMC for 3D Printing of Medications with Tailored Drug Release and Timed-Absorption. *Int. J. Pharm.* **2018**, *544* (1), 285–296. https://doi.org/10.1016/j.ijpharm.2018.04.010.

(250) Khizer, Z.; Akram, M. R.; Sarfraz, R. M.; Nirwan, J. S.; Farhaj, S.; Yousaf, M.; Hussain, T.; Lou, S.; Timmins, P.; Conway, B. R.; et al. Plasticiser-Free 3D Printed Hydrophilic Matrices: Quantitative 3d Surface Texture, Mechanical, Swelling, Erosion, Drug Release and Pharmacokinetic Studies. *Polymers (Basel).* **2019**, *11* (7). https://doi.org/10.3390/polym11071095.

(251) Ramukutty, S.; Ramachandran, E. Growth, Spectral and Thermal Studies of Ibuprofen Crystals. *Cryst. Res. Technol.* **2012**, *47* (1), 31–38. https://doi.org/10.1002/crat.201100394.

(252) Solanki, N. G.; Tahsin, M.; Shah, A. V.; Serajuddin, A. T. M. Formulation of 3D Printed Tablet for Rapid Drug Release by Fused Deposition Modeling: Screening Polymers for Drug Release, Drug-Polymer Miscibility and Printability. *J. Pharm. Sci.* **2018**, *107* (1), 390–401. https://doi.org/10.1016/j.xphs.2017.10.021.

(253) Kempin, W.; Domsta, V.; Grathoff, G.; Brecht, I.; Semmling, B.; Tillmann, S.; Weitschies, W.; Seidlitz, A. Immediate Release 3D-Printed Tablets Produced Via Fused Deposition Modeling of a Thermo-Sensitive Drug. *Pharm. Res.* **2018**, *35* (6). https://doi.org/10.1007/s11095-018-2405-6.

(254) Yu, D. G.; Branford-White, C.; Ma, Z. H.; Zhu, L. M.; Li, X. Y.; Yang, X. L. Novel Drug Delivery Devices for Providing Linear Release Profiles Fabricated by 3DP. *Int. J. Pharm.* **2009**, *370* (1–2), 160–166. https://doi.org/10.1016/j.ijpharm.2008.12.008.

(255) Jamróz, W.; Szafraniec, J.; Kurek, M.; Jachowicz, R. 3D Printing in Pharmaceutical and Medical Applications. *Pharm. Res.* **2018**, *35*, 176. https://doi.org/10.1007/s11095-018-2454-x.

(256) Chen, D.; Xu, X. Y.; Li, R.; Zang, G. A.; Zhang, Y.; Wang, M. R.; Xiong, M. F.; Xu, J. R.; Wang, T.; Fu, H.; et al. Preparation and In Vitro Evaluation of FDM 3D-Printed Ellipsoid-Shaped Gastric Floating Tablets with Low Infill Percentages. *AAPS PharmSciTech* **2020**, *21*, 6. https://doi.org/10.1208/s12249-019-1521-x.

(257) Krause, J.; Bogdahn, M.; Schneider, F.; Koziolek, M.; Weitschies, W. Design and Characterization of a Novel 3D Printed Pressure-Controlled Drug Delivery System. *Eur. J. Pharm. Sci.* **2019**, *140* (September 2018), 105060. https://doi.org/10.1016/j.ejps.2019.105060.

(258) Huang, S.; O'Donnell, K. P.; Keen, J. M.; Rickard, M. A.; McGinity, J. W.; Williams, R. O. A New Extrudable Form of Hypromellose: AFFINISOL™

HPMC HME. *AAPS PharmSciTech* **2016**, *17* (1), 106–119. https://doi.org/10.1208/s12249-015-0395-9.

(259) Kollamaram, G.; Croker, D. M.; Walker, G. M.; Goyanes, A.; Basit, A. W.; Gaisford, S. Low Temperature Fused Deposition Modeling (FDM) 3D Printing of Thermolabile Drugs. *Int. J. Pharm.* **2018**, *545* (1–2), 144–152. https://doi.org/10.1016/j.ijpharm.2018.04.055.

(260) Rowe, R. C. The Effect of the Molecular Weight of Ethyl Cellulose on the Drug Release Properties of Mixed Films of Ethyl Cellulose and Hydroxypropyl Methylcellulose. *Int. J. Pharm.* **1986**, *29* (1), 37–41. https://doi.org/10.1016/0378-5173(86)90197-3.

(261) Yousif, S. M.; Al-Marzouqi, A. H. Microencapsulation of Ibuprofen into Polyvinylpyrrolidone Using Supercritical Fluid Technology. *J. Chem. Eng. Process Technol.* **2016**, *07* (04). https://doi.org/10.4172/2157-7048.1000306.

(262) Piccinni, P.; Tian, Y.; Mcnaughton, A.; Fraser, J.; Brown, S.; Jones, D. S. Solubility Parameter-Based Screening Methods for Early- Stage Formulation Development of Itraconazole Amorphous Solid Dispersions. *J. Pharm. Pharmacol.* **2016**, *68*, 705–720. https://doi.org/10.1111/jphp.12491.

(263) Mallick, S.; Pattnaik, S.; Swain, K.; De, P. K.; Saha, A.; Mazumdar, P.; Ghoshal, G. Physicochemical Characterization of Interaction of Ibuprofen by Solid-State Milling with Aluminum Hydroxide. *Drug Dev. Ind. Pharm.* **2008**, *34*, 726–734. https://doi.org/10.1080/03639040801901868.

(264) Chai, X.; Chai, H.; Wang, X.; Yang, J.; Li, J.; Zhao, Y.; Cai, W.; Tao, T.; Xiang, X. Fused Deposition Modeling (FDM) 3D Printed Tablets for Intragastric Floating Delivery of Domperidone. *Sci. Rep.* **2017**, *7* (1), 1–9. https://doi.org/10.1038/s41598-017-03097-x.

(265) Crowley, M. M.; Schroeder, B.; Fredersdorf, A.; Obara, S.; Talarico, M.; Kucera, S.; McGinity, J. W. Physicochemical Properties and Mechanism of Drug Release from Ethyl Cellulose Matrix Tablets Prepared by Direct Compression and Hot-Melt Extrusion. *Int. J. Pharm.* **2004**, *269* (2), 509–

522. https://doi.org/10.1016/j.ijpharm.2003.09.037.

(266) Kumar, M. V.; Balasubramanian, V.; Rao, A. G. Hot Tensile Properties and Strain Hardening Behaviour of Super 304HCu Stainless Steel. *J. Mater. Res. Technol.* **2017**, *6* (2), 116–122. https://doi.org/10.1016/j.jmrt.2016.05.004.

(267) Afrin, N.; Chen, D. L.; Cao, X.; Jahazi, M. Strain Hardening Behavior of a Friction Stir Welded Magnesium Alloy. *Scr. Mater.* **2007**, *57* (11), 1004–1007. https://doi.org/10.1016/j.scriptamat.2007.08.001.

(268) Jin, H.; Gallerneault, M.; Lloyd, D. J. Low Work Hardening and Its Mitigation in Ultra-Fine Grained Aluminum Alloys. In *ICAA13*; Weiland, H., Rollett, A. D., Cassada, W. A., Eds.; Springer, Cham: Pittsburgh, 2012; pp 1741–1742. https://doi.org/10.1007/978-3-319-48761-8_260.

(269) Gao, G.; Zhang, H.; Gui, X.; Tan, Z.; Bai, B.; Weng, Y. Enhanced Strain Hardening Capacity in a Lean Alloy Steel Treated by a " Disturbed " Bainitic Austempering Process. *Acta Mater.* **2015**, *101*, 31–39. https://doi.org/10.1016/j.actamat.2015.08.071.

(270) Ma, D.; Djemai, A.; Gendron, C. M.; Xi, H.; Smith, M.; Kogan, J.; Li, L. Development of a HPMC-Based Controlled Release Formulation with Hot Melt Extrusion (HME). *Drug Dev. Ind. Pharm.* **2013**, *39* (7), 1070–1083. https://doi.org/10.3109/03639045.2012.702350.

(271) Zhu, Y.; Shah, N. H.; Waseem Malick, A.; Infeld, M. H.; Mcginity, J. W. Controlled Release of a Poorly Water-Soluble Drug from Hot-Melt Extrudates Containing Acrylic Polymers. *Drug Dev. Ind. Pharm.* **2006**, *32* (5), 569–583. https://doi.org/10.1080/03639040500528996.

(272) The Dow Chemical Company. *Chemistry of METHOCEL™ Cellulose Ethers-A Technical Review*; 2013.

(273) Elbadawi, M.; Muñiz, B.; Gavins, F. K. H.; Jie, J.; Gaisford, S.; Pérez, G.; Basit, A. W.; Cabalar, P.; Goyanes, A. M3DISEEN : A Novel Machine Learning Approach for Predicting the 3D Printability of Medicines. *Int. J. Pharm.* **2020**, *590*, 119837. https://doi.org/10.1016/j.ijpharm.2020.119837.

(274) Fina, F.; Goyanes, A.; Rowland, M.; Gaisford, S.; Basit, A. W. 3D Printing of Tunable Zero-Order Release Printlets. *Polymers (Basel).* **2020**, *12*, 1769. https://doi.org/10.3390/polym12081769.

(275) Nukala, P. K.; Palekar, S.; Patki, M.; Patel, K. Abuse Deterrent Immediate Release Egg-Shaped Tablet (Egglets) Using 3D Printing Technology : Quality by Design to Optimize Drug Release and Extraction. *AAPS PharmSciTech* **2019**, *20*, 80. https://doi.org/10.1208/s12249-019-1298-y.

(276) Tan, D. K.; Maniruzzaman, M.; Nokhodchi, A. Development and Optimisation of Novel Polymeric Compositions for Sustained Release Theophylline. *Polymers (Basel).* **2020**, *12*, 27. https://doi.org/10.3390/polym12010027.

(277) Gioumouxouzis, C. I.; Tzimtzimis, E.; Katsamenis, O. L.; Dourou, A.; Markopoulou, C.; Bouropoulos, N.; Tzetzis, D.; Fatouros, D. G. Fabrication of an Osmotic 3D Printed Solid Dosage Form for Controlled Release of Active Pharmaceutical Ingredients. *Eur. J. Pharm. Sci.* **2020**, *143*, 105176. https://doi.org/10.1016/j.ejps.2019.105176.

(278) Vo, A. Q.; Zhang, J.; Nyavanandi, D.; Bandari, S.; Repka, M. A. Hot Melt Extrusion Paired Fused Deposition Modeling 3D Printing to Develop Hydroxypropyl Cellulose Based Fl Oating Tablets of Cinnarizine. *Carbohydr. Polym.* **2020**, *246*, 116519. https://doi.org/10.1016/j.carbpol.2020.116519.

(279) Pereira, B. C.; Isreb, A.; Forbes, R. T.; Dores, F.; Habashy, R.; Petit, J.-B.; Alhnan, M. A.; Oga, E. F. ‘ Temporary Plasticiser ’: A Novel Solution to Fabricate 3D Printed Patient- Centred Cardiovascular ‘ Polypill ’ Architectures. *Eur. J. Pharm. Biopharm.* **2019**, *135*, 94–103. https://doi.org/10.1016/j.ejpb.2018.12.009.

(280) Lamichhane, S.; Park, J. B.; Sohn, D. H.; Lee, S. Customized Novel Design of 3D Printed Pregabalin Tablets for Intra-Gastric Floating and Controlled Release Using Fused Deposition Modeling. *Pharmaceutics* **2019**, *11* (11). https://doi.org/10.3390/pharmaceutics11110564.

(281) Gupta, S. S.; Solanki, N.; Serajuddin, A. T. M. Investigation of Thermal

and Viscoelastic Properties of Polymers Relevant to Hot Melt Extrusion, IV: Affinisol™ HPMC HME Polymers. *AAPS PharmSciTech* **2016**, *17* (1), 148–157. https://doi.org/10.1208/s12249-015-0426-6.

(282) Khan, K. A. The Concept of Dissolution Efficiency. *J. Pharm. Pharmacol.* **1975**, *27* (1), 48–49. https://doi.org/10.1111/j.2042-7158.1975.tb09378.x.

(283) Lu, Y.; Lin, P.; Huang, P.; Kuo, C.; Shalumon, K. T.; Chen, M.; Chen, J. Magnetic Graphene Oxide for Dual Targeted Delivery of Doxorubicin and Photothermal Therapy. *Nanomaterials* **2018**, *8*, 193. https://doi.org/10.3390/nano8040193.

Appendix

pharmaceutics

MDPI

Communication

Drop-On-Powder 3D Printing of Tablets with an Anti-Cancer Drug, 5-Fluorouracil

Kejing Shi [1], Deck K. Tan [1], Ali Nokhodchi [1,2,*] and Mohammed Maniruzzaman [1,*]

[1] School of Life Sciences, University of Sussex, Falmer, Brighton BN1 9QJ, UK; K.Shi@sussex.ac.uk (K.S.); D.Tan@sussex.ac.uk (D.K.T.)

[2] Drug Applied Research Center and Faculty of Pharmacy, Tabriz University of Medical Sciences, 5166/15731 Tabriz, Iran

* Correspondence: A.Nokhodchi@sussex.ac.uk (A.N.); M.Maniruzzaman@sussex.ac.uk or M.Maniruzzaman12@gmail.com (M.M.); Tel.: +441273872811 (A.N.); +441273877639 (M.M.)

Received: 12 February 2019; Accepted: 27 March 2019; Published: 1 April 2019

Abstract: This study reports the first case of an innovative drop-on-powder (DoP) three-dimensional (3D) printing technology to produce oral tablets (diameters of 10 mm and 13 mm) loaded with an anticancer model drug, 5-fluorouracil (FLU). For this study, a composition of the powder carrier containing $CaSO_4$ hydrates, vinyl polymer, and carbohydrate was used as the matrix former, whereas 2-pyrrolidone with a viscosity like water was used as a binding liquid or inkjet ink. All tablets were printed using a commercial ZCorp 3D printer with modification. The resultant tablets were subject to coating with various polymeric solutions containing the drug. The composition of the polymeric solutions was adjusted at drug: polymer(s) 1:1 (*w*/*w*) ratio. Either Soluplus® (SOL) alone or in combination with polyethylene glycol (PEG) was used to develop the coating solution of 2.5% (*w*/*v*) concentration. The particle size analysis, flow test, and particle morphology studies revealed mono-modal narrow size distribution, good flow properties, and porous loosely bound texture (of the tablets), respectively. Moreover, the advanced application of the fluorescence microscopy showed a homogenous distribution of the drug throughout the surface of the 3D printed tablets. The *in vitro* dissolution studies showed that the tablet compositions, dimensions, and the coating solution compositions influenced the release of the drug from the tablets. It can be concluded that our innovative DoP 3D printing technology can be used to fabricate personalized dosage forms containing optimized drug content with high accuracy and shape fidelity. This is particularly suitable for those drugs that are highly unstable in thermal processing and cannot withstand the heat treatment, such as in fused deposition modeling (FDM) 3D printing.

Keywords: 3D printing; drop-on-powder; powder-based 3D printing; personalized medicine; 5-fluorouracil; Soluplus

1. Introduction

Three-dimensional (3D) printing is an additive manufacturing technique, which is different from traditional machining techniques and has attracted a growing interest in rapid prototyping [1]. One of its major advantages is that it can fabricate complicated shapes and geometrics with higher possible shape fidelity and accuracy than the traditional fabrication techniques [2]. Nowadays, 3D printing is employed in medical devices, implants, tissue regeneration, pharmaceutical dosage form, and personalized medicine.

Powder-based (PB) 3D printing technology, also known as drop-on-powder (DoP) or binder jetting, was developed by the Massachusetts Institute of Technology (MIT) in the 1980s and was commercialized by Z-Corporation for producing different 3D printers [3]. It is regarded as the

first technological adaption of 3D printing for pharmaceutical demands [2]. This process utilizes an ink-jet head that can jet-dispense a liquid binder solution onto a flattened powder bed. Then, particles of the powder carrier can be adhered together by organic or inorganic binders to form an agglomerated object because of adhesive forces or a hydraulic cement setting reaction [4]. In this event, the final 3D objects with desired geometry are created by stacking agglomerated layers in sequence. As a result, the produced oral dosage forms, such as tablets, are similar to fast-disintegrating tablets because they are comprised mainly of powder with loosely bound particles. Although there are many different 3D printing techniques suitable for pharmaceutical applications, the first Food and Drug Administration (FDA) approved 3D printed medicine (Spritam®) was developed through TheriForm® technology, which is originally derived from a PB 3D printing technique [5]. Due to the printing nature, formulations, and process optimization, a 3D printed levetiracetam tablet has a highly porous internal environment and micron-scale pore size that can dramatically increase surface area, hence the ultra-rapid drug dissolution and release after oral administration [6].

Because of the benefits of its pharmaceutical application, such as easy adaptation and fixation, reduced development time, and favorable aesthetic results, DoP 3D printing technology can be better adapted to the manufacturing of dosage forms when compared to other 3D printing technology (i.e., fused deposition modeling (FDM)). One of the main reasons for this is that the starting materials (such as powders and binder solutions) have already been widely used in the pharmaceutical industry. However, there are some associated challenges, such as the additional drying process to eradicate residual solvents and to improve the physical resistance of the PB 3D printed constructs [2,7]. Still, it has immediate potential for unit dose fabrication. Moreover, with an appropriate process engineering and optimization, this possibly can be one of the first 3D printing processes suitable for fully scalable commercial exploitation.

Therefore, we report a first case of a DoP 3D printing process to develop anti-cancer drug loaded tablets with varying diameters (10 mm and 13 mm). We used 5-fluorouracil (FLU) as a model drug to prove the concept of our printing process. This model drug is highly potent and available in low dosage. Though FLU is fairly heat stable, the successful optimization and subsequent development of its tablets using DoP heat-less 3D printing will provide for an ideal platform to process and evaluate many other model drugs that are highly thermo-sensitive, such as biologics or macromolecules. Optimized powder carrier containing $CaSO_4$ hydrates were used as powder bed materials. The drug solution compositions were optimized using hydrophilic polymer combinations. This study proves that an optimized powder based 3D printing can also be used to develop pharmaceutical products using pharmaceutical grade excipients by eliminating the need for thermal processing. The latter can be a real issue for processing thermo-sensitive drugs. In addition, DoP is much easier and less time consuming than making filaments then using that filaments to fabricate tablets, as is the case in the FDM 3D printing.

2. Experimental Section

2.1. Materials

The model anticancer drug FLU with purity >98% was purchased from Hangzhou Longshine Bio-tech Co., Ltd. (Hangzhou, China). The printing $CaSO_4$ powder was obtained from EMCO Education Ltd. (Portsmouth, UK). Soluplus® was kindly donated by BASF, Germany. Polyethylene glycol (PEG) was procured from Sigma Aldrich (Gillingham, UK). All chemicals used were of analytical grade and used as received.

2.2. Experimental Methods

The tablets with diameters of 10 mm and 13 mm were printed using a ZCorp printer (Z-Corporation, Rock Hill, SC, USA) with a print layer thickness of ~100 µm. The tablet matrix was composed of a $CaSO_4$ based powder, which was a mixture of CaSO4 (<90%) and vinyl polymer (<20%)

with carbohydrate (<10%), whereas the liquid binding solution was an aqueous solution containing 2-pyrrolidinone, whose viscosity is similar to water. The approximate average weights of printed tablets with diameters of 13 mm were ~900 mg, and those with diameters of 10 mm were ~400 mg with an average thickness of 5 mm and 3 mm, respectively. The printing process only took <5 min for one tablet. The physical properties of the powder are listed in Table 1. The printing parameters such as binder volume, jet-dispensing speed, and drops fired were optimized and recorded throughout the printing process. The print head operated at a maximum temperature of 50 °C with a maximum current of 1.7 A and a fire voltage of 0.5 V, which was found to be optimal for the successful and smooth printing of the tablets. An AutoCAD design of the tablets was made using Solidworks (2017 SP5, Waltham, MA, USA) and transferred to the computer connected with the printer in stereolithographic (stl) file format prior to the actual printing process. The optimized composition of the pharmaceutical grade carrier powder utilized in the 3D printing process contained $CaSO_4$ hydrates (<90% *w*/*w*) and vinyl polymer. After the printing process was finished, all tablets were subject to a quick drying in the build box before being removed from the powder bed. This drying process was conducted to ensure that the printed tablets were robust enough to withstand the handling process and that any redundant powders were removed easily after the cycle. Since the aim of this study was to prove the concept of DoP printing for the fabrication of anti-cancer drug loaded tablets, only the powder suitable for printing with Z-Corp (e.g., $CaSO_4$) was used herein. This also eliminated any possibility for the intrusion of the performance and/or safety of the printer. Therefore, the incorporation of the drug in the tablet matrix was not performed at this stage. The coating aqueous solutions containing the drug FLU was optimized using hydrophilic polymers SOL and PEG. Various compositions were prepared as depicted in Table 2. The coating of the 3D printed tablets was performed using the drop-on-demand technique via utilizing micro-pipette and depositing the solution onto the surface of the tablet until a homogenous coating was achieved. As mentioned earlier, for the purpose of this proof of concept study, no additional materials except the suitable carrier powders were used in the printer. For this reason, the drug was added to the printed tablets by coating method.

Table 1. Properties of the powders used for printing matrices.

Printing Powder Carrier Properties				
Viscosity(cP_0)	**Flowability**		**Bulk Density (g/cm^3)**	**$D_{50\%}$, $D_{90\%}$ (μm)**
	Carr's Index	**Angle of Repose**		
220.8 (Torque: 18.4% Speed: 5.00 rpm)	25	22.05°	1.172	42.32, 80.12

Table 2. Drug coating solution compositions.

Tablets	Excipients	Solution A	Solution B	Solution C
Tablet (batch 1) (Diameter = 10 mm)	5-fluorouracil (mg)	2.5	2.5	2.5
	Soluplus (mg)	2.5	1.25	0
	Polyethylene glycol (PEG) (mg)	0	1.25	0
Tablet (Batch 2) (Diameter = 13 mm)	5-fluorouracil (mg)	5	5	5
	Soluplus (mg)	5	2.5	0
	PEG (mg)	0	2.5	0

Briefly, around 0.1 and 0.2 mL of the drug solution were dropped manually onto the surface of tablets (diameters of 10 mm and 13 mm) separately by using 20–200 μL Research® plus pipette (Eppendorf Ltd, Stevenage, UK). After that, the tablet samples were put into the oven at 50 °C for 1 h. The drying process was finished until the weight of tablets would not decrease.

The geometric primary particle size distribution of the printing powder was measured with a laser light diffraction analyzer (Helos/Rodos, Sympatec GmbH, Clausthal-Zellerfeld, Germany) equipped with the HELOS sensor and Windox software (version 5, Sympatec, Clausthal-Zellerfeld,

Germany). Detection of the particles was carried out using the R3 and R5 lenses with the detection range of 0.5–175 µm and 0.5–875 µm, respectively. The surface morphology of the printed tablets was examined by Jeol JMS 820 (Freising, Munich, Germany) at the accelerating voltage of 3 kV. The samples were mounted on an aluminum stub using adhesive carbon tape and were sputter coated with gold under vacuum (Edwards S-150 sputter coater, Edwards High Vacuum Co. International, Albany, NY, USA). As fluorescence and UV-Vis irradiation are important photo-physical properties of FLU, the homogeneity of FLU on the surface of 3D-printed tablets was checked with an SP8 confocal microscope (Leica, Microsystems (UK) Ltd., Milton Keynes, UK). Also, the 3D-printed tablet without the drug solution was analyzed for a negative control. *In vitro* dissolution tests under sink conditions were performed with a US Pharmacopeia (USP) type II paddle apparatus (708-DS Dissolution Apparatus, Agilent Technologies, Santa Clara, CA, USA) in 900 mL of phosphate-buffered saline (PBS) (pH 6.8) at 37 ± 0.3 °C with a paddle speed of 100 rpm. All samples were run in triplicate (n = 3). The drug concentration of the dissolution medium was measured automatically by using Cary 60 UV-Vis (Agilent Technologies) at a wavelength of 265 nm in a 1 cm cell versus a blank solution consisting of a phosphate buffer (pH 6.8). Then, the release profiles were plotted as a percentage of cumulative drug release versus time. Additionally, there was no interference from Soluplus® or PEG6000 on drug assay observed at the detection wavelength.

3. Results and Discussion

The powder-based 3D printing platform used the maximum layer resolution in accordance with the slicing fragments counted, which resulted in the estimated time for the printing of the whole series of the tablets at about 15–20 min (single tablet ~5 min). An interesting feature of this platform is that once the ideal formulation compositions and the processing parameters are optimized, this can be fairly scaled up for pilot scale manufacturing making it commercially viable process. The jet-dispensing rate plays a pivotal role in the texture and binding properties of the particles with the printed 3D objects (Figure 1). Our printing process was optimized so that all printed tablets were almost instantly ready for further evaluation, though an optional drying step can be introduced to produce tablets as robust as possible to withstand the handling process. This eliminates the wait-time for the eradication of the residual solvent. The process utilized an aqueous solution of 2-pyrrolidone, which is largely available in various pharmaceutical formulations [8]. The use of this binding liquid assisted in a smooth and faster printing process without any further post-processing steps. It has been reported that 2-pyrrolidone is an acceptable solvent to be used in drug delivery systems for humans. It is also widely present in foodstuffs and food additives [8].

The carrier powder was composed of pharmaceutical grade $CaSO_4$ granules, vinyl polymer, and carbohydrate with narrow particle size distribution. The particle size and shape of active and non-active pharmaceutical ingredients in most pharmaceutical products can affect various significant physical properties and quality attributes, such as physicochemical stability and dissolution rate [9]. In Figure 2b, as the mode average diameter according to the peak is around ~50 µm, the flowability of these particles may just be at the threshold of good flow. This can sometimes result in incomplete layers appearing during the printing process [5]. However, in our process, despite the moderate to poor flowability and because of the process optimization and engineering, various tablets with high accuracy and shape fidelity were still printed successfully.

The mean particle size distribution was found to be in the range of about 41.65–54.44 µm ($D_{50\%}$) with a volume mean diameter (VMD) of 41.46 µm (Figure 2b). The powder flowability test via both Carr's index and angle of repose estimation for formulation powders exhibited good flow properties. This is reflected on the calculated values of the Carr's index and angle of repose as 25 and 22.02 degrees, respectively. Moreover, the calculated bulk index value of the powder indicates that it rendered good compatibility as well (Table 1). It has been reported that the particle morphology of $CaSO_4$ hydrates based powder is good for high-performance composite material for strong, accurate, and high-definition model making. In an optimized process, by simply spraying the suitable binding

solution, this calcium sulfate hemihydrate ($CaSO_4 + nH_2O$) powder undergoes a self-hydration process, resulting in a semi-solid calcium plaster-like paste ($CaSO_4 \cdot \frac{1}{2}H_2O + 1\frac{1}{2}H_2O = CaSO_4 \cdot 2H_2O$) [4,10]. This process was adopted and repeated for each depositing layers in sequence until the 3D object was printed herein. As shown in Figure 2a, the tablets with various shape fidelity and dimensions were printed with high accuracy, uniformity, and reproducibility.

The surface morphology of the printed tablets examined via SEM is depicted in Figure 3. It is obvious from the SEM images that all printed tablets had a highly porous surface with matrix forming particles loosely bound with the binding liquid. This can be ideal for the formulation of fast disintegrating dosage forms, such as orally disintegrating tablets (ODTs). All of the tablet formulations exhibited micron-scale interconnected pore size. A high-resolution SEM image revealed the pore diameter in the region of about ~90 µm (Figure 3f). As a result, upon contact with an aqueous medium such as a dissolution solution, the surface area could be increased significantly, resulting in faster dissolution of the drug from the tablets.

The model anti-cancer drug, FLU, is sparingly soluble in water and slightly soluble in ethanol [11]. However, the solubility of FLU can be affected significantly by temperature, and it can be increased more than 12-fold by enhancing the temperature between 25 and 200 °C under a constant pressure of 5.1 MPa [12]. Additionally, Singh et al. pointed out that FLU has high thermal stability when the temperature is less than 278 °C [13]. Having considered this property, during the preparation of the drug-loaded coating solution, the temperature was increased to around 70 °C (i.e., in case of solution C (2.5% *w*/*v* FLU)) in order to increase the concentration of the drug in solution. As a result, the maximum concentration of the solution was optimized at 25 mg/mL.

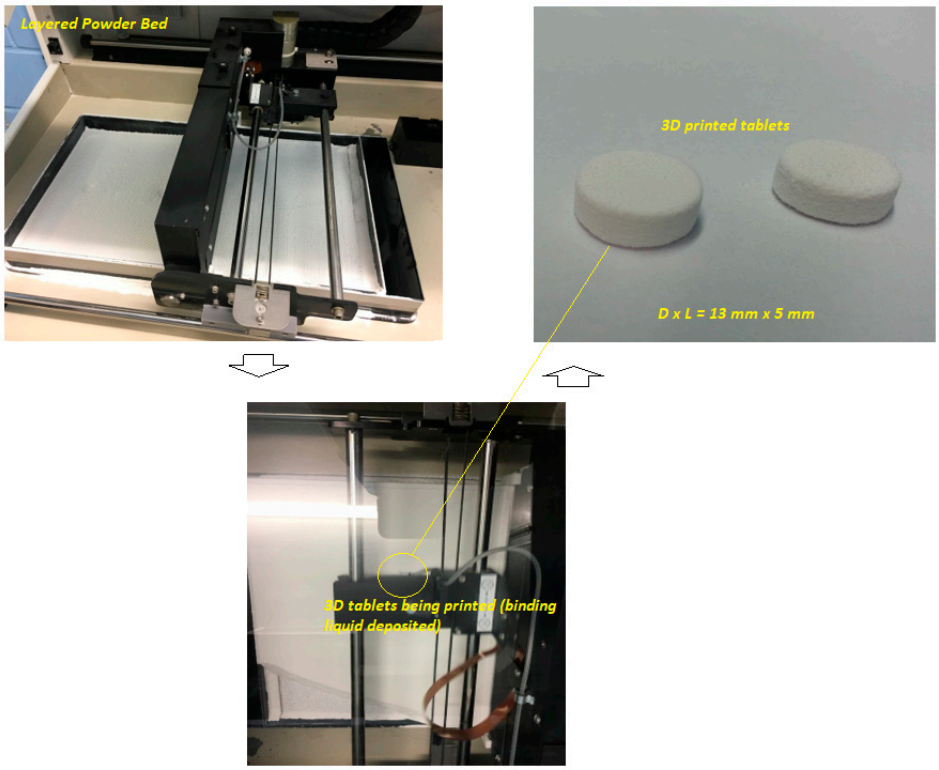

Figure 1. Schematic diagram of the printing process of drop-on-powder (DoP) three-dimensional (3D) printing process utilized in this study.

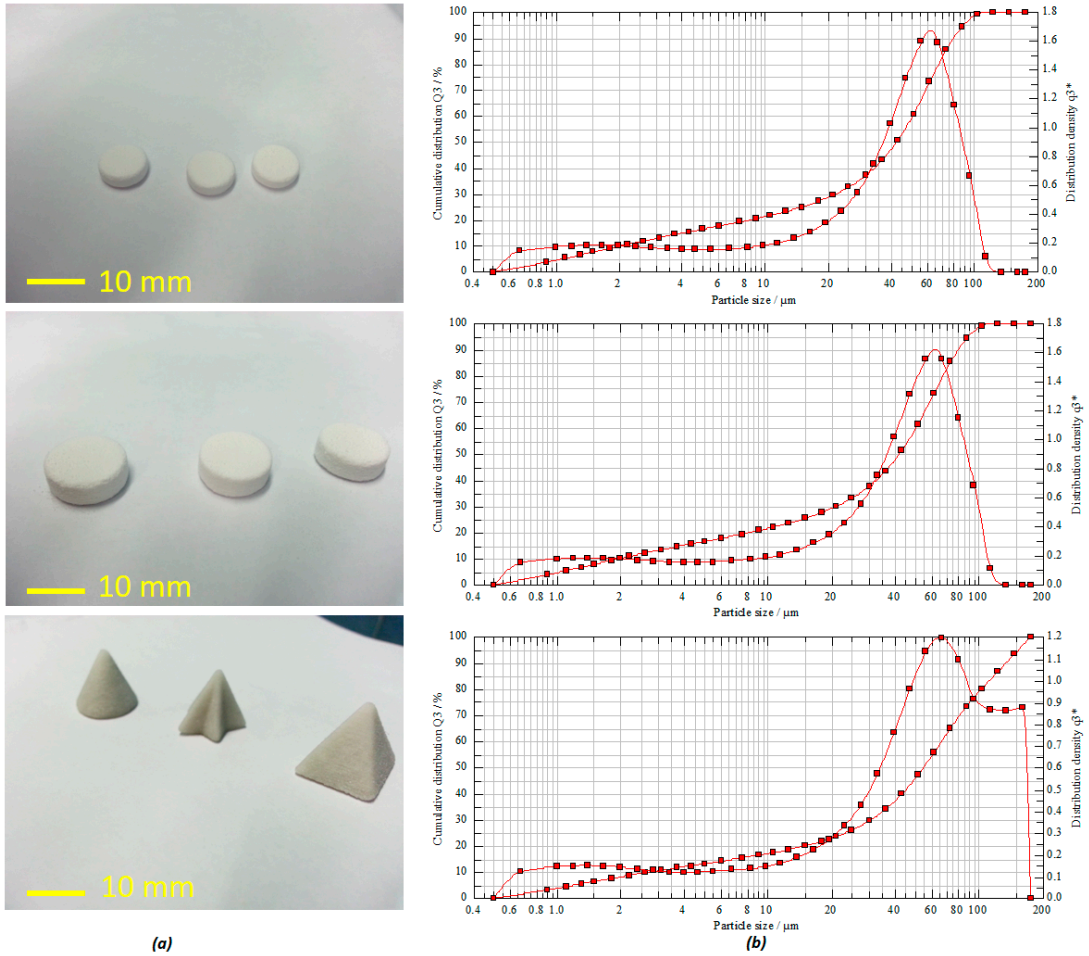

Figure 2. (**a**) 3D printed tablets with different shapes and dimensions; (**b**) volume-weighted particle size distribution (PSD) of the powder carriers used in the printing process.

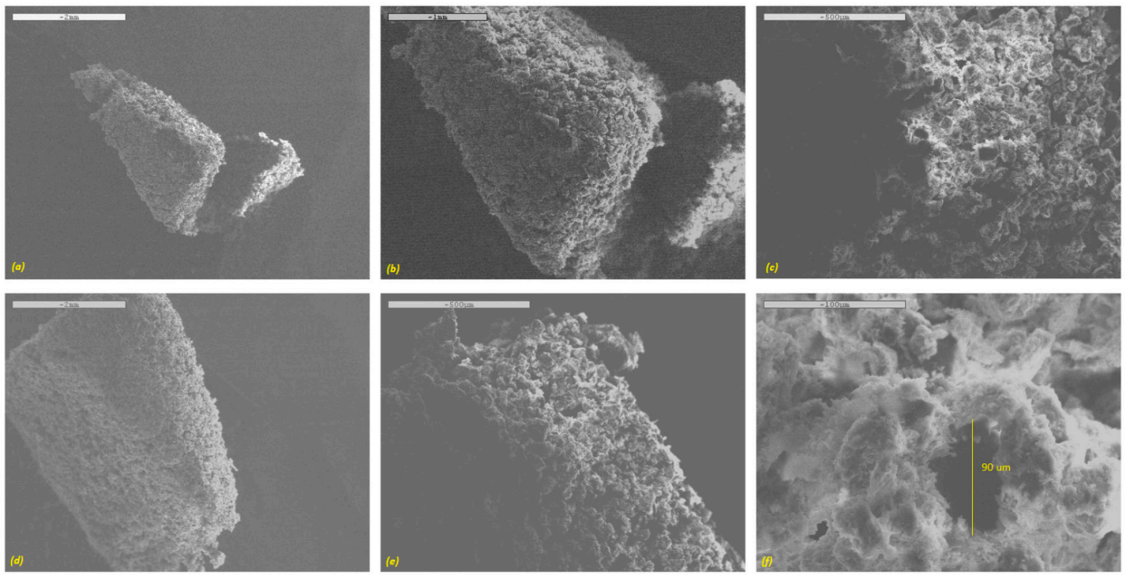

Figure 3. SEM images of the surface of DoP 3D printed tablets (**a**–**c**) 10 mm diameter and (**d**–**f**) 13 mm diameter.

Soluplus® (SOL) is a graft co-polymer of polyvinyl caprolactam (PVC)-polyvinyl acetate (PVA)-polyethylene glycol (PEG) that can help drug dispersed molecularly in its matrix in the preparation of solid dispersion. As a result, Thakral et al. proved Soluplus® can increase the water solubility of an anti-cancer drug with poor aqueous solubility—camptothecin—in a colon-targeted delivery system [14]. Their solid dispersion formulation of camptothecin in Soluplus® with citric acid had great potential for colorectal cancer therapy. Uddin et al. studied Soluplus® as a drug carrier and the coating formulations (consisting of drug-polymer solutions at various ratios) [15]. They found that Soluplus® helped the drug release for various anti-cancer substances (5-fluorouracil, curcumin, and cisplatin), especially for the water-insoluble drugs (curcumin and cisplatin) because of their solubilizing enhancement capacity. In addition, Homayouni et al. pointed out that this polymer can perform as a stabilizer and a solubilizing agent in poorly water-soluble drug formulation [16]. Because Soluplus® contains a polyethylene glycol backbone as the hydrophilic portion and vinyl caprolactam/vinyl acetate side chain as the lipophilic part, the significant amphipathic property gives it good surface activity, wettability, ability to enhance the aqueous solubility, and oral bioavailability [17,18]. As a result, all developed polymeric solutions (SOL alone or in combination with PEG) contained FLU dispersed homogeneously within the matrices.

In order to evaluate the homogeneity of the drug distribution upon depositing onto the formulated tablets, an advanced reverse optical microscopic analysis was conducted. As can be seen in Figure 4, an uncoated tablet without drug solution exhibited no fluorescence traces in the mapping image (Figure 4a). There were some bright green dots that may be attributed to some degree of contamination during the sample preparation or handling. These green dots were also present in the FLU loaded tablets, indicating that these are not relevant to the presence of the drug. It could also have been due to the presence of dust on the surface of the tablet. However, the images of tablets coated with drug solution showed significant differences compared to the tablet without drug solution. In contrast, the FLU loaded tablet surface showed a homogenous distribution of the drug throughout the surface of the tablets, represented by the dark green pattern. From these images, the edge of the tablet can be figured out easily. It can be concluded that the drug was coated homogeneously on the surface of these 3D printed tablets.

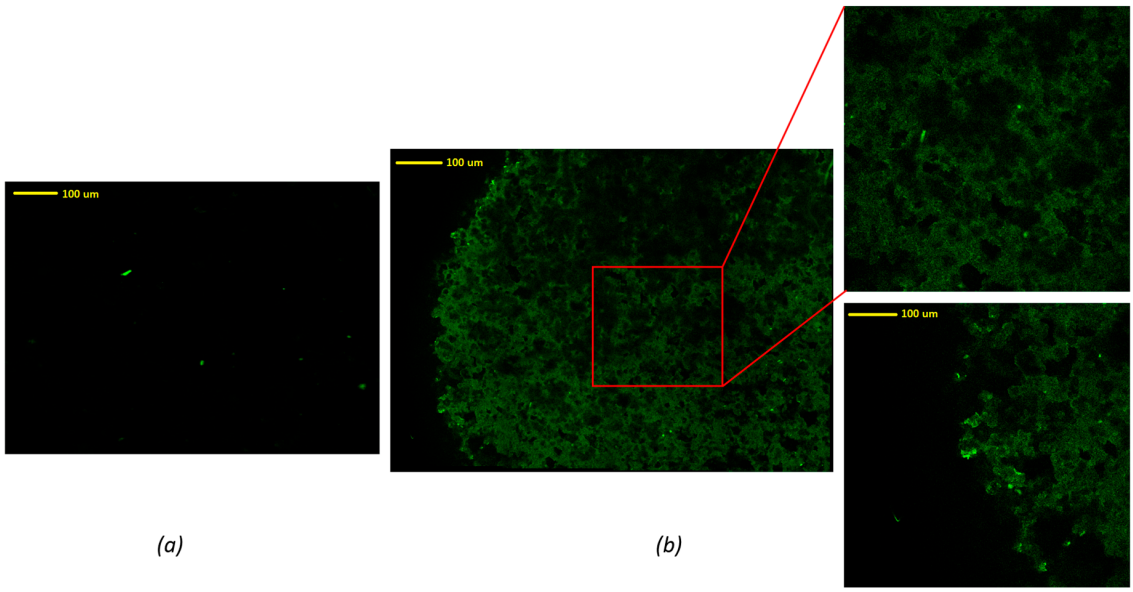

Figure 4. Confocal microscopic images of (**a**) tablets without drug solution, (**b**) tablets with drug solution C.

In vitro drug release profiles from both 10 mm and 13 mm tablets coated with FLU solution A, B, and C for 2 h are depicted in Figure 5. Tablets with a bigger diameter (13 mm) showed better dissolution behavior when compared with small tablets (Figure 5a). The probable reasons may have been the larger volume of 3D printed tablets for absorbing the drug solution and the larger surface area for partial hydration reaction in the dissolution media. The dissolution test was carried out for 6 h; as over 80% of the drug was released within the first 120 min, only data up to 120 min were picked up for further evaluations. The aim of the current research was not to show sustained release behavior of printed tablets. Rather, it was to show that the drug release from printed tablets can be modified to reach the dissolution profile needed. Asadi-Eydivand et al. pointed out that calcium sulphate hydrated powder could absorb moisture from the environment [10]. The comparison graphs of solutions A, B, and C clearly illustrate that all these drug solution coated tablets showed a sustained release over 2 h. Tablets coated with solutions A and B showed slightly slower release compared to that of solution C, which contained only FLU. About 90% of the drug had been released from polymeric solutions, whereas the bulk FLU solution showed about 100% release in 2 h. The slight delay in the release of the drug from the polymeric solution could be attributed to the chemistry of amphiphilic polymer, Soluplus®. It has been reported that Soluplus® tends to retard the release of the sparingly water-soluble drug upon swelling in the dissolution media [19]. Comparing the dissolution profiles of the 13 mm and the 10 mm tablets coated by solution C showed that these dissolution profiles were different (f_2 value of 43; f_2 value (similarity test); less than 50 indicates that they are different). This indicates that the size of printed tablets has a significant effect on the dissolution profiles of FLU. Comparing the effect of the coating solution showed that the type of solution cannot make a big difference (similarity factor f_2 was higher than 50). Nonetheless, our developed formulation compositions (solutions A and B) could be ideal for prolonging the release of the drug for a longer time or sustained release drug delivery, as may be required for chemotherapeutic drug delivery systems.

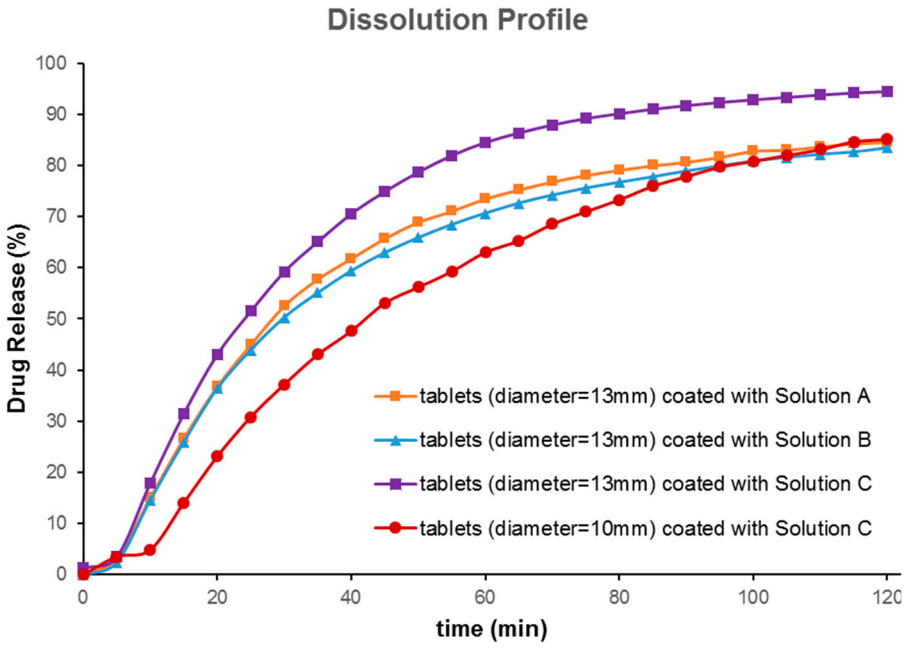

Figure 5. *In vitro* drug release profiles (under sink condition) of various printed tablets coated with solutions A, B, and C containing 5-fluorouracil (FLU) at pH 6.8 (n = 3).

4. Conclusions

The authors of the current research successfully demonstrated that an optimized DoP 3D printing process can be applied for the fabrication of oral dosage forms, such as tablets with varying shapes and morphology. A detailed investigation of the powder compositions revealed that the particle

morphology, flow, and compression properties play pivotal roles in powder based printing processes. The produced tablets were also coated with anticancer model drug solutions, where drug particles were seen homogenously dispersed throughout the surface of the printed tablets. Furthermore, it could be claimed that the DoP 3D printing process demonstrated here was able to adjust the dose, release rate, and loading of the drug substances by changing the formulation composition and the processing parameters. This method can be further scaled up for pilot scale manufacturing in the personalized medicines arena. In conclusion, it can be claimed that DoP 3D printing process reported herein can be exploited for a number of drugs, including thermolabile drugs, by optimizing the powder bed composition using pharmaceutical grade excipients such as polymers. This will indeed present this emerging technique at the forefront of additive manufacturing to the delivery of immediate potential for unit dose fabrication of personalized medicines.

Author Contributions: Conceptualization and planning, M.M.; methodology and experiments, K.S. and D.K.T.; software, D.K.T.; data analysis, K.S., D.K.T., M.M. and A.N.; writing—original draft preparation, K.S. and M.M.; writing—review and editing, M.M. and A.N.

Funding: This research received no external funding. The APC was funded by the authors' organization (University of Sussex, UK).

Conflicts of Interest: The authors declare no conflict of interest.

References

1. Moulton, S.E.; Wallace, G.G. 3-dimensional (3D) fabricated polymer based drug delivery systems. *J. Control. Release* **2014**, *193*, 27–34. [CrossRef] [PubMed]
2. Alhnan, M.A.; Okwuosa, T.C.; Sadia, M.; Wan, K.W.; Ahmed, W.; Arafat, B. Emergence of 3D Printed Dosage Forms: Opportunities and Challenges. *Pharm. Res.* **2016**, *33*, 1817–1832. [CrossRef] [PubMed]
3. Gharaie, S.H.; Morsi, Y.; Masood, S.H. Tensile properties of processed 3D printer ZP150 powder material. *Adv. Mater. Res.* **2013**, *699*, 813–816. [CrossRef]
4. Farzadi, A.; Solati-Hashjin, M.; Asadi-Eydivand, M.; Abu Osman, N.A. Effect of layer thickness and printing orientation on mechanical properties and dimensional accuracy of 3D printed porous samples for bone tissue engineering. *PLoS ONE* **2014**, *9*, e108252. [CrossRef] [PubMed]
5. Infanger, S.; Haemmerli, A.; Iliev, S.; Baier, A.; Stoyanov, E.; Quodbach, J. Powder bed 3D-printing of highly loaded drug delivery devices with hydroxypropyl cellulose as solid binder. *Int. J. Pharm.* **2018**, *555*, 198–206. [CrossRef] [PubMed]
6. Qi, S.; Craig, D. Recent developments in micro- and nanofabrication techniques for the preparation of amorphous pharmaceutical dosage forms. *Adv. Drug Deliv. Rev.* **2016**, *100*, 67–84. [CrossRef] [PubMed]
7. Maniruzzaman, M. (Ed.) *3D and 4D Printing Technology in Biomedical Applications: Process Engineering and Additive Manufacturing*; Wiley and Sons: Hoboken, NJ, USA, 2019; ISBN 978-3-527-34443-7.
8. Committee for Veterinary Medicinal Products: 2-Pyrrolidone—Summary Report. Available online: https://www.ema.europa.eu/documents/mrl-report/2-pyrrolidone-summary-report-committee-veterinary-medicinal-products_en.pdf. (accessed on 10 February 2019).
9. Shekunov, B.Y.; Chattopadhyay, P.; Tong, H.H.; Chow, A.W. Particle size analysis in pharmaceutics: principles, methods and applications. *Pharm. Res.* **2007**, *24*, 203–227. [CrossRef] [PubMed]
10. Asadi-Eydivand, M.; Solati-Hashjin, M.; Shafiei, S.S.; Mohammadi, S.; Hafezi, M.; Abu Osman, N.A. Structure, Properties, and In Vitro Behavior of Heat-Treated Calcium Sulfate Scaffolds Fabricated by 3D Printing. *PLoS ONE* **2016**, *11*, e0151216. [CrossRef] [PubMed]
11. Jeddipelly, S.R. Formulation and In-Vitro Evaluation of 5-Fluorouracil Microcapsules by Using Different Methods of Microencapsulation. Master's Thesis, The Tamil Nadu Dr. M.G.R. Medical University, Chennai, India, 2013.
12. Akay, S.; Kayan, B.; Yang, Y. Solubility and Chromatographic Separation of 5-Fluorouracil under Subcritical Water Conditions. *J. Chem. Eng. Data* **2017**, *62*, 1538–1543. [CrossRef]
13. Singh, P.; Tyagi, G.; Mehrotra, R.; Bakhshi, A.K. Thermal stability studies of 5-fluorouracil using diffuse reflectance infrared spectroscopy. *Drug Test. Anal.* **2003**, *1*, 240–244. [CrossRef] [PubMed]

14. Thakral, N.K.; Ray, A.R.; Bar-Shalom, D.; Eriksson, A.H.; Majumdar, D.K. Soluplus-solubilized citrated camptothecin–a potential drug delivery strategy in colon cancer. *AAPS PharmSciTech* **2012**, *13*, 59–66. [CrossRef] [PubMed]
15. Uddin, M.J.; Scoutaris, N.; Klepetsanis, P.; Chowdhry, B.; Prausnitz, M.R.; Douroumis, D. Inkjet printing of transdermal microneedles for the delivery of anticancer agents. *Int. J. Pharm.* **2015**, *494*, 593–602. [CrossRef] [PubMed]
16. Homayouni, A.; Sadeghi, F.; Varshosaz, J.; Garekani, H.F.; Nokhodchi, A. Promising dissolution enhancement effect of soluplus on crystallized celecoxib obtained through antisolvent precipitation and high pressure homogenization techniques. *Colloids Surf. B Biointerfaces* **2014**, *122*, 591–600. [CrossRef] [PubMed]
17. Yang, H.; Teng, F.; Wang, P.; Tian, B.; Lin, X.; Hu, X.; Zhang, L.; Zhang, K.; Zhang, Y.; Tang, X. Investigation of a nanosuspension stabilized by Soluplus(R) to improve bioavailability. *Int. J. Pharm.* **2014**, *477*, 88–95. [CrossRef] [PubMed]
18. Zeng, Y.C.; Li, S.; Liu, C.; Gong, T.; Sun, X.; Fu, Y.; Zhang, Z.R. Soluplus micelles for improving the oral bioavailability of scopoletin and their hypouricemic effect in vivo. *Acta Pharmacol. Sinica* **2017**, *38*, 424–433. [CrossRef] [PubMed]
19. Ayub, K.T.; Maniruzzaman, M.; Amin, P. Effect of melt extrudability and melt binding efficiency of polyvinyl caprolactam polyvinyl acetate polyethylene glycol graft copolymer (Soluplus®) on release pattern of hydrophilic and high dose drugs. *Mater. Sci. Eng. C* **2019**, *99*, 563–574. [CrossRef] [PubMed]

Colloids and Surfaces B: Biointerfaces 192 (2020) 111068

Contents lists available at ScienceDirect

Colloids and Surfaces B: Biointerfaces

journal homepage: www.elsevier.com/locate/colsurfb

Novel 3D printed device with integrated macroscale magnetic field triggerable anti-cancer drug delivery system

Kejing Shi[a], Rodrigo Aviles-Espinosa[b], Elizabeth Rendon-Morales[b], Lisa Woodbine[c], Mohammed Maniruzzaman[d,*], Ali Nokhodchi[a,*]

[a] Pharmaceutics Research Laboratory, School of Life Sciences, University of Sussex, Falmer, Brighton, BN1 9QJ, UK
[b] Robotics and Mechatronics Systems Research Centre, School of Engineering and Informatics, University of Sussex, Falmer, Brighton, BN1 9RH, UK
[c] Sussex Centre for Genome Damage and Stability, School of Life Sciences, University of Sussex, Falmer, Brighton, BN1 9RQ, UK
[d] Pharmaceutical Engineering and 3D Printing Lab, Division of Molecular Pharmaceutics and Drug Delivery, College of Pharmacy, The University of Texas at Austin, 2409 University Avenue, Austin, TX 78712, USA

ARTICLE INFO

Keywords:
3D printing
fused deposition modelling
FDM
magnetic field
polydimethylsiloxane sponge
triggerable drug delivery system
carbonyl iron
iron oxide
5-fluorouracil
personalized medicine

ABSTRACT

With the growing demand for personalized medicine and medical devices, the impact of on-demand triggerable (e.g., via magnetic fields) drug delivery systems increased significantly in recent years. The three-dimensional (3D) printing technology has already been applied in the development of personalized dosage forms because of its high-precision and accurate manufacturing ability. In this study, a novel magnetically triggerable drug delivery device composed of a magnetic polydimethylsiloxane (PDMS) sponge cylinder and a 3D printed reservoir was designed, fabricated and characterized. This system can realize a switch between "on" and "off" state easily through the application of different magnetic fields and from different directions. Active and repeatable control of the localized drug release could be achieved by the utilization of magnetic fields to this device due to the shrinking extent of the macro-porous magnetic sponge inside. The switching "on" state of drug-releasing could be realized by the magnetic bar contacted with the side part of the device because the times at which 50%, 80% and 90% (w/w) of the drug were dissolved are observed to be 20, 55 and 140 min, respectively. In contrast, the switching "off" state of drug-releasing could be realized by the magnetic bar placed at the bottom of the device as only 10% (w/w) of the drug could be released within 12 h. An anti-cancer substance, 5-fluorouracil (FLU), was used as the model drug to illustrate the drug release behaviour of the device under different strengths of magnetic fields applied. *In vitro* cell culture studies also demonstrated that the stronger the magnetic field applied, the higher the drug release from the deformed PDMS sponge cylinder and thus more obvious inhibition effects on Trex cell growth. All results confirmed that the device can provide a safe, long-term, triggerable and reutilizable way for localized disease treatment such as cancer.

1. Introduction

The objective of drug delivery systems is to provide predetermined drug release profiles ensuring optimal distribution and absorption of pharmaceutical compounds, which enhance therapeutic effectiveness and minimize side effects by offering a safer, more convenient, and efficient drug administration in humans with enhanced patient compliance [1,2]. Predetermined drug release profiles could be achieved by optimizing suitable drug delivery systems (DDSs) as such enhanced efficacy, safety, and patient compliance may be realized through optimal drug distribution and absorption in the targeted location at the (sub)cellular level [2,3]. However, it has been difficult for conventional drug delivery system to maintain drug concentration level within the narrow therapeutic concentration window for avoiding ineffectiveness (underdose) or toxicity (overdose), and it is often impossible to modify the drug release from these systems after administration [1,4,5]. Additionally, it may not always be appropriate for untunable monotonic drug release to be applied in some disease treatments which require variable release kinetics (including cancer, diabetes, pain, and myocardial infarction) [1,4]. Also, drugs are needed to be administered multiple times or continuously for achieving a long-acting drug release profile in some circumstances [4]. This may lead to patients' discomfort or inconvenience and even the addition of external devices. Therefore, it is important to design a drug delivery system, which can modulate drug release in terms of time, rate, and location. Such a drug delivery system would show considerable advances in delivering drugs, like

* Corresponding authors.
E-mail addresses: M.Maniruzzaman@austin.utexas.edu (M. Maniruzzaman), a.nokhodchi@sussex.ac.uk (A. Nokhodchi).

https://doi.org/10.1016/j.colsurfb.2020.111068
Received 18 February 2020; Received in revised form 11 April 2020; Accepted 18 April 2020
Available online 21 April 2020

painkillers, hormones, and chemotherapeutic agents [1].

Triggerable drug delivery systems (TDDSs), capable of releasing drug through applying external physical signals (such as magnetic field, ultrasound, pH, enzymes, temperature, electric, light, and near-infrared radiation) are gaining more and more attention in pharmaceutical sciences [1,6,7]. Such systems containing a large amount of drug can present remote, noninvasive, tunable, and reliable switching of therapeutic compound flux [4]. Hence, spatiotemporal management of drug availability could be realized through these triggerable drug delivery systems by the physicians or patients with the utilization of either the interaction between a 'responsive' material and the surrounding environment or a remotely controllable activation device [1,5,8]. Also, these systems loaded with a large amount of drug can achieve multiple dosing after a single administration through repeatable triggering [1]. However, there are still some limitations, like low controllability because of an initial burst release or a drug leakage via diffusion, difficulty in disposing of the systems after therapy, and increasing toxicity-associated risks due to the possible degradation of the matrix and the reduction of stability and reliability of the systems [1,5].

Implantable reservoir-based devices have been designed to overcome these limitations efficiently [9]. Targeted therapy could be achieved through these devices at different length scales with high anatomical variability [10]. The performing procedure and working environment will affect the features, sizes, and operation mechanisms significantly [5]. Herein, it is highly desirable to fabricate untethered macroscale triggerable drug delivery systems with low cost, simple preparation, facile operation, simplified structural morphology, and the ability to move through body channels and perform on-demand drug administration [5,11].

Although several external stimuli have been studied in TDDSs, controlled drug targeting through magnetic actuation is still one of the principal approaches because of many advantages, such as instantaneous and reversible response, remote actuation, non-destructive and high controllability, which are especially attractive for biomedical fabrication where the noncontact feature is particularly necessary *in vivo* environment with absolute safety [3,12,13]. Those magnetic systems also play an important role in cancer research due to the superior ability in chemotherapy by realizing: (1) selective delivery of the maximum fraction of anti-cancer molecules to the desired site without any increase in side effects to normal cells; (2) prior distribution of anti-cancer drug to targeted cells; (3) stable systemic drug concentration and (4) elimination of normal tissue clearance with the application of external magnetic field [3]. Various types of magnetic particles have been widely applied in these systems as switching carriers, including Fe_3O_4 particles [7,14], NdFeB powders [5] and carbonyl iron (CI) powders [12,13]. With the addition of magnetic enclosures, these magnetically responsive systems can move and deform due to applied magnetic fields [15]. Furthermore, with the manipulation of external permanent magnets, magnetically triggered drug delivery systems have the ability to remote locomotion through biological tissues in real-time because magnetic fields can transmit high force or torques wirelessly with multiple degrees of freedom to medical robots [5,16].

In recent years, personalized medicine has attracted increasing attention as it can provide patients with a superior treatment with a comprehensive consideration of their own pharmacogenomics, anatomical, and physical conditions [17]. It is reported that the inappropriate dosing or dosing combination has become the main reason for adverse effects from drug therapy [18]. This leads to an increased demand for a tailored method of dosage forms to suit patient needs instead of "One-size-fits-all" [18,19].

To address these challenges, three-dimensional printing (3DP) technology has been applied successfully because traditional DDSs cannot fulfil such criteria [17,19]. Because of its potential in personalized medicine, its applications in medical devices, implants, tissue engineering, and pharmaceutical dosage forms have attracted a great deal of attention [18]. This technology can achieve detailed and flexible spatial composition, and provide more available starting materials (like colloidal inks, bio-inks, and polymers) for the unprecedented complex and precise manufacture of 3D DDSs [2,20]. Various techniques, namely powder-based (PB), stereolithography (SLA), selective laser sintering (SLS), inkjet printing and fused deposition modelling (FDM) have been explored in the pharmaceutical applications [19]. Among them, FDM 3DP has gained the most attention due to its cost-effective, time-saving and versatile modalities of producing sophisticated solid objects [18,19].

Polylactic acid (PLA) is the most common material used for FDM because it is a non-toxic, renewable, thermoplastic, biodegradable and biocompatible polymer [20,21]. Additionally, its suitable properties like high mechanical strength, low coefficient of thermal expansion and processability for extrusion applications make this material ideal for pharmaceutical and biomedical applications [21]. Furthermore, various polymers, such as Pluronic, poly(vinyl alcohol) and polycaprolactone, could be blended with PLA to provide extra features with the addition of active pharmaceutical ingredients (APIs) to the final composite material in healthcare applications [20,21,22,23].

In this study, a magnetic-field triggerable drug delivery system with a 3D-printed reservoir and magnetic PDMS sponges was designed and characterized. This device can achieve highly precise and dynamic administration of drugs in an active and instant manner with only a permanent magnet.

2. Materials and Methods

2.1. Materials

A SYLGARD® 184 Silicone Elastomer prepolymer (Sylgard 184A, $M_w \approx 22\,000\ g{\cdot}mol^{-1}$) and the thermal curing agent (Sylgard 184B, $M_w \approx 15\,000\ g{\cdot}mol^{-1}$) were purchased from Dow Corning. Carbonyl iron (CI) powder with purity ≥ 97% was purchased from Sigma-Aldrich (Germany). The white granulated sugar was purchased from Sainsbury's (UK). The model anticancer drug 5-fluorouracil (FLU) with purity > 98% was purchased from Hangzhou Longshine Bio-tech Co., Ltd. (Hangzhou, China). The PLA filament (FilaPrint® premium PLA, 1.75 mm) was purchased from 3D FilaPrint Ltd. (Essex, UK). All chemicals used were of analytical or food grade and used as received.

2.2. Preparation of PDMS Sponges

An eco-friendly sugar templating method was applied to fabricate porous magnetic sponges in this study because the commercially available household sugar which is used as the mould could be removed easily through immersion in water afterwards [24]. Around 15 g sugar was thoroughly mixed with 0.5 mL water and pressed firmly in a Petri dish (diameter = 5 cm). Then the Petri dish was placed in a convection oven (Memmert, UF110, Schwabach, Germany) at 50 °C for around 1 h to dry the sugar for achieving a mould of connected sugar particles [1]. PDMS prepolymers and curing agents were mixed by a weight ratio of 10:1. Then the magnetic microparticles were blended with the well-mixed PDMS solution at different magnetic particle:PDMS weight ratios of 0:10 (0 w/w %), 3:10 (30 w/w %), 5:10 (50 w/w %), 10:10 (100 w/w %) or 15:10 (150 w/w %). After that, the mixture was poured onto the dried sugar mould and then the mixture was infiltrated into the sugar template because of capillary force [24]. The Petri dish was placed in the oven again at 70 °C for 3 h for the curing process. Finally, the cured blend was immersed in water to dissolve the sugar completely. After the removal of the sugar templates, 3D eco-friendly interconnected microporous PDMS sponges were formed.

2.3. Preparation and Characterization of the Reservoir

2.3.1. Design of the Reservoir

The model reservoir was designed using Solidworks (2017 SP5,

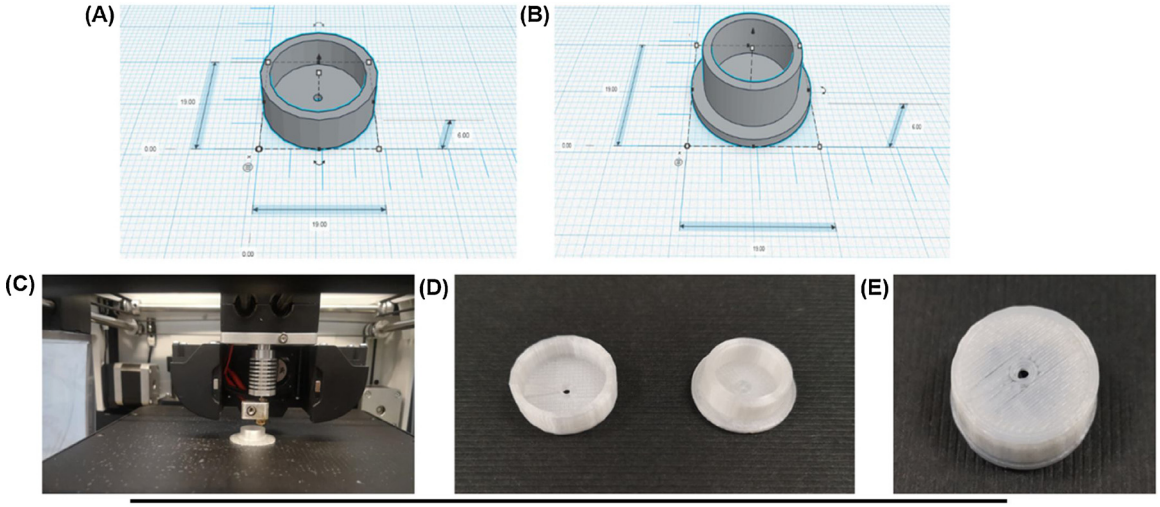

	weight (g)	diameter (mm)	height (mm)
top part	0.811±0.003	19.367±0.045	6.153±0.069
bottom part	0.980±0.005	19.385±0.029	6.662±0.050
whole reservoir	1.791±0.007	19.385±0.029	7.764±0.061

Fig. 1. Stereolithography images of (A) the bottom part and (B) the top part of the reservoir. (C) The printing process of the PLA reservoir with Robo R2. (D) Macroscopic appearance of 3D-printed PLA reservoir (left: bottom, right: top). (E) Macroscopic appearance of the assembled 3D-printed PLA reservoir loaded with 100% CI/PDMS sponge and drug solution. Dimensions and weight of the 3D printed reservoir are also shown ($n = 6$). The dimention and weight of each part was also added in this figure.

Waltham, MA, USA) and converted to a stereolithography file (.stl). For the ease of printing operation, the geometry of the 3D printed reservoirs was selected as cylinder shape because of the large surface area in contact with the building plate [25]. The currently optimized design was flat cylindrical with a smoothed edge and consisting of two parts: top and bottom (Fig. 1 A and B). The diameter and height of the reservoir are 19 mm and 7 mm respectively. The diameter and height of the hollow space for sponges are 12.5 mm and 5 mm respectively. In addition, there is a small aperture (diameter = 1.5 mm) at the centre of the top part surface.

2.3.2. FDM 3DP of the Reservoir

Printing was performed in a Robo R2 (San Diego, CA, USA) using a nozzle with a diameter of 0.4 mm for printing PLA 1.75 mm 3D printer filaments. The following settings were employed: the printing temperature (T_{print}) was set at 195 °C, $T_{platform}$ = 60 °C, infill pattern = light, layer height = 0.1 mm.

2.3.3. Appearance, dimensions, and microstructure of the reservoir

Samples prepared by FDM were photographed and were visually investigated. The diameter and height of the 3D printed reservoirs were measured with a vernier calliper. The radial expansion coefficient (E_r) of filaments was calculated according to Eq. 1, where D_f and D_0 represent the diameters of filament and die of printer respectively [26].

$$E_r(\%) = \frac{D_f}{D_0} \times 100\% \quad (1)$$

The printed reservoir (top and bottom part) was examined by Jeol JMS 820 scanning electron microscopy (Freising, Munich, Germany) at the accelerating voltage of 3 kV. The samples were mounted on an aluminium stub using adhesive carbon tape and were sputter-coated with gold under vacuum (Edwards S-150 sputter coater, Edwards High Vacuum Co. International, Albany, NY, USA).

2.4. Assemble and Drug Loading of the TDDS

2.4.1. Preparation of Drug Solution

The model drug in this study, 5-fluorouracil (FLU), is sparingly soluble in water and slightly soluble in ethanol [27], so it is necessary to design how to increase the dose of FLU loaded into the device. However, the solubility of 5-fluorouracil can be affected significantly by temperature as it can increase more than 12-fold by enhancing the temperature between 25 and 200 °C under the constant pressure of 5.1 MPa [28]. Additionally, Singh et al. point out that 5-fluorouracil has good thermal stability when the temperature is less than 278 °C [29]. Therefore, the temperature of the solution was increased in the preparing process.

2.4.2. Device Integration and Assembly

The sponge cylinders which can fit the shape of the hollow space of the reservoir bottom will be cut and then immersed into the drug solution. After the sponge cylinder absorbed enough drug solution, it was taken out and placed into the bottom hollow. Then the two parts of the reservoir were closed tightly.

2.4.3. Drug Loading of the Device

By comparing the weight change of the device before and after the drug loading process, the amount of drug loaded into the device could be calculated every time afterwards because the weight ratio of the drug to the solution is constant.

2.5. Dissolution Test under Sink Conditions

In vitro dissolution tests under sink conditions were performed with a US Pharmacopeia (USP) type I basket or type II paddle apparatus (708-DS Dissolution Apparatus, Agilent Technologies, USA) in 900 mL of PBS (pH 6.8) at 37 ± 0.3 °C with the paddle speed of 100 rpm according to different designed modes (Fig. 2). The drug concentration in the dissolution medium was measured automatically using Cary 60 UV-Vis (Agilent Technologies, USA) at a wavelength of 265 nm in a 1 cm

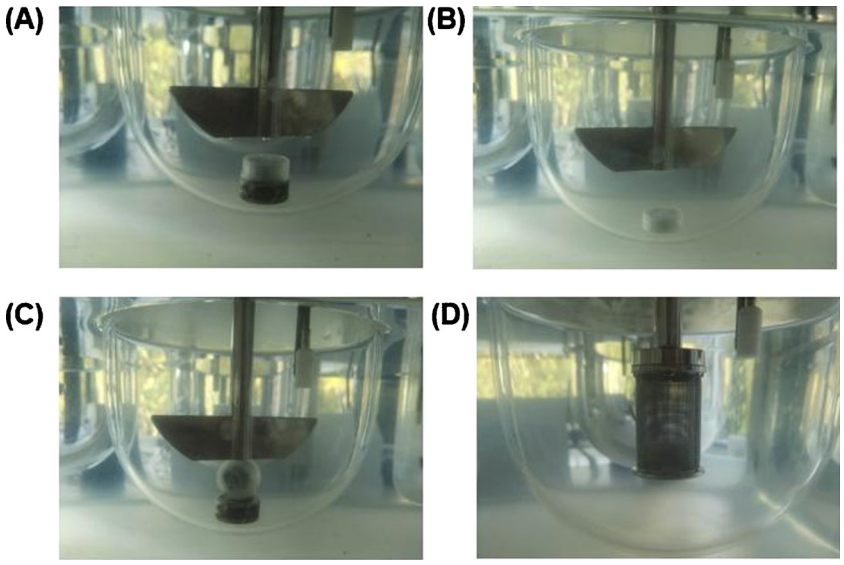

Fig. 2. Various modes for comparing the drug release from the device. (A) Mode 1: the device was laid flat on the magnet; (B) Mode 2: the device with no magnets; (C) Mode 3: the device was placed vertically on the magnet; (D) Mode 4: the device was placed in the basket without magnets.

cell versus a blank solution consisting of PBS (pH 6.8). All samples were run in triplicate ($n = 3$). Then the release profile could be plotted as a percentage of cumulative drug release versus time. The preliminary results showed that the materials used in 3D printing such as PLA does not interfere with drug detection and UV absorbance. The standard curve was prepared in the concentration of 0.625-20 μg/mL ($A = 0.0514C + 0.002$, $R^2 = 0.9995$) where A is the absorbance and C is the concentration (μg/ml).

To study the effect of the position of magnet versus device containing the sponge, various modes were employed. In Mode 1 (Fig. 2A), the device was lying on the magnet. In Mode 2 (Fig. 2B), there is no magnet. In Mode 3 (Fig. 2C), the device was standing on the magnet. In Mode 4 (Fig. 2D), the device was placed in the basket without magnet.

Neodymium grade N42 magnets were applied for providing different magnetic flux densities with a distance of 5 mm for the device during the dissolution testing (Table 1).

The similarity factor (f_2) in Eq. 2 was developed by Moore and Flanner as a model-independent mathematical method to analyze the closeness among these dissolution profiles [30]:

$$f_2 = 50 \times \log\{[1 + \frac{1}{n}\sum_{t=1}^{n}(R_t - T_t)^2]^{-0.5} \times 100\} \quad (2)$$

where n is the number of dissolution time points, R_t and T_t are the dissolution value of the reference and test sample at the time t, respectively.

The mathematical method of f_2 has been adopted by many guidance, like Food and Drug Administration (FDA) and European Medicines Agency (EMEA), as a criterion for measurement of the similarity between in vitro dissolution profiles [31]. As the value of f_2 equals to 100 when the two profiles are identical and the value is 50 when an average variation of 10% at all determined time points, a public standard for f_2 value between 50 and 100 can indicate the two dissolution profiles are similar, whereas the value of less than 50 can show the two profiles are different.

Table 1
Dimensions of magnets used in the current studies to provide different magnetic flux densities with 5 mm distance between the specimen and magnets

Magnets	A*	B	C	D
diameter (mm)	19.5	19.5	21.5	19.5
thickness (mm)	2.5	2.5	5.5	9.5
magnetic field (mT)	110	150	204	355

*The effect of this magnet was not further investigated as it did not show a significant deformation on sponges

2.6. Cell Studies of the Devices in Vitro with FLU Solution

2.6.1. Preparation of Sponges Samples Loaded with Drug Solution

As the sponge samples are very porous, it is easy for the drug solution penetrates the sponge and retained by the sponge. Three samples of each sponge formulation (diameter × thickness = 5 mm × 2 mm) were compressed gently in the drug solution until no air bubbles come out. After that, the sponge samples with drug solutions were taken out and leave them at room temperature.

2.6.2. Cell Lines

Trex cells can stably express green fluorescent protein (GFP) constructs. Cell lines were maintained in Dulbecco's modified Eagle medium (DMEM) supplemented with 10% fetal calf serum (FCS), penicillin/streptomycin and L-Glutamine at 37 °C and 5% CO_2.

2.6.3. Experimental Set-Up

Substrates were transferred to 12 well plates and sterilized with UV irradiation 30 min prior to adding cells. Cells were plated at a density of 0.4×10^5 on day 0. Day 1, substrates were transferred to new wells to avoid any effect of cell dissociation. Remaining cells were harvested using trypsin EDTA and counted using a hemocytometer to determine cell numbers. Cells were re-plated onto the transferred substrates in fresh media. Day 4, the substrates were washed three times with PBS. Remaining cells were trypsinized, counted and discarded as before. Images were taken prior to trypsinisation.

3. Results and Discussion

3.1. Fabrication and Characterization of Magnetic PDMS Sponges

Among all prepared magnetic PDMS sponges (Fig. 3), 100 w/w% CI/PDMS sponge was selected for the scaffold in this experiment as it exhibited the most deformation tendency at the given reflux under the given magnetic field. The underlying reasons being that the ferromagnetic particles were homogeneously distributed throughout the PDMS sponges as such it was enough to deform the sponges at a suitable extent to trigger drug release from the system. The lower or higher

Fig. 3. Photograph of the pure PDMS sponge cylinder, CI loaded PDMS cylinder and cube.

amount of CI particles in the formulation exhibited insufficient magnetic field sensitivity in the experimental set-up, respectively. Based on the preliminary results, 100% w/w CI/PDMS formulation was selected for the additional studies.

3.2. Fabrication and Characterization of the Reservoir

3.2.1. Printing the Device

The PLA filaments were transformed into reservoirs via a Robo R2 FDM 3D printer (Fig. 1C). The suitable size of the sponge cylinder was cut and subsequently installed into the PLA reservoir bottom before the top part assembling and drug loading. The reservoir could be opened later, meanwhile, both the reservoir and PDMS sponge cylinders could be washed completely and reutilized (Fig. 1B). These printed reservoirs showed satisfactory mechanical properties. These two parts of the reservoir are white, non-friable, plastic-like and can be closed tightly. The printed reservoirs show low variability in both size and weight (Fig. 1).

3.2.2. Characterization of 3D Printed Reservoirs

The extruded PLA filament was smooth and uniform with a diameter of 0.403 ± 0.001 mm. The value of E_r (100.75 %) reduced the possibility of die swelling, which may cause uneven filament blocking the feed nozzle (ø = 0.4 mm) of the printer. SEM analysis (Fig. 4) confirmed that the printed reservoir has a layered structure as the printing was conducted in a layer-by-layer manner.

3.3. Assemble and Drug Loading of the TDDS

The sponge cylinders with the diameter and height of 12.5 mm and 5 mm respectively were cut carefully and loaded into the hollow space of the reservoir bottom. Then the two parts of the reservoir can be closed tightly (Fig. 1E).

After the pure PDMS sponge or the CI-loaded PDMS sponge was assembled into the reservoir, around 0.3 mL solution could be loaded into the device because of the strong water absorption of the sponge samples. The dose of drug loaded into the device could be calculated by analyzing the weight change (weight of solution) of the device before and after the drug loading process. The maximum concentration of the FLU solution was optimized at 25 mg/mL [27]. As a result, the device containing around 7 ~ 8 mg FLU was assembled successfully.

3.4. Dissolution Test under Sink Conditions

It is assumed that the location of magnetic bar respect to the location of the reservoir containing sponge can deform sponge differently and this, in turn, releases the drug with different patterns when compared to the release behaviour of the device without magnets (Fig. 5). Some drug solutions can release from the small aperture gradually without magnets (Mode 2). When the magnet bar is contacted with the side part of the device, the magnetic sponge loaded with the drug solution can move close to the magnetic bar because of the magnetic field and drug solution is squeezed out through the small aperture (Mode 3). In contrast, the magnetic sponge and drug solution moves away from

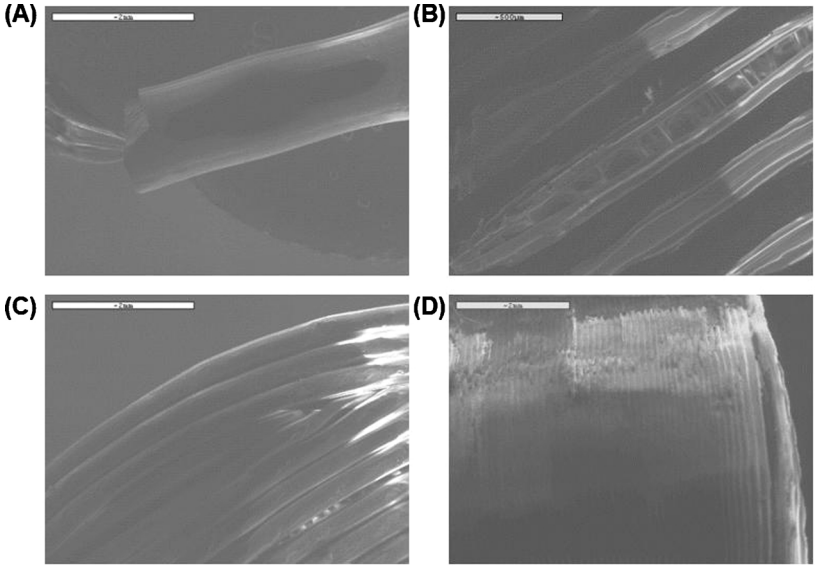

Fig. 4. SEM images of (A) PLA filaments, (B) the bottom surface of the reservoir, (C) the top surface of the reservoir, (D) the side surface of the reservoir.

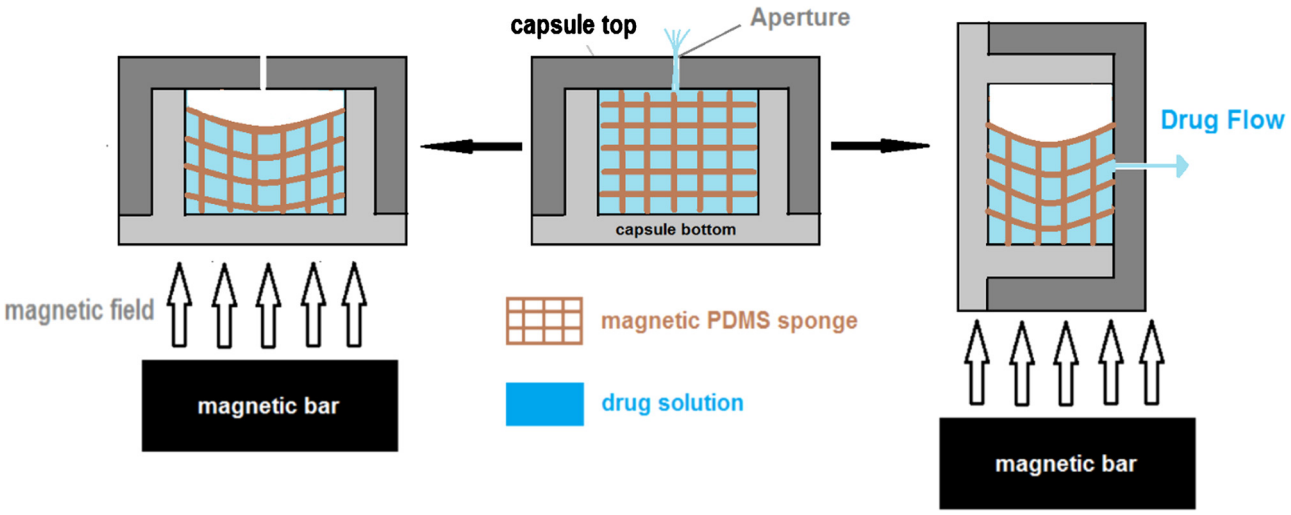

Fig. 5. A schematic cross-section view diagram showing the release mechanism of the device with the utilization of the magnetic field from different directions (left: Mode 1, middle: Mode 2, right: Mode 3).

the aperture when the magnetic bar is at the bottom of the device, so only a little amount of drug solution will be released (Mode 1). To prove this hypothesis, dissolution tests under sink conditions were carried out.

In vitro drug release profiles from the same drug-loaded device but with different utilizations of magnets are depicted in Fig. 6. The dissolution test was carried out for 12 h, and the results showed that over 80% of the drug released in Model 3 within the first 720 min.

When the device was standing on Magnet D (Model 1), the dissolution rate was faster than other models. The probable reasons may have been the drug solution could release from the small aperture because of the deformation caused by the magnetic field. In particular, the time at which 10%, 50%, 80% and 90% of the drug were dissolved ($T_{10\%}$, $T_{50\%}$, $T_{80\%}$ and $T_{90\%}$ respectively) are observed at < 5, 20, 55 and 140 min (Fig. 6). When Model 7 which the device was standing on Magnet B (the smaller magnetic field) and compared with Model 1 (the stronger magnetic field), the drug release was much faster from Model 1 (f_2= 40.58) mainly due to the more obvious deformation caused by a stronger magnetic field.

However, the drug release from the device which was lying on the magnet (Model 5) is dramatically slow. The comparison of dissolution profiles of Model 1 with model 5 demonstrated that the deformation of the magnetic sponge in Model 1 is more efficient than Model 5 because of the position of the small aperture and the size differences between the diameter and height of the sponge samples assembled in the reservoir (f_2= 9.71).

Besides, there are also significant differences between Models 1 and 2 (f_2= 30.03), Models 2 and 5 (f_2= 15.66). This indicates that the different utilizations of the external magnetic field have crucial influences on the dissolution behaviour of drug release from the device. The dissolution behaviours of the drug-loaded device are different in basket and paddle methods because of the obvious difference between Model 2 and 3 (f_2= 30.03), Model 4 and 5 (f_2= 50.56).

To prove the small aperture on the top of the reservoir is the main pathway for drug-releasing, the device without any aperture was designed, fabricated and analyzed (Model 6) in the same way as Model 2. During the 12 h, only 16% of drug loading was released from the device and the amount is much lower than that of Model 2. This indicates that the drug solution is mainly released from the small aperture. However, the slower drug release in Model 8 when compared with Model 5 indicates that the weaker magnetic field can release less drug in Mode 1.

It can be concluded that the switching “on” state in the release pattern from the device can be triggered when the magnet is employed like Model 1, and the switching “off” drug-releasing of the device can also be realized when we change the position of the magnets like Model 8. Consequently, the release of drugs from this device can be controlled repeatedly and quickly. All these features make this novel implantable drug delivery device a promising candidate to tailor and control the release of therapeutic substances in local disease therapy. The device could be navigated to the target site *in vivo* wirelessly with the application of magnetic fields. With the development of this TDDS, the anticancer agent (FLU) could be navigated to the target site and released at an adjustable rate in accordance with patients’ specific conditions for minimizing adverse effects during cancer treatment. Herein, the bioavailability of FLU could be enhanced significantly. Furthermore, this device shows superior potential in hormone deficiencies and chronic pain treatments. Desirable doses of these drugs, like hormones and painkillers, can be released by loading these drug solutions of various concentrations into the drug delivery system.

3.5. Cell Studies in vitro

It is necessary to analyze the cell inhibition behaviour of FLU loaded 3D printed reservoir and sponge samples. The assessment of cell numbers of Trex cells was designed as follows. The cell numbers in Fig. 7 (Group B1, B9 with B11, Group B2 with B10) display that these PDMS sponges, especially CI loaded PDMS sponge without the drug can inhibit the growth of Trex cells to some extent, but the number of Trex cells still increased within 4 days because there are no FLU solution. Through comparing data of groups under the same conditions just except for applying magnetic fields (Group B9 with B10, Group B1 with B2, and Group B3 with B4), it can be concluded that stronger magnet will lead to more drugs being released from the deformation of magnetic sponges and more obvious inhibition effects on Trex cell growth. Importantly, sponge samples loaded with a higher concentration of FLU solution (Group B3 with B5, Group B4 with B6) present a stronger inhibition effect on Trex cells. The results showed that there is no difference between Group 7 and 8 and this is not surprising because the magnet would not trigger the release of drug solution loaded in the device when the magnets were placed at the bottom of the whole device as reflected by the results highlighted in the dissolution section.

In summary, stronger magnetic fields can lead to larger deformations of CI-loaded PDMS sponge cylinders and a higher volume of drug solution will be released from the drug-loaded magnetic PDMS sponges. By adjusting the concentration of the drug solution, the dose of the drug could be changed. Because the prepared magnetic sponge sample can release a specific volume of drug solution under the same magnetic field, the lower loaded solution concentration can lead to the lower loaded dose of the drug. With the assembly of a 3D printed PLA

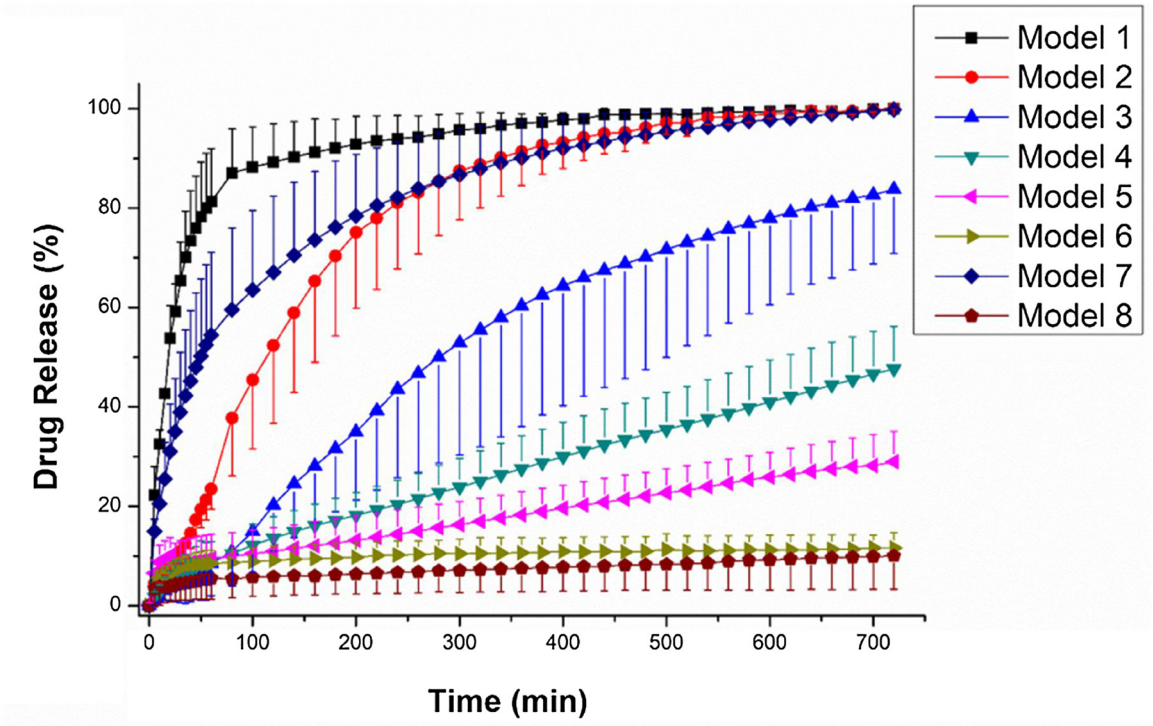

Model	Apparatus	Magnet	Mode	Aperture	$T_{10\%}$	$T_{50\%}$	$T_{80\%}$	$T_{90\%}$
1	Paddle	D	3	√	<5 min	20 min	55 min	140 min
2	Paddle	×	2	√	25 min	120 min	240 min	340 min
3	Basket	×	4	√	80 min	280 min	640 min	-
4	Basket	D	1	√	80 min	-	-	-
5	Paddle	D	1	√	80 min	-	-	-
6	Paddle	×	2	×	220 min	-	-	-
7	Paddle	B	3	√	<5 min	50 min	220 min	360 min
8	Paddle	B	1	√	720 min	-	-	-

Fig. 6. *In vitro* mean drug release profiles (± SD) (under sink condition) in PBS (pH 6.8) of device loaded with 25 mg/mL FLU solution (n = 3). Different models and the time at which 10%, 50%, 80% and 90% of the drug were dissolved are clarified underneath the dissolution profiles for the comparison of drug release behaviours of the device.

reservoir, there will be no obvious difference of released dose of drug from the whole device between the device having magnets placed underneath and the device alone without magnets.

4. Conclusion

In this experiment, we designed and developed a novel implantable drug delivery device assembled from a magnetic PDMS sponge cylinder and a 3D-printed PLA reservoir to provide a triggerable and remotely controllable system for on-demand drug delivery in localized disease treatment. This device utilizes different extrinsic magnetic fields for offering a tunable force to trigger drug release through reversible magnetic sponge deformations. The geometric shape and dimensions of the reservoir could be adjusted easily through FDM 3D printing technology according to the requirement of patients. In addition, the drug-releasing dose and timing can be reliably and flexibly controlled by different applications of the magnetic field to fit the prescribed needs. Furthermore, this device has the potential to be optimized as a safe and long-term implant because of its large drug loading ability. It can be the key component of a multi-functional, implantable and smart drug delivery system for the controlled release of therapeutic substances to avoid frequent injection or various sophisticated dosing regimens. In the future, combining the device with *i.e.* sensing system can also offer protection for biosensors because biofouling and exposure to the body may lead to the failure of biosensors *in vivo*.

CRediT author statement

Kejing Shi: Investigation, draft preparation
Rodrigo Aviles-Espinosa: Investigation
Elizabeth Rendon-Morales: Investigation
Lisa Woodbine: Investigation
Mohammed Maniruzzaman: Conceptualization, Supervision, Reviewing and Editing
Ali Nokhodchi: Supervision, Conceptualization, Writing- Reviewing and Editing

Conflict of Interest

The authors declare no conflict of interest.

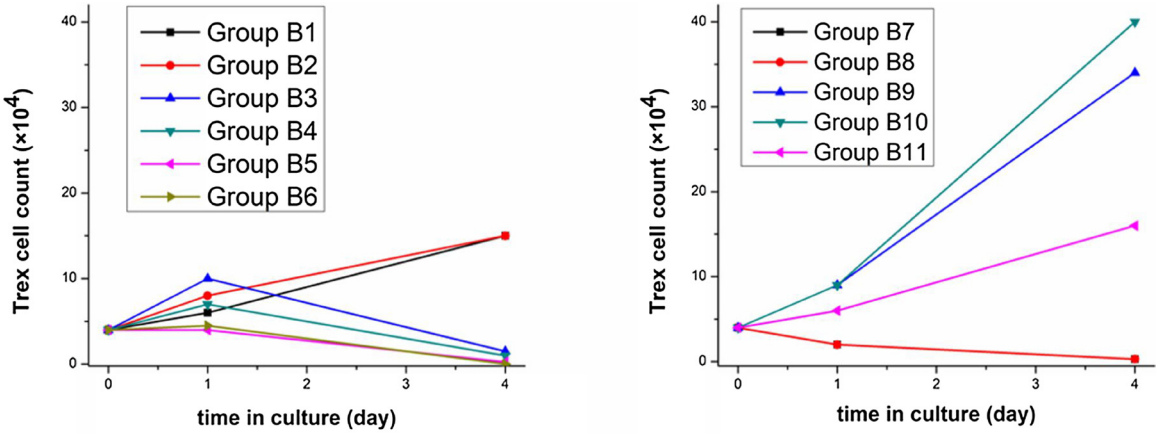

Group	Magnet	Sponge	FLU Solution	PLA Reservoir
B1	B	CI/PDMS=100 wt%	×	×
B2	C	CI/PDMS=100 wt%	×	×
B3	B	CI/PDMS=100 wt%	12.5 mg/mL	×
B4	C	CI/PDMS=100 wt%	12.5 mg/mL	×
B5	B	CI/PDMS=100 wt%	25 mg/mL	×
B6	C	CI/PDMS=100 wt%	25 mg/mL	×
B7	×	CI/PDMS=100 wt%	12.5 mg/mL	√
B8	B	CI/PDMS=100 wt%	12.5 mg/mL	√
B9	B	×	×	×
B10	C	×	×	×
B11	B	pure PDMS	×	×

Fig. 7. Numbers of Trex cells under different conditions. 3D printed PLA reservoir and sponge samples loaded with different solutions under different magnetic fields (for better clarification the composition for each group was added in the table attached to the figure).

Acknowledgement

The authors thanks China Scholarship Council (CSC) for financial support of Kejing Shi.

References

[1] A. Shademani, H. Zhang, J.K. Jackson, M. Chiao, Active Regulation of On-Demand Drug Delivery by Magnetically Triggerable Microspouters, Adv. Funct. Mater. 27 (2017), https://doi.org/10.1002/adfm.201604558.
[2] S.E. Moulton, G.G. Wallace, 3-dimensional (3D) fabricated polymer based drug delivery systems, J. Control. Release. 193 (2014) 27–34, https://doi.org/10.1016/j.jconrel.2014.07.005.
[3] J.L. Arias, V. Gallardo, F. Linares-Molinero, A.V. Delgado, Preparation and characterization of carbonyl iron/poly(butylcyanoacrylate) core/shell nanoparticles, J. Colloid Interface Sci. 299 (2006) 599–607, https://doi.org/10.1016/j.jcis.2006.03.005.
[4] B.P. Timko, T. Dvir, D.S. Kohane, Remotely triggerable drug delivery systems, Adv. Mater. 22 (2010) 4925–4943, https://doi.org/10.1002/adma.201002072.
[5] V. Iacovacci, G. Lucarini, L. Ricotti, P. Dario, P.E. Dupont, A. Menciassi, Untethered magnetic millirobot for targeted drug delivery, Biomed. Microdevices. 17 (2015), https://doi.org/10.1007/s10544-015-9962-9.
[6] M. Sitti, H. Ceylan, W. Hu, J. Giltinan, M. Turan, S. Yim, E. Diller, Biomedical Applications of Untethered Mobile Milli/Microrobots, Proc. IEEE. 103 (2015) 205–224, https://doi.org/10.1109/JPROC.2014.2385105.
[7] X. Zhao, J. Kim, C.A. Cezar, N. Huebsch, K. Lee, K. Bouhadir, D.J. Mooney, Active scaffolds for on-demand drug and cell delivery, Proc. Natl. Acad. Sci. 108 (2011) 67–72, https://doi.org/10.1073/pnas.1007862108.
[8] A.Y. Rwei, J.L. Paris, B. Wang, W. Wang, C.D. Axon, M. Vallet-Regí, R. Langer, D.S. Kohane, Ultrasound-triggered local anaesthesia, Nat. Biomed. Eng. 1 (2017) 644–653, https://doi.org/10.1038/s41551-017-0117-6.
[9] J.M. Maloney, S.A. Uhland, B.F. Polito, N.F. Sheppard, C.M. Pelta, J.T. Santini, Electrothermally activated microchips for implantable drug delivery and biosensing, J. Control. Release. 109 (2005) 244–255, https://doi.org/10.1016/j.jconrel.2005.09.035.
[10] W. Kempin, C. Franz, L.C. Koster, F. Schneider, M. Bogdahn, W. Weitschies, A. Seidlitz, Assessment of different polymers and drug loads for fused deposition modeling of drug loaded implants, Eur. J. Pharm. Biopharm. 115 (2017) 84–93, https://doi.org/10.1016/j.ejpb.2017.02.014.
[11] S.A. Stewart, J. Domínguez-Robles, V.J. McIlorum, E. Mancuso, D.A. Lamprou, R.F. Donnelly, E. Larrañeta, Development of a biodegradable subcutaneous implant for prolonged drug delivery using 3D printing, Pharmaceutics. 12 (2020), https://doi.org/10.3390/pharmaceutics12020105.
[12] S. Jiang, Y. Hu, H. Wu, Y. Zhang, Y. Zhang, Y. Wang, Y. Zhang, W. Zhu, J. Li, D. Wu, J. Chu, Multifunctional Janus Microplates Arrays Actuated by Magnetic Fields for Water/Light Switches and Bio-Inspired Assimilatory Coloration, Adv. Mater. 31 (2019) 1–8, https://doi.org/10.1002/adma.201807507.
[13] J.H. Kim, S.M. Kang, B.J. Lee, H. Ko, W.G. Bae, K.Y. Suh, M.K. Kwak, H.E. Jeong, Remote Manipulation of Droplets on a Flexible Magnetically Responsive Film, Sci. Rep. 5 (2015) 1–10, https://doi.org/10.1038/srep17843.
[14] K. Cai, Z. Luo, Y. Hu, X. Chen, Y. Liao, L. Yang, L. Deng, Magnetically triggered reversible controlled drug delivery from microfabricated polymeric multireservoir devices, Adv. Mater. 21 (2009) 4045–4049, https://doi.org/10.1002/adma.200900593.
[15] X. Hu, G. Nian, X. Liang, L. Wu, T. Yin, H. Lu, S. Qu, W. Yang, Adhesive Tough Magnetic Hydrogels with High Fe 3 O 4 Content, 108747. Interfaces. 11 (2019) 10292–10300, https://doi.org/10.1021/acsami.8b20937.
[16] F. Munoz, G. Alici, H. Zhou, W. Li, M. Sitti, Analysis of Magnetic Interaction in Remotely Controlled Magnetic Devices and its Application to a Capsule Robot for Drug Delivery, IEEE/ASME Trans, Mechatronics. 23 (2018) 298–310, https://doi.org/10.1109/TMECH.2017.2764902.
[17] K. Pietrzak, A. Isreb, M.A. Alhnan, A flexible-dose dispenser for immediate and extended release 3D printed tablets, Eur. J. Pharm. Biopharm. 96 (2015) 380–387, https://doi.org/10.1016/j.ejpb.2015.07.027.
[18] M.A. Alhnan, T.C. Okwuosa, M. Sadia, K.W. Wan, W. Ahmed, B. Arafat, Emergence of 3D Printed Dosage Forms: Opportunities and Challenges, Pharm. Res. 33 (2016) 1817–1832, https://doi.org/10.1007/s11095-016-1933-1.

[19] C.I. Gioumouxouzis, A.-T. Chatzitaki, C. Karavasili, O.L. Katsamenis, D. Tzetzis, E. Mystiridou, N. Bouropoulos, D.G. Fatouros, Controlled Release of 5-Fluorouracil from Alginate Beads Encapsulated in 3D Printed pH-Responsive Solid Dosage Forms, AAPS PharmSciTech. 19 (2018) 3362–3375, https://doi.org/10.1208/s12249-018-1084-2.

[20] K. Liang, S. Carmone, D. Brambilla, J.-C. Leroux, 3D printing of a wearable personalized oral delivery device: A first-in-human study, Sci. Adv 4 (2018) eaat2544 http://advances.sciencemag.org/.

[21] J. Domínguez-Robles, N. Martin, M. Fong, S. Stewart, N. Irwin, M. Rial-Hermida, R. Donnelly, E. Larrañeta, Antioxidant PLA Composites Containing Lignin for 3D Printing Applications: A Potential Material for Healthcare Applications, Pharmaceutics. 11 (2019) 165, https://doi.org/10.3390/pharmaceutics11040165.

[22] J. Fu, X. Yu, Y. Jin, 3D printing of vaginal rings with personalized shapes for controlled release of progesterone, Int. J. Pharm. 539 (2018) 75–82, https://doi.org/10.1016/j.ijpharm.2018.01.036.

[23] D. Li, G. Guo, R. Fan, J. Liang, X. Deng, F. Luo, Z. Qian, PLA/F68/Dexamethasone implants prepared by hot-melt extrusion for controlled release of anti-inflammatory drug to implantable medical devices: I. Preparation, characterization and hydrolytic degradation study, Int. J. Pharm. 441 (2013) 365–372, https://doi.org/10.1016/j.ijpharm.2012.11.019.

[24] S.J. Choi, T.H. Kwon, H. Im, D. Il Moon, D.J. Baek, M.L. Seol, J.P. Duarte, Y.K. Choi, A polydimethylsiloxane (PDMS) sponge for the selective absorption of oil from water, ACS Appl. Mater. Interfaces. 3 (2011) 4552–4556, https://doi.org/10.1021/am201352w.

[25] Q. Li, H. Wen, D. Jia, X. Guan, H. Pan, Y. Yang, S. Yu, Z. Zhu, R. Xiang, W. Pan, Preparation and investigation of controlled-release glipizide novel oral device with three-dimensional printing, Int. J. Pharm. 525 (2017) 5–11, https://doi.org/10.1016/j.ijpharm.2017.03.066.

[26] Y. Yang, H. Wang, H. Li, Z. Ou, G. Yang, 3D printed tablets with internal scaffold structure using ethyl cellulose to achieve sustained ibuprofen release, Eur. J. Pharm. Sci. 115 (2018) 11–18, https://doi.org/10.1016/j.ejps.2018.01.005.

[27] K. Shi, D. Tan, A. Nokhodchi, M. Maniruzzaman, Drop-On-Powder 3D Printing of Tablets with an Anti-Cancer Drug, 5-Fluorouracil, Pharmaceutics. 11 (2019) 150, https://doi.org/10.3390/pharmaceutics11040150.

[28] S. Akay, B. Kayan, Y. Yang, Solubility and Chromatographic Separation of 5-Fluorouracil under Subcritical Water Conditions, J. Chem. Eng. Data. 62 (2017) 1538–1543, https://doi.org/10.1021/acs.jced.7b00015.

[29] P. Singh, G. Tyagi, R. Mehrotra, A.K. Bakhshi, Thermal stability studies of 5-fluorouracil using diffuse reflectance infrared spectroscopy, Drug Test. Anal. 1 (2009) 240–244, https://doi.org/10.1002/dta.41.

[30] J.W. Moore, H.H. Flanner, Mathematical Comparison of Dissolution Profiles, Pharm. Technol. 20 (1996) 64–74.

[31] F. Xie, S. Ji, Z. Cheng, In vitro dissolution similarity factor (f2) and in vivo bioequivalence criteria, how and when do they match? Using a BCS class II drug as a simulation example, Eur. J. Pharm. Sci. 66 (2015) 163–172, https://doi.org/10.1016/j.ejps.2014.10.002.

ACS Biomaterials SCIENCE & ENGINEERING

pubs.acs.org/journal/abseba

Article

Magnetic Field Triggerable Macroporous PDMS Sponge Loaded with an Anticancer Drug, 5-Fluorouracil

Kejing Shi, Rodrigo Aviles-Espinosa, Elizabeth Rendon-Morales, Lisa Woodbine, Jonathan P. Salvage, Mohammed Maniruzzaman,* and Ali Nokhodchi*

Cite This: *ACS Biomater. Sci. Eng.* 2021, 7, 180−195

Read Online

ACCESS | Metrics & More | Article Recommendations

ABSTRACT: This study aims to prepare, optimize, and characterize magnetic-field-sensitive sugar-templated polydimethylsiloxane (PDMS) sponges for localized delivery of an anticancer drug, 5-fluorouracil (FLU). For this purpose, different concentrations of carbonyl iron (CI) and magnetite Fe_3O_4 nanopowders were embedded as magnetosensitive materials in PDMS resins for the fabrication of macroporous sponges via a sugar-template process. The process is environmentally friendly and simple. The fabricated interconnected macroporous magnetic particles loaded PDMS sponges possess flexible skeletons and good recyclability because of their recoverability after compression (deformation) without any breakdown. The prepared magnetic PDMS sponges were evaluated for their morphology (SEM and EDS), porosity (absorbency), elastic modulus, deformation under a magnetic field, thermostability, and *in vitro* cell studies. All physicochemical and magnetomechanical analysis confirmed that the optimized magnetic-field-sensitive PDMS sponge can provide an efficient method for delivering an on-demand dose of anticancer drug solutions at a specific location and timing with the aid of controlled magnetic fields.

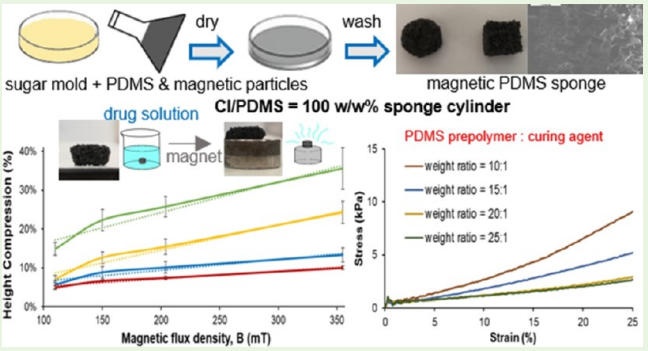

KEYWORDS: *Magnetic field, polydimethylsiloxane, sponge, triggerable drug delivery system, carbonyl iron, iron oxide, nanoparticles, 5-fluorouracil, personalized medicine*

1. INTRODUCTION

Macroporous sponges, dispersions of gas into a solid matrix to form a porous solid structure, fabricated from polymers, metals, ceramics, and glasses have been extensively studied as drug delivery carriers in pharmaceutical fields, such as wound dressing, ocular formulation, and buccal drug delivery, as well as in tissue engineering.[1,2] These porous scaffolds can provide a three-dimensional (3D) environment for tissue volume preservation, cell interaction support, and biological agent delivery.[1] The normal mechanism to release drugs from these porous scaffolds is via passive release (e.g., scaffold degradation and molecular diffusion), which limits the dose accuracy and on-demand delivery.[1] However, through the optimized design and tailoring of porous biomaterials, active porous scaffolds that can deliver bioactive substances under the control of external stimuli such as light, magnetic field, electricity, or ultrasound could be realized.[1]

Porous polymer structures have been widely developed in various technological areas, such as membranes for separation and purification, water desalination, hemodialysis, scaffolds for tissue engineering, solid supports for biosensors, biomedicines, and catalysts.[3,4] Among them, soft elastomers (like natural rubber, polyimide, and silicone rubber) have been used as magnetically responsive materials because through designing different microstructures, several functions could be achieved.[5,6] There are many advantages of silicon rubber, like low viscosity, thermostability, chemical stability, and high tendency to form linear structures.[7] Porous silicones are commercially available with low surface tension, high wetting ability, and good recyclability.[8] These properties make them good candidates for medical and pharmaceutical applications. Polydimethylsiloxane (PDMS), one of the most commonly used silicone polymers, has been widely employed in biomedical applications such as surgical implants, pacemaker encapsulants, catheters, and contact lenses.[8] A porous PDMS structure could be used as a microfilter and porous microchannels for gas sensors in microfluidic systems.[3] It has

Received: November 14, 2020
Accepted: December 1, 2020
Published: December 11, 2020

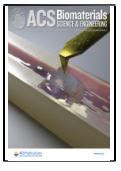

been proven that the PDMS sponge is a kind of porous and hydrophobic polymer with attractive features like large absorption capacity, high porosity, lightweight, low density, low surface tension, good elasticity (to be bent to any shape), repeated compressibility (in either air or liquids without collapsing), and excellent recyclability.[9−12] Additionally, the PDMS sponge shows a superior thermal property between 0 and 400 °C, so it is stable in actual experimental conditions.[8] Although PDMS sponges possess these suitable properties, the silicon substrate is not biodegradable and the activation of drug release from traditional devices is not reversible.[13] Therefore, PDMS was selected as the scaffold material for fabricating the sponges with stochastic porous structures in this study because of its special properties such as chemical inertness, thermal stability, biocompatibility, low toxicity, high flexibility, non-flammability, ease of fabrication, low manufacturing costs, optical transparency, and gas permeability.[8,9,11,14,15]

There are many approaches to fabricating porous PDMS structures, like templating with self-assembled colloidal microspheres, emulsion polymerization, surface treatment using a CO_2-pulsed laser, phase separation, one-pot method with the reaction of $NaHCO_3$ and HCl, NaCl microparticles templating with dimethicone, and suspension polymerization with gelatin as the surfactant.[3,8,16] However, these methods are expensive, time-consuming, and difficult to manipulate the shapes and sizes of porous structures because of sophisticated fabrication procedures.[3,16] Zhao *et al.* pointed out that PDMS sponges must be washed repeatedly with ethanol and dichloromethane to remove the NaCl microparticles completely, which is not the case when sugar was used.[17] Furthermore, the porosity of sponges made from salt molds is lower because the thick pore wall decreased significantly, and the compressive modulus is higher. Also, it has been proven that the sponge pores of sugar molds are more amorphous because of higher connectivity.[14] In this study, a simple, cheap, and eco-friendly sugar templating method was applied to fabricate porous PDMS sponges using commercial household sugar.

It has been reported that magnetic responsive scaffolds can achieve real-time control over diffusion-based drug release through reversible deformation.[14] Among them, magnetic elastomer (a mixture of magnetic nano/microparticles homogeneously embedded in an elastic polymeric matrix) has attracted increasing applications in vibration control and radio absorbing such as strong elasticity, large elastic deformation, reversible and simultaneous mechanical properties under magnetic fields.[6,18] The polymer matrix and magnetic particles are two main components in a magneto-rheological elastomer.[18] In this case, magnetic nanoparticles could be employed as switching carriers during the fabrication of PDMS sponges so that the sponges can deform immediately and reversibly in response to magnetic fields.[13,19,20] Magnetic particles (including iron, nickel powder, magnetite, and permalloy) have been widely applied in biomedical devices, like cellular therapy, tissue repair, drug delivery, magnetic resonance imaging (MRI), and especially in the fabrication of magnetically triggerable drug delivery systems (TDDSs).[6,13] The content of embedded magnetic particles and the strength of external magnetic fields can be adjusted to achieve desirable deformation and locomotion of TDDSs.[20] In recent years, iron oxide nanoparticles have attracted much consideration in different applications because of their various physical and chemical properties (e.g., super-paramagnetism, surface-to-volume ratio, large surface area, and easy separation methodology).[21] Carbonyl iron (CI) is a unique form of elemental iron with a small particle size and very low toxicity (LD_{50}: 50 g/kg).[22] As a novel food additive or iron supplementation, CI has therapeutic potential for iron deficiency anemia because of its safety and potent bioavailability.[23] In addition, the relatively high permeability and high saturation magnetization at the microwave frequency band make CI have the potential to be used as an electromagnetic wave absorbing material.[6,24] It has been proven that black iron oxide Fe_3O_4 (magnetite) particles are biocompatible, can respond quickly to an extrinsic magnetic field, and display fast reverse behavior once the magnetic field is removed.[13,21,25] Therefore, these two kinds of magnetic particles are promising candidates in the fields of biomaterials, implant technology, and biosensors for biomedical applications.

Despite their good magnetic-field sensitivity and water absorbency, the effects of the sugar template and the weight ratio of the prepolymer and the curing agent of PDMS have not been investigated. A novel method of measuring the deformation of prepared magnetic PDMS sponge cylinders was developed in this study with the manipulation of a bright-field microscopy metrology system. Also, *in vitro* cell studies were conducted to illustrate the inhibition behavior from drug-loaded sponges. All these inspired the authors of the current research to develop a simple, economical, and effective approach to fabricate different magnetic PDMS porous sponges as a component of smart stimuli-responsive drug delivery systems for the localized on-demand delivery of chemotherapeutic drugs.

2. MATERIALS AND METHODS

2.1. Materials. A Sylgard 184 silicone elastomer prepolymer (Sylgard 184A, $M_w \approx 22{,}000$ g·mol^{-1}) and the thermal curing agent (Sylgard 184B, $M_w \approx 15{,}000$ g·mol^{-1}) were donated by Dow Corning Ltd. (Barry, UK). Carbonyl iron powder (purity ≥97%) and Fe_3O_4 powder (<5 μm) with a purity of 95% were purchased from Sigma-Aldrich (Darmstadt, Germany). White granulated sugar and demerara sugar were purchased from Sainsbury's Supermarkets Ltd. (London, UK) and Co-operative Group Ltd. (Manchester, UK), respectively. The model anticancer drug 5-fluorouracil (FLU) with purity >98% was purchased from Hangzhou Longshine Bio-tech Co., Ltd. (Hangzhou, China). All chemicals used were of analytical or food grade and used as received.

2.2. Preparation of Macroporous Sponges. About 15 g of sugar was fully mixed with around 0.5 mL of water with a spatula and then pressed firmly in a Petri dish (diameter = 5 cm) to form a flat surface. To obtain a mold of connected sugar particles, the Petri dish with sugar was placed in a convection oven (Memmert, UF110, Schwabach, Germany) at 50 °C for around 1 h to achieve fusion of sugar.[19,26]

PDMS sponges were prepared by polymerization of the blend of the prepolymer and a thermal curing agent (with a weight ratio of 10:1).[27] The ferromagnetic particles were then loaded in the well-mixed PDMS at 0, 30, 50, 100, and 150% (w/w) of the weight of the PDMS in the formulation.

The blend of PDMS (prepolymer and a curing agent) and magnetic microparticles were vortexed and sonicated for 10 min to achieve a homogeneous dispersion because the strong polarity and high density make these magnetic particles difficult to be well dispersed in common solvents.[24] After that, the well-mixed blend was poured onto the dried sugar mold and then infiltrated into the sugar template because of capillary force.[9,16] The Petri dish was placed in the oven again at 70 °C for 3 h for the curing process. Finally, the cured blend was immersed in water to dissolve sugar completely with an ultrasonic cleaning bath (Fisherbrand FB15050, Leicestershire,

https://dx.doi.org/10.1021/acsbiomaterials.0c01608
ACS Biomater. Sci. Eng. 2021, 7, 180−195

UK) at 50 °C. The obtained sponges containing magnetic particles were removed from the ultrasonic bath and dried in the oven at 60 °C for 1 h. After the complete removal of sugar templates, 3D interconnected macroporous PDMS sponges were formed.

2.3. Optimization of the Sponges. According to Choi *et al.*, the less uniform the sugar particles are, the higher the porosity of the PDMS sponge can be achieved.[9] PDMS sponges replicated with different sugar templates were fabricated and characterized for comparison. Besides, sponges prepared with different weight ratios of the prepolymer and the curing agent of PDMS were prepared and analyzed.

2.3.1. Particle Size Analysis of Sugar. Data were collected over selected scanning electron microscopy (SEM) images of sugar samples. The average particle size of each kind of sugar was calculated from 100 random individual measurements through ImageJ software (National Institutes of Health, USA). Particle size distribution graphs were plotted and analyzed using OriginPro 8.5.

2.3.2. PDMS Sponges Prepared with Different Sugar Molds. The demerara sugar and the mixture of granulated and demerara sugar (in a weight ratio of 1:1) were employed as templates for the preparation of PDMS sponges. All other conditions of the fabrication process were the same as in section 2.2.

2.3.3. PDMS Sponge Formulation Optimization. To explore differences among sponges prepared with different prepolymer/curing agent weight ratios, PDMS prepolymer and curing agents were blended by weight ratios of 15:1, 20:1, 25:1, and 30:1 followed by the same process of CI particle addition.

2.4. Characterization of PDMS Sponge Properties.

2.4.1. Physical Appearance. A Celestron 44347 TetraView LCD digital microscope (Celestron LLC, Torrance, CA, USA) was used to check the uniformity of sugar particles for sponge molds. The formed sponges were physically evaluated concerning color, transparency, brittleness, and integrity. A ROTEK digital microscope (Shenzhen, China) was employed to obtain the surface image of fabricated sponges.

2.4.2. Scanning Electron Microscopy (SEM) and Energy-Dispersive X-ray Spectroscopy (EDS). The PDMS sponge samples were mounted on 12.5 mm diameter aluminum pin stubs (Agar Scientific, UK) using Leit-C conductive carbon cement (Agar Scientific, UK) and sputter-coated with 4 nm of platinum using a Q150T-ES sputter coater (Quorum Technologies, UK) to improve sample conductivity.

SEM imaging and EDS analysis were performed under high vacuum using a Zeiss Sigma FEG-SEM (Carl Zeiss, UK) and AZtec EDS system (Oxford Instruments, UK). The SEM working condition parameters were 20 kV accelerating voltage, 60 μm column aperture, and 8.5 mm working distance, using an Everhart−Thornley secondary electron detector (Carl Zeiss, UK) for imaging. The EDS analysis used a 10-frame acquisition per map, 20 μs pixel dwell time, AZtec software signal processer time setting 5, and an X-Max 80 mm^2 silicon drift detector (SDD) (Oxford Instruments, UK) for X-ray signal detection.

2.4.3. X-ray Diffraction (XRD). XRD measurements were performed using a Siemens D500 X-ray diffractometer (Munich, Germany). The samples were scanned between 2θ of 5 and 50° using 0.01° step width and 1 s time count. The divergence slit was 1 mm, and the scatter slit was 0.6 mm. The X-ray wavelength was 0.154 nm in the Cu source and at a voltage of 40 kV.

2.4.4. Porosity (Absorbency) Measurement. During the leaching process, the porous structure is generated by dissolving sugar in the sponge, which makes the drug delivery system more porous. Hence, the total pore volume of sponges could be used for the mathematical calculation of the porosity value.[2] Dried sponge cubes (1 × 1 × 0.5 cm, length × width × height) were weighed (m_s) and placed in distilled water at room temperature. Then the sponge cubes were compressed gently to let air bubbles come out, so the sponges were filled with water after the removal of the force from the sponge. Finally, the sponges were taken out of the water after water absorption equilibrium and were weighed again (m) to calculate the volume of absorbed water in the sponge cubes (V_w). The water absorbency (N_w) of the sample was calculated using eq 1.[10] The porosity of the sponge was eventually determined by both the volume of the sponge cube (V_s) and the volume of absorbed water as $V_w/V_s \times 100$ in eq 2. The bulk density (ρ) of the sponge was calculated with eq 3. Because the structure of the sugar template has a significant effect on the porosity of the PDMS sponge,[9] three separate samples (different fabricated molds) were used to attain the average value of each kind of sponge. All experiments were conducted at room temperature.

$$N_w = \frac{m - m_s}{m_s} \times 100 \quad (1)$$

$$\text{porosity}(\%) = \frac{V_w}{V_s} \times 100 = \frac{m_w}{\rho_w \times V_s} \times 100 = \frac{m - m_s}{1\frac{g}{cm^3} \times V_s} \times 100 \quad (2)$$

$$\rho = \frac{m_s}{v} = \frac{m_s}{0.5\text{cm}^3} \quad (3)$$

2.4.5. Compression Test. To do the compression test, all the fabricated PDMS sponges were cut into cylinders (12 mm in diameter and 7 mm in height). A texture analyzer (TA.XT Plus, Texture Technologies, Scarsdale, NY, USA) and a radiused cylinder probe (P/0.5R) were used for measuring the elasticity moduli of all PDMS sponge samples. The modulus of elasticity (E) of the sample was calculated with eq 4, and it could be represented as the slope of the stress−strain curve in the elastic region. The stress (σ) is the pressing force, which brings the deformation to the object. The strain (ε) is defined as the ratio of the height change of the object due to the deformation to its original height.[28] These PDMS samples were compressed with a trigger force of 0.005 kg at a test speed of 2.00 mm/s. All samples were run in triplicate (n = 3).

$$E = \frac{\sigma}{\varepsilon} \quad (4)$$

2.4.6. Measurement of Sponge Deformation under a Magnetic Field. Magnetic PDMS sponge cylinders (diameter × thickness = 12 mm × 7 mm) with various contents of magnetic particles were placed on a microscope glass slide (thickness = 1 mm). Magnet D (Table 1)

Table 1. Dimensions of Neodymium Grade N42 Magnets Used in the Current Studies to Provide Different Magnetic Flux Densities with a Distance of 5 mm

magnets	A	B	C	D
diameter (mm)	19.5	19.5	21.5	19.5
thickness (mm)	2.5	2.5	5.5	9.5
magnetic field (mT)	110	150	204	355

was placed underneath the sponge cylinder (attached on a glass slide) to provide a magnetic field strength (magnetic flux density) of 355 mT for compressing these sponge cylinders. Then the displacement of the front surface of each sponge cylinder in three different locations under different magnetic flux densities and the average deformation were recorded. Three separate sponge samples from independently fabricated sugar molds were applied for the deformation measurements (n = 3).

A noncontact rig for characterizing the compression of magnetic sponges was designed. This method is based on a bright-field microscopy (BFM) metrology system (Figure 1) consisting of an Olympus PLN4X (working distance of 18.5 mm, a numerical aperture of 0.1, Olympus Corporation, Tokyo, Japan), a tube lens with a focal length of 180 mm, and an Imaging Source DMK31BF03 CCD camera (The Imaging Source Europe GmbH, Bremen, Germany) mounted on top of a custom-made linear stage having a coarse resolution of around 3.3 μm.

As the sponges are made of PDMS and ferromagnetic particles, the illumination source was placed parallel to the measurement device, i.e., facing toward the surface of the sample. The sponges under test were fixed on microscope slides and positioned at the focal point of

https://dx.doi.org/10.1021/acsbiomaterials.0c01608
ACS Biomater. Sci. Eng. 2021, 7, 180−195

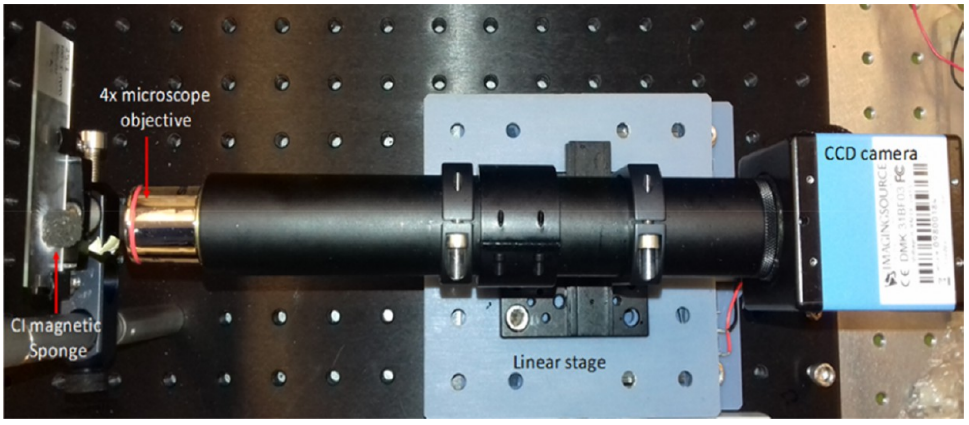

Figure 1. Bright-field microscopy metrology system.

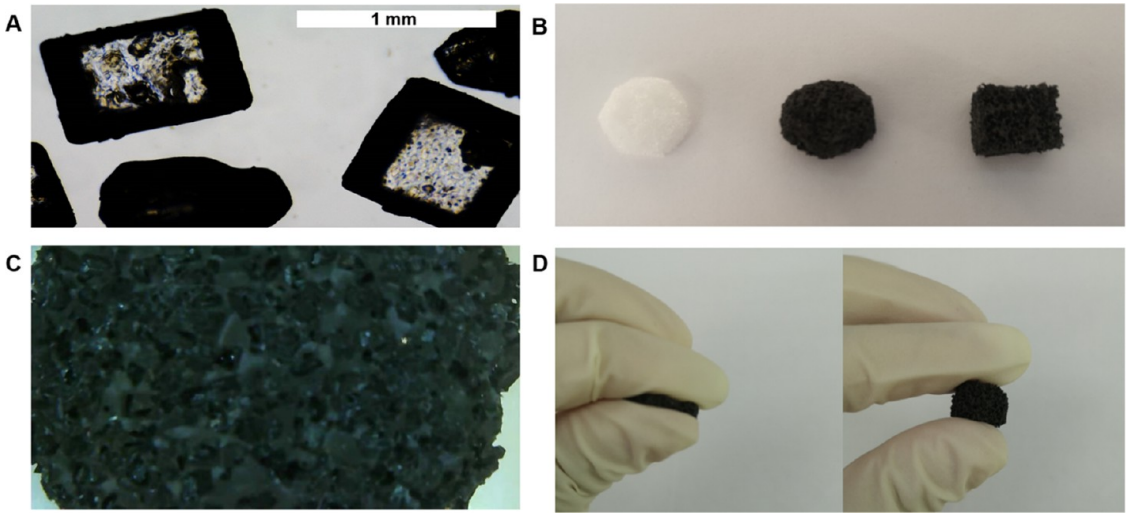

Figure 2. (A) Optical microscope image of granulated sugar particles. (B) Photograph of the pure PDMS sponge cylinder, CI-loaded PDMS cylinder, and Fe_3O_4-loaded PDMS cube fabricated with the granulated sugar template. (C) Macroscopic appearance of the 100 w/w % CI/PDMS cylinder surface. (D) Manual compression and recovery of the 100 w/w % CI/PDMS sponge cylinder.

the metrology system. The measurements were performed by applying different magnetic field strengths using custom-designed neodymium grade N42 magnets (Table 1).

By placing the magnets in contact with the back of the microscope slide, visible deformation was observed. This was measured by employing the bright-field measurement device without making contact with the actual sponge (i.e., opposed to contacting methods based on the use of a calliper) to determine the average deformation of the sponge at different magnetic field strengths.

By focusing the microscope on the magnetic sponge surface, the reference position was recorded. Then, placing the magnet near the magnetic sponge, a deformation was produced, taking the sample out of the focal plane. By refocusing the measuring device and recording the linear stage digital readout, the deformation was accurately measured.

2.4.7. Dielectric Constant (Relative Permittivity) Measurement. The dielectric constant (relative permittivity) is measured with an LCR meter (4274A multifrequency LCR meter 100 Hz to 100 kHz, HP/Agilent, Japan) and a parallel plate capacitor (dielectric loss test Jig TJ155B/1, Marconi Instruments Ltd., UK) with two disks (25.4 mm in diameter). The sponge sample was sandwiched between the two plates, so the capacitance (C) was measured out on the screen. As the area of parallel plates (A) is 5.07×10^{-4} m^2, the separation (d) is the thickness of the sponge sample, and the permittivity of space (ε_0) is 8.854×10^{-12} F/m, the relative permittivity of the dielectric material between the plates (k or ε_r) could be calculated with eq 5.

$$k = \frac{\varepsilon}{\varepsilon_0} = \frac{Cd}{\varepsilon_0 A} \tag{5}$$

2.4.8. Recyclability. The measurement of repeated absorption and desorption on water absorbency of sponges is applied for the evaluation of their reusability. To achieve absorption equilibrium, the sponge cylinder samples (diameter × thickness = 12 mm × 7 mm) was immersed in water at room temperature and was compressed gently until no air bubbles came out. Then the absorbency value was calculated by weighing the sponge samples with absorbed water. The samples were squeezed and dried in an oven at 60 °C until the weight was stable. The absorption−desorption procedure was repeated 10 times to check if the absorbency property of the sponge remained intact.

2.4.9. Thermogravimetric Analysis (TGA). TGA was performed with a TGA Q50 (TA Instruments, Leatherhead, UK) to measure the degradation temperature of fabricated PDMS sponges. Around 5 mg of each sample was placed in an open aluminum pan and then heated from 20 °C at a heating rate of 10 °C/min up to 500 °C with 25 mL/min purified nitrogen purging. Data were recorded and analyzed with the TA Universal Analysis software (TA Instruments-Waters LLC, New Castle, DE, USA).

2.5. Cell Culture Studies of the Devices *In Vitro* with FLU Solution. *2.5.1. Preparation of Sponges Samples Loaded with Drug Solution.* As the sponge samples are very porous, it is easy for them to absorb the drug solution inside. The solubility of FLU in water is very low and could be increased significantly at higher

https://dx.doi.org/10.1021/acsbiomaterials.0c01608
ACS Biomater. Sci. Eng. 2021, 7, 180−195

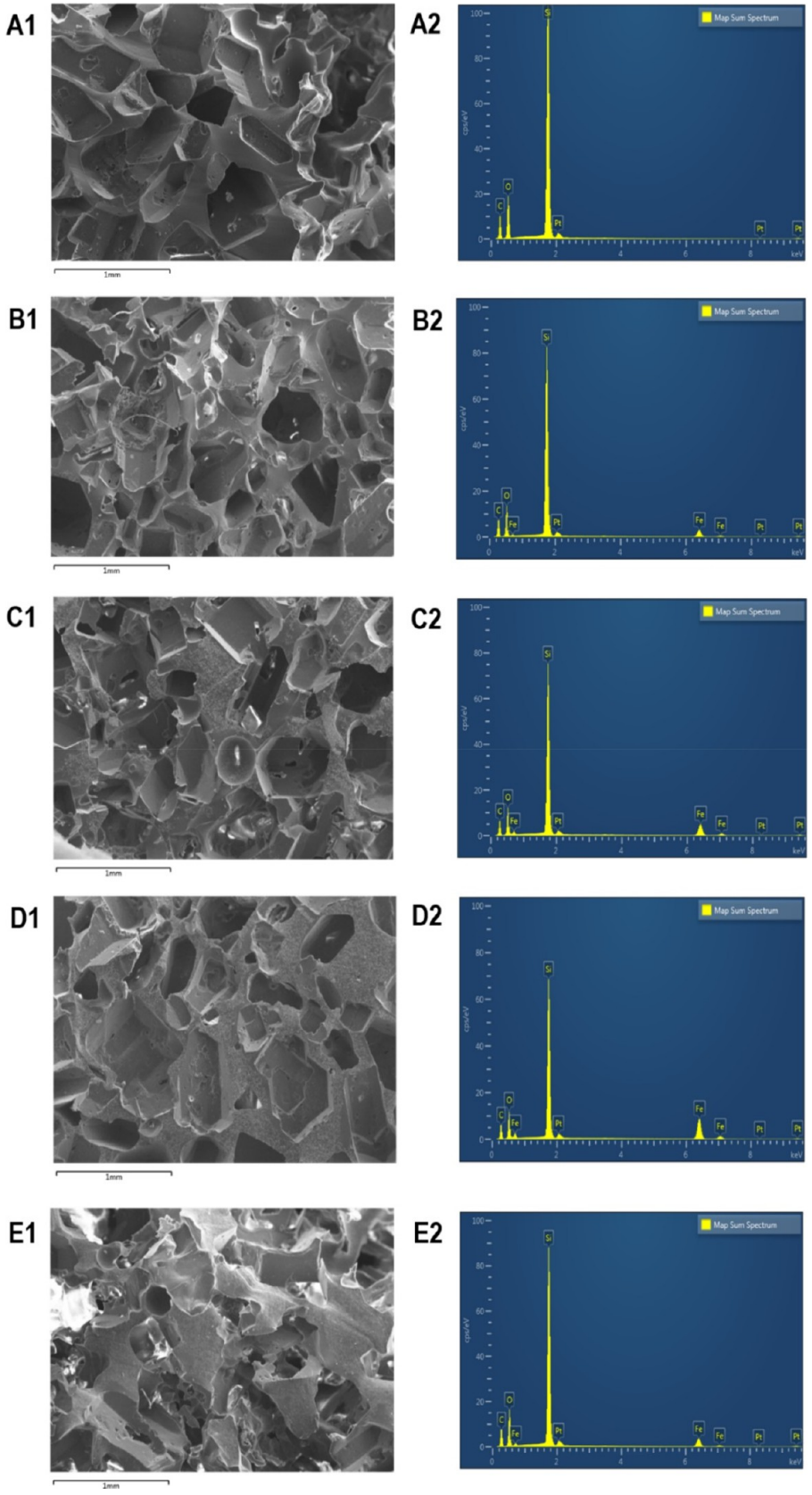

Figure 3. SEM images of the morphology and EDS spectra in the cross section of (A) pure PDMS sponges, (B) 30 w/w % CI/PDMS sponges, (C) 100 w/w % CI/PDMS sponges, (D) 150 w/w % CI/PDMS sponges, and (E) 30 w/w % Fe_3O_4/PDMS sponges.

temperatures; therefore, the temperature was increased to 70 °C to load more drug in a limited volume of water during the FLU solution preparation.[29] Three samples of each kind of sponge (diameter × thickness = 5 mm × 2 mm) were immersed in the drug solution

https://dx.doi.org/10.1021/acsbiomaterials.0c01608
ACS Biomater. Sci. Eng. 2021, 7, 180−195

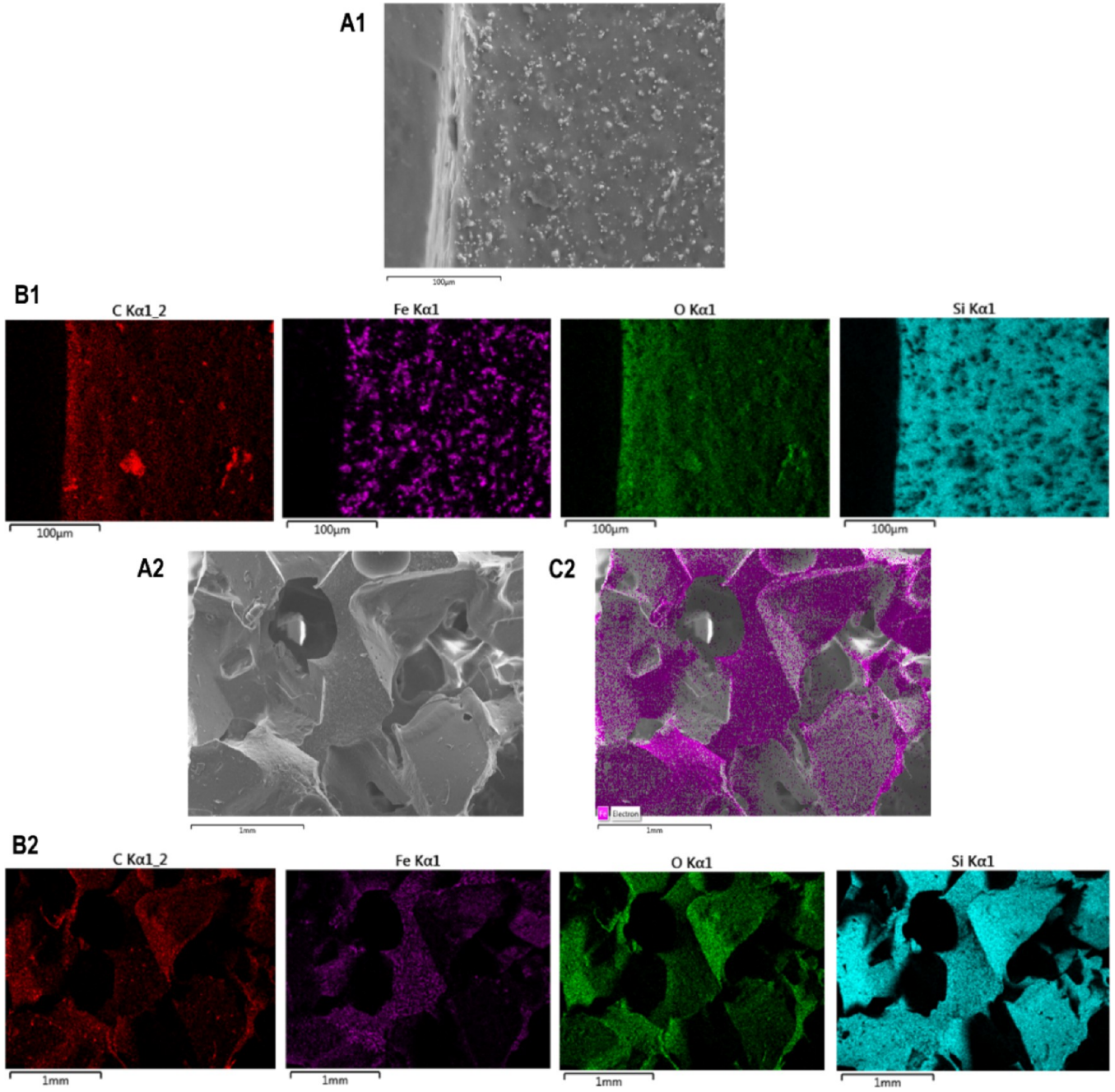

Figure 4. Cross-sectional (A) SEM images, (B) multielement EDS mapping of C, Fe, O, and Si, and (C) SEM-EDS digital image of element Fe in 100 w/w % CI/PDMS sponges.

(FLU) with a concentration of 25 mg/mL or 12.5 mg/mL. After the complete absorption of the drug solution, the sponge samples were taken out and left at room temperature for 3 days before sterilization.

2.5.2. Cell Lines. HeLa cells stably express green fluorescent protein (GFP) constructs. Cell lines were maintained in Dulbecco's modified Eagle's medium (DMEM) supplemented with 10% fetal calf serum (FCS), penicillin/streptomycin, and L-glutamine at 37 °C and 5% CO_2.

2.5.3. Experimental Setup. Substrates were sterilized and transferred to 12-well plates. Cells were plated at a density of 0.4×10^5 on day 0. On day 1, media in wells were changed. On day 1 or 2, substrates were transferred to new wells and the remaining cells were trypsinized using trypsin EDTA and counted using a hemocytometer. Cells were replated onto the substrates in fresh media. On day 4, substrates were washed three times with PBS and transferred to new wells and fresh media. Remaining cells were trypsinized, counted, and discarded.

3. RESULTS AND DISCUSSION

3.1. Characterization of Magnetic Sponges. In this study, pure PDMS sponges and magnetic PDMS sponges with different concentrations of magnetic microparticles were fabricated and sectioned into different thicknesses by using the water-soluble sugar template. The macroporous sponges with interconnected pores, larger pore sizes, a higher concentration of magnetic particles, and lower compressive moduli were selected as the main scaffold in this study. The main reasons behind the selection of sponges were that sponges with large pore sizes and high connectivity can

https://dx.doi.org/10.1021/acsbiomaterials.0c01608
ACS Biomater. Sci. Eng. 2021, 7, 180−195

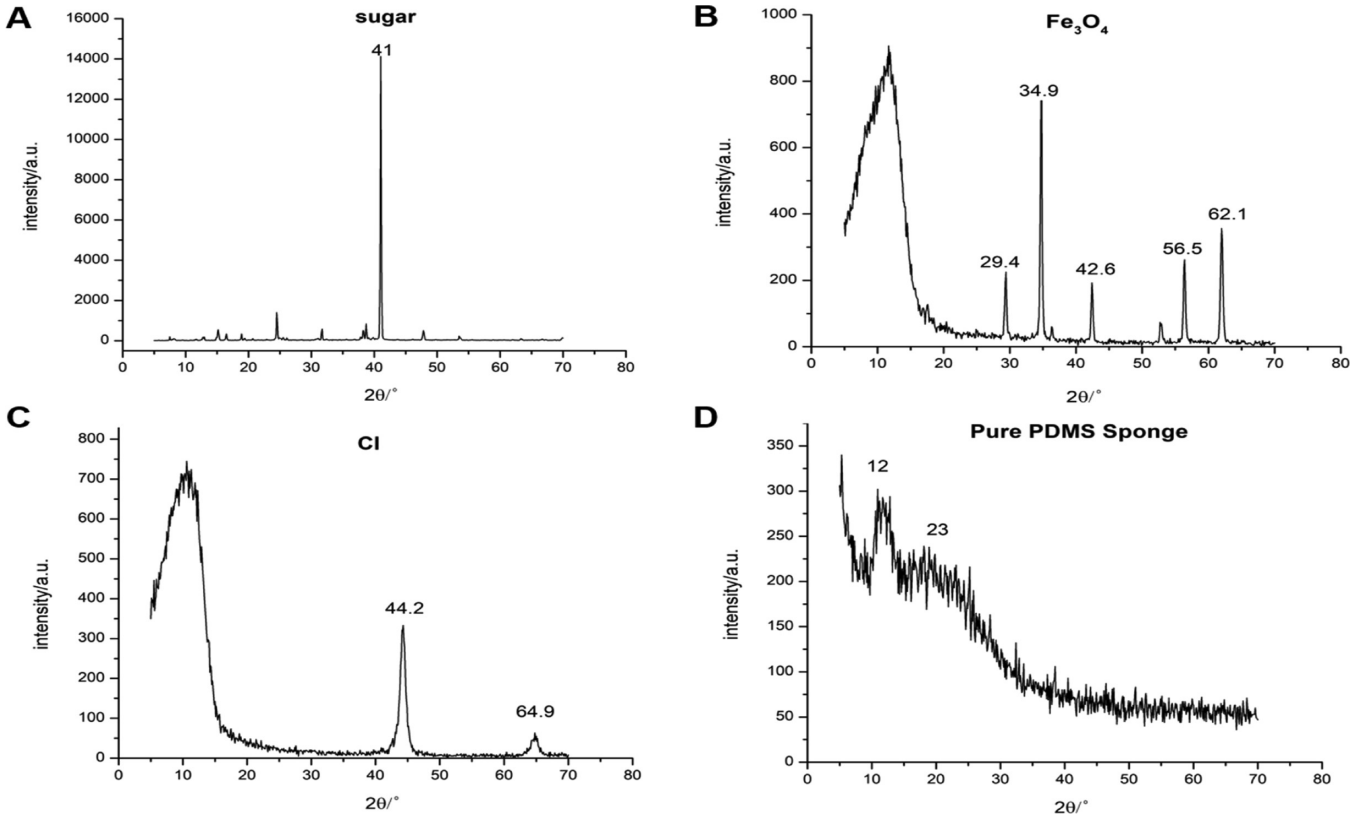

Figure 5. XRD patterns of raw materials (sugar, Fe_3O_4, and CI) and PDMS sponges.

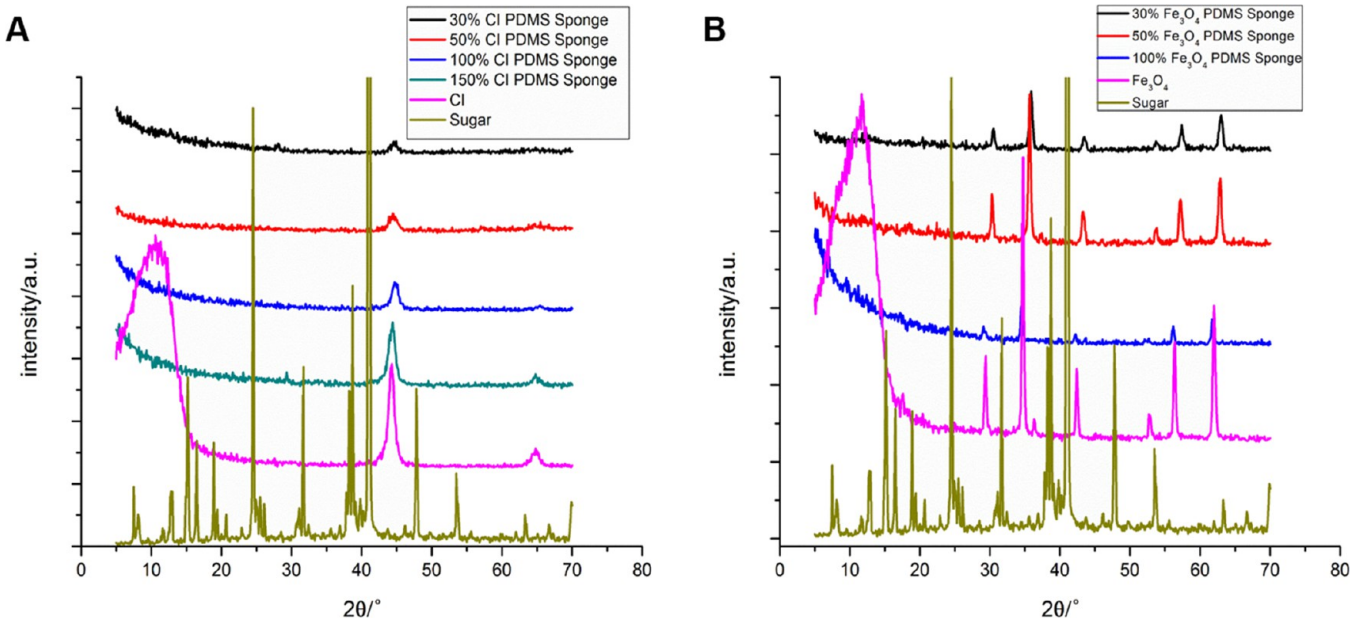

Figure 6. Comparison of XRD patterns of raw materials (sugar and Fe_3O_4/CI) with corresponding (A) Fe_3O_4-loaded and (B) CI-loaded PDMS sponges.

preserve and transport drug more efficiently, and a higher magnetic particle density can produce a higher body force under the same magnetic field, and sponges with lower compressive moduli have the potential to show larger deformation (leads to a more obvious effect on drug release) when subject to the same body force.[1]

3.1.1. Physical Appearance of Sponges. The optical microscope image of granulated sugar particles (Figure 2A) reveals that the size of granulated sugar particles used in this experiment is not so uniform. This will help to increase the porosity of PDMS sponges because the less uniform the sugar particles are, the higher the porosity of the sponges is.[9]

Macroporous sponges of various shapes and dimensions (Figure 2B) can readily be fabricated and cut to accommodate specific requirements. Additionally, large-scale production of PDMS sponges can be accessible through the proposed sugar-

https://dx.doi.org/10.1021/acsbiomaterials.0c01608
ACS Biomater. Sci. Eng. 2021, 7, 180−195

Table 2. Calculated Mean ± Standard Deviation Values of Bulk Density, Porosity, and Water Absorption of Different Kinds of PDMS Sponge Samples Prepared with Granulated Sugar (n = 3)

composition	concentration of magnetic particles (%)	bulk density (g/cm^3)	porosity (%)	water absorption (%)
pure PDMS sponge	0	0.31 ± 0.02	64.97 ± 5.50	145.51 ± 6.15
CI/PDMS = 30 wt % sponge	23.08	0.35 ± 0.01	63.57 ± 2.44	128.33 ± 10.10
CI/PDMS = 50 wt % sponge	33.33	0.43 ± 0.06	61.90 ± 4.37	119.01 ± 12.56
CI/PDMS = 100 wt % sponge	50	0.49 ± 0.06	59.04 ± 2.93	102.87 ± 5.48
CI/PDMS = 150 wt % sponge	60	0.56 ± 0.02	41.01 ± 2.16	63.10 ± 10.30
Fe_3O_4/PDMS = 30 wt % sponge	23.08	0.46 ± 0.12	53.96 ± 3.36	117.18 ± 11.85
Fe_3O_4/PDMS = 50 wt % sponge	33.33	0.49 ± 0.20	49.71 ± 1.42	83.08 ± 14.58

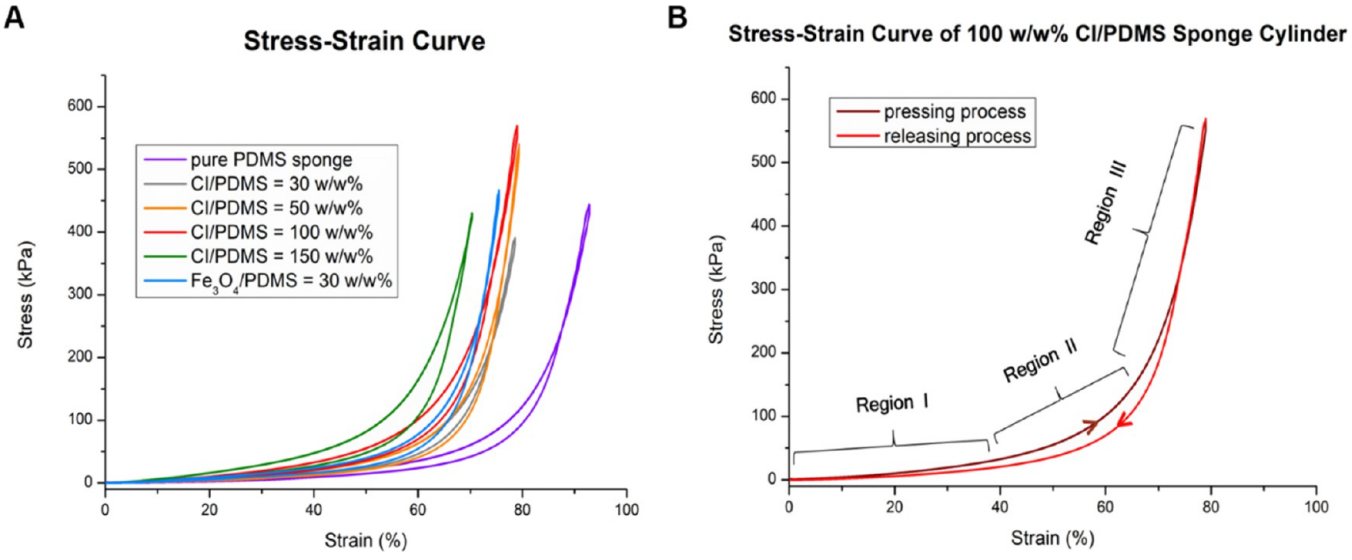

Figure 7. (A) Compressive stress−strain curves of various PDMS sponge cylinders prepared with granulated sugar molds. (B) Illustration of different phases (the brown curve represents the pressing process with three regions, and the red curve represents the releasing process) in the stress−strain curve of 100 w/w % CI/PDMS sponge cylinders.

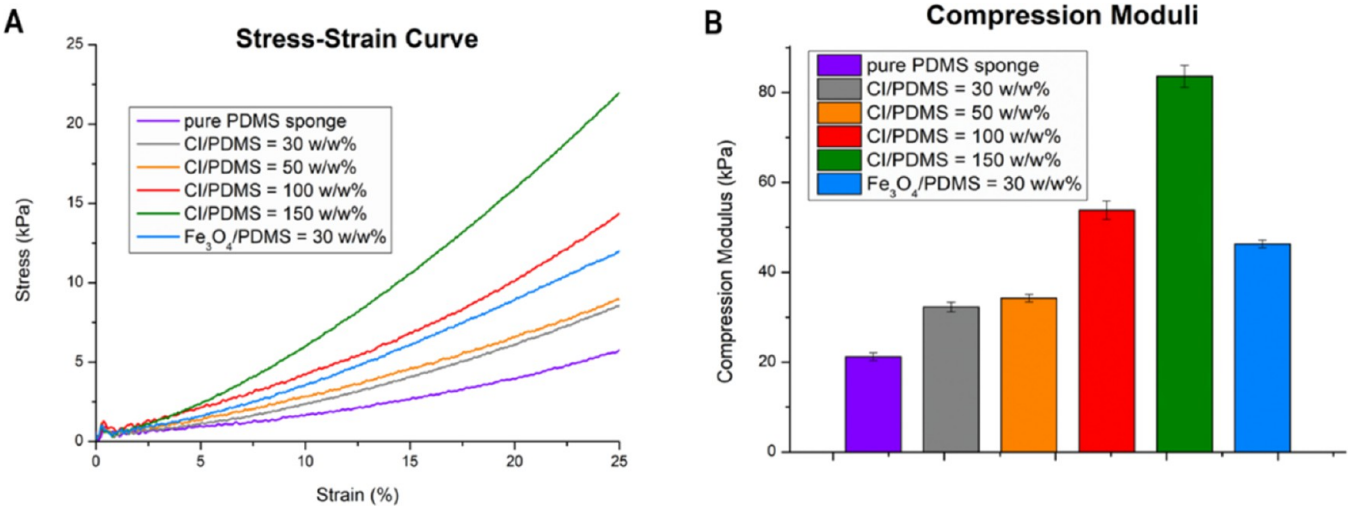

Figure 8. (A) Compressive stress−strain curves with a maximum strain of 25% for various magnetic particle loaded PDMS sponges prepared with granulated sugar molds. (B) Calculated compression moduli of sponges with different concentrations of magnetic particles. The average ± standard deviation is represented by the error bars (n = 3).

templating process as the total production processing time only lasts for a few hours.[9]

The highly porous pure PDMS sponge was white, soft, and highly flexible. Highly monodisperse Fe_3O_4 microparticles with a diameter of <5 μm were embedded in sponges at predetermined concentrations (30, 50, and 100 w/w % of the PDMS). These sponges are black and porous. The sponges become stiffer when the concentration of Fe_3O_4 microparticles increases due to the stiffness of the magnetic microparticles.

Unlike Fe_3O_4, CI microparticles can be used to prepare 30, 50, 100, and 150 (w/w % of the weight of PDMS) CI-loaded PDMS sponges, which could be due to the lower density of CI

https://dx.doi.org/10.1021/acsbiomaterials.0c01608
ACS Biomater. Sci. Eng. 2021, 7, 180−195

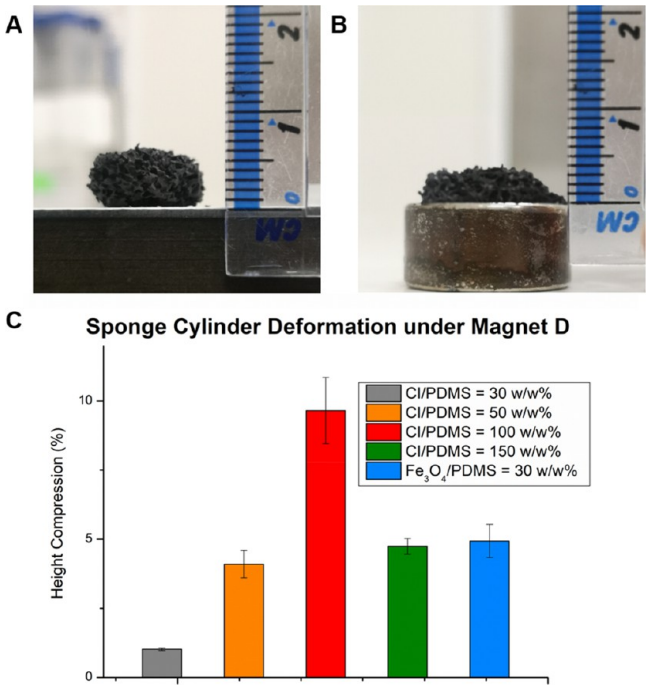

Figure 9. (A) Image of the original shape of the 100 w/w % CI/PDMS sponge. (B) The deformed shape of the 100 w/w % CI/PDMS sponge under Magnet D. (C) Average configuration changes of sponges prepared with granulated sugar molds under Magnet D; the average ± standard error is represented by the error bars (n = 3).

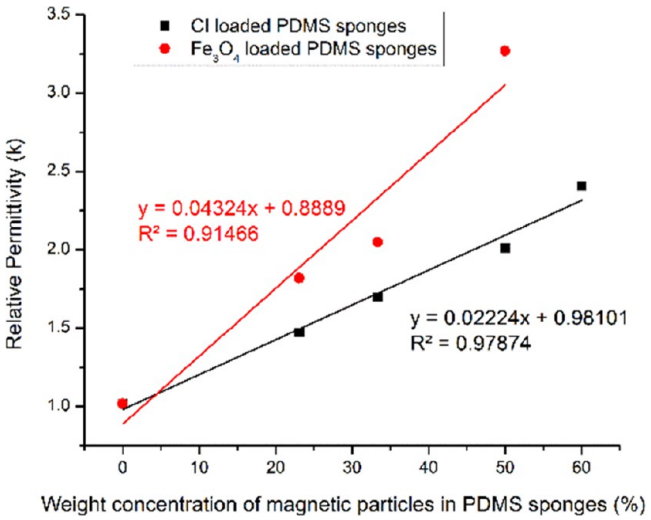

Figure 10. Comparison of the relative permittivity values of Fe_3O_4-loaded PDMS sponges and CI-loaded PDMS sponges.

(1.45 g/cm^3) than of Fe_3O_4 (5.2 g/cm^3).[25,30,31] These sponges are dark gray and porous (Figure 2C). The sponges also become stiffer when the concentration of CI microparticles increases.

As shown in Figure 2D, the fabricated magnetic PDMS sponges display rarely observed structural flexibility in porous materials.[9] These sponges show significant compliance and springiness for a remarkable volume reduction of more than 50% in manual compression. Additionally, these sponges can be bent to a large extent without breaking apart, and they are reversible to their original shape. It is inferred that these sponges are suitable for recycling. Furthermore, the absorbed solution in PDMS sponges can be removed and reutilized through slightly squeezing sponges manually because of the springiness nature of these PDMS sponges.

3.1.2. SEM and EDS Analysis. From these SEM images of thin sponge slices (Figure 3), no obvious difference in the morphology or distribution of magnetic particles is discovered among all these PDMS sponges. It is illustrated in Figure 3 that all sponge samples possess a similar open network of pores with a large surface area and a perfect porous structure. It indicates that the mixture of magnetic particles and PDMS (prepolymer and curing agents) filled the sugar mold completely and was capable of forming porous scaffolds.[32] The interconnected pores of these sponge samples were spread evenly across PDMS, and their pore size is around 200−500 μm, mainly because the same sugar template was used. With the addition of magnetic particles, the surface of the sponge becomes rugged. As magnetic particles were wrapped completely, the risk of oxidation will be minimized, the stability will be enhanced, and surface roughness will be increased.[6,18,24] However, the rough surface and the 3D interconnected pores of magnetic powder loaded PDMS sponges could enhance the hydrophobic property of the sponges.[8]

In conjunction with advanced SEM, EDS has been widely applied as a chemical microanalysis technology because of its many advantages, such as high-resolution imaging, semi-quantitative elemental analysis, and qualitative X-ray elemental maps.[33] It is difficult to fabricate sponges with both high contents of magnetic particles and superior distribution of magnetic particles at the same time due to the tendency for these Fe_3O_4 and CI particles with large surface areas and high free energy to cluster and precipitate.[20] To investigate the chemical composition and spatial distribution of magnetic particles in sponges, EDS was also used in this study.

The EDS analysis of the cross-sectional area in these sponges showed various distributions of elements (Figure 3). The pure PDMS sponges only exhibited a large number of signals of C, O, and Si as well as trace amounts of Pt because of the sputter coating process. With the addition of CI particles in the PDMS sponges, the signals of Fe increased whereas the signals of Si decreased gradually.

Multielemental EDS mapping images of C, Fe, O, and Si are shown in Figure 4. The bright spots of these elements in corresponding maps indicate a homogeneous distribution of these elements in the field of view of the partial cross section. Furthermore, the magnetic particles showed no agglomeration, and they were distributed in PDMS uniformly.

3.1.3. XRD Analysis. XRD measurements are important to analyze the dispersion of magnetic particles in these fabricated magnetic PDMS sponges. The XRD diffractograms (Figure 5) of raw materials and pure PDMS sponges show that white granulated sugar, Fe_3O_4, and CI particles all have a crystalline nature because of sharp intense peaks throughout their diffraction patterns, whereas the XRD pattern of pure PDMS sponges is mostly in the amorphous state as it shows a halo pattern. The XRD patterns of Fe_3O_4 particles exhibit five peaks at 2θ of 29.4, 34.9, 42.6, 56.5, and 62.1°, and that of CI shows two peaks at 2θ of 44.2 and 64.9°, which are the main peaks for these two chemicals.[7,34,35] Two broad and low intensity peaks at around 12 and 23° from the pattern of pure PDMS sponges confirm their amorphous nature because it has been revealed that the XRD diffraction peak at around 24° is one of the

https://dx.doi.org/10.1021/acsbiomaterials.0c01608
ACS Biomater. Sci. Eng. 2021, 7, 180−195

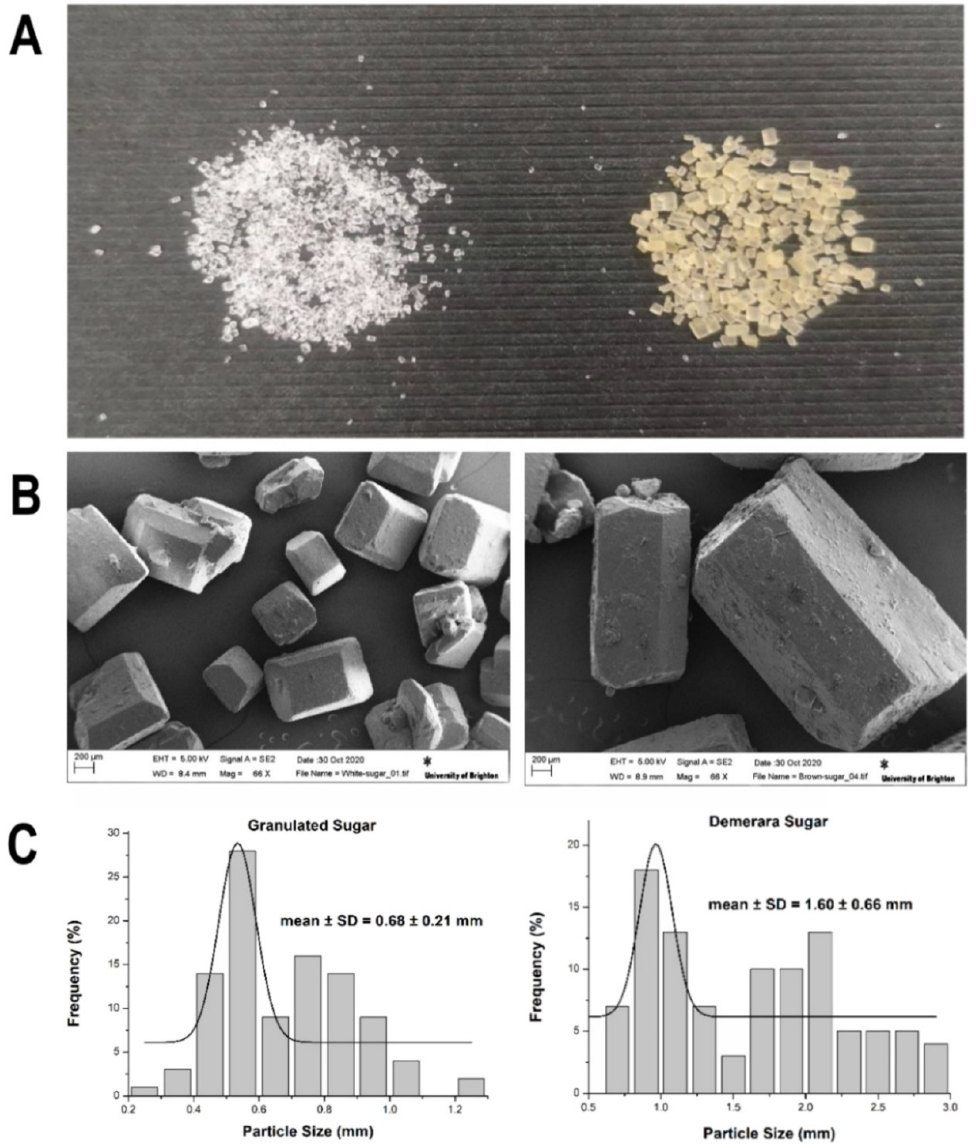

Figure 11. (A) Photographs, (B) SEM images, and (C) the particle size frequency diagrams of granulated sugar and demerara sugar.

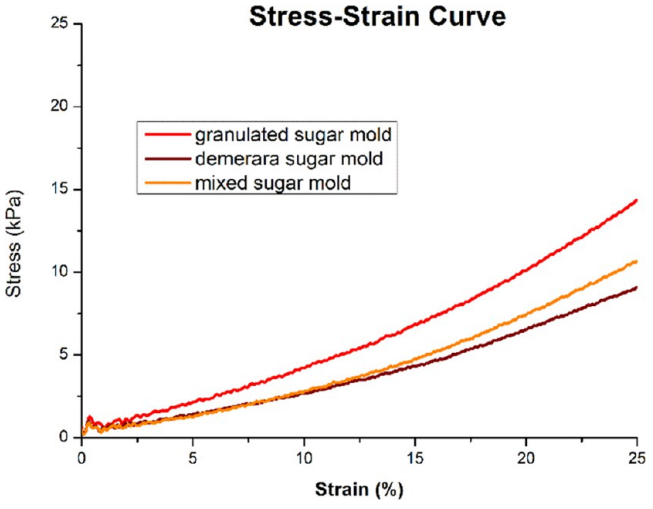

Figure 12. Compressive stress−strain curves with a maximum strain of 25% for 100 w/w % CI/PDMS sponges prepared with different sugar molds.

evidence for the existence of large quantities of amorphous materials.[7,35]

There are obvious sharp intense peaks in all diffraction patterns of Fe_3O_4/PDMS sponges and CI/PDMS sponges, so they all have a crystalline nature. The comparisons of XRD traces (Figure 6) of different Fe_3O_4-loaded PDMS sponges/CI-loaded PDMS sponges and Fe_3O_4/CI were made to find out the relationship between the peaks of Fe_3O_4-loaded/CI-loaded PDMS sponges with raw materials. Most peaks in Fe_3O_4-loaded/CI-loaded PDMS sponges are inconsistent with the peaks of Fe_3O_4/CI. Consequently, a certain amount of crystalline Fe_3O_4/CI can be confirmed in these Fe_3O_4-loaded/CI-loaded PDMS sponges through these graphs. Furthermore, there is also no trace of sugars in the formulation, which means that all sugars have been washed away during the leaching process. However, 100% Fe_3O_4/PDMS sponges seemed to have reduced the crystallinity because the mixture of Fe_3O_4 and PDMS solution was so sticky that Fe_3O_4 cannot penetrate through the sugar mold to form the sponge. As a result, most Fe_3O_4 particles were agglomerated at the top surface of the

https://dx.doi.org/10.1021/acsbiomaterials.0c01608
ACS Biomater. Sci. Eng. 2021, 7, 180−195

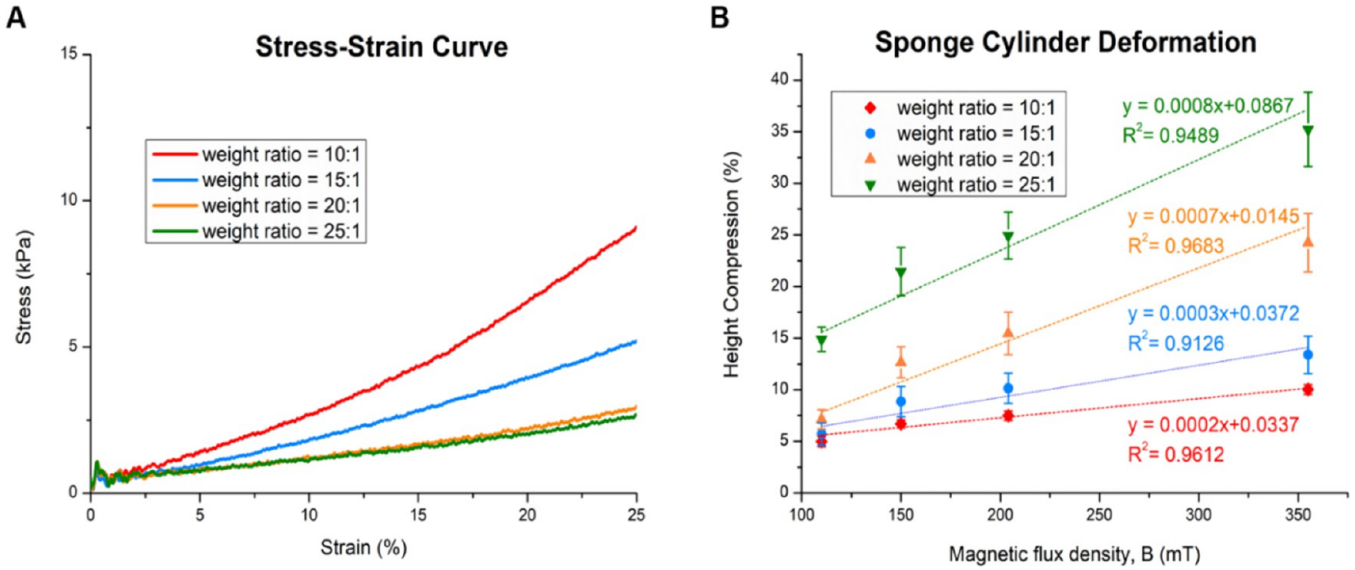

Figure 13. (A) Compressive stress−strain curves with a maximum strain of 25% for 100 w/w % CI/PDMS prepared with the demerara sugar mold and various weight ratios of PDMS prepolymer and curing agents. (B) Height compression of sponges versus different magnetic fields; the average ± standard error is represented by the error bars (n = 3).

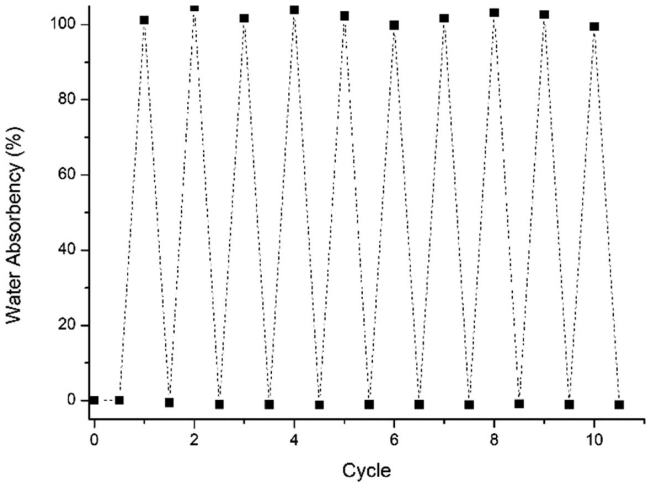

Figure 14. Demonstration of recyclability of 100 w/w % CI/PDMS sponge cylinders (prepared with demerara sugar and PDMS prepolymer/curing agents = 25:1 w/w).

sugar mold in the fabricating process of 100 w/w % Fe_3O_4/PDMS sponges.

Since the specimens for XRD studies were selected from the midsection of the mold for all formulations, this proves less penetration of Fe_3O_4 in the sponges due to the unsatisfactory penetration of 100 w/w % Fe_3O_4/PDMS through the sugar mold. Because it has been proven that the nonuniform distribution of magnetic particles could lead to poor magnetic and mechanical properties, this sponge was not used in the following experiments.[20,36]

3.1.4. Porosity of Sponges. As can be seen from Table 2, pure PDMS sponges exhibited the highest porosity and water absorption. However, the differences among the porosity values of CI/PDMS sponge samples with weight ratios of 30, 50, and 100 w/w % PDMS are not very remarkable. The porosity of 150 w/w % CI/PDMS sponges is the lowest. Also, the porosity values of 30 and 50 w/w % Fe_3O_4/PDMS sponges are much lower than the same ratio of CI/PDMS sponges. The possible reason is the higher density of Fe_3O_4 than of CI. By immersing these sponges fabricated from the granulated sugar mold directly in water, up to 146 wt % of the original weight could be absorbed. These PDMS sponges were immediately wetted in water, although higher absorption was expected to achieve in long immersion times. This time-independent absorbing property also illustrates the strong water absorption of these sponges. Furthermore, the standard deviations of the water absorption of Fe_3O_4-loaded PDMS sponges are higher than those of CI-loaded PDMS sponges.

According to Jurin's law (eq 6), the height of liquid (h) in a capillary tube is associated with the surface tension (γ) of the liquid, the contact angle (θ) of the liquid, the mass density (ρ), and the tube radius (r).[37] Although these sponges were all prepared with the granulated sugar mold, the depth of liquid columns of the PDMS and magnetic particle blend penetrated in the sugar mold is lower because of the higher density of the magnetic PDMS blend. The slow penetration of the solution can completely remove the air between sugar crystals from the sugar template compared to the fast penetration of pure PDMS. As a result, the sponges prepared with magnetic PDMS blends show thicker walls inside the sponge. After the leaching process, the magnetic PDMS sponge can show lower porosity as the density of PDMS blends increases. This is true as when the concentration of magnetic particles increases in the PDMS solution (in which the density of the solution will increase accordingly), the porosity of the sponges decreases as a result of the high density of the solution (Table 2).

$$h = \frac{2\gamma\cos\theta}{\rho g r} \tag{6}$$

Additionally, the absorption capacity of these PDMS sponges after multiple cycles was normalized by the initial weight gain. Complete removal of remaining water of the PDMS sponge in an oven can ensure the PDMS sponge could be recycled.[10]

3.1.5. Mechanical Testing. The inclusion of heterogeneous materials can affect the mechanical properties of PDMS sponges, so compressive stress−strain curves were used to

https://dx.doi.org/10.1021/acsbiomaterials.0c01608
ACS Biomater. Sci. Eng. 2021, 7, 180−195

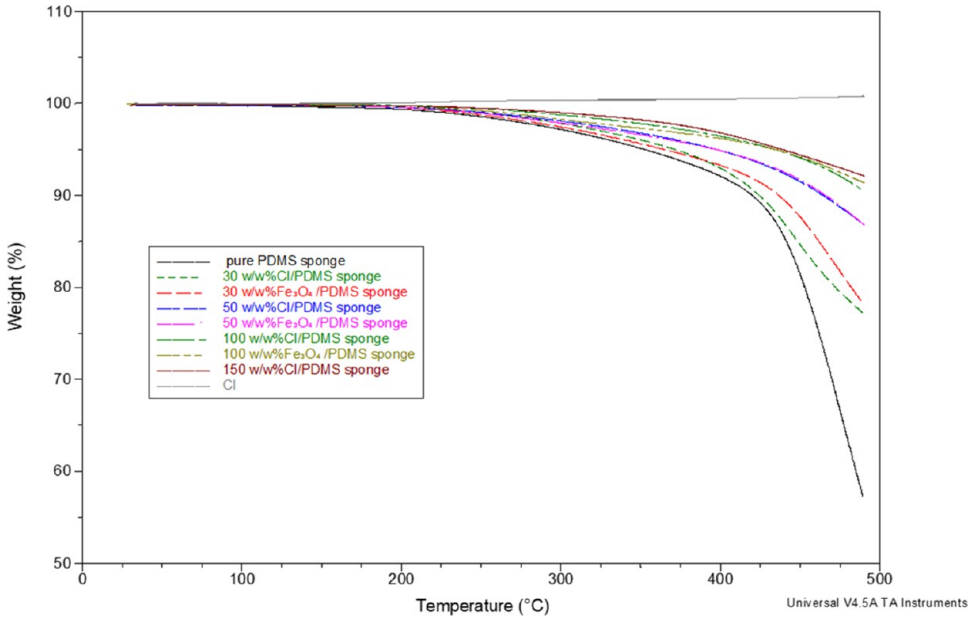

Figure 15. TGA thermal traces of CI particles, pure fabricated PDMS sponge, and various magnetic PDMS sponge samples. The initial weight shows 100%.

Table 3. Sponge Samples Loaded with Different Solutions and under Different Magnetic Fields

group	magnet	sponge	FLU solution
A1	B	×	×
A2	C	×	×
A3	×	pure PDMS	×
A4	×	pure PDMS	25 mg/mL
A5	B	pure PDMS	×
A6	B	pure PDMS	25 mg/mL
A7	C	pure PDMS	25 mg/mL
A8	×	CI/PDMS = 100 wt %	×
A9	×	CI/PDMS = 100 wt %	25 mg/mL
A10	B	CI/PDMS = 100 wt %	×
A11	C	CI/PDMS = 100 wt %	×
A12	B	CI/PDMS = 100 wt %	25 mg/mL
A13	C	CI/PDMS = 100 wt %	25 mg/mL
A14	B	CI/PDMS = 100 wt %	12.5 mg/mL
A15	C	CI/PDMS = 100 wt %	12.5 mg/mL

analyze their moduli.[38] Figure 7A exhibits the measured stress−strain data of various prepared PDMS sponge cylinders fabricated with the granulated sugar mold, which proves that these porous materials possess a three-phase behavior (Figure 7B).[32] At the beginning of curves, the intact sponges deform linearly with respect to the stress. Region I was depicted as the elastic region. This region is followed by a relative plateau (Region II), in which the curves demonstrate that these scaffolds are buckled and collapsed. With the increase of stress (Region III), the PDMS sponges are crushed together and exhibit great mechanical performances. During the releasing process, these curves can return to the origin without plastic deformation. The cycled compression−relaxation test of these sponges illustrated their excellent reversible deformation ability.[14] Obvious hysteresis loops could be found in all stress−strain curves. The area inside the loop represents the energy lost during the pressing−releasing cycle. This is mainly attributed to the viscoelastic characteristics of these PDMS sponges. It indicates that strong mechanical strength could be applied to these prepared PDMS sponges as they possess high deformability. As expected, pure PDMS sponges showed the maximum strain at about 90%, which started decreasing with the increase in the content of magnetic iron particles. This is because of the stiffness of the crystalline particles. However, the presence of the iron particles contributed to the enhanced stress values of the sponges where a maximum stress of about 500 kPa was observed for CI-loaded PDMS sponges compared to about 450 kPa for pure PDMS sponges. Nonetheless, all developed sponges exhibited 70% more strain values with the capacity of full deformation.

The measured data within the elastic region (Region I) are shown in the stress−strain curves (Figure 8A). Based on the slope of strain versus stress, the elastic moduli of these sponge samples can be calculated. The measured elastic modulus of prepared PDMS sponges is between 20 and 90 kPa (Figure 8B), which is significantly lower than those of rubber (10485.76−104857.6 kPa) and bulk PDMS materials (786.432 kPa).[9]

As shown in Figure 8B, the compression modulus will increase when the CI/PDMS w/w % ratio is increased because the interaction between the CI particles and the polymer scaffold was strengthened.[6] The possible reason for these enhanced moduli is the increased rigidity of the sponge samples because of the participation of magnetic microparticles. However, the sponge samples with lower compression moduli are more desirable because they can deflect more under the same external magnetic field. The surface properties of embedded particles have a crucial effect on the physicochemical interaction between the filler materials and the polymer scaffold network, which then can further influence the mechanical properties of the composites.[6] Therefore, these PDMS sponges with excellent mechanical properties and resilience from large deformations could be potentially applied in drug-releasing devices and implantable biomedical devices.

3.1.6. Sponge Deformation under a Magnetic Field. As shown in Figure 9A,B, the height of prepared sponge cylinders can decrease obviously under the magnetic field provided by

https://dx.doi.org/10.1021/acsbiomaterials.0c01608
ACS Biomater. Sci. Eng. 2021, 7, 180−195

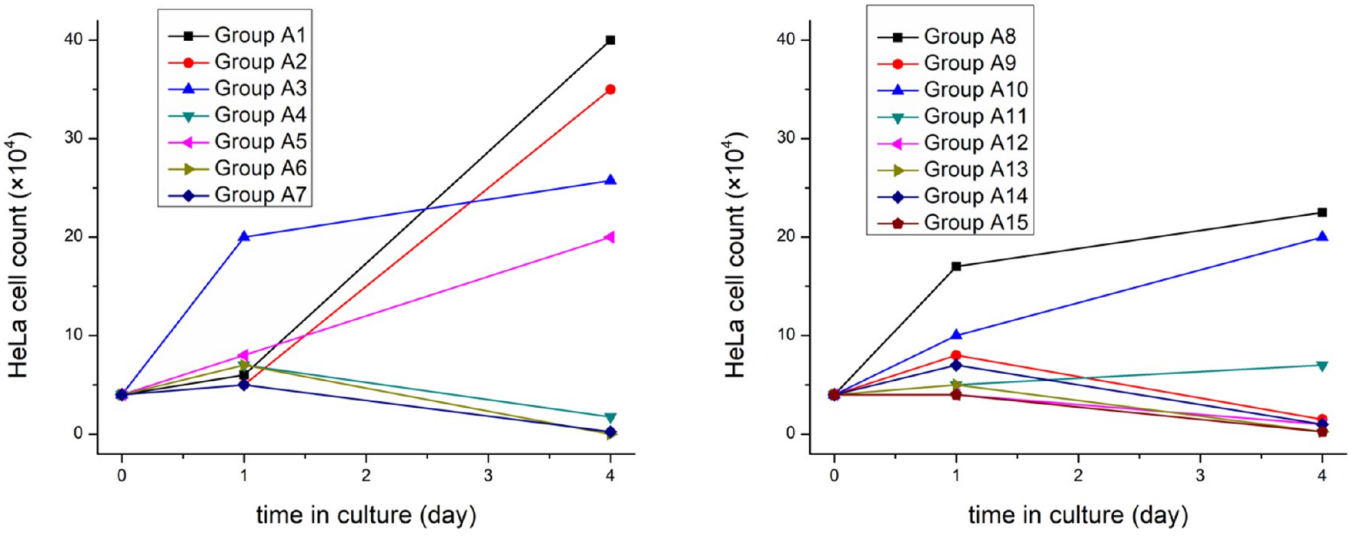

Figure 16. Numbers of HeLa cells under different conditions.

Magnet D (Table 1). At the same time, the volume of the interconnected pores of sponges will be minimized. Like manual compression (Figure 2D), all deformations due to the magnetic force could be reversible. The deformation of these magnetic sponge samples increases linearly as a function of magnetic field strength. Under Magnet D, the height changes were compared to sponge samples of different magnetic particle concentrations shown in Figure 9C. When the CI concentration in PDMS sponges was increased, a stronger magnetic force might be applied to the magnetic PDMS sponge in a specific magnetic field and the volume variations subsequently might increase. It is clear from the figure that the sponge with the lowest CI concentration (CI/PDMS = 30 w/w %) presents the least compression. The sponge with a CI/PDMS weight ratio of 150 w/w % shows less deformation, similar to the 50 w/w % CI/PDMS sponge and 30 w/w % Fe_3O_4/PDMS sponge.

The 100% w/w % CI/PDMS sponge showed the maximum compression. The possible reason is the enhanced rigidity of 150 w/w % CI/PDMS sponges because of the excess addition of magnetic particles. Thus, the enhanced compression modulus weakened the effect of magnetic fields on the deformation degree. Furthermore, sponges with an Fe_3O_4/PDMS weight ratio of 30% show significantly more deformation than the same weight ratio of CI/PDMS sponges.

Given its deformation of 10%, the sponge prepared with the most magnetic-field-sensitive weight ratio of CI and PDMS (100 w/w %) in the experiment was selected for further sponge optimization studies.

3.1.7. Dielectric Constant (Relative Permittivity) Measurement. In this study, embedded magnetic particles in polymer scaffolds can also be regarded as conductive fillers for improving the conductivity of this material.[39] The dielectric constant of a material is its absolute permittivity represented as a ratio relative to the permittivity of vacuum or free space. The value could show how easily this material can become polarized by the imposition of an electric field on an insulator. From Figure 10, it is obvious that the relative permittivity value of the pure PDMS sponge is the lowest. When the concentration of magnetic powders increases, the relative permittivity value also increases. When compared with the relative permittivity value of water ($\varepsilon_r(H_2O)$ = 78) at room temperature, the relative permittivity for these sponge samples is very low.[40]

Through the comparison of relative permittivity values of Fe_3O_4-loaded and CI-loaded PDMS sponges (Figure 10), the PDMS sponges loaded with Fe_3O_4 show higher relative permittivity when the concentrations of magnetic powders are the same. The correlation coefficient (R^2) values of the trendlines are 0.979 and 0.915, respectively (very close to 1), so the data fit the lines well. As a result, the relative permittivity of PDMS sponge samples loaded with different concentrations of magnetic powders could be predictable with these equations included in Figure 10. As the magnetic particles were uniformly embedded on the PDMS scaffold, the holistic impedance matching was enhanced.[24]

When external pressure is applied, the sponge is compressed and air-holes shrink.[41] According to eq 5, the capacitance (C) of the PDMS sponge will increase primarily due to the reduction in thickness of sponge samples (d). Capacitance has been used as one of the conversion mechanisms for transforming external pressure signals (including stretch and compression) into electrical signals in the applications of implantable flexible pressure sensors, such as wearable devices, intelligent robots, and electronic skin.[32,39] In recent years, various PDMS-based porous conductive sponges were developed and were considered as ideal scaffolds for stretchable flexible sensors and piezoresistive sensors because of their exceptional deformability, failure strain, synchronous reflection to stimulations, and magnetic-mechanic-electric coupling properties.[18,39] Consequently, the prepared PDMS sponges have the potential to be applied in wireless flexible pressure sensors as a dielectric layer to overcome the disadvantages of most flexible sensors, like weak stretchability, low gauge factor, and long hysteresis.[41]

3.2. Optimization of Sponges. To investigate the influence of the fabrication process on the deformation of these PDMS sponges under varying magnetic fields, 100 w/w % CI/PDMS sponges prepared in the same way just except different sugar molds and/or different weight ratios of PDMS prepolymer and curing agents were characterized for comparison.

3.2.1. Particle Size Analysis of Sugar. The calculated average particle sizes (P_m) of granulated sugar and demerara

https://dx.doi.org/10.1021/acsbiomaterials.0c01608
ACS Biomater. Sci. Eng. 2021, 7, 180−195

sugar (Figure 11A,B) are 0.68 and 1.60 mm, respectively. The particle size frequency diagrams are shown in Figure 11C. As a result, PDMS sponges prepared with the demerara sugar mold may show weaker stiffness because the interconnected pore size is much bigger than those of sponges prepared with granulated sugar. For increasing the porosity of sponges, the mixture of granulated and demerara sugar was employed as the sugar mold for fabrication as well.

3.2.2. Sponges Prepared with Different Sugar Molds. The stress−strain curves with a maximum strain of 25% for 100 w/w % CI/PDMS sponge cylinders (diameter × thickness = 12 mm × 7 mm) fabricated with different sugar molds are shown in Figure 12. The sponge cylinder fabricated with the granulated sugar mold is more rigid and resistant to compression than the demerara sugar mold and the mixed sugar mold, which could be explained by the smaller interconnected pore size. Consequently, PDMS sponge cylinders prepared with demerara sugar or mixed sugar particles will possess a looser structure, higher porosity, less rigidity, and may show more deformation under the same magnetic field because of the less uniform sugar particle size.[14]

3.2.3. PDMS Sponge Formulation Optimization. According to Li *et al.*, the PDMS prepared with different prepolymer and curing agent weight ratios will show different compression modulus values.[6] 100 w/w % CI/PDMS sponges prepared with PDMS prepolymer and curing agent weight ratios of 15:1, 20:1, 25:1, and 30:1 were fabricated with the demerara sugar mold aiming to overcome the problems encountered when using the previous prepolymer/curing agent ratio (10:1). The sponge sample prepared with a weight ratio of 30:1 had an increased viscosity, and therefore, it was difficult to be fully cured. According to Figure 13A, the rigidity of sponge decreases when the prepolymer and curing agent weight ratio increases. The compressive modulus of 100 w/w % CI/PDMS sponges prepared with the demerara sugar mold was decreased significantly when the curing agent content decreased. The possible reason is the low cross-linking density of the sponge with the lower ratio of curing agents.[14] However, inadequate cross-linking may cause unwanted stickiness and relatively low recoverability. Hence, a less amount of curing agents is added into the PDMS prepolymer in the preparation process, and the PDMS sponges will show more deformation under magnetic fields.

As it can be observed from the graphs, the 100 w/w % CI/PDMS sponge cylinder prepared with demerara sugar and PDMS prepolymer/curing agents = 25:1 w/w shows the maximum compression as a function of the applied magnetic field. Generally, decreasing the curing agent's concentration can lead to softer PDMS sponges and consequently increases the volume change under a specific magnetic field. The R^2 values of all trendlines are close to 1, so the data fit these lines well. Based on the equation mentioned in Figure 13B, the deformation of each kind of sponge cylinder (diameter × thickness = 12 mm × 7 mm) in a given magnetic field could easily be predicted.

3.2.4. Recyclability. After finishing all tests on the sponges, an attempt was made to test their recyclability, which is a crucial property in actual applications.[11] The most fragile 100 w/w % CI/PDMS sponge prepared with demerara sugar (PDMS prepolymer/curing agents = 25:1 w/w) was selected as the model for the recyclability test. The results showed that the sponge cylinder weight was constant before absorption and after desorption of water. The sponge samples exhibited almost no change in their absorption capacities and their weights after 10 absorbing/desorbing cycles shown in Figure 14.

3.2.5. Thermal Characterization. The TGA analysis (Figure 15) of CI particles exhibits a slight ring trend, possibly due to oxidation of the particles caused by the impurity of the nitrogen gas.[7] The fabricated PDMS sponges showed almost no weight loss below 100 °C, which is related to the relatively low weight ratio of absorbed moisture.[34] Their weight loss begins from 200 °C, mainly due to the onset of thermal degradation. With the temperature increasing to 400 °C, significant weight loss for these sponge samples (especially the pure PDMS sponge) occurred as a result of the decomposition of methyl groups.[8,11] Also, it was observed that the pure PDMS sponge sample shows the highest weight loss, indicating the most obvious chemical degradation. When the ferromagnetic particle (Fe_3O_4 or CI) concentration of the PDMS sponge is the same, the weight loss of PDMS sponges remains constant. With the increase of ferromagnetic particles in the PDMS sponge, the total weight loss will decrease. It indicates that the introduction of magnetic particles can improve the thermostability of the PDMS matrix.[7] Furthermore, the degradation at a processing temperature will be decreased and the degradation rate will be slowed down owing to the interactions between the PDMS matrix and embedded magnetic particles.[7] Karimzadeh *et al.* proved that the TGA curve of bare Fe_3O_4 nanoparticles shows only 1.6% weight loss between 25 and 200 °C and no obvious weight loss from 200 to 600 °C.[42] This result is consistent with our hypothesis that the degradation is mainly due to PDMS whereas bare ferromagnetic particles are thermally stable even at elevated temperatures. Consequently, these fabricated magnetic PDMS sponges will remain thermally stable during the preparing process and under real operating conditions.

3.3. Cell Studies *In Vitro*. To explore the inhibition behaviors of different sponges, different magnetic fields, and different concentrations of FLU solution on the growth of cancerous cells, various groups of assessments were designed (Table 3). By comparing the numbers of HeLa cells in 4 days, the differences in the inhibition of HeLa cells among these groups could be observed.

Comparing Group A3 with A5, Group A1 with A2, and Groups A8 and A10 with A11 in terms of the number of cells (Figure 16), it is obvious that a stronger magnetic field can exhibit stronger inhibition effects on the growth of HeLa cells. Similarly, the increase of HeLa cell numbers in groups with these PDMS sponges (especially CI-loaded PDMS sponges) is not as obvious as the increase in groups without sponge samples as reflected by the data of Groups A1 and A5 with A10 and Group A2 with A11. The possible reason is that the volumes of PDMS sponge samples in the well plates affect the growth of HeLa cells because the number of cells in all these groups still shows an increasing trend. Additionally, sponge samples loaded with FLU solution (both 12.5 and 25 mg/mL) can kill almost all HeLa cells within 4 days (Groups A4, A6, A7, A9, and A12−15). The differences between pure PDMS sponges (Groups A4, A6, and A7) and CI-loaded PDMS sponges (Groups A9, A12, and A13) under various magnetic fields illustrate that the main reason for the decrease in cell numbers in Group A13 is the addition of a magnetic field, which can trigger the release of FLU solution from magnetic sponges. Also, there is no significant difference in cell numbers between Groups A12 and A14, Groups A13 and A15. The possible reason may be both concentrations of FLU solutions

https://dx.doi.org/10.1021/acsbiomaterials.0c01608
ACS Biomater. Sci. Eng. 2021, 7, 180−195

are high enough to inhibit the growth of the HeLa cells. Lower concentrations will be applied in the future to test the effect of various FLU concentrations loaded into the sponges on the growth of cancerous cells. Also, drug release dynamics based on magnetic PDMS sponge types and external magnetic fields will be further explored.

4. CONCLUSIONS

In the current research, various PDMS sponges were successfully fabricated with different magnetic particles and different sugar molds with different weight ratios of PDMS prepolymer and curing agents. The sugar templating method for fabricating porous scaffolds has the advantages of low cost, flexible formulation design, simple process, and no other materials required. By controlling the fabrication process, required porous scaffolds for drug delivery systems with suitable porosity and magnetic field sensitivity could be prepared. Besides, the study showed that the optimized magnetic sponges can be reused as the water absorption capacity of the prepared CI-loaded PDMS sponge did not change after 10 cycles. All these promising features and simple fabrication make the CI-loaded PDMS sponge a superior scaffold for delivering drug solutions in local treatment of diseases and further applications on innovative medical devices.

AUTHOR INFORMATION

Corresponding Authors

Mohammed Maniruzzaman − *Pharmaceutical Engineering and 3D Printing (PharmE3D) Lab, Division of Molecular Pharmaceutics and Drug Delivery, College of Pharmacy, The University of Texas at Austin, Austin, Texas 78712, United States*; Email: M.Maniruzzaman@austin.utexas.edu

Ali Nokhodchi − *Pharmaceutics Research Laboratory, School of Life Sciences, University of Sussex, Brighton BN1 9QJ, U.K.*; orcid.org/0000-0002-3244-2482; Email: a.nokhodchi@sussex.ac.uk

Authors

Kejing Shi − *Pharmaceutics Research Laboratory, School of Life Sciences, University of Sussex, Brighton BN1 9QJ, U.K.*

Rodrigo Aviles-Espinosa − *Robotics and Mechatronics Systems Research Centre, School of Engineering and Informatics, University of Sussex, Brighton BN1 9RH, U.K.*

Elizabeth Rendon-Morales − *Robotics and Mechatronics Systems Research Centre, School of Engineering and Informatics, University of Sussex, Brighton BN1 9RH, U.K.*

Lisa Woodbine − *Sussex Centre for Genome Damage and Stability, University of Sussex, Brighton BN1 9RQ, U.K.*

Jonathan P. Salvage − *School of Pharmacy and Biomolecular Sciences, University of Brighton, Brighton BN2 4GJ, U.K.*

Complete contact information is available at: https://pubs.acs.org/10.1021/acsbiomaterials.0c01608

Notes

The authors declare no competing financial interest.

REFERENCES

(1) Zhao, X.; Kim, J.; Cezar, C. A.; Huebsch, N.; Lee, K.; Bouhadir, K.; Mooney, D. J. Active Scaffolds for On-Demand Drug and Cell Delivery. *Proc. Natl. Acad. Sci.* **2011**, *108*, 67−72.

(2) Hazzah, H. A.; Farid, R. M.; Nasra, M. M. A.; El-Massik, M. A.; Abdallah, O. Y. Lyophilized Sponges Loaded with Curcumin Solid Lipid Nanoparticles for Buccal Delivery: Development and Characterization. *Int. J. Pharm.* **2015**, *492*, 248−257.

(3) Cha, K. J.; Kim, D. S. A Portable Pressure Pump for Microfluidic Lab-on-a-Chip Systems Using a Porous Polydimethylsiloxane (PDMS) Sponge. *Biomed. Microdevices* **2011**, *13*, 877−883.

(4) Gu, Y.; Miki, N. A Microfilter Utilizing a Polyethersulfone Porous Membrane with Nanopores. *J. Micromech. Microeng.* **2007**, *17*, 2308−2315.

(5) Jiang, S.; Hu, Y.; Wu, H.; Zhang, Y.; Zhang, Y.; Wang, Y.; Zhang, Y.; Zhu, W.; Li, J.; Wu, D.; Chu, J. Multifunctional Janus Microplates Arrays Actuated by Magnetic Fields for Water/Light Switches and Bio-Inspired Assimilatory Coloration. *Adv. Mater.* **2019**, *31*, 1807507.

(6) Li, J.; Zhang, M.; Wang, L.; Li, W.; Sheng, P.; Wen, W. Design and Fabrication of Microfluidic Mixer from Carbonyl Iron − PDMS Composite Membrane. *Microfluid. Nanofluid.* **2011**, *10*, 919−925.

(7) Perales-Martínez, I. A.; Palacios-Pineda, L. M.; Lozano-Sánchez, L. M.; Martínez-Romero, O.; Puente-Cordova, J. G.; Elías-Zúñiga, A. Enhancement of a Magnetorheological PDMS Elastomer with Carbonyl Iron Particles. *Polym. Test.* **2017**, *57*, 78−86.

(8) Guo, J.; Wang, J.; Wang, W.; Bai, Z.; Zhang, Z.; Zhang, Y.; Zhang, S. The Fabrication of 3D Porous PDMS Sponge for Oil and Organic Solvent Absorption. *Environ. Prog. Sustainable Energy* **2019**, *38*, S86−S92.

(9) Choi, S.-J.; Kwon, T.-H.; Im, H.; Moon, D.-I.; Baek, D. J.; Seol, M.-L.; Duarte, J. P.; Choi, Y.-K. A Polydimethylsiloxane (PDMS) Sponge for the Selective Absorption of Oil from Water. *ACS Appl. Mater. Interfaces* **2011**, *3*, 4552−4556.

(10) Si, P.; Wang, J.; Guo, J.; Li, S.; Cai, W.; Xu, H. Mussel-Inspired One-Step Modification of a Porous Structured Surface with Self-Cleaning Properties for Oil Sorption. *New J. Chem.* **2015**, *39*, 6823−6829.

(11) Guo, J.; Wang, J.; Zhang, S.; Ma, X.; Qiu, Z.; Peng, X.; Ying, J.; Wang, Y.; Wu, G. One-Step Modification of PU Sponges for Selective Absorption of Oil-Water Mixtures. *New J. Chem.* **2017**, *41*, 90−96.

(12) Shi, K.; Aviles-espinosa, R.; Rendon-morales, E.; Woodbine, L.; Maniruzzaman, M.; Nokhodchi, A. Novel 3D Printed Device with Integrated Macroscale Magnetic Field Triggerable Anti-Cancer Drug Delivery System. *Colloids Surf., B* **2020**, *192*, 111068.

(13) Cai, K.; Luo, Z.; Hu, Y.; Chen, X.; Liao, Y.; Yang, L.; Deng, L. Magnetically Triggered Reversible Controlled Drug Delivery from Microfabricated Polymeric Multireservoir Devices. *Adv. Mater.* **2009**, *21*, 4045−4049.

(14) Shi, J.; Zhang, H.; Jackson, J.; Shademani, A.; Chiao, M. A Robust and Refillable Magnetic Sponge Capsule for Remotely Triggered Drug Release. *J. Mater. Chem. B* **2016**, *4*, 7415−7422.

(15) Zhang, H.; Chiao, M. Anti-Fouling Coatings of Poly-(Dimethylsiloxane) Devices for Biological and Biomedical Applications. *J. Med. Biol. Eng.* **2015**, *35*, 143−155.

(16) Li, J.; Zhang, Y. Porous Polymer Films with Size-Tunable Surface Pores. *Chem. Mater.* **2007**, *19*, 2581−2584.

(17) Zhao, X.; Li, L.; Li, B.; Zhang, J.; Wang, A. Durable Superhydrophobic/Superoleophilic PDMS Sponges and Their Applications in Selective Oil Absorption and in Plugging Oil Leakages. *J. Mater. Chem. A* **2014**, *2*, 18281−18287.

(18) Ding, L.; Xuan, S.; Pei, L.; Wang, S.; Hu, T.; Zhang, S.; Gong, X. Stress and Magnetic Field Bimode Detection Sensors Based on Flexible CI/CNTs − PDMS Sponges. *ACS Appl. Mater. Interfaces* **2018**, *10*, 30774−30784.

(19) Shademani, A.; Zhang, H.; Jackson, J. K.; Chiao, M. Active Regulation of On-Demand Drug Delivery by Magnetically Triggerable Microspouters. *Adv. Funct. Mater.* **2017**, *27*, 1604558.

(20) Hu, X.; Nian, G.; Liang, X.; Wu, L.; Yin, T.; Lu, H.; Qu, S.; Yang, W. Adhesive Tough Magnetic Hydrogels with High Fe_3O_4 Content. *ACS Appl. Mater. Interfaces* **2019**, *11*, 10292−10300.

(21) Ali, A.; Zafar, H.; Zia, M.; Ul Haq, I.; Phull, A. R.; Ali, J. S.; Hussain, A. Synthesis, Characterization, Applications, and Challenges of Iron Oxide Nanoparticles. *Nanotechnol. Sci. Appl.* **2016**, *9*, 49−67.

(22) Arias, J. L.; Gallardo, V.; Linares-Molinero, F.; Delgado, A. V. Preparation and Characterization of Carbonyl Iron/Poly-

(Butylcyanoacrylate) Core/Shell Nanoparticles. *J. Colloid Interface Sci.* **2006**, *299*, 599−607.
(23) Zhu, Q.; Qian, Y.; Yang, Y.; Wu, W.; Xie, J.; Wei, D. Effects of Carbonyl Iron Powder on Iron Deficiency Anemia and Its Subchronic Toxicity. *J. Food Drug Anal.* **2016**, *24*, 746−753.
(24) Quan, B.; Gu, W.; Chen, J.; Xu, G.; Ji, G. Integrating Carbonyl Iron with Sponge to Enable Lightweight and Dual-Frequency Absorption. *Nanotechnology* **2019**, *30*, 195703.
(25) Ghazanfari, M. R.; Kashefi, M.; Shams, S. F.; Jaafari, M. R. Perspective of Fe_3O_4 Nanoparticles Role in Biomedical Applications. *Biochem. Res. Int.* **2016**, *2016*, 1.
(26) Wang, J.; Guo, J.; Si, P.; Cai, W.; Wang, Y.; Wu, G. Polydopamine-Based Synthesis of an $In(OH)_3$ -PDMS Sponge for Ammonia Detection by Switching Surface Wettability. *RSC Adv.* **2016**, *6*, 4329−4334.
(27) Chemical, T. D. C. SYLGARD ™ 184 Silicone Elastomer APPLICATIONS. *Silicone Elastomer Tech. Data Sheet* **2017**, 4. Form No. 11−3184-01 C.
(28) Beer, F. P.; Johnston, E. R.; DeWolf, J. T.; Mazurek, D. F. *Mechanics of Materials*, Seventh Ed.; New York, 2015; DOI: 10.4135/9781452276076.n265.
(29) Shi, K.; Tan, D.; Nokhodchi, A.; Maniruzzaman, M. Drop-On-Powder 3D Printing of Tablets with an Anti-Cancer Drug, 5-Fluorouracil. *Pharmaceutics* **2019**, *11*, 150.
(30) Bernardes, C. E. S.; Canongia Lopes, J. N.; Da Piedade, M. E. M. All-Atom Force Field for Molecular Dynamics Simulations on Organotransition Metal Solids and Liquids. Application to $M(CO)_n$ (M = Cr, Fe, Ni, Mo, Ru, or W) Compounds. *J. Phys. Chem. A* **2013**, *117*, 11107−11113.
(31) Blaney, L. Magnetite (Fe_3O_4): Properties, Synthesis, and Applications. *Lehigh Rev.* **2007**, *15*−*2007*, 5. Paper
(32) Song, Y.; Chen, H.; Su, Z.; Chen, X.; Miao, L.; Zhang, J.; Cheng, X.; Zhang, H. Highly Compressible Integrated Supercapacitor−Piezoresistance-Sensor System with CNT−PDMS Sponge for Health Monitoring. *Small* **2017**, *13*, 1702091.
(33) Chang, H.-H.; Cheng, C.-L.; Huang, P.-J.; Lin, S.-Y. Application of Scanning Electron Microscopy and X-Ray Microanalysis : FE-SEM , ESEM-EDS , and EDS Mapping for Studying the Characteristics of Topographical Microstructure and Elemental Mapping of Human Cardiac Calcified Deposition. *Anal. Bioanal. Chem.* **2014**, *406*, 359−366.
(34) Liu, Y.; Wang, X.; Feng, S. Nonflammable and Magnetic Sponge Decorated with Polydimethylsiloxane Brush for Multitasking and Highly Efficient Oil − Water Separation. *Adv. Funct. Mater.* **2019**, *29*, 1902488.
(35) Beshkar, F.; Khojasteh, H.; Salavati-niasari, M. Recyclable Magnetic Superhydrophobic Straw Soot Sponge for Highly Efficient Oil / Water Separation. *J. Colloid Interface Sci.* **2017**, *497*, 57−65.
(36) Tang, J.; Tong, Z.; Xia, Y.; Liu, M.; Lv, Z.; Gao, Y.; Lu, T.; Xie, S.; Pei, Y.; Fang, D.; et al. Super Tough Magnetic Hydrogels for Remotely Triggered Shape Morphing. *J. Mater. Chem. B* **2018**, *6*, 2713−2722.
(37) Liu, S.; Li, S.; Liu, J. Jurin's Law Revisited : Exact Meniscus Shape and Column Height. *Eur. Phys. J. E* **2018**, *41*, 46.
(38) Yin, T.; Wu, L.; Wu, T.; Mao, G.; Nian, G.; Chen, Z.; Hu, X.; Wang, P.; Xiang, Y.; Yu, H.; Qu, S.; Yang, W. Ultrastretchable and Conductive Core / Sheath Hydrogel Fibers with Multifunctionality. *J. Polym. Sci., Part B: Polym. Phys.* **2019**, *57*, 272−280.
(39) Hu, T.; Xuan, S.; Ding, L.; Gong, X. Stretchable and Magneto-Sensitive Strain Sensor Based on Silver Nanowire-Polyurethane Sponge Enhanced Magnetorheological Elastomer. *Mater. Des.* **2018**, *156*, 528−537.
(40) Pawliszyn, J. *Theory of Solid-Phase Microextraction*; Elsevier Inc.: 2012; DOI: 10.1016/B978-0-12-416017-0.00002-4.
(41) Kou, H.; Zhang, L.; Tan, Q.; Liu, G.; Dong, H.; Zhang, W.; Xiong, J. Wireless Wide-Range Pressure Sensor Based on Graphene/PDMS Sponge for Tactile Monitoring. *Sci. Rep.* **2019**, *9*, 3916.
(42) Karimzadeh, I.; Aghazadeh, M.; Doroudi, T.; Ganjali, M. R.; Kolivand, P. H. Superparamagnetic Iron Oxide (Fe_3O_4) Nanoparticles Coated with PEG/PEI for Biomedical Applications: A Facile and Scalable Preparation Route Based on the Cathodic Electrochemical Deposition Method. *Adv. Phys. Chem.* **2017**, *2017*, 1−7.

https://dx.doi.org/10.1021/acsbiomaterials.0c01608
ACS Biomater. Sci. Eng. 2021, 7, 180−195

International Journal of Pharmaceutics 597 (2021) 120315

Contents lists available at ScienceDirect

International Journal of Pharmaceutics

journal homepage: www.elsevier.com/locate/ijpharm

Role of release modifiers to modulate drug release from fused deposition modelling (FDM) 3D printed tablets

Kejing Shi [a], Jonathan P. Slavage [b], Mohammed Maniruzzaman [c,*], Ali Nokhodchi [a,*]

[a] Pharmaceutics Research Laboratory, School of Life Sciences, University of Sussex, Falmer, Brighton BN1 9QJ, UK
[b] School of Pharmacy and Biomolecular Sciences, University of Brighton, Brighton BN2 4GJ, UK
[c] Pharmaceutical Engineering and 3D Printing Lab, Division of Molecular Pharmaceutics and Drug Delivery, College of Pharmacy, The University of Texas at Austin, 2409 University Avenue, Austin, TX 78712, USA

ARTICLE INFO

Keywords:
Hot melt extrusion
3D printing
Fused deposition modelling
Sustained release
Ethyl cellulose
Polymers
Personalized medicine

ABSTRACT

Although hot melt extrusion (HME) has been used in combination with fused deposition modelling (FDM) three-dimensional printing (3DP), suitable feedstock materials such as polymeric filaments with optimum properties are still limited. In this study, various release modifying excipients, namely, poly(vinyl alcohol) (PVA), Soluplus®, polyethylene glycol (PEG) 6000, Eudragit® RL PO/RS PO, hydroxypropyl methylcellulose (HPMC) K4M/E10M/K100M, Kollidon® vinyl acetate 64 (VA 64)/17PF/30, were used as a release modulating tool to control the drug release from 3D printed sustained release tablets. Ibuprofen (as the model drug) and ethyl cellulose (as the polymeric matrix), along with various release modifiers, were blended and extruded into filaments through a twin-screw extruder. Then these filaments were printed into cylindrical tablets through FDM 3DP technique and their surface morphology, thermal stability, solid-state, mechanical properties, dose accuracy and drug release behaviors were investigated. The solid-state analysis of 3D printed tablets exhibited the amorphous nature of the drug dispersed in the polymer matrices. Although all these prepared filaments could be successfully printed without failing during the FDM 3DP process, the mechanical characterization showed that the filament stiffness and brittleness could be adjusted significantly by changing the type of release modifiers. Moreover, *in vitro* drug release studies revealed that the drug release could simply be controlled over 24 h by only changing the type of release modifiers. All ibuprofen (IBP) loaded 3D printed tablets with ethyl cellulose (EC) matrix, especially with PEG as the release modifier, showed great potential in releasing IBP in a zero-order reaction. In conclusion, all the results illustrated that the HME/FDM approach and optimized formulation compositions can be an attractive option for the development of pharmaceutical tablets and implants where adjustable drug release patterns are necessary.

1. Introduction

In pharmaceutical applications, three-dimensional printing (3DP) is an emerging additive manufacturing technique, which produces solid objects by depositing successive layers under the control of computer-aided software (Alhnan et al., 2016; Goyanes et al., 2015b). This promising technique has been widely applied in many domains, such as fashion, architecture, defence, aerospace, automotive engineering and disease therapy (Goyanes et al., 2015b; Melocchi et al., 2016; Stewart et al., 2020). In the pharmaceutical industry, 3DP could be used to fabricate dosage forms with flexible shapes, multiple drugs and modulated drug release kinetics (Homaee Borujeni et al., 2020). However, many shortcomings of commercial feeding materials need to be taken into consideration, such as poor extrudability, biocompatibility, printability, drug loading and stability (Kadry et al., 2018).

Hot melt extrusion (HME) was first used in the plastic and rubber industry, since the 1970s, it has been promoted in pharmaceutical research as a method of preparing solid dispersions through distributing poorly soluble drugs into a polymeric matrix for manufacturing various dosage forms (e.g. implants, granules, pellets, films) (Homaee Borujeni et al., 2020; Quinten et al., 2009; Zhang et al., 2017). An early investigation revealed that the percentage of drug loading into the polymers would be low when drugs were loaded through impregnation/incubation in organic solvents as a function of passive diffusion (soaking)

* Corresponding authors.
E-mail addresses: M.Maniruzzaman@austin.utexas.edu (M. Maniruzzaman), a.nokhodchi@sussex.ac.uk (A. Nokhodchi).

https://doi.org/10.1016/j.ijpharm.2021.120315
Received 17 December 2020; Received in revised form 21 January 2021; Accepted 23 January 2021
Available online 1 February 2021

(Kempin et al., 2017; Nasereddin et al., 2018). In recent years, HME has been used in combination with fused deposition modelling (FDM) 3DP, which is one of the most promising 3DP technologies in pharmaceutical applications to date (Alhnan et al., 2016; Kadry et al., 2018; Khizer et al., 2019; Pietrzak et al., 2015). Consequently, HME is of great importance in providing an increasing number of materials processable by FDM, increasing the drug loading capacity of filaments, and achieving on-demand fabrication of a unit dose for patients.

FDM, often known as fused filament fabrication (FFF), is a thermal extrusion-based technique. In an FDM 3D printer, polymer filaments were extruded through a hot-end or a heated nozzle to create objects layer by layer on a build plate (Alhijjaj et al., 2016; Goyanes et al., 2015b). After the build plate moves down, the next layer is then deposited onto the previous layer to fabricate a 3D solid object (Goyanes et al., 2017, 2015a). Additionally, FDM allows the fabrication of drug delivery systems (DDSs) with almost any shape, which makes it promising for implants administration at application sites with high anatomical variability (Kempin et al., 2017). As FDM 3DP has the potential to fabricate single-unit dosage forms, the active pharmaceutical ingredient (API) or the API-loaded carriers can be either incorporated within a polymer matrix or encapsulated in complex polymer structures through this technology (Gioumouxouzis et al., 2018). Nevertheless, the main limitation of FDM 3DP in pharmaceutical applications is the required high temperature for softening polymer filaments, which may cause the degradation of a large number of APIs and excipients especially those that are susceptible to heat (Alhnan et al., 2016). Recently, direct pellets/powder extrusion 3DP technique was developed to fabricate printlets directly from powder materials without the need for hot melt extruded filaments (Goyanes et al., 2019; Ong et al., 2020). This single-step manufacturing technology show great potential for preclinical studies and on-demand personalized therapy with the development of equipment (Fanous et al., 2020).

Pharmaceutical polymers have been widely applied in HME formulations, such as synthetic cellulose derivatives, methacrylate polymers, polyvinyl pyrrolidone (PVP), polyethylene oxide (PEO) and pyrrolidone-co-vinyl acetate (Maru et al., 2011). However, only 30 materials are available commercially for the FDM process, whereas there are more than 3000 materials that are suitable for other HME-based processes (Fuenmayor et al., 2018). It is difficult to fabricate suitable hot melt extruded filaments for the following 3D printing process due to the importance of filament mechanical characteristics (Elbadawi et al., 2020). Melt-blending can provide a cost-effective, convenient and mature solution through combining two or more different polymers with various properties into a single matrix material (Fuenmayor et al., 2018; Kadry et al., 2018). As a result, the final dosage form can be designed and fabricated with suitably flexible properties to overcome material shortcomings of polymers for the FDM process.

Conventional manufacture of zero-order release dosage forms is complicated, time-consuming, difficult and low in flexibility (Fina et al., 2020). In recent years, additive manufacturing technology has been developed into a promising platform to fabricate sustained-release tablets or implants with many advantages, such as the ability to prepare objects in almost any shape to meet the growing need for personalized medicine (Jamróz et al., 2018; Kempin et al., 2017). It has been proved that 3DP can be of great importance in many practical medical applications which are required to meet a wide range of anatomical and pathological requirements, like vaginal rings and localized cancer treatment (Kempin et al., 2017; Stewart et al., 2020). In addition, although the HME can be used to improve the solubility and bioavailability of poorly soluble drugs, the combination of HME and FDM 3DP into a continuous process can become a promising strategy for the preparation of patient-centered and abuse-deterrent dosage forms of opioids (Nukala et al., 2019), offer a cost-effective and convenient manufacturing platform for sustained release DDSs (Tan et al., 2020), fabricate zero-order release dosage forms consisting of an insoluble shell and a controlled release core (Fina et al., 2020), create osmotically controlled dosage forms with a core–shell structure for achieving sustained and/or delayed-release (Gioumouxouzis et al., 2020), develop floating zero-order release dosage forms with complex hollow structure (Vo et al., 2020), provide an alternative to the development of multi-layer polypills with optimized release profiles for individualized therapy (Pereira et al., 2019), and prolong the drug release from dosage forms in a continuous and controlled manner simultaneously (Homaee Borujeni et al., 2020).

Table 1
Composition of the filament formulations for HME.

Group number	Filaments	Ibuprofen, (% w/w)	EC (% w/w)	Release modifier (w/w)
G1	F1	20	80	–
G2	F2	20	60	20% PVA
G3	F3	20	60	20% Soluplus
G4	F4	20	60	20% PEG 6000
G5	F5	20	60	20% Eudragit RSPO
G6	F6	20	60	20% Eudragit RLPO
G7	F7	20	60	20% HPMC K4M
G8	F8	20	60	20% HPMC E10M
G9	F9	20	60	20% HPMC K100M
G10	F10	20	60	20% Kollidon VA 64
G11	F11	20	60	20% Kollidon 17 PF
G12	F12	20	60	20% Kollidon 30
G13	F13	20	60	15% Kollidon VA 64, 5% TEC
G14	F14	20	60	10% Kollidon VA 64, 10% Eudragit RSPO

The purposes of this research were (1) to develop suitable materials for preparing HME filaments and FDM 3DP of sustained-release tablets, (2) to compare the impact of different release modifiers on the mechanical properties and drug dissolution behaviors of filaments and FDM 3D printed tablets, and (3) to test the applicability of these processes in the preparation of 3D printed objects for achieving adjustable drug release profiles. For these purposes, a comprehensive evaluation of the suitability of a series of ethyl cellulose (EC) formulations containing both ibuprofen (IBP) and a range of release modifiers for HME and FDM 3DP processes was conducted. In the current research, tablets were also prepared using a manual tablet compression machine by mixing all raw materials prior to direct compression and compared with 3D printed tablets.

2. Materials and methods

2.1. Materials

The model drug ibuprofen (IBP) was purchased from Spectrum Chemical Manufacturing Corp. (New Brunswick, NJ, USA). EC (Ethocel® Standard 10 premium) and hydroxypropyl methylcellulose (HPMC) Methocel® K4M Premium CR were kindly donated by Colorcon Ltd. (Dartford, UK). HPMC Methocel® E10M Premium CR was obtained from Dow Chemical Company (Michigan, USA). HPMC Benecel™ K100M PHARM XR was donated by Ashland Industries Europe GmbH (Schaffhausen, Switzerland). Poly(vinyl alcohol) (PVA) with the average molecular weight of 22,000 was purchased from Acros Organics (Geel, Belgium). Soluplus®, Kollidon® 17 PF, 30 and vinyl acetate 64 (VA64) were obtained from BASF (Ludwigshafen, Germany). Polyethylene glycol (PEG 6000) was procured from Alfa Aesar (Lancashire, UK). Eudragit® RL PO and RS PO powder were obtained from Evonik Industries AG (Darmstadt, Germany). Triethyl citrate (TEC) was purchased from Thermo Fisher Scientific Inc. (Geel, Belgium). Absolute ethanol (≥99.8%) was purchased from Sigma-Aldrich Co. Ltd. (Dorset, UK). All chemicals used were of analytical grade and used as received.

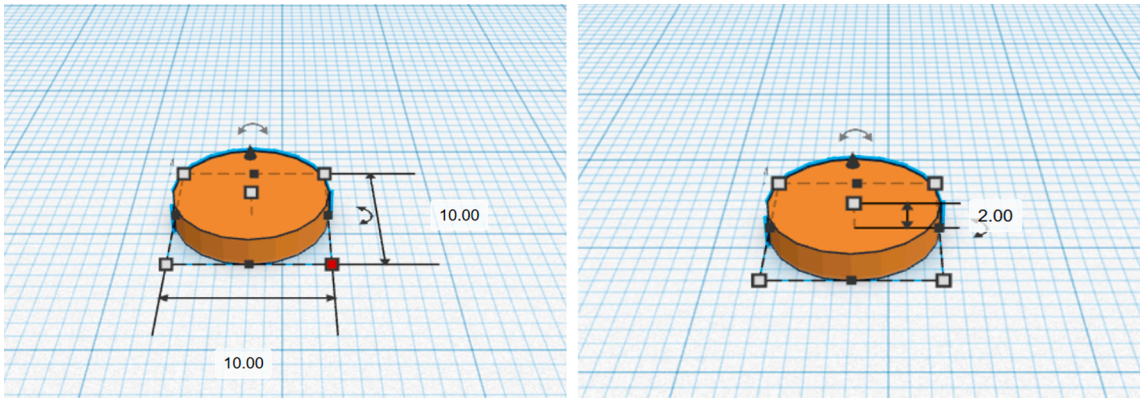

Fig. 1. Designed CAD model of the tablet (diameter × height = 10 × 2 mm) for FDM 3DP.

2.2. Preparation of physical mixtures

All materials (except PEG 6000 and TEC) were placed in a convection oven (Memmert, UF110, Schwabach, Germany) at 50 °C for approximately 2 h before use, because the removal of residual moisture can help prevent these powders from aggregating and sticking on the feeder surface of the hot melt extruder at high processing temperature. Physical mixtures were prepared by dry mixing of the composition as outlined in Table 1 using a mortar and pestle for 5 min. Then, powder mixtures were further mixed with a Turbula blender (T2F, Willy A. Bachofen AG, Muttenz, Switzerland) for 10 min. Before the extrusion process, the blend was left overnight for better migration of the plasticizer TEC (liquid form) into the polymer (Quinten et al., 2009).

2.3. Thermogravimetric analysis (TGA)

TGA was performed with a TGA Q50 (TA Instruments, Leatherhead, UK) to measure water content and degradation temperature of raw materials. Around 5 mg of each sample was placed in an open aluminium pan and then heated from 25 °C to 500 °C at a heating rate of 20 °C/min under 20 mL/min purified nitrogen gas for purging. Data were recorded and analyzed with the TA Universal Analysis 2000 software (TA Instruments-Waters LLC, New Castle, DE, USA).

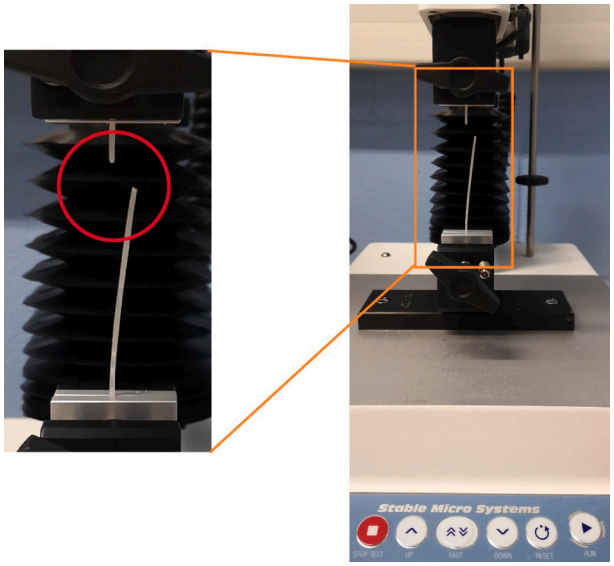

Fig. 2. The rig of filaments texture analysis.

2.4. Preparation of polymeric filaments

The powder mixtures were fed into a 10 mm twin-screw extruder L/D 20 (assembled by Point 1 Control System Ltd., Stoke-on-Trent, UK) at a screw speed of 60 rpm. As IBP has a plasticizing effect, the glass transition temperature (T_g) of EC and the processing temperature during HME should decrease (De Brabander et al., 2002). Hence, the extrusion temperatures of four heating zones and the die along the extrusion barrel were set at 80, 100, 100, 100 and 100 °C respectively. The extruded filaments were collected with a filament winder (FilaFab™, D3D Innovations Limited, Bristol, UK).

2.5. 3DP of tablets

The model tablet (diameter × height = 10 × 2 mm) was designed online on TinkerCAD (https://www.tinkercad.com/) and then downloaded as a stereolithographic (stl.) file format (Fig. 1). The stl. file was then imported into a MakerBot Replicator 2X 3D Printer (MakerBot Inc., Brooklyn, NY, USA), which was equipped with two MK8 dual-head extruders (diameter = 0.4 mm). Model tablets were printed with 100% infill density. The layer height was set at 0.2 mm. The printing was performed at 178 °C whereas the build plate was set to 65 °C.

2.6. Characterization of tablets

The weight, diameter and thickness of tablets from each batch were assessed for uniformity (n = 3). The diameter and thickness of 3D printed tablets were measured using a digital micrometer (Series 293 MDC-MX Lite, Mitutoyo Ltd., Hampshire, UK). Then the weight of tablets was measured accurately using a digital analytical balance (Sartorius, 0.1 mg).

2.7. Scanning electron microscopy (SEM)

SEM imaging was performed under high vacuum using a Zeiss Sigma FEG-SEM (Carl Zeiss, UK). The SEM working condition parameters were 5 kV accelerating voltage with a 30 μm column aperture, using an Everhart-Thornley secondary electron detector (Carl Zeiss, UK) for imaging.

2.8. Differential scanning calorimetry (DSC) analysis

A differential scanning calorimeter (DSC) 4000 system (Perkin Elmer, Waltham, MA, USA) was utilized to conduct a thermal analysis of all raw materials, physical mixtures, extruded filaments, and 3D printed tablets. Samples (approximately 5 mg) were accurately weighed and placed in a 40 μL aluminium pan (Mettler Toledo GmbH, Greifensee, Switzerland). All experiments were conducted under a nitrogen

Table 2
Kinetic release model equations in this study.

Model	Equation	Parameters
Zero-order	$F = k_0 \cdot t$	k_0– zero-order release constant
First-order	$F = 100 \cdot (1 - e^{-k_1 \cdot t})$	k_1– first-order release constant
Higuchi	$F = k_H \cdot t^{0.5}$	k_H– Higuchi release constant
Korsmeyer-Peppas	$F = k_{KP} \cdot t^n$	k_{KP}– release constant with structural & geometric information n – diffusional exponent indicating release mechanism

(F is the fraction or percentage of drug released in time t).

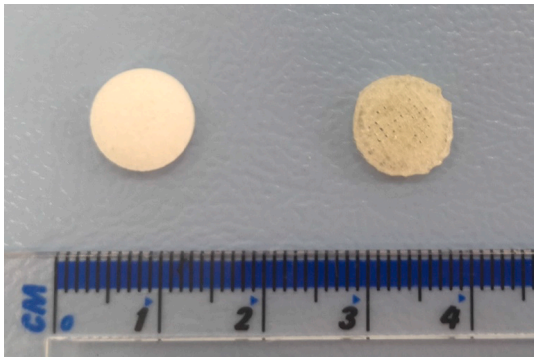

Fig. 3. Images of the directly compressed physical mixtures tablet (left) and the 3D printed tablet (right).

environment (flow rate = 20 mL/min). All samples were heated from 25 °C to 200 °C at 20 °C /min. The data were collected using Pyris software version 5.0 (Perkin Elmer, Waltham, MA, USA).

2.9. X-ray powder diffraction (XRPD)

XRPD measurements were performed using a Siemens D500 X-ray Diffractometer (Munich, Germany). The samples were scanned between 2 Theta (θ) from 5° to 50° at a step width of 0.01° and 1 s time count. The divergence slit was 1 mm and the scatter slit was 0.6 mm. The X-ray wavelength was 0.154 nm in Cu source and at a voltage of 40 kV.

2.10. Mechanical characterization

A TA.XT plusC Texture Analyser (Stable Micro Systems Ltd., Godalming, UK) equipped with a 50 kg load cell and tensile grips (A/TG) probe was used to measure the tensile strength of extruded filaments which were accurately cut into 10 cm segments (diameter × length = 1.75 mm × 10 cm). The filament pieces were fixed vertically between two screw-down grips. The original distance between two grips was set to 8 cm and then stretched gradually at an elongation speed of 1 mm/s until the filament was broken (Fig. 2). The stress and strain values were collected through the Exponent Software version 7.0.3.0 (Stable Micro Systems Ltd., Godalming, UK). Then the elastic modulus could be calculated according to the elastic region (linear region) in the stress–-strain curve. At least three replicates were conducted for each batch of extruded filaments.

2.11. Tablets prepared by direct compression

A manual tablet compression machine (Model MTCM-I, Globe Pharma, USA) equipped with 10 mm diameter flat-faced punches was used to prepare tablet compacts of physical mixtures. All punches and dies were carefully cleaned before the compression process.

For a better comparison between 3D printed tablets and tablets prepared via direct compression, based on the weights of prepared 3D printed tablets (Table 2), physical mixtures of the same weight in each group were accurately weighed and filled into the die manually (Fig. 3). Tablets were compressed at 30 MPa for 3 s dwell time.

2.12. Determination of drug content

Around 30 mg segments of hot melt extruded filaments or 3D-printed tablets were placed into a volumetric flask with 25 mL ethanol under magnetic stirring until the segments were completely dissolved. Then the homogenous solution was filtered through a 10 mL SOL-M^{TM} syringe (SOL-MILLENNIUM Medical Group, Aichwald, Germany) and a 0.45 μm Fisherbrand^{TM} syringe filter (Fisher Scientific International, Inc., Guangzhou, China). The amount of IBP was determined with a Biochrom WPA Biowave II^{+} UV/Visible Spectrophotometer (Biochrom Ltd., Cambourne, UK) at an absorption wavelength of 264 nm. To calculate the concentration of IBP in ethanol, the calibration curve was prepared in the range of 3.125–100 μg/mL ($A = 0.0014C + 0.0046, R^2 = 0.9956$) where A represents the absorbance and the C represents the concentration (μg/mL). There was no interference between IBP and the other materials at the wavelength. The drug loading and dose accuracy were calculated according to Eqs. (1) and (2). All measurements were conducted in triplicate ($n = 3$).

$$Drug\ Loading = \frac{Amount\ of\ drug}{Amount\ of\ drug + polymers} \times 100\% \quad (1)$$

$$Dose\ Accuracy = \frac{Calculated\ drug\ loading}{Theoretical\ drug\ loading} \times 100\% \quad (2)$$

2.13. In vitro drug release studies

In vitro dissolution tests under sink conditions were performed with a USP type II paddle apparatus (708-DS Dissolution Apparatus, Agilent Technologies, Santa Clara, CA, USA) in 900 mL of phosphate-buffered saline (PBS) solution (pH = 7.2) at 37 ± 0.3 °C with a paddle speed of 100 rpm. All samples were run in triplicate ($n = 3$). At different time intervals (0, 20, 40, 60, then every 60 min up to 24 h) the dissolution medium was automatically pumped into UV spectrophotometer. The drug concentration of the dissolution medium was measured automatically by using Cary 60 UV–Vis (Agilent Technologies) at a wavelength of 221 nm in a 1 cm cell versus a blank solution consisting of PBS solution (pH = 7.2). The solubility of IBP in this medium is 4.48 ± 0.08 mg/mL at 37 °C (De Brabander et al., 2003). The calibration curve from 0.78125 to 25 μg/mL was prepared ($A = 0.0424C + 0.0024$, $R^2 = 0.9997$) to calculate the concentration of IBP. Then, the release profiles were plotted as a percentage of cumulative drug release versus time. Additionally, there is no interference from other raw materials on the drug assay observed at the detection wavelength.

An add-in program (DDSolver) in Microsoft Excel (Zhang et al., 2010) was used to evaluate the drug release kinetics of the acquired dissolution curves by fitting the data to various equations listed in Table 2. The zero-order drug release model where the dissolution rate is constant is regarded as the ideal model for release data as this type of drug release pattern can maintain the drug concentration in blood plasma at a constant level for prolonged periods (Samaha et al., 2009; Williams, 2018). The first-order model (the dissolution rate is exponential) has been used to describe drug absorption, elimination and decomposition (Samaha et al., 2009; Williams, 2018). The Higuchi model (square root time-dependent) mainly describes drug release as a diffusion process according to Fick's law (Higuchi, 1963; Samaha et al., 2009). The Korsmeyer-Peppas model (relating exponentially the drug release to the elapsed time) could be used to analyze the drug release mechanism (Quinten et al., 2009) (Homaee Borujeni et al., 2020). In the case of cylindrical tablets, the value of n could be used as an approximation to describe the mechanism of drug release. The $n < 0.45$ (Fickian

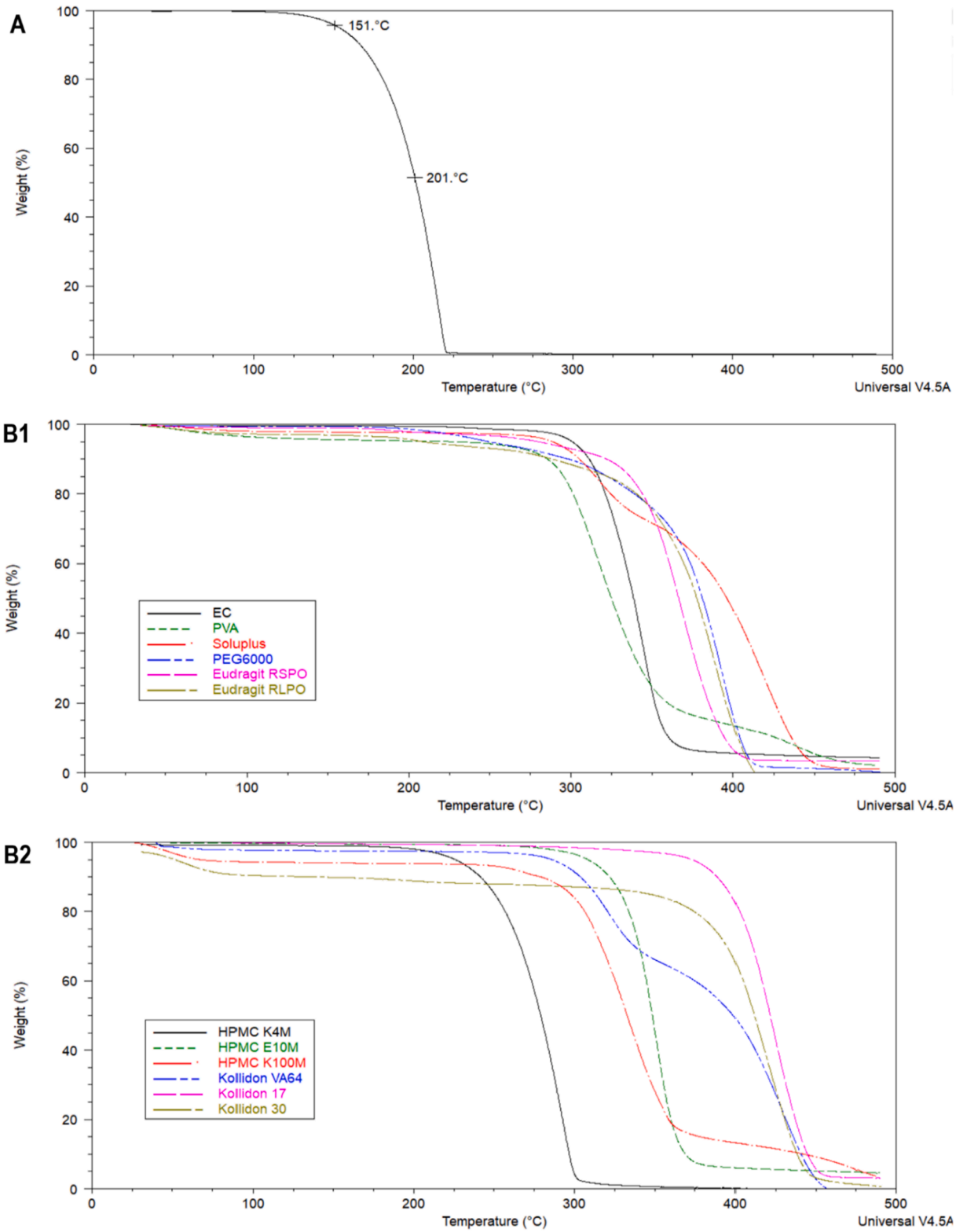

Fig. 4. Thermal degradation profiles of (A) IBP and (B) other raw materials.

diffusion), $0.45 < n < 0.89$ (anomalous transport) and $n > 0.89$ (case-II transport) (Peppas and Sahlin, 1989). It is noteworthy that only the portion of the dissolution curve where $F < 60\%$ should be used to calculate the exponent n (Peppas and Sahlin, 1989). n value of 0.45 or 0.89 is an indication of diffusion or erosion mechanism, respectively.

Two statistical criteria, the adjusted coefficient of determination (R^2_{adj}) and the Akaike Information Criteria (AIC) were applied to determine the most suitable model for fitting dissolution data (Ilyés et al., 2019; Quinten et al., 2009). When comparing different models for a given dissolution profile, the model with the highest value of R^2_{adj} and the lowest value of AIC could be regarded as the best fit among all models (Samaha et al., 2009; Zhang et al., 2010).

3. Results and discussion

3.1. Materials selection

IBP is one of the most commonly used non-steroidal anti-inflammatory drugs (NSAIDs) (Ramukutty and Ramachandran, 2012). Its short biological half-life (2 h) makes this drug suitable for sustained DDSs development (De Brabander et al., 2003). Solid dispersions of IBP with various carriers have been investigated in recent years for improving the solubility and dissolution properties of IBP, even though IBP shows poor pharmaceutical behaviors and flow properties (Al-hamidi et al., 2010; Samaha et al., 2009). Moreover, IBP has a high tendency to adhere to punches during direct compression (Ramukutty and Ramachandran, 2012). IBP was selected as the model drug in this study mainly due to its plasticizing effect on EC, which has been studied by many research groups (De Brabander et al., 2002; Yang et al., 2018).

EC is a well-known polymer to be used in the manufacture of tablets by direct compression for achieving sustained release profiles (De Brabander et al., 2003). EC with various molecular weights is suitable for HME because of its excellent thermo-plasticity when the temperature is higher than its T_g (129–133 °C) (Maru et al., 2011; Quinten et al., 2009). As a result, EC formulations without plasticizers could only be extruded at temperatures above 133 °C and the extrudates will be too brittle to be further printed through FDM (Quinten et al., 2009). With the addition of traditional plasticizers (e.g. dibutyl sebacate), the extrusion process will become easier by decreasing the T_g and melt viscosity of EC, then the risk of thermal decomposition of the API will be minimized because of the lower processing temperature (Quinten et al., 2009). Many studies have illustrated that the addition of IBP to the HME formulations can lower the extrusion temperature significantly and increase the stability due to the plasticizing effect of IBP (De Brabander et al., 2003, 2002; Yang et al., 2018). However, the drug release rate from the IBP and EC hot melt extrudates is very slow due to the water insolubility and inertia of EC (De Brabander et al., 2003; Quinten et al., 2009; Yu et al., 2009). Consequently, other polymers were also introduced to modify the drug release behavior of FDM 3D printed tablets fabricated from hot melt extruded filaments of IBP and EC matrix. In this way, HME can provide an effective combining method for melt-blending different polymers into one homogenous final dosage form (Fuenmayor et al., 2018). Because the printability of filaments will be affected significantly by the physicochemical properties of the starting materials, the hot melt extruded filaments were characterized comprehensively (Jamróz et al., 2018).

In the current research, release modifiers with different viscosity grades were added to IBP-EC hot melt extruded matrix separately to modulate the drug release. Although FDM 3DP is a promising method for preparing controlled release dosage forms, the high compactness and high density of FDM 3D printed objects place a significant restriction on the drug release through diffusion (Homaee Borujeni et al., 2020; Yang et al., 2018). In this situation, the introduction of erosive polymers (e.g. PVA, Soluplus, HPMC) into the 3D printed matrix is an efficient method for improving the drug release through surface erosion of the intact matrix in the dissolution media (Goyanes et al., 2015b; Homaee Borujeni et al., 2020). Yang et al. (2018) have used PVA and HPMC K100LV as release modifiers in combination with IBP and EC because HPMC can increase the drug release through water uptake, swelling and erosion. PVA possesses great thermo-plasticity and mechanical properties, so PVA filaments are one of the commercially available filaments for FDM 3DP (Chen et al., 2020; Liang et al., 2018; Palekar et al., 2019). Similarly, Soluplus is another swellable polymer for HME in pharmaceutical applications due to its outstanding thermal stability and extrudability, although pure Soluplus filaments are too brittle for FDM 3D printers (Alhijjaj et al., 2016). Traditional plasticizers, such as TEC and various grades of PEG, show a facilitating effect on FDM 3DP for increasing the melt flow properties of thermoplastic polymers and decreasing the T_g (Nasereddin et al., 2018). The pH-independent swelling behavior and low permeability make Eudragit RL and RS promising release modifiers for release retardation because the drug release from these two water-insoluble polymers is mainly governed by the diffusion mechanism in many studies of 3DP (Kempin et al., 2017; Krause et al., 2019; Pietrzak et al., 2015). Various grades of HPMC are processable in HME without the addition of plasticizers and they are the most widely used polymers in drug-loaded filament development for sustained drug release 3D printed tablets (Huang et al., 2016; Khizer et al., 2019). Kollidon® VA64 (a copolymer of polyvinylpyrrolidone and vinyl acetate) has been used as a water-soluble polymer matrix material in the HME process, but the pure Kollidon® VA64 filaments are so brittle that would collapse in the 3D printer (Fuenmayor et al., 2018; Solanki et al., 2018). To the best of our knowledge, Kollidon® 17 PF and 30 have not been employed in the FDM 3DP technology, but Kollamaram et al. (2018) proved that Kollidon® 12PF is a suitable excipient for FDM 3DP (Kollamaram et al., 2018). Kollidon® 12PF and 17PF are soluble low molecular polyvinylpyrrolidone which is used as common solubilizing agents and crystallization inhibitors . Similarly, Kollidon® 30 (medium-molecular polyvinylpyrrolidone) could also be applied as a solubilizing agent and a crystallization inhibitor.

In the development of sustained DDSs, high drug loading should be considered due to the requirement for high amounts of drug and low volume of drug systems (De Brabander et al., 2003). As IBP shows a plasticizing effect on EC and has a significant effect on improving the thermo-plasticity of EC during the HME process, therefore, sufficient IBP was necessary to ensure the processability of hot melt extruded filaments in the following FDM printing process (De Brabander et al., 2002) (Yang et al., 2018). According to Yang et al. (2018), FDM 3D printed tablets with 20% ibuprofen perform better than tablets prepared with other drug contents from 16% to 24% in printing quality.

3.2. Thermal analysis

3.2.1. TGA analysis

The processing temperature plays an important role in this study because higher processing temperature will lead to a higher risk of thermal API decomposition (Quinten et al., 2009). It has also been shown that printing quality could be affected significantly by printing temperatures (Yang et al., 2018). Objects printed through lower temperatures tend to be more viscous in the heater and show weaker bond strength between layers, which then lead to nozzle blockage and the disintegration of final products (Yang et al., 2018). However, if the printing temperature is too high, thermolabile drugs and polymers will degrade (Pietrzak et al., 2015). Hence, the TGA was conducted to compare the thermal decomposition pattern of all raw materials.

As shown in Fig. 4A, the start point of IBP thermal degradation is around 151 °C, and 201 °C is regarded as the degradation acceleration peak. All other raw materials (Fig. 4B) exhibited no obvious weight loss up to 220 °C, where the thermal degradation begins to occur for HPMC K4M. Among these materials, Kollidon 30 and HPMC K100M both demonstrated an obvious weight loss below 100 °C, which is related to the relatively higher weight ratio of absorbed moisture. Therefore, all other polymers applied in this study are thermally stable up to around 300 °C. In addition, Pietrzak et al. (2015) pointed out that FDM 3DP temperature is required to be at least 40–50 °C higher than the ideal HME processing temperature. The possible reason is the difference between the heating durations of HME (longer than 5 min under shear mixing of powder mixtures) and 3DP (normal extrusion rate of extruded filaments at 3 mm^3/s through the heated nozzle) (Pietrzak et al., 2015). To minimize the decomposition of the API during extrusion and printing processes, printing temperatures were tested from 150 °C to determine the lowest processable printing temperature. Based on the results, all fabricated filaments could only be printed until 178 °C.

Hence, 178 °C was selected as the optimum printing temperature without compromising the quality of the print as well as the products. Apart from IBP, no significant weight loss of other excipients could be

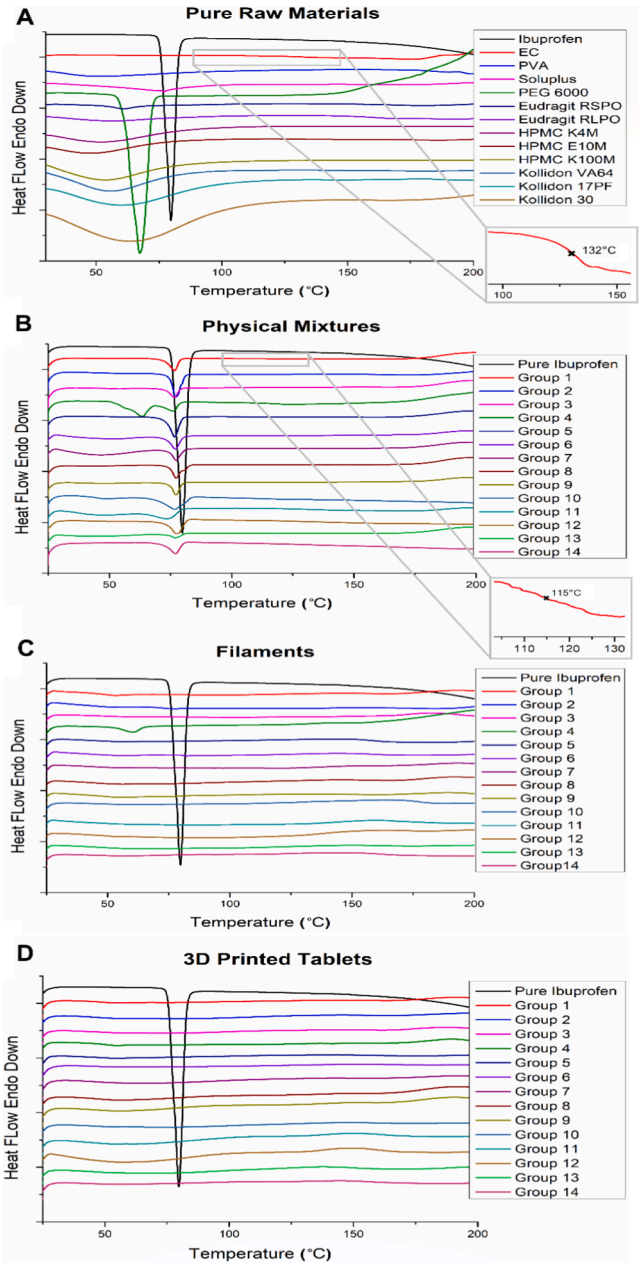

Fig. 5. DSC thermograms of (A) pure raw materials, (B) physical mixtures, (C) hot melt extruded filaments and (D) 3D printed tablets of each group.

observed in the HME zone (80–100 °C) nor the FDM printing zone (178 °C). Therefore, the drug content test was necessary to evaluate the amount of IBP loaded in the filaments and printed tablets after repetitive exposure to high temperature.

3.2.2. DSC analysis

The optimal processing temperatures during extrusion and printing processes should be determined by both the melting and degradation temperature values of IBP and other raw materials to minimize degradation and incomplete incorporation of the model drug in the carrier. For evaluating the solid-state of the drug in the extruded filaments and 3D printed tablets, DSC and XRPD analyses were applied. As shown in Fig. 5A, the DSC profile of IBP showed a sharp endothermic peak with an onset temperature of about 78.9 °C. The melting point of IBP also confirmed its crystalline state. EC and other excipients (except for PEG 6000 which is a semi-crystalline substance) showed no endothermic peaks, indicating that they are in an amorphous state. The DSC thermograms of physical mixtures of all formulations exhibited an IBP endothermic peak but with smaller intensity due to the low amount of IBP (20 w/w%) compared to DSC traces of pure IBP. Additionally, it could be due to partial drug-polymer miscibility and interaction (Piccinni et al., 2016). The presence of the characteristic endothermic peak of IBP in all physical mixtures indicates that the mixing process cannot change the solid states of the API and excipients (Fig. 5B). However, a complete absence of the IBP endothermic peak in the IBP loaded extruded filaments (Fig. 5C) and 3D printed tablets (Fig. 5D) from all groups was attributed to the conversion of IBP from the crystalline state to the amorphous state during the HME process (Yang et al., 2018). The single shift in the baseline of unprocessed EC powder was observed at around 132 °C, which could be attributed to its T_g (De Brabander et al., 2002). Additionally, De Brabander et al. (2002) pointed out that the T_g of amorphous IBP was determined at −43.6 °C. According to the Gordon-Taylor equation, the significant decrease in the T_g of EC from 132 °C to 115 °C reflects the miscibility between IBP and EC in the physical mixtures of Group 1 (IBP and EC without release modifiers) because the T_g of physical mixtures lies between the T_g of two individual components (Maniruzzaman et al., 2013). This decreasing effect of IBP on the T_g of EC can also confirm that IBP showed the plasticizing effect and mobility enhancing effect on EC chains (Homaee Borujeni et al., 2020). It is noteworthy that the endothermic peak of PEG could be observed in F4 filaments instead of 3D printed tablets because semi-crystalline PEG was transformed into the amorphous state mainly during the printing process.

3.3. Surface morphology

The filaments of F1, F5 and F6 were translucent and others have a slightly white opaque appearance (Fig. 6). This indicates that most release modifiers of each group still existed in the form of particles after the HME process to some extent except F5 and F6 (Chai et al., 2017).

As shown in Fig. 7A and B, no defects, bubbles or holes were observed on the cross-section or surface of all drug-loaded filaments. Homogeneous morphology and the absence of drug crystals in SEM images of Group 1 (Fig. 7A1 and B1) illustrated that IBP was distributed evenly in the EC matrix of IBP containing filaments (Homaee Borujeni et al., 2020). However, a small number of IBP crystals could be seen in the filaments of Groups 2 and 9 at high magnification when compared with other groups. The external surface of hot melt extruded filaments in Groups 1, 3, 4, 5 and 6 was smoother, possibly due to the better coalescence of the API and polymers during processing (Quinten et al., 2009). On the contrary, the roughness imperfections on the surface of filaments in Group 2, and Group 7 to Group 14 might be contributed to the low processing temperature during HME (80–100 °C) which is not high enough for melt flowing and mixing of EC and release modifiers (Homaee Borujeni et al., 2020). According to Crowley et al. (2004), the processing temperature has a significant effect on the surface morphology of extrudates because lower processing temperature is related to visible crystalline API particles and higher processing temperature can lead to striated appearance. The images of 3D printed tablets (Fig. 7C and D) illustrated that IBP was distributed in the tablets homogenously after further exposure to heat. The excellent surface morphology of all these hot melt extruded filaments and 3D printed tablets confirmed that the formulation composition of 14 groups is suitable for HME and FDM 3DP processes.

The physical characteristics of tablets printed with filaments were evaluated. As shown in Table 3, the ability of fabricated filaments to reproduce the predesigned 3D structure was high. The tablets in each group were found to have uniform weights, diameters and heights with acceptable variation (Table 2 and Fig. 8). The weight variations seen for these batches could be attributed to the differences among the fluidity potentials of these release modifiers (Ilyés et al., 2019). Raw materials with enhanced mechanical and rheological properties can lead to higher extrusion rate, then bigger and heavier final tablets could be produced.

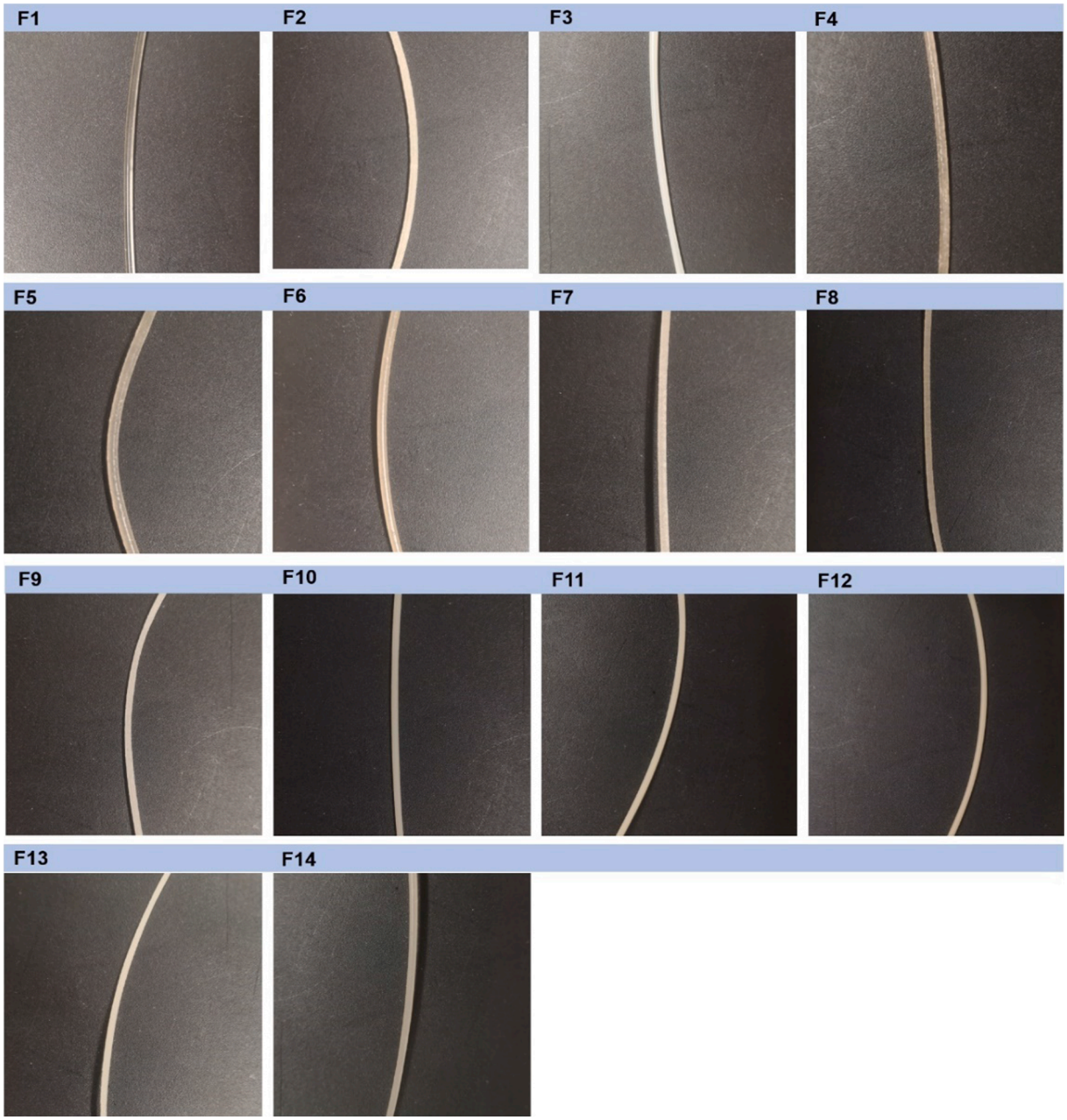

Fig. 6. Images of hot melt extruded filaments containing IBP.

The geometry of these tablets is relatively constant with similar surface area/volume ratios from 1.32 to 1.40. Because the mechanical strength of these tablets was high, therefore, the friability values were zero, conventional hardness test methods are not feasible for FDM 3D printed formulations (Homaee Borujeni et al., 2020; Lamichhane et al., 2019).

3.4. XRPD analysis

XRPD studies were conducted to analyze the physicochemical properties of raw materials and the crystalline-amorphous transformation of the API through the preparing process. XRPD diffractograms of raw materials (Fig. 9) were illustrated to identify the original solid-state of IBP, polymer and various release modifiers. Diffraction patterns of IBP showed an obvious crystalline nature due to multiple sharp intense peaks at around 6.2°, 12.3°, 16.7°, 19.1°, 20.2° and 22.4° (2-theta position), whereas other raw materials showed the halo structure which is an indication of amorphous nature of these materials with an exception of PEG (Mallick et al., 2008). The diffraction pattern of PVA and PEG 6000 revealed a complete agreement of their semi-crystalline nature (Alhijjaj et al., 2016; Kempin et al., 2018; Palekar et al., 2019).

The XRPD traces of raw materials, physical mixtures, hot melt extruded filaments and 3D printed tablets for each batch are shown in Fig. 10. The peaks of XRPD traces of physical mixtures are in good consistent with peaks of IBP in each batch because EC and most of the release modifiers (Soluplus, Eudragit RL PO/RS PO, HPMC K4M/E10M/K100M, Kollidon VA 64/17PF/30) exist in the amorphous state. No characteristic peaks for IBP were detected in the diffractograms for the extruded filaments and 3D printed tablets, confirming the absence of crystalline IBP in the extruded filaments and 3D printed tablets with the 20 w/w% drug load. It suggests that HME and 3DP processes had a significant effect on the crystallinity of the API. The XRPD diffractograms of drug-loaded hot melt extruded filaments and 3D printed tablets from all groups only reflect the EC characteristic peaks. Multiple high-

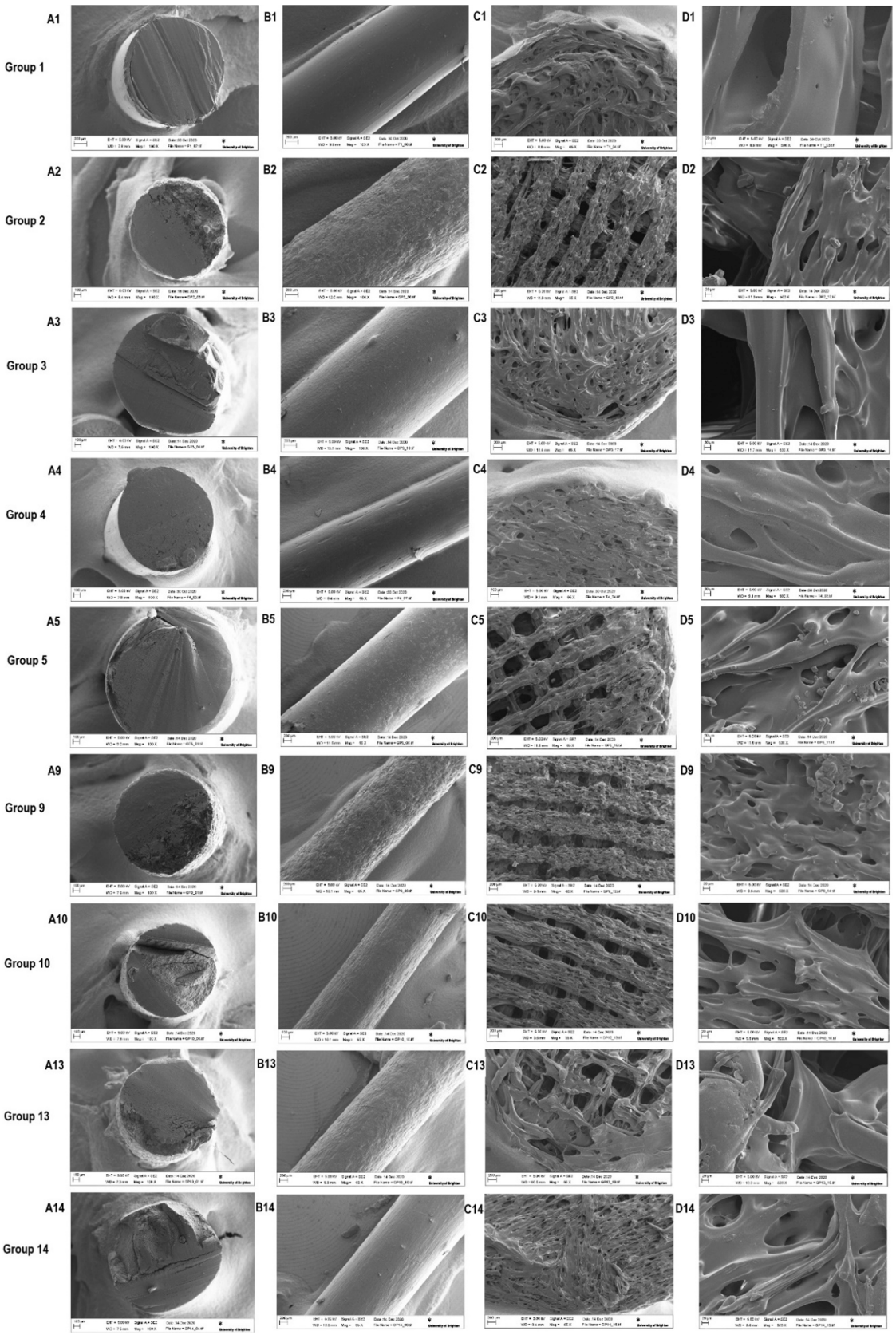

Fig. 7. SEM images of (A) cross-section, (B) surface of filaments, (C) and (D) top surface of 3D printed tablets loaded with IBP in Group 1, 2, 3, 4, 5, 9, 10, 13 and 14.

Table 3
Physical parameters for 3D printed tablets ($n = 3$, mean ± SD).

3DP Tablets	Weight (mg)	Diameter (mm)	Height (mm)	Volume (mm^3)	Density (mg/mm^3)	Surface area (mm^2)	Surface area/volume
Group 1	116.00 ± 5.02	9.67 ± 0.12	2.21 ± 0.09	162.43 ± 3.18	0.71 ± 0.04	214.07 ± 1.87	1.32 ± 0.03
Group 2	119.73 ± 5.65	9.74 ± 0.15	2.14 ± 0.13	159.20 ± 12.35	0.75 ± 0.03	214.41 ± 7.92	1.35 ± 0.06
Group 3	144.97 ± 1.12	9.84 ± 0.19	2.13 ± 0.09	162.09 ± 11.35	0.90 ± 0.06	217.99 ± 8.84	1.35 ± 0.05
Group 4	137.17 ± 1.00	9.71 ± 0.24	2.12 ± 0.11	156.57 ± 9.71	0.88 ± 0.05	212.53 ± 8.60	1.36 ± 0.05
Group 5	116.17 ± 4.10	9.82 ± 0.10	2.10 ± 0.04	158.59 ± 5.67	0.73 ± 0.03	216.00 ± 4.58	1.36 ± 0.02
Group 6	118.73 ± 4.36	9.78 ± 0.15	2.09 ± 0.05	156.90 ± 6.84	0.76 ± 0.05	214.30 ± 6.22	1.37 ± 0.03
Group 7	126.13 ± 4.55	9.58 ± 0.01	2.14 ± 0.05	154.62 ± 3.37	0.82 ± 0.05	208.77 ± 1.45	1.35 ± 0.02
Group 8	130.53 ± 0.78	9.80 ± 0.12	2.02 ± 0.05	152.25 ± 6.48	0.86 ± 0.03	212.97 ± 5.39	1.40 ± 0.03
Group 9	135.47 ± 5.06	9.85 ± 0.12	2.07 ± 0.01	157.62 ± 3.59	0.86 ± 0.05	216.36 ± 4.26	1.37 ± 0.01
Group 10	116.43 ± 3.32	9.64 ± 0.09	2.03 ± 0.05	148.24 ± 5.80	0.79 ± 0.05	207.43 ± 4.45	1.40 ± 0.03
Group 11	113.20 ± 1.40	9.76 ± 0.23	2.01 ± 0.02	150.68 ± 7.36	0.75 ± 0.04	211.41 ± 8.69	1.40 ± 0.01
Group 12	102.37 ± 3.40	9.61 ± 0.21	2.15 ± 0.04	155.90 ± 10.07	0.66 ± 0.04	210.06 ± 9.16	1.35 ± 0.03
Group 13	103.30 ± 1.30	9.51 ± 0.11	2.12 ± 0.08	150.53 ± 8.97	0.69 ± 0.03	205.34 ± 6.16	1.37 ± 0.04
Group 14	118.10 ± 1.61	9.70 ± 0.05	2.11 ± 0.04	156.00 ± 4.21	0.76 ± 0.02	212.09 ± 2.90	1.36 ± 0.02

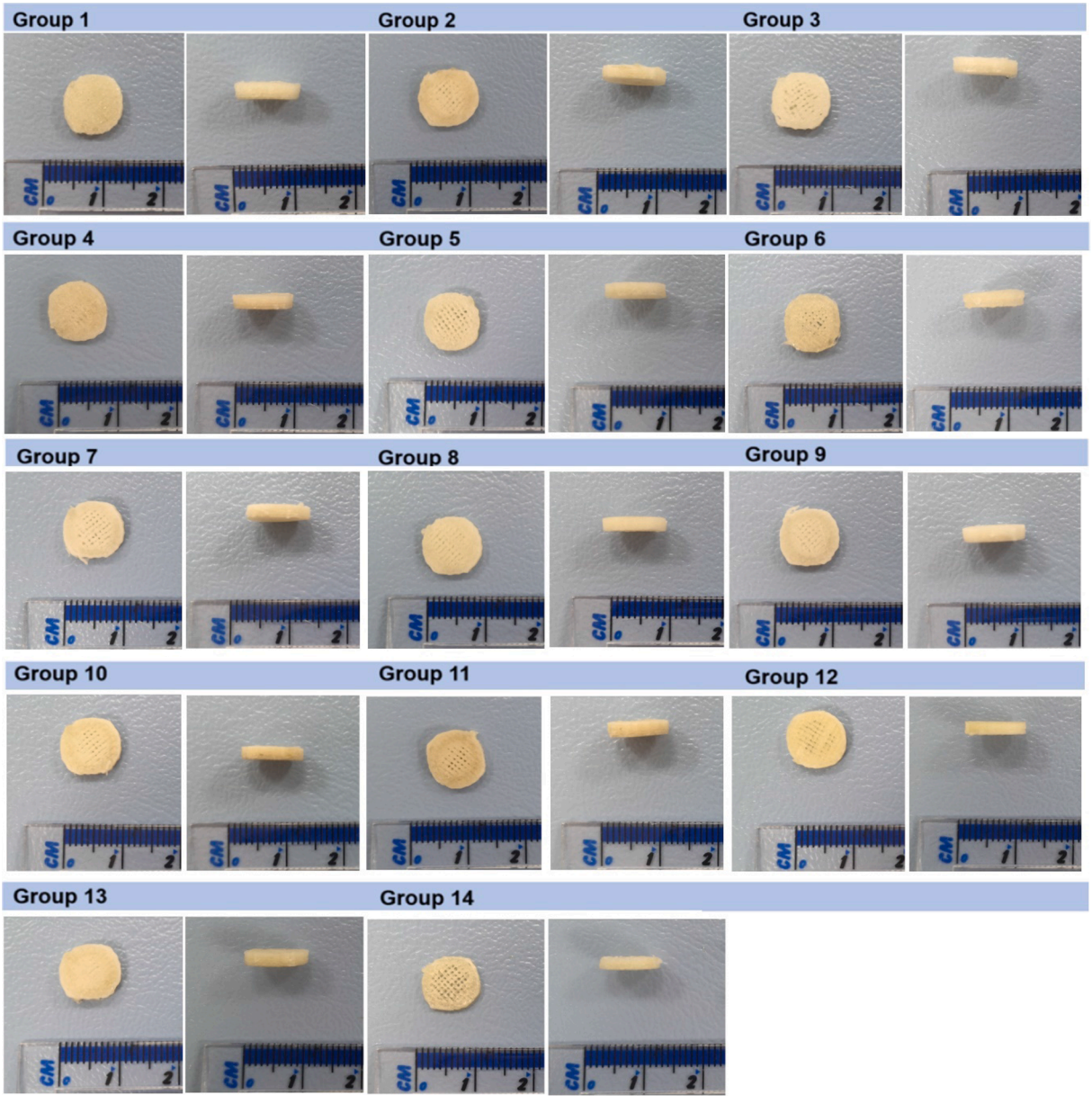

Fig. 8. Images of 3D printed tablets prepared with hot melt extruded filaments.

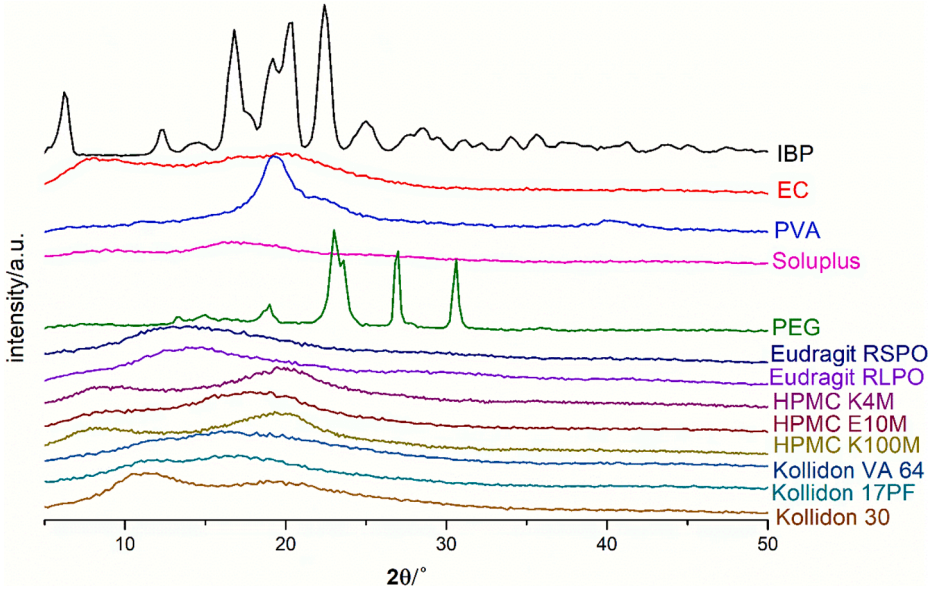

Fig. 9. XRPD diffractograms of raw materials.

intensity peaks of IBP were not seen in the XRPD patterns of filaments or 3D printed tablets, mainly because of the formation of the IBP solid dispersion in the filaments or 3D printed tables which overshadowed its crystalline nature (Kadry et al., 2018).

3.5. Mechanical properties

Elasticity, stiffness, homogenous dimension and drug distribution are key factors for filaments to be printed into high-quality dosage forms with FDM technology (Jamróz et al., 2018). Most pharmaceutical polymers possess high viscosity and poor melt flow properties, which are undesirable factors for FDM (Nasereddin et al., 2018). The filaments are required to possess both suitable stiffness and elasticity (Dumpa et al., 2020). Otherwise, those filaments could not be printed successfully due to several states, such as fragmentation (related to high brittleness), shear/erosion (related to lower resistance to traction), buckle (high viscosity and /or low column strength) and so forth (Ilyés et al., 2019; Jamróz et al., 2018).

Mechanical properties of hot melt extruded filaments were evaluated using a texture analyzer to predict the printability of these filaments during the FDM 3DP process (Liang et al., 2018). Commercial polylactic acid (PLA) filaments (FilaPrint® premium PLA, 1.75 mm, 3D FilaPrint Ltd., Essex, UK) without drug deposition were used as the reference standard (Fig. 11). The yield strength (elastic limit) represents the maximum stress that the filament could tolerate before permanent deformation happens. The ultimate tensile strength is represented by the highest point in the stress–strain curve because it is the minimum stress (ratio of applied force to the cross-sectional area filaments) that the material will break during the stretching process. The elastic modulus (Young's modulus) could be represented by the slope of the elastic region (linear part) in the stress–strain curve (Homaee Borujeni et al., 2020). The elastic modulus was calculated to evaluate the stiffness of filaments. To guarantee the filaments could tolerate the operation in drive gears of the 3D printer, the elongation at break (the ratio of increase in length to original length) is needed to be higher (Homaee Borujeni et al., 2020; Ilyés et al., 2019). Furthermore, stiffer filaments show higher Young's modulus and less brittle filaments show higher elongation at break (Zhang et al., 2017).

Obviously, the commercial PLA filaments showed higher yield strength, Young's modulus and tensile strength when compared with hot melt extruded IBP loaded EC filaments due to higher stiffness (Fig. 12). Filaments prepared without release modifiers (F1) were used to ascertain the original printing properties of IBP and EC. It is noteworthy that filaments prepared without release modifiers (F1) exhibited slightly higher elongation at break than PLA filaments because of lower brittleness. Filaments extruded with only IBP and EC (F1) displayed significantly higher tensile strength of 30 MPa than all other fabricated filaments with the addition of various release modifiers (F2-14). Additionally, their elongation at break (7.88%) was also the highest. Nasereddin et al. (2018) have pointed out that pure Soluplus filaments showed almost no strain bearing capacity, which is in agreement with the low elongation at break of F3 filaments. The IBP-EC filaments with the addition of Kollidon VA 64 (F10) and Kollidon 30 (F12) showed similar mechanical properties. The addition of TEC in F13 can lower the brittleness and stiffness of filaments in F10, whereas the addition of Eudragit RSPO in F14 can increase the stiffness and brittleness slightly.

As shown in Table 4, the addition of these release modifiers decreased the stiffness and increased the brittleness because of the significant decrease in both tensile strengths and elongations at the break. No obvious difference could be observed among F7, F8 and F9, indicating that the mechanical properties of filaments prepared with the addition of HPMC K4M, E10M and K100M are similar. Similar trends could be found in F5 (Eudragit RSPO) and F6 (Eudragit RLPO) even though F5 showed the second-highest elongation at break (6.90%) among all these 14 batches. The addition of plasticizer (TEC) can increase the strain bearing ability and decrease the elastic modulus of F13 compared to F10 filaments (Dumpa et al., 2020; Homaee Borujeni et al., 2020; Nasereddin et al., 2018).

The strain hardening behavior could be applied as a parameter to evaluate the conditions for material processing as it has a significant influence on the strength and ductility (Vinoth Kumar et al., 2017). As shown in Eq. (3), the strain hardening capacity (H_c) was defined as a ratio of the ultimate tensile strength (σ_{UTS}) to the yield strength (σ_y). According to Hall-Petch relationship, materials with the higher H_c value are considered as ideal because they reflect homogeneous yielding and the increase in formability and grain size (Afrin et al., 2007; Jin et al., 2012). Strain hardening capacity is related to the material condition as higher hardening capacity will lead to higher ductility (Gao et al., 2015). As shown in Table 4, the values of H_c in F1 and F4 to F7 are all obviously higher than that of commercial PLA filaments. Among them, the addition of HPMC E10M (F8), K4M (F7) and PEG 6000 (F4) can increase the value of H_c in IBP-EC filaments (F1). However, the hardening capacity values of filaments in F3, F10, F11, F12 and F14 are 0. In this case, these extruded filaments experienced a sudden fracture during the tensile test

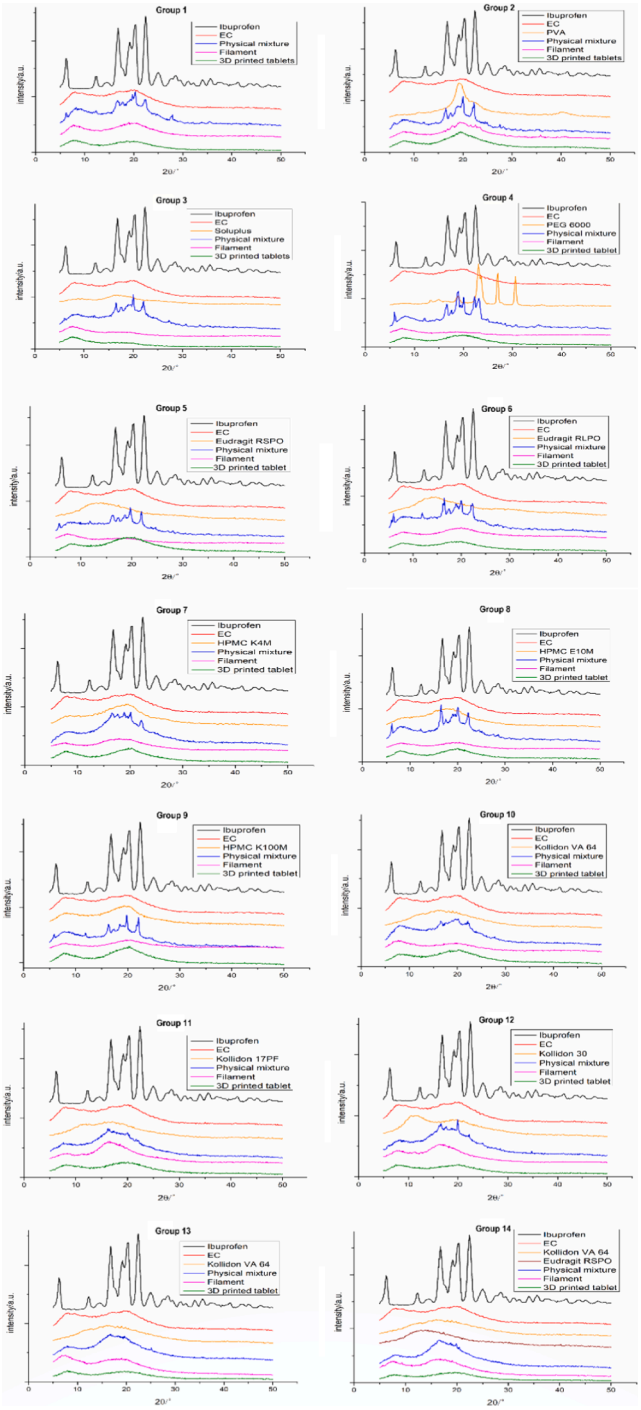

Fig. 10. Comparison of XRPD diffractograms of each group.

without the strain hardening process.

$$H_c = \frac{\sigma_{UTS}}{\sigma_y} - 1 \tag{3}$$

All these prepared filaments showed no breaking or squeezing problems during the 3DP process, indicating suitable mechanical properties of these filaments for FDM 3DP and the fabrication of high-quality 3D printed tablets.

3.6. Drug content determination

During the HME and FDM processes for developing amorphous dispersions, identifying drug loading is vitally important for checking the chemical and physical stability of the final formulation (Huang et al., 2016). Ethanol was used to completely dissolve EC based filaments and 3D printed tablets (Quinten et al., 2009). The percentage of IBP in the filaments and 3D printed tablets was shown in Table 5. Reasonable under-content or overage is common and acceptable in pharmaceutical products across regulatory agencies (Kadry et al., 2018). This indicates that there is no major loss or degradation of IBP during the extrusion and printing processes. The good drug content uniformity in IBP containing filaments and 3D printed tablets illustrated that the HME process can provide an effective method for loading IBP into EC polymer matrix homogeneously and minimizing the drug content differences among the 3D printed tablets (Homaee Borujeni et al., 2020). Consequently, the drug loading in the filaments or 3D printed tablets was 20 w/w%, which allowed for adjusting the amount of IBP by controlling the total weight of the final products.

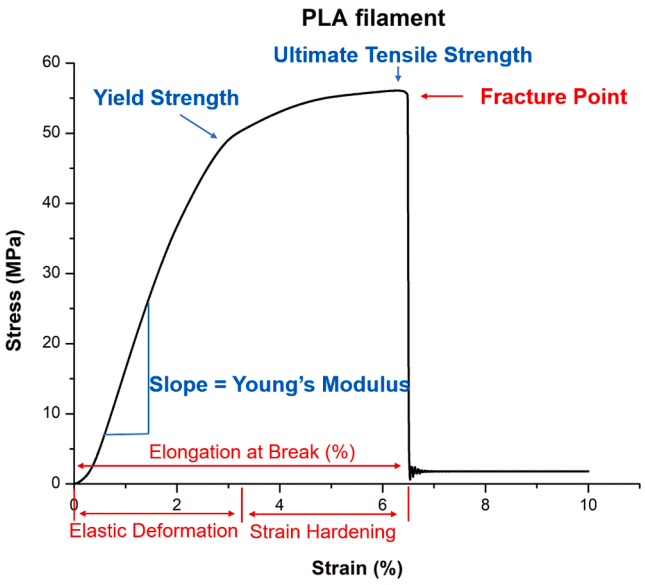

Fig. 11. Illustration of the stress-strain curve of commercial PLA filaments.

3.7. In vitro dissolution studies

The drug dissolution behavior from hot melt extruded filament segments, 3D printed tablets, directly compressed physical mixture tablets were evaluated. The main polymer in this study was EC, which is barely soluble in water and has been applied in producing sustained-release tablets by direct compression (De Brabander et al., 2003; Zhang et al., 2017). As expected, the directly compressed physical mixture tablets (in Group 1) released only 37% of IBP within 24 h (Fig. 13A). However, tablets from other groups exhibited different dissolution behaviors. Typically, the dissolution rate of tablets from Groups 7, 8 and 9 (physical mixtures of IBP, EC and HPMC) showed the fastest among all fourteen formulations studied, although the addition of PVA, Soluplus, PEG and Kollidon can also enhance drug release to some extent in Groups 2, 3, 4 and 10–12. On the contrary, the incorporation of Eudragit RSPO (Group 5) or RLPO (Group 6) showed a reduction in drug release.

Generally, the drug release rate from filament segments (Fig. 13B) is much lower than directly compressed physical mixture tablets due to the compacted nature of the molten polymers. It is clear from the results, the addition of Soluplus in F3 has an increasing effect on the dissolution rate of the IBP and EC matrix when compared with other filaments. Many researchers proved that Soluplus, a water-soluble polymer, could be used to increase the dissolution of poorly soluble drugs during the preparation of hot melt extruded solid dispersions (Alhijjaj et al., 2016).

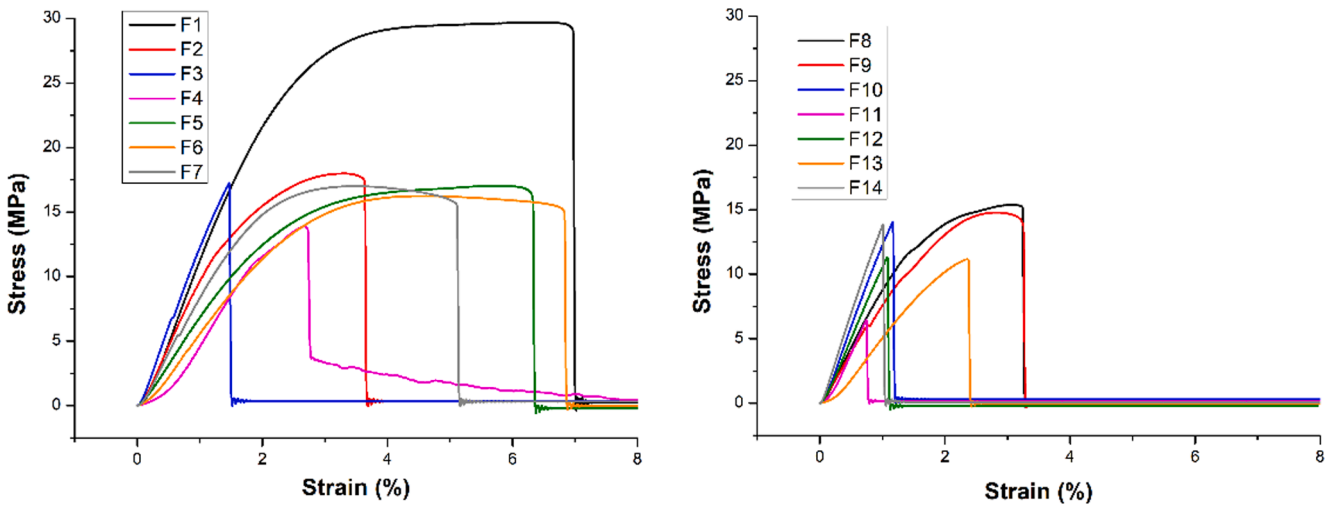

Fig. 12. Stress-Strain curves of various IBP-loaded EC filaments.

Table 4
Mechanical properties of hot melt extruded IBP-loaded EC filaments (n = 3, mean ± SD).

Filament	Yield strength (MPa)	Tensile strength (MPa)	Elastic modulus (MPa)	Elongation at break (%)	Strain hardening capacity
PLA	50.43 ± 0.97	54.64 ± 2.02	2171.62 ± 62.13	6.38 ± 0.17	0.08 ± 0.06
F1	26.59 ± 3.30	32.71 ± 4.29	1099.37 ± 0.06	7.88 ± 1.29	0.23 ± 0.01
F2	16.84 ± 0.28	17.59 ± 0.54	1015.58 ± 116.19	2.96 ± 0.97	0.04 ± 0.01
F3	15.48 ± 2.40	15.48 ± 2.40	1272.24 ± 96.03	1.28 ± 0.30	0 ± 0
F4	13.05 ± 2.09	15.15 ± 0.40	697.12 ± 140.55	2.81 ± 0.06	0.26 ± 0.01
F5	15.50 ± 0.86	17.99 ± 1.39	701.82 ± 32.67	6.90 ± 0.79	0.16 ± 0.03
F6	14.18 ± 0.42	15.52 ± 1.01	932.81 ± 47.35	4.53 ± 3.27	0.09 ± 0.04
F7	12.66 ± 0.35	17.46 ± 0.66	916.60 ± 114.56	4.31 ± 1.15	0.38 ± 0.09
F8	11.43 ± 0.02	17.02 ± 2.35	961.00 ± 159.81	2.99 ± 0.37	0.54 ± 0.13
F9	13.09 ± 0.26	14.84 ± 0.08	707.00 ± 129.50	2.96 ± 0.42	0.13 ± 0.02
F10	11.67 ± 2.98	11.67 ± 2.98	1068.67 ± 227.76	1.13 ± 0.07	0 ± 0
F11	5.23 ± 1.63	5.23 ± 1.63	825.05 ± 60.01	0.65 ± 0.16	0 ± 0
F12	12.19 ± 1.41	12.19 ± 1.41	966.50 ± 120.75	1.48 ± 0.54	0 ± 0
F13	8.89 ± 2.02	9.51 ± 2.49	457.27 ± 79.36	2.79 ± 0.90	0.06 ± 0.04
F14	9.66 ± 3.51	9.66 ± 3.51	1183.67 ± 202.46	0.80 ± 0.20	0 ± 0

Table 5
Drug loading and dose accuracy (mean ± standard deviation) of filaments and 3D printed tablets in each group.

Group	Theoretical drug loading (%)	Filaments		3D Printed Tablets	
		Drug Loading (%)	Dose Accuracy (%)	Drug Loading (%)	Dose Accuracy (%)
G1	20	20.09 ± 0.10	100.47 ± 0.52	19.94 ± 0.05	99.70 ± 0.24
G2	20	20.72 ± 0.13	103.62 ± 0.64	19.98 ± 0.20	99.88 ± 1.00
G3	20	20.14 ± 0.20	100.72 ± 1.01	20.06 ± 0.14	100.32 ± 0.71
G4	20	19.98 ± 0.06	99.92 ± 0.30	20.07 ± 0.06	100.37 ± 0.29
G5	20	19.99 ± 0.18	99.94 ± 0.89	20.28 ± 0.10	101.39 ± 0.50
G6	20	19.98 ± 0.04	99.92 ± 0.20	20.03 ± 0.99	100.14 ± 4.94
G7	20	20.03 ± 0.26	100.16 ± 1.29	20.00 ± 0.40	99.98 ± 1.99
G8	20	19.97 ± 0.29	99.86 ± 1.45	19.96 ± 0.17	99.79 ± 0.87
G9	20	19.97 ± 0.28	99.83 ± 1.40	20.05 ± 0.11	100.25 ± 0.57
G10	20	20.42 ± 0.42	102.12 ± 2.11	19.96 ± 0.27	99.78 ± 1.35
G11	20	20.38 ± 0.07	101.92 ± 0.37	19.93 ± 0.61	99.67 ± 3.07
G12	20	20.08 ± 0.11	100.42 ± 0.57	19.97 ± 0.42	99.86 ± 2.12
G13	20	20.75 ± 0.17	103.75 ± 0.83	20.01 ± 0.61	100.05 ± 3.06
G14	20	19.92 ± 0.44□	□99.62 ± 2.19	20.16 ± 0.19	100.82 ± 0.94

Although Soluplus has promising thermostability and extrudability in pharmaceutical HME, pure hot melt extruded Soluplus filaments are not FDM printable (Alhijjaj et al., 2016). The excellent thermoplastic and FDM printability of PVA make it a benchmark release modifier in this study (Alhijjaj et al., 2016). Similarly, PEG was also applied to improve the FDM printability of the blends and have a plasticizing effect on poorly water-soluble drugs (Alhijjaj et al., 2016). Many studies pointed out that diffusion is the main mechanism for the API to be released from the insoluble macromolecular matrix of Eudragit (Pietrzak et al., 2015). Eudragit® RLPO and RSPO are both copolymers of acrylic and methacrylic acid esters (Zhu et al., 2006). Eudragit® RLPO exhibits more permeable to aqueous media than Eudragit® RSPO because of the higher molar ratio of ionizable groups (Zhu et al., 2006). As a result, the drug release rates of extruded filaments and physical mixture tablets in Group 6 are both slightly higher than those in Group 5. Commonly, sustained-release compacts prepared with higher viscosity grades of HPMC result in a decrease in the drug release rate because of stronger polymer entanglement and slower polymer erosion (De Brabander et al., 2003). However, it has been proved that hot melt extrudates prepared with IBP, EC and higher viscosity grades of HPMC will show a faster drug release rate and higher initial burst drug release when compared with similar extrudates containing lower viscosity grades of HPMC (De Brabander et al., 2003; Quinten et al., 2009). The possible reasons are: (1) the high drug load and the presence of EC can weaken the HPMC chains

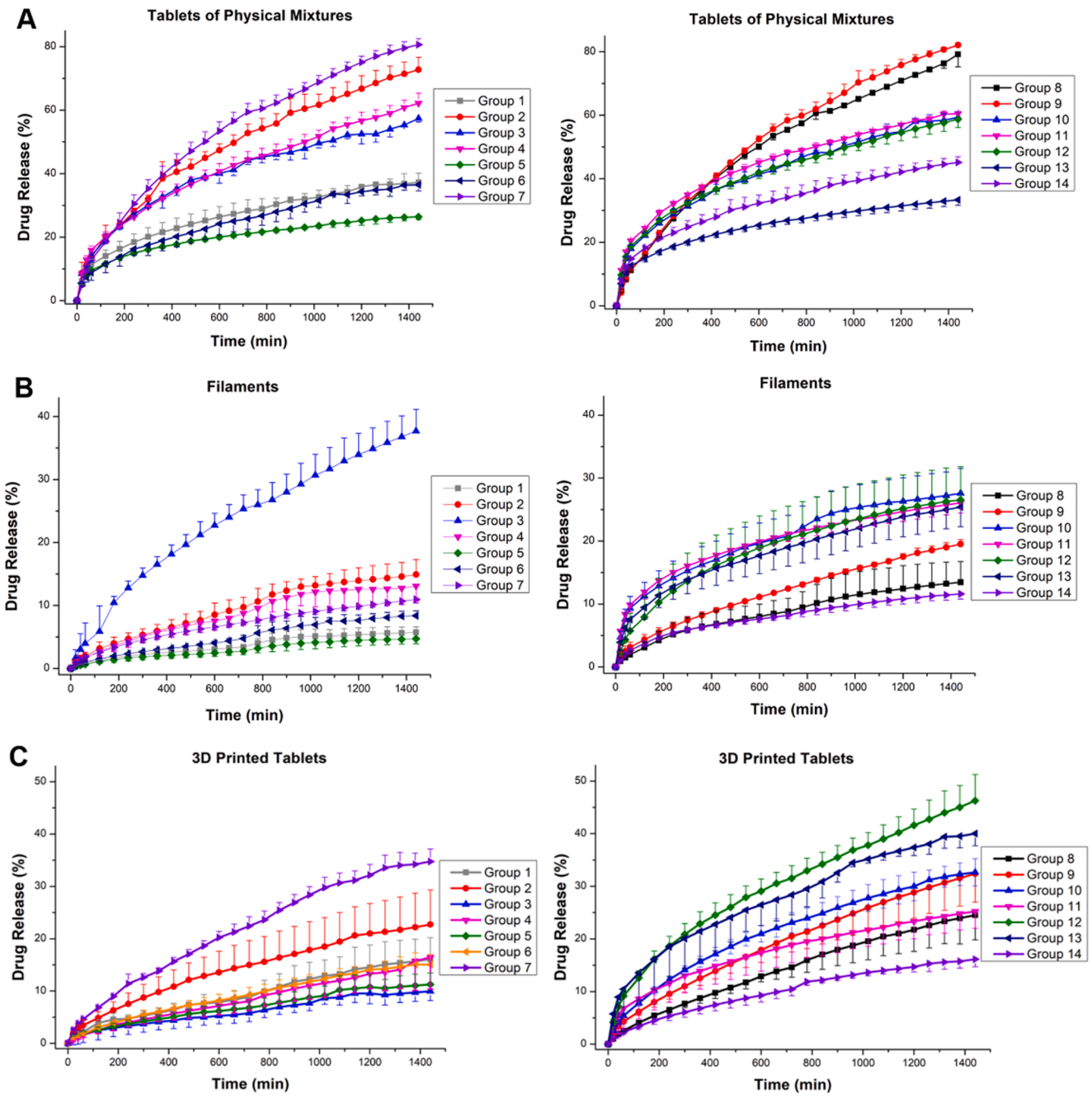

Fig. 13. In vitro drug release study of (A) physical mixture tablets, (B) filament pieces and (C) 3D printed tablets ($n = 3$).

entangled within the matrix; (2) the higher water uptake and swelling capability of higher viscosity HMPC grades can make the matrix more accessible to the dissolution medium (De Brabander et al., 2003; Quinten et al., 2009). The viscosity of HPMC used in this study was in the order of K4M < E10M < K100M (The Dow Chemical Company, 2013). This is in good agreement with the order of drug release rates for their filaments (Fig. 13B). It can be observed that the Kollidon® VA64, 17PF and 30 showed similar increasing effects on the dissolution rate of hot melt extruded filaments of the IBP-EC matrix. It is noteworthy that the dissolution rate of F14 decreased significantly with the addition of Eudragit ® RSPO when compared with F10 as it can be seen that F5 showed the lowest dissolution rate among all groups. All these data indicate that the behavior of polymers in their physical mixture and in the filament is entirely different and the drug release from filaments cannot be predicted based on the dissolution data of physical mixtures of IBP and polymers.

The dissolution efficiency, the area under the dissolution curve, was calculated to analyze whether the behavior of the release modifier added to the formulation is the same trend when it is subjected to HME or 3DP process (Khan, 1975). The results were shown in Fig. 14. The figure shows that the data are scattered everywhere, and no pattern and correlation can be deduced from the figures. This indicates that the behavior of polymers (release modifiers) can be changed via HME or 3DP processes.

Generally, the dissolution profiles of 3D printed tablets (Fig. 13B) showed a slightly faster release than filaments (Fig. 13C) because of the denser structure of filaments generated via thermal treatment during the HME process (Yang et al., 2018). Tablets of Group 1 released only 16% of IBP within 24 h. The incorporation of Soluplus (Group 3), PEG (Group 4) and Eudragit (Groups 5 & 6) decreased the drug release rate.

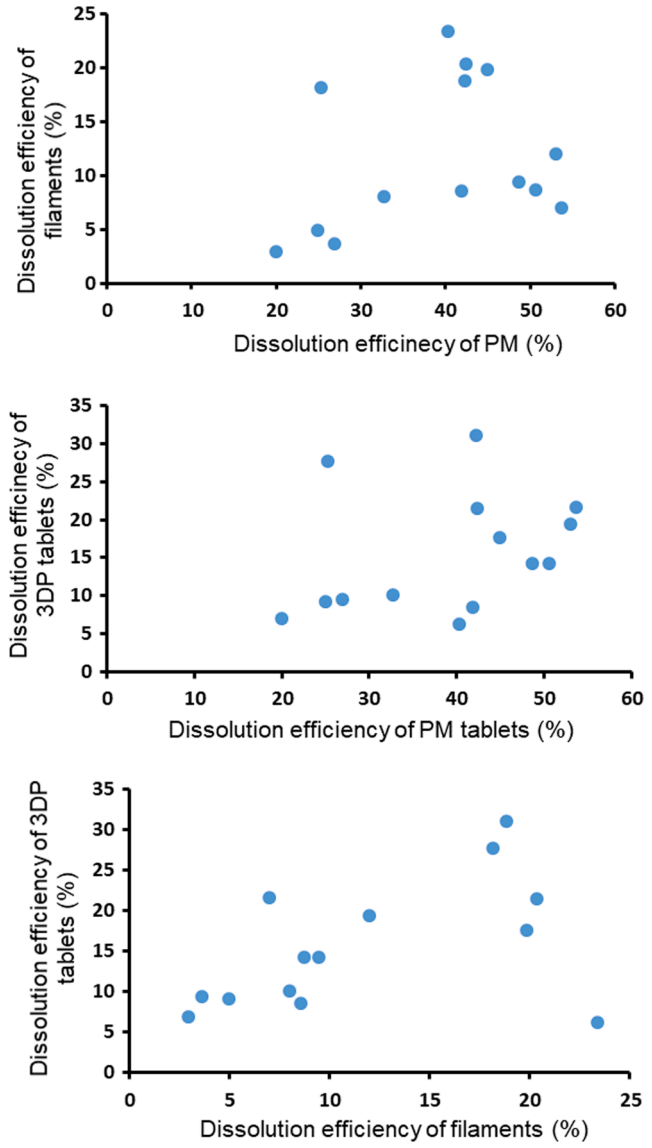

Fig. 14. Correlating dissolution efficiency of physical mixture tablets, filaments and 3DP tablets.

However, other release modifiers can enhance the drug release rate. When Kollidon 30 was applied as the release modifier (Group 12), 3D printed tablets had the highest release rate with more than 47% drug content released after 24 h, which is two times higher than in Group 1.

Consequently, these fabricated IBP-EC 3D printed tablets showed various dissolution profiles with the polymer blending method. By changing the type and concentration of release modifiers, the drug release rate from 3D printed tablets could be modulated and adjusted. If the drug release rate from these 3D printed tablets is required to be further enhanced, lower fill density could be applied because an increase in the surface area/mass ratio of tablets can lead to the improvement in water permeation and drug diffusion (Yang et al., 2018).

3.8. Determination of drug release kinetics

The dissolution data of tablets prepared by direct compression and 3DP were plotted based on the zero-order, first-order, Higuchi and Korsmeyer-Peppas equations and calculated kinetic parameters with fitting results are summarized in Table 6. The best fit for the kinetics of almost all tablets was obtained with the Korsmeyer-Peppas model. The n values of 3D printed tablets ($0.45 < n < 0.89$) in all groups suggest the anomalous transport and the mechanism of drug release were governed by diffusion and matrix swelling, whereas the n values of physical mixture tablets are much lower and in some groups (Groups 1, 3, 5, 10–14) are less than 0.45 (indicating Fickian diffusion) (Homaee Borujeni et al., 2020). In each group, 3D printed tablets showed significantly higher n values than physical mixture tablets except Groups 7–9 (with the addition of HPMC). The possible reason is the high swelling capacity of HPMC makes HPMC swell and form a viscous layer, the diffusion and swelling rates are comparable in physical mixture tablets (Quinten et al., 2009). Hence, the release of IBP from IBP loaded 3D printed tablets of all groups could occur by diffusion of water through EC and release modifiers matrix and swelling/relaxation of chains between EC and release modifiers (Homaee Borujeni et al., 2020). Among them, the 3D printed tablets from Group 4 showed the highest n value (0.817) indicates that IBP release of these tablets almost followed zero-order kinetic, and this is consistent with the parameters in zero-order model because of its highest R^2_{adj}(0.9876) and lowest AIC (53.15) values among all groups. It is necessary to mention that 3D printed tablets from all groups (except Group 10–13) presented a near-zero-order release with $R^2_{adj} > 0.9$.

IBP loaded 3D printed tablets showed significantly lower release rate of IBP than directly compressed physical mixture tablets (Fig. 13). Therefore, the HME and FDM printing processes not only decreased the IBP release rate from 3D printed tablets but also changed the drug release mechanism from the diffusion of directly compressed tablets to the diffusion and erosion of 3D printed tablets. Furthermore, these IBP loaded 3D printed tablets show great potential in releasing IBP in a zero-order reaction.

4. Conclusion

In this study, we successfully fabricated various solid dispersion filaments with ibuprofen in an EC/release modifiers matrix through the HME process, which all showed high printability for FDM 3DP. All these 3D printed tablets possess elegant appearance, suitable mechanical properties, and good constancy in both physical parameters and drug content. It has been proved that by only changing the release-modifying agents, a tunable release profile of the model drug from various 3D printed tablets can be achieved. To our knowledge, this is the first research for adjusting the drug release behavior of IBP by adding various release modifiers to the EC matrix. Hot melt extruded filaments prepared with a proportion of 20% IBP, 60% EC and 20% release modifiers (w/w) exhibited high processability for the preparation of tablets using FDM 3DP process. Sustained-release tablets with different dissolution behaviors were fabricated by coupling HME and FDM 3DP processes. Consequently, the sustained release of IBP from these dosage forms showed significant potential in minimizing its plasma fluctuations and side effects, as well as enhancing its patient compliance.

This study proved the suitability of preparing several modified dosage forms of IBP and EC using FDM technology with various pharmaceutical-grade polymers. All these results illustrated that these dosage forms developed in this study are promising candidates for sustained release devices (tablets) and implants development.

CRediT authorship contribution statement

Kejing Shi: Investigation, Methodology, Writing - original draft. **Jonathan P. Slavage:** Investigation, Methodology. **Mohammed Maniruzzaman:** Conceptualization, Supervision, Writing - review & editing. **Ali Nokhodchi:** Conceptualization, Supervision, Writing - review & editing.

Declaration of Competing Interest

The authors declare that they have no known competing financial

Table 6
Drug release kinetics parameters for various drug release models.

Group	Parameter	Tablets of Physical Mixtures				Filaments				3D printed tablets			
		Zero-order	First-order	Higuchi	Korsmeyer-Peppas	Zero-order	First-order	Higuchi	Korsmeyer-Peppas	Zero-order	First-order	Higuchi	Korsmeyer-Peppas
1	R^2_{adj}	0.691	0.792	0.983	0.999	0.928	0.934	0.977	0.998	0.961	0.970	0.973	0.992
	AIC	183	172	105	35	49	47	11	−34	101	93	57	48
	n	——	——	——	0.408	——	——	——		——	——	——	0.696
2	R^2_{adj}	0.780	0.964	0.997	0.999	0.923	0.989	0.982	0.997	0.921	0.944	0.995	0.999
	AIC	502	401	245	150	98	93	72	23	122	113	36	−13
	n	——	——	——	0.542	——	——	——		——	——	——	0.610
3	R^2_{adj}	0.514	0.795	0.971	0.986	0.914	0.954	0.989	0.999	0.966	0.971	0.914	0.983
	AIC	515	470	352	302	157	140	97	27	51	47	99	33
	n	——	——	——	0.424	——	——	——	0.626	——	——	——	0.672
4	R^2_{adj}	0.629	0.833	0.996	0.998	0.912	0.928	0.976	0.989	0.988	0.991	0.967	0.9974
	AIC	496	450	238	188	102	96	58	43	53	45	67	−1
	n	——	——	——	0.453				0.640	——	——	——	0.817
5	R^2_{adj}	0.178	0.357	0.922	0.997	0.941	0.945	0.961	0.993	0.916	0.930	0.973	0.996
	AIC	452	439	318	166	27	26	20	−25	79	76	45	6
	n	——	——	——	0.344	——	——	——	0.669	——	——	——	0.648
6	R^2_{adj}	0.798	0.868	0.987	0.997	0.964	0.968	0.938	0.983	0.942	0.958	0.966	0.999
	AIC	401	377	251	174	51	48	66	27	97	92	82	15
	n	——	——	——	0.478	——	——	——	0.771	——	——	——	0.685
7	R^2_{adj}	0.843	0.991	0.993	0.999	0.886	0.903	0.998	1.000	0.937	0.973	0.985	0.999
	AIC	499	335	322	136	95	91	−15	−77	147	125	102	47
	n	——	——	——	0.647	——	——	——	0.572	——	——	——	0.660
8	R^2_{adj}	0.872	0.989	0.989	1.000	0.891	0.905	0.998	1.000	0.984	0.994	0.973	0.999
	AIC	208	141	138	28	89	85	3	−61	99	74	91	1
	n	——	——	——	n = 0.651	——	——	——	0.581	——	——	——	0.737
9	R^2_{adj}	0.879	0.997	0.987	0.999	0.934	0.954	0.995	1.000	0.953	0.984	0.979	1.000
	AIC	208	110	149	20	115	105	38	−16	138	113	102	1
	n	——	——	——	0.684	——	——	——	0.619	——	——	——	0.674
10	R^2_{adj}	0.572	0.788	0.976	0.999	0.530	0.624	0.974	0.996	0.834	0.929	0.998	0.998
	AIC	216	197	138	65	171	165	93	48	161	148	51	46
	n	——	——	——	0.404	——	——	——	0.384	——	——	——	0.553
11	R^2_{adj}	0.392	0.704	0.951	0.999	0.246	0.386	0.917	0.999	0.782	0.842	0.999	0.999
	AIC	227	207	159	51	184	179	125	20	152	145	15	4
	n	——	——	——	0.358	——	——	——	0.318	——	——	——	0.445
12	R^2_{adj}	0.470	0.740	0.964	0.998	0.800	0.852	0.995	0.996	0.894	0.953	0.999	0.999
	AIC	221	204	151	64	151	143	55	50	172	150	47	49
	n	——	——	——	0.377	——	——	——	0.475	——	——	——	0.518
13	R^2_{adj}	0.286	0.479	0.927	0.999	0.588	0.675	0.985	0.999	0.871	0.931	0.996	0.998
	AIC	198	190	139	31	165	160	77	16	168	151	77	58
	n	——	——	——	0.326	——	——	——	0.402	——	——	——	0.474
14	R^2_{adj}	0.492	0.672	0.965	0.997	0.709	0.743	0.995	0.997	0.914	0.932	0.987	0.999
	AIC	204	192	132	65	119	116	6	−9	110	104	61	–23
	n	——	——	——	0.376	——	——	——	0.461	——	——	——	0.631

interests or personal relationships that could have appeared to influence the work reported in this paper.

Acknowledgment

Kejing Shi (KS) thanks China Scholarship Council (CSC) and The University of Sussex for financial support during her PhD study. KS also thanks Deck Khong Tan to train her on hot melt extruder.

References

Afrin, N., Chen, D.L., Cao, X., Jahazi, M., 2007. Strain hardening behavior of a friction stir welded magnesium alloy. Scr. Mater. 57 (11), 1004–1007. https://doi.org/10.1016/j.scriptamat.2007.08.001.

Al-Hamidi, H., Edwards, A.A., Mohammad, M.A., Nokhodchi, A., 2010. To enhance dissolution rate of poorly water-soluble drugs: Glucosamine hydrochloride as a potential carrier in solid dispersion formulations. Colloids Surf. B Biointerfaces 76 (1), 170–178. https://doi.org/10.1016/j.colsurfb.2009.10.030.

Alhijjaj, M., Belton, P., Qi, S., 2016. An investigation into the use of polymer blends to improve the printability of and regulate drug release from pharmaceutical solid dispersions prepared via fused deposition modeling (FDM) 3D printing. Eur. J. Pharm. Biopharm. 108, 111–125. https://doi.org/10.1016/j.ejpb.2016.08.016.

Alhnan, M.A., Okwuosa, T.C., Sadia, M., Wan, K.-W., Ahmed, W., Arafat, B., 2016. Emergence of 3D Printed Dosage Forms: Opportunities and Challenges. Pharm. Res. 33 (8), 1817–1832. https://doi.org/10.1007/s11095-016-1933-1.

Chai, X., Chai, H., Wang, X., Yang, J., Li, J., Zhao, Y., Cai, W., Tao, T., Xiang, X., 2017. Fused deposition modeling (FDM) 3D printed tablets for intragastric floating delivery of domperidone. Sci. Rep. 7, 1–9. https://doi.org/10.1038/s41598-017-03097-x.

Chen, D., Xu, X.Y., Li, R., Zang, G.A., Zhang, Y., Wang, M.R., Xiong, M.F., Xu, J.R., Wang, T., Fu, H., Hu, Q., Wu, B., Yan, G.R., Fan, T.Y., 2020. Preparation and In vitro Evaluation of FDM 3D-Printed Ellipsoid-Shaped Gastric Floating Tablets with Low Infill Percentages. AAPS PharmSciTech 21, 6. https://doi.org/10.1208/s12249-019-1521-x.

Crowley, M.M., Schroeder, B., Fredersdorf, A., Obara, S., Talarico, M., Kucera, S., McGinity, J.W., 2004. Physicochemical properties and mechanism of drug release from ethyl cellulose matrix tablets prepared by direct compression and hot-melt extrusion. Int. J. Pharm. 269 (2), 509–522. https://doi.org/10.1016/j.ijpharm.2003.09.037.

de Brabander, C., van den Mooter, G., Vervaet, C., Remon, J.P., 2002. Characterization of ibuprofen as a nontraditional plasticizer of ethyl cellulose. J. Pharm. Sci. 91 (7), 1678–1685. https://doi.org/10.1002/jps.10159.

De Brabander, C., Vervaet, C., Remon, J.P., 2003. Development and evaluation of sustained release mini-matrices prepared via hot melt extrusion. J. Control. Release 89 (2), 235–247. https://doi.org/10.1016/S0168-3659(03)00075-0.

Mallick, S., Pattnaik, S., Swain, K., De, P.K., Saha, A., Mazumdar, P., Ghoshal, G., 2008. Physicochemical Characterization of Interaction of Ibuprofen by Solid-State Milling with Aluminum Hydroxide. Drug Dev. Ind. Pharm. 34 (7), 726–734. https://doi.org/10.1080/03639040801901868.

Dumpa, N.R., Bandari, S., Repka, M.A., 2020. Novel gastroretentive floating pulsatile drug delivery system produced via hot-melt extrusion and fused deposition modeling 3D printing. Pharmaceutics 12, 52. https://doi.org/10.3390/pharmaceutics12010052.

Elbadawi, M., Muñiz, B., Gavins, F.K.H., Jie, J., Gaisford, S., Pérez, G., Basit, A.W., Cabalar, P., Goyanes, A., 2020. M3DISEEN : A novel machine learning approach for predicting the 3D printability of medicines. Int. J. Pharm. 590, 119837 https://doi.org/10.1016/j.ijpharm.2020.119837.

Fanous, M., Gold, S., Muller, S., Hirsch, S., Ogorka, J., Imanidis, G., 2020. Simplification of fused deposition modeling 3D-printing paradigm : Feasibility of 1-step direct powder printing for immediate release dosage form production. Int. J. Pharm. 578, 119124 https://doi.org/10.1016/j.ijpharm.2020.119124.

Fina, F., Goyanes, A., Rowland, M., Gaisford, S., Basit, A.W., 2020. 3D Printing of Tunable Zero-Order Release Printlets. Polymers (Basel). 12, 1769. https://doi.org/10.3390/polym12081769.

Fuenmayor, E., Forde, M., Healy, A.V., Devine, D.M., Lyons, J.G., McConville, C., Major, I., 2018. Material considerations for fused-filament fabrication of solid dosage forms. Pharmaceutics 10, 1–27. https://doi.org/10.3390/pharmaceutics10020044.

Gao, G., Zhang, H., Gui, X., Tan, Z., Bai, B., Weng, Y., 2015. Enhanced strain hardening capacity in a lean alloy steel treated by a " disturbed " bainitic austempering process. Acta Mater. 101, 31–39. https://doi.org/10.1016/j.actamat.2015.08.071.

Gioumouxouzis, C.I., Chatzitaki, A.-T., Karavasili, C., Katsamenis, O.L., Tzetzis, D., Mystiridou, E., Bouropoulos, N., Fatouros, D.G., 2018. Controlled Release of 5-Fluorouracil from Alginate Beads Encapsulated in 3D Printed pH-Responsive Solid Dosage Forms. AAPS PharmSciTech 19 (8), 3362–3375. https://doi.org/10.1208/s12249-018-1084-2.

Gioumouxouzis, C.I., Tzimtzimis, E., Katsamenis, O.L., Dourou, A., Markopoulou, C., Bouropoulos, N., Tzetzis, D., Fatouros, D.G., 2020. Fabrication of an osmotic 3D printed solid dosage form for controlled release of active pharmaceutical ingredients. Eur. J. Pharm. Sci. 143, 105176. https://doi.org/10.1016/j.ejps.2019.105176.

Goyanes, A., Allahham, N., Trenfield, S.J., Stoyanov, E., Gaisford, S., Basit, A.W., 2019. Direct powder extrusion 3D printing: Fabrication of drug products using a novel single-step process. Int. J. Pharm. 567, 118471. https://doi.org/10.1016/j.ijpharm.2019.118471.

Goyanes, A., Chang, H., Sedough, D., Hatton, G.B., Wang, J., Buanz, A., Gaisford, S., Basit, A.W., 2015a. Fabrication of controlled-release budesonide tablets via desktop (FDM) 3D printing. Int. J. Pharm. 496 (2), 414–420. https://doi.org/10.1016/j.ijpharm.2015.10.039.

Goyanes, A., Fina, F., Martorana, A., Sedough, D., Gaisford, S., Basit, A.W., 2017. Development of modified release 3D printed tablets (printlets) with pharmaceutical excipients using additive manufacturing. Int. J. Pharm. 527 (1-2), 21–30. https://doi.org/10.1016/j.ijpharm.2017.05.021.

Goyanes, A., Wang, J., Buanz, A., Martínez-Pacheco, R., Telford, R., Gaisford, S., Basit, A.W., 2015b. 3D Printing of Medicines: Engineering Novel Oral Devices with Unique Design and Drug Release Characteristics. Mol. Pharm. 12 (11), 4077–4084. https://doi.org/10.1021/acs.molpharmaceut.5b00510.

Higuchi, T., 1963. Mechanism of sustained-action medication. Theoretical analysis of rate of release of solid drugs dispersed in solid matrices. J. Pharmaceirtical Sci. 52 (12), 1145–1149. https://doi.org/10.1002/jps.2600521210.

Homaee Borujeni, S., Mirdamadian, S.Z., Varshosaz, J., Taheri, A., 2020. Three-dimensional (3D) printed tablets using ethyl cellulose and hydroxypropyl cellulose to achieve zero order sustained release profile. Cellulose 27 (3), 1573–1589. https://doi.org/10.1007/s10570-019-02881-4.

Huang, S., O'Donnell, K.P., Keen, J.M., Rickard, M.A., McGinity, J.W., Williams, R.O., 2016. A New Extrudable Form of Hypromellose: AFFINISOL^{TM} HPMC HME. AAPS PharmSciTech 17, 106–119. https://doi.org/10.1208/s12249-015-0395-9.

Ilyés, K., Kovács, N.K., Balogh, A., Borbás, E., Farkas, B., Casian, T., Marosi, G., Tomuță, I., Nagy, Z.K., 2019. The applicability of pharmaceutical polymeric blends for the fused deposition modelling (FDM) 3D technique: Material considerations–printability–process modulation, with consecutive effects on in vitro release, stability and degradation. Eur. J. Pharm. Sci. 129, 110–123. https://doi.org/10.1016/j.ejps.2018.12.019.

Jamróz, W., Szafraniec, J., Kurek, M., Jachowicz, R., 2018. 3D printing in pharmaceutical and medical applications. Pharm. Res. 35, 1–22. https://doi.org/10.1007/s11095-018-2454-x.

Jin, H., Gallerneault, M., Lloyd, D.J., 2012. Low Work Hardening and Its Mitigation in Ultra-Fine Grained Aluminum Alloys. In: Weiland, H., Rollett, A.D., Cassada, W.A. (Eds.), ICAA13. Springer, Cham, Pittsburgh, pp. 1741–1742. https://doi.org/10.1007/978-3-319-48761-8-260.

Kadry, H., Al-Hilal, T.A., Keshavarz, A., Alam, F., Xu, C., Joy, A., Ahsan, F., 2018. Multi-purposable filaments of HPMC for 3D printing of medications with tailored drug release and timed-absorption. Int. J. Pharm. 544 (1), 285–296. https://doi.org/10.1016/j.ijpharm.2018.04.010.

Kempin, W., Domsta, V., Grathoff, G., Brecht, I., Semmling, B., Tillmann, S., Weitschies, W., Seidlitz, A., 2018. Immediate Release 3D-Printed Tablets Produced Via Fused Deposition Modeling of a Thermo-Sensitive Drug. Pharm. Res. 35 (6) https://doi.org/10.1007/s11095-018-2405-6.

Kempin, W., Franz, C., Koster, L.C., Schneider, F., Bogdahn, M., Weitschies, W., Seidlitz, A., 2017. Assessment of different polymers and drug loads for fused deposition modeling of drug loaded implants. Eur. J. Pharm. Biopharm. 115, 84–93. https://doi.org/10.1016/j.ejpb.2017.02.014.

Khan, K.A., 1975. The concept of dissolution efficiency. J. Pharm. Pharmacol. 27, 48–49. https://doi.org/10.1111/j.2042-7158.1975.tb09378.x.

Khizer, Z., Akram, M.R., Sarfraz, R.M., Nirwan, J.S., Farhaj, S., Yousaf, M., Hussain, T., Lou, S., Timmins, P., Conway, B.R., Ghori, M.U., 2019. Plasticiser-free 3D printed hydrophilic matrices: Quantitative 3d surface texture, mechanical, swelling, erosion, drug release and pharmacokinetic studies. Polymers (Basel). 11 (7), 1095. https://doi.org/10.3390/polym11071095.

Kollamaram, G., Croker, D.M., Walker, G.M., Goyanes, A., Basit, A.W., Gaisford, S., 2018. Low temperature fused deposition modeling (FDM) 3D printing of thermolabile drugs. Int. J. Pharm. 545 (1-2), 144–152. https://doi.org/10.1016/j.ijpharm.2018.04.055.

Krause, J., Bogdahn, M., Schneider, F., Koziolek, M., Weitschies, W., 2019. Design and characterization of a novel 3D printed pressure-controlled drug delivery system. Eur. J. Pharm. Sci. 140, 105060. https://doi.org/10.1016/j.ejps.2019.105060.

Vinoth Kumar, M., Balasubramanian, V., Gourav Rao, A., 2017. Hot tensile properties and strain hardening behaviour of Super 304HCu stainless steel. J. Mater. Res. Technol. 6 (2), 116–122. https://doi.org/10.1016/j.jmrt.2016.05.004.

Lamichhane, S., Park, J.B., Sohn, D.H., Lee, S., 2019. Customized novel design of 3D printed pregabalin tablets for intra-gastric floating and controlled release using fused deposition modeling. Pharmaceutics 11. https://doi.org/10.3390/pharmaceutics11110564.

Liang, K., Carmone, S., Brambilla, D., Leroux, J.-C., 2018. 3D printing of a wearable personalized oral delivery device: A first-in-human study. Sci. Adv. 4 (5), eaat2544. https://doi.org/10.1126/sciadv.aat2544.

Maniruzzaman, M., Morgan, D.J., Mendham, A.P., Pang, J., Snowden, M.J., Douroumis, D., 2013. Drug-polymer intermolecular interactions in hot-melt extruded solid dispersions. Int. J. Pharm. 443 (1-2), 199–208. https://doi.org/10.1016/j.ijpharm.2012.11.048.

Maru, S.M., de Matas, M., Kelly, A., Paradkar, A., 2011. Characterization of thermal and rheological properties of zidovidine, lamivudine and plasticizer blends with ethyl cellulose to assess their suitability for hot melt extrusion. Eur. J. Pharm. Sci. 44 (4), 471–478. https://doi.org/10.1016/j.ejps.2011.09.003.

Melocchi, A., Parietti, F., Maroni, A., Foppoli, A., Gazzaniga, A., Zema, L., 2016. Hot-melt extruded filaments based on pharmaceutical grade polymers for 3D printing by fused deposition modeling. Int. J. Pharm. 509 (1-2), 255–263. https://doi.org/10.1016/j.ijpharm.2016.05.036.

Nasereddin, J.M., Wellner, N., Alhijjaj, M., Belton, P., Qi, S., 2018. Development of a Simple Mechanical Screening Method for Predicting the Feedability of a Pharmaceutical FDM 3D Printing Filament. Pharm. Res. 35 (8) https://doi.org/10.1007/s11095-018-2432-3.

Nukala, P.K., Palekar, S., Patki, M., Patel, K., 2019. Abuse Deterrent Immediate Release Egg-Shaped Tablet (Egglets) Using 3D Printing Technology : Quality by Design to Optimize Drug Release and Extraction. AAPS PharmSciTech 20, 80. https://doi.org/10.1208/s12249-019-1298-y.

Ong, J.J., Awad, A., Martorana, A., Gaisford, S., Stoyanov, E., Basit, A.W., Goyanes, A., 2020. 3D printed opioid medicines with alcohol-resistant and abuse-deterrent properties. Int. J. Pharm. 579, 119169. https://doi.org/10.1016/j.ijpharm.2020.119169.

Palekar, S., Nukala, P.K., Mishra, S.M., Kipping, T., Patel, K., 2019. Application of 3D printing technology and quality by design approach for development of age-appropriate pediatric formulation of baclofen. Int. J. Pharm. 556, 106–116. https://doi.org/10.1016/j.ijpharm.2018.11.062.

Peppas, N.A., Sahlin, J.J., 1989. A simple equation for the description of solute release. III. Coupling of diffusion and relaxation. Int. J. Pharm. 57 (2), 169–172. https://doi.org/10.1016/0378-5173(89)90306-2.

Pereira, B.C., Isreb, A., Forbes, R.T., Dores, F., Habashy, R., Petit, J.-B., Alhnan, M.A., Oga, E.F., 2019. ' Temporary Plasticiser ': A novel solution to fabricate 3D printed patient- centred cardiovascular ' Polypill ' architectures. Eur. J. Pharm. Biopharm. 135, 94–103. https://doi.org/10.1016/j.ejpb.2018.12.009.

Piccinni, P., Tian, Y., Mcnaughton, A., Fraser, J., Brown, S., Jones, D.S., 2016. Solubility parameter-based screening methods for early- stage formulation development of itraconazole amorphous solid dispersions. J. Pharm. Pharmacol. 68, 705–720. https://doi.org/10.1111/jphp.12491.

Pietrzak, K., Isreb, A., Alhnan, M.A., 2015. A flexible-dose dispenser for immediate and extended release 3D printed tablets. Eur. J. Pharm. Biopharm. 96, 380–387. https://doi.org/10.1016/j.ejpb.2015.07.027.

QUINTEN, T., BEER, T., VERVAET, C., REMON, J., 2009. Evaluation of injection moulding as a pharmaceutical technology to produce matrix tablets. Eur. J. Pharm. Biopharm. 71 (1), 145–154. https://doi.org/10.1016/j.ejpb.2008.02.025.

Ramukutty, S., Ramachandran, E., 2012. Growth, spectral and thermal studies of ibuprofen crystals. Cryst. Res. Technol. 47 (1), 31–38. https://doi.org/10.1002/crat.v47.110.1002/crat.201100394.

Samaha, D., Shehayeb, R., Kyriacos, S., 2009. Modeling and comparison of dissolution profiles of diltiazem modified-release formulations. Dissolution Technol. 16, 41–46. https://doi.org/10.14227/DT160209P41.

Solanki, N.G., Tahsin, M.d., Shah, A.V., Serajuddin, A.T.M., 2018. Formulation of 3D Printed Tablet for Rapid Drug Release by Fused Deposition Modeling: Screening Polymers for Drug Release, Drug-Polymer Miscibility and Printability. J. Pharm. Sci. 107 (1), 390–401. https://doi.org/10.1016/j.xphs.2017.10.021.

Stewart, S., Domínguez-Robles, J., McIlorum, V., Mancuso, E., Lamprou, D., Donnelly, R., Larrañeta, E., 2020. Development of a biodegradable subcutaneous implant for prolonged drug delivery using 3D printing. Pharmaceutics 12 (2), 105. https://doi.org/10.3390/pharmaceutics12020105.

Tan, D.K., Maniruzzaman, M., Nokhodchi, A., 2020. Development and Optimisation of Novel Polymeric Compositions for Sustained Release Theophylline. Polymers (Basel). 12, 27. https://doi.org/10.3390/polym12010027.

The Dow Chemical Company, 2013. Chemistry of METHOCELTM Cellulose Ethers-A Technical Review.

Vo, A.Q., Zhang, J., Nyavanandi, D., Bandari, S., Repka, M.A., 2020. Hot melt extrusion paired fused deposition modeling 3D printing to develop hydroxypropyl cellulose based fl oating tablets of cinnarizine. Carbohydr. Polym. 246, 116519. https://doi.org/10.1016/j.carbpol.2020.116519.

Williams, G.R., 2018. Kinetics. In: Aulton, M.E., Taylor, K.M. (Eds.), Aulton's Pharmaceutics: The Design and Manufacture of Medicines. Churchill Livingstone, pp. 114–127.

Yang, Y., Wang, H., Li, H., Ou, Z., Yang, G., 2018. 3D printed tablets with internal scaffold structure using ethyl cellulose to achieve sustained ibuprofen release. Eur. J. Pharm. Sci. 115, 11–18. https://doi.org/10.1016/j.ejps.2018.01.005.

Yu, D.-G., Branford-White, C., Ma, Z.-H., Zhu, L.-M., Li, X.-Y., Yang, X.-L., 2009. Novel drug delivery devices for providing linear release profiles fabricated by 3DP. Int. J. Pharm. 370 (1-2), 160–166. https://doi.org/10.1016/j.ijpharm.2008.12.008.

Zhang, J., Feng, X., Patil, H., Tiwari, R.V., Repka, M.A., 2017. Coupling 3D printing with hot-melt extrusion to produce controlled-release tablets. Int. J. Pharm. 519 (1-2), 186–197. https://doi.org/10.1016/j.ijpharm.2016.12.049.

Zhang, Y., Huo, M., Zhou, J., Zou, A., Li, W., Yao, C., Xie, S., 2010. DDSolver: An add-in program for modeling and comparison of drug dissolution profiles. AAPS J. 12 (3), 263–271. https://doi.org/10.1208/s12248-010-9185-1.

Zhu, Y., Shah, N.H., Waseem Malick, A., Infeld, M.H., McGinity, J.W., 2006. Controlled Release of a Poorly Water-Soluble Drug from Hot-Melt Extrudates Containing Acrylic Polymers. Drug Dev. Ind. Pharm. 32 (5), 569–583. https://doi.org/10.1080/03639040500528996.